Circulations de fluides et mécanismes de déformation dans les Schistes Lustrés Liguro-Piémontais : implications pour le fonctionnement des zones de subduction

Clément Herviou

Sorbonne Université

ED 398 - Géosciences, Ressources Naturelles et Environnement

Institut des Sciences de la Terre de Paris

Circulations de fluides et mécanismes de déformation dans les Schistes Lustrés Liguro-Piémontais : Implications pour le fonctionnement des zones de subduction

Thèse de doctorat en Sciences de la Terre présentée par

Clément HERVIOU

Pour obtenir le grade de

Docteur de Sorbonne Université

Thèse soutenue publiquement le 09 Mai 2022 devant le Jury composé de :

Michel Ballèvre	Professeur – Université de Rennes 1 (Géosciences Rennes)	Rapporteur
Marco Scambelluri	Professore – Università degli Studi di Genova (DISTAV)	Rapporteur
Laurent Jolivet	Professeur – Sorbonne Université (ISTeP)	Examinateur
Jaime D. Barnes	Professor – University of Texas at Austin	Examinatrice
Åke Fagereng	Reader – Cardiff University	Examinateur
Philippe Agard	Professeur – Sorbonne Université (ISTeP)	Directeur de thèse
Anne Verlaguet	Maitre de Conférences – Sorbonne Université (ISTeP)	Co-directrice de thèse
Alexis Plunder	Ingénieur géologue – BRGM	Invité

Jeune bouquetin (en place) sur les serpentinites du Monte Rocciavrè

Remerciements

Et voilà, c'est fini … Alors que s'achève un cycle de quasi 10 ans sur le campus de Jussieu, il me revient la tâche la plus difficile, celle de trouver les mots justes pour remercier toutes les personnes qui ont contribué à cette thèse.

Ce travail n'aurait jamais pu voir le jour sans mes directeurs de thèse, Philippe et Anne. Philippe, je te remercie pour ton soutien sans faille dans les bons moments comme dans les étapes plus difficiles de cette thèse. Merci d'avoir réussi à composer avec « ma tête dure » et pour ton exigence sans limite, même sur les versions 32 des figures, qui a forcément tiré ce travail vers le haut. Je te remercie sincèrement pour le cadre scientifique et humain que tu m'as fourni durant ces années, tout d'abord au labo : les interactions avec tes autres doctorants, notamment à travers le bureau magique 303b, m'ont permis de créer des liens professionnels et d'amitié qui dureront et sans qui cette thèse n'aurait pas la même allure. En dehors du labo, merci pour ces week-ends d'escapades dans les durs mois de rédaction de papiers/thèse et pour toutes les opportunités, souvent à coups de « ZIP-OH » (E-FIRE, Pise, 4EU+, etc…). Cependant, je ne te remercie pas pour toutes les parties de Uno où tu as fait le choix d'avantager ce tricheur de Mathieu (aka chouchou). Et désolé pour tous ces montages Illustrator qui ne te mettent pas nécessairement en valeur. Au fait, tu connais Guillaume Bonnet ? Anne, merci de m'avoir soutenu depuis le début ! 4 stages et une thèse, ça commence à faire un bon bout de temps qu'on travaille ensemble ! Depuis la L3 tu as cru en moi, tu ne m'as pas lâché et tu m'as permis de découvrir tous les rouages de la recherche. Je n'en serais pas là sans toi, sans ton soutien, et je ne l'oublierais pas. Merci pour ton exigence à toute épreuve et à toute échelle qui m'a vraiment permis de toujours plus me creuser la tête, pour essayer d'améliorer ce travail de thèse. Enfin, je te remercie sincèrement pour toutes les relectures et suggestions. Merci également à Alexis Plunder et Hugues Raimbourg, qui ont suivis certaines étapes de ce travail d'un peu plus loin et avec qui les interactions scientifiques ont beaucoup apporté à certains volets de cette thèse.

Merci à Michel Ballèvre, Marco Scambelluri, Jaime Barnes, Åke Fagereng et Laurent Jolivet qui ont accepté de faire partie de ce jury de thèse et de juger ce travail. Je tiens particulièrement à remercier chaleureusement Laurent pour sa bienveillance, son enthousiasme et sa passion si communicative de la géologie qui m'ont été d'une grande aide durant les comités de suivis de cette thèse. Merci

également à Christian Chopin et Alberto Vitale Brovarone pour leurs conseils enrichissants lors de ces comités.

Viens maintenant le moment de remercier les collègues et amis du laboratoire, je vais tout d'abord commencer par les autochtones du 3ème étage de l'ISTeP, véritable famille depuis mes premiers pas dans le couloir, en 2016. Tout d'abord, je remercie Benoît D., véritable soutien tout au long de cette thèse. Merci Benoît, pour ton accueil et ton amitié dès le M1. Merci pour toutes ces pauses café de déblocages scientifiques pour commencer la journée dans les rails et surtout merci pour tes nombreuses aides avec Matlab qui ont sauvées les volets bubulles de cette thèse. Merci également pour ta rigueur scientifique exemplaire qui me pousse à être toujours plus exigeant et enfin merci pour tes messages et invitations dans les moments de mous psychologiques. Merci à Michael complétant cette belle équipe du café de 8h et pour tous les coups de pouce avec illustrator ! Merci à Nico, Michel et Omar, le terrible trio d'ingénieurs, pour les moments de rigolades et pour avoir toujours rendu les sessions analytiques plus faciles et plus amusantes. Mention spéciale à Nico pour les discussions souvent philosophiques mais toujours déplacées et merci pour tous les outils que je t'ai taxé ! Merci à Marc pour les moments Chouffe, à Marco pour les trop nombreux scans et pour toutes les petites attentions. Merci également à Claudio et Loïc pour les discussions toujours instructives, vous nous manquez au 3eme. Enfin merci aux doctorants passés, présents, futurs : tout d'abord Mathieu, merci pour ton accueil dès les premiers jours, pour tes conseils depuis la L3. Je n'en serais pas ici sans ton soutien. Par contre arrête de tricher au Uno chouchou. L'histoire se souviendra que je suis tombé à Verdun par TA FAUTE. Merci à Guillaume, ton retour fracassant depuis Santa Barbara a été un véritable déclic. Merci pour tout tes conseils scientifiques et pour les fous rires quotidiens, merci encore pour ton appui pour le postdoc et surtout fais gaffe aux vaches piémontaises, elles te trouvent appétissant. Merci à Michele de m'avoir montré la voie de la pétro bien faite, à travers sa passion bréchique ! Merci également aux voisins du couloir : Tiphaine, Sarah et au nouveau piou-piou Hippobyte. Enfin merci à mes collègues du bureau 303b où règne une véritable émulsion scientifique à mi-chemin entre génie, absurdité et démence : Tout d'abord, merci à Ben, le beauf perchois, grand frère de thèse. Merci pour toutes ces réponses à mes questions lors de l'initiation de cette thèse, pour m'avoir ouvert la voie vers les Schistes Lustrés et pour les branlées au basket. Merci à Toto, aka l'éponge aka polatôt, pour ces moments de décompression au bar, pour les conseils scientifiques et les coups de mains avec Matlab. Merci également pour les fous rires comme dans la fontaine (le jacuzzi) de Montdauphin. Merci à Kévin (Kiwine pour les intimes), l'analphabète carpophobe, partenaire ultime de jeux à la con (lucarne de l'ISTeP, Ping box) mais aussi de kébabs

et autres adanas. Véritable binôme, ayant notamment partagé toutes les galères de terrain, cette thèse aurait été clairement moins drôle sans toi. Ton recrutement en tant que porteur de cailloux, à mon service, dès ton M1, avait commencé à donner le ton. Merci pour tous ces moments en mode glaçons dans le torrent, merguez on the grill, chips lustrés, à Dodavek, Add Blue, Calabourdane, calzone fritte, rodéo Jimny, et bivouac sur matelas percé. Quand Ben a fini sa thèse, il m'a dit qu'il me laissait les Schistes Lustrés, moi je ne te laisse RIEN, même pas le contact bizuuuuuuu. Bon allez, je te laisse la Pointe de la Sassa... Excuse-moi encore de t'avoir autant martyrisé au ping pong (21-2 branlée du siècle, gros coup de coco). Merci également à la nouvelle recrue Louisette, aka Marie Denise, aka têt cal, merci pour les fous rires et les relectures en mode Marie-Pierre, tu gères.

Je tiens également à remercier toutes les personnes de l'ISTeP qui m'ont simplifié la vie par leurs aides administratives, scientifiques ou tout simplement par leur présence. Encore une fois j'ai une pensée spéciale pour les doctorants et ex-doctorants de l'ISTeP et notamment Marie et Manon, les copines du 4eme ! Merci pour le soutien et pour les bons moments notamment lors de la traversée de la Tchéquie. Merci à tous les autres et notamment à J-B, Dia, Tan, Camille, Thiébaut, Adeline, Yasir et Maylis.

Merci également à Marie-Camille Caumon pour m'avoir accueilli à Nancy durant les longues semaines de Raman sur inclusions fluides et à Damien D. pour l'accès au Raman et les parties endiablées de basket à l'ENS. Merci à Kristijan R. pour les nombreux accueils à Orléans et pour toutes les discussions scientifiques. Merci à Thierry, mon Suisse préféré pour les discussions autour d'une bière. Merci aux collègues américains et internationaux du groupe E-FIRE pour les bons moments passés sur le terrain.

Je remercie également très chaleureusement Kennet Flores, qui m'accueille dès Juillet dans son équipe de recherche à Chapel Hill !

Voici maintenant le moment de remercier tous les amis qui ont pu me soutenir durant ce projet de thèse. Merci à Alex et Morgan, les frères, membre du trio mortel de Master pour les parties de billards, les bières, les burgers et pour ces vacances salvatrices aux Canaries juste avant de commencer cette thèse. Mention spéciale à Morgan, qui en m'accompagnant sur le terrain a connu la douleur du bivouac en fin de saison sous la pluie et la neige. Merci à Ziad, ma شرموطة, pour ton soutien et ton amitié dès le M1. Je me souviendrais toujours de ton arrivée en France, ou après deux semaines à manger des croissants tu as enfin compris que ce n'était pas vraiment un repas. Merci à Flo et Bart, amis dès la première année de fac. On en a fait du chemin depuis les bancs des amphis A, B et C.

Vous m'avez vu passer de l'exclusion des cours magistraux à la rédaction d'une thèse, c'était quand même très mal engagé. Merci à tous les amis de fac, particulièrement Charlotte, Emma, Claire, Karim, Olivia, Roxane, Rabii, Fabien, Alex M mais surtout ma team ultime des cloches Pierre, Arnaud, Martin, Alex B. Enfin, merci à Yvan, présent depuis le début, qui m'a vu passer par les pires étapes pour finalement m'en sortir, j'ai beaucoup de chances de t'avoir à mes côtés.

Merci également à Pascal Barrier pour son accueil à LaSalle Beauvais lors de mes stages de 3eme et de seconde et à Philippe Berger-Sabatel sans qui ma collection minéralogique serait bien pauvre. Votre soutien m'a permis d'affirmer cette passion de toujours pour la Géologie à des moments où j'aurais pu m'en détacher.

Pour finir, merci à ma famille sans qui cette passion d'enfance pour la Géologie n'aurait jamais pu se concrétiser de cette façon. Lorsque je suis rentré dans un magasin de minéraux à mes 6 ans personne n'aurait pu imaginer ce qui allait suivre. Merci à mes parents de m'avoir permis de toujours entretenir cette passion, notamment en me permettant de parcourir l'Europe à la recherche de minéraux. Merci d'avoir cru en moi, quand, en primaire, je vous ai dit que je voulais devenir Géologue, même si ça devait ressembler à un rêve d'enfant farfelu. Par votre soutien vous m'avez permis de rêver et de faire de mon rêve un métier. Merci également pour toutes les aides et sacrifices que cela a impliqué. Merci aussi pour la voiture, sans qui l'échantillonnage de cette thèse serait bien moins riche. Ce bout de métal m'a servi de refuge et de lit pendant les longs mois de terrain seul et m'as permis de parcourir les Schistes Lustrés de fond en comble. Merci à mes grands-parents et à ma tante qui m'ont toujours soutenu et sans qui cette passion n'aurait jamais vu le jour. Le billet de 10 francs des vacances de l'été 2000 a tout lancé ! Merci à mon frère et à ma belle-sœur pour leur soutien et à Piou Andrea que je vais enfin pouvoir regarder grandir. Merci également à tous mes tantes, oncles, cousins, cousines, pour tous ces bons moments passés dans le Sud-Ouest et pour leur soutien de toujours. Enfin, merci à ma Julie, cette thèse est aussi la tienne. Merci d'avoir compris l'importance que ce travail avait pour moi, merci de ton soutien, de ton appui depuis le début. Tu es celle qui as le plus cru en moi durant toutes ces années, je n'aurais pas pu réussir sans toi. Cette thèse a été ma raison de vivre durant ces trois dernières années, j'y ai consacré toute mon énergie, tout mon temps et toute ma passion. Ce travail m'a privé de vous pendant trop longtemps et j'espère pouvoir rattraper les moments perdus à vos côtés dans les années à venir.

A mes parents

Résumé de la thèse

Les travaux scientifiques de la dernière décennie reconnaissent aux fluides libérés dans les zones de subduction, à la faveur des réactions successives de déstabilisation des minéraux hydratés, une influence décisive sur la déformation des roches, y compris la nucléation de séismes ou de glissements lents asismiques. Cependant, la caractérisation de ces fluides naturels en termes de composition, abondance, répartition ou modalités de migration, demeure assez limitée. Ce travail de thèse tente d'y remédier par la compilation et l'acquisition de données pétrologiques, géochimiques, lithostratigraphiques, radiochronologiques et structurales systématiques dans le domaine Liguro-Piémontais des Alpes occidentales, où des fragments de lithosphère océanique subduits affleurent de façon continue et permettent d'étudier les processus se déroulant entre ~30 et 80 km de profondeur en subduction.

Ce travail s'est tout d'abord attaché à fournir un cadre détaillé des conditions métamorphiques enregistrées par les écailles de subduction Liguro-Piémontaises et à affiner leur position paléogéographique dans le domaine océanique. L'ensemble des données permet de mettre en évidence la présence d'une distribution trimodale d'unités avec une augmentation des conditions métamorphiques des unités Liguro-Piémontaises supérieures (LPU ; 320-400°C- 1.2-1.9 GPa), aux unités médianes (LPM ; 415-475°C- 1.7-2.2 GPa) et aux unités inférieures (LPL ; 500-580°C- 2.2-2.8 GPa). Les unités supérieures et médianes métamorphisées dans le faciès schiste bleu sont dominées par les sédiments (>90%) tandis que les unités inférieures de faciès éclogite sont bien plus riches en roches mafiques et ultramafiques (>40%).

Dans les unités supérieures et médianes, les nombreuses veines de haute pression à lawsonite et Fe-Mg carpholite observées dans les méta-sédiments des Schistes Lustrés constituent des témoins directs de la circulation de fluides lors de la subduction alpine. L'étude statistique des textures des veines permet de mettre en évidence leur formation par des mécanismes incrémentaux de fracturation, dans un régime de dilatation entre des plans de cisaillement particulièrement faibles, et de proposer un lien avec des glissements lents en subduction. Les inclusions fluides piégées dans ces veines contiennent des salinités modérées avec de faibles quantités de CO_2 et de CH_4, suggérant une alimentation locale par des fluides circulant de manière pervasive dans les roches, en accord avec l'étude statistique de distribution des veines. Certaines veines, situées au voisinage des unités de marge continentale, contiennent des salinités plus fortes, suggérant une infiltration de fluides

provenant des niveaux évaporitiques présents dans ces marges et une ouverture du système jusqu'à l'échelle hectométrique à kilométrique. La tendance générale de décroissance des salinités avec l'augmentation du grade métamorphique dans les unités supérieures et médianes est interprétée comme reflétant la dilution progressive des salinités des fluides de pores initiaux par les fluides libérés par les réactions métamorphiques.

Dans les méta-sédiments des unités inférieures, les inclusions fluides dans les grenats, piégées au pic d'enfouissement, contiennent un fluide aqueux à CO_2-CH_4 dans les conditions du faciès éclogite. Les salinités plus fortes que dans les unités supérieures et médianes suggèrent une infiltration de fluides externes provenant des roches mafiques et/ou ultramafiques, volumétriquement importantes dans ces unités. Les fortes salinités mesurées dans des veines à jadéite (assemblage du pic de faciès schiste bleu) et veines/matrices de brèches à omphacite ± grenat (assemblage du pic éclogitique) des méta-gabbros sont interprétées comme héritées de la phase d'altération hydrothermale à haute température.

Dans les contacts tectoniques entre écailles Liguro-Piémontaises, des talcschistes à dolomite ont été découverts. L'étude des compositions des minéraux, de la géochimie des roches totales, des inclusions fluides et les datations U-Pb sur titanite ont permis de montrer que ces roches se sont formées par la transformation de serpentinites via l'infiltration de fluides des sédiments, au pic d'enfouissement des unités. Ces roches riches en carbonates et en éléments mobiles dans le fluide pourraient avoir un impact sur le cycle profond du carbone et la composition du coin mantellique lors de leur déstabilisation aux conditions sub-arc.

Les profondeurs du pic d'enfouissement des unités supérieures (~35-45 km), médianes (~55-65 km) et inférieures (~70-80 km) sont similaires à celles déduites pour l'écaillage et le sous-plaquage dans les zones de subduction modernes et fossiles, reflétant des changements majeurs du couplage mécanique à l'interface des plaques. L'écaillage des unités LPU et LPM aurait principalement été contrôlé par des contrastes lithostratigraphiques majeurs tels que des niveaux très pélitiques, ou la partie supérieure du manteau serpentinisé. En revanche, des réactions de déshydratation majeures comme la déstabilisation de grandes quantités de lawsonite dans les méta-sédiments pourraient être à l'origine de l'écaillage des unités inférieures éclogitiques, sous de fortes pressions de fluide et engendrant une fragilisation des roches. La rétroaction positive entre déformation et infiltration de fluides dans les contacts lithologiques serpentinites/sédiments, amenant à la formation de talc, pourrait également avoir contribué à l'écaillage des unités Liguro-Piémontaises.

Abstract

In the last decade, the major role of fluids liberated in subduction zones, through successive dehydration reactions, on rock deformation mechanisms including nucleation of earthquakes and slow slip events has been acknowledged. However, the characterization of these fluids in terms of composition, volume, distribution and migration mechanisms remain largely unconstrained. This thesis aims to better characterize these fluids through systematic compilation and acquisition of petrological, geochemical, lithostratigraphic, radiochronological and structural data in the Liguro-Piemont domain of the Western Alps, where fragments of subducted oceanic lithosphere are continuously exposed and allow the study of processes occurring between ~30 and 80 km depth in subduction zones.

This work first focused on providing a detailed framework of the metamorphic conditions recorded by the Liguro-Piemont subduction slices and refining their paleogeographic position in the oceanic domain. All these data highlight the presence of a trimodal distribution of units with an increase in metamorphic conditions from the Liguro-Piemont Upper units (LPU; 320-400°C- 1.2-1.9 GPa), to the Middle units (LPM; 415-475°C- 1.7-2.2 GPa) and to the Lower units (LPL; 500-580°C- 2.2-2.8 GPa). The LPU and LPM units metamorphosed under blueschist-facies conditions are dominated by sediments (>90%) while the eclogite-facies LPU units are much richer in mafic and ultramafic rocks (>40%).

In the LPU and LPM units, numerous lawsonite- and Fe-Mg-carpholite-bearing high-pressure veins have been observed in the Schistes Lustrés metasediments and are considered as direct evidences of fluid circulation during the Alpine subduction. The statistical study of vein textures highlights their formation by incremental dilational fracturing mechanisms between extremely weak shear planes and suggests a possible link with slow slip in subduction. Fluid inclusions trapped in these veins contain moderate salinities with low amounts of CO_2 and CH_4, suggesting a local fluid release and a pervasive circulation of fluid through the rocks, in agreement with the statistical study of vein distribution. A few veins, situated close to continental margin units, contain higher salinities suggesting fluid infiltration from the evaporitic levels embedded in these margins and fluid migration up to the hectometer/kilometer scale. The general trend of decreasing salinities with increasing metamorphic grade in the LPU and LPM units is interpreted to reflect the progressive dilution of initial pore fluid salinities by fluids released by metamorphic reactions.

In the metasediments from the LPL units, the study of fluid inclusions in garnet formed during peak burial revealed the presence of an aqueous CO_2-CH_4 fluid at eclogite-facies conditions. Salinities higher than in the LPU and LPM metasediments suggest an infiltration of external fluids from the mafic and/or ultramafic rocks, which represent a large volume of LPL units. High salinities measured in jadeite veins (blueschist-facies) and omphacite ± garnet veins/breccia matrices (eclogite-facies) of the metagabbros are interpreted as inherited from a phase of hydrothermal alteration at high temperature.

In the tectonic contacts between Liguro-Piemont slices, dolomite-bearing talcschists have been discovered. Mineral compositions, bulk-rock geochemistry, fluid inclusions and U-Pb titanite geochronology have shown that these rocks formed by intense infiltration of fluids from the surrounding sediments into serpentinites, at peak burial conditions. These rocks containing large amounts of carbonates and large concentrations of fluid-mobile elements could impact the deep carbon cycle and the mantle wedge composition through their destabilization at sub-arc conditions.

Finally, the peak burial depths of the LPU (~35-45 km), LPM (~55-65 km), and LPL (~70-80 km) units are similar to those inferred for offscraping and underplating in both modern and fossil subduction zones, reflecting major changes in mechanical coupling at the plate interface. Slicing of LPU and LPM units was likely controlled by major lithostratigraphic contrasts such as highly pelitic horizons or the upper part of the serpentinized mantle. On the other hand, major dehydration reactions such as lawsonite destabilization in the metasediments could be responsible for the offscraping of the LPL eclogitic units, under high fluid pressures and rock embrittlement. Finally, a positive feedback between deformation and fluid infiltration, leading to talc formation, in the lithological contacts between serpentinites and sediments could also have contributed to the slicing of the Liguro-Piemont units.

Table des matières

Chapitre I - Introduction et problématiques

Zone de cisaillement de faciès schiste bleu dans un méta-gabbro. Col de Saint-Véran.

I. Introduction et problématiques

I.1. Déshydratation des roches et implications pour la déformation en subduction

Les zones de subduction, où une plaque lithosphérique plonge sous une autre plaque tectonique chevauchante, sont le foyer de séismes dévastateurs et d'éruptions volcaniques intenses (Ruff et Kanamori, 1980 ; Tatsumi, 1986 ; Stern, 2002) qui ont des conséquences parfois dramatiques sur les populations (e.g. séisme de sumatra de 2004, plus de 250000 morts). La compréhension de la dynamique de ces zones de convergence, très répandues à la surface de la Terre (> 55000 km ; Lallemand, 1999 ; Stern, 2002 ; Fig. I.1) représente un enjeu majeur pour l'évaluation des risques naturels et des mécanismes moteurs de la tectonique des plaques.

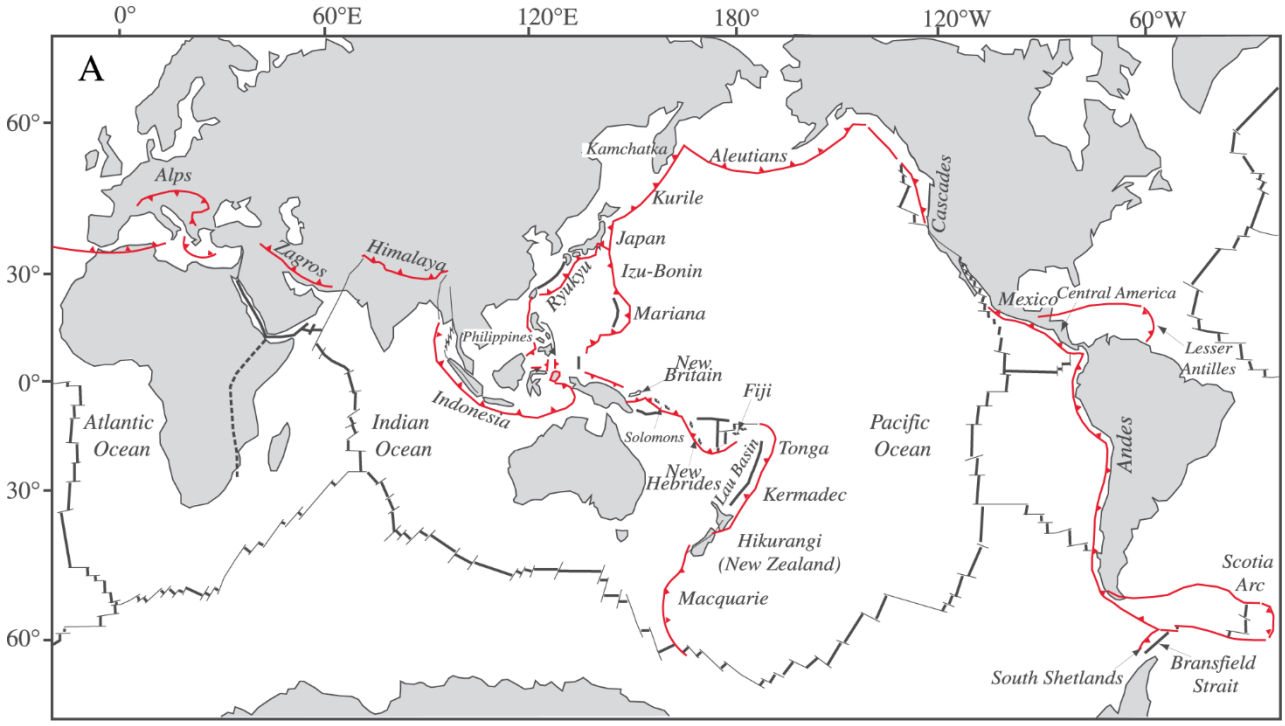

Figure I.1 *: Zones de subduction et limites de plaques en convergence (en rouge). Modifié d'après Lallemand (1999) et Stern (2002).*

D'importantes quantités de fluides sont libérées dans les zones de subduction car la lithosphère océanique est naturellement hydratée. D'une part, par la présence de fluides dans les sédiments, à l'intérieur des pores et dans les minéraux de la fraction pélitique (entre autres : smectite : ~27 wt% H_2O ; Opal-A et -CT : ~11 wt% H_2O ; e.g. Kastner et al., 1991) mais aussi par le biais de l'hydrothermalisme océanique qui provoque la formation de phases hydratées par réactions

métamorphiques entre les minéraux anhydres des roches mafiques et l'eau de mer (entre autres : saponite : ~18 wt% H_2O ; chlorites : 12 wt% H_2O ; amphiboles : ~2 wt% H_2O ; épidote : ~1.8 wt% H_2O ; e.g. Alt et al., 1996). Ces réactions peuvent aussi impliquer l'hydratation, du manteau lithosphérique, par serpentinisation, particulièrement dans les contextes de dorsale lente où le manteau est exhumé le long de détachements océaniques (brucite : ~31 wt% H_2O ; lizardite et chrysotile : ~13 wt% H_2O ; e.g. Moody, 1976).

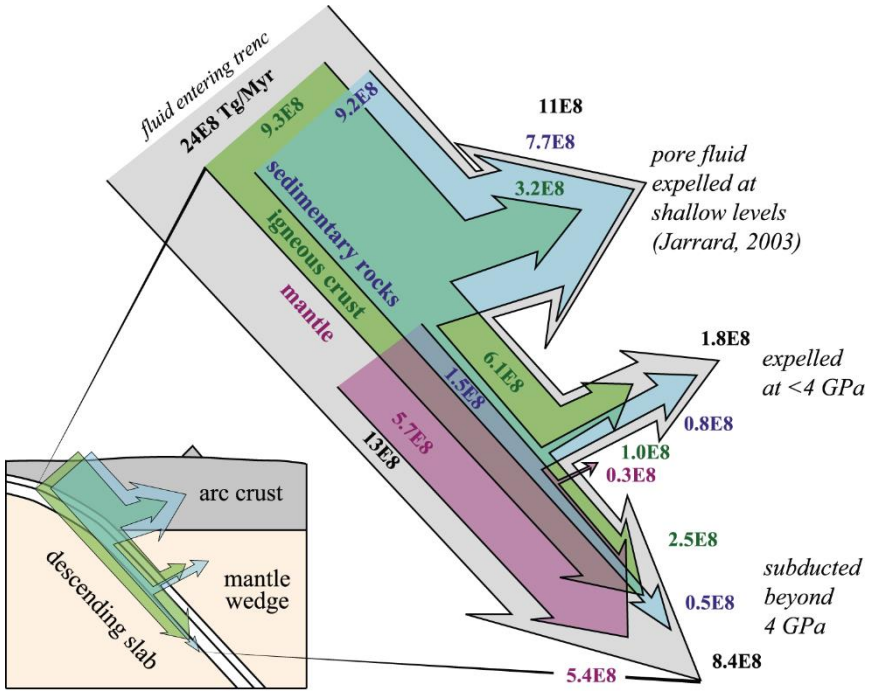

***Figure I.2** : Flux global de H_2O de la fosse jusqu'aux profondeurs d'arrière-arc lors de la subduction de la lithosphère océanique. La taille des flèches dépend de la magnitude des flux donnés en Tg/Ma. D'après Hacker (2008).*

Lors de l'enfouissement de la lithosphère océanique en subduction, la principale source de fluides sur les 10-15 premiers kilomètres est l'expulsion, lors de la compaction des sédiments, des fluides interstitiels contenus dans les pores (Kastner et al., 1991 ; Fig. I.2). Plus en profondeur, l'augmentation progressive des conditions de pression-température provoque la déstabilisation successive des minéraux hydratés et permet la libération de fluides dans la lithosphère et à l'interface des plaques (Fig. 2 ; Rüpke et al., 2004 ; Schmidt et Poli, 2014 ; Hacker, 2008). En effet, les minéraux ne sont stables que dans un champ précis de conditions pression-température et leur déstabilisation lors de l'enfouissement entraine généralement la formation de phases moins hydratées. Le régime thermique de la subduction, principalement lié à l'âge de la lithosphère subduite, et la composition des roches vont donc largement contrôler la profondeur à laquelle les réactions métamorphiques libérant le fluide se produiront (Fig. I.3). Ainsi chaque zone de subduction, aura un régime de déshydratation spécifique, en fonction de son régime thermique propre, de ses sédiments contenant des fractions argileuses variables et de sa lithosphère océanique plus ou moins hydratée. (Fig. I.3, I.4a-i).

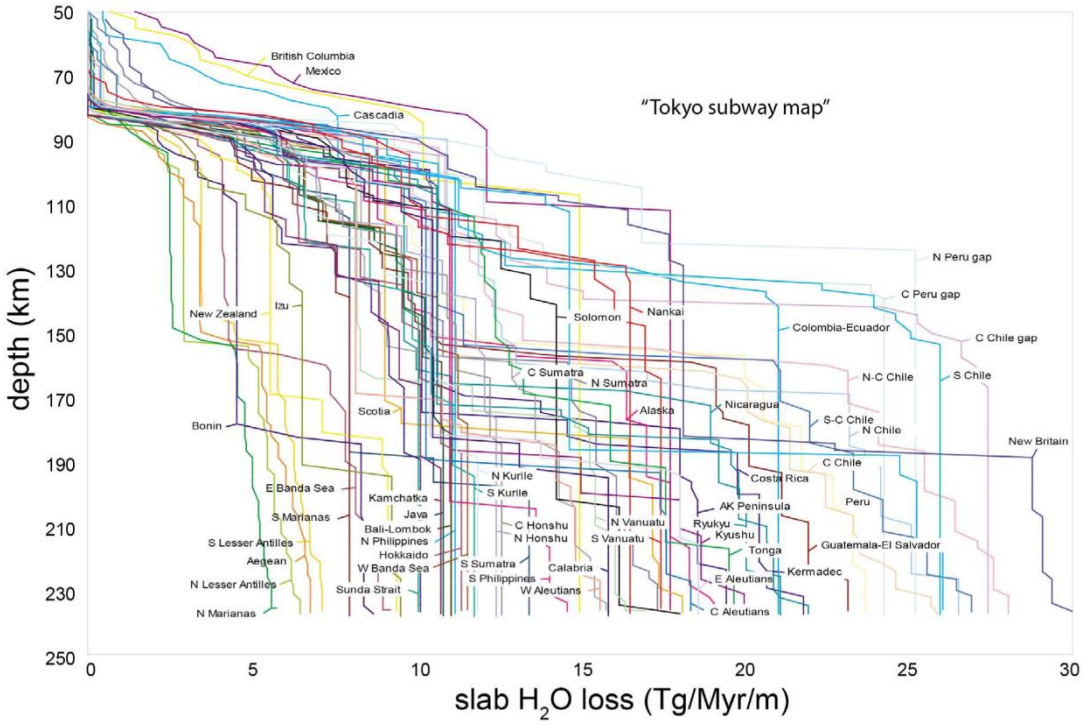

Figure I.3 *: La « Tokyo subway map » montrant le flux d'H_2O perdu par le panneau plongeant en fonction de la profondeur pour une compilation de zones de subduction actives. D'après Van Keken et al. (2011).*

Quand la température de la plaque est suffisamment faible, les minéraux hydratés (notamment antigorite, chlorite, lawsonite) sont stabilisés jusqu'à de grandes profondeurs. La déstabilisation de ces minéraux à une centaine de kilomètres de profondeur (profondeurs sub-arc) dans le manteau sous-continental de la plaque supérieure provoque ensuite la fusion partielle du coin mantellique et la formation du volcanisme d'arc (Tatsumi, 1986, 1989).

Depuis une quinzaine d'année l'impact de la libération de fluides sur la déformation cassante des roches et la sismicité est au centre des discussions (e.g. Hacker et al., 2003). La transition du faciès schiste bleu au faciès éclogite est considérée comme un palier de déshydratation majeur du panneau plongeant (palier à ~80 km sur la figure I.2 ; fléchissement des isoplèthes d'H_2O à ~550°C sur la figure I.3 ; Peacock, 1993 ; Van Keken et al., 2011 ; Paulatto et al., 2017). Il a été montré que la limite entre ces deux faciès coïncide avec la profondeur de localisation des séismes de profondeurs intermédiaires, suggérant un affaiblissement et une déformation cassante des roches aux profondeurs du faciès éclogite (Fig. I.5 ; Hacker et al., 2003 ; Kita et al., 2006 ; Abers et al., 2006, 2013).

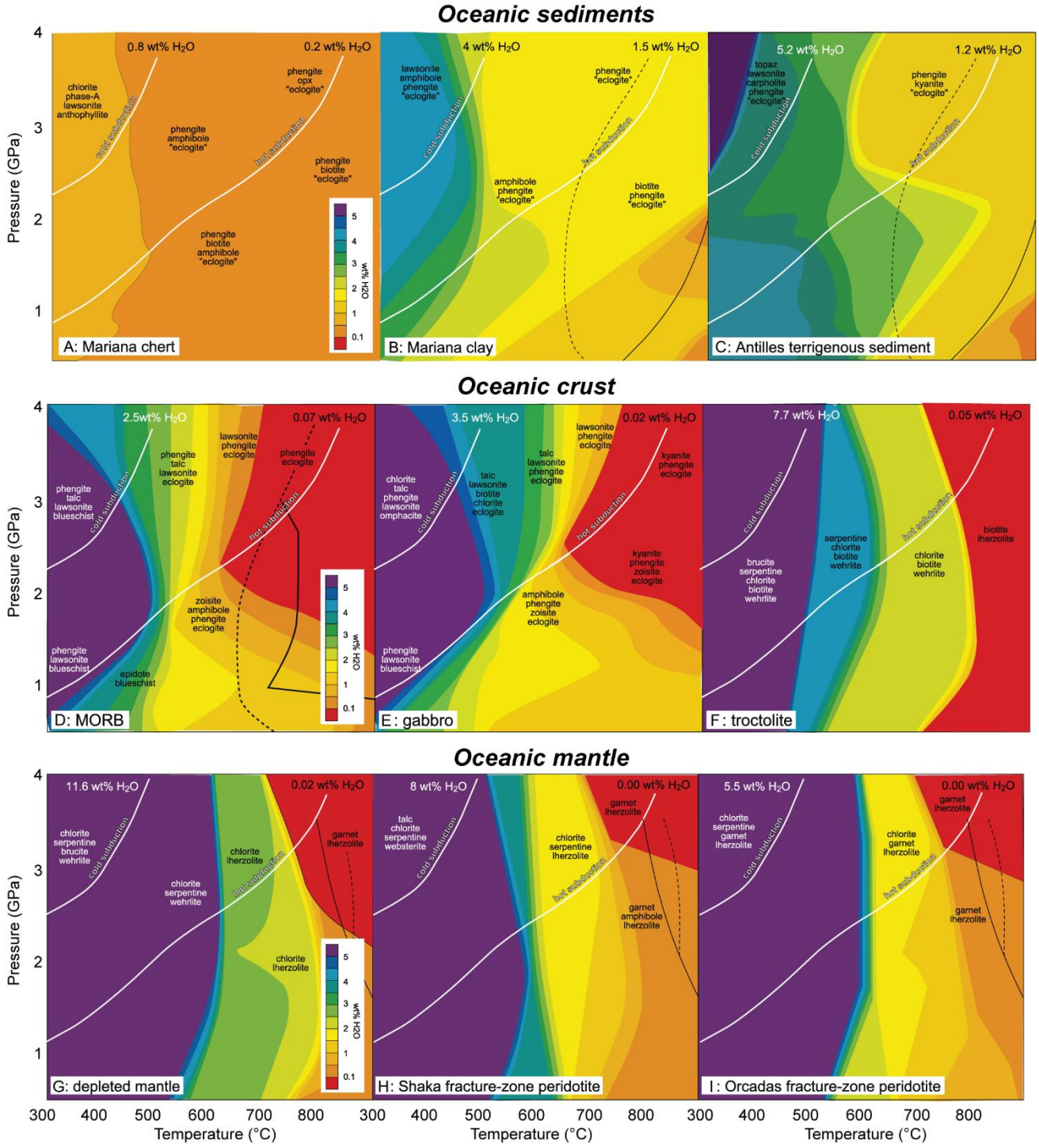

Figure I.4 *: Diagrammes de phases montrant l'évolution du contenu en H_2O dans : A) à C) les minéraux des sédiments océaniques ; D) à F) des roches de la croûte océanique et G) à I) du manteau pour des panneaux plongeant chaud et froid. Les solidus des roches saturées en H_2O et complètement déshydratées sont respectivement montrés par des pointillés et une ligne continue noire. Modifié d'après Hacker (2008).*

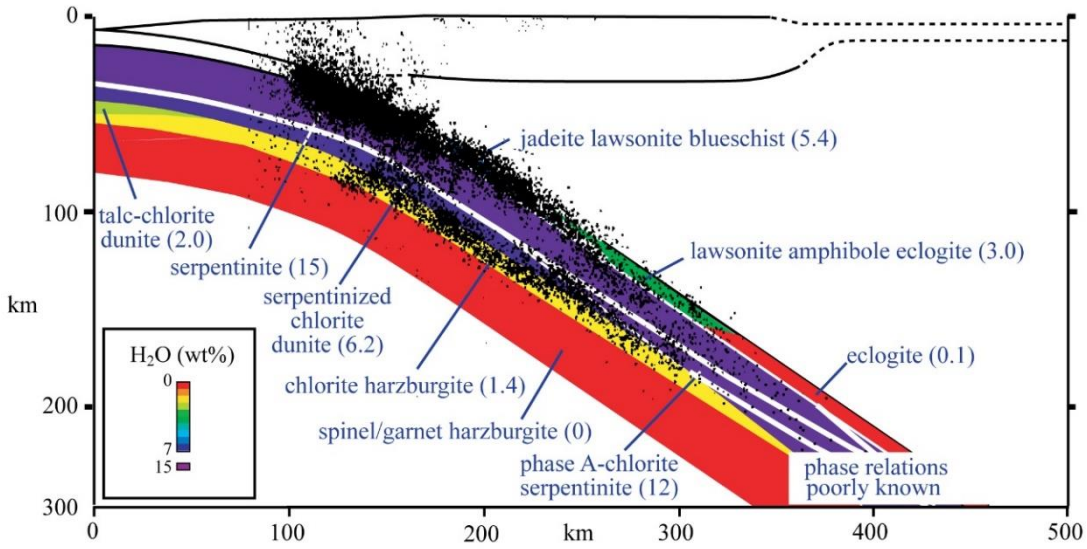

Figure I.5 *: Corrélations entre séismes relocalisés (points noirs) et faciès métamorphiques dans la zone de subduction de Tohoku (Japon). Modifié d'après Hacker et al. (2003).*

Récemment, des glissements lents asismiques souvent accompagnés de trémors non volcaniques ont été identifiés dans des zones de subduction actives et la responsabilité des fluides est régulièrement évoquée pour leur nucléation (e.g. Obara, 2002). Ces évènements appelés « slow slip events » (SSEs), « low-frequency earthquakes » (LFEs), « very-low-frequency earthquakes » (VLFEs) et « episodic tremor and slips » (ETS) sont tous caractérisés par des durées, des récurrences et des déplacements spécifiques et se produisent principalement à des profondeurs et température de 25-55 km et 350°C (Fig. I.6a, b ; Obara et Kato, 2016 ; Behr et Bürgmann, 2021). A ces profondeurs, une transition rhéologique majeure est présente : on passe d'une zone sismogénique où l'interface des plaques est couplée et où les roches se déforment principalement de façon cassante, à une portion juxtaposée au coin mantellique, généralement considérée comme découplée et où les roches se déforment majoritairement de façon ductile (Lay et al., 2012 ; Peacock et Hyndman, 1999 ; Agard et al., 2018). Dans cette zone de transition où la plupart des glissements lents se produisent, une couche caractérisée par de faibles vitesses d'ondes S, de forts coefficients de poisson et de forts ratio V_p/V_s cohérent avec la présence de fluides à des pressions presque lithostatiques est imagée dans la plupart des zones de subduction (Audet et al., 2009 ; Peacock et al., 2011 ; Bostock, 2013 ; Audet et Bürgmann, 2014 ; Fig. I.6c, d). Cet horizon pourrait se localiser, selon les auteurs, dans la croûte océanique du panneau plongeant ou bien dans les sédiments sous-plaqués en base de croûte continentale (Abers et al., 2009 ; Calvert et al., 2011 ; Hansen et al., 2012 ; Bostock, 2013 ; Paulatto et al., 2017 ; Delph et al., 2018, 2021 ; Behr et Bürgmann, 2021 ; Tewksbury-Christle et Behr, 2021).

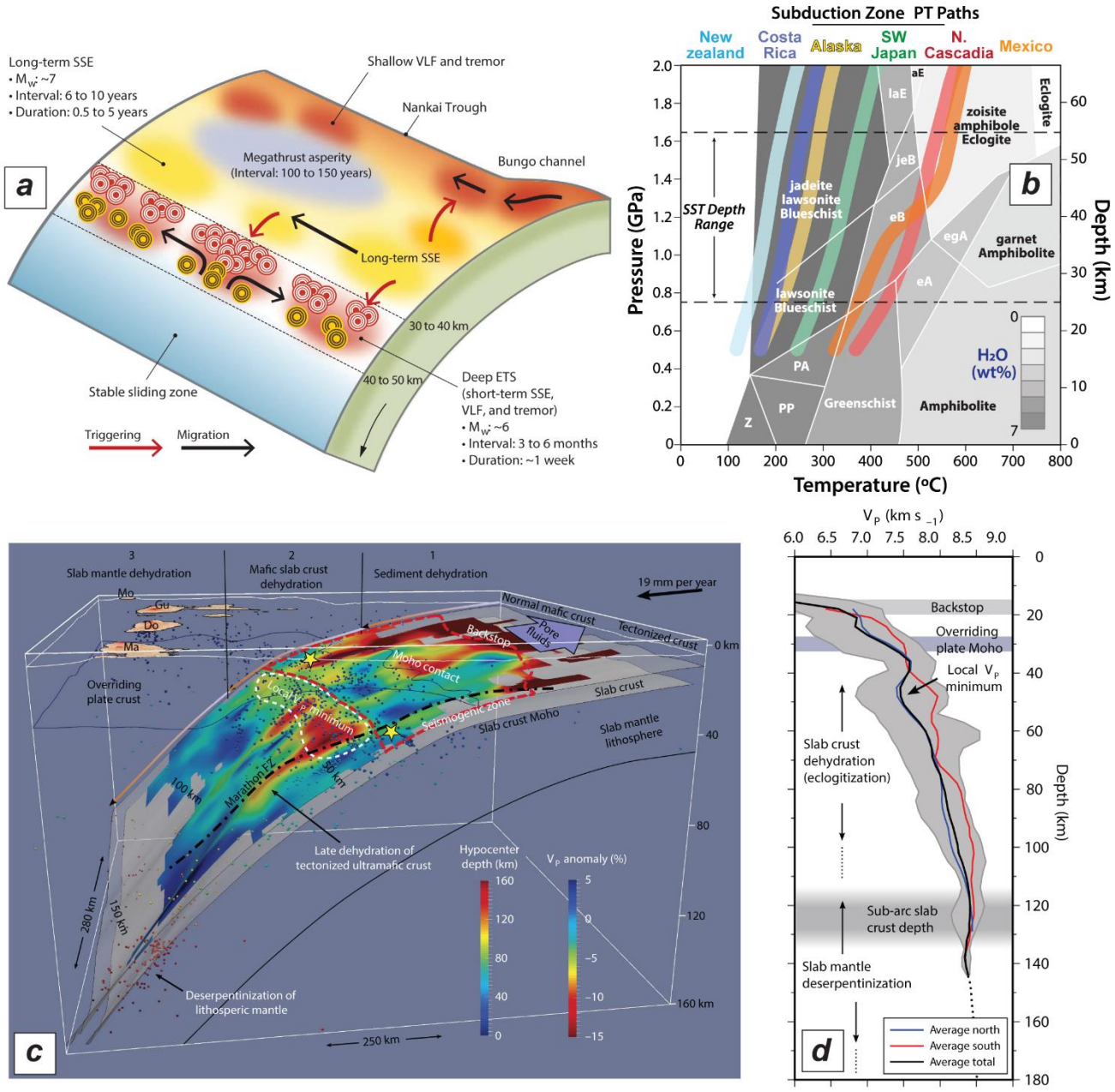

Figure I.6 *: Glissements lents asismiques en subduction. A) Vision schématique de la distribution hétérogène des types variés de séismes lents dans la zone de subduction de Nankai (Japon). Les flèchent indiquent les interactions entre les SSEs de longue durée et les autres séismes lents. Modifié d'après Obara et Kato (2016). B) Faciès pression-température et quantité d'eau contenue dans les minéraux aux profondeurs de nucléation des glissement lents et trémors. SST = slow slip and tremors. Modifié d'après Behr et Bürgmann (2021). C) Représentation 3D de l'anomalie des ondes P et des séismes le long du panneau plongeant des petites Antilles. D'après Paulatto et al. (2017). D) Evolution de la vitesse moyenne des ondes S le long du panneau plongeant des petites Antilles. Modifié d'après Paulatto et al. (2017).*

La région où se déclenchent les glissements lents et trémors étant considérée comme un environnement riche en fluide et avec des pressions de fluide fortes, le rôle des fluides est donc régulièrement invoqué dans la nucléation de ces évènements (Obara, 2002 ; Saffer et Tobin, 2011). Il a notamment été proposé que la récurrence des ETS pourrait être contrôlée par le transfert de silice via le fluide libéré lors de la déstabilisation des minéraux : la précipitation de silice à l'interface réduirait la porosité, entrainant des surpressions de fluides fréquente et une plus forte récurrence des ETS (Audet et Bürgmann, 2014).

Cependant, les sources de fluides et les liens clairs entre déshydratation, circulation de fluides et déformation cassante restent à mettre en évidence. Ces processus généralement d'échelle métrique à hectométrique ne peuvent pas être illustrés par les méthodes géophysiques traditionnellement utilisées pour l'étude des zones de subduction actives (méthodes sismiques, GPS, InSAR et magnétotelluriques) et il est donc nécessaire d'étudier des zones de subduction fossiles dans lesquelles des roches enfouies en profondeur sont maintenant exhumées à la surface de la Terre.

Comment les circulations de fluides et déformations passées sont-elles enregistrées dans les roches ? Quels témoignages de changement de la dynamique de subduction en profondeur peuvent être retrouvés dans des échantillons naturels ?

I.2. Les roches de haute pression-basse température, témoins fossiles des processus de subduction

Les ophiolites (et/ou fragments ophiolitiques) sont des morceaux de lithosphère océanique (manteau, croûte et sédiments océaniques) que l'on trouve généralement au cœur des orogènes (Coleman, 1971 ; Dewey et Bird, 1971 ; Dilek et Furnes, 2011 ; Fig. I.7a). Certains de ces fragments, maintenant exhumés sur les marges continentales, contiennent des assemblages minéralogiques témoignant de leur formation dans des conditions de haute pression-basse température (HP-BT) caractéristiques d'un enfouissement en zone de subduction (Fig. I.7b).

Figure I.7 *(page suivante) : Localisation des ophiolites et des roches HP-BT sur Terre. A) Distribution globale des ophiolites et des systèmes orogéniques. Modifié d'après Dilek et Furnes (2011). B) Distribution globale des roches de faciès schiste bleu et éclogite exhumées et des régions où des glissements lents ont été détectées. Modifié d'après Behr et Bürgmann (2021).*

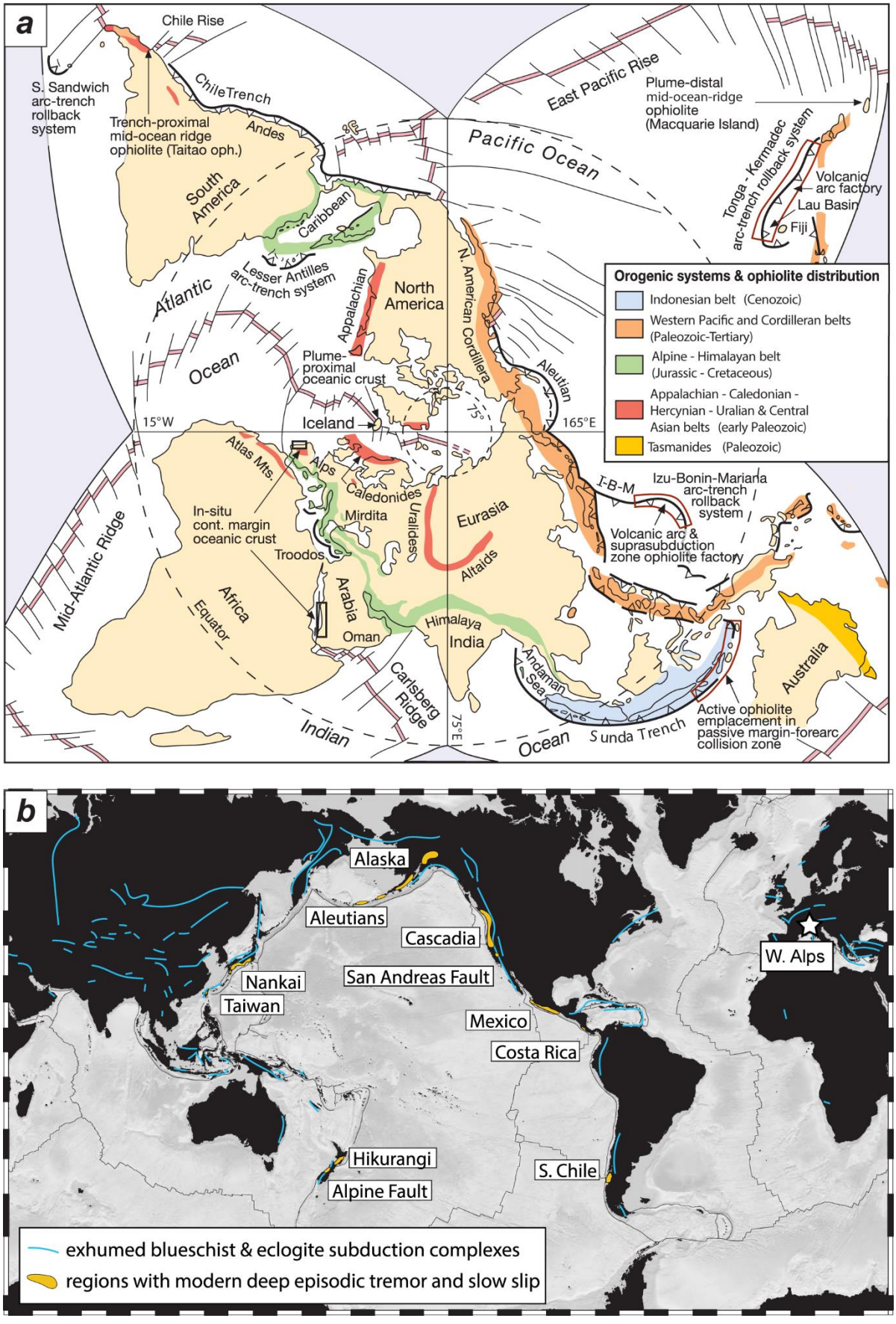
a
Chile Rise
S. Sandwich arc-trench rollback system
Trench-proximal mid-ocean ridge ophiolite (Taitao oph.)
ChileTrench
Andes
South America
Caribbean
Lesser Antilles arc-trench system
Atlantic
Ocean
Appalachian
North America
Plume-proximal oceanic crust
15°W
Iceland
East Pacific Rise
Plume-distal mid-ocean-ridge ophiolite (Macquarie Island)
Pacific Ocean
Tonga - Kermadec arc-trench rollback system
Volcanic arc factory
Lau Basin
Fiji
N. American Cordillera
75°
Aleutian
165°E
Orogenic systems & ophiolite distribution
Indonesian belt (Cenozoic)
Western Pacific and Cordilleran belts (Paleozoic-Tertiary)
Alpine - Himalayan belt (Jurassic - Cretaceous)
Appalachian - Caledonian - Hercynian - Uralian & Central Asian belts (early Paleozoic)
Tasmanides (Paleozoic)
Atlas Mts.
Alps
Caledonides
Uralides
Eurasia
Altaids
Mirdita
In-situ cont. margin oceanic crust
Troodos
Mid-Atlantic Ridge
Africa
Equator
Arabia
Oman
Himalaya
India
Carlsberg Ridge
Indian
Ocean
75°E
I-B-M
Izu-Bonin-Mariana arc-trench rollback system
Volcanic arc & suprasubduction zone ophiolite factory
Andaman Sea
Sunda Trench
Australia
Active ophiolite emplacement in passive margin-forearc collision zone
b
Alaska
Aleutians
Cascadia
San Andreas Fault
Nankai
Taiwan
Mexico
Costa Rica
W. Alps
Hikurangi
Alpine Fault
S. Chile
exhumed blueschist & eclogite subduction complexes
regions with modern deep episodic tremor and slow slip

En effet, durant la convergence, du matériel océanique est arraché à la plaque plongeante et accrété frontalement ou sous-plaqué à la plaque supérieure (Karig et Sharmann, 1975 ; Scholl et al., 1980 ; Platt, 1986). A faibles profondeurs, l'accrétion de la partie supérieure de la croûte océanique entraine la formation de prismes d'accrétion dominés par les sédiments (e.g., Von Huene et Scholl, 1991). A plus grande profondeur, l'écaillage de la plaque plongeante engendre l'empilement et l'exhumation d'écailles profondes avec des histoires de subduction distinctes (Plunder et al., 2012 ; Angiboust et al., 2013, 2016, 2018, 2022 ; Tewksbury-Christle et al., 2021). Les roches de haute pression, véritables témoins des processus de subduction, ont été reconnues de part et d'autre du globe (Fig. I.7b) et leur caractérisation permet de reconstruire l'histoire des subductions fossiles et des mouvements de convergence des plaques tectoniques sur Terre (Ernst, 1988 ; Maruyama, 1996 ; Tsujimori et al., 2006b ; Guillot et al., 2009 ; Agard et al., 2009 ; 2018).

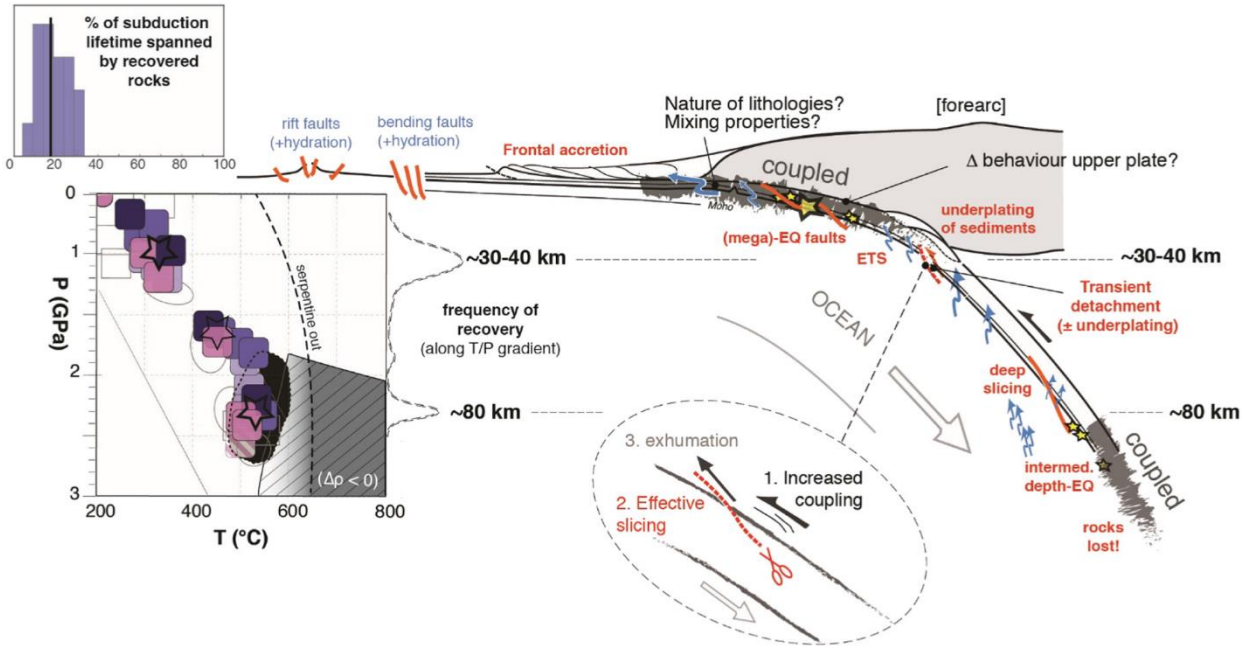

Figure I.8 *: Couplage, écaillage et exhumation en subduction. Le premier histogramme montre que les roches HP-BT sont écaillées durant un intervalle de temps court de la durée de vie des zones de subduction. Le champ pression-température montre les deux gammes de profondeurs principales enregistrées par les roches HP-BT exhumées (~30-40 km et 80 ± 10 km). Modifié d'après Agard et al. (2018).*

L'arrachement de matériel océanique du panneau plongeant et son accrétion à la plaque supérieure implique une augmentation du couplage mécanique entre les plaques (Agard et al., 2016, 2018 ; Fig. I.8), le déplacement vers le bas du niveau décollement de l'interface (Kimura et Ludden, 1996 ; Kimura et al., 2007) et donc la localisation de la déformation dans des zones de faiblesses (Kimura

et Ludden, 1996 ; Kimura et al., 2007 ; Angiboust et al., 2012c ; Ruh et al., 2015). Une compilation des roches HP-BT retrouvées dans le monde a permis d'identifier que l'écaillage et donc le couplage mécanique entre plaques a lieu (Fig. I.8) : (i) à des profondeurs caractéristiques (principalement à ~30-40 km et 80 km de profondeur ; Agard et al., 2018 ; Plunder et al., 2015), (ii) de façon transitoire (Agard et al., 2009 ; Monié et Agard, 2009) et peut (iii) se produire simultanément à plusieurs profondeurs (Bonnet et al., 2018).

Bien que le rôle des sédiments (Behr et Becker, 2018), de la serpentinisation du panneau plongeant et/ou du coin mantellique (Agard et al., 2009, 2016 ; Guillot et al., 2009, 2015 ; Ruh et al., 2015), et des fluides (e.g., Agard et al., 2020) soient évoqués, les mécanismes conduisant au couplage des plaques et à l'écaillage du panneau plongeant restent largement débattus.

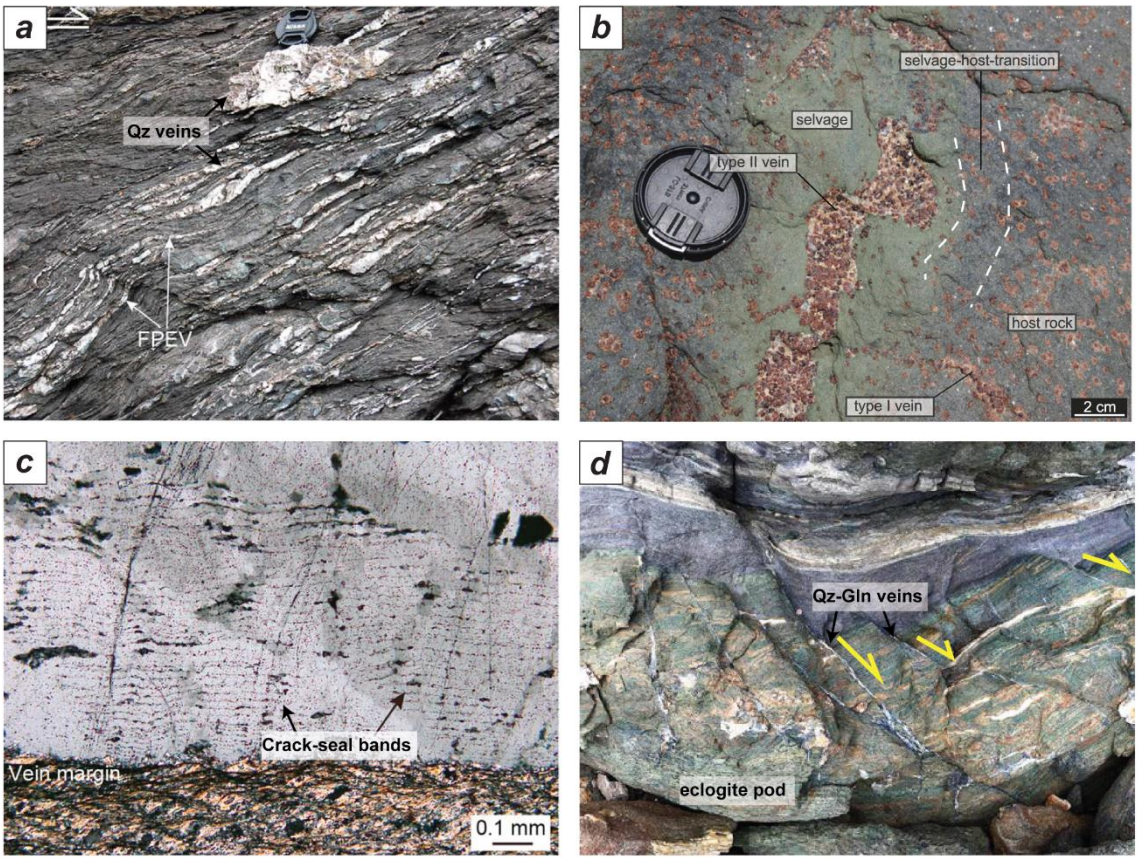

Figure I.9 *: Veines métamorphiques de roches HP-BT. A) Grandes quantités de veines de quartz dans les méta-sédiments du prisme de Shimanto (Japon). FPEV = foliation-parallel extension veins. Modifié d'après Ujiie et al. (2018). B) Veines à grenat-quartz-phengite dans un bloc éclogitique du Pouébo Eclogite Mélange (Nouvelle-Calédonie). D'après Taetz et al. (2018). C) Bandes d'inclusions dans une veine de type « crack-seal » du prisme de Shimanto (Japon). Ce type de veine se forme par des cycles successifs de fracturation, d'infiltration de fluide et de cristallisation. Chaque bande est interprétée comme un incrément de déplacement sur une surface de glissement. Modifié d'après Ujiie et al. (2018). D) Veines de cisaillement à quartz-glaucophane recoupant un boudin d'éclogite, Syros (Grèce). Modifié d'après Kotowski et Behr (2019).*

Dans les roches, les veines métamorphiques formées par la croissance de cristaux dans une fracture sont ubiquistes et considérées comme les témoins préservés du passage de fluides et des interactions fluides-roches (e.g. Oliver et Bons, 2001 ; Bons et al., 2012). Elles sont particulièrement abondantes dans les sédiments des prismes d'accrétion exhumées (Fisher et Byrne, 1990 ; Fisher et al., 1995 ; Meneghini et al., 2009 ; Fig. I.9a). A l'inverse, dans les roches HP-BT enfouies à plus grande profondeur (faciès schiste bleu et éclogite) elles sont plus rares, et la découverte de veines contenant des assemblages minéralogiques attestant de leur formation à haute pression est d'une importance clé pour comprendre les mécanismes de circulations de fluides en subduction (Spandler et Hermann, 2006 ; John et al., 2008 ; Taetz et al., 2018 ; Fig. I.9b). L'observation des textures des veines est souvent utilisée pour tenter de caractériser les liens entre circulations de fluides, fracturation et mécanismes de déformation à grande échelle en subduction (Fagereng et al., 2010 ; 2011 ; Ujiie et al., 2018 ; Fig. I.9c). Dans les roches HP-BT profondes (faciès schiste bleu et éclogite), la présence de veines est généralement considérée comme un marqueur principal de déformation cassante dans le régime ductile (Angiboust et al., 2017 ; Hertgen et al., 2017 ; Behr et al., 2018 ; Kotowski et Behr, 2019 ; Fig. I.9d).

La plupart des études caractérisant textures, minéralogie et géochimie des veines métamorphiques dans les roches HP-BT se sont concentrées soit sur les sédiments des prismes d'accrétion peu profonds (e.g., Fisher et al., 1995 ; Rossetti et al., 2010 ; Vannuchi et al., 2010 ; Raimbourg et al., 2015), soit sur les roches mafiques et ultramafiques de faciès éclogitiques (Philippot et Selverstone, 1991 ; Scambelluri et al., 1997 ; Gilio et al., 2020). L'évolution des compositions de fluides ainsi que des mécanismes de formation des veines et de transfert de fluides en fonction de la profondeur reste largement à caractériser.

Comment évoluent les compositions de fluides le long du panneau plongeant ? Quels sont les mécanismes et échelles de migration des fluides en profondeur ? Quels sont les impacts des circulations de fluides sur les mécanismes d'écaillage en subduction ?

I.3. Le domaine Liguro-Piémontais Alpin, l'exemple parfait pour étudier l'évolution en profondeur des processus de subduction

Les Alpes occidentales sont le résultat de la fermeture des océans Valaisans et Liguro-Piémontais, large d'environ 100 à 1000 km, au cours d'une subduction lente (~1cm/an) vers l'Est- Sud-Est sous Adria/Apulia (Fig. I.10a, b ; Le Pichon et al., 1988 ; Schmid et al., 1996, 2017 ; Lapen et al., 2003 ; Handy et al., 2010 ; Agard et Handy, 2021). La subduction de ces domaines océaniques à propagation lente (Lagabrielle et Cannat, 1990) s'est initiée au Crétacé supérieur et terminée il y a environ 35 Ma (Stampfli et al., 1998 ; Schmid et al., 2017 ; Fig. I.10b). Cette subduction océanique s'est ensuite prolongée par la subduction du continent Briançonnais (Chopin, 1984 ; Rubatto et Hermann, 2003) avant l'initiation de la collision entre l'Eurasie et Adria/Apulia (Simon-Labric et al., 2009 ; Bellahsen et al., 2014 ; Fig. I.10b).

Des vestiges de la lithosphère océanique Liguro-Piémontaise sont maintenant exposés dans les zones internes des Alpes occidentales et forment un empilement de nappes appelé domaine Liguro-Piémontais (Agard, 2021 ; Agard et Handy, 2021 ; Fig. I.10c-e). Les méta-sédiments, les Schistes Lustrés sont volumétriquement dominants dans ce complexe et sont d'âge Jurassique supérieur à Crétacé supérieur (Fig.10e ; De Wever et Caby, 1981 ; Lemoine et al., 1984 ; Lagabrielle, 1987). Ces sédiments correspondent à une séquence initiale de 200 à 400 m de dépôts pélagiques et hémipélagiques sur les fonds océaniques (marnes, argiles et calcaires métamorphisés sous la forme de calcschistes, méta-pélites et marbres ; Lemoine et al., 1984 ; Lemoine et Tricart, 1986 ; Lemoine, 2003 ; Deville et al., 1992 ; Michard et al., 1996) emballant des volumes variables de roches mafiques et ultramafiques (Fig. I.10e).

Après un pic d'enfouissement entre 60 et ~40 Ma (e.g., Agard et al., 2002 ; Rubatto et Hermann, 2003), ces roches furent arrachées au panneau plongeant sous la forme d'écailles et exhumées entre l'Eocène supérieur et le Miocène (Agard et al., 2002, 2009 ; Schwartz et al., 2007, 2020 ; Malusà et al., 2005 ; Angiboust et Glodny, 2020 ; Fig. I.10b). Cet empilement d'écailles constitue maintenant un complexe d'accrétion profond (Platt, 1986 ; Marthaler et Stampfli, 1989 ; Agard et al., 2009, 2018 ; Agard, 2021) construit par des sous-plaquages successifs et où les unités structuralement supérieures auraient été écaillées en premier (Kimura et al., 2007 ; Dumitru et al., 2010 ; Plunder et al., 2012 ; Agard et Vitale-Brovarone, 2013 ; Angiboust et al., 2016, 2022 ; Fig. I.10b).

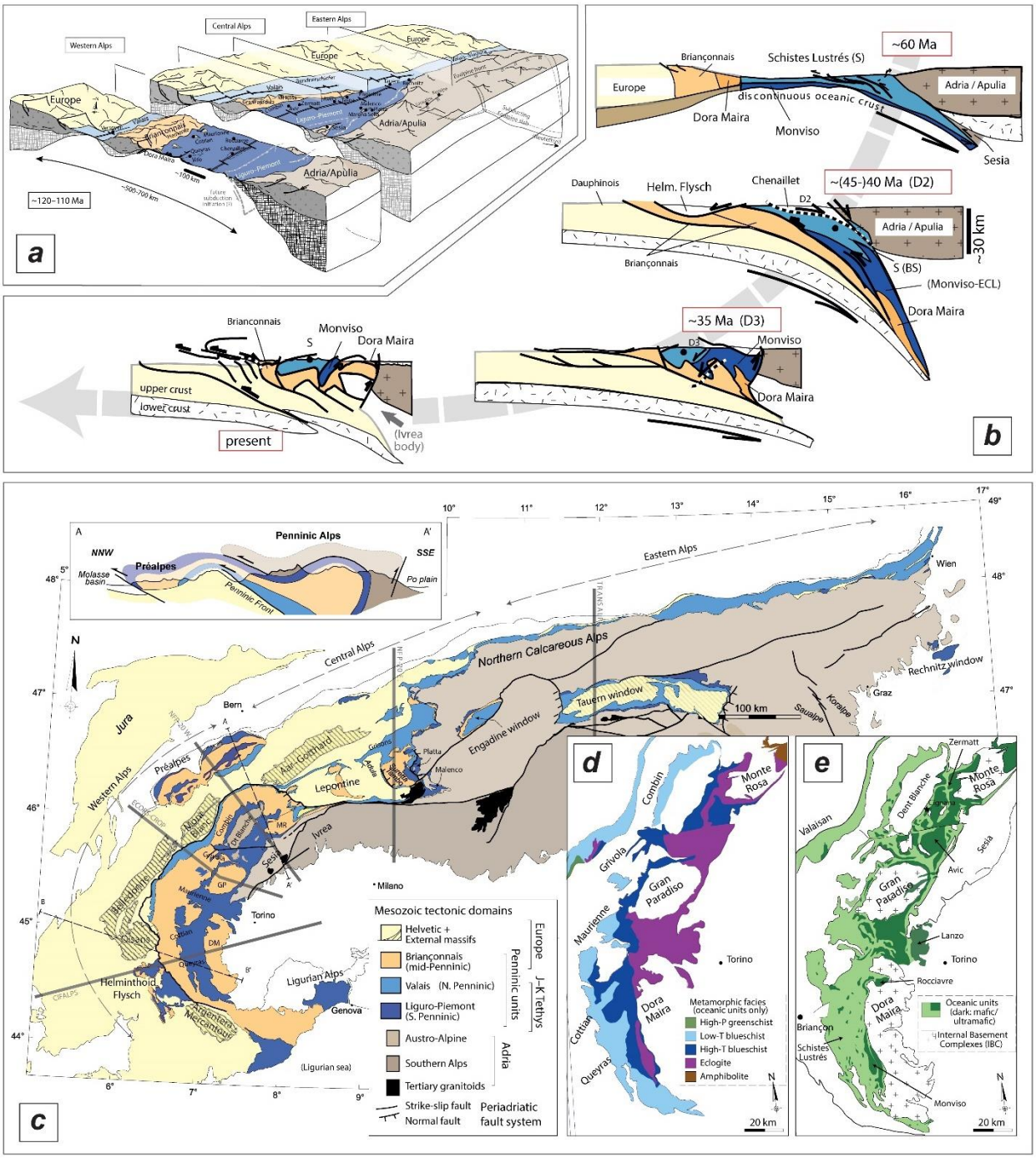

Figure I.10 *: Contexte géologique des Alpes occidentales et du domaine Liguro-Piémontais. A) Vision schématique 3D du domaine alpin à ~120 Ma. B) Schéma de l'évolution tectonique du domaine Liguro-Piémontais des Alpes occidentales, de la subduction océanique jusqu'à la collision. C) Schéma structural global de la chaine alpine. D) Distribution des faciès métamorphiques à travers les domaines Valaisan et Liguro-Piémontais des Alpes occidentales. E) Distribution des sédiments, des roches mafiques et ultramafiques à travers les domaines Valaisan et Liguro-Piémontais des Alpes occidentales. Figures modifiées d'après Agard (2021) et Agard et Handy (2021).*

D'environ 200 km de long et 50 km de large, le domaine Liguro-Piémontais Ouest-alpin est parmi les complexes de subduction les plus grands, les mieux préservés et les plus étudiés permettant un accès quasi-direct aux processus se produisant entre ~30 et 80 km de profondeur dans les zones de subduction (Berger et Bousquet, 2008 ; Agard et al., 2009 ; 2018, Agard, 2021).

Dans ce complexe une distinction majeure est présente entre une zone de faciès éclogite et où les roches mafiques et ultramafiques sont dominantes (unités MUM de Agard, 2021) et une zone de faciès schiste bleu dominée par les méta-sédiments (unités S de Agard, 2021 ; Dal Piaz, 1974b ; Caby et al., 1978 ; Droop et al., 1990 ; Pognante, 1991 ; Agard, 2021). A l'intérieur de ces deux zones, différentes écailles, généralement trois ou quatre, ont été identifiées sur différents transects du domaine Liguro-piémontais (Fudral, 1996 ; Agard et al., 2001a ; Tricart et Schwartz, 2006 ; Lagabrielle et al., 2015). Cependant les contacts tectoniques préservant la juxtaposition initiale des unités écaillées lors de la subduction sont souvent obscurcis par les phases de déformation ultérieures et presque impossible à suivre sur de grandes distances. En conséquence, très peu d'études (e.g., Deville et al., 1992) ont essayées de faire des corrélations Nord-Sud entre les écailles tectoniques à l'échelle du domaine, donc la distribution et l'extension des écailles sont très peu contraintes. Une connaissance détaillée du contexte tectonométamorphique est cependant critique pour étudier et comprendre les processus reliés à la subduction le long du domaine Liguro-Piémontais.

Quelles sont les corrélations spatiales entre les écailles de subduction le long du domaine Liguro-Piémontais ? Comment évoluent les structures, la lithostratigraphie, les assemblages minéralogiques et les conditions de pression-température à travers ce complexe de subduction ?

I.4. Veines métamorphiques dans le domaine Liguro-Piémontais : quelles contraintes sur les circulations de fluides en subduction ?

Les méta-sédiments de faciès schiste bleu du domaine Liguro-Piémontais, comme ceux des prismes d'accrétion exhumés, contiennent de grandes quantités de veines, principalement constituées de quartz et de carbonates (Fig. I.11a ; e.g., Henry et al., 1996). Dans certaines veines, plus rares, le quartz est accompagné de minéraux caractéristiques de conditions de haute pression : la lawsonite

et la Fe-Mg carpholite (Fig. I.11b-d) Ces minéraux, très hydratés (~12 wt% H_2O) sont très abondants dans les Schistes Lustrés (Caron, 1974 ; Goffé et Chopin, 1986 ; Sicard-Lochon, 1987) et la lawsonite peut localement constituer jusqu'à 30-45 vol% des roches (Lefeuvre et al., 2020).

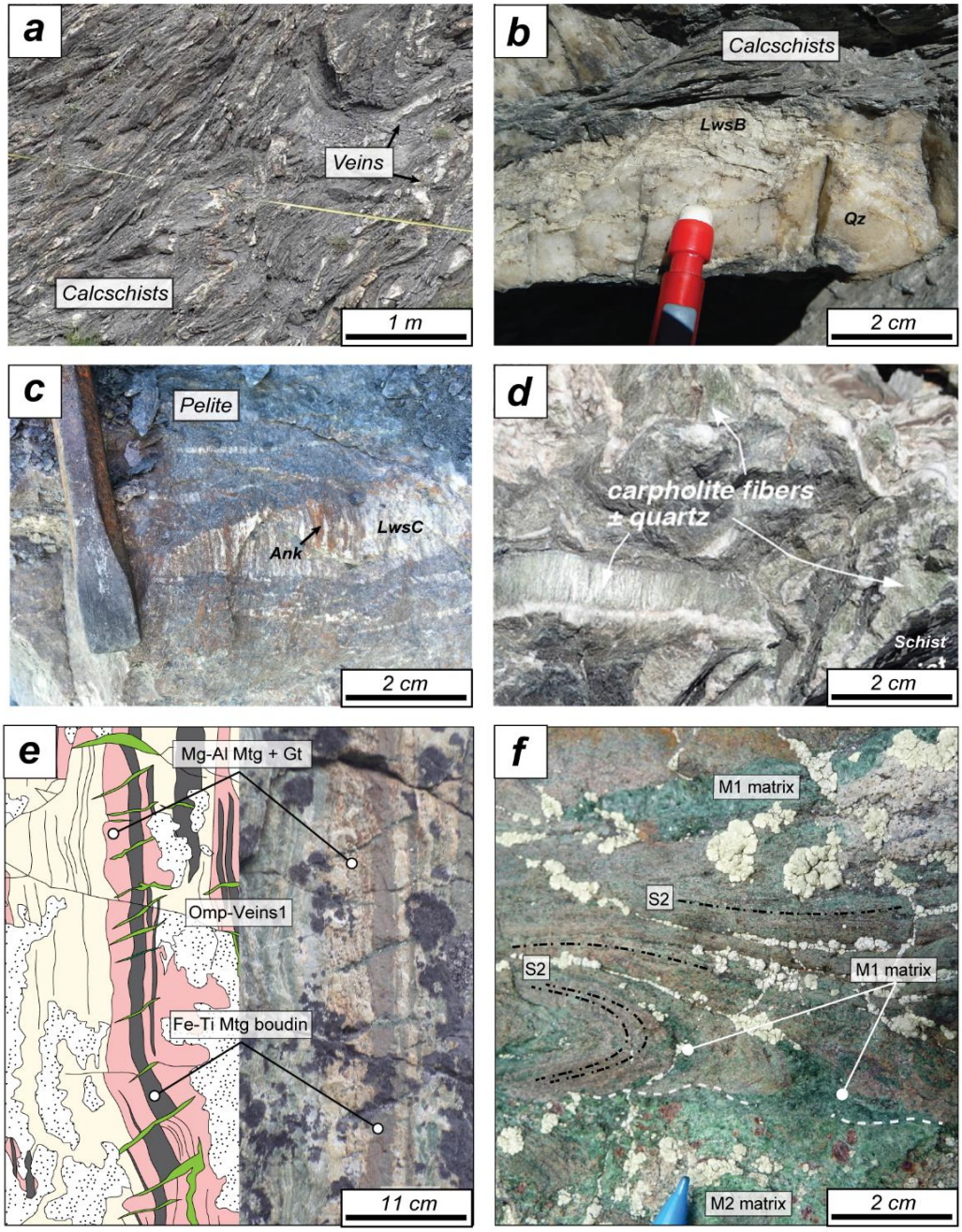

Figure I.11 *: Veines métamorphiques dans le domaine Liguro-Piémontais. A) Affleurement riche en veine dans les Schistes Lustrés. Modifié d'après Agard (2021). B) Veine à fibres de lawsonite B et de quartz dans les Schistes Lustrés. Modifié d'après Lefeuvre et al. (2020). C) Fente de tension à fibres de lawsonite C et d'ankérite dans les Schistes Lustrés. Modifié d'après Lefeuvre et al. (2020). D) Veine à fibres de Fe-Mg carpholite et de quartz dans les Schistes Lustrés. Modifié d'après Agard (2021). E) Veines d'omphacite dans un méta-gabbro de faciès éclogite du massif du Monviso. Modifié d'après Locatelli et al. (2019b). Brèches éclogitiques avec clastes de méta-gabbros Fe-Ti et matrices à grenat-omphacite. Modifié d'après Locatelli et al. (2019b).*

Plusieurs types de lawsonite ont notamment été décrits (Lefeuvre et al., 2020) : (i) les lawsonites A sont des cristaux prismatiques sombres retrouvés directement dans les calcschistes ; (ii) les lawsonites B, dans les veines, correspondent à des cristaux de couleur crème allongés parallèlement aux épontes des veines et accompagnés de quartz et parfois d'ankérite (Fig. I.11b) et enfin (iii) les lawsonites C correspondent également à des cristaux allongés de couleur crème associés à des fibres d'ankérite et de quartz mais orientés perpendiculairement aux épontes de fentes de tension qui les contiennent (Fig. I.11c). Ces veines de lawsonite, témoins des circulations de fluides en subduction, ont uniquement été décrites dans les unités structuralement supérieures qui ont étés enfouies aux profondeurs de nucléation des glissements lents et trémors (Fig. I.6b). La présence de ces nombreux minéraux hydratés suggère une production de fluide limitée à ces profondeurs, contrairement aux suggestions des études géophysiques. Les mécanismes responsables de la formation de ces veines ainsi que la représentativité de leur présence à travers le domaine Liguro-Piémontais Ouest-alpin restent à déterminer.

Par rapport aux méta-sédiments, les roches meta-basiques sont presque entièrement dépourvues de veines. Les principaux marqueurs de circulations de fluides sont des veines métamorphiques constituées d'assemblages à omphacite ± grenat (assemblage éclogitique) recoupant la foliation mylonitique des méta-gabbros de faciès éclogite (Fig. I.11e ; Philippot, 1987 ; Philippot et Selverstone, 1991 ; Philippot et al., 1998 ; Angiboust et al., 2011 ; Spandler et al., 2011 ; Locatelli et al., 2018, 2019a, b). Dans les zones de cisaillement pluri-kilométriques du massif du Monviso, des brèches dont les matrices contiennent des assemblages minéralogiques du faciès éclogite attestent d'épisodes successifs de déformation cassante et d'infiltration de fluides dans le domaine ductile en subduction (Fig. I.11f ; Angiboust et al., 2012a, 2014a ; Locatelli et al., 2018, 2019a, b).

De façon générale les études isotopiques et des éléments traces dans les méta-sédiments du domaine Liguro-Piémontais tendent à montrer la dominance d'un système tamponné par les roches avec des infiltrations de fluides externes limités (Henry et al., 1996 ; Bebout et al., 2013 ; Epstein et al., 2020) à part à proximité des contacts tectoniques majeurs (Jaeckel et al., 2018 ; Epstein et al., 2021). Dans les grandes zones de cisaillements ou au niveau des contacts lithologiques entre méta-sédiments et roches mafiques/ultramafiques, des infiltrations de fluides externes dans les blocs mafiques et ultramafiques ont également été identifiées (Spandler et al., 2011 ; Lafay et al., 2013 ; Angiboust et al., 2014a ; Debret et al., 2016, 2018 ; Inglis et al., 2019 ; Tartarotti et al., 2019 ; Vitale-Brovarone et al., 2020b ; Rotondo et al., 2021). L'identification systématique des sources principales de fluides ayant circulés dans les différents réservoirs (méta-sédiments, roches mafiques et

ultramafiques), en fonction de l'évolution du gradient métamorphique ainsi que l'ampleur et les échelles d'infiltration de fluides externes au niveau des contacts lithologiques et tectoniques restent cependant à déterminer.

Comment évoluent les fluides métamorphiques à travers un complexe HP-BT ? Quels enseignements sur l'évolution des compositions de fluides et des mécanismes de transfert de fluide dans un panneau plongeant pouvons-nous tirer de l'étude des veines métamorphiques ? Quels sont les mécanismes de formation de veines à haute pression et peuvent-elles enregistrer des processus de déformation grande échelle en subduction ? Quels impacts ont les libérations de fluides sur les mécanismes d'écaillages et de transformation des roches ?

I.5. Objectifs, méthodologie et structure de la thèse

En essayant de répondre aux nombreuses problématiques posées dans cette introduction, cette thèse a pour objectif d'apporter des contraintes sur les mécanismes de circulations de fluides, de déformation associés, et sur les potentielles implications des fluides sur les processus d'écaillage dans les zones de subduction. Le domaine Liguro-Piémontais alpin fournissant des roches enfouies entre ~30 et 80 km de profondeur lors de la subduction alpine est donc une cible parfaitement adaptée pour cette étude.

Du terrain à l'analyse géochimique d'échelle micrométrique

Un grand travail d'observations, de mesures et d'échantillonnage sur le terrain (3 mois ½ en six missions) a été effectué afin d'identifier et de traquer les marqueurs principaux de circulations de fluides à haute pression à travers le domaine Liguro-Piémontais des Alpes occidentales. Ce travail de terrain a également permis de combler les zones de faible échantillonnage des études précédentes afin de permettre un suivi complet des évolutions métamorphiques le long de ce complexe. Les 315 échantillons collectés ont ensuite été étudiés par de nombreuses méthodes pétrologiques, géochimiques et statistiques permettant d'aboutir aux **cinq volets** (**chapitres II, III, IV, V, VI**) présentés dans ce manuscrit entre la présente introduction et la discussion :

Le **chapitre II** est un article publié dans la revue Lithos en 2021. Ce volet présente l'analyse d'inclusions fluides primaires piégées dans les veines de haute pression des méta-sédiments et des

roches mafiques d'un transect très étudié dans le domaine Liguro-Piémontais (Queyras-Monviso) où le cadre structural est bien contraint. Une approche statistique par spectroscopie Raman a été utilisée pour analyser le contenu en gaz et les salinités de ces petites portions de fluides piégées au pic pression-température. Une compilation exhaustive des données d'inclusions fluides primaires dans les zones de subduction océaniques fossiles est également présentée afin de comparer les résultats obtenus à une base de donnée mondiale.

Le **chapitre III** est un article publié dans la revue Tectonophysics en 2022. Ce chapitre présente une compilation globale des données pression-température-temps, lithostratigraphiques et structurales des écailles de subduction Liguro-Piémontaises. A travers l'apport de nouvelles données pétrologiques (spectroscopie Raman sur matière carbonée, contenu en Si des phengites, pseudosection) et lithostratigraphiques (ratio sédiments vs mafiques-ultramafiques et surface des écailles), ce travail cherche à fournir un modèle global de distribution des unités et des conditions métamorphiques du domaine Liguro-Piémontais afin de pouvoir en déduire des informations sur les mécanismes d'écaillage en subduction. Cette démarche était nécessaire pour pouvoir réaliser ensuite une étude de circulation des fluides à l'échelle du complexe (**chapitre VI**).

Le **chapitre IV** est une ébauche d'article en préparation pour la revue Journal of Structural Geology. Ce volet présente la mesure d'épaisseur de veines, de leur espacement, de leur regroupement et d'espacements de bandes de crack-seal dans les Schistes Lustrés. L'observation des textures et l'application de lois statistiques aux données collectées a permis ensuite de définir des mécanismes de formation de ces veines, de circulation des fluides et de proposer des implications pour la rupture en base de zone sismogénique.

Le **chapitre V** est une ébauche d'article en préparation pour Earth and Planetary Science Letters. Ce chapitre présente la découverte et l'étude de talc-schistes à carbonates observés à proximité des contacts tectoniques entre les unités Liguro-Piémontaises. L'analyse des inclusions fluides primaires, des assemblages et compositions minéralogiques et des éléments majeurs, mineurs et traces sur roche totale a permis de caractériser l'origine de ces roches. La datation de ces échantillons a ensuite été réalisée par géochronologie U-Pb sur sphène en collaboration avec Guillaume Bonnet (UCSB/ISTeP). Toutes ces analyses ont permis de proposer de nouveaux mécanismes d'écaillages du panneau plongeant alpin par rétroaction positive entre fluides et déformation.

Le **chapitre VI** est une nouvelle analyse des inclusions fluides primaires dans les veines de haute pression du domaine Liguro-Piémontais. En s'appuyant sur le modèle structural du **chapitre III** et sur

les mécanismes de formation des veines et de circulation des fluides proposés dans les **chapitre IV et V**, ce chapitre vise à étendre les observations faites dans le **chapitre II** grâce à l'étude de 3 coupes majeures (Savoy-Susa, Alpes Cottiennes, Queyras-Monviso). Avec 1585 inclusions étudiées dans plus de 70 échantillons, ce volet contient la plus grande base de données d'inclusions fluides en subduction jamais collectée et fera l'objet d'un article avec une soumission prévue dans la revue Geochemistry, Geophysics, Geosystems.

Le **chapitre VII** présente une discussion générale intégrant l'ensemble des données des différents volets dans le but d'aboutir à un modèle global de circulations des fluides en fonction de la profondeur, lors de la subduction alpine, et de ces implications sur la déformation et sur les mécanismes d'écaillage.

Le **chapitre VIII** permet de conclure et de soulever des perspectives d'études permettant de répondre aux nouvelles problématiques ouvertes par ce travail de thèse.

Enfin dans les **annexes** de ce manuscrit, deux travaux auxquels j'ai été associé durant ma thèse sont présentés. Le premier, est un article publié dans la revue American Mineralogist par L. Masci et collaborateurs. Ce travail, contenant une partie des résultats de ma thèse de Master 1, présente l'étude du contenu en Fe^{3+} des chlorites et discute de ces implications pour les substitutions et la thermobarométrie dans ces minéraux. Le deuxième est une ébauche d'article en préparation par B. Lefeuvre et collaborateurs pour la revue Contributions to Mineralogy and Petrology. A travers l'étude des roches totales, des éléments majeurs et traces dans les minéraux et des isotopes du strontium, ce travail présente les variations compositionnelles des lawsonites des Schistes Lustrés le long d'un transect dans les unités Liguro-Piémontaises supérieures des Alpes Cottiennes.

Chapitre II - Evolution des compositions de fluide le long d'un transect majeur (Queyras-Monviso)

Veine de lawsonite B et C dans les Schistes Lustrés. Punta Bagna.

II. Evolution des compositions de fluide le long d'un transect majeur (Queyras-Monviso)

II.1. Résumé du chapitre

Le transect Queyras-Monviso du complexe des Schistes Lustrés est un empilement de nappes constituées de fragments de lithosphère océanique et subduites dans les conditions des faciès schiste bleu à éclogite. Cette étude apporte des données de salinité et des contenus en gaz d'inclusions fluides primaires piégées dans les veines de haute pression de méta-sédiments et de méta-gabbros de ces unités (445 inclusions fluides dans 22 échantillons). Ces données permettent d'avoir un accès aux compositions des fluides présents aux conditions du pic d'enfouissement entre ~30 et 80 km de profondeur. L'étude de ces inclusions fluides le long du grade métamorphique illustre donc l'évolution de la composition des fluides lors de l'enfouissement le long d'une zone de subduction froide. Les inclusions fluides piégées dans les veines à lawsonite et à Fe-Mg carpholite des méta-sédiments contiennent des fluides aqueux faiblement salés (salinité moyenne de 4.6 wt.% eq. NaCl) avec de faibles quantités de CO_2 et de CH_4 à l'intérieur de la phase vapeur. La décroissance de la salinité observée avec l'augmentation du grade métamorphique est interprétée comme reflétant la dilution progressive des fluides de pores initiaux, ayant une salinité proche de celle de l'eau de mer, par des fluides faiblement salés et libérés localement par les réactions de déshydratation. De plus rares échantillons avec des salinités fortes ont été identifiés dans l'unité structuralement supérieure, dominée par les sédiments. Ces salinités fortes suggèrent l'infiltration de saumures provenant des unités de marge continentale, riches en évaporites. Le CO_2 et le CH_4 (et de rares potentiels hydrocarbures) sont vraisemblablement libérés localement par des interactions entre le fluide, les carbonates et les horizons pélitiques riches en matière carbonée.

Dans les méta-gabbros, les inclusions fluides de veines de haute pression à omphacite enregistrent des salinités plus fortes (salinités moyenne de 17 wt% eq. NaCl) avec de faibles quantités de N_2 uniquement trouvées dans les veines éclogitiques. Dans ces veines, une grande variété de minéraux (calcite, micas blancs, sels) indique des systèmes chimiques complexes. Ces salinités fortes sont interprétées comme partiellement héritées de l'altération hydrothermale à haute température des gabbros résultant en une séparation des phases et la formation de saumures. La déstabiliation progressive des amphiboles hydrothermales, riches en Cl, en glaucophane (faciès schiste bleu), puis

en omphacite (faciès éclogite) ainsi que la libération des saumures piégées dans les inclusions fluides pourraient expliquer la salinité forte des inclusions fluides des méta-gabbros. Ces inclusions fluides enregistrent donc la libération progressive du Cl dans la phase fluide lors de l'augmentation du grade métamorphique. Les signatures des fluides des méta-sédiments et des méta-basites apparaissent caractéristiques de chaque type de roche. La signature locale et les conditions oxydo-reductrices furent donc préservées dans les unités, potentiellement grâce à une circulation de fluide restreinte et transitoire (à l'échelle de l'hectomètre au plus).

Les inclusions fluides des méta-sédiments alpins ont des salinités et des contenus en gaz comparables à ceux des autres fragments de lithosphère océanique subduits à travers le monde. Les salinités des méta-gabbros alpins sont cependant plus fortes que celles enregistrées dans ces autres zones de subduction fossiles. Ces différences pourraient être liées à (1) une altération hydrothermale à plus haute température engendrant la formation de saumures dans les méta-gabbros alpins (par rapport aux roches méta-volcaniques) ou (2) à une infiltration plus restreinte de fluides externes provenant des sédiments par rapport aux blocs des mélanges de subduction.

II.2. Article 1: Along-dip variations of subduction fluids: The 30–80 km depth traverse of the Schistes Lustrés complex (Queyras-Monviso, W. Alps). Lithos, Avril 2021.

Lithos 394–395 (2021) 106168

Contents lists available at ScienceDirect

Lithos

journal homepage: www.elsevier.com/locate/lithos

Research Article

Along-dip variations of subduction fluids: The 30–80 km depth traverse of the Schistes Lustrés complex (Queyras-Monviso, W. Alps)

Clément Herviou [a,*], Anne Verlaguet [a], Philippe Agard [a], Michele Locatelli [b], Hugues Raimbourg [c], Benjamin Lefeuvre [a], Benoit Dubacq [a]

[a] Sorbonne Université, CNRS-INSU, Institut des Sciences de la Terre de Paris, ISTeP UMR 7193, F 75005 Paris, France
[b] Dipartimento di Scienze della Terra, Ambiente e Vita (DISTAV), Università di Genova, Italy
[c] Institut des Sciences de la Terre d'Orléans (ISTO), UMR7327 Université d'Orléans, CNRS-INSU, Bureau de Recherches Géologiques et Minières (BRGM), 45071 Orléans, France

ARTICLE INFO

Article history:
Received 18 December 2020
Received in revised form 29 March 2021
Accepted 11 April 2021
Available online 16 April 2021

Keywords:
Fluid inclusions
Subduction fluids
Schistes Lustrés
Western Alps
Fluid-rock interactions
Salinity variations

ABSTRACT

The Queyras-Monviso traverse of the Schistes Lustrés complex, is a stack of underplated nappes of oceanic rocks subducted from blueschist- to eclogite-facies conditions.

This study reports on salinities and gas contents of primary fluid inclusions trapped in high pressure veins from metasediments and metamafic rocks (445 fluid inclusions in 22 samples). These data provide snapshots of the compositions of fluids present at peak burial conditions, varying from ~30 to 80 km depth and illustrate the evolution of fluid composition with burial along a cold subduction zone.

Fluid inclusions trapped in lawsonite- and carpholite-bearing veins in metasediments contain moderately saline aqueous fluids (average salinity of 4.6 wt% NaCl eq.) with subordinate amounts of CO_2 and CH_4 in the vapor phase. The observed salinity decrease with increasing grade is interpreted as reflecting progressive dilution of initial seawater-like pore fluid by low-salinity fluids released locally by dehydration reactions. Less-frequently measured higher salinities in the uppermost metasedimentary-dominated tectonic unit suggest brine infiltration from embedded blocks of margin units containing evaporites. CO_2 and CH_4 (and scarce potential hydrocarbons) appear to be locally released from fluid interaction with carbonates and carbonaceous matter-rich pelitic horizons, respectively.

Fluid inclusions in high pressure omphacite veins in metagabbros record higher salinities (mean salinity about 17 wt% NaCl eq.) with small amounts of N_2 in eclogitic veins only, and a variety of minerals (calcite, white mica, salts) indicative of complex chemical systems. These high salinities are interpreted as partly inherited from seafloor high-temperature hydrothermal alteration of gabbros, resulting in phase separation and brine formation. Progressive breakdown of hydrothermal Cl-rich amphibole to glaucophane (blueschist-facies) and then omphacite (eclogite-facies) and release of brines trapped in fluid inclusions could account for the high salinity fluids. Therefore, in metagabbros, fluid inclusions record progressive release of Cl in the fluid phase with increasing grade.

Fluid signatures of metasediments and metamafics appear characteristic of each rock type. Local fluid signatures and redox conditions were preserved within units, possibly due to restricted and transient fluid circulation (at the hm-scale at most).

Fluid inclusions in Alpine metasediments show salinities and gas contents comparable with other subducted fragments of oceanic lithosphere worldwide, whereas fluid salinities of Alpine metagabbros are higher than salinities recorded elsewhere, either due to (1) higher-temperature hydrothermal alteration and brine formation in Alpine metagabbros (compared to metavolcanics) or (2) more restricted infiltration by sediment-derived fluids compared to block-in-mélange subduction complexes.

1. Introduction

Large amounts of fluids are released in subduction zones by progressive dehydration of hydrothermalized portions of the oceanic lithosphere and of its sedimentary cover (Hacker, 2008; Rupke et al., 2004; Schmidt and Poli, 2014). Fluid release and fluid migration have major mechanical and chemical consequences in rocks: the presence of a free fluid phase strongly impacts rheology, e.g. fracturing and intermediate-depth earthquake and slow slip event generation (Hacker et al., 2003; Hyndman et al., 2015; Obara, 2002); the amount and composition of fluids, in part controlled by permeability, dictates

* Corresponding author.
E-mail address: clement.herviou@sorbonne-universite.fr (C. Herviou).

https://doi.org/10.1016/j.lithos.2021.106168
0024-4937/

the magnitude of chemical changes and mass transfer. Characterizing major fluid sources, amounts and pathways in subduction zones is therefore a prerequisite to assessing their impact on subduction dynamics (Bebout and Penniston-Dorland, 2016).

Fluids are elusive in essence and their compositions are mostly inferred from isotopic and trace element studies from exhumed fossil subduction zones (Spandler and Pirard, 2013). A direct access to deep fluid compositions is nevertheless provided by primary fluid inclusions (FI) trapped in high pressure low temperature (HP-LT) minerals (e.g., Frezzotti and Ferrando, 2015; Scambelluri and Philippot, 2001; Touret and Frezzotti, 2003). Despite common re-equilibration of FI densities during exhumation and difficulty to preserve V-X properties of FI trapped at prograde or peak metamorphic conditions (Bodnar, 2003b; Diamond, 2003; Küster and Stöckhert, 1997; Raimbourg et al., 2018; Tarantola et al., 2012; Vityk and Bodnar, 1995a, 1995b), several studies have shown that their pristine compositions may be genuinely preserved (Diamond et al., 2010; Diamond and Tarantola, 2015; Sterner and Bodnar, 1989).

Former studies of subduction FI have so far mostly focused on shallow metasediments from exhumed accretionary wedges (e.g., Brantley et al., 1998; Smith and Yardley, 1999; Raimbourg et al., 2015) or mafic and ultramafic rocks from deep eclogitic metamorphic terranes (e.g., Philippot and Selverstone, 1991; Giaramita and Sorensen, 1994; Fig. 1; Table 1). As shown by the compilation of Fig. 1, only few studies have provided information on fluid compositions in blueschist-facies metapelites (Agard et al., 2000; El-Shazly and Sisson, 2004) despite their (i) considerable fluid content stored in hydrous minerals (e.g., Bousquet et al., 2008; Lefeuvre et al., 2020) and (ii) potential to retain some elements to great depths (Bebout et al., 2013; Busigny et al., 2003), and thereby contribute to a significant fraction of fluids released at depth and element recycling. Moreover, the evolution of fluid compositions with increasing P-T conditions remains poorly documented in both sedimentary and mafic protoliths and somewhat ambiguous. Local dehydration and progressive dilution of pore water has been proposed to explain the decrease of fluid salinity in prehnite-pumpellyite- to blueschist-facies Franciscan metasediments (Sadofsky and Bebout, 2004), whereas preservation of hydrothermal salinities up to eclogite-facies conditions has been proposed for Alpine mafic rocks (e.g., Philippot et al., 1998). To assess wether such trends are representative across subduction zones, there is a need for statistical data on the evolution of fluid composition with depth in both mafic rocks and sediments, i.e. on a continuous transect of a single subduction zone.

In the Western Alps, several tectonic slices buried from ~30 km to ~80 km during subduction of the Liguro-Piemont ocean are continuously exposed in the Schistes Lustrés complex (SL; Agard et al., 2001, 2009). They comprise oceanic metasediments with variable mafic and ultramafic fragments and have preserved prograde to peak metamorphic assemblages and abundant veins with HP minerals (Goffé and Chopin, 1986; Lefeuvre et al., 2020; Philippot, 1987). They provide the opportunity to study the evolution of fluid compositions and pathways across depths along a former subduction plate interface (Agard et al., 2018). Isotopic and trace element data of this dominantly metasedimentary suite suggest the dominance of a rock-buffered system with only limited external fluid infiltration (Bebout et al., 2013; Busigny et al., 2003; Cook-Kollars et al., 2014; Henry et al., 1996), except along major tectonic contacts (Angiboust et al., 2011, 2014; Epstein et al., 2021; Jaeckel et al., 2018; Locatelli et al., 2018; Spandler et al., 2011). The current dataset of primary FI of HP veins shows aqueous low to moderately saline fluid compositions in the shallowest SL (Agard et al., 2000; locally CO_2-bearing: Raimbourg et al., 2018) and moderate to highly-saline fluids in the deep mafic and ultramafic eclogite-facies rocks (Nadeau et al., 1993; Philippot et al., 1998; Philippot and Selverstone, 1991; Scambelluri et al., 1997).

The aim of the present study is to characterize the composition of fluids trapped in FI from HP veins formed at or close to peak burial, across subduction depths and for two major fluid-reservoirs/sources, i.e. metasediments and metamafic rocks. To obtain a statistically meaningful dataset representative of the evolution of fluid composition with burial, we report analyses of 445 FI in 22 samples collected along the Queyras-Monviso transect of the Alpine subduction zone. We then discuss possible fluid sources, evaluate the relative contributions of

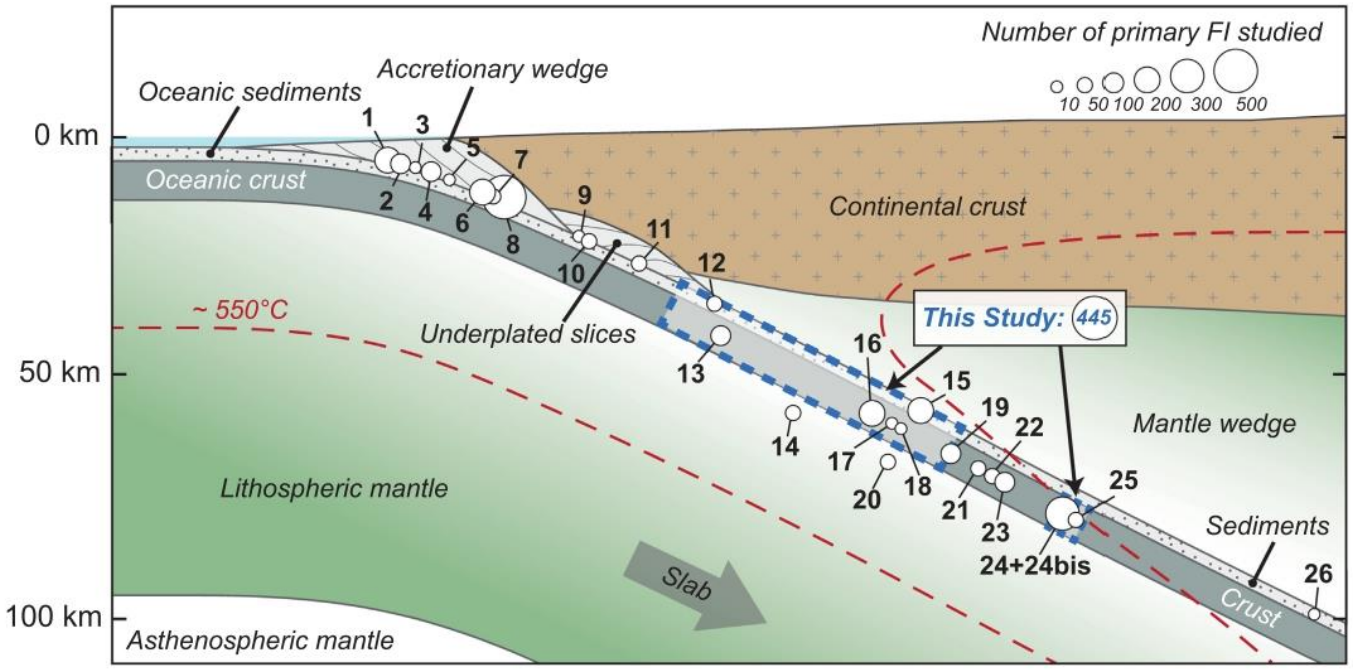

Fig. 1. Compilation of exhumed oceanic subduction rocks for which primary FI were analyzed in the literature, placed on a schematic subduction zone according to their estimated burial depth. The scope of this study is represented by red-border rectangles. References for studies of both fluid inclusions and P-T estimates are reported in Table 1. The size of the circles corresponds to the number of salinity values from primary FI available for each oceanic subduction compiled in Table 1. The lower bound of the smallest circle corresponds to 0 or unspecified in the corresponding studies.

Table 1
List of exhumed oceanic subduction zones compiled in Figs. 1 and 14 and corresponding references for fluid inclusion and P-T estimate studies.

n°	Locality	FI references	P (kbar)	T (°C)	P-T references
1	Helmyntoïdes Flysch, W. Alps	Raimbourg et al. (2018)	?	~270	Raimbourg et al. (2018)
2	Robertson Bay, Antarctica	Rossetti et al. (2006)	2	200–250	Rossetti et al. (2006)
3	Chugach Complex, Alaska	Sisson et al. (1989)	2.5	400–650	Sisson et al. (1989)
4	Kodiak, Alaska	Brantley et al. (1998); Vrolijk (1987); Vrolijk et al. (1988)	2.6 ± 0.4	269	Brantley et al. (1998)
5	Costal Belt, Franciscan Complex, USA	Sadofsky and Bebout (2004)	<3	~125	Blake Jr (1988); Terabayashi and Maruyama (1998)
6	Shimanto Belt, Japan	Raimbourg et al. (2014, 2015, 2018)	3–5	~250	Toriumi and Teruya (1988); Raimbourg et al. (2014)
7	Franciscan Complex - Central Belt, USA	Sadofsky and Bebout (2004)	3–5.6	150-260	Blake Jr (1988); Terabayashi and Maruyama (1998)
8	Otago Schist, New Zealand	Smith and Yardley (1999)	4–5	~390	Yardley (1982); Jamieson and Craw (1987)
9	Southern Appenines, Italy	Invernizzi et al. (2008)	6–8	250–350	Monaco and Tortorici (1995)
10	Franciscan Complex - Eastern Belt	Sadofsky and Bebout (2004)	6–8.3	180-330	Blake Jr (1988); Terabayashi and Maruyama (1998)
11	Franciscan Complex - Diablo Range	Sadofsky and Bebout (2004)	7.4–10.5	130–260	Ernst (1993); Terabayashi and Maruyama (1998)
12	Schistes Lustrés LPU, W. Alps	Agard et al. (2000); Raimbourg et al. (2018)	12–13	300–350	Agard et al. (2001)
13	Rio San Juan Complex, Rep. Dom.	Kawamoto et al. (2018)	12–17	350–500	Schertl et al. (2012); Hertwig et al. (2016)
14	Cerro de Almirez, Betic Cordillera	Scambelluri et al. (2001)	16–19	680–710	Padrón-Navarta et al. (2010)
15	Sapi-Shergol, Himalaya	Sachan et al. (2017)	~19	~470	Groppo et al. (2016)
16	Tianshan, China	Gao and Klemd (2001)	18–21	480–600	Gao et al. (1999); Gao and Klemd (2000)
17	Tauern Window, E. Alps	Luckscheiter and Morteani (1980); Selverstone et al. (1992)	19.5 ± 2.5	590 ± 20	Spear and Franz (1986); Holland (1979)
18	Sanbagawa eclogites, Japan	Yoshida et al. (2015)	~20.5	525–565	Endo (2010)
19	Syros, Cyclades	Barr (1990)	22 ± 2	530 ± 30	Laurent et al. (2018)
20	Erro-Tobbio, Ligurian Alps	Scambelluri et al. (1997)	20–25	550–600	Messiga et al. (1995)
21	Samana Peninsula, Rep. Dom.	Giaramita and Sorensen (1994)	22–24	610–625	Escuder-Viruete and Pérez-Estaún (2006)
22	Franciscan Complex eclogites, USA	Giaramita and Sorensen (1994)	22–25	550–620	Tsujimori et al. (2006)
23	Voltri eclogites, Ligurian Alps	Vallis and Scambelluri (1996)	23–25	500–525	Starr et al. (2020)
24 + 24bis	Monviso, W. Alps	Philippot and Selverstone (1991) + Nadeau et al. (1993)	26	550	Angiboust et al. (2011)
25	Rocciavre, W. Alps	Philippot et al. (1998)	25–29	460–610	Ghignone et al. (2020)
26	Lago di Cignana, W. Alps	Frezzotti et al. (2011, 2014); Frezzotti (2019)	>32	590–605	Groppo et al. (2009)

inherited sedimentary and/or hydrothermal fluids and of local devolatilization reactions and/or external deeper fluids, and finally discuss implications for fluid-rock interactions and evolution of fluid composition along the subduction plate interface.

2. Geological setting

2.1. Fragments of subducted oceanic lithosphere in the Western Alps

The Western Alps formed as a result of an east- to south-east-dipping and slow (~1 cm/yr) subduction of the ~700 km wide Valais and Liguro-Piemont oceans below Adria/Apulia (Agard and Handy, 2021; Handy et al., 2010; Lapen et al., 2003; Le Pichon et al., 1988; Schmid et al., 1996, 2017). Subduction of these slow-spreading oceanic domains (Lagabrielle and Cannat, 1990) started in the late Cretaceous and was over by ~35 Ma (Schmid et al., 2017; Stampfli et al., 1998).

Remants of subducted Liguro-Piemont oceanic lithosphere are now exposed in the internal domain of the Western Alps and form a nappe stack known as the Schistes Lustrés complex (SL; Agard et al., 2009; Agard, 2021). Metasediments are volumetrically dominant in this complex and range from late Jurassic (De Wever and Caby, 1981; Lagabrielle, 1987) to late Cretaceous (Lagabrielle, 1987; Lemoine et al., 1984). They correspond to an initial ~200–400 m thick sequence of pelagic seafloor deposits (marls, shales and limestones metamorphosed as calcschists, pelites and marbles; Lemoine et al., 1984; Lemoine and Tricart, 1986; Deville et al., 1992; Michard et al., 1996) now embedding variable amounts of mafic and ultramafic rocks. During subduction, these metasediments were buried to contrasting depths and were intensely folded, leading to a consequent thickening of the initial sedimentary pile (Agard et al., 2002; Tricart and Schwartz, 2006). Agard et al. (2009) have roughly estimated that approximatively 30% to 50% of the sedimentary deposits were offscraped from the downgoing subducting plate and exhumed, whereas only ~5% of the oceanic crust and serpentinized mantle did.

2.2. Tectono-metamorphic evolution of the Schistes Lustrés complex

Based on lithostratigraphic and tectono-metamorphic contrasts, several units were identified in the SL complex (Agard et al., 2009; Lagabrielle, 1987). A major distinction is between the blueschist- (BS) facies metasedimentary-dominated units and the metamafic-ultramafic-dominant eclogite-facies units cropping out eastward of and tectonically below the BS-facies units (Fig. 2a; Dal Piaz, 1974; Caby et al., 1978; Droop et al., 1990; Pognante, 1991). These groups of units are separated by a major extensional tectonic contact (Ballèvre et al., 1990; Ballèvre and Merle, 1993; Philippot, 1990). Three distinct groups, from west to east, can be recognized in the SL complex (Agard, 2021; Fudral, 1996; Fudral et al., 1987; Lagabrielle et al., 2015; Plunder et al., 2012): (1) the upper units (LPU) exposed on the westernmost part of the SL complex are mostly made of low- to medium-temperature BS-facies calcschists and pelites with minor mafic-ultramafic fragments; (2) the middle units (LPM) comprise medium- to high-temperature BS-facies calcschists, generally more carbonate-rich, with more oceanic slivers than the LPU; (3) the lower units (LPL) comprise transitional BS-eclogite-facies to eclogite-facies km-scale bodies of mafic and ultramafic rocks together with minor amounts of metasediments. In places, a distinction (not made in the following, for the sake of clarity) can be made between metasedimentary-rich tectonic slices (e.g., around Susa; Agard et al., 2001; Ghignone et al., 2020) and mafic/ultramafic units several km-long (e.g., Monviso; Lombardo, 1978; Locatelli et al., 2019a). The latter directly overly the internal crystalline massifs in the easternmost part of the SL complex.

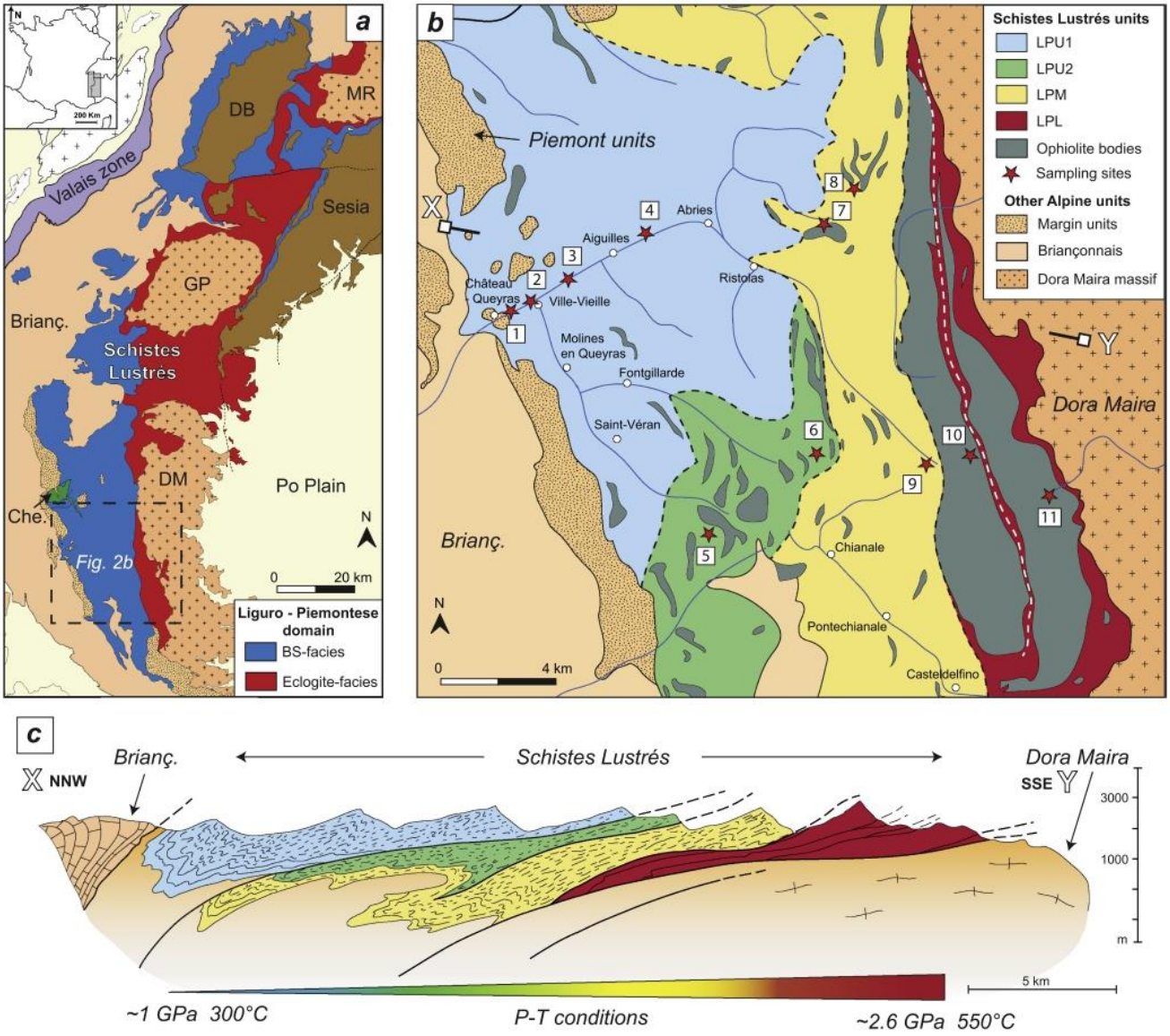

Fig. 2. Map and cross-section of the studied area. A) Simplified geological map of the Western Alps with focus on the Schistes Lustrés complex and the distribution of metamorphic facies within. The studied area is outlined by the black dashed square. DB: Dent Blanche; MR: Monte Rosa; GP: Gran Paradiso; DM: Dora Maira; Briançonnais; Che.: Chenaillet. B) Simplified geological map of the studied area with distribution of tectonometamorphic units after Lagabrielle (1987). Studied outcrops are localized by stars and described in Table 2. C) Schematic cross-section of the studied traverse and eastward-increasing gradient of peak metamorphic conditions (modified after Lagabrielle, 1987) with P-T estimates from Agard et al. (2001), Schwartz et al. (2013) and Angiboust et al. (2012b).

P-T estimates show an eastward, almost continuous increase in metamorphic grade from the upper (1.2 GPa-300 °C) to the lower units (~2.5 GPa-550 °C), along a ~ 8 °C/km metamorphic gradient (Agard et al., 2001; Beyssac et al., 2002; Gabalda et al., 2009; Plunder et al., 2012; Schwartz et al., 2013).

Several deformation stages were identified and dated in the SL complex of the Cottian Alps (Agard et al., 2001, 2002; see also Ghignone et al., 2020): the first episode (D1) relates to the development of early fabrics, km-scale folds and crystallization of peak metamorphic assemblages at ~62–55 Ma. A second phase (D2) at ~51–45 Ma corresponds to the ductile east-vergent deformation accompanying early exhumation under BS-facies conditions. The third fabric (D3), between ~38 and 35 Ma, is marked by top-to-the-west ductile to brittle deformation associated with greenschist-facies exhumation, and coincides with the final ductile exhumation of large mafic-ultramafic complexes such as Monviso (Angiboust and Glodny, 2020). Two late fabrics (D4 and D5; Tricart and Schwartz, 2006), marked by small-scale boudinage and west-dipping normal faulting, characterize the final ductile-brittle transition during late exhumation.

2.3. The Queyras-Monviso traverse

This study focuses on the southern SL complex where subducted oceanic fragments buried at different depths are particularly well-exposed along the Queyras-Monviso traverse and provide access to fluid-rock interactions during subduction. In this area, four major units were identified (Fig. 2b, c; Lagabrielle, 1987; Lagabrielle et al., 2015).

Peak burial conditions across the traverse were constrained by mineralogical assemblages of meta-ophiolitic bodies (e.g., Angiboust et al., 2012b; Locatelli et al., 2018; Schwartz, 2000; Tricart and Schwartz, 2006) and maximum temperatures derived from the Raman spectroscopy of carbonaceous material (Angiboust et al., 2012b;

Schwartz et al., 2013). From west to east, the two first units comprise metasedimentary-dominated low- to medium-temperature blueschists, while the third one was buried up to medium- to high-temperature BS-facies conditions. Lithologies and P-T conditions suggest that these slices are similar to the LPU and LPM cropping out further north in the Cottian Alps and Savoy (Agard, 2021; Agard et al., 2001; Plunder et al., 2012), and will be referred to below as LPU1, LPU2 and LPM (Figs. 2b, c; 3). The last unit on this traverse corresponds to the Monviso massif, a large mafic-ultramafic body comprising at least two sub-units metamorphosed at the BS- eclogite-facies transition and lawsonite-bearing eclogite-facies (Schwartz et al., 2000; Angiboust et al., 2012b; Locatelli et al., 2018; Fig. 3), which can be regarded as an analogue to the LPL of the Cottian Alps, Savoy and Aosta-Valais (Agard, 2021; Agard et al., 2001; Angiboust et al., 2009; Deville et al., 1992; Plunder et al., 2012).

After peak burial between 62 and 55 Ma for LPU and LPM (Agard et al., 2002) and around 50–45 Ma for the Monviso LPL (Garber et al., 2020; Rubatto and Angiboust, 2015; Rubatto and Hermann, 2003), the four units of the Queyras-Monviso transect were exhumed from late Eocene to Miocene times (Angiboust and Glodny, 2020; Schwartz et al., 2007, 2020).

3. High pressure metamorphic veins

3.1. High pressure veins in the Schistes Lustrés complex

Metamorphic veins, as well as mineralized fractures and shear zones, provide access to fluid-rock interactions and fluid circulation pathways. BS-facies metasediments of the SL complex contain numerous veins (Fig. 4a), as for most former subduction complexes of various grades (Fisher and Byrne, 1990; Meneghini et al., 2009; Muñoz-Montecinos et al., 2020; Raimbourg et al., 2015; Sadofsky and Bebout, 2004; Vannucchi, 2001). Cartwright and Buick (2000) estimated that veins can make up to 30% of outcrops and commonly 5–10% of BS-facies metasediments in Alpine Corsica. Late veins, not studied here, are filled by quartz ± calcite ± albite ± chlorite assemblages and relate to D2 and D3 exhumation events (Agard et al., 2000).

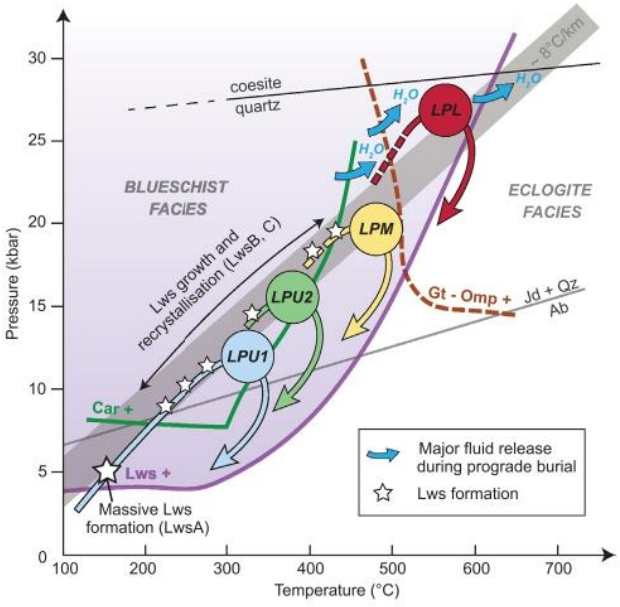

Fig. 3. Metamorphic evolution of the Schistes Lustrés complex units. P-T estimates are from Agard et al. (2001), Schwartz et al. (2013) and Angiboust et al. (2012b). Lawsonite and carpholite stability fields for metasediments are reported from Lefeuvre et al. (2020), Bebout et al. (2013) and Pourteau et al. (2014). Garnet-omphacite stability field for metamafic rocks is after Angiboust and Agard (2010). Fluid release associated with carpholite or lawsonite breakdown, or garnet formation, is indicative and corresponds to generalized P-T conditions. Lws: lawsonite; Car: carpholite; Jd: jadeite; Qz: quartz; Ab: albite.

In metasediments, veins formed during (peak) burial are quartz-bearing and characterized by HP minerals such as lawsonite and Fe-Mg carpholite (Fig. 4a–f). These hydrous minerals, which contain 12 wt% H_2O, are abundant in the SL complex (Caron, 1974; Goffé and Chopin, 1986; Sicard-Lochon, 1987), with lawsonite and lawsonite pseudomorphs making up to 40–45 vol% of the host-rock in places (Lefeuvre et al., 2020).

Fe-Mg carpholite in the schist is commonly replaced by chlorite and white mica during exhumation and only preserved as micrometric needles inside quartz crystals (Agard et al., 2000, 2001; Goffé and Chopin, 1986) or in meter-scale quartz-pods/veins subparallel to the main D1/D2 foliation (Agard et al., 2000).

Lawsonite is less sensitive to retrogression and better preserved throughout the SL complex. Several lawsonite types were identified in the LPU of the Cottian Alps by Lefeuvre et al. (2020) and can be recognized across the entire SL complex. We hereafter use the abbreviations defined in Lefeuvre et al. (2020): (1) LwsA are mostly found in pelitic calcschists as dark prismatic crystals filled with inclusions of organic matter; (2) LwsB consist of cream-coloured elongated fibers with long axis parallel to the vein walls and aligned with quartz crystals ± minor ankerite; LwsB occurs in pluri-centimetric to metric veins subparallel to the present schistosity (Fig. 4b, c, e); (3) LwsC co-crystallizes with quartz and ankerite as cream-coloured fibers perpendicular to the walls of mm- to cm-large tensile veins (Fig. 4d, f). While LwsA crystals in the host calcschists formed early on during prograde metamorphism, several generations of LwsB- and LwsC-bearing veins appear to have formed along the prograde P-T path up to peak burial depths, through dissolution-precipitation processes and lawsonite-forming reactions (Lefeuvre et al., 2020; Fig. 3).

Compared to metasediments, metamafic rocks from the SL complex are almost devoid of veins (Fig. 4g, h). Studies reporting direct evidence of fluid circulation during burial to peak conditions focused on (1) glaucophane shear-bands in BS-facies metagabbroic bodies (Debret et al., 2016; Schwartz, 2000), (2) omphacite-bearing veins in eclogite-facies rocks of Monviso and Rocciavre bodies (Philippot, 1987; Philippot et al., 1998; Philippot and Kienast, 1989; Philippot and Selverstone, 1991), (3) eclogitic breccias of Monviso (Angiboust et al., 2012a; Locatelli et al., 2018) and (4) kyanite-bearing veins in Zermatt-Saas eclogites (Fry and Barnicoat, 1987; Widmer and Thompson, 2001).

In Monviso, brecciated Fe-Ti-metagabbros crop out in major shear zones (Intermediate and lower shear zones; Angiboust et al., 2012a, Locatelli et al., 2018). Different generations of veins and eclogitic breccia matrices were characterized (Locatelli et al., 2018) (1): the first generation of vein (V1) and matrix (M1) is almost exclusively composed of omphacite whereas (2) the second generation of vein (V2) and matrix (M2) is filled by omphacite and garnet; (3) the last matrix generation (M3) is composed of lawsonite pseudomorphs and relics of garnet and omphacite. Thermodynamic modelling and trace elements analysis of omphacite and garnet in these veins and matrices allowed to identify the progressive opening of the system to external fluid infiltrations (Locatelli et al., 2018, 2019b): from metric at peak conditions (V1 veins and M1 matrix) to possibly decametric opening at early retrograde conditions (V2 veins and M2) and hectometric to kilometric opening at retrograde conditions (M3).

3.2. High pressure veins and sampling along the Queyras-Monviso traverse

Outcrops were selected across the LPU1, LPU2, LPM and LPL units of the Queyras-Monviso traverse (Table 2). HP veins can locally reach around 20–25 vol% of the outcrop (Fig. 4a). Fresh lawsonite-bearing veins were found in LPU1, LPU2 and LPM, and creamy-coloured lawsonite crystals were observed in both LwsB (Fig. 4b, c, e) and LwsC veins (Fig. 4d, f). The abundance of lawsonite-bearing veins strongly

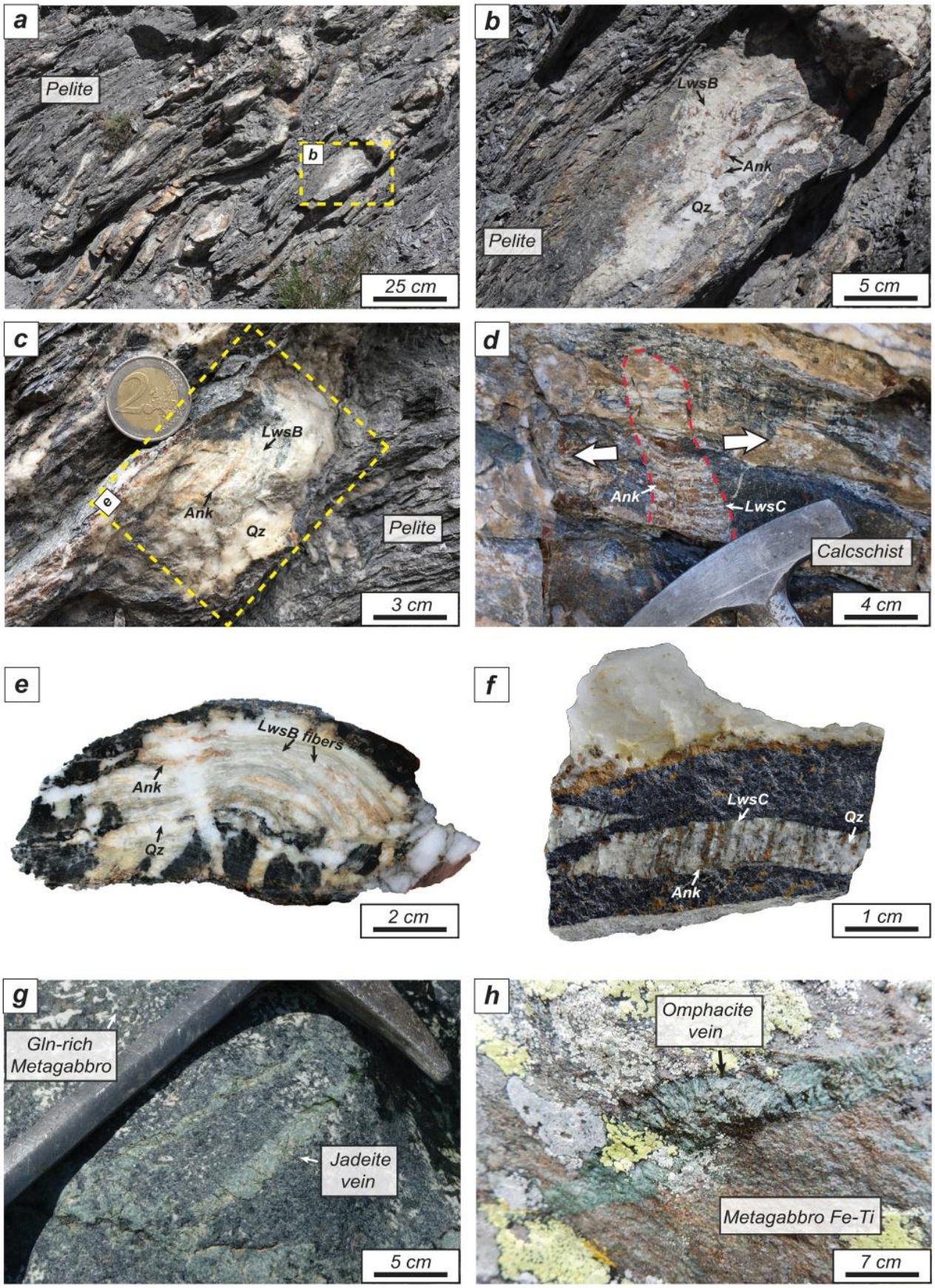

Fig. 4. Field observations. A) Metapelitic outcrop from LPU1 exposing a huge density of veins. B), C) Quartz-lawsonite-ankerite vein showing elongated creamy-coloured LwsB crystals parallel to vein walls. D) Small tensile LwsC vein with ankerite and quartz. E) Closer-view of C sample exposing the association of LwsB fibers with ankerite and quartz. F) Close-up view of LwsC 'en échelon' veins illustrating the association of LwsC with quartz and ankerite. G) Metagabbroic blueschist-facies block from LPU1 containing few veins of greenish-jadeite. H) Close view of omphacite-bearing veins crosscutting an eclogite-facies garnet-rich metagabbro from LPL. Lws: lawsonite; Ank: ankerite; Qz: quartz; Gln: glaucophane.

depends on lithology (see Lefeuvre et al., 2020): they are much more abundant in calcschists containing roughly similar amounts of pelites and carbonates in fine alternations than in carbonate-dominated host rocks (where only calcite ± ankerite veins are present). LwsB-bearing veins are abundant in LPU1, but far less abundant than LwsC tension gashes in LPU2 and LPM.

Fewer Fe-Mg carpholite-bearing veins were observed along this the traverse (which is more carbonate-rich than that of the Cottian Alps) and only one sample containing carpholite needles in a *syn*-foliation quartz vein from LPU1 was collected. Chloritoid is present across most of LPM, showing that carpholite is not stable anymore (Fig. 3; as for the Cottian Alps: Agard et al., 2001; Bebout et al., 2013). By comparison with BS-facies metasediments, eclogite-facies metasediments lack diagnostic veins and/or show strongly transposed veins so that no clear example of peak burial vein could be found in these rocks.

BS-facies metagabbro bodies exhibit jadeite-rich clinopyroxene-bearing peak assemblages, i.e. lawsonite-jadeite-glaucophane in LPU1 and zoisite-jadeite-glaucophane in LPM (Saliot, 1979; Schwartz, 2000; Tricart and Schwartz, 2006) and cm-scale jadeite-veins that could be sampled (Fig. 4g). In eclogite-facies metamafics, we used samples of omphacite ± garnet bearing veins (Fig. 4h) and matrices of eclogitic breccias from Monviso massif of LPL unit (see Locatelli et al., 2018, 2019b).

Outcrops 1 to 4 belong to LPU1 and correspond to metasediments (Fig. 2b, Table 2; 1: east of Château-Queyras; 3: between Ville-Vieille and Aiguilles, Malafosse locality; 4: between Aiguilles and Abriès, Le Gouret locality), except for the outcrop 2 lawsonite-jadeite-glaucophane-bearing metagabbro block (west of Ville-Vieille, close to Guil river). LPU1 samples comprise LwsB- and LwsC-bearing veins (outcrops 1, 3 and 4), one jadeite-bearing vein (outcrop 2) and one carpholite-bearing vein (outcrop 3).

Outcrops 5 and 6 belong to LPU2 (Fig. 2b, Table 2; 5: vallée de la Blanche, near Clausis chapel; 6: bottom of Pain de Sucre, near Col Agnel) and correspond to LwsB- and LwsC-bearing veins in metasediments.

Outcrops 7 to 9 belong to LPM (Fig. 2b, Table 2; 7: Pelvas d'Abries, Col d'Urine; 8: Col Bouchet; 9: between Refuge du Viso and Col Valanta). LPM samples comprise LwsB- and/or LwsC-bearing veins in metasediments (outcrops 8 and 9) and one jadeite-bearing vein (outcrop 7).

Outcrops 10 and 11 belong to LPL (Fig. 2b, Table 2; 10: Intermediate Shear Zone, near Lago Superiore; 11: Lower Shear Zone, east of Rifugio Quintino Sella). Both correspond to Fe-Ti metagabbro blocks metamorphosed, mylonitized and brecciated under eclogite-facies conditions. Omphacite-bearing veins V1 and V2 (see Locatelli et al., 2018, 2019b) crosscutting the mylonitic foliation and M2 matrix of eclogitic breccias were sampled in outcrop 10. M1 matrix of eclogitic breccias was studied in outcrop 11.

4. Analytical strategy and methods

4.1. Fluid inclusion micro-textural analysis and selection

Fluid inclusion (FI) analyses were performed on 100 μm thick double-polished sections. FI were observed using optical microscopy, in order to characterize their morphology, gas/liquid ratios and textural location within crystals. To characterize the pristine fluids present during crystal growth, only fluid inclusions showing good textural evidences of primary entrapment were selected (Fig. 5 a–f; i.e., fluid inclusions either isolated or in non-planar clusters inside mineral grains; Roedder, 1984; Van den Kerkhof and Hein, 2001). The FI were carefully examined and we selected inclusions with the most regular shapes in order to avoid as much as possible post-entrapment modification of FI chemistry. FI aligned on trails crosscutting several mineral grains, considered as secondary inclusions in recrystallized fractures, were not considered in this study.

4.2. Fluid salinity: Microthermometric versus Raman spectroscopy measurements

Microthermometric measurements were carried out on a subset of quartz and omphacite fluid inclusions at ISTeP (Sorbonne Université) using an optical microscope equipped with a Linkam THMSG600 heating-freezing stage (−196 °C to +600 °C) controlled by a Linkam TMS-93 programmer via LinkSys software v.2.15. Ice melting and liquid-vapor homogenization temperatures were reproducible within 0.1 °C (~0.2 wt% NaCl eq.) and 1 °C, respectively. Salinity was estimated from ice-melting temperatures using the equation of Bodnar (1993). Eutectic temperatures were also measured in FI from omphacite veins, in which a complex salt system was assumed. Values are reported in Sup. mat. 1.

In the studied samples, homogenization temperatures (Th) showed a large scatter, suggesting density reequilibration of FI due to deformation during exhumation (Bodnar, 2003b; Diamond, 2003; Raimbourg et al., 2018; Tarantola et al., 2012; Vityk and Bodnar, 1995a, 1995b), as already observed in fluid inclusions trapped in HP conditions in the SL complex (Agard et al., 2000; Philippot and Selverstone, 1991). Th and density measurements were not further performed since our study focuses on fluid compositions and such data would have been meaningless.

Ice-melting temperatures (Tm_{ice}) were difficult to obtain for most FI due to their small size (most FI <10 μm), and only few Tm_{ice} measurement were obtained in Monviso omphacite due to the FI thick walls and stretched, motionless gas bubbles. This resulted in a very limited number of salinity data for most samples.

Salinity can also be determined by Raman spectroscopy with an accuracy of ±0.4 wt% NaCl eq., owing to recent calibrations performed at GeoRessources laboratory (Université de Lorraine, Nancy; Caumon et al., 2013, 2015; Tarantola and Caumon, 2015) as the Raman spectrum of liquid water in the OH stretching vibrations is a function of salinity (Fig. 6). Raman spectroscopy data of our FI set were collected with the very same spectrometers used for calibration in the works above (see § 4.3). Salinities measured by both microthermometry and Raman spectroscopy for a subset of samples (Sup. mat. 1; Fig. 7) are similar within the sum of the respective uncertainties of each method (0.6 wt% NaCl eq.): they plot on the 1:1 line in Fig. 7, showing the validity and good accuracy of Raman spectroscopy for salinity measurements in our samples. This further shows that Raman spectroscopy can be confidently used to determine salinity in all our FI, which enables acquiring a statistically robust dataset for a large number of samples (445 FI studied in 22 samples).

4.3. Raman spectroscopy for salinity, gas and mineral analysis

Most studied FI are two-phase (liquid-vapor) and only some contain daughter mineral phases (three-phase inclusions). Salinity, gas content and nature of daughter minerals of the 445 studied FI were determined by Raman spectroscopy, by focusing the laser on the liquid phase, gas bubble and minerals respectively. Raman measurements were performed at GeoRessources laboratory (Université de Lorraine, Nancy) using a LabRAM HR and a LabRAM spectrometer (Horiba Jobin-Yvon®) equipped with a liquid nitrogen-cooled CCD detector, a 600 groove.mm^{-1} grating for salinity measurements and a 1800 groove.mm^{-1} grating for gas analysis. The excitation light was provided by an Ar^{+} laser (Stabilite 2017, Newport Spectra-Physics) at 514.532 nm at a power of 200, 160 or 120 mW, focused on the sample using a 100× objective (Olympus).

Salinities were determined using the method described in Caumon et al. (2013, 2015) and Tarantola and Caumon (2015). Raman spectrum of water in the studied FI were acquired and salinity were determined using the intensity ratio of two defined positions (3260 and 3425 cm^{-1}) after subtraction of a linear baseline.

Table 2
Studied samples and corresponding outcrop localities and estimated P-T conditions P-T conditions estimated from host-rock and segregation parageneses in: [(1)] Schwartz et al. (2013); [(2)] Agard et al. (2001); [(3)] Locatelli et al. (2018). Lws: lawsonite; Qz: quartz; Ank: ankerite; Chl: chlorite; Ph: phengite; Jd: jadeite; Gln: glaucophane; Cal: calcite; Omp: omphacite; Grt: garnet; Ap: apatite; Rt: rutile.

Outcrop	Unit	Peak T / P	Sample #	Host rock	Segregation mineralogy	Longitude	Latitude
1. Château-Queyras	LPU1	332 °C[(1)]/ ~10–13 kbar[(2)]	1LwsB	Calcschist	Lws-Qz-Ank + late Chl and Ph	6.793083	44.757933
			1LwsC				
2. Guil river		328 °C[(1)]/ ~10–13 kbar[(2)]	2Jd	Metagabbro	Jd-Gln + late Cal	6.817350	44.761550
3. Malafosse		336 °C[(1)]/ ~10–13 kbar[(2)]	3LwsB	Calcschist	Lws-Qz + late Chl and Ph	6.840083	44.771133
			3LwsC		Lws-Qz-Ank		
			3Car		Car-Qz + late Chl		
4. Gouret		336–367 °C[(1)]/ ~10–13 kbar[(2)]	4LwsB		Lws-Qz-Ank + late Chl and Ph	6.887066	44.788583
			4LwsC				
5. Blanche	LPU2	356 °C[(1)]/ ~12–13 kbar[(2)]	5LwsB	Calcschist	Lws-Qz-Ank-Cal + late Chl and Ph	6.925016	44.662983
			5LwsC				
6. Pain de Sucre		373 °C[(1)]/ ~13–16 kbar[(2)]	6LwsB			6.990050	44.693683
			6LwsC		Lws-Qz-Ank + late Chl, Ph and Cal		
7. Pelvas	LPM	389–402 °C[(1)]/ ~18–20 kbar[(2)]	7Jd	Metagabbro	Jd-Gln	6.995666	44.796806
8. Bric Bouchet		402 °C[(1)]/ ~18–20 kbar[(2)]	8LwsC	Calcschist	Lws-Qz-Ank + late Chl and Ph	7.015416	44.811850
9. Valanta		469 °C[(1)]/ ~20 kbar[(2)]	9LwsB		Lws-Qz-Ank + late Chl, Ph and Cal	7.063700	44.683667
			9LwsC		Lws-Qz-Ank + late Chl and Ph		
10. ISZ	LPL	580 °C/ 27 kbar[(3)]	10OmpV1a	Metagabbro	Omp-Ap	7.087500	44.693889
			10OmpV1b				
		560 °C/ 24 kbar[(3)]	10OmpV2a		Omp-Grt		
			10OmpV2b				
			10OmpM2				
11. LSZ		580 °C/ 27 kbar[(3)]	11OmpM1		Omp-Rt	7.134166	44.670000

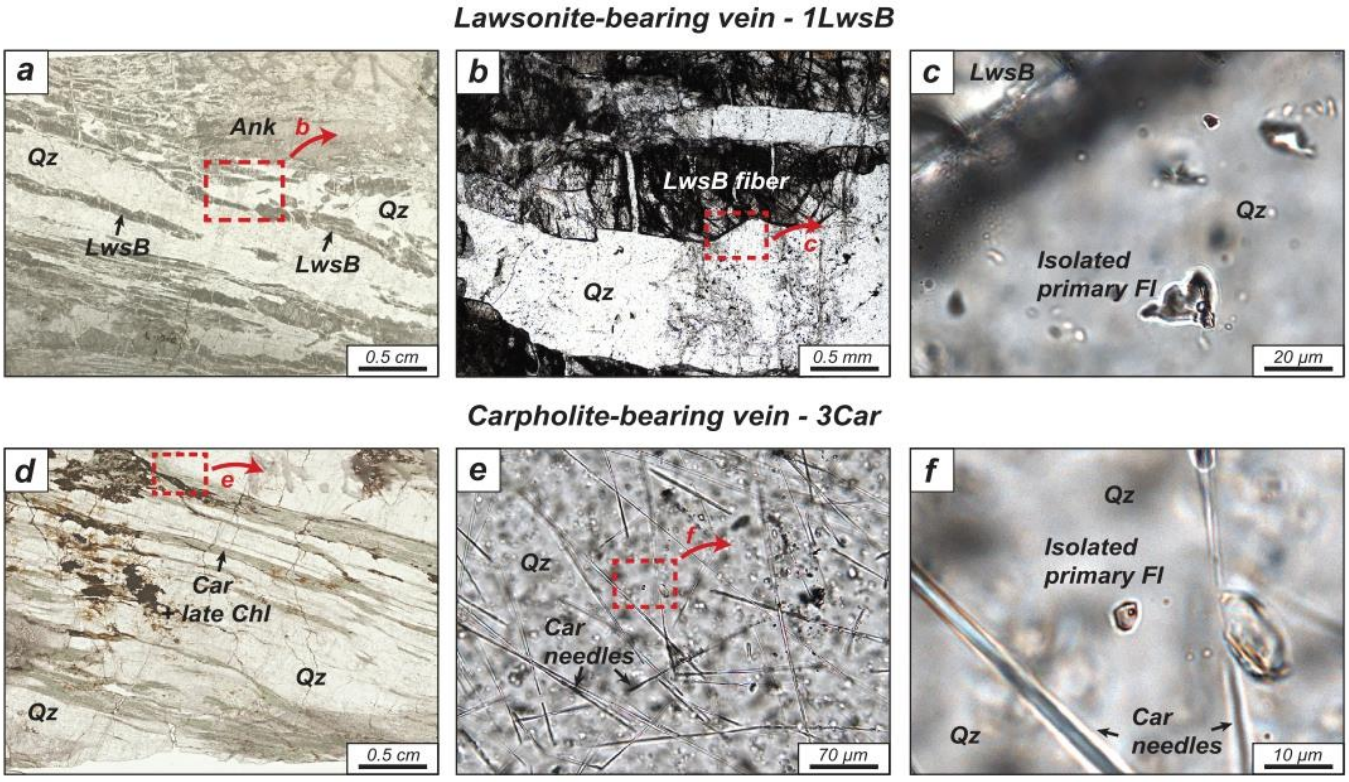

Fig. 5. Microphotographs of veins illustrating mineral crystallization textures and trapped primary fluid inclusions. A) Thick-section of LwsB-bearing vein from LPU1. B) Closer-view of A) showing textural equilibrium between lawsonite (Lws) and quartz (Qz) fibers. C) Closer-view of B) showing isolated primary fluid inclusions in the quartz co-crystallizing with lawsonite. D) Thick section of carpholite (Car)-bearing vein sample from LPU1. E) Closer-view of D) exposing quartz full of carpholite needles. F) Closer-view of E) showing an isolated primary fluid inclusion in quartz co-crystallizing with carpholite.

For gas analysis, Raman spectra were corrected using an ICS function (Intensity Correction System) to normalize the instrument response with wavelength. Gas spectra were identified using peak positions compiled by Frezzotti et al. (2012). CO_2 was detected by the presence of the Fermi diad (Fermi, 1931; 1285 and 1388 cm^{-1} peaks, Fig. 8a), CH_4 by the major band at 2917 cm^{-1} (Fig. 8a) and N_2 by the major band at 2331 cm^{-1} (Fig. 8b). Presence of N_2 in the inclusion was then confirmed by subtraction of the atmospheric N_2 peak area on the main band of N_2 detected in inclusion. For CO_2-CH_4 mixtures, peak areas were computed after substraction by a linear baseline. Molar proportions of each gas in

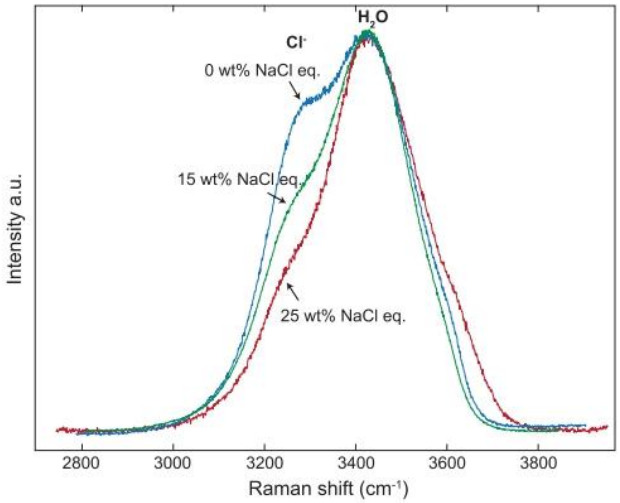

Fig. 6. Raman spectra of the liquid phase of three fluid different inclusions in quartz of LwsB-bearing veins and in omphacite from eclogitic breccia matrices. The variable shape of the chlorinity band allows calculation of salinity following the method of Caumon et al. (2013). a.u.: arbitrary unit.

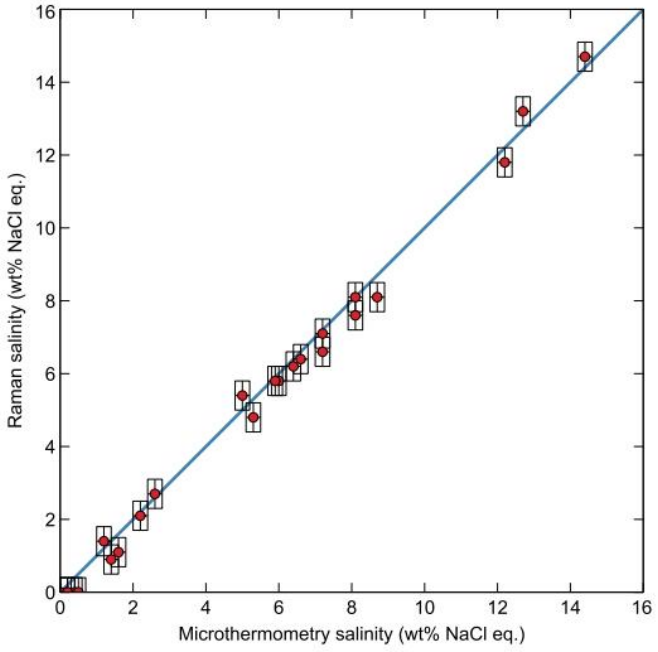

Fig. 7. Salinity estimated by microthermometry versus salinity estimated by Raman spectroscopy in the same inclusions. Taking into account the respective uncertainties of these methods (0.2 wt% NaCl eq. for microthermometry and 0.4 wt% NaCl eq. for Raman considering the methodology of Caumon et al., 2013) all points are crossing the 1:1 line showing the validity and accuracy of Caumon et al. (2013) method in our samples.

the mixtures were determined using the respective area and the corresponding relative Raman scattering cross-section (RRSCS; Wopenka and Pasteris, 1987). We choose to use the recent values of Le et al. (2019, 2020) for RRSCS of CO_2 (1.40 ± 0.03 for the 1388 cm^{-1} peak and 0.89 ± 0.02 for the 1285 cm^{-1} peak) and CH_4 (7.73 ± 0.16 for the major band at 2917 cm^{-1}).

Daughter minerals were identified using the data compilation of Frezzotti et al. (2012).

5. Petrography and microstructural analysis of fluid inclusions

5.1. Lawsonite-bearing veins (LPU1-LPU2-LPM)

All studied samples of LwsB-bearing veins contain idiomorphic-fibrous crystals of lawsonite. These fibers are parallel to the vein walls, generally several cm-long and mm-thick and always exhibit fine alternation with quartz fibers and commonly ankerite (Fig. 5a, b). Lawsonite is frequently pseudomorphed in the veins by fine-grained assemblages of phengite, chlorite and calcite, as previously reported (Lefeuvre et al., 2020; Sicard-Lochon, 1987; Vitale Brovarone et al., 2014). Similar features are observed in LwsC-bearing veins except that fibers are smaller, more often replaced by the late-greenschist facies assemblage (phengite, chlorite, calcite) and ankerite is always present in apparent equilibrium with quartz and LwsC fibers.

FI were systematically studied in quartz co-crystallizing with lawsonite ± ankerite fibers (Fig. 5a–c). Although FI are commonly very densely packed, hampering a correct assessment of their primary or secondary nature (Fig. 9a), some are found in quartz grain cores as isolated inclusions or in non-planar-clusters indicating primary entrapment. Inclusion sizes are 5–15 μm and rarely reach 20 μm. These inclusions are mostly two-phase (L + V; Fig. 9b, c) with a vapor bubble occupying typically ~10–20% of the inclusion volume. These inclusions commonly show a well-defined slightly elongate shape (Fig. 9b–e), but some exhibit angular shapes suggesting post-entrapment modification (Fig. 9d). A small number of isolated primary FI are monophase (L), suggesting metastability. Out of over 250 FI from lawsonite-bearing veins, only four (all from sample 1LwsB) are three-phased (L + V + S), with two of them containing a cubic highly-refractive crystal (Fig. 9e).

5.2. Carpholite-bearing veins (LPU1)

In the carpholite–bearing sample (outcrop 3), almost all carpholite crystals are replaced by retrograde chlorite. Preserved fresh carpholite occurs as needle clusters in quartz, highlighting co-crystallization of carpholite and quartz during BS-facies conditions (Fig. 5d–f).

FI were only characterized in quartz crystals hosting carpholite needles (Fig. 5f) and are very similar to those of lawsonite veins. Primary FI are biphase (L + V), 5–20 μm in size and occur as isolated or in non-planar clusters (see also Agard et al., 2000). The vapor bubble also represents ~10–20% of the inclusion volume, and the FI generally have regular shapes.

5.3. Jadeite-bearing veins (LPU1 and LPM)

Jadeite-bearing veins are composed of jadeite idiomorphic green crystals with multiple orientations (Fig. 9f) and few glaucophane crystals generally filling fractures.

FI have a well-defined tubular shape and are generally small in 2Jd sample (LPU1, a few micrometers, rarely up to 20 μm), while slightly bigger in 7Jd sample (LPM, 5–20 μm in size, rarely up to 25 μm). All these inclusions are systematically oriented parallel to the c-axis of jadeite crystals and occur as isolated or in non-planar clusters (Fig. 9f), suggesting primary entrapment. These inclusions are generally biphase (L + V) but few monophase (L), biphase (L + S; 2/23 in 2Jd) or triphase FI (L + V + S; 2/23 in 2Jd) were identified. The vapor bubble generally occupies ~5–10% of the inclusion total volume in 2Jd sample and ~ 20% in 7Jd sample.

5.4. V1 and V2 omphacite (± garnet) bearing veins (LPL)

V1 veins are almost parallel to the eclogitic foliation. They are filled by pluri-millimeter-long fibrous and euhedral omphacite crystals. These crystals are generally oriented perpendicular to the vein walls and show concentric-zoning. V2 veins are filled with omphacite and

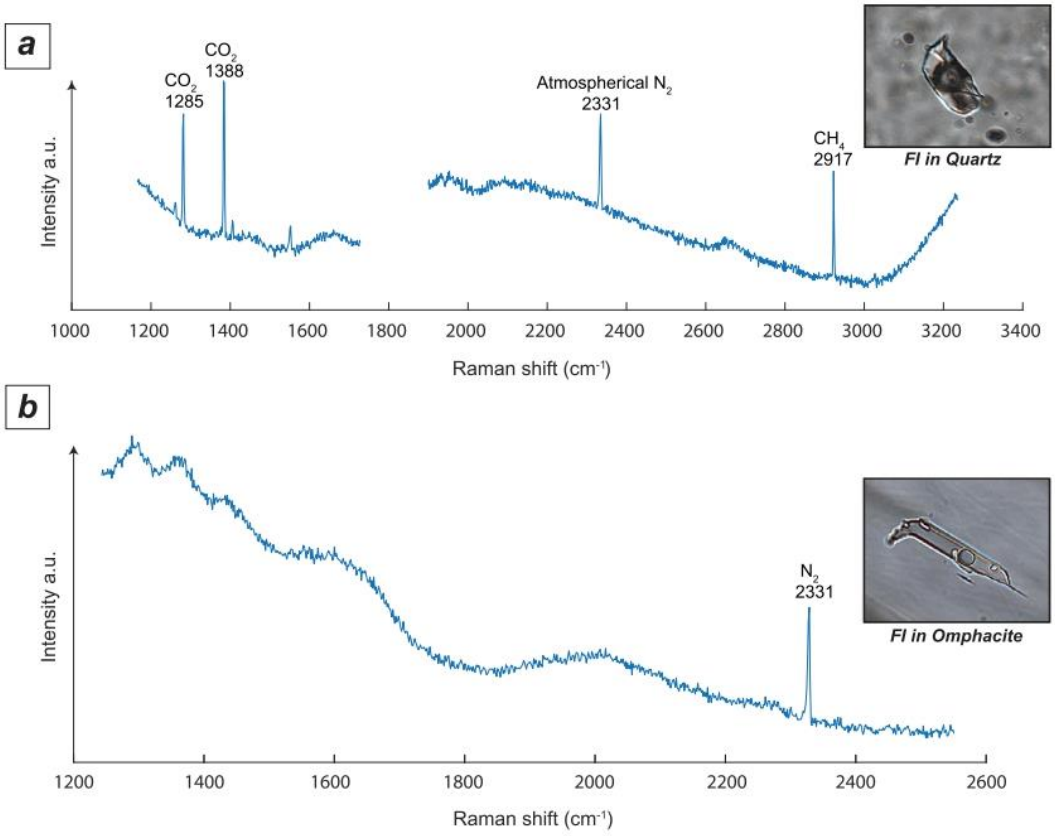

Fig. 8. Raman spectra of the main gases identified FI vapor bubbles. a) CO_2 presence was detected by identification of the Fermi diad (Fermi, 1931; 1285 and 1388 cm^{-1} peaks) and CH_4 by appearance of the 2917 cm^{-1} peak (Frezzotti et al., 2012). b) N_2 is characterized by a peak at 2331 cm^{-1} (Frezzotti et al., 2012) and calculated by substraction of atmospherical N_2 peak area (outside the FI). a.u.: arbitrary unit.

garnet. Garnet is idiomorphic, mm-sized, while omphacite crystals are slightly smaller than in V1 veins.

In both vein types, most primary FI are concentrated in the core of omphacite crystals, to which their dense clustering gives a darkish color (Fig. 9g). These inclusions occur as isolated or in non-planar clusters. They are tubular-shaped, typically 10–20 μm large and up to ~40 μm, and are always oriented parallel to the c-axis of omphacite (Fig. 9h, i). There are as many biphase (L + V) as triphase (L + V + S; Fig. 9h, i) inclusions, and the vapor bubble generally occupies 15–20% of the inclusion total volume. Triphase inclusions generally contain one or several transparent anisotropic solids and some a cubic-shaped darkish-coloured opaque solid. In many of these inclusions, material recrystallized on the inclusion borders, creating thick internal walls that squeeze the (often elongate) gas bubble. The refraction index suggests it could be omphacite.

5.5. M1 omphacite-bearing and M2 omphacite-garnet-bearing matrices (LPL)

M1 matrix of Monviso eclogitic breccias is almost entirely made of light-green idiomorphic crystals of omphacite with minor apatite, while M2 matrix is dominantly composed of euhedral omphacite crystals with idiomorphic zoned garnets.

In M1 matrix, FI are isolated or in non-planar clusters and oriented parallel to the omphacite-c axis, again suggesting primary entrapment. Most inclusions are 5–10 μm sized, generally biphase (L + V) and rarely triphase (L + V + S; 5/24), containing a colorless solid. The vapor bubble has an almost constant volume representing 10–15% of the inclusion total volume.

M2 matrix primary FI are relatively similar: 5 to 15 μm in size, rarely 20 μm, parallel to the omphacite c-axis. These inclusions are biphase (L + V) and only two triphase (over 19; L + V + S) were observed, one with an opaque solid, the other with a colorless solid. The vapor bubble generally occupied ~10% of the inclusion total volume. As for the omphacite-bearing veins, some inclusions expose thick walls of recrystallized material.

6. Fluid inclusion chemistry

276 FI from metasedimentary veins, 43 FI from BS mafic samples and 126 FI from eclogitic mafic samples were analyzed by Raman spectroscopy to determine fluid salinity, gas content and the nature of daughter minerals.

6.1. Fluid inclusion salinity

6.1.1. Lawsonite and carpholite veins (LPU1, LPU2 and LPM)

The fluid salinity estimated in primary FI from lawsonite-bearing quartz veins generally shows low to intermediate salt concentrations (mean: 4.8 wt% NaCl eq.; median: 3.2 wt% NaCl eq.) and fairly variable values (standard deviation sd: 4.1). Detailed salinity values for lawsonite-bearing veins in each outcrop are (mean; median; sd; in wt% NaCl eq and FI numbers): outcrop 1 (11 wt%; 7.8 wt%; 8.1; $n = 34$); outcrop 3 (1.8 wt%; 1.8 wt%; 1.4; $n = 33$); outcrop 4 (6.4 wt%; 6.3 wt%; 3.2; $n = 44$); outcrop 5 (6.1 wt%; 3.9 wt%; 5.8; n = 44); outcrop 6 (2.8 wt%; 2.6 wt%; 2.3; n = 44); outcrop 8 (4.3 wt%; 3.2 wt%; 4.1; $n = 14$) and outcrop 9 (1.2 wt%; 0.9 wt%; 1.2; $n = 41$). No obvious salinity difference between LwsB- and LwsC-bearing veins was detected in any sample. The carpholite-

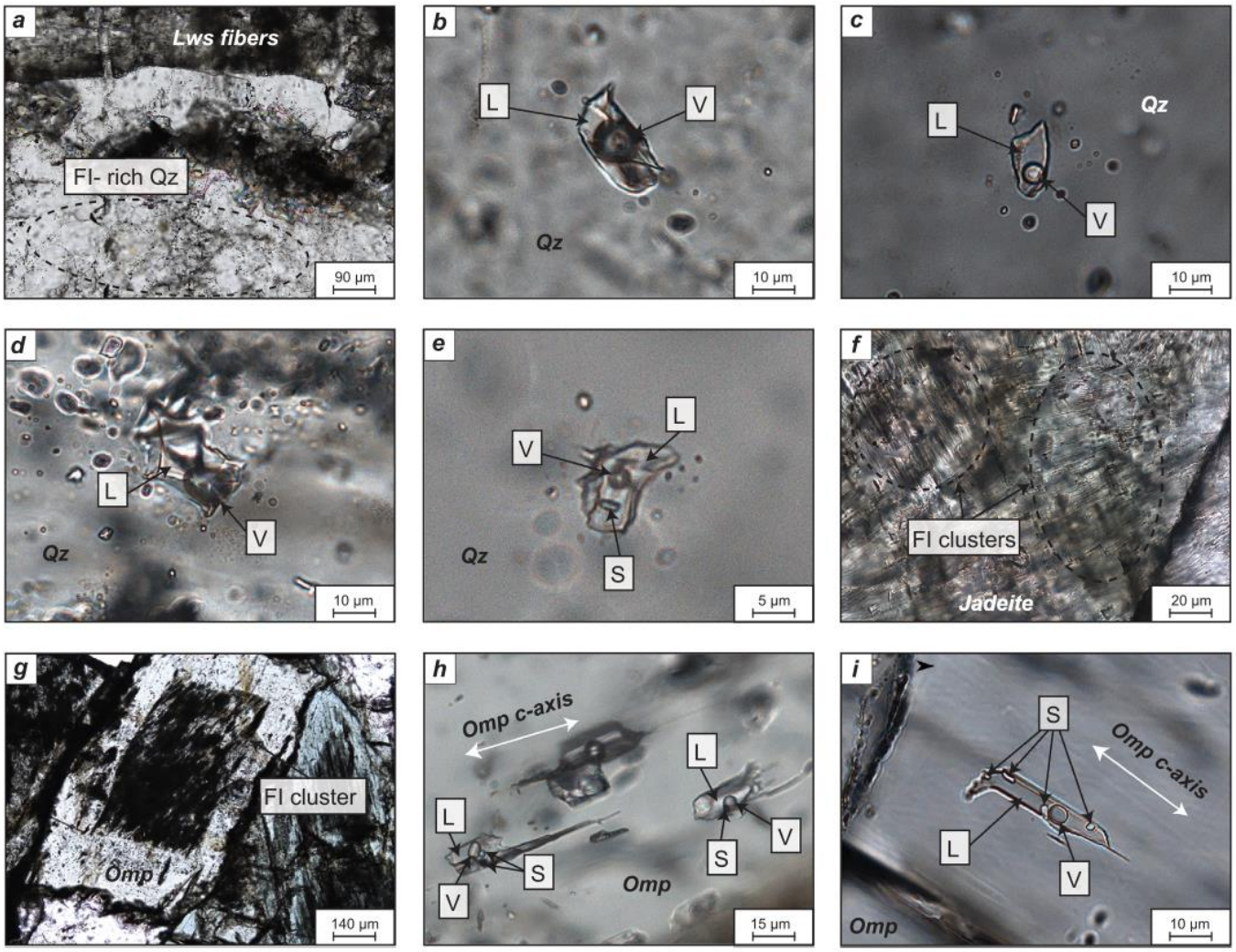

Fig. 9. Microphotographs of fluid inclusions. A) FI-rich quartz (Qz) showing textural equilibrium with LwsB fibers. B) and C) Biphase (liquid L + vapor V) well-defined inclusions in quartz from lawsonite (Lws)-bearing veins. D) Biphase (L + V) fluid inclusion with irregular shape, in quartz from a lawsonite-bearing vein. E) Rare triphase (L + V+ solid S) fluid inclusion in quartz from LwsB outcrop1 vein. F) Distribution of FI clusters in jadeite crystals. All these primary inclusions are oriented parallel to c-axis of the clinopyroxene. G) Zoned crystal of omphacite (Omp) from a V2 vein. Note the presence of the FI-rich dark core. H) Biphase and triphase FI in omphacite from V1 vein. The inclusions are oriented parallel to omphacite c-axis and triphase inclusions contain various colorless and opaque solids. I) Triphase 25 µm-long fluid inclusion from a V2 vein. The FI is oriented parallel to omphacite c-axis and contains four colorless solids.

bearing sample from outcrop 3 has a low-salinity range similar to the lawsonite-bearing samples from the same outcrop (2.4 wt%; 2.7 wt%; 1.5; $n = 22$).

Since a clear eastward increase in metamorphic grade is observed along this traverse (Fig. 3), measured salinities are presented as a function of longitude (Fig. 10a). Vein salinities in metasedimentary rocks show a decreasing trend of average salinity towards the east, from outcrop 1 (11 wt% NaCl eq.) to outcrop 9 (1.2 wt% NaCl eq.). This trend is further illustrated in Fig. 10b–d, where salinity data are represented in cumulative bar-charts for each unit. In each chart, salinities follow an approximate normal Gaussian distribution truncated at low values and show a decreasing salinity trend at the unit scale, from LPU1 (5.8 wt%; 4.2 wt%; 5.8; $n = 133$) to LPU2 (4.4 wt%; 3.1 wt%; 4,68; $n = 88$) and to LPM (2.0 wt%; 1.3 wt%; 2.63; $n = 55$). In LPU1, FI salinity is highly variable (sd: 5.8), particularly for outcrop 1 where salinities are frequently above 10 wt% NaCl eq. and even >25 wt% NaCl equivalent. Measured salinities for this unit are generally above early Cretaceous seawater salinity (~ 3.2–3.7 wt%; Hay et al., 2006), whereas in LPU2 and LPM salinities are mostly close or lower to seawater salinity.

6.1.2. Jadeite-bearing veins (LPU1 and LPM)

In BS-facies jadeite-bearing veins, FI salinity is generally higher than in surrounding metasediments (16.4 wt%; 11.8 wt%; 9.4; $n = 43$). Intermediate values of salinity are found for 2Jd sample from LPU1 (Fig. 10a, b; 9.1 wt%, 9.1 wt%; 2.8; $n = 23$), while fluid salinity is higher in 7Jd sample from LPM (Fig. 10a, c; 24.6 wt%. 28.4 wt%; 7.1; $n = 20$).

6.1.3. V1 and V2 omphacite (±garnet) bearing veins (LPL)

Eclogite-facies omphacite-bearing veins from LPL share similar salinity ranges. These salinities are intermediate to high for both V1 (Fig. 10a, e; 14.6 wt%; 13.3 wt%; 5.4; $n = 37$) and V2 (Fig. 10a, e; 14.6 wt%; 14.8 wt%; 4.1; $n = 46$).

Eutectic temperatures measured in 10OmpV1 sample range from −22.0 °C to −24.3 °C (Sup. mat. 1). These temperatures are lower than pure H_2O-NaCl eutectic temperature (−21.2 °C) and close to H_2O-NaCl-KCl eutectic temperature (−22.9 °C; Bodnar, 2003a), suggesting the presence of both NaCl and KCl. Minor presence of $MgCl_2$ and/or CaCl2 could account for the lowest eutectic temperatures (eutectic temperatures: H_2O-NaCl-$MgCl_2$: -35 °C; H_2O-NaCl-$CaCl_2$: -52 °C; Davis et al., 1990; Bodnar, 2003a).

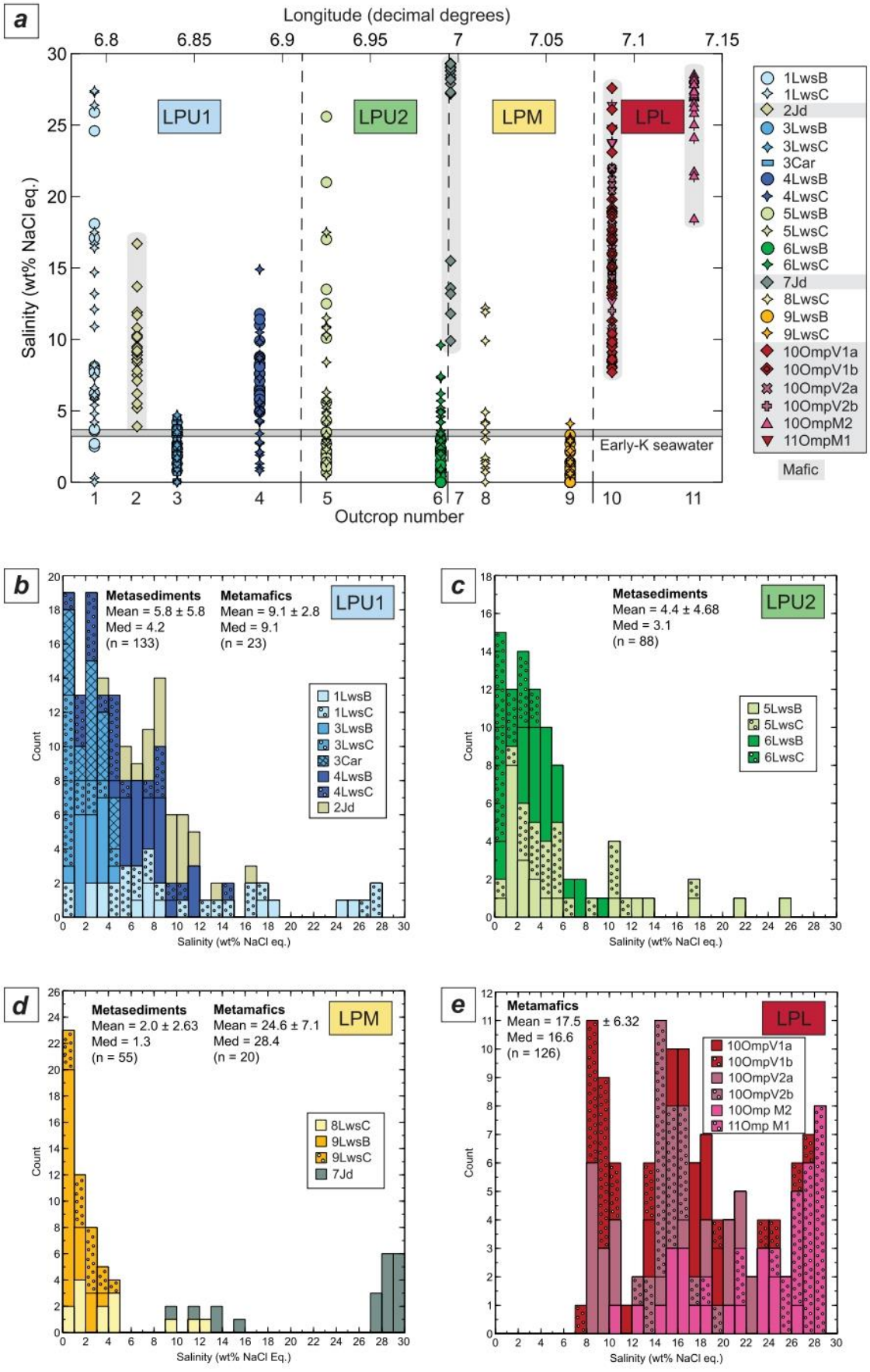
a
Longitude (decimal degrees)
6.8
6.85
6.9
6.95
7
7.05
7.1
7.15
Salinity (wt% NaCl eq.)
LPU1
LPU2
LPM
LPL
Early-K seawater
Outcrop number
1LwsB
1LwsC
2Jd
3LwsB
3LwsC
3Car
4LwsB
4LwsC
5LwsB
5LwsC
6LwsB
6LwsC
7Jd
8LwsC
9LwsB
9LwsC
10OmpV1a
10OmpV1b
10OmpV2a
10OmpV2b
10OmpM2
11OmpM1
Mafic
b
Metasediments
Mean = 5.8 ± 5.8
Med = 4.2
(n = 133)
Metamafics
Mean = 9.1 ± 2.8
Med = 9.1
(n = 23)
LPU1
Count
Salinity (wt% NaCl eq.)
c
Metasediments
Mean = 4.4 ± 4.68
Med = 3.1
(n = 88)
LPU2
d
Metasediments
Mean = 2.0 ± 2.63
Med = 1.3
(n = 55)
Metamafics
Mean = 24.6 ± 7.1
Med = 28.4
(n = 20)
LPM
Salinity (wt% NaCl Eq.)
e
Metamafics
Mean = 17.5 ± 6.32
Med = 16.6
(n = 126)
LPL
10OmpV1a
10OmpV1b
10OmpV2a
10OmpV2b
10Omp M2
11Omp M1

6.1.4. M1 Omphacite-bearing and M2 omphacite-garnet-bearing matrices (LPL)

As in omphacite-bearing veins, salinity of fluids trapped in matrices from eclogitic breccias are clearly higher than seawater salinity, with high values for both M1 (Fig. 10a, e; 26.4 wt%; 27.2 wt%; 2.6; $n = 24$) and M2 matrix (Fig. 10a, e; 18.9 wt%; 17.4 wt%; 4.6; $n = 19$).

6.2. Fluid inclusion gas content

6.2.1. BS-facies metasediments: Lawsonite- and carpholite-bearing veins

In FI vapor bubble from metasedimentary veins, the two peaks constituting the fermi diad of CO_2 (1285 cm^{-1} and 1388 cm^{-1}) and the 2907 cm^{-1} peak of CH_4 were identified in most of our inclusions and a Raman signal strong enough to make quantitative measurements was obtained in 110 FI. The molar proportion of each gas in the CO_2-CH_4 gas mixtures is represented according to FI salinity (Fig. 11). LwsC-bearing vein FI generally contain proportionnaly more CH_4 in CO_2-CH_4 mixtures (CO_2%; Mean: 29.4%; Med: 25.4%; n = 44) than in LwsB- (CO_2%; Mean: 67%; Med: 82%; $n = 57$) and carpholite-bearing veins (CO_2%; Mean: 88.1%; Med: 90.4%; $n = 9$). Contrary to salinity, gas ratios do not show any particular correlation with P-T conditions.

In very few FI from LPU2 Lws-bearing veins (2 FI over 46 analyzed in 5LwsB and 5LwsC samples), several peaks were identified in the 2800–3000 cm^{-1} region (Fig. 12). These peaks correspond to the symmetrical and asymmetrical stretching vibrations of CH_2 and CH_3. These spectra, exclusively detected inside fluid inclusions, were carefully compared to the Raman spectra of the glue and oil used for sample preparation (Sup. mat. 2) and showed systematically different patterns. Distribution of peak positions corresponds to saturated hydrocarbons and fits well with pentane spectra (Sterin et al., 1980). These FI, visually identical to the aqueous ones (biphase, L + V), thus contain potential liquid and gaseous hydrocarbons (HC) heavier than CH_4 without any detectable trace of water or other gas species.

6.2.2. BS-facies metamafics: Jadeite-bearing veins

In jadeite-bearing vein samples from LPU1 and LPM, no gas (other than H_2O vapor) was detected in the vapor bubble of aqueous inclusions. Nevertheless, potential hydrocarbon spectra similar to those of Lws-bearing veins were detected in 3/26 FI of 2Jd sample (LPU1) and in 5/24 FI of 7Jd sample (LPM). These hydrocarbons were identified in monophase (L) and few biphase (L + S) inclusions.

6.2.3. Eclogite-facies metamafics: Omphacite-bearing veins and matrices

N_2 was frequently detected in omphacite-bearing veins V1 (in 10/17 FI) and V2 (in 18/29 FI), in particular in triphase (L + V + S) and in few biphase (L + V) inclusions. N_2 was similarly detected in M2 matrix (in 5/13 FI) in the biphase and the only triphase inclusions. Conversely, no gas (other than H_2O) was detected in the bubble of analyzed aqueous FI from M1 matrix.

6.3. Solids in fluid inclusions

In Lws-bearing veins, only four FI, all from 1LwsB and showing very high salinity (i.e. salinity exceeding NaCl-saturation value in water at room temperature), contain solids. Calcite was identified by Raman analysis in two of them. The other two FI contain colorless solids undetectable by Raman spectroscopy, with a cubic habit resembling that of salt crystals, which is in good agreement with the high salinity determined for these inclusions. We posit that these solids are daughter minerals formed by fluid supersaturation with respect to salts under post-entrapment decreasing P-T conditions. Similar crystals probably failed to nucleate due to metastability in the other rare high salinity inclusions of this sample (Bodnar, 1994, 2003a).

In Jd3 bearing-sample, calcite was detected in two aqueous FI and a white mica was detected in one aqueous FI and one HC-rich FI. These solids were only found in rare inclusions and are not systematically present in all FI of a cluster. Such crystals are regarded as having formed by post-trapping reactions between the fluid and the host mineral.

In omphacite-bearing veins and matrices from Monviso, Raman spectra of the FI thick walls are systematically similar to host omphacite spectra but with different peak intensity ratios, which suggests that these walls are made of omphacite with different orientations, ie. omphacite recrystallized during decreasing P-T conditions. About half of the FI from V1 and V2 veins contain solids, calcite being the more common (19 occurrences). Calcite was frequently detected in clustered FI with similar phase ratio (liquid/gas/solid) suggesting that these solids are daughter minerals. White micas were detected in three calcite-bearing inclusions in these veins and could have formed by post-trapping fluid-host mineral reactions. Opaque cubic solids (7 occurrences in calcite-bearing FI) could not be identified because they were systematically too mobile under the laser. These opaque solids could have formed by post-trapping fluid-host mineral reactions, or were accidentally trapped in these inclusions. An opaque solid was also detected in one FI from M2 matrix and calcite detected in two FI from M1 matrix. Finally, in 12 FI, colorless solids remained undetected by Raman spectroscopy. Such crystals are very small and may have too low Raman signals to be detected. However, most of them occur in highly-saline FI (i.e., salinity close to or exceeding salt-saturation values in water at room temperature) from omphacite-bearing matrices and veins, and could therefore be salt crystals. However, during microthermometric measurements, none of these crystals could be dissolved in FI even at temperatures about 450–500 °C.

7. Discussion

7.1. Validity of salinity data

7.1.1. Possible origin for salinity variations

Salinity data appear homogeneous for some localities (e.g., #3, 6, 9) but exhibit large variations in others, in both metasediments (e.g., LPU1: 1LwsB, 1LwsC; LPU2: 5LwsB, 5LwsC; Fig. 10a–c) and metamafics (localities #7,10; LPM and LPL; Fig. 10a, e). Such variations may either reflect sequential trapping during vein growth of fluids with variable salt concentrations or post-entrapment modification of inclusions. Although the least deformed lawsonite-bearing HP veins were sampled, some quartz crystals in metasediments may have been slightly deformed during retrograde exhumation (D2, D3). This process affects fluid inclusion shape and density, but chemistry is supposed to be largely preserved, at least for intact FI (Diamond et al., 2010).

However, partial leakage of fluid inclusions with preferential release of small amounts of H_2O (i.e., increasing salinity; Bakker and Jansen, 1990, 1991, 1994; Hall and Sterner, 1993) cannot be excluded, and could account for the few outliers with higher salinity in outcrops 2, 5 and 8. For outcrop 5, this interpretation is also supported by the slightly irregular shapes of high-salinity FI indicating potential partial leakage, whereas FI with clustered salinities have a more regular shape. In contrast, the large salinity range observed for outcrop 1 is difficult to explain by post-entrapment partial leakage only since most fluid

Fig. 10. Raman spectroscopy-derived salinity of analyzed fluid inclusions in metasediments and metamafic rocks. A) Measured fluid inclusion salinity for each outcrop, plotted with increasing longitude. Rock units on the Queyras-Monviso transect are characterized by increasing P-T conditions from West (on the left of the graph) to East (right of the graph), thus increasing longitude reflects increasing burial depth. A general salinity-decrease trend with increasing burial depth is observed in metasediments from LPU1 to LPM, while metamafics are generally more saline in both blueschist- and eclogite-facies slices. A 0.4 wt% NaCl eq. uncertainty for salinity values is represented after Caumon et al. (2013). B to E) Cumulative Bar-chart of salinity for each tectonometamorphic unit illustrating the salinity-decrease trend with increasing burial depth in metasediments and the highest salinities in metamafics.

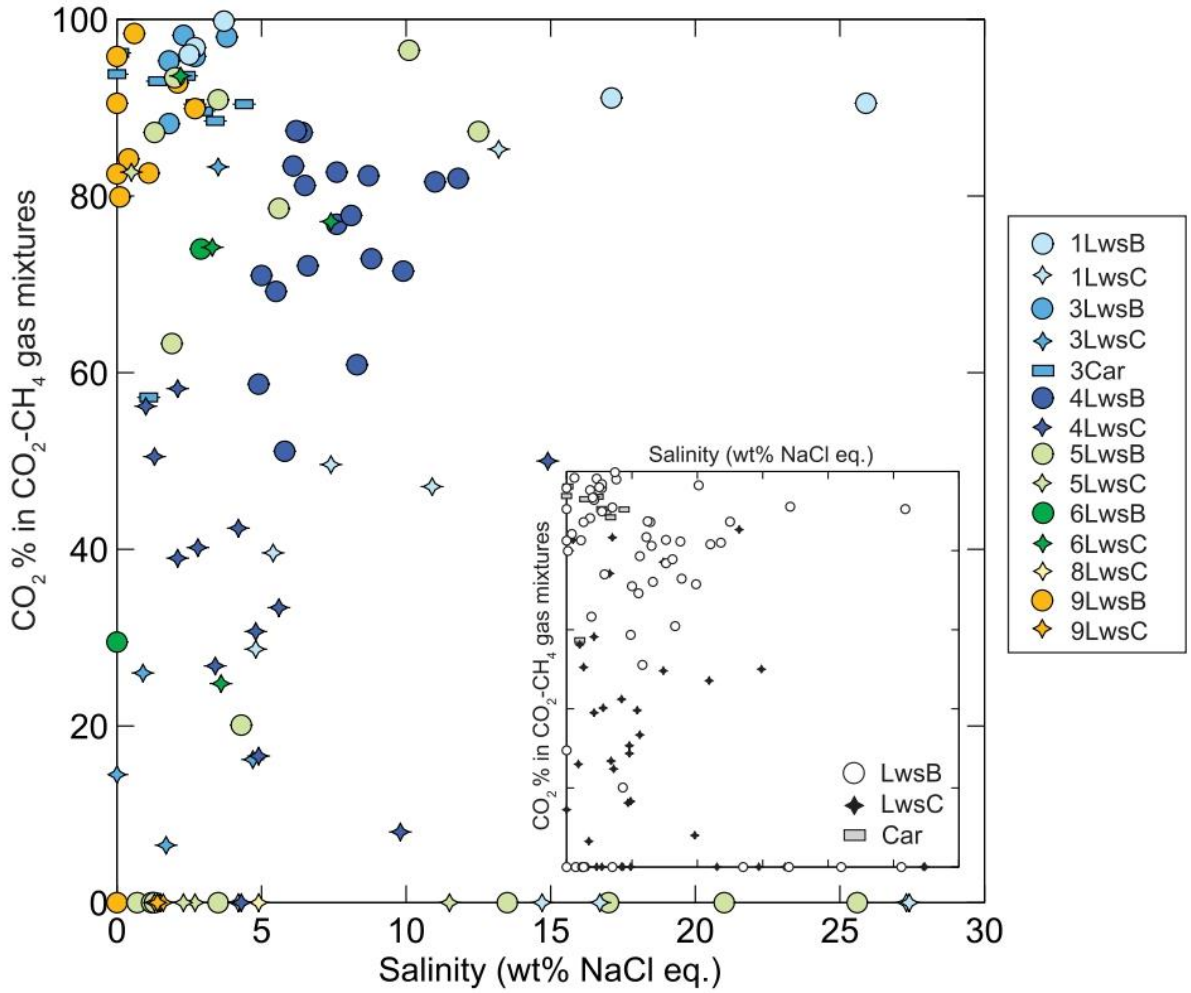

Fig. 11. Salinity versus gas content in fluid inclusions from metasediments. Salinity of the liquid phase and amount (mol%) of CO_2 in the CO_2-CH_4 gas mixtures of vapor bubbles were determined from Raman spectroscopy analyses. LwsB- and Car-bearing veins generally contain more CO_2 than CH_4, while LwsC-bearing vein gas content is dominated by CH_4. A 0.4 wt % NaCl eq. uncertainty for salinity values is represented after Caumon et al. (2013). Simplified graph with all veins in black and white color is on lower right with same units and axes.

inclusions show regular shapes, even for LwsC vein high-salinity data, and rather suggests entrapment of a variably saline fluid. Note that as we only analyzed FI with the most regular shapes, the link between FI morphology and potential partial leakage is however too weak to allow discarding any outlier. All data are thus considerd in Fig. 10a–e.

In mafic outcrop 10 from Monviso LPL, all vein and matrix generations show large salinity ranges (Fig. 10e). The absence of macroscopic deformation of vein and matrix omphacite and the higher salinities reported for low-strained omphacite, compared to mylonitic omphacite of the surrounding rock (Nadeau et al., 1993), likely discard a systematic deformation-induced salinity increase in FI.

7.1.2. Validity of Raman salinity measurements

A few FI from Monviso LPL veins and matrices nevertheless contain colorless crystals undected by Raman spectroscopy, that could be salt crystals, but could not be dissolved in the liquid phase even at temperatures of 450–500 °C. This was also observed on similar Monviso omphacite vein FI by Philippot and Selverstone (1991) and Nadeau et al. (1993), who reported FI decrepitation at about 500 °C before any dissolution of daughter crystals. If these crystals are salts, these FI could have experienced deformation-induced salinity increase and their present-day salinities would be underestimated by Raman measurements, which indicate the salinity of the fluid coexisting with the salt crystal.

Crystallization of other secondary phases in FI during exhumation could also account for changes in fluid salinity (Frezzotti and Ferrando, 2015). Indeed, most fluid inclusions in eclogitic veins and matrices are coated by thick walls of material crystallized from the fluid, reflecting decreasing mineral solubility with decreasing P-T conditions. The refraction index and Raman analyses suggest that most of this coating could be newly-formed omphacite, but a variety of other solids were also observed in these fluid inclusions, both in this study and a previous one on similar omphacite veins (Philippot and Selverstone, 1991). Such secondary crystallization, in particular of H_2O-rich white mica, may slightly modify fluid inclusion salinity (Frezzotti and Ferrando, 2015).

In some FI, measured salinities exceed salt-saturation values in water at room temperature (Fig. 10a–e; salinities up to 30 wt% NaCl eq., while saturation is at 23.2 wt% NaCl eq.) although no salt crystal could be observed. This is true for most FI of mafic outcrops 7 and 11 and also concerns a few FI from mafic outcrop 10 and metasedimentary outcrops 1 and 5 (Fig. 10a–e). This could be explained by halite metastability in this salinity range. Indeed, halite hardly nucleates for salinities <30–35 wt% NaCl, as shown by the restricted amount of microthermometrically-derived salinities in the 23–35 wt% NaCl eq. range (Bodnar, 2003a) and may be sluggish in experiments even for

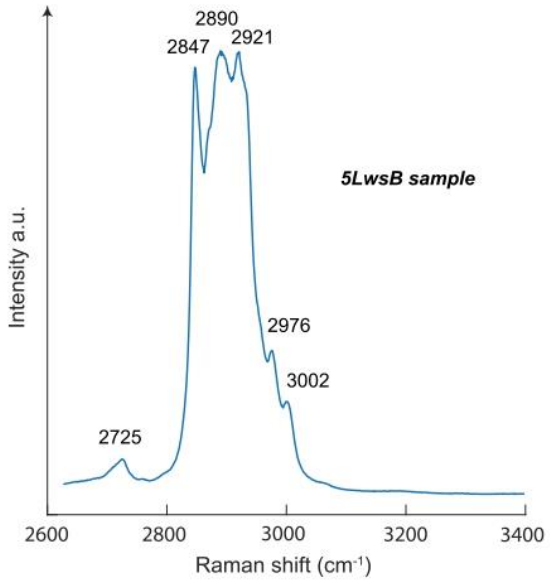

Fig. 12. Raman spectra of potential hydrocarbons identified in the liquid phase of a FI from quartz of LwsB-bearing vein. CH_2 is identified by its characteristic symmetrical (~2850) and asymmetrical (~2890) stretching vibrations while CH_3 is identified by its characteristic symmetrical (~2920–2930) and asymmetrical (~2960–2970) stretching vibrations. Peak distribution is very consistent with saturated hydrocarbon spectra and especially pentane (Sterin et al., 1980). a.u.: arbitrary unit.

salinities of 40 wt% NaCl eq. (Bodnar, 1994). Such metastability was recently observed by Brooks et al. (2019) in FI from Sifnos, Greece.

Alternatively, the absence of salt nucleation may truly indicate that the fluid is not saturated with respect to any of the salt species. Salinities are indeed calculated from Raman-derived chlorinities in a simplified system, considering NaCl as the unique salt species. While NaCl is generally the dominant species, the presence of a variety of secondary minerals in FI from Monviso mafic samples (in veins in particular) suggests that the salt system could be much more complex. Eutectic temperatures measured for sample 10OmpV1 (Sup. Mat. 1) suggest the presence of both NaCl and KCl, with potentially minor amounts of $MgCl_2$ and/or $CaCl_2$. The presence of other salts was similarly inferred from the low eutectic temperatures measured in similar omphacite veins from Monviso (Philippot and Selverstone, 1991) and Rocciavre (Philippot et al., 1998).

7.2. Fluids in BS-facies metasediments: Composition and potential sources

7.2.1. Local vs exotic source of fluid?

Lawsonite- and carpholite-bearing veins exhibit mostly low to moderate salinity aqueous fluids (in NaCl eq., mean 1.2–11 wt%, med 0.9–7.8 wt%) with small amounts of CO_2 and CH_4 in the vapor phase of some fluid inclusions. CH_4 is commonly interpreted as formed by hydrocarbon cracking during prograde metamorphism (Mangenot et al., 2021; Mullis, 1979; Mullis et al., 1994) and is the dominant gas species recorded in low-temperature metasediments from accretionary wedges (Raimbourg et al., 2014, 2015, 2018; Sadofsky and Bebout, 2004; Vrolijk, 1987; Vrolijk et al., 1988). In contrast, CO_2 content tends to increase at higher temperatures (i.e., >270 °C, Mullis et al., 1994; Tarantola et al., 2007) and may become dominant over CH_4 below the brittle-ductile transition (Raimbourg et al., 2018). In the SL calcschists, CH_4 and CO_2 may be locally-derived, from the reduced carbonaceous material of pelitic layers and from carbonate-rich horizons, respectively. CO_2 may in part form by oxidation of CH_4 (Tarantola et al., 2007, 2009), so that variations in the CO_2/CH_4 ratio among different veins may also reflect local changes in redox conditions depending on lithology (Cannaò and Malaspina, 2018; Tarantola et al., 2009).

Potential hydrocarbons heavier than CH_4 were identified in only two FI from metasediments, in both liquid and vapor phases from non-aqueous inclusions. Hydrocarbons are generally restricted to diagenetic conditions and undergo cracking during burial. However, liquid hydrocarbons (aromatic and aliphatic) and wet gas (C_2H_6) were found in primary FI from metamorphic minerals (quartz, calcite and lawsonite) in similar BS-facies metapelites from the Briançonnais and interpreted as preserved from metanogenesis during burial (Goffé, 1982; Goffé and Velde, 1984; Goffé and Villey, 1984). Hydrocarbons reported here may therefore have been trapped early during burial (thereby escaping cracking) and liberated later on during lawsonite formation as a phase immiscible with the local aqueous fluid, as attested by the absence of water in these inclusions. Alternatively, hydrocarbons may have formed by polymerization of methane trapped in inclusions (Kolesnikov et al., 2009).

Fluids analyzed in lawsonite- and carpholite-bearing veins present a wide range of salinities, from 1.2 to 11 wt% NaCl eq. for mean values. Most outcrops record salinities close to or lower than seawater salinity (i.e., 3.5 wt% NaCl eq. for modern seawater, 3.2–3.7 and up to 4.2 wt% NaCl eq. for lower Cretaceous and upper Jurassic seawater, respectively; Hay et al., 2006), as for FI in metasedimentary sequences from accretionary wedges (Brantley et al., 1998; Raimbourg et al., 2014, 2015, 2018; Rossetti et al., 2006; Sadofsky and Bebout, 2004; Smith and Yardley, 1999; Yardley and Graham, 2002) and unsubducted sediments analogous to the SL metamorphic sediments (Helmintoïdes flysch, Fig. 13a; Raimbourg et al., 2018). Such salinities could reflect the mixing between seawater-like fluids initially present in sediment pores and grain boundaries with H_2O-rich fluid released upon dehydration during progressive burial (e.g., Raimbourg et al., 2015), hence advocating for locally-derived fluids.

In contrast, outcrops 1 and 4 of LPU1 show salinities greater than that of seawater, as previously reported for carpholite-bearing veins of upper SL units to the north and south of the study area (Agard et al., 2000; mean salinity ~9 wt% NaCl eq.). Outcrop 1 presents a particularly wide range of salinities, with high mean values (Fig. 10a, b; mean: 11 wt % NaCl eq.; med: 7.8 wt% NaCl eq.; sd = 8.1) and some FI above the salt-saturation threshold (up to 27 wt% NaCl eq.). While preferential H_2O-loss during post-entrapment leakage of FI could explain part of the highest salinity outliers (see § 7.1; Hall and Sterner, 1993), the large scatter of salinities of outcrop 1 rather reflects trapping of fluids with variable salinity, either derived from compositionally distinct adjacent protoliths or far-travelled.

A potential hypothesis, to account for the higher salinity in the metasediments in LPU1, is the ingression of an external fluid derived from metamafics, as the latter rocks show higher salinities than metasediments (Fig. 10a–e). This hypothesis is nevertheless not relevant, as: i) LPU1 contains only few mafic bodies located far away from the studied outcrops and ii) where larger-scale and more abundant mafic bodies are found, as in LPM, metasediments trapped fluids with salinities lower than that of seawater (Fig. 10a–d). Fragments of Triassic Piemont metacarbonates embedded in LPU1 oceanic metasediments, which are found ~150 m away from outcrop 1 (Fig. 2b), are a more likely source of exotic fluids: these fragments regarded as former extensional allochtons (with a Briançonnais affinity) are commonly associated with evaporate-rich deposits akin to producing saline brines during prograde metamorphism. The mixing of variable amounts of infiltrating brines and locally-derived low-saline fluids could explain the wide salinity range of fluids trapped in the HP veins of LPU1 (Fig. 13c). FI from metamorphosed continental margins also generally exhibit higher salinity fluids than oceanic-derived accretionary sequences (Yardley and Graham, 2002).

Infiltration at prograde to peak burial depths, during the formation of Lws-bearing veins, by fluids derived from dehydrating fragments of Piemont units has tectonic implications for the past location of LPU1: this unit must have been located close to portions of the stretched continental margin units. Two alternative scenarios can be envisioned

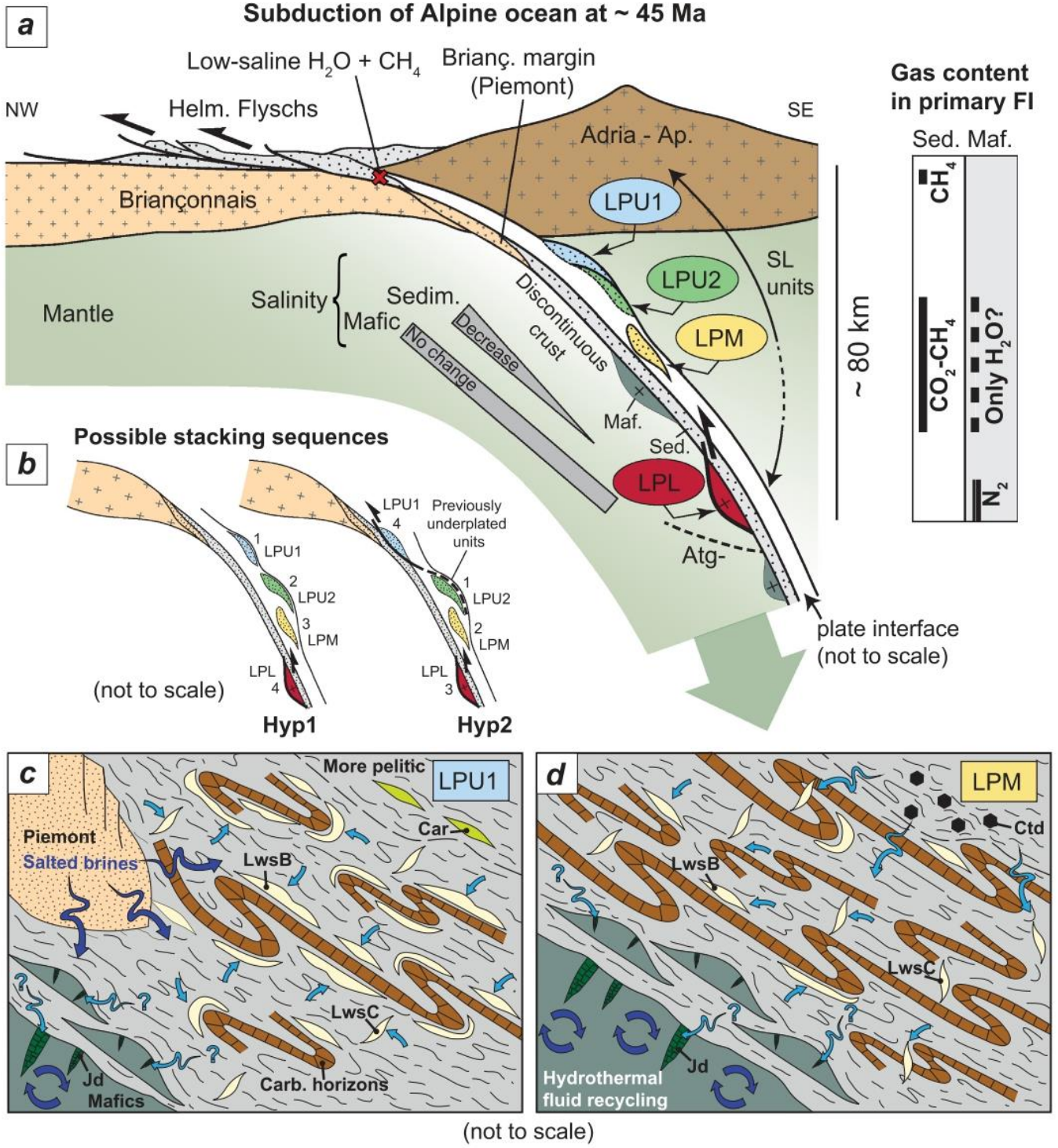

Fig. 13. Tentative model of fluid circulation in the Schistes Lustrés complex and geodynamic implications. A) Sketch of W. Alps subduction zone at ~45 Ma. Fluids from blueschist-facies metasediments are low saline with small amounts of CO_2 and CH_4 and expose a decreasing trend of salinity values along depth. In metagabbros, primary fluids are highly saline and can contain small amounts of N_2 in eclogites. By comparison, unsubducted Helmyntoïdes Flyschs from the alpine accretionary wedge contain low saline fluids with low CH_4 content (Raimbourg et al., 2018). B) Reconstruction of the two possible slicing and stacking sequences of Schistes Lustrés complex units. Its structural upper position in the present day Schistes Lustrés suggests that LPU1 could have been the first detached unit. However, the presence of margin blocks embedded in LPU1 sugest that LPU1 could also correspond to the oceanic units closest to the Piemont margin, thus the latest to be buried and detached from the subducting slab. C) and D) Schematic fluid circulation in LPU1 and LPM at peak burial conditions. FI: fluid inclusions; Sed./Sedim: sediments; Maf.: mafic rocks; Atg-: antigorite-out reaction; Carb.: carbonate-rich layer; Lws: lawsonite; Car: carpholite; Jd: jadeite; Ctd: chloritoide.

(Fig. 13b): (i) before tectonic slicing from the downgoing slab, the oceanic LPU1 was located next to the Briançonnais stretched continental margin and was subducted and detached from the slab last (Fig. 13b). It could even represent sequences directly deposited on a Triassic substratum (Lagabrielle, 1987); (ii) LPU1 was the unit furthest away from the Briançonnais margin but nevertheless contained extensional allochthons and/or olistostromes, such as the Piemont blocks to the west of LPU1 (Fig. 2b). In this case LPU1 would have been the first of the recovered units to have been subducted and detached from the slab, which would explain the tectonic stacking observed today more easily (Fig. 13b).

7.2.2. Salinity reduction with increasing grade?

In addition to local salinity variations, primary FI trapped in HP-LT metasedimentary assemblages show a trend of decreasing salinity with increasing burial depth: LPU1, LPU2 and LPM yield mean fluid salinities of 5.8, 4.4 and 2.0 wt% NaCl eq. respectively (Fig. 10a–d). While the high salinities of LPU1 are at least in part lithologically-controlled, the salinity decrease between LPU2 and LPM could reflect (i) a change in fluid salinity with increasing grade or (ii) initial protolith heterogeneities.

Heterogeneities in sediment compositions are common in SL metasediments and reflected by m- to hm-scale variations in carbonate versus pelitic contents (Fudral, 1996; Lagabrielle et al., 2015). Heterogeneous chlorine concentrations and isotopic values, interpreted as inherited from protoliths heterogeneities (Barnes et al., 2019), could explain some of the salinity variations observed between LPU1, LPU2 and LPM since Cl is highly fluid-mobile and directly controls salinity. Contrary to subducted metasediments of the Franciscan complex, whose decrease in bulk-rock Cl-content with increasing grade likely reflects the release of Cl-rich fluids during progressive dehydration (Catalina Schist, Barnes et al., 2019), no systematic change was detected in the SL complex, even at depth of partial destabilization of the main Cl-hosts (i.e., chlorite and white mica). This advocates for Cl retention in rocks, consistent with the release of a low-saline aqueous fluid such as observed in LPU2 and LPM.

Salinity decrease with increasing burial depth is nevertheless documented in the Franciscan complex (Sadofsky and Bebout, 2004) and attributed to the progressive dilution of initial seawater-like pore fluid by successive dehydration reactions releasing H_2O (Raimbourg et al., 2015; Sadofsky and Bebout, 2004; Smith and Yardley, 1999; Yardley and Graham, 2002). In the studied traverse, lawsonite is stable across grade and cannot contribute to fluid dilution: it starts forming early along the prograde path (~180 °C, LwsA type; Lefeuvre et al., 2020; Fig. 3) and keeps recrystallizing in veins with incremental deformation until peak burial (LwsB-C types). However, progressive dilution of fluid salinity by dehydration reactions is expected from the breakdown of water-rich Fe-Mg carpholite (~12 wt% H_2O; Agard et al., 2001; Bebout et al., 2013; Fig. 3; 13d), which occurs at the temperatures and depths reached in the eastern sector of LPU2 and in LPM. This hypothesis is supported by the fact that the lawsonite veins selected for this study, the freshest and least deformed hence formed close to the peak P-T conditions of each unit, sampled the deepest fluid compositions.

7.3. Fluids in BS- and eclogite-facies metamafics: Composition and potential sources

7.3.1. Preservation of hydrothermal signatures?

In BS-facies metamafic blocks, FI in jadeite-bearing veins are dominantly aqueous with salinities higher than in the surrounding sediments (mean values: 9.1 in LPU1 and 24.6 wt% NaCl eq. in LPM; Fig. 10a, b, d). High salinities are also recorded in fluids trapped in omphacite-bearing veins and matrices from Monviso (17.5 wt% NaCl eq.; Fig. 10a, e). The low eutectic temperatures associated to a variety of secondary minerals (calcite, white mica, salt crystals) as well as fluid salinities above the water NaCl-saturation threshold in some FI lacking salt crystals (see § 7.1) suggest entrapment of a various salt-rich fluid (NaCl-KCl ± minor amounts of $MgCl_2$ and/or $CaCl_2$) in BS- and eclogite-facies metamafics.

Similar highly saline fluids in omphacite-bearing samples from Monviso (vein and whole-rock; Philippot and Selverstone, 1991; Nadeau et al., 1993) and low-strain omphacite from Rocciavre (Philippot et al., 1998) were interpreted as inherited from hydrothermal alteration based on: (i) the similar $\delta^{18}O$ values (of pyroxene and whole-rock) in eclogites and hydrothermally altered crust, (ii) the similar δD of hydrothermal chlorite and amphibole in non-subducted mafic rocks (Chenaillet gabbros) and of omphacite in Monviso veins (Nadeau et al., 1993), (iii) the similarity between FI salinity and $\delta^{18}O$ signature of eclogitic veins and those of altered oceanic crust and unmetamorphosed ophiolites (Philippot et al., 1998).

Near-ridge high-temperature (> 500 °C) hydrothermal alteration of gabbros in reaction zones is classically accompanied by phase separation leading to the formation of brines (up to ~40–50 wt% NaCl eq.) and vapor phases (e.g., Alt et al., 2010; Castelain et al., 2014; Delaney et al., 1987; Kelley et al., 1992; Kelley and Delaney, 1987; Nehlig, 1991; Vanko, 1988; Verlaguet et al., 2020). In contrast to the upward migration of low-density vapor phases, less-buoyant brines may be stored at depth in gabbro porosity (Fontaine et al., 2007; Fontaine and Wilcock, 2006) and trapped as fluid inclusions in newly-formed amphibole (and epidote). Hydrothermal amphibole commonly hosts several tenths of wt% of Cl, and up to 4 wt% were analyzed in hydrothermal amphiboles from oceanic gabbros (Ito and Anderson, 1983; Vanko, 1986). Significant amounts of chlorine were found in amphibole from the Chenaillet ophiolite and in relict hydrothermal amphibole from LPU1 and LPU2 BS-facies metagabbros (up to 0.3 wt%; Debret et al., 2016).

During subduction of hydrothermally-altered gabbros up to BS-facies conditions, progressive breakdown of amphibole + plagioclase (± chlorite, epidote) to glaucophane + jadeite + lawsonite/zoisite will release only small fluid amounts (if any). The fluid released is expected to be Cl-rich, since glaucophane and lawsonite contain less Cl than hydrothermal amphibole (Debret et al., 2016), and may therefore have a high salinity. Mixing of this Cl-rich fluid with small volumes of brines released from amphibole FI could account for the high and variable salinity of BS-facies jadeite veins (Fig. 10a, b, d).

A much larger fluid release is expected during glaucophane and lawsonite breakdown to omphacite + garnet in eclogite-facies rocks (Fig. 3; Angiboust and Agard, 2010). This fluid probably has a lower salinity than that released under BS-facies conditions since glaucophane and lawsonite contain only moderate amounts of Cl and brines provided by the final destabilization of relictual hydrothermal amphibole are volumetrically insignificant. The moderate salinity of some omphacite-bearing veins and matrices in Monviso (Fig. 10a, e) may reflect dilution of the high-salinity BS-facies fluid by progressive glaucophane breakdown into omphacite.

While no gas other than H_2O vapor was detected in BS-facies metamafics, N_2 is present in some FI from Monviso eclogites. N_2 is frequently detected in eclogite-facies FI (Andersen et al., 1989, 1990, 1993; Klemd et al., 1992; Mukherjee and Sachan, 2009; Selverstone et al., 1992) and generally interpreted as inherited from the breakdown of pre-eclogitic minerals hosting NH_{4+} (e.g., amphibole, feldspar). Ammonium, bound as NH_{4+} in K-Na-Ca-bearing minerals, was found in BS-facies metagabbros along the investigated SL traverse (Busigny et al., 2011). N_2 may therefore have been retained in glaucophane under BS-facies conditions (as NH_{4+} substituting for Na) and later released and trapped in FI when glaucophane broke down to omphacite under eclogite-facies conditions (Fig. 3).

The intermediate-to-high salinity and gas content detected in our FI in metamafics could therefore in part be inherited from variations in the degree of hydrothermal alteration predating subduction, thereby explaining the contrasts between samples (i.e., between 7Jd and 2Jd, or between Monviso outcrops 10 and 11; Fig. 10a, b, d, e). This conclusion is supported by the $\delta^{37}Cl$ and $\delta^{65}Cu$ signature of relictual hydrothermal amphibole, which attests to the preservation of the

hydrothermal imprint throughout Alpine subduction (Busigny et al., 2011, 2018; Selverstone and Sharp, 2013).

7.3.2. Mixing with externally-derived fluids?

Several FI in BS-facies metagabbros contain potential hydrocarbons heavier than CH_4 without water, which did not mix with the local high-salinity fluid (i.e., eight FI in samples 2Jd and 7Jd, similar to the two FI in outcrop 5 lawsonite-bearing veins). This likely advocates for fluid infiltration from surrounding metasediments since metamafic rocks are generally devoid of organic matter (Fig. 13c). Dissolution and mobilization of carbonaceous material in the fluid was identified at metasediments-metamafics contacts in the SL complex (Vitale Brovarone et al., 2020b). Previous trace element and isotopic studies on these Queyras metamafic blocks furthermore argued for infiltration of volatiles from the surrounding metasediments (Debret et al., 2016, 2018; Inglis et al., 2017; Lafay et al., 2013). However, fluid infiltration from metasediments was probably limited, since mafic blocks and surrounding metasediments still have different salinities (Fig. 10a–e), and likely restricted to block rims and deformed zones (Debret et al., 2016; Schwartz, 2000), as suggested by the preservation of rare magmatic pyroxene and hydrothermal amphibole in block cores (Debret et al., 2016; Philippot et al., 1998).

Hydrocarbons, whether or not derived from sedimentary fluids, could result from deep abiotic generation by polymerization of methane through a reversible reaction (forming ethane, propane, butane; Kolesnikov et al., 2009). Recent experimental and field data have suggested that CH_4 and other hydrocarbons can be stable at HP conditions and up to deep upper-mantle conditions (McCollom, 2013; Sverjensky et al., 2020; and references therein). Saturated hydrocarbons are formed in HP experiments by carbonate reduction (Tao et al., 2018) or transformation of dissolved organic species (Huang et al., 2017; Li, 2017). Immiscible abiotic CH_4 produced by carbonate reduction (Vitale Brovarone et al., 2017) and deep serpentinization (Vitale Brovarone et al., 2020a) was reported in HP ultramafic rocks from the Western Alps. Dissolved organic molecules, still present at UHP metamorphic conditions as shown by aqueous FI in deeply subducted metasediments (Frezzotti, 2019; Frezzotti et al., 2011), could also contribute to form hydrocarbons at BS-facies conditions.

Monviso Fe-Ti-metagabbros allow studying fluid ingression during progressive brecciation and strain localization at eclogite-facies conditions (Angiboust et al., 2012a; Locatelli et al., 2018). Thermodynamic modelling and trace element compositions suggest that omphacite crystallization in V1 veins and M1 matrix reflects final glaucophane and lawsonite breakdown in Mg-rich gabbros, while the omphacite from V2 veins and M2 matrix formed at incipient retrograde conditions without local fluid production and in the presence of some serpentinite-derived fluids (Locatelli et al., 2019b). The salinity of V2 and M2 omphacite FI does not deviate significantly, however, from that of V1 veins, suggesting either remobilization and entrapment of local remnant fluids (i.e., FI or grain boundary fluids) or that external fluid input was minimal (consistent with only incipient opening of the system; Locatelli et al., 2019b) and/or had a similar salinity. In ultramafic rocks, deserpentinization through the brucite-out reaction (as is the case in Monviso; Gilio et al., 2020) was shown to result in the formation of highly saline FI (Scambelluri et al., 1997), whereas the antigorite-out reaction produces less saline FI (Scambelluri et al., 2001).

7.4. Implications on fluid circulation during subduction of the SL complex

This study shows that salinities and gas signatures of HP metasedimentary FI can be accounted for by the progressive dilution of a local residual pore seawater-like fluid by successive dehydration reactions accompanying subduction. There is no strong evidence for infiltration of external fluids, except in LPU1 where high salinity fluids reflect hm-scale fluid circulation of brines from nearby Piemont blocks. This concurs with the conclusions from whole-rock trace element and isotopic studies that SL metasediments represent a rock-buffered system with only limited external fluid infiltration (Barnes et al., 2019; Bebout et al., 2013; Cook-Kollars et al., 2014; Epstein et al., 2020; Henry et al., 1996).

Gas contents do not show systematic variations with increasing grade but the $CO_2/(CO_2\text{-}CH_4)$ ratio does with lawsonite vein type in all metasedimentary units (Fig. 11). In particular, LwsC crack veins reflecting cm-scale element transport from vein walls (Fig. 4d, f), mostly restricted to pelite-rich horizons, systematically contain higher CH_4 amounts. This suggests local fluid derivation from reduced carbonaceous material contained in pelites. Conversely, the larger LwsB-bearing veins (up to dm-wide, m-long; Fig. 4a–c, e) systematically higher $CO_2/(CO_2\text{-}CH_4)$ ratios suggest that the fluid produced by dehydration of pelitic horizons interacted with more distant carbonate layers, as also recorded by in-situ trace element signatures (Lefeuvre, 2020).

This spatial control on gas contents points to local variations of the redox state in the fluid, which hardly homogenizes at the m-scale. We interprete the small cm-scale LwsC tensile veins, which preserve their redox/CH_4-rich signature, as short-lived tectonic events accompanied by local fluid-rock interaction. In contrast, mass transfer and element redistribution across lithological horizons (Lefeuvre et al., 2020) could operate through fluid circulation in networks outlined by the larger-scale, longer-lived Lws-B veins, thereby explaining the calcite isotopic homogenization at the hm-scale (Cook-Kollars et al., 2014; Henry et al., 1996). There is however no evidence for larger scale infiltration of external fluid inside the SL units (Barnes et al., 2019; Bebout et al., 2013; Cook-Kollars et al., 2014; Epstein et al., 2020; Henry et al., 1996) and high fluid flow seems restricted to contacts between units (e.g., Epstein et al., 2021; Jaeckel et al., 2018). Although the presence of potential hydrocarbons hints towards element transfer between metasediments and metamafics, fluid circulations were probably more restricted in metamafic blocks, as suggested by the preservation of magmatic pyroxene in the undeformed cores of metagabbro blocks and locally-derived high-salinity fluids. This conclusion is strengthened by trace element data in metagabbros and serpentinites of the Monviso LPL unit, suggesting rather closed-system conditions upon burial and up to peak conditions (Lafay et al., 2013; Locatelli et al., 2019b; Spandler et al., 2011).

7.5. Comparison with other subduction zones

Fluid compositions trapped at peak burial in FI of the SL units are compared to those from other oceanic subducted fragments worldwide (Fig. 14; Table 1). Studies of shallow subduction depths mostly rely on metasediments (< 430 °C, about 20 kbar) whereas studies of eclogite-facies conditions mostly do on metamafic samples (reflecting processes controlling rock recovery in subduction zones; Agard et al., 2018).

Similar salinity ranges and gas contents are recorded in trapped primary FI from BS-facies metasediments worldwide (Agard et al., 2000; Raimbourg et al., 2018; Sachan et al., 2017; Sadofsky and Bebout, 2004). Rather low-salinity fluids (<5 wt% NaCl eq.) characterize low-grade to BS-facies metasedimentary rocks from accretionary wedges (Brantley et al., 1998; Smith and Yardley, 1999; Sadofsky and Bebout, 2004; Rossetti et al., 2006; Raimbourg et al., 2015, 2018). The evolution of fluid compositions in metasediments beyond BS-facies conditions remains uncertain due to only few studies. It may involve progressive dilution by locally-derived dehydration fluids, as observed in SL metasediments (this study) or in the Franciscan complex (Sadofsky and Bebout, 2004). Yet FI in Himalayan BS-facies metasediments record higher salinities (about 12 wt% NaCl eq.; Fig. 14; Sachan et al., 2017).

Metamafics from the various eclogitic terranes seem to be characterized by medium to highly saline primary FI (Luckscheiter and Morteani, 1980; Nadeau et al., 1993; Philippot et al., 1998; Philippot and Selverstone, 1991; Selverstone et al., 1992; Yoshida et al., 2015). They show a diverse set of solid inclusions (this study; Philippot and

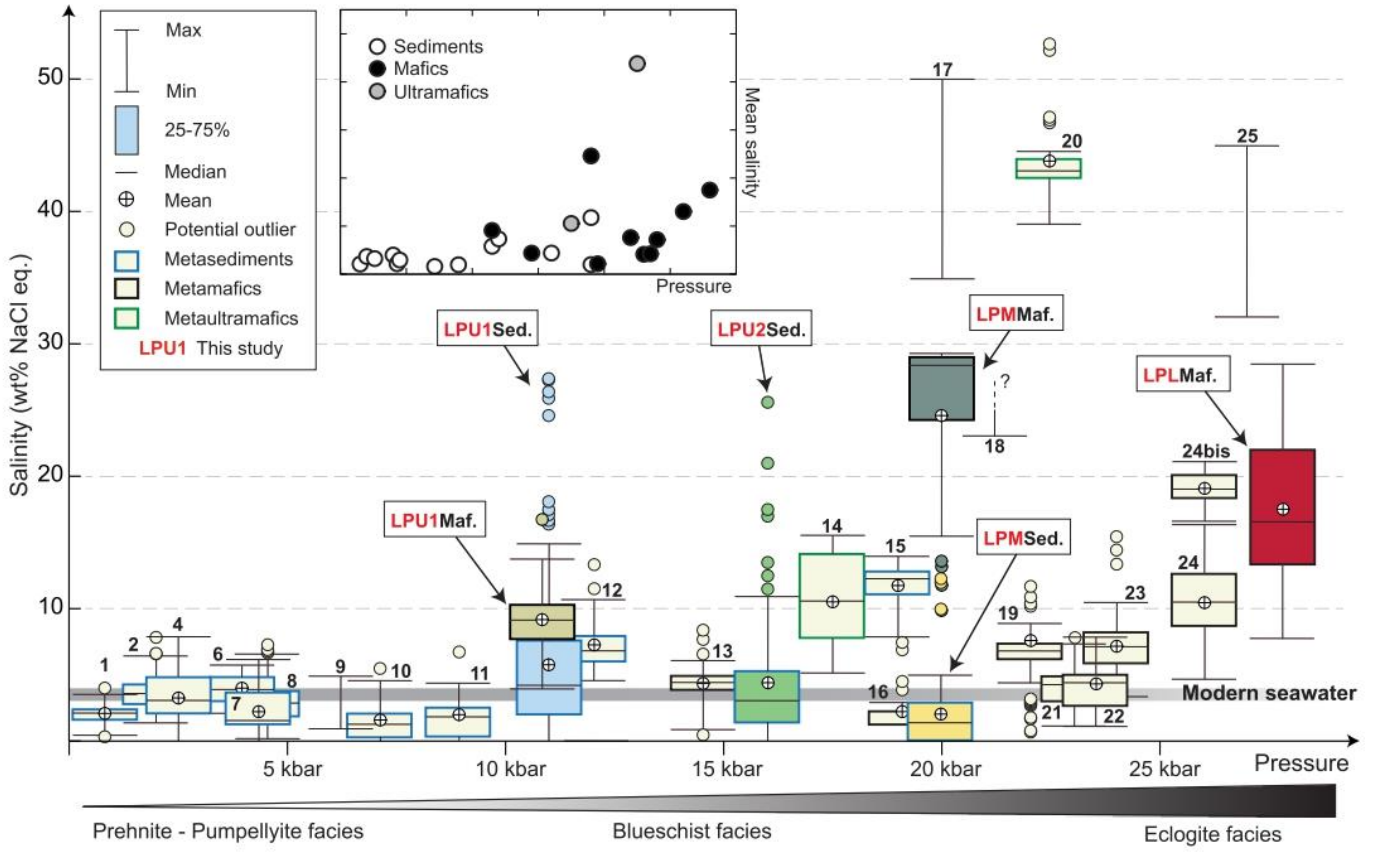

Fig. 14. Compilation of fluid salinity in primary fluid inclusions from exhumed oceanic subduction rocks. Salinity data series are represented as boxplots and plotted depending on the estimated peak pressure conditions of host rocks. A simplified graph representing mean salinity depending on peak pressure is at the top of the figure. Data series from our study have red names. References for the FI studies and corresponding P-T conditions data are reported in Table 1. Maf.: metamafic rocks; Sed.: metasediments.

Selverstone, 1991; Selverstone et al., 1992), indicative of complex salt systems ($NaCl \pm KCl \pm CaCl_2 \pm FeCl_2 \pm MgCl_2$), and eclogites from oceanic and continental subduction commonly contain N_2 or CO_2 in the FI bubble (Andersen et al., 1989; El-Shazly and Sisson, 1999; Selverstone et al., 1992). Cogenetic monophase gaseous N_2-$CO_2 \pm CH_4$-bearing FI were interpreted as representing immiscible fluids at peak burial conditions (Andersen et al., 1990; Andersen et al., 1993; Klemd et al., 1992; Mukherjee and Sachan, 2009; Selverstone et al., 1992).

FI from Alpine metagabbros are by far the most studied and record the highest salinities under both BS-facies and eclogitic conditions (10–45 wt% NaCl eq.; this study; Nadeau et al., 1993; Philippot and Selverstone, 1991; Philippot et al., 1998), reflecting at least partial inheritance from high-temperature amphibolite-facies hydrothermal alteration (Nadeau et al., 1993; Philippot et al., 1998). In comparison, ultramafic rocks having experienced antigorite breakdown above 600 °C exhibit lower salinity FI (Cerro de Amirez, Scambelluri et al., 2001) than only partially dehydrated serpentinites (Erro Tobbio, Scambelluri et al., 1997).

Localities outside the Alps (Fig. 14; e.g., Tianshan, Dominican Republic, Syros, Franciscan complex; Barr, 1990; Giaramita and Sorensen, 1994; Gao and Klemd, 2001; Kawamoto et al., 2018) record significantly lower fluid salinities (2–7 wt% NaCl eq.; Fig. 14), though still higher than for metasediments. Contrary to the Alpine case study, eclogites from the Franciscan complex, Samana Peninsula (Giaramita and Sorensen, 1994) and Rio San Juan jadeitites (Kawamoto et al., 2018) correspond to mafic blocks in subduction mélanges (Agard et al., 2018): they may have experienced greater fluid circulation, thereby explaining the lower salinity values. In the Franciscan complex, eclogitic mafic blocks show slightly higher salinities than surrounding metasediments (Giaramita and Sorensen, 1994; Sadofsky and Bebout, 2004), suggesting that their initial fluid salinity was higher than that of the infiltrating sediment-derived (low-saline) fluids. Alternatively, since these mafic blocks are mostly metavolcanics they may have trapped initially low-salinity seawater-like fluids (Philippot et al., 1998): hydrothermalization of basalts indeed generally occurs under greenschist-facies conditions, preventing phase separation, brine trapping and formation of Cl-rich phases.

8. Conclusions

This study reports on salinities and gas contents of primary fluid inclusions (FI) trapped in high pressure veins from metasediments and metamafic rocks along the Queyras-Monviso traverse of the Schistes Lustrés complex (Western Alps). Results provide snapshots of fluids present at peak burial conditions from ~30 to 80 km depth, along a cold subduction zone.

Fluids trapped in metasediments are moderately saline aqueous fluids (mean salinity of 4.6 wt% NaCl eq.) with small amounts of CO_2 and CH_4 in the vapor phase. FI in metamafic HP veins record higher salinities (mean salinity about 17 wt% NaCl eq.) with small amounts of N_2 in eclogitic veins only, and a variety of daughter minerals (calcite, white mica, salts) indicative of complex chemical systems. These fluid signatures are consistent with literature data and appear characteristic of each rock type.

Salinity decreases with increasing grade in the studied metasediments, which is interpreted to reflect progressive dilution of initial seawater-like pore fluid by fresh fluids released locally by successive dehydration reactions. Higher salinities in the uppermost metasedimentary-dominated tectonic unit suggest brine infiltration from embedded continental margin fragments of former extensional

allochtons, which are commonly associated with evaporate-rich deposits. CO_2 and CH_4 (and scarce potential hydrocarbons) appear to be locally released from fluid interaction with carbonates and carbonaceous matter-rich pelitic horizons, respectively.

In metagabbros, high salinities are interpreted as partly inherited from seafloor high-temperature hydrothermal alteration resulting in brine formation. Progressive breakdown of hydrothermal Cl-rich amphiboles to glaucophane (BS-facies) and then omphacite (eclogite-facies) and release of trapped FI brines could account for the high salinity fluids trapped in FI. Therefore, fluid inclusions record progressive release of Cl in the fluid phase with increasing grade.

FI in Alpine metasediments show salinities and gas contents comparable with other subducted fragments of oceanic lithosphere worldwide, whereas fluid salinities of Alpine metagabbros are higher than salinities recorded elsewhere. These higher salinities may result from (1) higher-temperature hydrothermal alteration and brine formation in Alpine metagabbros (compared to metavolcanics) or (2) more restricted infiltration by sediment-derived fluids compared to block-in-mélange subduction complexes.

This study suggests that fluids released in subduction zones from the different rock reservoirs are mostly aqueous but present variable salinities and gas contents. Characteristic local fluid signatures and redox conditions within units reflect restricted and transient fluid circulation. Conversely, lithological contrasts, often localizing fluid circulations, may take part in fluid mixing.

Declaration of Competing Interest

The authors declare that they have no known competing financial interests or personal relationships that could have appeared to influence the work reported in this paper.

Acknowledgments

This study was partly funded by the BRGM in the frame of the RGF-Alpes project, by ISTeP and by the project "Zooming in between plates" (Marie Curie International Training Network no. 604713) to P. Agard. The authors thank M-C. Caumon and V-H Le for analytical support and discussion, E. Delairis and M. Moroni for technical support with samples. We also thank A. Plunder, L. Jolivet, A. Vitale-Brovarone, K. Rajic, C. Chopin; G. Bonnet, T. Gyomlai, M. Soret and K. Mendes for insightful discussions. The manuscript benefited from the useful suggestions of three anonymous reviewers and the Special Issue Editor, S. Angiboust.

Appendix A. Supplementary data

Supplementary data to this article can be found online at https://doi.org/10.1016/j.lithos.2021.106168.

References

Agard, P., 2021. Subduction of oceanic lithosphere in the Alps: selective and archetypal from (slow-spreading) oceans. Earth Sci. Rev. 103517.
Agard, P., Handy, M., 2021. Ocean subduction dynamics in the Alps. Elements 17, 9–16.
Agard, P., Goffé, B., Touret, J.L.R., Vidal, O., 2000. Retrograde mineral and fluid evolution in high-pressure metapelites (Schistes lustrés unit, Western Alps). Contrib. Mineral. Petrol. 140, 296–315. https://doi.org/10.1007/s004100000190.
Agard, P., Jolivet, L., Goffe, B., 2001. Tectonometamorphic evolution of the Schistes Lustres complex; implications for the exhumation of HP and UHP rocks in the Western Alps. Bull. Soc. Géol. France 172, 617–636. https://doi.org/10.2113/172.5.617.
Agard, P., Monie, P., Jolivet, L., Goffe, B., 2002. Exhumation of the Schistes Lustres complex: in situ laser probe 40Ar/39Ar constraints and implications for the Western Alps. J. Metamorph. Geol. 20, 599–618. https://doi.org/10.1046/j.1525-1314.2002.00391.x.
Agard, P., Yamato, P., Jolivet, L., Burov, E., 2009. Exhumation of oceanic blueschists and eclogites in subduction zones: timing and mechanisms. Earth Sci. Rev. 92, 53–79. https://doi.org/10.1016/j.earscirev.2008.11.002.
Agard, P., Plunder, A., Angiboust, S., Bonnet, G., Ruh, J., 2018. The subduction plate interface: rock record and mechanical coupling (from long to short timescales). Lithos 320–321, 537–566. https://doi.org/10.1016/j.lithos.2018.09.029.
Alt, J.C., Laverne, C., Coggon, R.M., Teagle, D.A.H., Banerjee, N.R., Morgan, S., Smith-Duque, C.E., Harris, M., Galli, L., 2010. Subsurface structure of a submarine hydrothermal system in ocean crust formed at the East Pacific Rise, ODP/IODP Site 1256. Geochem. Geophys. Geosyst. 11. https://doi.org/10.1029/2010GC003144.
Andersen, T., Burke, E.A.J., Austrheim, H., 1989. Nitrogen-bearing, aqueous fluid inclusions in some eclogites from the Western Gneiss Region of the Norwegian Caledonides. Contrib. Mineral. Petrol. 103, 153–165. https://doi.org/10.1007/BF00378501.
Andersen, T., Austrheim, H., Burke, E.A.J., 1990. Fluid inclusions in granulites and eclogites from the Bergen Arcs, Caledonides of W. Norway. Mineral. Mag. 54, 145–158. https://doi.org/10.1180/minmag.1990.054.375.02.
Andersen, T., Austrheim, H., Burke, E.A.J., Elvevold, S., 1993. N2 and CO2 in deep crustal fluids: evidence from the Caledonides of Norway. Chem. Geol. 108, 113–132. https://doi.org/10.1016/0009-2541(93)90320-l.
Angiboust, S., Agard, P., 2010. Initial water budget: the key to detaching large volumes of eclogitized oceanic crust along the subduction channel? Lithos 120, 453–474.
Angiboust, S., Glodny, J., 2020. Exhumation of eclogitic ophiolitic nappes in the W. Alps: New age data and implications for crustal wedge dynamics. Lithos 356–357, 105374. https://doi.org/10.1016/j.lithos.2020.105374.
Angiboust, S., Agard, P., Jolivet, L., Beyssac, O., 2009. The Zermatt-Saas ophiolite: the largest (60-km wide) and deepest (c. 70-80 km) continuous slice of oceanic lithosphere detached from a subduction zone? Terra Nova 21, 171–180. https://doi.org/10.1111/j.1365-3121.2009.00870.x.
Angiboust, S., Agard, P., Raimbourg, H., Yamato, P., Huet, B., 2011. Subduction interface processes recorded by eclogite-facies shear zones (Monviso, W. Alps). Lithos 127, 222–238. https://doi.org/10.1016/j.lithos.2011.09.004.
Angiboust, S., Agard, P., Yamato, P., Raimbourg, H., 2012a. Eclogite breccias in a subducted ophiolite: a record of intermediate-depth earthquakes? Geology 40, 707–710. https://doi.org/10.1130/G32925.1.
Angiboust, S., Langdon, R., Agard, P., Waters, D., Chopin, C., 2012b. Eclogitization of the Monviso ophiolite (W. Alps) and implications on subduction dynamics. J. Metamorph. Geol. 30, 37–61. https://doi.org/10.1111/j.1525-1314.2011.00951.x.
Angiboust, S., Pettke, T., De Hoog, J.C.M., Caron, B., Oncken, O., 2014. Channelized fluid flow and eclogite-facies metasomatism along the Subduction Shear Zone. J. Petrol. 55, 883–916. https://doi.org/10.1093/petrology/egu010.
Bakker, R.J., Jansen, J.B.H., 1990. Preferential water leakage from fluid inclusions by means of mobile dislocations. Nature 345, 58–60.
Bakker, R.J., Jansen, J.B.H., 1991. Experimental post-entrapment water loss from synthetic CO2-H2O inclusions in natural quartz. Geochim. Cosmochim. Acta 55, 2215–2230.
Bakker, R.J., Jansen, J.B.H., 1994. A mechanism for preferential H2O leakage from fluid inclusions in quartz, based on TEM observations. Contrib. Mineral. Petrol. 116, 7–20.
Ballèvre, M., Merle, O., 1993. The Combin Fault: compressional reactivation of a late Cretaceous-early Tertiary detachment fault in the Western Alps. Schweiz. Mineral. Petrogr. Mitt. 73, 205–227. https://doi.org/10.5169/SEALS-55570.
Ballèvre, M., Lagabrielle, Y., Merle, O., 1990. Tertiary ductile normal faulting as a consequence of lithospheric stacking in the western Alps. Mém. Soc. Géol. France 156, 227–236.
Barnes, J.D., Penniston-Dorland, S.C., Bebout, G.E., Hoover, W., Beaudoin, G.M., Agard, P., 2019. Chlorine and lithium behavior in metasedimentary rocks during prograde metamorphism: a comparative study of exhumed subduction complexes (Catalina Schist and Schistes Lustrés). Lithos 336–337, 40–53. https://doi.org/10.1016/j.lithos.2019.03.028.
Barr, H., 1990. Preliminary fluid inclusion studies in a high-grade blueschist terrain, Syros, Greece. Mineral. Mag. 54, 159–168. https://doi.org/10.1180/minmag.1990.054.375.03.
Bebout, G.E., Penniston-Dorland, S.C., 2016. Fluid and mass transfer at subduction interfaces—the field metamorphic record. Lithos 240–243, 228–258. https://doi.org/10.1016/j.lithos.2015.10.007.
Bebout, G.E., Agard, P., Kobayashi, K., Moriguti, T., Nakamura, E., 2013. Devolatilization history and trace element mobility in deeply subducted sedimentary rocks: Evidence from Western Alps HP/UHP suites. Chem. Geol. 342, 1–20. https://doi.org/10.1016/j.chemgeo.2013.01.009.
Beyssac, O., Goffé, B., Chopin, C., Rouzaud, J.N., 2002. Raman spectra of carbonaceous material in metasediments: a new geothermometer. J. Metamorph. Geol. 20, 859–871. https://doi.org/10.1046/j.1525-1314.2002.00408.x.
Blake Jr., M.C., 1988. Metamorphic and tectonic evolution of the Franciscan complex, northern California. Metamorphism and Crustal Evolution of the Western United States, pp. 1035–1060.
Bodnar, R.J., 1993. Revised equation and table for determining the freezing point depression of H2O-NaCl solutions. Geochim. Cosmochim. Acta 57, 683–684.
Bodnar, R.J., 1994. Synthetic fluid inclusions: XII. The system H2O-NaCl. Experimental determination of the halite liquidus and isochores for a 40 wt% NaCl solution. Geochim. Cosmochim. Acta 58, 1053–1063.
Bodnar, R.J., 2003a. Introduction to aqueous-elecrolyte fluid inclusions. In: Samson, I., Anderson, A., Marshall, D. (Eds.), Fluid Inclusions: Analysis and Interpretation. 32. Mineral Association of Canada, Short Course, pp. 81–100.
Bodnar, R.J., 2003b. Re-equilibration of fluid inclusions. In: Samson, I., Anderson, A., Marshall, D. (Eds.), Fluid Inclusions: Analysis and Interpretation. 32. Mineral Association of Canada, Short Course, pp. 213–230.
Bousquet, R., Oberhänsli, R., Goffé, B., Wiederkehr, M., Koller, F., Schmid, S.M., Schuster, R., Engi, M., Berger, A., Martinotti, G., 2008. Metamorphism of metasediments at the scale of an orogen: a key to the Tertiary geodynamic evolution of the Alps. Geol. Soc. Lond., Spec. Publ. 298, 393–411. https://doi.org/10.1144/SP298.18.
Brantley, S.L., Fisher, D.M., Deines, P., Clark, M.B., Myers, G., 1998. Segregation veins: evidence for the deformation and dewatering of a low-grade metapelite. Deformation-Enhanced Fluid Transport in the Earth's Crust and Mantle. The Mineralogical Society, pp. 267–288.
Brooks, H.L., Dragovic, B., Lamadrid, H.M., Caddick, M.J., Bodnar, R.J., 2019. Fluid capture during exhumation of subducted lithologies: a fluid inclusion study from Sifnos, Greece. Lithos 332, 120–134.

Busigny, V., Cartigny, P., Philippot, P., Ader, M., Javoy, M., 2003. Massive recycling of nitrogen and other fluid-mobile elements (K, Rb, Cs, H) in a cold slab environment: evidence from HP to UHP oceanic metasediments of the Schistes Lustrés nappe (western Alps, Europe). Earth Planet. Sci. Lett. 215, 27–42. https://doi.org/10.1016/S0012-821X(03)00453-9.

Busigny, V., Cartigny, P., Philippot, P., 2011. Nitrogen isotopes in ophiolitic metagabbros: a re-evaluation of modern nitrogen fluxes in subduction zones and implication for the early Earth atmosphere. Geochim. Cosmochim. Acta 75, 7502–7521. https://doi.org/10.1016/j.gca.2011.09.049.

Busigny, V., Chen, J., Philippot, P., Borensztajn, S., Moynier, F., 2018. Insight into hydrothermal and subduction processes from copper and nitrogen isotopes in oceanic metagabbros. Earth Planet. Sci. Lett. 498, 54–64. https://doi.org/10.1016/j.epsl.2018.06.030.

Caby, R., Kienast, J.-R., Saliot, P., 1978. Structure, métamorphisme et modèle d'évolution tectonique des Alpes occidentales. Revue Géogra. Phys. Géol. Dyn. Paris 20, 307–322.

Cannaò, E., Malaspina, N., 2018. From oceanic to continental subduction: Implications for the geochemical and redox evolution of the supra-subduction mantle. Geosphere 14, 2311–2336. https://doi.org/10.1130/GES01597.1.

Caron, J.-M., 1974. Rapports entre diverses" generations" de lawsonite et les deformations dans les Schistes lustres des Alpes cottiennes septentrionales (France et Italie). Bull. Soc. Géol. France 7, 256–263.

Cartwright, I., Buick, I.S., 2000. Fluid generation, vein formation and the degree of fluid-rock interaction during decompression of high-pressure terranes: the Schistes Lustrés, Alpine Corsica, France. J. Metamorph. Geol. 18, 607–624. https://doi.org/10.1046/j.1525-1314.2000.00280.x.

Castelain, T., McCaig, A.M., Cliff, R.A., 2014. Fluid evolution in an Oceanic Core Complex: a fluid inclusion study from IODP hole U1309 D—Atlantis Massif, 30°N, Mid-Atlantic Ridge. Geochem. Geophys. Geosyst. 15, 1193–1214. https://doi.org/10.1002/2013GC004975.

Caumon, M.-C., Dubessy, J., Robert, P., Tarantola, A., 2013. Fused-silica capillary capsules (FSCCs) as reference synthetic aqueous fluid inclusions to determine chlorinity by Raman spectroscopy. Eur. J. Mineral. 25, 755–763. https://doi.org/10.1127/0935-1221/2013/0025-2280.

Caumon, M.-C., Tarantola, A., Mosser-Ruck, R., 2015. Raman spectra of water in fluid inclusions: I. Effect of host mineral birefringence on salinity measurement: effect of mineral birefringence on salinity measured by Raman spectroscopy. J. Raman Spectrosc. 46, 969–976. https://doi.org/10.1002/jrs.4708.

Cook-Kollars, J., Bebout, G.E., Collins, N.C., Angiboust, S., Agard, P., 2014. Subduction zone metamorphic pathway for deep carbon cycling: I. Evidence from HP/UHP metasedimentary rocks, Italian Alps. Chem. Geol. 386, 31–48. https://doi.org/10.1016/j.chemgeo.2014.07.013.

Dal Piaz, G.V., 1974. Le métamorphisme de haute pression et basse température dans l'évolution structurale du bassin ophiolitique alpino-apenninique. Schweiz. Mineral. Petrogr. Mitt. 54, 399–424.

Davis, D.W., Lowenstein, T.K., Spencer, R.J., 1990. Melting behavior of fluid inclusions in laboratory-grown halite crystals in the systems NaCl-H2O, NaCl-KCl-H2O, NaCl-MgCl2-H2O, and NaCl-CaCl2-H2O. Geochim. Cosmochim. Acta 54, 591–601.

De Wever, P., Caby, R., 1981. Datation de la base des schistes lustrés postophiolitiques par des radiolaires (Oxfordien-Kimmeridgien moyen) dans les Alpes Cottiennes (Saint Véran, France). Comptes Rendus de l'Acad. Sci. Paris 292, 467–472.

Debret, B., Koga, K.T., Cattani, F., Nicollet, C., Van den Bleeken, G., Schwartz, S., 2016. Volatile (Li, B, F and Cl) mobility during amphibole breakdown in subduction zones. Lithos 244, 165–181. https://doi.org/10.1016/j.lithos.2015.12.004.

Debret, B., Bouilhol, P., Pons, M.L., Williams, H., 2018. Carbonate transfer during the Onset of Slab Devolatilization: New Insights from Fe and Zn Stable Isotopes. J. Petrol. 59, 1145–1166. https://doi.org/10.1093/petrology/egy057.

Delaney, J.R., Mogk, D.W., Mottl, M., 1987. Quartz-cemented breccias from the Mid-Atlantic Ridge: Samples of a high-salinity hydrothermal upflow zone. J. Geophys. Res. 92, 9175–9192.

Deville, E., Fudral, S., Lagabrielle, Y., Marthaler, M., Sartori, M., 1992. From oceanic closure to continental collision: a synthesis of the" Schistes lustrés" metamorphic complex of the Western Alps. Geol. Soc. Am. Bull. 104, 127–139.

Diamond, L.W., 2003. Introduction to gas-bearing, aqueous fluid inclusions. In: Samson, I., Anderson, A., Marshall, D. (Eds.), Fluid inclusions: Analysis and Interpretation. 32. Mineral Association of Canada, Short Course, pp. 101–158.

Diamond, L.W., Tarantola, A., 2015. Interpretation of fluid inclusions in quartz deformed by weak ductile shearing: Reconstruction of differential stress magnitudes and pre-deformation fluid properties. Earth Planet. Sci. Lett. 417, 107–119. https://doi.org/10.1016/j.epsl.2015.02.019.

Diamond, L.W., Tarantola, A., Stünitz, H., 2010. Modification of fluid inclusions in quartz by deviatoric stress. II: experimentally induced changes in inclusion volume and composition. Contrib. Mineral. Petrol. 160, 845–864. https://doi.org/10.1007/s00410-010-0510-6.

Droop, G.T.R., Lombardo, B., Pognante, U., 1990. Formation and distribution of eclogite facies rocks in the Alps. In: Carswell, D.A. (Ed.), Eclogite Facies Rocks: Glasgow. Blackie, United Kingdom, pp. 225–229.

El-Shazly, A.K., Sisson, V.B., 1999. Retrograde evolution of eclogite facies rocks from NE Oman: evidence from fluid inclusions and petrological data. Chem. Geol. 154, 193–223. https://doi.org/10.1016/S0009-2541(98)00132-6.

El-Shazly, A.K., Sisson, V.B., 2004. Fluid inclusions in carpholite-bearing metasediments and blueschists from NE Oman: Constraints on P-T evolution. Eur. J. Mineral. 16, 221–233. https://doi.org/10.1127/0935-1221/2004/0016-0221.

Endo, S., 2010. Pressure-temperature history of titanite-bearing eclogite from the Western Iratsu body, Sanbagawa Metamorphic Belt, Japan: Titanite eclogite from Sanbagawa Belt. Island Arc 19, 313–335. https://doi.org/10.1111/j.1440-1738.2010.00708.x.

Epstein, G.S., Bebout, G.E., Angiboust, S., Agard, P., 2020. Scales of fluid-rock interaction and carbon mobility in the deeply underplated and HP-Metamorphosed Schistes Lustrés, Western Alps. Lithos 354–355, 105229. https://doi.org/10.1016/j.lithos.2019.105229.

Epstein, G.S., Bebout, G.E., Angiboust, S., 2021. Fluid and mass transfer along transient subduction interfaces in a deep paleo-accretionary wedge (Western Alps). Chem. Geol. 559, 119920. https://doi.org/10.1016/j.chemgeo.2020.119920.

Ernst, W.G., 1993. Metamorphism of Franciscan tectonostratigraphic assemblage, Pacheco Pass area, east-central Diablo Range, California coast ranges. Geol. Soc. Am. Bull. 105, 618–636.

Escuder-Viruete, J., Pérez-Estaún, A., 2006. Subduction-related P–T path for eclogites and garnet glaucophanites from the Samaná Peninsula basement complex, northern Hispaniola. Int. J. Earth Sci. (Geol Rundsch) 95, 995–1017. https://doi.org/10.1007/s00531-006-0079-5.

Fermi, E., 1931. Über den ramaneffekt des kohlendioxyds. Z. Phys. 71, 250–259.

Fisher, D., Byrne, T., 1990. The character and distribution of mineralized fractures in the Kodiak Formation, Alaska: Implications for fluid flow in an underthrust sequence. J. Geophys. Res. 95, 9069. https://doi.org/10.1029/JB095iB06p09069.

Fontaine, F.J., Wilcock, W.S.D., 2006. Dynamics and storage of brine in mid-ocean ridge hydrothermal systems. J. Geophys. Res. 111. https://doi.org/10.1029/2005JB003866.

Fontaine, F.J., Wilcock, W.S.D., Butterfield, D.A., 2007. Physical controls on the salinity of mid-ocean ridge hydrothermal vent fluids. Earth Planet. Sci. Lett. 257, 132–145. https://doi.org/10.1016/j.epsl.2007.02.027.

Frezzotti, M.L., 2019. Diamond growth from organic compounds in hydrous fluids deep within the Earth. Nat. Commun. 10, 4952. https://doi.org/10.1038/s41467-019-12984-y.

Frezzotti, M.L., Ferrando, S., 2015. The chemical behavior of fluids released during deep subduction based on fluid inclusions. Am. Mineral. 100, 352–377. https://doi.org/10.2138/am-2015-4933.

Frezzotti, M.L., Selverstone, J., Sharp, Z.D., Compagnoni, R., 2011. Carbonate dissolution during subduction revealed by diamond-bearing rocks from the Alps. Nat. Geosci. 4, 703–706. https://doi.org/10.1038/ngeo1246.

Frezzotti, M.L., Tecce, F., Casagli, A., 2012. Raman spectroscopy for fluid inclusion analysis. J. Geochem. Explor. 112, 1–20. https://doi.org/10.1016/j.gexplo.2011.09.009.

Frezzotti, M.-L., Huizenga, J.-M., Compagnoni, R., Selverstone, J., 2014. Diamond formation by carbon saturation in C–O–H fluids during cold subduction of oceanic lithosphere. Geochim. Cosmochim. Acta 143, 68–86. https://doi.org/10.1016/j.gca.2013.12.022.

Fry, N., Barnicoat, A.C., 1987. The tectonic implications of high-pressure metamorphism in the western Alps. J. Geol. Soc. 144, 653–659. https://doi.org/10.1144/gsjgs.144.4.0653.

Fudral, S., 1996. Etude géologique de la suture tethysienne dans les Alpes franco-italiennes Nord-Occidentales de la Doire Ripaire (Italie) à la région de Bourg Saint-Maurice. PhD thesis Université de Savoie.

Fudral, S., Deville, E., Marthaler, M., 1987. Distinction de trois ensembles d'unités dans les «Schistes lustrés» compris entre la Vanoise et le Val de Suse (Alpes franco-italiennes septentrionales): aspects lithostratigraphiques, paléogéographiques et géodynamiques. Comptes rendus de l'Académie des sciences. Série 2. Mécanique, Physique, Chimie, Sci. l'univers, Sci. Terre 305, 467–472.

Gabalda, S., Beyssac, O., Jolivet, L., Agard, P., Chopin, C., 2009. Thermal structure of a fossil subduction wedge in the Western Alps. Terra Nova 21, 28–34. https://doi.org/10.1111/j.1365-3121.2008.00849.x.

Gao, J., Klemd, R., 2000. Eclogite occurrences in the Southern Tianshan high-pressure belt, Xinjiang, Western China. Gondwana Res. 3, 33–38.

Gao, J., Klemd, R., 2001. Primary fluids entrapped at blueschist to eclogite transition: evidence from the Tianshan meta-subduction complex in northwestern China. Contrib. Mineral. Petrol. 142, 1–14.

Gao, J., Klemd, R., Zhang, L., Wang, Z., Xiao, X., 1999. P-T path of high-pressure/low-temperature rocks and tectonic implications in the western Tianshan Mountains, NW China. J. Metamorph. Geol. 17, 621–636. https://doi.org/10.1046/j.1525-1314.1999.00219.x.

Garber, J.M., Smye, A.J., Feineman, M.D., Kylander-Clark, A.R.C., Matthews, S., 2020. Decoupling of zircon U–Pb and trace-element systematics driven by U diffusion in eclogite-facies zircon (Monviso meta-ophiolite, W. Alps). Contrib. Mineral. Petrol. 175, 55. https://doi.org/10.1007/s00410-020-01692-2.

Ghignone, S., Borghi, A., Balestro, G., Castelli, D., Gattiglio, M., Groppo, C., 2020. HP tectono-metamorphic evolution of the Internal Piedmont Zone in Susa Valley (Western Alps): New petrologic insight from garnet+chloritoid-bearing micaschists and Fe–Ti metagabbro. J. Metamorph. Geol. 1–26.

Giaramita, M.J., Sorensen, S.S., 1994. Primary fluids in low-temperature eclogites: evidence from two subduction complexes (Dominican Republic, and California, USA). Contrib. Mineral. Petrol. 117, 279–292. https://doi.org/10.1007/BF00310869.

Gilio, M., Scambelluri, M., Agostini, S., Godard, M., Pettke, T., Agard, P., Locatelli, M., Angiboust, S., 2020. Fingerprinting and relocating tectonic slices along the plate interface: evidence from the Lago Superiore unit at Monviso (Western Alps). Lithos 352-353, 105308.

Goffé, B., 1982. Définition du faciès A Fe Mg carpholite-chloritoïde, un marqueur du métamorphisme de HP-BT dans les métasédiments alumineux. PhD thesis Université Pierre et Marie Curie-Paris VI.

Goffé, B., Chopin, C., 1986. High-pressure metamorphism in the Western Alps: zoneography of metapelites, chronology and consequences. Schweiz. Mineral. Petrogr. Mitt. 66, 41–52. https://doi.org/10.5169/SEALS-50880.

Goffé, B., Velde, B., 1984. Contrasted metamorphic evolutions in thrusted cover units of the Brianqonnais zone (French Alps): a model for the conservation of HP-LT metamorphic mineral assemblages. Earth Planet. Sci. Lett. 68, 351–360.

Goffé, B., Villey, M., 1984. Texture d'un matériel carboné impliqué dans un métamorphisme haute pression-basse température (Alpes françaises). Les hautes

pressions influencent-elles la carbonification ? Bull. Mineral. 107, 81–91. https://doi.org/10.3406/bulmi.1984.7795.

Groppo, C., Beltrando, M., Compagnoni, R., 2009. The *P-T* path of the ultra-high pressure Lago Di Cignana and adjoining high-pressure meta-ophiolitic units: insights into the evolution of the subducting Tethyan slab. J. Metamorph. Geol. 27, 207–231. https://doi.org/10.1111/j.1525-1314.2009.00814.x.

Groppo, C., Rolfo, F., Sachan, H.K., Rai, S.K., 2016. Petrology of blueschist from the Western Himalaya (Ladakh, NW India): Exploring the complex behavior of a lawsonite-bearing system in a paleo-accretionary setting. Lithos 252–253, 41–56. https://doi.org/10.1016/j.lithos.2016.02.014.

Hacker, B.R., 2008. H_2O subduction beyond arcs. Geochem. Geophys. Geosyst. 9. https://doi.org/10.1029/2007GC001707.

Hacker, B.R., Peacock, S.M., Abers, G.A., Holloway, S.D., 2003. Subduction factory 2. Are intermediate-depth earthquakes in subducting slabs linked to metamorphic dehydration reactions? J. Geophys. Res. 108. https://doi.org/10.1029/2001JB001129.

Hall, D.L., Sterner, S.M., 1993. Preferential water loss from synthetic fluid inclusions. Contrib. Mineral. Petrol. 114, 489–500. https://doi.org/10.1007/BF00321753.

Handy, M.R., Schmid, S.M., Bousquet, R., Kissling, E., Bernoulli, D., 2010. Reconciling plate-tectonic reconstructions of Alpine Tethys with the geological–geophysical record of spreading and subduction in the Alps. Earth Sci. Rev. 102, 121–158.

Hay, W.W., Migdisov, A., Balukhovsky, A.N., Wold, C.N., Flögel, S., Söding, E., 2006. Evaporites and the salinity of the ocean during the Phanerozoic: Implications for climate, ocean circulation and life. Palaeogeogr. Palaeoclimatol. Palaeoecol. 240, 3–46. https://doi.org/10.1016/j.palaeo.2006.03.044.

Henry, C., Burkhard, M., Goffé, B., 1996. Evolution of synmetamorphic veins and their wallrocks through a Western Alps transect: no evidence for large-scale fluid flow. Stable isotope, major- and trace-element systematics. Chem. Geol. 127, 81–109. https://doi.org/10.1016/0009-2541(95)00106-9.

Hertwig, A., McClelland, W.C., Kitajima, K., Schertl, H.-P., Maresch, W.V., Stanek, K., Valley, J.W., Sergeev, S.A., 2016. Inherited igneous zircons in jadeitite predate high-pressure metamorphism and jadeitite formation in the Jagua Clara serpentinite mélange of the Rio San Juan complex (Dominican Republic). Contrib. Mineral. Petrol. 171, 48. https://doi.org/10.1007/s00410-016-1256-6.

Holland, T.J.B., 1979. High water activities in the generation of high pressure kyanite eclogites of the Tauern Window, Austria. J. Geol. 87, 1–27. https://doi.org/10.1086/628388.

Huang, F., Daniel, I., Cardon, H., Montagnac, G., Sverjensky, D.A., 2017. Immiscible hydrocarbon fluids in the deep carbon cycle. Nat. Commun. 8, 15798. https://doi.org/10.1038/ncomms15798.

Hyndman, R.D., McCrory, P.A., Wech, A., Kao, H., Ague, J., 2015. Cascadia subducting plate fluids channelled to fore-arc mantle corner: ETS and silica deposition. J. Geophys. Res. Solid Earth 120, 4344–4358. https://doi.org/10.1002/2015JB011920.

Inglis, E.C., Debret, B., Burton, K.W., Millet, M.-A., Pons, M.-L., Dale, C.W., Bouilhol, P., Cooper, M., Nowell, G.M., McCoy-West, A.J., Williams, H.M., 2017. The behavior of iron and zinc stable isotopes accompanying the subduction of mafic oceanic crust: a case study from Western Alpine ophiolites. Geochem. Geophys. Geosyst. 18, 2562–2579. https://doi.org/10.1002/2016GC006735.

Invernizzi, C., Bigazzi, G., Corrado, S., Leo, P.D., Schiattarella, M., Zattin, M., 2008. New thermobaric constraints on the exhumation history of the Liguride accretionary wedge, southern Italy. Ofioliti 33, 21–32.

Ito, E., Anderson, A.T., 1983. Submarine metamorphism of gabbros from the Mid-Cayman rise: Petrographic and mineralogic constraints on hydrothermal processes at slow-spreading ridges. Contrib. Mineral. Petrol. 82, 371–388. https://doi.org/10.1007/BF00399714.

Jaeckel, K., Bebout, G.E., Angiboust, S., 2018. Deformation-enhanced fluid and mass transfer along Western and Central Alps paleo-subduction interfaces: significance for carbon cycling models. Geosphere 14, 2355–2375. https://doi.org/10.1130/GES01587.1.

Jamieson, R.A., Craw, D., 1987. Sphalerite geobarometry in metamorphic terranes: an appraisal with implications for metamorphic pressure in the Otago Schist. J. Metamorph. Geol. 5, 87–99. https://doi.org/10.1111/j.1525-1314.1987.tb00371.x.

Kawamoto, T., Hertwig, A., Shertl, H.-P., Maresch, W.V., 2018. Fluid inclusions in jadeitite and jadeite-rich rock from serpentinite mélanges in northern Hispaniola: Trapped ambient fluids in a cold subduction channel. Lithos 308-309, 227–241.

Kelley, D.S., Delaney, J.R., 1987. Two-phase separation and fracturing in mid-ocean ridge gabbros at temperatures greater than 700°C. Earth Planet. Sci. Lett. 83, 53–66. https://doi.org/10.1016/0012-821X(87)90050-1.

Kelley, D.S., Robinson, P.T., Malpas, J.G., 1992. Processes of brine generation and circulation in the oceanic crust: Fluid inclusion evidence from the Troodos Ophiolite, Cyprus. J. Geophys. Res. 97, 9307. https://doi.org/10.1029/92JB00520.

Klemd, R., Van den Kerkhof, A.M., Horn, E.E., 1992. High-density CO 2 -N 2 inclusions in eclogite-facies metasediments of the Mfinchberg gneiss complex, SE Germany. Contrib. Mineral. Petrol. 111, 409–419.

Kolesnikov, A., Kutcherov, V.G., Goncharov, A.F., 2009. Methane-derived hydrocarbons produced under upper-mantle conditions. Nat. Geosci. 2, 566–570. https://doi.org/10.1038/ngeo591.

Küster, M., Stöckhert, B., 1997. Density changes of fluid inclusions in high-pressure low-temperature metamorphic rocks from Crete: a thermobarometric approach based on the creep strength of the host minerals. Lithos 41, 151–167. https://doi.org/10.1016/S0024-4937(97)82010-5.

Lafay, R., Deschamps, F., Schwartz, S., Guillot, S., Godard, M., Debret, B., Nicollet, C., 2013. High-pressure serpentinites, a trap-and-release system controlled by metamorphic conditions: example from the Piedmont zone of the western Alps. Chem. Geol. 343, 38–54. https://doi.org/10.1016/j.chemgeo.2013.02.008.

Lagabrielle, Y., 1987. Les ophiolites: Marqueurs de l'histoire tectonique des domaines océaniques. PhD thesis Brest.

Lagabrielle, Y., Cannat, M., 1990. Alpine Jurassic ophiolites resemble the modern Central Atlantic basement. Geology 18, 319–322.

Lagabrielle, Y., Vitale Brovarone, A., Ildefonse, B., 2015. Fossil oceanic core complexes recognized in the blueschist metaophiolites of Western Alps and Corsica. Earth Sci. Rev. 141, 1–26. https://doi.org/10.1016/j.earscirev.2014.11.004.

Lapen, T.J., Johnson, C.M., Baumgartner, L.P., Mahlen, N.J., Beard, B.L., Amato, J.M., 2003. Burial rates during prograde metamorphism of an ultra-high-pressure terrane: an example from Lago di Cignana, western Alps, Italy. Earth Planet. Sci. Lett. 215, 57–72. https://doi.org/10.1016/S0012-821X(03)00455-2.

Laurent, V., Lanari, P., Naïr, I., Augier, R., Lahfid, A., Jolivet, L., 2018. Exhumation of eclogite and blueschist (Cyclades, Greece): Pressure-temperature evolution determined by thermobarometry and garnet equilibrium modelling. J. Metamorph. Geol. 36, 769–798.

Le Pichon, X., Bergerat, F., Roulet, M., 1988. Plate kinematics and tectonics leading to the Alpine belt formation: a new analysis. Geol. Soc. Am. Special Issue 218, 111–131.

Le, V.-H., Caumon, M.-C., Tarantola, A., Randi, A., Robert, P., Mullis, J., 2019. Quantitative measurements of composition, pressure, and density of microvolumes of CO_2 –N_2 Gas mixtures by Raman Spectroscopy. Anal. Chem. 91, 14359–14367. https://doi.org/10.1021/acs.analchem.9b02803.

Le, V.-H., Caumon, M.-C., Tarantola, A., Randi, A., Robert, P., Mullis, J., 2020. Calibration data for simultaneous determination of P-V-X properties of binary and ternary CO2 - CH4 - N2 gas mixtures by Raman spectroscopy over 5–600 bar: Application to natural fluid inclusions. Chem. Geol. 552, 119783. https://doi.org/10.1016/j.chemgeo.2020.119783.

Lefeuvre, B., 2020. La lawsonite dans les métasédiments en base de zone sismogénique: géochimie, échelles de migration des fluides et rôle de la déformation dans les Schistes Lustrés. PhD thesis. Sorbonne Université Paris.

Lefeuvre, B., Agard, P., Verlaguet, A., Dubacq, B., Plunder, A., 2020. Massive formation of lawsonite in subducted sediments from the Schistes Lustrés (W. Alps): Implications for mass transfer and decarbonation in cold subduction zones. Lithos 370–371, 105629. https://doi.org/10.1016/j.lithos.2020.105629.

Lemoine, M., Tricart, P., 1986. Les Schistes lustrés piémontais des Alpes Occidentales: approche stratigraphique, structurales et sédimentologique. Eclogae Geol. Helv. 79, 271–294. https://doi.org/10.5169/SEALS-165835.

Lemoine, M., Marthaler, M., Caron, M., Sartori, M., Amaudric du Chaffaut, S., 1984. Découverte de foraminifères planctoniques du Crétacé supérieur dans les schistes lustrés du Queyras (Alpes occidentales). Conséquences paléogéographiques et tectoniques. Comptes-rendus des séances de l'Académie des sciences. Série 2. Mécanique-physique, chimie, sci. l'univers, sci. terre 299, 727–732.

Li, Y., 2017. Immiscible C-H-O fluids formed at subduction zone conditions. Geochem. Perspect. Lett. 3, 12–21. https://doi.org/10.7185/geochemlet.1702.

Locatelli, M., Verlaguet, A., Agard, P., Federico, L., Angiboust, S., 2018. Intermediate-depth brecciation along the subduction plate interface (Monviso eclogite, W. Alps). Lithos 320–321, 378–402. https://doi.org/10.1016/j.lithos.2018.09.028.

Locatelli, M., Federico, L., Agard, P., Verlaguet, A., 2019a. Geology of the southern Monviso metaophiolite complex (W-Alps, Italy). J. Maps 15, 283–297. https://doi.org/10.1080/17445647.2019.1592030.

Locatelli, M., Verlaguet, A., Agard, P., Pettke, T., Federico, L., 2019b. Fluid pulses during stepwise brecciation at intermediate subduction depths (Monviso Eclogites, W. Alps): first internally then externally sourced. Geochem. Geophys. Geosyst. 20, 5285–5318. https://doi.org/10.1029/2019GC008549.

Lombardo, B., 1978. Osservazioni preliminari sulle ofioliti metamorfiche del Monviso (Alpi Occidentali). Rendiconti Della Soc. Ital. Mineral. E Petrol. 34, 235–305.

Luckscheiter, B., Morteani, G., 1980. The fluid phase in eclogites, glaucophane-bearing rocks and amphibolites from the central tauern window as deduced from fluid inclusion studies. TMPM Tschermaks Petr. Mitt. 27, 99–111. https://doi.org/10.1007/BF01082401.

Mangenot, X., Tarantola, A., Mullis, J., Girard, J.P., Le, V.H., Eiler, J.M., 2021. Geochemistry of clumped isotopologues of CH4 within fluid inclusions in Alpine tectonic quartz fissures. Earth Planet. Sci. Lett. 561, 116792.

McCollom, T.M., 2013. Laboratory simulations of abiotic hydrocarbon formation in earth's deep subsurface. Rev. Mineral. Geochem. 75, 467–494. https://doi.org/10.2138/rmg.2013.75.15.

Meneghini, F., Marroni, M., Moore, J.C., Pandolfi, L., Rowe, C.D., 2009. The processes of underthrusting and underplating in the geologic record: structural diversity between the Franciscan complex (California), the Kodiak complex (Alaska) and the Internal Ligurian units (Italy). Geol. J. 44, 126–152. https://doi.org/10.1002/gj.1144.

Messiga, B., Scambelluri, M., Piccardo, G.B., 1995. Chloritoid-bearing assemblages in mafic systems and eclogite-facies hydration of alpine Mg-Al metagabbros (Erro-Tobbio Unit, Ligurian Western Alps). Eur. J. Mineral. 7, 1149–1168. https://doi.org/10.1127/ejm/7/5/1149.

Michard, A., Goffé, B., Chopin, C., Henry, C., 1996. Did the Western Alps develop through an Oman-type stage? The geotectonic setting of high-pressure metamorphism in two contrasting Tethyan transects. Eclogae Geol. Helv. 89, 43–80.

Monaco, C., Tortorici, L., 1995. Tectonic role of ophiolite-bearing terranes in the development of the Southern Apennines orogenic belt. Terra Nova 7, 153–160. https://doi.org/10.1111/j.1365-3121.1995.tb00684.x.

Mukherjee, B.K., Sachan, H.K., 2009. Fluids in coesite-bearing rocks of the Tso Morari complex, NW Himalaya: evidence for entrapment during peak metamorphism and subsequent uplift. Geol. Mag. 146, 876–889. https://doi.org/10.1017/S0016756809990069.

Mullis, J., 1979. The system methane-water as a geologic thermometer and barometer from the external part of the Central Alps. Bull. Mineral. 102, 526–536. https://doi.org/10.3406/bulmi.1979.7301.

Mullis, J., Dubessy, J., Poty, B., O'Neil, J., 1994. Fluid regimes during late stages of a continental collision: physical, chemical, and stable isotope measurements of fluid inclusions in fissure quartz from a geotraverse through the Central Alps, Switzerland.

Geochim. Cosmochim. Acta 58, 2239–2267. https://doi.org/10.1016/0016-7037(94)90008-6.

Muñoz-Montecinos, J., Angiboust, S., Cambeses, A., García-Casco, A., 2020. Multiple veining in a paleo–accretionary wedge: the metamorphic rock record of prograde dehydration and transient high pore-fluid pressures along the subduction interface (Western Series, Central Chile). Geosphere 16, 765–786. https://doi.org/10.1130/GES02227.1.

Nadeau, S., Philippot, P., Pineau, F., 1993. Fluid inclusion and mineral isotopic compositions (HCO) in eclogitic rocks as tracers of local fluid migration during high-pressure metamorphism. Earth Planet. Sci. Lett. 114, 431–448. https://doi.org/10.1016/0012-821X(93)90074-J.

Nehlig, P., 1991. Salinity of oceanic hydrothermal fluids: a fluid inclusion study. Earth Planet. Sci. Lett. 102, 310–325. https://doi.org/10.1016/0012-821X(91)90026-E.

Obara, K., 2002. Nonvolcanic Deep Tremor Associated with Subduction in Southwest Japan. Science 296, 1679–1681. https://doi.org/10.1126/science.1070378.

Padrón-Navarta, J.A., Hermann, J., Garrido, C.J., López Sánchez-Vizcaíno, V., Gómez-Pugnaire, M.T., 2010. An experimental investigation of antigorite dehydration in natural silica-enriched serpentinite. Contrib. Mineral. Petrol. 159, 25–42. https://doi.org/10.1007/s00410-009-0414-5.

Philippot, P., 1987. "Crack seal" vein geometry in eclogitic rocks. Geodin. Acta 1, 171–181.

Philippot, P., 1990. Opposite vergence of Nappes and crustal extension in the French-Italian western Alps. Tectonics 9, 1143–1164. https://doi.org/10.1029/TC009i005p01143.

Philippot, P., Kienast, J.-R., 1989. Chemical-microstructural changes in eclogite-facies shear zones (Monviso, Western Alps, North Italy) as indicators of strain history and the mechanism and scale of mass transfer. Lithos 23, 179–200. https://doi.org/10.1016/0024-4937(89)90004-2.

Philippot, P., Selverstone, J., 1991. Trace-element-rich brines in eclogitic veins: implications for fluid composition and transport during subduction. Contrib. Mineral. Petrol. 106, 417–430. https://doi.org/10.1007/BF00321985.

Philippot, P., Agrinier, P., Scambelluri, M., 1998. Chlorine cycling during subduction of altered oceanic crust. Earth Planet. Sci. Lett. 12.

Plunder, A., Agard, P., Dubacq, B., Chopin, C., Bellanger, M., 2012. How continuous and precise is the record of P-T paths? Insights from combined thermobarometry and thermodynamic modelling into subduction dynamics (Schistes Lustrés, W. Alps). J. Metamorph. Geol. 30, 323–346. https://doi.org/10.1111/j.1525-1314.2011.00969.x.

Pognante, U., 1991. Petrological constraints on the eclogite- and blueschist facies metamorphism and P-T-t paths in the Western Alps. J. Metamorph. Geol. 9, 5–17. https://doi.org/10.1111/j.1525-1314.1991.tb00501.x.

Pourteau, A., Bousquet, R., Vidal, O., Plunder, A., Duesterhoeft, E., Candan, O., Oberhänsli, R., 2014. Multistage growth of Fe–Mg–carpholite and Fe–Mg–chloritoid, from field evidence to thermodynamic modelling. Contrib. Mineral. Petrol. 168, 1090.

Raimbourg, H., Thiéry, R., Vacelet, M., Ramboz, C., Cluzel, N., Le Trong, E., Yamaguchi, A., Kimura, G., 2014. A new method of reconstituting the P–T conditions of fluid circulation in an accretionary prism (Shimanto, Japan) from microthermometry of methane-bearing aqueous inclusions. Geochim. Cosmochim. Acta 125, 96–109. https://doi.org/10.1016/j.gca.2013.09.025.

Raimbourg, H., Vacelet, M., Ramboz, C., Famin, V., Augier, R., Palazzin, G., Yamaguchi, A., Kimura, G., 2015. Fluid circulation in the depths of accretionary prisms: an example of the Shimanto Belt, Kyushu, Japan. Tectonophysics 655, 161–176. https://doi.org/10.1016/j.tecto.2015.05.023.

Raimbourg, H., Famin, V., Palazzin, G., Mayoux, M., Jolivet, L., Ramboz, C., Yamaguchi, A., 2018. Fluid properties and dynamics along the seismogenic plate interface. Geosphere 14, 469–491. https://doi.org/10.1130/GES01504.1.

Roedder, E., 1984. Fluid inclusions. Reviews in Mineralogy. Vol. 12. Mineralogical Society of America, p. 644.

Rossetti, F., Tecce, F., Aldega, L., Brilli, M., Faccenna, C., 2006. Deformation and fluid flow during orogeny at the palaeo-Pacific active margin of Gondwana: the early Palaeozoic Robertson Bay accretionary complex (North Victoria Land, Antarctica). J. Metamorph. Geol. 24, 33–53. https://doi.org/10.1111/j.1525-1314.2005.00620.x.

Rubatto, D., Angiboust, S., 2015. Oxygen isotope record of oceanic and high-pressure metasomatism: a P–T–time–fluid path for the Monviso eclogites (Italy). Contrib. Mineral. Petrol. 170, 44. https://doi.org/10.1007/s00410-015-1198-4.

Rubatto, D., Hermann, J., 2003. Zircon formation during fluid circulation in eclogites (Monviso, Western Alps): implications for Zr and Hf budget in subduction zones. Geochim. Cosmochim. Acta 67, 2173–2187.

Rupke, L., Morgan, J., Hort, M., Connolly, J., 2004. Serpentine and the subduction zone water cycle. Earth Planet. Sci. Lett. 223, 17–34. https://doi.org/10.1016/j.epsl.2004.04.018.

Sachan, H.K., Kharya, A., Singh, P.C., Rolfo, F., Groppo, C., Tiwari, S.K., 2017. A fluid inclusion study of blueschist-facies lithologies from the Indus suture zone, Ladakh (India): Implications for the exhumation of the subduction related Sapi-Shergol ophiolitic mélange. J. Asian Earth Sci. 146, 185–195. https://doi.org/10.1016/j.jseaes.2017.05.025.

Sadofsky, S.J., Bebout, G.E., 2004. Field and isotopic evidence for fluid mobility in the franciscan complex: forearc paleohydrogeology to depths of 30 kilometers. Int. Geol. Rev. 46, 1053–1088. https://doi.org/10.2747/0020-6814.46.12.1053.

Saliot, P., 1979. La jadéite dans les Alpes françaises. Bull. Mineral. 102, 391–401. https://doi.org/10.3406/bulmi.1979.7335.

Scambelluri, M., Philippot, P., 2001. Deep fluids in subduction zones. Lithos 55, 213–227. https://doi.org/10.1016/S0024-4937(00)00046-3.

Scambelluri, M., Piccardo, G., Philippot, P., Robbiano, A., Negretti, L., 1997. High salinity fluid inclusions formed from recycled seawater in deeply subducted alpine serpentinite. Earth Planet. Sci. Lett. 148, 485–499. https://doi.org/10.1016/S0012-821X(97)00043-5.

Scambelluri, M., Bottazzi, P., Trommsdorff, V., Vannucci, R., Hermann, J., Gomez-Pugnaire, M.T., Lopez-Sanchez, V., 2001. Incompatible element-rich fluids released by antigorite breakdown in deeply subducted mantle. Earth Planet. Sci. Lett. 192, 457–470.

Schertl, H.-P., Maresch, W.V., Stanek, K.P., Hertwig, A., Krebs, M., Baese, R., Sergeev, S.S., 2012. New occurrences of jadeitite, jadeite quartzite and jadeite-lawsonite quartzite in the Dominican Republic, Hispaniola: petrological and geochronological overview. Eur. J. Mineral. 24, 199–216. https://doi.org/10.1127/0935-1221/2012/0024-2201.

Schmid, S.M., Pfiffner, O.A., Froitzheim, N., Schönborn, G., Kissling, E., 1996. Geophysical-geological transect and tectonic evolution of the Swiss-Italian Alps. Tectonics 15, 1036–1064. https://doi.org/10.1029/96TC00433.

Schmid, S.M., Kissling, E., Diehl, T., van Hinsbergen, D.J.J., Molli, G., 2017. Ivrea mantle wedge, arc of the Western Alps, and kinematic evolution of the Alps–Apennines orogenic system. Swiss J. Geosci. 110, 581–612. https://doi.org/10.1007/s00015-016-0237-0.

Schmidt, M.W., Poli, S., 2014. Devolatilization during subduction. Treatise on Geochemistry. Elsevier, pp. 669–701 https://doi.org/10.1016/B978-0-08-095975-7.00321-1.

Schwartz, S., 2000. La zone piémontaise des Alpes Occidentales: un paléocomplexe de subduction. Arguments Métamorphiques, Géochronologiques et Structuraux. PhD thesis Université Claude Bernard-Lyon I.

Schwartz, S., Lardeaux, J.-M., Guillot, S., Tricart, P., 2000. Diversité du métamorphisme éclogitique dans le massif ophiolitique du Monviso (Alpes occidentales, Italie). Geodin. Acta 13, 169–188. https://doi.org/10.1080/09853111.2000.11105371.

Schwartz, S., Lardeaux, J.M., Tricart, P., Guillot, S., Labrin, E., 2007. Diachronous exhumation of HP-LT metamorphic rocks from South-Western Alps: evidence from fission-track analysis. Terra Nova 19, 133–140. https://doi.org/10.1111/j.1365-3121.2006.00728.x.

Schwartz, S., Guillot, S., Reynard, B., Lafay, R., Debret, B., Nicollet, C., Lanari, P., Auzende, A.L., 2013. Pressure–temperature estimates of the lizardite/antigorite transition in high pressure serpentinites. Lithos 178, 197–210. https://doi.org/10.1016/j.lithos.2012.11.023.

Schwartz, S., Gautheron, C., Ketcham, R.A., Brunet, F., Corre, M., Agranier, A., Pinna-Jamme, R., Haurine, F., Monvoin, G., Riel, N., 2020. Unraveling the exhumation history of high-pressure ophiolites using magnetite (U-Th-Sm)/He thermochronometry. Earth Planet. Sci. Lett. 543, 116359. https://doi.org/10.1016/j.epsl.2020.116359.

Selverstone, J., Sharp, Z.D., 2013. Chlorine isotope constraints on fluid-rock interactions during subduction and exhumation of the Zermatt-Saas ophiolite. Geochem. Geophys. Geosyst. 14, 4370–4391. https://doi.org/10.1002/ggge.20269.

Selverstone, J., Franz, G., Thomas, S., Getty, S., 1992. Fluid variability in 2 GPa eclogites as an indicator of fluid behavior during subduction. Contrib. Mineral. Petrol. 112, 341–357. https://doi.org/10.1007/BF00310465.

Sicard-Lochon, E., 1987. La Lawsonite et Ses Pseudomorphoses. PhD thesis Université Claude Bernard-Lyon I.

Sisson, V.B., Hollister, L.S., Onstott, T.C., 1989. Petrologic and age constraints on the origin of a low-pressure/high-temperature metamorphic complex, southern Alaska. J. Geophys. Res. 94, 4392–4410. https://doi.org/10.1029/JB094iB04p04392.

Smith, M.P., Yardley, B.W.D., 1999. Fluid evolution during metamorphism of the Otago Schist, New Zealand: (I) evidence from fluid inclusions. J. Metamorph. Geol. 17, 173–186. https://doi.org/10.1046/j.1525-1314.1999.00189.x.

Spandler, C., Pirard, C., 2013. Element recycling from subducting slabs to arc crust: a review. Lithos 170–171, 208–223. https://doi.org/10.1016/j.lithos.2013.02.016.

Spandler, C., Pettke, T., Rubatto, D., 2011. Internal and External Fluid sources for Eclogite-facies Veins in the Monviso Meta-ophiolite, Western Alps: Implications for Fluid Flow in Subduction zones. J. Petrol. 52, 1207–1236. https://doi.org/10.1093/petrology/egr025.

Spear, F.S., Franz, G., 1986. P-T evolution of metasediments from the Eclogite Zone, south-central Tauern Window, Austria. Lithos 19, 219–234. https://doi.org/10.1016/0024-4937(86)90024-1.

Stampfli, G.M., Mosar, J., Marquer, D., Marchant, R., Baudin, T., Borel, G., 1998. Subduction and obduction processes in the Swiss Alps. Tectonophysics 296, 159–204. https://doi.org/10.1016/S0040-1951(98)00142-5.

Starr, P.G., Broadwell, K.S., Dragovic, B., Scambelluri, M., Haws, A.A., Caddick, M.J., Smye, A.J., Baxter, E.F., 2020. The subduction and exhumation history of the Voltri Ophiolite, Italy: evaluating exhumation mechanisms for high-pressure metamorphic massifs. Lithos 376-377, 105767.

Sterin, K.E., Aleksanyan, V.T., Zhizhin, G.N., 1980. Raman Spectra of Hydrocarbons (Pergamon. ed).

Sterner, S.M., Bodnar, R.J., 1989. Synthetic fluid inclusions - VII. Re-equilibration of fluid inclusions in quartz during laboratory-simulated metamorphic burial and uplift. J. Metamorph. Geol. 7, 243–260. https://doi.org/10.1111/j.1525-1314.1989.tb00587.x.

Sverjensky, D., Daniel, I., Brovarone, A.V., 2020. The changing character of carbon in fluids with pressure: organic geochemistry of Earth's upper mantle fluids. In: Manning, C.E., Lin, J., Mao, W.L. (Eds.), Geophysical Monograph Series. Wiley, pp. 259–269 https://doi.org/10.1002/9781119508229.ch22.

Tao, R., Zhang, L., Tian, M., Zhu, J., Liu, X., Liu, J., Höfer, H.E., Stagno, V., Fei, Y., 2018. Formation of abiotic hydrocarbon from reduction of carbonate in subduction zones: constraints from petrological observation and experimental simulation. Geochim. Cosmochim. Acta 239, 390–408. https://doi.org/10.1016/j.gca.2018.08.008.

Tarantola, A., Caumon, M.-C., 2015. Raman spectra of water in fluid inclusions: II. Effect of negative pressure on salinity measurement: Effect of negative pressure on salinity measured by Raman spectroscopy. J. Raman Spectrosc. 46, 977–982. https://doi.org/10.1002/jrs.4668.

Tarantola, A., Mullis, J., Vennemann, T., Dubessy, J., de Capitani, C., 2007. Oxidation of methane at the CH4/H2O–(CO2) transition zone in the external part of the Central Alps, Switzerland: evidence from stable isotope investigations. Chem. Geol. 237, 329–357. https://doi.org/10.1016/j.chemgeo.2006.07.007.

Tarantola, A., Mullis, J., Guillaume, D., Dubessy, J., de Capitani, C., Abdelmoula, M., 2009. Oxidation of CH4 to CO2 and H2O by chloritization of detrital biotite at 270±5 °C in the external part of the Central Alps, Switzerland. Lithos 112, 497–510. https://doi.org/10.1016/j.lithos.2009.04.008.

Tarantola, A., Diamond, L.W., Stünitz, H., Thust, A., Pec, M., 2012. Modification of fluid inclusions in quartz by deviatoric stress. III: Influence of principal stresses on inclusion density and orientation. Contrib. Mineral. Petrol. 164, 537–550. https://doi.org/10.1007/s00410-012-0749-1.

Terabayashi, M., Maruyama, S., 1998. Large pressure gap between the Coastal and Central Franciscan belts, northern and Central California. Tectonophysics 285, 87–101. https://doi.org/10.1016/S0040-1951(97)00194-7.

Toriumi, M., Teruya, J., 1988. Tectono-metamorphism of the Shimanto Belt. Mod. Geol. 12, 303–324.

Touret, J.L.R., Frezzotti, M.-L., 2003. Fluid inclusions in high pressure and ultrahigh pressure metamorphic rocks. In: Papp, G., Weiszburg, T.G., Carswell, D.A., Compagnoni, R., Rolfo, F. (Eds.), Ultrahigh Pressure Metamorphism. Mineralogical Society of Great Britain and Ireland, Budapest, pp. 467–487 https://doi.org/10.1180/EMU-notes.5.15.

Tricart, P., Schwartz, S., 2006. A north-south section across the Queyras Schistes lustrés (Piedmont zone, Western Alps): Syn-collision refolding of a subduction wedge. Eclogae Geol. Helv. 99, 429–442. https://doi.org/10.1007/s00015-006-1197-6.

Tsujimori, T., Matsumoto, K., Wakabayashi, J., Liou, J.G., 2006. Franciscan eclogite revisited: Reevaluation of the P–T evolution of tectonic blocks from Tiburon Peninsula, California, U.S.a. Mineral. Petrol. 88, 243–267. https://doi.org/10.1007/s00710-006-0157-1.

Vallis, F., Scambelluri, M., 1996. Redistribution of high-pressure fluids during retrograde metamorphism of eclogite-facies rocks (Voltri Massif, Italian Western Alps). Lithos 39, 81–92. https://doi.org/10.1016/S0024-4937(96)00012-6.

Van den Kerkhof, A.M., Hein, U.F., 2001. Fluid inclusion petrography. Lithos 55, 27–47.

Vanko, D.A., 1986. High-chlorine amphiboles from oceanic rocks: product of highly-saline hydrothermal fluids? Am. Mineral. 71, 51–59.

Vanko, D.A., 1988. Temperature, pressure, and composition of hydrothermal fluids, with their bearing on the magnitude of tectonic uplift at mid-ocean ridges, inferred from fluid inclusions in oceanic layer 3 rocks. J. Geophys. Res. 93, 4595–4611.

Vannucchi, P., 2001. Monitoring paleo-fluid pressure through vein microstructures. J. Geodyn. 32, 567–581. https://doi.org/10.1016/S0264-3707(01)00048-5.

Verlaguet, A., Bonnemains, D., Mével, C., Escartín, J., Andreani, M., Bourdelle, F., Boiron, M.-C., Chavagnac, V., 2020. Fluid circulation along an oceanic detachment fault: insights from fluid inclusions in silicified brecciated fault rocks (Mid-Atlantic Ridge at 13°20′ N). Geochem. Geophys. Geosyst. https://doi.org/10.1029/2020GC009235.

Vitale Brovarone, A., Alard, O., Beyssac, O., Martin, L., Picatto, M., 2014. Lawsonite metasomatism and trace element recycling in subduction zones. J. Metamorph. Geol. 32, 489–514. https://doi.org/10.1111/jmg.12074.

Vitale Brovarone, A., Martinez, I., Elmaleh, A., Compagnoni, R., Chaduteau, C., Ferraris, C., Esteve, I., 2017. Massive production of abiotic methane during subduction evidenced in metamorphosed ophicarbonates from the Italian Alps. Nat. Commun. 8, 14134. https://doi.org/10.1038/ncomms14134.

Vitale Brovarone, A., Sverjensky, D.A., Piccoli, F., Ressico, F., Giovannelli, D., Daniel, I., 2020a. Subduction hides high-pressure sources of energy that may feed the deep subsurface biosphere. Nat. Commun. 11, 3880. https://doi.org/10.1038/s41467-020-17342-x.

Vitale Brovarone, A., Tumiati, S., Piccoli, F., Ague, J.J., Connolly, J.A.D., Beyssac, O., 2020b. Fluid-mediated selective dissolution of subducting carbonaceous material: implications for carbon recycling and fluid fluxes at forearc depths. Chem. Geol. 549, 119682. https://doi.org/10.1016/j.chemgeo.2020.119682.

Vityk, M.O., Bodnar, R.J., 1995a. Do fluid inclusions in high-grade metamorphic terranes preserve peak metamorphic density during retrograde decompression? Am. Mineral. 80, 641–644.

Vityk, M.O., Bodnar, R.J., 1995b. Textural evolution of synthetic fluid inclusions in quartz during reequilibration, with applications to tectonic reconstruction. Contrib. Mineral. Petrol. 121, 309–323. https://doi.org/10.1007/BF02688246.

Vrolijk, P., 1987. Tectonically driven fluid flow in the Kodiak accretionary complex, Alaska. Geology 15, 466–469.

Vrolijk, P., Myers, G., Moore, J.C., 1988. Warm fluid migration along tectonic melanges in the Kodiak Accretionary complex, Alaska. J. Geophys. Res. 93, 10313–10324. https://doi.org/10.1029/JB093iB09p10313.

Widmer, T., Thompson, A.B., 2001. Local origin of high pressure vein material in eclogite facies rocks of the Zermatt-Saas-Zone, Switzerland. Am. J. Sci. 301, 627–656. https://doi.org/10.2475/ajs.301.7.627.

Wopenka, B., Pasteris, J.D., 1987. Raman intensities and detection limits of geochemically relevant gas mixtures for a laser Raman microprobe. Anal. Chem. 59, 2165–2170.

Yardley, B.W.D., 1982. The early metamorphic history of the Haast Schists and related rocks of New Zealand. Contrib. Mineral. Petrol. 81, 317–327. https://doi.org/10.1007/BF00371686.

Yardley, B.W.D., Graham, J.T., 2002. The origins of salinity in metamorphic fluids: origins of salinity in metamorphic fluids. Geofluids 2, 249–256. https://doi.org/10.1046/j.1468-8123.2002.00042.x.

Yoshida, K., Hirajima, T., Ohsawa, S., Kobayashi, T., Mishima, T., Sengen, Y., 2015. Geochemical features and relative B–Li–Cl compositions of deep-origin fluids trapped in high-pressure metamorphic rocks. Lithos 226, 50–64. https://doi.org/10.1016/j.lithos.2015.03.002.

Supplementary Material en annexe – 3

Chapitre III – Corrélations spatiales entre écailles Liguro-Piémontaises et implications pour les mécanismes d'écaillage en subduction

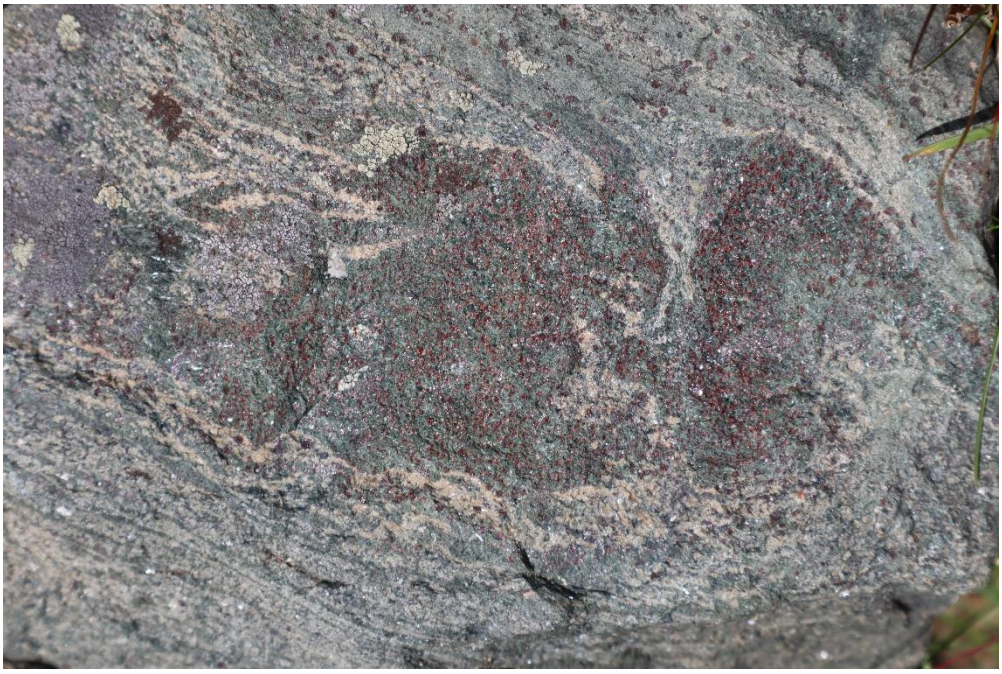

Boudin d'éclogite dans un bloc de méta-basaltes. Lago Laus.

III. Corrélations spatiales entre écailles Liguro-Piémontaises et implications pour les mécanismes d'écaillage en subduction

III.1. Résumé du chapitre

Des fragments subduits de lithosphère océanique sont exposés de façon continue dans le domaine Liguro-Piémontais des Alpes occidentales. En combinant de nouvelles données pétrologiques, avec celles de la littérature, nous fournissons un cadre détaillé des conditions du pic métamorphique enregistrées par les différentes écailles de subduction. Cette cartographie haute résolution confirme la présence d'une forte augmentation du grade métamorphique vers l'Est à travers le domaine comme à l'intérieur de certaines écailles. La compilation des données lithostratigraphiques, structurales ainsi que radiochronologiques et l'estimation des ratio sédiments/mafiques-ultramafiques pour chaque écaille a permis d'affiner l'origine initiale de ces unités tectonométamorphiques à l'intérieur du domaine océanique.

Le modèle proposé permet de restaurer les géométries de la subduction alpine aux conditions du pic d'enfouissement. Les résultats montrent une distribution trimodale d'unités avec une augmentation du grade métamorphique depuis les unités supérieures (LPU ; 320-400°C- 1.2-1.9 GPa) aux unités médianes (LPM ; 415-475°C- 1.7-2.2 GPa) et inférieures (LPL ; 500-580°C- 2.2-2.8 GPa). Les unités LPU et LPM, de faciès schiste bleu, sont dominées par les sédiments (>90%), tandis que les unités LPL, de faciès éclogite, sont bien plus riches en roches mafiques et ultramafiques (>40%). Ces caractéristiques, accompagnées de distinctions lithostratigraphiques, reflètent des différences initiales de paléogéographie et/ou des mécanismes responsables de l'arrachement de matériel au panneau plongeant.

Les profondeurs du pic d'enfouissement des unités LPU, LPM, et LPL sont similaires à celles déduites pour l'écaillage et le sous-plaquage dans les zones de subduction actives et fossiles. Les données pétrologiques et lithostratigraphiques suggèrent que l'écaillage des unités LPU et LPM aurait principalement été contrôlé par des contrastes lithostratigraphiques : (i) dans les niveaux pélitiques ou (2) le long des contacts dans la partie supérieure du manteau serpentinisé. En revanche, dans les unités inférieures, les réactions de déshydratation majeures (comme la déstabilisation de la lawsonite dans les sédiments) auraient potentiellement contrôllées leur écaillage dans les conditions du faciès

éclogite et potentiellement sous des conditions de fortes pressions de fluide et une fragilisation des roches.

III.2. Article 2: Subducted fragments of the Liguro-Piemont ocean, Western Alps: spatial correlations and offscraping mechanisms during subduction. Tectonophysics, Février 2022.

Tectonophysics 827 (2022) 229267

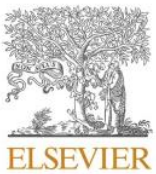

Contents lists available at ScienceDirect

Tectonophysics

journal homepage: www.elsevier.com/locate/tecto

Subducted fragments of the Liguro-Piemont ocean, Western Alps: Spatial correlations and offscraping mechanisms during subduction

Clément Herviou [a,*], Philippe Agard [a], Alexis Plunder [b], Kevin Mendes [a], Anne Verlaguet [a], Damien Deldicque [c], Nadaya Cubas [a]

[a] Sorbonne Université, CNRS-INSU, Institut des Sciences de la Terre de Paris, ISTeP UMR 7193, F-75005 Paris, France
[b] BRGM, F-45060 Orléans, France
[c] Laboratoire de Géologie, Ecole Normale Supérieure PSL, F-75005 Paris, France

ARTICLE INFO

Keywords:
Oceanic subduction
Liguro-Piemont
Schistes Lustrés
Western Alps
Tectonic slicing
HP-LT metamorphism

ABSTRACT

Fragments of subducted slow-spreading oceanic lithosphere are exposed continuously in the Liguro-Piemont domain of the Western Alps. By combining new and literature petrological data, interpolated maps of maximum temperatures, maximum Si contents of phengite as a proxy for peak pressure and thermodynamic modelling, we provide a detailed framework of the peak metamorphic conditions experienced by the distinct subduction slices. High-resolution mapping confirms the marked eastward increase in metamorphic grade throughout the domain, as well as within some slices. The compilation of lithostratigraphic, structural and radiochronological data and the estimation of sediment/mafic-ultramafic ratio for each slice allow refining the origin of these tectonometamorphic units within the former oceanic domain. The refined structural sketchmap allows to restore the geometries of the Alpine subduction at peak burial conditions. Results point to a trimodal distribution of the units with an increase in metamorphic conditions from the Upper (LPU; 320-400°C- 1.2-1.9 GPa) to the Middle (LPM; 415-475°C- 1.7-2.2 GPa) and to the Lower units (LPL; 500-580°C- 2.2-2.8 GPa). The blueschist-facies LPU and LPM units are dominated by sediments (>90%), whereas the eclogitic LPL units are far richer in mafic-ultramafic rocks (>40%). These characteristics, along with lithostratigraphic differences, reflect major differences in their initial paleogeography and/or in the mechanisms responsible for material offscraping from the downgoing slab. The peak burial depths of the LPU, LPM and LPL units are similar to those inferred for slicing and underplating in both modern and fossil subduction zones. Petrological and lithostratigraphic data suggest that the offscraping of the LPU and LPM units was mostly controlled by lithological contrasts, within pelagic shales or along contacts within the uppermost serpentinized mantle. In contrast, major dehydration reactions (such as lawsonite breakdown in sediments) likely controlled the offscraping of the LPL units at eclogite-facies conditions, possibly through high fluid pressure conditions and rocks embrittlement.

1. Introduction

Subduction zones trigger devastating earthquakes and volcanic eruptions (e.g. Ruff and Kanamori, 1980; Tatsumi, 1986; Stern, 2002). Understanding mechanical coupling and mass transfer occurring at the subduction plate boundary, and the complex interplay of short and long-term processes, is therefore critical to decipher subduction dynamics and risk assessment (Rüpke, 2004; Agard et al., 2018; Behr and Bürgmann, 2021). During convergence, some material is removed from the downgoing plate (the 'slab') sporadically and accreted, or 'underplated', to the upper one (Karig and Sharman, 1975; Scholl et al., 1980; Platt, 1986). At shallow depth, offscraping at the roof of the oceanic crust results in the formation of accretionary wedges dominated by sediments (Platt, 1988). Deeper accretion also takes place along the subduction plate interface (Willner, 2005; Agard et al., 2009) and leads to the juxtaposition, and later exhumation, of deeply subducted slices with distinctive subduction histories (Plunder et al., 2012, 2015; Angiboust et al., 2013, 2014, 2016, 2018; Tewksbury-Christle et al., 2021). The removal of oceanic material from the slab, and potential accretion to the upper plate, require the down-stepping of the plate interface décollement into the slab (Kimura et al., 1996; Kimura et al., 2007), hence an increase in mechanical coupling (Agard et al., 2016, 2020) and

* Corresponding author.
E-mail address: clement.herviou@sorbonne-universite.fr (C. Herviou).

https://doi.org/10.1016/j.tecto.2022.229267
Received 8 December 2021; Received in revised form 10 February 2022; Accepted 14 February 2022
Available online 22 February 2022

strain localization into weakness zones (Kimura et al., 1996; Kimura et al., 2007; Angiboust et al., 2012c; Ruh et al., 2015). The worldwide record of blueschist- and eclogite-facies subducted oceanic fragments shows that this happens transiently (Agard et al., 2009; Monié and Agard, 2009; Bonnet et al., 2018) and at non-random depths (Plunder et al., 2015; Agard et al., 2018).

The processes leading to coupling and slicing in the slab are still debated, despite suggestions that large sediment inputs (Behr and Becker, 2018) and serpentinization of the slab (Ruh et al., 2015) or of the mantle wedge (Agard et al., 2009, 2016; Guillot et al., 2009, 2015), or fluid-mediated deformation mechanisms (Agard et al., 2020), may enhance the lubrication of the plate interface, and thereby promote decoupling (Agard et al., 2018; Garber et al., 2020b). More specifically, what are the mechanical processes driving deep slicing of the downgoing plate and the recovery of slivers at the surface? Do rock recovery clusters correspond to downdip changes of the mechanical behavior along the plate interface or to lithological heterogeneities? How do dehydration reactions impact slab fragments, from the base of the seismogenic zone down to sub-arc depths?

Since direct access through deep drilling is limited to the few first kilometers (e.g. Tobin et al., 2019), the investigation of fossil subduction fragments with a diagnostic high pressure low temperature (HP-LT) imprint is paramount. In the Western Alps, remnants of subducted slow-spreading oceanic lithosphere (Lagabrielle and Cannat, 1990) are exposed along the 200 km-long and up to 50 km-wide Liguro-Piemont domain (L-P; or Piemonte-Liguria domain; Deville et al., 1992; Agard, 2021; Agard and Handy, 2021). This nappe-stack is one of the largest, better-preserved and most studied examples of fossil subduction complexes, spanning a range from ~30 to 80 km depth (Berger and Bousquet, 2008; Agard et al., 2002, 2018; Agard, 2021), and providing an access to subduction processes along those depths (Bebout et al., 2013; Herviou et al., 2021).

In the L-P domain, a major distinction can be made between the metamafic-ultramafic dominated (MUM units of Agard, 2021) eclogite-facies units and the metasedimentary dominated (S units of Agard, 2021) blueschist (BS)-facies units (Dal Piaz, 1974b; Caby et al., 1978; Droop et al., 1990; Pognante, 1991; Agard et al., 2001a). Within these distinct zones, several slices, generally three to four in total, were identified along different transects of the L-P domain (Fudral, 1996; Agard et al., 2001a; Tricart and Schwartz, 2006; Lagabrielle et al., 2015). However, tectonic contacts preserving the pristine, initial juxtaposition of the units sliced during subduction are often obscured by later deformation and almost impossible to follow over great distances. Consequently, very few studies (e.g. Deville et al., 1992) have attempted to correlate these tectonic slices across the entire domain, and their extension and distribution across the L-P domain remain poorly known. A detailed knowledge of this tectonometamorphic set-up is nevertheless critical to reconstruct the 2D and 3D geometries and to understand subduction-related processes along the L-P domain.

In the Liguro-Piemont domain, metamafic and ultramafic bodies are generally embedded in volumetrically dominant sediments. These sediments, more sensitive to P-T changes (Goffé and Chopin, 1986; Bousquet et al., 2008) are also cropping out continuously along the complex and across the different slices. They provide the opportunity to follow in detail the evolution of (i) the index mineralogy (Goffé et al., 2004; Bousquet et al., 2008), (ii) the variation of their stratigraphic succession (Deville et al., 1992; Lemoine, 2003), (iii) the maximum temperature experienced by these rocks during peak burial (Beyssac et al., 2002), and (iv) the peak pressure, through adequate indicators (Agard et al., 2001a, 2001b).

This study tightly and systematically combines lithostratigraphic, structural and petrologic data, both new and from the literature, across the entire L-P domain of the Western Alps, in order to precise its tectonometamorphic set-up. A refined model of the distribution of equivalent tectonic slices along the L-P complex is proposed. We then discuss the mechanisms driving the recovery of the distinct rock types (MUM versus S units) from selective depths and the insights gained on Alpine subduction dynamics, as well as on the processes driving slab slicing and nappe stacking at depth.

2. Geological setting

2.1. Fragments of subducted oceanic lithosphere in the Western Alps

The Western Alps formed as a result of an east- to south-east-dipping and slow (~1 cm/yr) subduction of the 100 to 1000 km wide Valais and Liguro-Piemont oceans below Adria/Apulia (Le Pichon et al., 1988; Schmid et al., 1996, 2017; Lapen et al., 2003; Handy, 2010; Agard and Handy, 2021). Subduction of these slow-spreading oceanic domains (Lagabrielle and Cannat, 1990) started in the Late Cretaceous and was over by ~35 Ma (Stampfli et al., 1998; Schmid et al., 2017). Subduction of oceanic material was followed by a phase of continental subduction (Chopin, 1984; Rubatto and Hermann, 2001; Bonnet et al., 2022) before Eurasia-Adria/Apulia collision started (Simon-Labric et al., 2009; Bellahsen et al., 2014).

Remnants of subducted Liguro-Piemont oceanic lithosphere are now exposed in the internal domain of the Western Alps and form a nappe-stack known as the Liguro-Piemont (L-P) domain (Agard, 2021; Agard and Handy, 2021; Fig. 1a) or Schistes Lustrés complex (Caron, 1977; Agard et al., 2001a, 2009), owing to their characteristic sedimentary features. Metasediments (Schistes Lustrés s.s.) are volumetrically dominant in this complex and range from the Late Jurassic (De Wever and Caby, 1981; Lagabrielle, 1987) to the Late Cretaceous (Lemoine et al., 1984; Lagabrielle, 1987). They correspond to an initial ~200-400 m thick sequence of pelagic and hemipelagic seafloor deposits (marls, shales and limestones metamorphosed as calcschists, metapelites and marbles; Lemoine et al., 1984; Lemoine and Tricart, 1986; Lemoine, 2003; Deville et al., 1992; Michard et al., 1996) embedding variable amounts of mafic and ultramafic rocks (Fig. 1a). The serpentinized mantle generally contains sparse pockets of Jurassic mafic material (e.g. Decrausaz et al., 2021) highlighting the discontinuous character of the oceanic crust (Lagabrielle, 1987; see Agard, 2021 and references therein). Exposed fragments of L-P lithosphere often preserve pre-alpine oceanic structures (Lagabrielle et al., 2015; Balestro et al., 2018, 2019; Decrausaz et al., 2021).

During subduction, these rocks were buried between ~30 and 80 km depth (Agard et al., 2002, 2009) and were intensely folded, leading to significant thickening of the initial sedimentary pile (Agard et al., 2002; Tricart and Schwartz, 2006). Agard et al. (2009) roughly estimated that approximatively 30% to 50% of the sedimentary deposits were scraped off from the downgoing plate and exhumed, whereas only ~5% of the oceanic crust and serpentinized mantle were.

After a peak burial between 60 and ~40 Ma (e.g. Agard et al., 2002; Rubatto and Hermann, 2003), these rocks were detached as slices from the subducting plate and were exhumed from the Late Eocene to the Miocene (Agard et al., 2002, 2009; Schwartz et al., 2007, 2020; Malusà et al., 2005; Angiboust and Glodny, 2020). This complex stack of slices formed a deep accretionary complex, probably built by progressive underplating (Platt, 1986; Marthaler and Stampfli, 1989; Agard et al., 2009, 2018; Agard, 2021), where structurally upper slices may have been underplated earlier (Kimura et al., 2007; Dumitru et al., 2010; Plunder et al., 2012; Agard and Vitale-Brovarone, 2013; Angiboust et al., 2016).

Rocks from the Western Alps L-P domain, metamorphosed under BS- to eclogite-facies conditions, exhibit an almost continuous increase of metamorphic grade from west (~1.2 GPa-330°C) to east (~2.5 GPa-550°C), along a ~8°C metamorphic gradient characteristic of subduction zones (Agard et al., 2001a; Gabalda et al., 2009; Plunder et al., 2012; Schwartz et al., 2013; Agard, 2021). This gradient is recognizable by the evolution of metamorphic mineral assemblages and notably by the subtle evolution of index minerals in metasediments (Goffé and Chopin, 1986; Agard et al., 2001a; Goffé et al., 2004; Bousquet et al.,

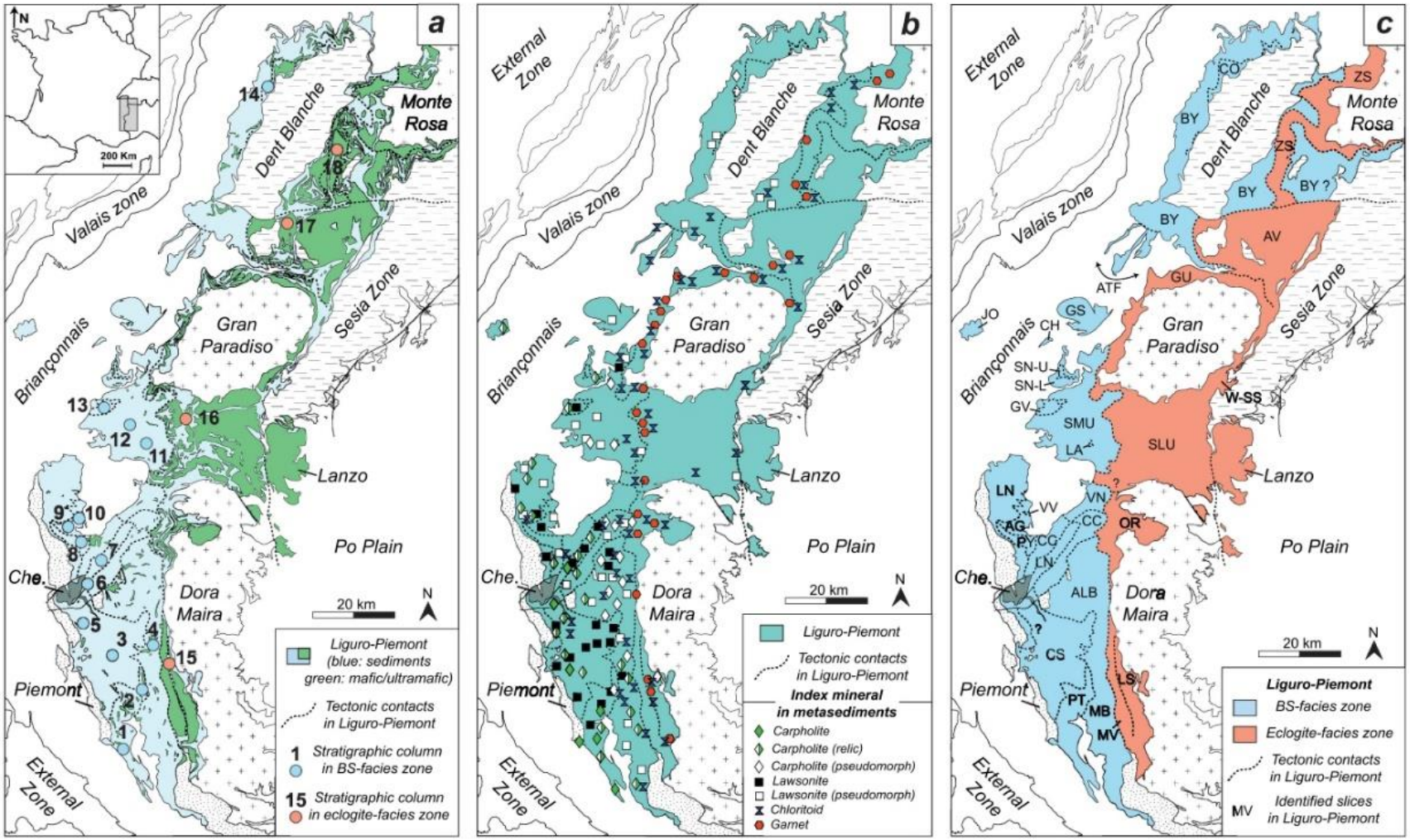

Fig. 1. Maps of the Western Alps focused on the Liguro-Piemont (L-P) domain. A) Distribution of sediments and mafic-ultramafic rocks across the L-P domain and location of the stratigraphic columns presented in Fig. 3b and the tectonic contacts separating L-P slices. B) Zoneography of index metamorphic minerals of L-P metasediments, both from field observations (this study) and compiled from literature (Bocquet, 1974; Agard et al., 2001a; Goffé et al., 2004; Bousquet et al., 2008; Manzotti et al., 2021). C) Distribution of blueschist- and eclogite-facies metamorphism across the L-P domain and location of the L-P tectonic slices described in literature. References for the different slices are in the text (see §3). Che: Chenaillet. Abbreviations for the tectonic slices: AG: Aigle; ALB: Albergian; ATF: Avise-Tsaboc-Feluma; AV: Avic; BY: By unit; CC: Cerogne-Ciantiplagna; CH: Chardonnet klippe; CO: Cornet; CS: Calcschist unit; GU: Grivola-Urtier; GS: Grande-Sassière klippe; GV: Grand Vallon klippe; JO: Jovet klippe; LA: Lamet klippe; LN: Lago Nero; LS: Lago Superiore; MB: Mirabouc-Bouchet; MV: Monviso unit; OR: Orsiera-Rocciavrè; PT: Pelvas-Taillante; PY: Puys; SLU: Savoy Lower Unit; SMU: Savoy Middle Unit; SN-L: Lower Sana klippe; SN-U: Upper Sana klippe; VN: Venaus; VV: Vin Vert; W-SS: West-Sesia unit; ZS: Zermatt-Saas.

2008; Fig. 1b). For example, in the western part of the Schistes Lustrés complex, and especially south of Ambin massif, Fe-Mg carpholite is frequently present in pelitic layers (Fig. 1b; Goffé and Chopin, 1986; Agard et al., 2001a). Further east, Fe-Mg capholite gradually disappears at the expense of chloritoid (Fig. 1b; Goffé and Chopin, 1986; Agard et al., 2001a). In both areas lawsonite can be observed in the metasedimentary matrix as well as in metamorphic veins (Caron, 1974; Bocquet, 1974; Saliot, 1978; Lefeuvre et al., 2020; Herviou et al., 2021). Finally, the easternmost part of the L-P domain is characterized by the occurrence of garnet, generally coexisting with chloritoid (Agard et al., 2001a; Plunder et al., 2012; Ghignone et al., 2021a). In these metasediments, Fe-Mg carpholite is characteristic of low-temperature BS-facies while chloritoid generally appears in high-temperature BS-facies (Goffé and Chopin, 1986; Goffé et al., 2004). Lawsonite is present over a wide range of P-T conditions in these BS-facies rocks (Herviou et al., 2021), whereas the presence of garnet is indicative of eclogite-facies metamorphism (Agard et al., 2001a; Plunder et al., 2012; Vitale Brovarone et al., 2014) except for rare spessartine and grossular-rich garnet in marbles (Ballèvre and Lagabrielle, 1994; Manzotti et al., 2021).

Besides this metamorphic gradient, several units/slices were identified in the L-P domain of the Western Alps based on lithostratigraphic and tectonometamorphic contrasts (Lagabrielle, 1987; Fudral, 1996; Agard, 2021). In particular, the metamafic-ultramafic dominated eclogite-facies units crop out eastward of and tectonically below the BS-facies metasedimentary-dominated units (Fig. 2c; Dal Piaz, 1974b; Caby et al., 1978; Droop et al., 1990; Pognante, 1991; respectively MUM and S units of Agard, 2021 and Agard and Handy, 2021). These zones are separated by a major extensional tectonic contact (Philippot, 1990; Ballèvre et al., 1990; Ballèvre and Merle, 1993). Inside these different zones, distinct slices, generally 3 to 4 were described in different transects of the L-P domain (Lagabrielle, 1987; Fudral, 1996; Agard, 2021) and are described in the next section.

3. Subduction slices across the Western Alps Liguro-Piemont domain

3.1. Valais-Aosta transect

In this northern zone, the identification of a major sharp divide was first made in the Zermatt-Saas area by Bearth (1959, 1962, 1967).

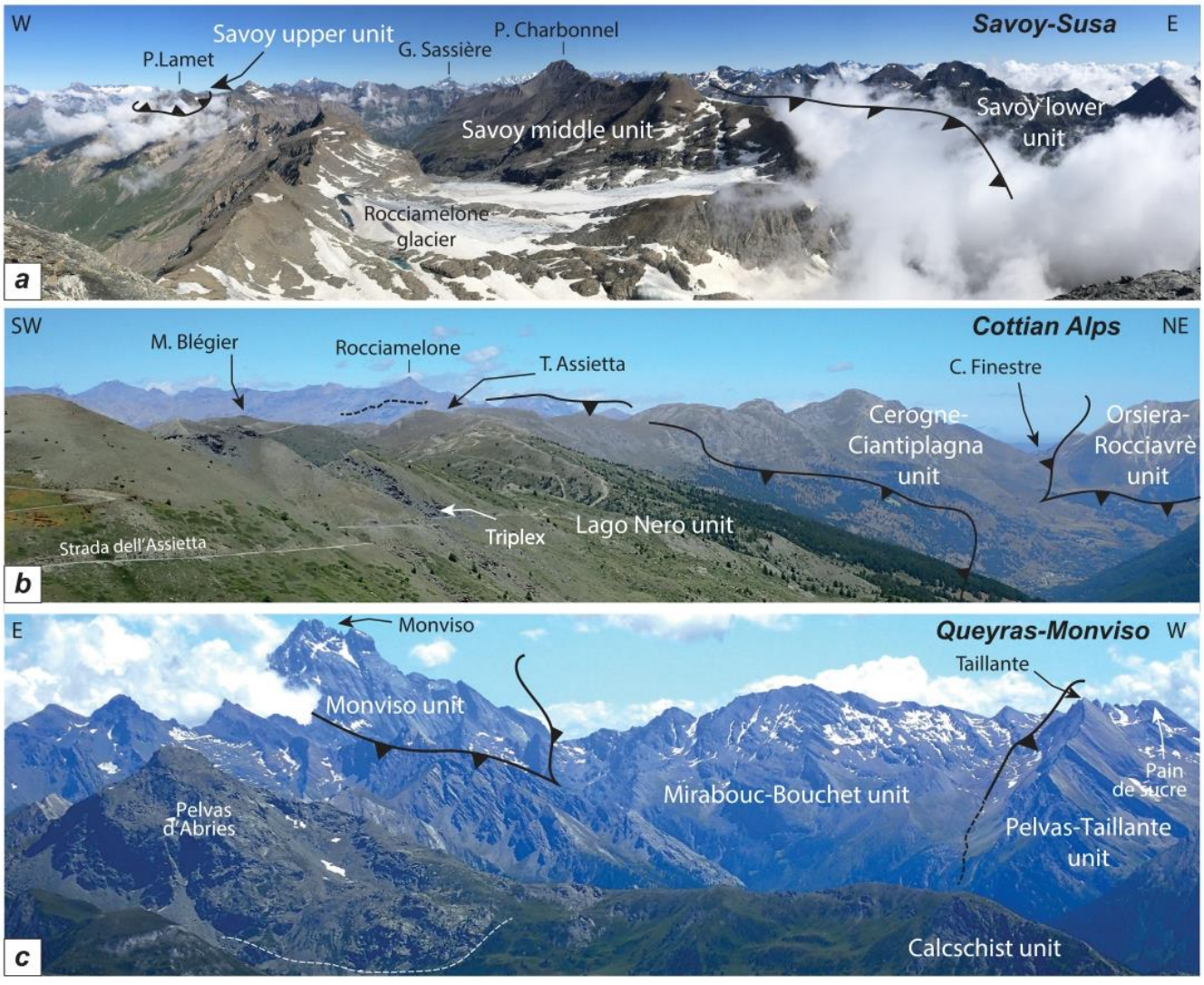

Fig. 2. Panoramic pictures of the Liguro-Piemont domain exposing the present slice-stacking. A) Savoy-Susa transect from Rocciamelone summit. B) Cottian Alps transect. C) Queyras-Monviso transect from Bric-Froid summit. B) and C) are modified after Agard (2021).

Kienast (1973), Dal Piaz (1974a, 1974b) and Caby et al. (1976, 1978) later described a similar divide in the Aosta Valley. These authors identified a zone of "Lower Schistes Lustrés" rich in mafic and ultramafic rocks metamorphosed in eclogite-facies that they distinguish from a zone of "Upper Schistes Lustrés" only metamorphosed in blueschist- and greenschist-facies and almost devoid of ophiolites. The eclogite-facies slices or Zermatt-Saas zone are cropping out eastward of the Dent Blanche klippe and are tectonically overlain by the blueschist slices named Combin zone (or Tsaté Nappe). These zones are separated by a Late Cretaceous-Early Tertiary extensional fault, the Combin fault (Ballèvre and Merle, 1993, Fig. 1a-c).

Different tectonic slices were identified in the Zermatt-Saas zone: the Zermatt-Saas and Avic slices found on both sides of the Aosta fault (ZS and AV in Fig. 1c; Dal Piaz et al., 2010; Polino et al., 2015). Thermodynamic modelling, multi-equilibrium thermobarometry and Raman Spectroscopy on Carbonaceous Material (RSCM) allowed to estimate peak P-T conditions around 550 ± 50°C and 2.5 ± 0.5 GPa for the Zermatt-Saas unit (Bucher et al., 2005; Bucher and Grapes, 2009; Angiboust et al., 2009; Angiboust and Agard, 2010; Negro et al., 2013; Zanoni et al., 2016) and around 550 ± 50°C and 2.1-2.3 GPa for the Avic unit (Martin et al., 2008; Angiboust et al., 2009; Angiboust and Agard, 2010; Dragovic et al., 2020). While the homogeneity of the P-T conditions recorded in these two units may hint to largely coherent slices (Angiboust et al., 2009), these two units show at smaller scale a series of tectonic slices separated by serpentinite layers (Angiboust and Agard, 2010). Near Lago di Cignana, a small 2 km^2 ZS slice contains diamond- and coesite-bearing metasediments indicative of ultra-high pressure (UHP) conditions of 2.8-3.2 GPa and 600°C (Reinecke, 1991, 1998; Compagnoni and Rolfo, 2003; Groppo et al., 2009; Frezzotti et al., 2011). Finally, south of the Avic unit, an eclogite-facies slice is cropping out around the Gran Paradiso massif, the Grivola-Urtier unit (GU in Fig. 1c; Bocchio et al., 2000; Dal Piaz et al., 2010; Polino et al., 2015). P-T conditions of 550°C, 2.3-2.5 GPa are estimated for this slice mostly made of calcschists enveloping mafic blocks (Bousquet, 2008; see also Reynard and Ballèvre, 1988).

Based on multiple methods, most peak burial ages range between 40 and 50 Ma for the Zermatt-Saas unit (Bowtell et al., 1994; de Meyer et al., 2014; Skora et al., 2015; Weber et al., 2015; Rebay et al., 2018), between 42-46 Ma for the Avic unit (Dal Piaz et al., 2001; Dragovic et al., 2020) and between 40 and 49 Ma for the Lago di Cignana slice (Rubatto et al., 1998; Amato et al., 1999; Lapen et al., 2003; Gouzu et al., 2006, 2016; Skora et al., 2015). For the Grivola-Urtier unit, peak burial ages were constrained between 42 and 48 Ma by Rb-Sr and Ar-Ar on white mica in both metasediments and metamafics (Dal Piaz et al., 2001; Villa et al., 2014) and between 55 and 60 Ma by Lu-Hf on bulk garnet-omphacite or garnet-glaucophane assemblages (Villa et al., 2014). D1 syn-peak deformation stage is dated at 48 Ma while D2 syn-BS facies exhumation is dated at 40 Ma (Villa et al., 2014). K-Ar data on white-micas from two localities of the Grivola-Urtier unit gave 54-39 Ma ages (Delaloye and Desmons, 1976).

In the BS-facies Combin zone, below the Dent Blanche klippe, the presence of a synformal stack of slices was inferred from the distribution of RSCM temperatures (Negro et al., 2013; Angiboust et al., 2014; Manzotti et al., 2021), possibly two or three slices (Angiboust et al., 2014). Recently, Manzotti et al. (2021), based on petrological data and field observations, suggested the presence of two slices, the Cornet unit separated from the underlying By unit by a major tectonic discontinuity (respectively CO and BY in Fig. 1c). Based on this distinction, peak temperatures range between 364 and 422°C in the Cornet unit and between 421 and 530°C in the By unit (Negro et al., 2013; Angiboust et al., 2014; Decrausaz et al., 2021; Manzotti et al., 2021). The large By unit may comprise several slices (Broilliot and Aouilletta slices; Ellero and Loprieno, 2018; Polino et al., 2015), but their extension is unknown. Peak pressures are estimated at 1.6-1.7 GPa for the By unit and 0.8-0.9 GPa for the Cornet unit (Manzotti et al., 2021). The D2 to D3 exhumation-related episodes of these units were dated between 41 and 37 Ma (Reddy et al., 2003; Angiboust et al., 2014). Potentially independent tectonic slices, rooted in the Briançonnais area and belonging to the complex Valsavarenche mega-fold (Bucher et al., 2003), crop out around the Valgrisenche, Val de Rhêmes and Valsavarenche valleys. These slices, grouped in the Avise-Tsaboc-Feluma unit (ATF in Fig. 1c), seem to have recorded BS-facies conditions (Debelmas et al., 1991; Caby, 1996; Polino et al., 2015). In the Avise area, D1 deformation was dated a 45.4 Ma and followed by a 39.5 Ma D2 deformation. Finally, a slice may be present in the eastern side of Grand Paradiso between the Grivola-Urtier slice and the Sesia complex, featured as a thin tongue of BS-facies L-P rocks in literature maps and cross-sections (Ballèvre et al., 1986; Dal Piaz et al., 2001; West-Sesia, i.e. W-SS in Fig. 1c).

3.2. Savoy-Susa transect

A similar contrast between the BS-facies "Upper Schistes Lustrés" and eclogite-facies "Lower Schistes Lustrés" was observed in the Savoy area by Bocquet (1974), Caby et al. (1976), Chopin (1979) and Robert (1979), and in the Susa Valley by Pognante (1980, 1984). Chopin (1979) first distinguished two sets of slices within the BS-facies zone, with the "Upper Unit" characterized by low-grade BS-facies metamorphism atop the "Intermediate Unit" composed by a thick series of calcschist metamorphosed in BS-facies. Based on lithostratigraphic and structural arguments, Deville (1987), Fudral et al. (1987) and Fudral (1996) refined Chopin's (1979) distinction by also suggesting the presence of three units in the Savoy region and by mapping their distribution. These units are the eclogite-facies "Lower Oceanic Unit", the BS-facies "Middle Oceanic Unit" and the "Upper Oceanic Unit" also metamorphosed in BS-facies.

The "Upper Oceanic Unit" (Savoy Upper Unit) crops out as rare klippen scattered across the region (Lamet, Jovet, Sana, Grand Vallon; respectively LA, JO, SN-U and GV in Fig. 1c, see also 2a). Their limited extent across the area precludes assessing whether they are independent slices or instead correspond to a single one. Nevertheless, the Grand Vallon klippe (Fig. 1c) contains a stratigraphic succession distinct from the other "Upper Oceanic Unit" klippen (Deville, 1986, 1987; Fudral, 1996). Its detrital-rich sediments were dated as Late Maastrichtian by the presence of foraminifera, as for the unmetamorphosed Helminthoid Flysch (Deville, 1986). Such deposits are rarely encountered in the Schistes Lustrés, suggesting that this klippe constitutes an independent slice (Deville, 1986; Deville et al., 1992; Fudral, 1996). The "Upper Oceanic Unit" is characterized by a low-grade BS-facies, marked by the presence of Fe-Mg carpholite or lawsonite and absence of chloritoid (Fig. 1b). Peak burial temperatures range between 376 and 404°C in the Savoy region (Gabalda et al., 2009; Plunder et al., 2012). No pressure or age constraints are available for these tectonic slices.

The "Middle Oceanic Unit" (Savoy Middle Unit, i.e. SMU in Fig. 1c) predominates in this region and seems to be made of several slices with uncertain boundaries (Fudral, 1996). These slices mostly crop out across the Haute-Maurienne valley and have also been identified in the Grande Sassière and Chardonney klippen and at the base of the Sana klippe (Deville, 1987, Fudral, 1996; respectively GS, CH and SN-L in Fig. 1c). Near Susa, a distinct Venaus slice was recognized (Polino et al., 2002; Cadoppi et al., 2002; VN in Fig. 1c) within the previously defined Savoy slices (Fudral, 1996). The "Middle Oceanic Unit" is mostly made of massive calcschist slices and characterized by the presence of chloritoid, lawsonite and relics of Fe-Mg carpholite (Fig. 1b). Peak P-T are 384-503°C and 1.6-1.9 GPa (Rolland et al., 2000; Gabalda et al., 2009; Plunder et al., 2012). Recent in situ Ar-Ar white-mica dating of the "Middle Oceanic Unit" around Susa gave ages for an early foliation S1 between 49 and 40 Ma, while retrograde fabrics (S2 and mylonitic foliation) range between 40 and 37 Ma (Ghignone et al., 2021b). Previous Ar-Ar dating on white mica for this unit gave 42-37 Ma ages (Chopin and Maluski, 1980).

The eclogite-facies "Lower Oceanic Unit" (Savoy Lower Unit, i.e. SLU in Fig. 1c) crops out in the eastern part of the Haute-Maurienne area,

immediately above the Gran Paradiso massif (Fig. 2a; Chopin, 1979) and in the Susa, Viu and Ala Valleys (Fig. 1c). At least two slices named Ciamarella-Gran Uia and Averole where recognized in this unit (Fudral, 1996), but their exact distribution remains uncertain. A large slice of eclogitized mantle is also present in the eastern part of this transect, the Lanzo massif (Lagabrielle et al., 1990; Debret et al., 2013; Fig. 1a, b, c). Its ultramafic lithology contrasts with those of the "Lower Oceanic Unit", and whether it represents oceanic or sub-continental mantle is disputed (Bodinier et al., 1991; Müntener et al., 2005; Pelletier and Müntener, 2006; Piccardo et al., 2007). The "Lower Oceanic Unit" is characterized by the appearance of garnet coexisting with chloritoid, suggesting the existence of a pressure gap with the "Middle Oceanic Unit" (Plunder et al., 2012; Vitale Brovarone et al., 2014). Estimated peak P-T are 460-570°C and 2.2-2.9 GPa (Rolland et al., 2000; Gabalda et al., 2009; Plunder et al., 2012; Ghignone et al., 2021a). Recent in-situ Ar-Ar dating on an early S1 foliation gave 47-42 Ma ages, while retrograde fabrics (S2 and mylonitic foliation) range between 40 and 36 Ma (Ghignone et al., 2021b). Previous Ar-Ar on white micas data for the HP stages of this unit yielded a wide range between 68 and 39 Ma (Chopin and Maluski, 1980).

3.3. Cottian Alps transect

In this transect, the different L-P units are particularly well-exposed across a long ridge between Susa and the Chisone valley, which constitutes a reference cross-section (Caron, 1977; Agard et al., 2001a, 2001b, 2009; Agard, 2021; Fig. 2b). A strong eastward metamorphic gradient was identified by the progressive increase of the tschermak substitution in white-mica (which serves as proxy for pressure; Velde, 1967; Massonne and Schreyer, 1987) and by the evolution of index minerals in sediments (Agard et al., 2001a, 2001b; Fig. 1b). These trends are also reflected in the eastward increase of RSCM temperatures (Beyssac et al., 2002). In this region, as well, a zone of BS-facies metasedimentary-dominant slices stands out from an eclogite-facies zone containing more metamafics and ultramafic rocks (Agard, 1999; Agard et al., 2001a; Fig.1a, c). These zones are separated by a major tectonic contact, well exposed at the Finestre Pass (Fig. 2b; Ballèvre et al., 1990; Agard et al., 2001a).

Several tectonic slices were described in the BS-facies zone. Structurally on top, the Lago Nero unit (Polino et al., 2002; Barféty et al., 2006; LN in Fig. 1c, see also 2b) shows Fe-Mg carpholite-bearing metasediments and the appearance of chloritoid in the eastern outcrops (Agard et al., 2001a, 2001b). These rocks also contain massive amounts of lawsonite (Lefeuvre et al., 2020). Peak P-T range from 300-350°C-1.2-1.3 GPa at west to ~380°C- 1.8 GPa at east (Agard, 1999; Agard et al., 2001a, 2001b; Beyssac et al., 2002; Gabalda et al., 2009). The Lago Nero unit was considered as analogous to the "Oceanic Upper Unit" of the Savoy transect (Plunder et al., 2012; Agard, 2021). Below this slice, five BS-facies tectonic slices were identified: (i) the Cerogne-Ciantiplagna unit (Polino et al., 2002; Cadoppi et al., 2002; CC in Fig. 1c, see also 2b); (ii) the Albergian unit, separated from the Cerogne-Ciantiplagna unit by a major tectonic contact nicely exposed in the Chisone valley (Polino et al., 2002; ALB in Fig. 1c); (iii) the Puys unit, considered as an equivalent of the Venaus slice from the Savoy-Susa transect (Polino et al., 2002; Barféty et al., 2006; PY in Fig. 1c); (iv) the Aigle unit (Polino et al., 2002; Barféty et al., 2006; AG in Fig. 1c) and (v) the small Vin Vert unit (Polino et al., 2002; Barféty et al., 2006; VV in Fig. 1c) immediately above the Ambin massif. The Cerogne-Ciantiplagna and Albergian units are characterized by the presence of chloritoid (Fig. 1b) and peak P-T conditions of 423-463°C- ~1.9 GPa (Agard et al., 2001a, 2001b; Beyssac et al., 2002). These slices were inferred to be equivalent to the "Middle Oceanic Unit" of the Savoy-Susa transect (Plunder et al., 2012; Agard, 2021). The Puys, Aigle and Vin Vert slices are essentially lacking P-T constraints, although a RSCM temperature of 386°C was estimated in the Aigle unit (Gabalda et al., 2009). In metasediments from the Lago Nero and Albergian units, several deformation stages were identified and dated (Agard et al., 2001a, 2002; see also Ghignone et al., 2021a). D1 deformation relates to the development of early fabrics, km-scale folds and crystallization of peak metamorphic assemblages at 61-55 Ma for the Lago Nero unit and 64-49 Ma for the Albergian unit. A second phase (D2), dated at 51-43 Ma for the Lago Nero, corresponds to the ductile east-vergent deformation accompanying early exhumation under BS-facies conditions. The third fabric (D3), between ~38 and 36 Ma for the Lago Nero unit, is marked by top-to-the-west ductile to brittle deformation associated with greenschist-facies exhumation. Two K-Ar ages on white mica from the Lago Nero unit gave 67-62 Ma ages (Delaloye and Desmons, 1976).

In the eclogite-facies zone, the presence of different slices is unclear. In the Orsiera-Rocciavrè unit (OR in Fig. 1c, Cadoppi et al., 2002), the Rocciavrè massif is a large eclogitic gabbroic and ultramafic body containing negligible amounts of metasediments (Pognante, 1985). In contrast, to the west, from Monte Orsiera to Finestre pass, mafic and ultramafic rocks are embedded in metasediments that seem to be volumetrically equivalent to the ophiolitic bodies (Fig. 1c). The existence of a tectonic contact between these two parts of the unit was suggested by Cadoppi et al. (2002). Metasediments contain garnet and chloritoid (Fig. 1b) and their estimated P-T conditions are 500-542°C and ~2-2.1 GPa (Agard, 1999; Agard et al., 2001a, 2001b; Beyssac et al., 2002; Gabalda et al., 2009). No recent P-T estimates are available for the mafic rocks. The Orsiera-Rocciavrè unit is interpreted as the southern extension of the "Lower Oceanic Unit" of the Savoy-Susa transect (Plunder et al., 2012). In metasediments from the Orsiera-Rocciavrè unit, the same D1 to D3 events of BS-facies slices were described (Agard et al., 2001b). An early-HP stage, close to D1 deformation is dated at 61-53 Ma by in situ Ar-Ar in white mica, whereas D2 is dated at 46-42 Ma and D3 at 42-38 Ma (Agard et al., 2002). In Rocciavrè metagabbros, Rb-Sr on phengite with high Si content gave a 46 Ma age (Angiboust and Glodny, 2020).

3.4. Queyras-Monviso and Ubaye transects

Along these southernmost transects, the BS-facies slices are separated from eclogite-facies units by a major extensional contact (Philippot, 1990; Ballèvre et al., 1990; Fig. 2c).

Three BS-facies slices were identified in the Queyras region around the Guil valley, from west to east (Lagabrielle, 1987; Lagabrielle and Polino, 1988; Lagabrielle et al., 2015): (i) the Calcschist unit (CS in Fig. 1c, see also 2c), almost devoid of ophiolitic material, is characterized by Fe-Mg carpholite and lawsonite occurrences (Herviou et al., 2021; Fig. 1b, c); (ii) the Pelvas-Taillante unit (PT in Fig. 1c, see also 2c) also contains Fe-Mg carpholite and lawsonite occurrences, and chloritoid appears in the eastern part (Fig. 1b); (iii) the Mirabouc-Bouchet unit (MB in Fig. 1c, see also 2c), which is characterized by the presence of lawsonite and chloritoid (Fig. 1b). Estimated P-T conditions are 320-340°C- ~1 GPa for the Calcschist unit, 338-373°C- ~1.2 GPa for the Pelvas-Taillante Unit and 383-469°C- ~1.3 GPa for the Mirabouc-Bouchet unit (Schwartz, 2000; Tricart and Schwartz, 2006; Schwartz et al., 2013).

The eclogite-facies zone of this transect corresponds to the Monviso massif, a large mafic-ultramafic body (Lombardo et al., 1978) comprising at least two tectonic slices (Schwartz et al., 2000a; Angiboust et al., 2012b; Locatelli et al., 2018, 2019a). The Monviso Unit (MV in Fig.1c, see also 2c), to the west, recorded 476-498°C- ~2.2 GPa P-T conditions (Angiboust et al., 2012b; Schwartz et al., 2013) and the Lago Superiore unit to the east (LS in Fig. 1c, see also 2c) recorded 514-580°C-2.5-2.8 GPa (Groppo and Castelli, 2010; Angiboust et al., 2012b; Schwartz et al., 2013; Locatelli et al., 2018). Metasediments from these two slices are characterized by garnet-chloritoid-bearing assemblages (Fig. 1b).

The Lago Superiore unit peak-burial conditions were dated between 50 and 45 Ma by multiple methods (Duchène et al., 1997; Rubatto and Hermann, 2003; Rubatto and Angiboust, 2015; Garber et al., 2020a).

The D2 and D3 exhumation-related deformation episodes were dated at 38-37 Ma and 35 Ma in the Lago Superiore and Monviso slices (Angiboust and Glodny, 2020; Rb-Sr on phengite). For the BS-facies slices, a 42-40 Ma Ar-Ar age on white mica, supposedly close to peak P-T conditions, was obtained for the Calcschist unit (Lanari, 2012). In the Pelvas-Taillante unit, two ages between 43 and 41 Ma were obtained by bulk K-Ar on white mica (Delaloye and Desmons, 1976). Finally, Ar-Ar dating on white mica on a sample from the Mirabouc-Bouchet unit gave 68-58 Ma for an early S1 fabric (prograde to peak?), 45 Ma for a second fabric (S2) and a <30 Ma age for a S3 foliation (Lanari, 2012). D3 deformation in the same slice was dated at ~35 Ma by Rb-Sr on phengite (Angiboust and Glodny, 2020). All these BS- and eclogite-facies units were stacked and exhumed from late Eocene to Miocene times (Angiboust and Glodny, 2020; Schwartz et al., 2007, 2020). Along the Ubaye transect, an eastward metamorphic increase was identified from the Briançonnais units to the Liguro-Piemont domain (Michard et al., 2004), with no distinction of L-P slices. We will consider that the Queyras-Monviso slices extend across this valley (Fig. 1c).

4. Compilation of lithostratigraphic data and size of the recovered slices

4.1. Stratigraphic columns of the different slices

In order to identify similarities between the tectonic slices of the different transects and gain information on the paleogeography of the L-P slices (Fig. 3a), we compiled lithostratigraphic columns across the Western Alps L-P domain (Fig. 3b).

In the Western Alps, the Chabrière series (stratigraphic column 1, Fig. 1a, 3b; Lemoine et al., 1970; Tricart, 1974) is considered as the characteristic and idealized sequence of L-P deposits. This stratigraphic column allowed to differentiate the L-P series deposited on an oceanic basement from the Gondran-type series (Lemoine, 1959, 1971), which are made of sediments deposited on the Piemont/Pre-Piemont continental margins (Fig. 1a-c; Lemoine, 1971; Elter, 1971; Bourbon et al., 1979; Lemoine et al., 1986). The Chabrière-type series starts with radiolarian cherts or shales deposited on an oceanic basement. This formation, dated between the Oxfordian and the Kimmeridgian (De Wever and Caby, 1981; De Wever et al., 1987a, 1987b; Lagabrielle, 1987) corresponds to the first argillite-dominated episode of the series (A2; Fig. 3b; Lemoine, 2003), characterizing sediments deposited below the CCD. These A2 deposits are often composed by manganese-rich quartzite layers instead of cherts (Chopin, 1978, 1979). Overlying the cherts, there is a level of whitish to bluish marbles attributed to the Late Jurassic (Tithonian and up to Berriasian?) by analogy with the "Calpionelles Limestones" of the Ligurian Appenines (Decandia and Elter, 1969, 1972; Lagabrielle, 1987). This formation corresponds to the first calcareous-dominated episode of the series (C3; Fig. 3b; Lemoine, 2003), with deposition above the CCD. The above, younger formation, made of shales with intercalations of calcareous beds with a characteristic reddish patina, is named "Replatte formation" (Lemoine et al., 1970). This formation is attributed to the Lower Cretaceous by analogy with the "Palombini shales" of the Ligurian Appenines (Lemoine et al., 1970; Lemoine and Tricart, 1986; Lagabrielle, 1987). Just above, there is a characteristic formation of black shales, often called the "Roche Noire formation" (Fig. 3b; Tricart, 1974), assigned to the Mid-Cretaceous (Aptian-Albian?) given their similarity with the "Val Lavagna Schists" of Ligurian Appenines (Decandia and Elter, 1972; Tricart, 1974; Lagabrielle, 1987). These two Lower Cretaceous formations correspond to the second argillite-dominated episode of the series (A3; Fig. 3b; Lemoine, 2003). For the sake of clarity, we herein use A3a for the "Replatte formation" and A3b for the "Roche Noire formation" (Fig. 3b). Finally, these series end by a thick and fairly homogeneous formation of massive calcschists dated as Late Cretaceous (Cenomanian-Turonian) by the presence of planktonic foraminifera in various localities (Marthaler, 1984; Lemoine et al., 1984; Lagabrielle, 1987; Deville, 1987). In scarce places the L-P series ends with a formation of Maastrichtian calcareous flyschs considered as lateral equivalents of the unsubducted Helminthoid Flysch (Deville, 1986; Deville et al., 1992). These Late Cretaceous formations correspond to the last calcareous-dominated deposit of the series (C4; Fig. 3b; Lemoine, 2003; C4a is used below for the Cenomanian-Turonian calcschists and C4b for the Maastrichtian flyschs). Some of these C4 flyschs may correspond to trench-filling deposits (Marthaler, 1984). The different formations of the Chabrière-type series generally contain detritic and breccia horizons made of continental and/or oceanic material (e.g., Deville et al., 1992) not considered here.

The Chabrière series therefore consists of pelagic/hemipelagic and rarer clastic deposits overlying mafic and ultramafic rocks. Changes of the stratigraphic record and/or tectonic repetition of this succession may help reveal the distinct paleogeography and/or preferential zones of detachment inside the sequences (Kimura et al., 1996).

In the Western Alps L-P domain, stratigraphic columns equivalent to the Chabrière series were described in several of the blueschist-facies slices.

In the Queyras-Ubaye region, the complete Chabrière series was observed in the Pelvas-Taillante slice (Fig. 1a, 3b, stratigraphic columns 1,2; Lemoine et al., 1970; Tricart, 1974; Lemoine and Tricart, 1986; Lagabrielle, 1987). In the Calcschist unit, the deposits are mainly made of a thick C4a calcschist formation overlying a thin A3b formation (Fig. 3b, stratigraphic column 3; Lagabrielle, 1987; Deville et al., 1992). The lack of Jurassic deposits and ophiolites led the authors to suggest that the Calcschist unit sediments may have been deposited on continental margin rather than oceanic basement (Lagabrielle, 1987; Deville et al., 1992). The lithostratigraphic column of the Mirabouc-Bouchet (Fig. 1a, 3b, stratigraphic column 4; Lagabrielle, 1987) is close to the complete Chabrière series but differs by the absence of A2 cherts and the presence of a thick C4a calcschist formation.

In the Cottian Alps region, a series close to the Chabrière one was described in the Lac des Cordes (Fig. 1a, 3b, stratigraphic column 5; Dumont et al., 1984; Lemoine and Tricart, 1986). This series is nevertheless lacking the Middle Jurassic cherts and contains a A3a calcschist formation instead of the Replatte formation. In general, Chabrière-type series were identified in the Lago Nero (Fig. 1a, 3b, stratigraphic columns 6 and 7; Caron, 1977; Polino and Lemoine, 1984; Lemoine and Tricart, 1986) and Aigle slices (Fig. 1a, 3b, stratigraphic column 9; Barféty et al., 2006). C4a is characterized by a calcareous flysch rather than calcschists in the Lago Nero locality (Fig. 3b, stratigraphic column 6; Polino and Lemoine, 1984). Deposits in the Puys slice consist of undifferentiated Cretaceous calcschists probably corresponding to C4a (Fig. 1a, 3b; stratigraphic column 8; Barféty et al., 2006), whereas the Vin Vert slice contains massive C4a calcschists and C3 marbles (Fig. 1a, 3b; stratigraphic column 10; Barféty et al., 2006). Very few sedimentary descriptions are available for the Cerogne-Ciantiplagna and Albergian slices. The Cerogne-Ciantiplagna sediments nevertheless mostly comprise massive calcschists with very few pelitic alternations (Fig. 2b), as for C4a calcschists. For the Albergian slice, where ophiolites are present in greater amounts (Fig. 1a), the sedimentary sequence rather corresponds to a Chabrière-like series analogous to that of the Mirabouc-Bouchet unit (Caron, 1977; Fig. 1a, 3b, stratigraphic column 4).

Around the Savoy region, different series where identified in the Savoy Upper Unit klippen. In most of them, such as for the Lamet klippe (Fig. 1a, 3b, stratigraphic column 11; Fudral, 1996), the metasediments correspond to C4a calcschists whereas the Grand Vallon klippe is composed by the Maastrichtian C4b flysch (Fig. 1a, 3b, stratigraphic column 13; Deville, 1986, 1987; Deville et al., 1992). However, the Savoy Middle Unit stratigraphic column seems to correspond to an incomplete Chabrière-type series (Fig. 1a, 3b, stratigraphic column 12; Fudral, 1996; Deville et al., 1992): these C4 calcschists overly deposits markedly from the A3 sediments, and this series may therefore lack Lower Cretaceous sediments.

Finally, around the Valais region, the Combin sediments resemble a

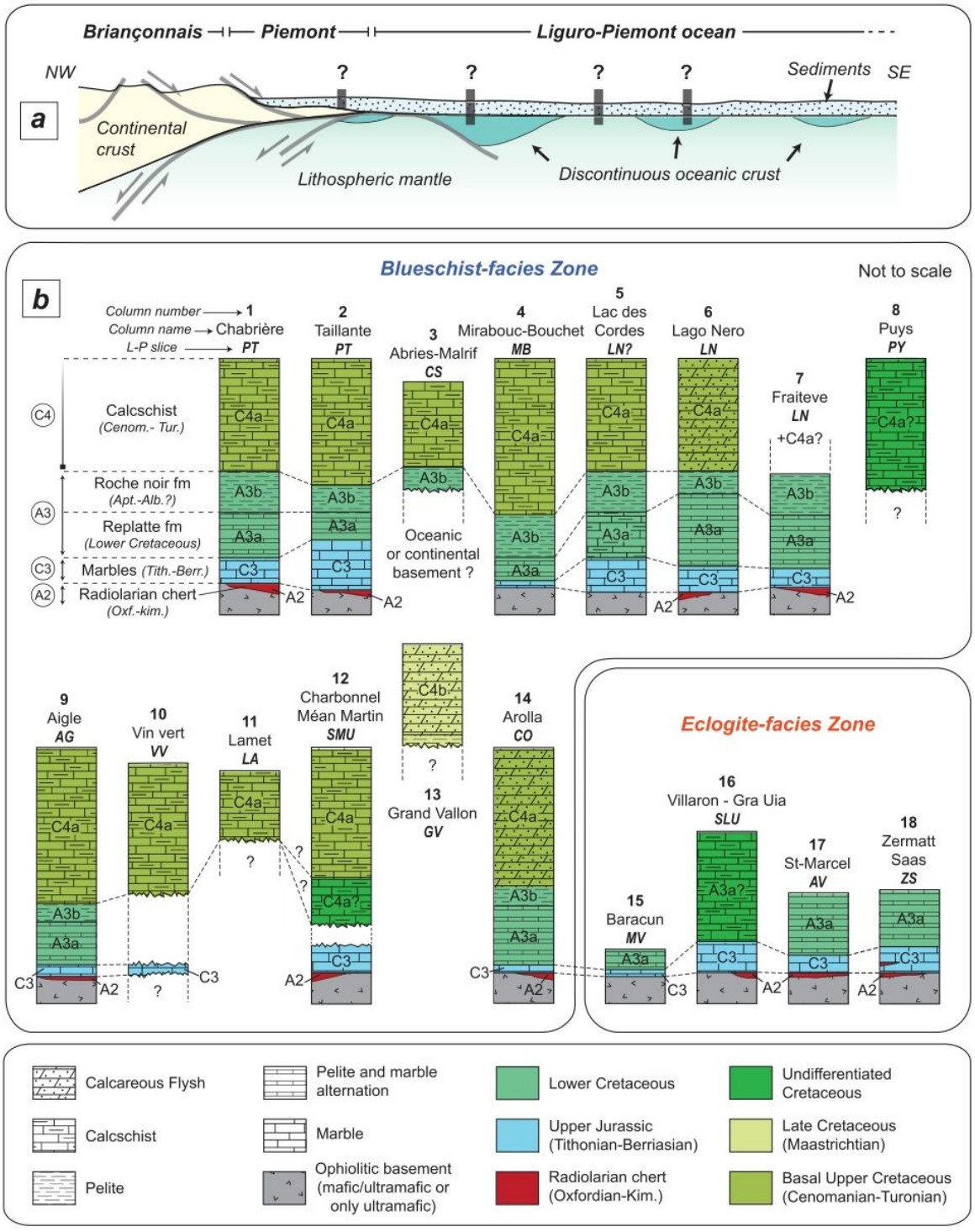

Fig. 3. Stratigraphy and paleogeography of the Liguro-Piemont rocks. A) Schematic cross-section of the European margin and Liguro-Piemont ocean before subduction with emphasis on the paleogeograhic unknowns. Grey sticks with question marks correspond to potential locations for the stratigraphic columns of Fig. 3b. B) Compilation of stratigraphic columns of the L-P domain. Description, references of the different stratigraphic columns, stratigraphic formations and events are in the text (§4.1). Location of the stratigraphic columns across the L-P complex are in Fig. 1a. Stratigraphic column 1 (Chabrière-series) corresponds to the reference complete succession of L-P deposits ranging from Middle-Upper Jurassic to Upper Cretaceous deposits. Most of the blueschist-facies slices have an almost similar stratigraphic succession with only few formations missing. Few blueschist-facies slices (column 3, 8, 10, 11, 13) (almost) only have Upper Cretaceous sediments. All stratigraphic colums from eclogite-facies slices are devoid of Upper Cretaceous. Abbreviations for the tectonic slices: AV: Avic; AG: Aigle; CS: Calcschist unit; CO: Cornet; GV: Grand Vallon klippe; LA: Lamet klippe; LN: Lago Nero; MB: Mirabouc-Bouchet; MV: Monviso unit; PT: Pelvas-Taillante; SLU: Savoy Lower Unit; SMU: Savoy Middle Unit; VV: Vin Vert; ZS: Zermatt-Saas.

Chabrière-like series with C4 composed by a calcareous flysch (Fig. 1a, 3b, stratigraphic column 14; Marthaler, 1984; Sartori, 1987; Kunz, 1988; Marthaler and Stampfli, 1989; Stampfli and Marthaler, 1990; Deville et al., 1992).

In the eclogite-facies slices, stratigraphic columns are always lacking Upper Cretaceous formations (Fig. 1a, 3b, stratigraphic columns 15-18; Lagabrielle, 1987; Sartori, 1987; Stampfli and Marthaler, 1990; Deville et al., 1992; Balestro et al., 2019; Tartarotti et al., 2021). These sedimentary series are generally exposing A2 cherts and C3 marbles, overlain by Lower Cretaceous A3a Replatte-like deposits or calcschists. In these slices, the thickness variation of the sedimentary-series is interpreted as reflecting deposition on a rugged seafloor (De Togni et al., 2021).

4.2. Sediment/ophiolitic ratios and surface extension of the slices

The ratio of sedimentary versus ophiolitic material (mafic and ultramafic rocks) cropping out in each L-P slice was calculated using imagej©. This software was also used to compute the approximate aerial exposure of each L-P slice using the geological outlines of the 1:250000 BRGM maps (Gap; Annecy and Thonons-les-Bains). For the different contours we used 1:50000 ISPRA maps (Aosta; Bardonecchia; Chatillon, Monte Cervino and Susa), 1:50000 BRGM maps (Lanslebourg-Mont d'Ambin; Névache-Bardonecchia-Modane; Tignes) and some articles/PhD. theses (Lagabrielle, 1987; Fudral, 1996; Lagabrielle et al., 2015; Manzotti et al., 2021). The Chenaillet and Lanzo massifs (Fig. 1a-c) were not considered in the calculations.

The results highlight the predominance of sediments in the Western Alps L-P domain (71%; Table 1). Almost all BS-facies slices surfaces have more than 90% (Table 1) of sediments except for the Combin domain (By + Cornet slices) where numerous volcano-sedimentary horizons (prasinites) are mapped, but where sediments still prevail (76%; Table 1). The whole BS-facies zone surface only contains 9% of mafic and ultramafic rocks (Table 1). The eclogite-facies slices surfaces drastically differ from the BS-facies slices (Table 1). Indeed, four out of the six studied areas contain less than 40% of sediments, whereas the two remaining areas contain around 60% of sediments (Table 1). The whole eclogite-facies zone displays 62% of mafic and ultramafic rocks at the surface. Finally, in the two slices for which few metamorphic informations are available (Avise-Tsaboc-Feluma and West-Sesia; Fig. 1c) sediments predominate (more than 90%; Table 1).

The outcropping surface of the L-P slices ranges from a few km^2 in the Savoy Upper Unit klippen (less than 1 km^2 for the Lamet klippe; Table 1) to several hundred of km^2 (Table 1). In the blueschist-facies zone, most of the slices (14 over 19) represent less than 100 km^2, whereas the Lago Nero and Calcschist units are respectively around 130 and 160 km^2 (Table 1). The three remaining zones correspond to greater surfaces but the poor knowledge of the boundaries between the slices imposed some grouping (By+Cornet, Savoy Middle Unit, Albergian+Mirabouc Bouchet; Table 1). In the eclogite-facies zone, most of the slices are larger than 100 km^2 (5 over 6; Table 1), which may suggest the presence of several slices in these areas.

5. Evolution of temperature and pressure in the Western Alps Liguro-Piemont slices

5.1. Raman spectroscopy of carbonaceous material temperatures

5.1.1. Methodology

The abundance of carbonaceous material in the almost continuously exposed L-P metasediments allows quantifying the maximum temperature (T_{max}) experienced by these metasediments during peak burial, using the Raman Spectra of Carbonaceous Material technique (RSCM; Beyssac et al., 2002, 2003). Despite previous studies across the L-P domain of the Western Alps, large gaps remain across the studied transects (Beyssac et al., 2002; Gabalda et al., 2009; Angiboust et al., 2009, 2012b, 2014; Angiboust and Agard, 2010; Plunder et al., 2012; Negro et al., 2013; Decrausaz et al., 2021; Manzotti et al., 2021; see Fig. 4a). Complementary sampling (108 new samples added to the existing 289 ones) was therefore conducted to constrain the maximum temperature of the entire domain (as for the Central Alps; Wiederkehr et al., 2011), as well as to characterize the thermal imprint of individual tectonic slices (Fig. 4a). Note that two samples, one from this study and another form Schwartz et al. (2013), belong to the west-Chenaillet

Table 1
Lithological ratio (sediment versus mafic-ultramafic) and aerial exposure of the Liguro-Piemont slices. See text (§4.2) for details in the methodology.

Slice	Metamorphic zone	Sediments %	Mafic-ultramafic %	~ outcroping surface (km^2)
All Liguro-Piemont domain	Blueschist and eclogite facies zones	71	29	2477
All Blueschist-facies slices	Blueschist-facies zone	91	9	1516
All Eclogite-facies slices	Eclogite-facies zone	38	62	961
Aigle + Vin vert	Blueschist-facies zone	98	2	20
Albergian + Mirabouc-Bouchet	"	96	4	258
Cerogne-Ciantiplagna	"	95	5	78
Chardonnet klippe (Savoy Middle Unit)	"	100	0	2
Combin (By + Cornet)	"	76	24	433
Calcschist unit	"	99	1	161
Grande-Sassière klippe (Savoy Middle Unit)	"	99	1	38
Grand Vallon klippe (Savoy Upper Unit)	"	100	0	9
Jovet klippe (Savoy Upper Unit)	"	100	0	9
Lamet klippe (Savoy Upper Unit)	"	100	0	<1
Lago Nero	"	99	1	134
Pelvas-Taillante	"	90	10	70
Puys	"	99	1	14
Savoy Middle Unit	"	98	2	181
Lower Sana klippe (Savoy Middle Unit)	"	96	4	14
Upper Sana klippe (Savoy Upper Unit)	"	91	9	3
Venaus	"	99	1	28
Avise-Tsaboc-Feluma	?	99	1	28
West-Sesia	?	93	7	34
Avic unit	Eclogite-facies zone	28	72	211
Grivola-Urtier	"	61	39	113
Monviso unit + Lago Superiore	"	40	60	101
Orsiera-Rocciavrè	"	59	41	70
Savoy Lower Unit	"	36	64	314
Zermatt-Saas	"	35	65	152

Gondran sediments, which may rather correspond to Piemont margin deposits (Fig. 4a; Lemoine, 1971).

Raman spectra of carbonaceous material, were obtained using a Renishaw inVia Spectrometer at ENS Paris. The excitation light was provided by a laser (Cobolt Fandango) at 514.5 nm and at a power of 50 mW, focused on the sample using a x100 objective (Leica). Thirteen to seventeen spectra per sample were acquired in the 1000-2000 cm^{-1} range; acquisition time was 30-90 seconds with 10% of laser power following the spectral acquisition parameters of Beyssac et al. (2002). Peak position, baseline correction and band width were determined using Peakfit© software and Matlab© codes. Temperatures were determined using Beyssac et al. (2002) method for most of the samples (105 samples) and using Lahfid et al. (2010) method for the very rare low-temperature samples (<330°C; 3 samples). The RSCM data from the literature and this study were then interpolated using the inverse distance weighted interpolation method of QGis© software (Fig. 4b, c). Temperature estimates, mineralogy and GPS coordinates of the samples can be found in Sup. mat. 1.

5.1.2. Results

RSCM temperatures and their interpolation illustrate the eastward increase of metamorphic grade across the Western Alps L-P domain (Fig. 4a-c). This is particularly conspicuous south of the Gran Paradiso massif, where western samples recorded 300-350°C peak temperatures while eastward samples are generally greater than 500°C (Fig. 4a-c). The distribution of the L-P tectonic contacts allows studying the specific maximum temperature of each slice (Fig. 4c). It reveals the presence of both intra-slice metamorphic gradients, where temperature overlaps rather smoothly across the slices, and temperature gaps matching tectonic contacts (Fig. 4c). For example, some BS-facies slices (Fig. 1c; §3) are dominantly in bluish-color in the interpolation maps, exposing temperatures below 400°C, while others have greenish to yellowish colors outlining a temperatures range between 400°C and 500°C (Fig. 4b-c). The eclogite-facies slices exhibit almost only orange to red colors suggesting temperatures above 500°C (Fig. 4b-c). More irregular patterns in the temperature interpolation, especially south of Gran Paradiso massif, result from the lack of data in these areas (Fig. 4b).

The temperature distribution for each slice (mean, median, standard deviation, number of samples and temperature range) is compiled in Table 2. While many slices show a wide range of temperatures, reflecting their internal metamorphic gradient (Table 2; Fig. 4a-c), the mean-median temperatures of slices appear clustered around three temperature ranges in each of the four studied transect (Valais-Aosta, Savoy-Susa, Cottian Alps and Queyras-Monviso; Table 2). These clusters are around 350-390°C (Cornet, Savoy Upper Unit, Lago Nero, Puys, Aigle, Calcschist Unit and Pelvas-Taillante), 415-475°C (By, West-Sesia, Savoy Middle Unit, Venaus, Vin Vert, Cerogne-Ciantiplagna, Albergian, Mirabouc-Bouchet) and 490-540°C (Zermatt-Saas, Avic, Grivola-Urtier, Avise-Tsaboc-Feluma, Savoy Lower Unit, Orsiera-Rocciavrè, Monviso and Lago Superiore). Temperatures indeed follow a trimodal distribution with Gaussian-like curves centered around 370-380°C, 460-470°C and 530-550°C (Fig. 5a). Cumulative histograms of the RSCM temperatures for each transect, where individual slices were grouped into the three distinct temperature clusters (Fig. 5b-e), show that these groups have specific temperature distributions and only overlap around the minimum and/or maximum values (Fig. 5b-e).

5.2. Si^{max} values of phengite

5.2.1. Methodology

Tschermak substitution ($Al^{IV} + Al^{VI} = Si^{IV} + Fe^{VI}$, Mg^{VI}) in phengite is known to be highly sensitive to pressure variations in K-feldspar- or talc-bearing assemblages (Velde, 1967; Massonne and Schreyer, 1987, 1989; Massonne, 1995) and in HP-LT metapelites (Saliot and Velde, 1982; Massonne, 1992; Jolivet et al., 1996, 1998; Goffé and Bousquet, 1997; Bousquet et al., 1998, 2002; Agard et al., 2001a, 2001b). The maximum Si values ($Si^{max}Ph$) of highly substituted early phengite therefore provide an estimate of the peak pressure experienced by the rocks during burial (Si values also depend on rock composition, see §6 below). This is a minimum value since phengite may have reequilibrated during the retrograde path. In the Western Alps L-P domain, the map of $Si^{max}Ph$ isopleths revealed an eastward increase in peak-pressure along the Cottian Alps transect (Agard, 1999; Agard et al., 2001a). In the Savoy-Susa transect, the differences between the Savoy Lower Unit and the Savoy Middle Unit are further supported by their contrasting $Si^{max}Ph$ values (Plunder et al., 2012).

In order to map out the peak pressure distribution across the Western Alps L-P domain, emphasis was placed on the southern half of the domain (Cottian Alps to Ubaye valley), where a strong eastward metamorphic gradient was detected along several transects (Agard et al., 2001a; Gabalda et al., 2009; Schwartz et al., 2013). This is also where numerous slices were identified and very few P-T constraints are available for most of them (see § 3.3; 3.4). Thirty-two samples were selected (see Sup. mat. 1 for location and mineralogy). In each sample, the different generations of white mica were carefully studied in order to locate early, highly substituted phengite. In optimal samples, where up to three successive schistosities (S1, S2 and S3) could be recognized, similar to those of Agard et al., 2001a; Fig. 6a-b), phengite from the S1 generation was selected.

Electron Probe Microanalyis (EPMA) was performed at Camparis (Sorbonne Université, Paris) using both Cameca SX-5 and SX-100 instruments. Point measurements were made in classical analytical conditions (15 kV acceleration voltage, 10 nA beam current allowing ~2 µm beam size in wavelength-dispersive spectroscopy mode) using diopside (Ca, Mg, Si), $MnTiO_3$ (Mn, Ti), orthoclase (K, Al), Fe_2O_3 (Fe), albite (Na) and Cr_2O_3 (Cr) as standards for calibration of elements in parentheses. Representative electron microprobe compositions of phengite are presented in Sup. mat. 2.

Phengite structural formulae were calculated on an 11 oxygen basis and the $Si^{max}Ph$ value of each sample is considered as a proxy for the minimum peak-pressure recorded by the rocks. In order to complete this dataset $Si^{max}Ph$ value from the same region were compiled from literature (Bocquet, 1974; Liewig, 1981; Agard et al., 2001a; Bonnet et al., 2022). Selected $Si^{max}Ph$ values from this work and from the literature are given in Sup. mat. 3.

5.2.2. Results

Phengite microprobe data are shown in the muscovite-celadonite-pyrophyllite ternary diagram (Fig. 7a). Most analyses plot close to the muscovite-celadonite axis, i.e. along the tschermak substitution trend (Fig. 7a), and generally contain less than 20% of pyrophyllite. We discard phengite containing more than 20% of pyrophyllite to avoid considering Si values related to the pyrophyllitic substitution rather than to peak pressure (see Agard et al., 2001b).

$Si^{max}Ph$ values range between 3.25 and 3.67 atoms per formula units (a.p.f.u.) highlighting a large range of tschermark substitution. Selected $Si^{max}Ph$ values from our data and the literature were plotted against their corresponding RSCM temperatures (Fig. 7b). Most of the points expose a relatively clear trend of $Si^{max}Ph$ increase with temperature, evidencing a subduction-related HP-LT gradient in these rocks (Fig. 7b). Some points, especially for high temperature (> to 440°C), are plotting away from the trend. These points may represent samples where the most substituted phengite formed at peak burial was not preserved.

The selected $Si^{max}Ph$ are superimposed on the simplified structural sketch map of the Cottian Alps-Queyras region in order to discern the evolution of peak-pressure across the L-P domain (Fig. 8). Except for samples that may not have preserved peak Si values (Fig. 7b), these data reveal an increase of $Si^{max}Ph$ values from west (generally lower than 3.35 a.p.f.u.) to east (generally greater than 3.55 a.p.f.u.), consistent with previous findings on specific sections (Agard et al., 2001a, 2001b) and with the strong eastward increase in metamorphic grade. Our dense sample distribution allows to draw approximate $Si^{max}Ph$ isopleths for

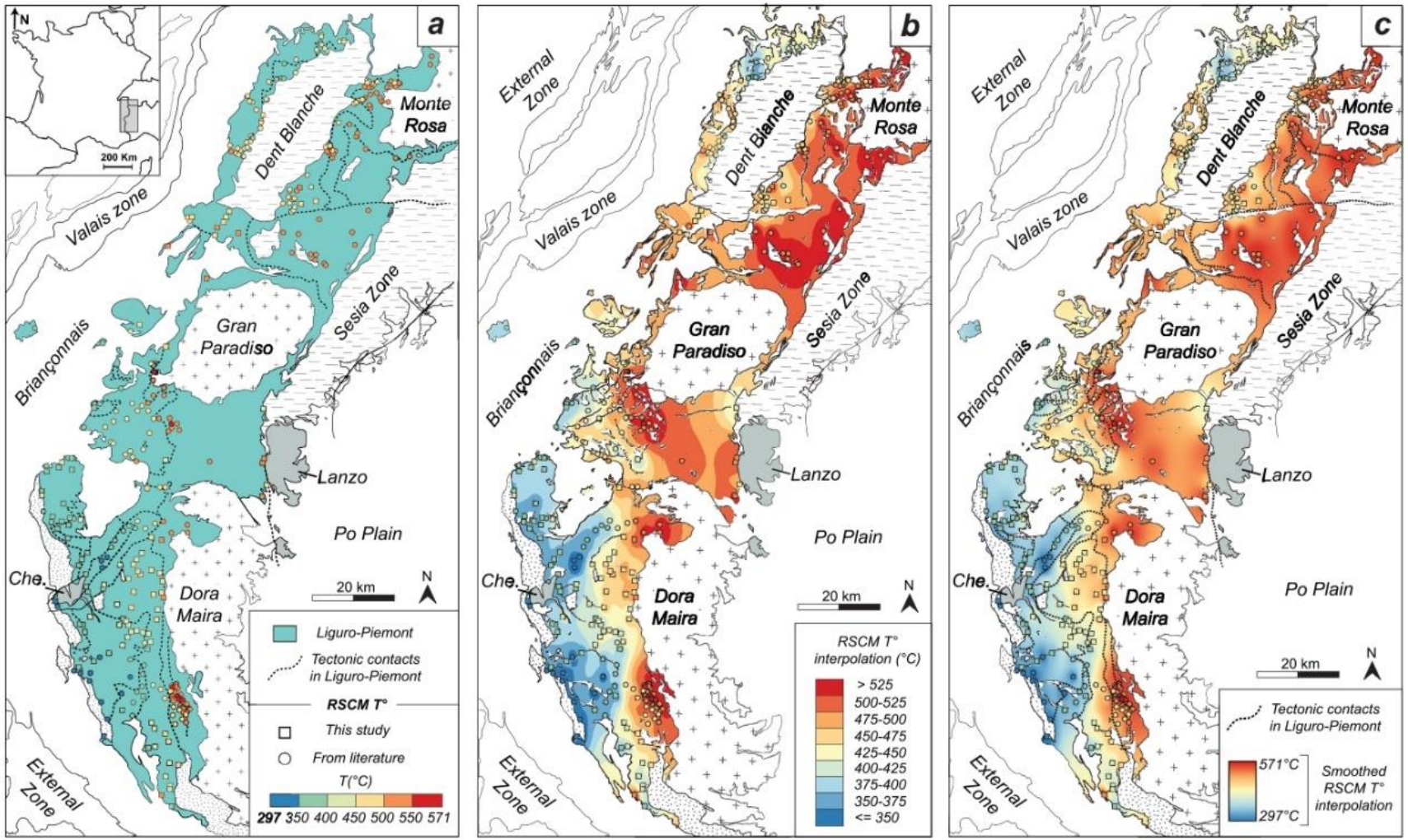

Fig. 4. Distribution and interpolation of RSCM temperatures across the Liguro-Piemont domain. A) RSCM temperatures and L-P tectonic contacts across the domain notably highlighting the eastward metamorphic gradient. B) Interpolation of RSCM temperatures across the L-P domain with 25°C intervals. C) Smoothed interpolation of RSCM temperatures across the domain and tectonic contacts of the L-P slices. This map as C) highlights the burial temperature recorded by rocks across the whole L-P domain and the specific temperature range of each tectonic slice. Some slices have blue color corresponding to 300-400°C while other have green-to yellow colors highlighting ~400-500°C T_{max}. Finally, easternmost slices (eclogite-facies) have orange-to red colors corresponding to T_{max} above 500°C. Most of the slices expose an internal eastward increase in T_{max}. For the three maps, square symbols correspond to our samples (108 samples) while round symbols correspond to RSCM temperatures compiled from literature (289 samples; Beyssac et al., 2002; Gabalda et al., 2009; Angiboust et al., 2009, 2012b, 2014; Angiboust and Agard, 2010; Plunder et al., 2012; Negro et al., 2013; Schwartz et al., 2013; Decrausaz et al., 2021; Manzotti et al., 2021). Samples description, temperature and mineral assemblages as well as compiled RSCM temperatures from literature are presented in Sup. mat. 1.

Table 2
RSCM temperatures of the Liguro-Piemont slices. All the compiled RSCM temperatures (from this study and literature) are presented in Sup. Mat 1.

Transect	Slice	Mean T (°C)	Med. T (°C)	sd	n samples	T range (°C)	References
Valais-Aosta	Cornet (Combin)	390	392	18	21	364-422	Negro et al. (2013); Angiboust et al. (2014); Decrausaz et al. (2021); Manzotti et al. (2021)
"	By (Combin)	476	474	25	106	421-532	This study; Angiboust and Agard (2010); Negro et al. (2013); Angiboust et al. (2014); Decrausaz et al. (2021); Manzotti et al. (2021)
"	Zermatt-Saas	533	536	12	26	495-546	Angiboust et al. (2009); Angiboust and Agard (2010); Negro et al. (2013)
"	Avic	538	538	7	12	523-547	Angiboust et al. (2009); Angiboust and Agard (2010)
"	Grivola-Urtier	499	483	31	3	479-534	This study
"	Avise-Tsaboc-Feluma	/	/	/	1	522	This study
"	West-Sesia	/	/	/	1	433	This study
Savoy-Susa	Savoy Upper Unit	384	377	14	4	376-404	This study; Gabalda et al. (2009); Plunder et al. (2012)
"	Savoy Middle Unit	445	449	36	31	384-503	This study; Gabalda et al. (2009); Plunder et al. (2012)
"	Venaus	/	/	/	1	484	This study
"	Savoy Lower Unit	530	533	21	24	471-580	This study; Gabalda et al. (2009); Plunder et al. (2012)
Cottian Alps	Lago Nero	372	373	20	33	330-423	This study; Beyssac et al. (2002); Gabalda et al. (2009)
"	Puys	/	/	/	1	364	This study
"	Aigle	373	377	15	3	357-386	This study; Gabalda et al. (2009)
"	Vin Vert	414	414	3	2	413-416	This study
"	Cerogne-Ciantiplagna	421	423	34	5	373-463	This study; Beyssac et al. (2002)
"	Albergian	452	453	29	16	386-491	This study
"	Orsiera-Rocciavrè	517	517	22	8	483-542	This study; Beyssac et al. (2002); Gabalda et al. (2009)
Queyras-Monviso	Calcschist unit	364	349	43	14	320-437	This study; Schwartz et al. (2013)
"	Pelvas-Taillante	355	362	17	10	319-363	This study; Schwartz et al. (2013)
"	Mirabouc-Bouchet	427	419	34	29	376-517	This study; Schwartz et al. (2013)
"	Monviso unit	488	489	8	7	476-498	Angiboust et al. (2011); Schwartz et al. (2013)
"	Lago Superiore	536	534	14	37	514-571	Angiboust et al. (2011); Schwartz et al. (2013)

0.10 a.p.f.u. steps and to map out the distribution of estimated peak pressure across the L-P domain (Fig. 8). A finer resolution would nevertheless be necessary to scrutinize the pressure evolution across individual tectonic contacts between the L-P slices (Fig. 1c), except maybe for the contact between the BS and eclogite-facies slices, which appears close to the Si 3.55 a.p.f.u. isopleth.

6. Themodynamic modelling for an average composition, peak pressure and dehydration in the tectonic slices

6.1. Methodology

In order to compare the peak pressure of the different slices, a reference P-T pseudosection was calculated with the Perple_X software (version 6.9.1; Connolly, 1990, 2005, 2009; Fig. 9a). The updated thermodynamic database is that of Holland and Powell (1998), with the corresponding solution models (for chloritoid, Fe-Mg carpholite, garnet, phengite) except for chlorite (after Holland et al., 1998). For this pseudosection, we used the bulk composition CBas912m of Henry et al., 1996; Fig. 9a) since that is considered as a representative L-P calcschist (and was already used for the Schistes Lustrés by Bebout et al., 2013). The used Na_2O-CaO-K_2O-FeO-MgO-Al_2O_3-SiO_2-H_2O (NaCaKFMASH) chemical system is assumed to describe realistically most of the L-P metasediments. Manganese is largely restricted to garnet cores and was thus neglected in the calculations. TiO_2 and BO_3 are only present in accessory phases (rutile, titanite, tourmaline). Cr_2O_3 is minor and dominantly stored in phengite (and/or lawsonite) and was therefore neglected. The pseudosection was calculated with H_2O in excess in the P-T range of 0.9-2.5 GPa and 300-600°C encompassing most of the peak P-T conditions in the Western Alps L-P domain. The Si-in-phengite isopleths (a.p.f.u.), shown on the P-T grid (Fig. 9a), are relatively flat-lying, outlining the good sensitivity of the phengitic tschermak substitution to pressure variations. The relative peak pressure conditions were determined from the intersection of $Si^{max}Ph$ values (along Si-in-phengite isopleths) of this study and literature samples with their respective RSCM temperatures. The estimated P-T ranges for the studied slices are given in Table 3 (see Sup. mat. 3 for all P-T estimations). These pressure estimates must be considered with caution since the Si content in phengite depends, to a minor extent, on each bulk rock composition. Varying randomly the weight percent of each system component by a few percents results in pressure variations of ± 0.1-0.15 GPa.

In order to track the evolution of metamorphic assemblages during burial, mineral proportions were calculated along the 8°C/km gradient inferred for the Western Alps (Fig. 9b; Agard et al., 2001a; Agard, 2021). We computed the evolution of water content bound in minerals along the same gradient (Fig. 9c) to identify the major dehydration steps and assess their potential impact on slicing mechanisms.

6.2. Results

The pseudosection reproduces mineral assemblages observed in L-P sediments (Fig. 1a, 9a, b). Quartz and phengite are the dominant phases and are present in all fields (Fig. 9a, b). Fe-Mg carpholite is present in low-grade sediments and progressively disappears at the expense of chloritoid (Fig. 9a, b). Across a 8°C/km gradient, garnet appears around ~525°C and ~2.2 GPa. This is in good agreement with the almost systematic lack of garnet in BS-facies slices (Fig. 1a; §2.2, 3). Along the same gradient lawsonite is stable up to ~575°C and ~2.4 GPa, fitting with the presence of lawsonite in the ~470°C peak P-T assemblages of the L-P domain (Herviou et al., 2021). The major mismatch is the presence of Na-bearing silicates (glaucophane, jadeite) and kyanite in minor proportions above 2 GPa (glaucophane <6 vol%; jadeite ~1 vol%; kyanite 6-7 vol%), as already noticed by Bebout et al. (2013). The amount of mineral-bound water first decreases significantly when crossing the chloritoid-in reaction (Fig. 9b-c), and then progressively as Fe-Mg carpholite (~12% H_2O) is gradually replaced by chloritoid (~7.5% H_2O; Fig. 9b). At higher grade two major steps of dehydration are observed along this gradient (Fig. 9b, c): (i) the first one corresponds to chlorite breakdown at ~500°C and 2 GPa (~3.5 to ~2.8 wt% H_2O in the system), followed by final disappearance of carpholite (ii) the second one to lawsonite and chloritoid breakdown reactions, at ~575°and 2.4 GPa (~2.5 to ~1.2 wt% H_2O in the system).

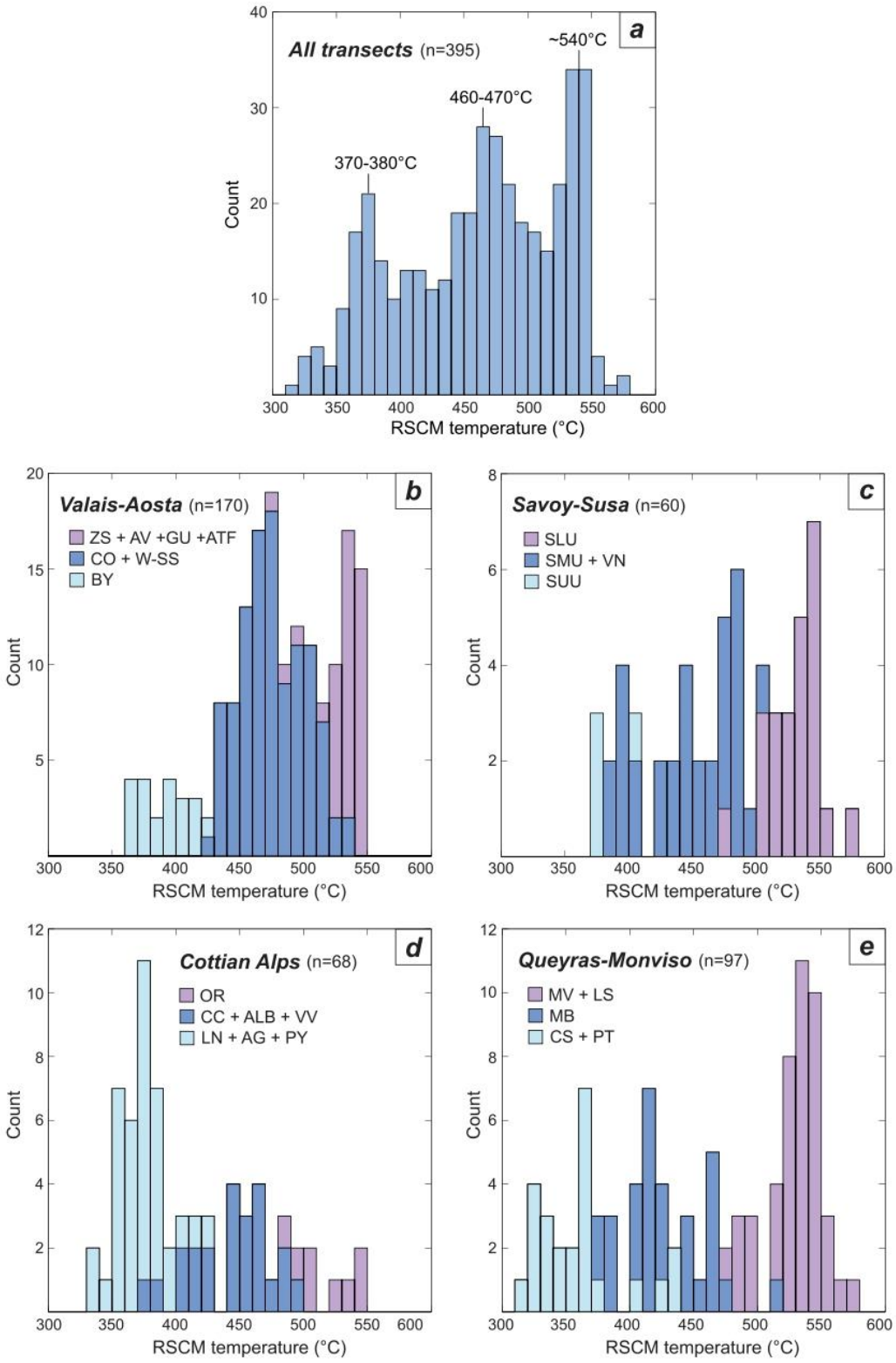

Fig. 5. Statistical distribution of RSCM temperatures in Liguro-Piemont domain. A) Bar chart of all RSCM temperatures showing a trimodal distribution with peaks at 370-380°C, 460-470°C and ~540°C. B) to E) Cumulative bar charts of RSCM temperatures along Valais-Aosta, Savoy-Susa, Cottian Alps and Queyras-Monviso transects, all showing the same three temperature clusters of A). Slices were color-coded according to their specific temperature ranges (Table 1). Fo all charts, RSCM temperatures are both from this study and compiled from literature (see Fig. 4 caption)

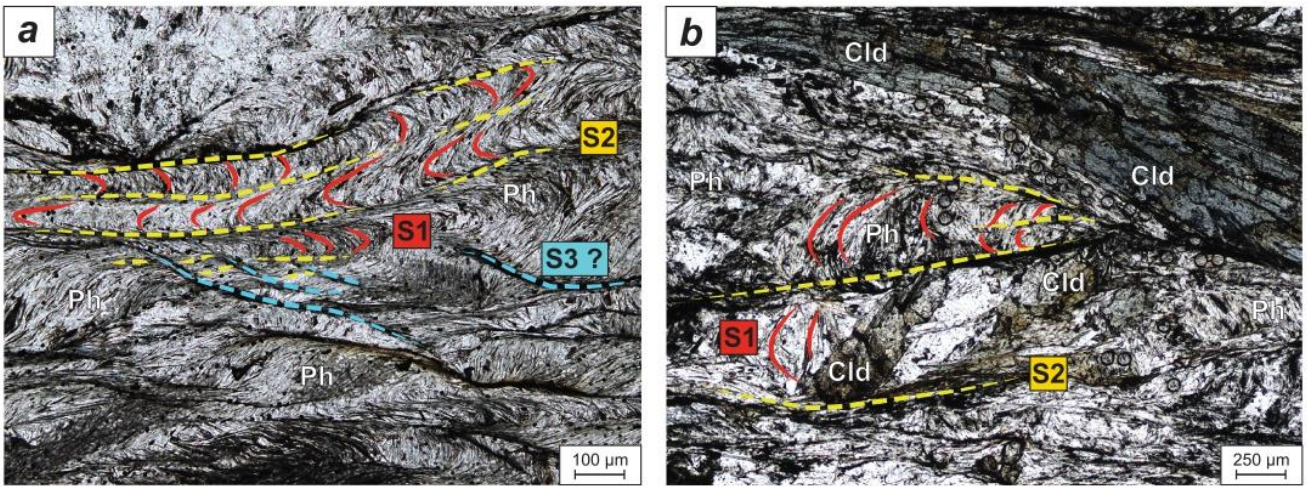

Fig. 6. Microphotographs highlighting the successive deformation structures observed in our representative metasedimentary samples. A) to B) S1 and S2 foliation are marked by phengite (Ph) and chlorite crystals. D3 deformation corresponds to small shear bands cross-cutting S1 and S2. Index minerals, such as chloritoid (Cld), lawsonite, Fe-Mg carpholite or garnet often show textural equilibrium with S1 phengite.

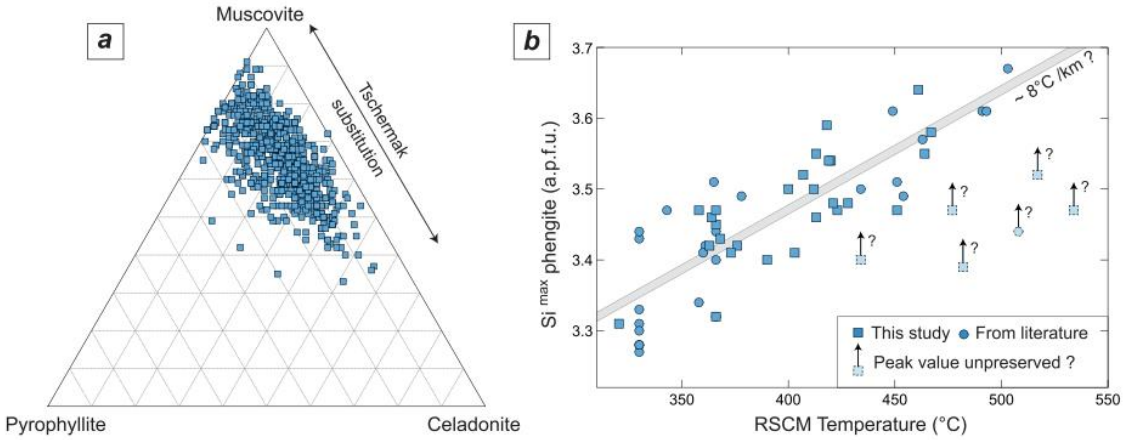

Fig. 7. Phengite composition. A) Ternary diagram of point electron microprobe analyses of phengite. B) Maximum Si values of phengite ($Si^{max}Ph$; peak pressure indicator) versus RSCM temperatures of the same samples or samples from the same locality. Most samples plot on a linear trend, highlighting the increase of $Si^{max}Ph$ with temperature and the efficiency of Si value use as peak pressure indicator. Square/round symbols correspond to our samples/literature $Si^{max}Ph$ (Bocquet, 1974; Liewig, 1981; Agard et al., 2001a; Bonnet et al., 2022). Light-blue symbols with dotted contours correspond to samples in which phengite with peak burial Si values was not preserved or not found. Representative compositions of analyzed phengite are presented in Sup. mat. 2 and selected $Si^{max}Ph$ values are presented in Sup. mat. 3.

Peak pressures estimated using the $Si^{max}Ph$ and RSCM temperatures intersection range between ~1.3 and 2.5 GPa (Table 3; Sup. mat. 3). Above 500°C, however, pressure determination is limited by the steepening of the Si-in-phengite isopleths (Fig. 9a). The obtained pressures are in good agreement with data available from literature, at least for Cottian Alps (Agard et al., 2001a, 2001b). Indeed, for Lago Nero slice, the pressures obtained range between ~1.3 GPa at west to ~1.9 GPa at east (Table 1) versus 1.2-1.3 and 1.8 GPa for Agard et al. (2001a) in the same samples. In Albergian slice, peak pressure ranges between 1.8 and 2.3 GPa (Table 3) with most samples clustering around 2 GPa (Sup. mat. 3) while Agard et al. (2001a) obtained ~1.9-2 GPa in the same slice. These pressures are a bit higher than those of Agard et al. (2001a) but fit the 2-2.3 GPa peak pressure recently estimated by Corno et al. (2021) for extensional allochtons embedded within the Albergian slice (Corno et al., 2019; Fig. 1a-c). For the Orsiera-Rocciavrè sediments, we obtained slightly higher pressure (~2.2 to ~2.5 GPa; Table 3) than Agard et al. (2001a; 2-2.1 GPa). These values nevertheless fit better with the eclogitic sediments of the other L-P slices (Bousquet, 2008; Angiboust et al., 2012b; Plunder et al., 2012), as well as the 8°C/km gradient of the Western Alps. In the Puys, Vin Vert and Cerogne-Ciantiplagna units, where no pressure estimates exist, the obtained ranges are repectively 1.7-1.8 GPa, 2.1 GPa and 1.7- ~2.2 GPa.

For the Queyras-Monviso BS-facies slices, the estimated pressures are higher than the scarce literature values. Pressure is in the range 1.4-2 GPa for the Calcschist unit, 1.4-1.7 GPa for the Pelvas-Taillante unit and 1.9- ~2.4 GPa for the Mirabouc-Bouchet unit (with most data around 1.9-2 GPa in the latter unit; Table 3; Sup. mat. 3). These pressure values significantly contrast with those previously estimated for metamafic rocks of the same slices (Schwartz, 2000; Tricart and Schwartz, 2006), i.e. respectively ~1 GPa (for ~300°C), ~1.2 GPa and ~1.3 GPa (for ~450°C). These older P-T estimates align along a ~16-17 °C/km gradient, which seems inconsistent with the HP-LT gradient usually considered for Western Alps (Agard, 2021), suggesting that peak pressure was strongly underestimated in these previous works. Finally, the estimated peak pressure for the Lago-Superiore slice is >2.4 GPa (Table 3), in good agreement with literature data (see §3.4; Angiboust

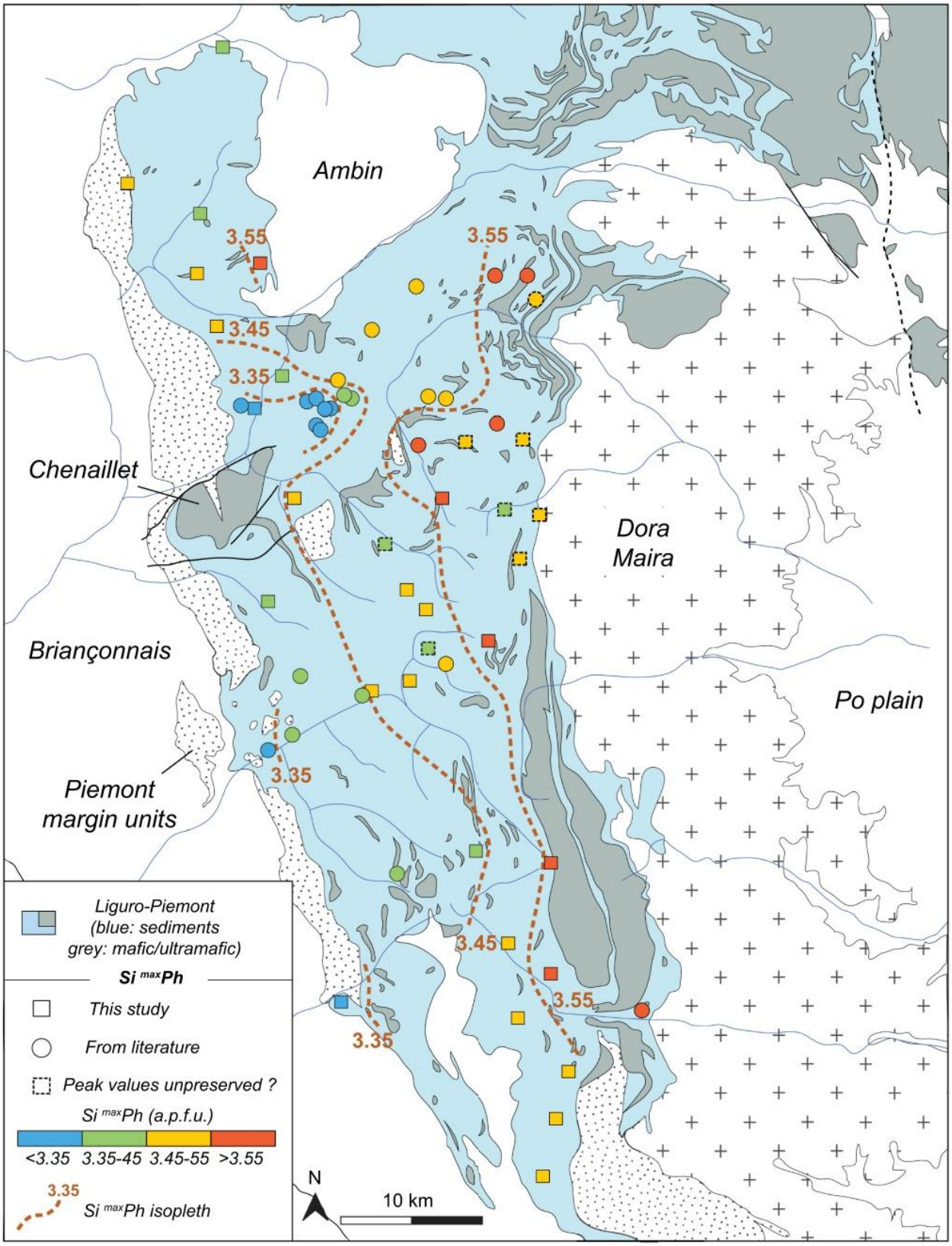

Fig. 8. Distribution of maximum Si values of phengite ($Si^{max}Ph$) across the L-P domain, in Cottian Alps and Queyras-Monviso region. $Si^{max}Ph$ values progressively increase toward east, showing an eastward pressure gradient as highlighted for temperature in Fig. 4a-c. Square symbols correspond to our samples while round symbols correspond to literature data (see Fig. 7 caption). Symbols with dotted contours correspond to samples where peak burial Si values were not preserved or foundd. Selected $Si^{max}Ph$ values are presented in Sup. mat. 3.

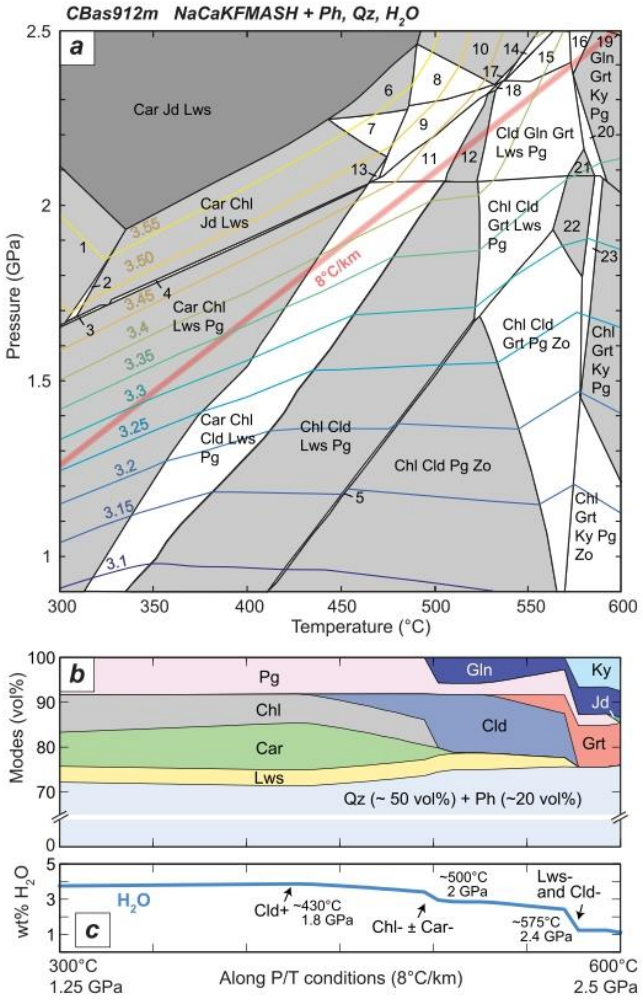

Fig. 9. Thermodynamic modelling for a representative composition of Liguro-Piemont metasediments. A) Pseudosection (system NaCaKFMASH, with all assemblages containing quartz, phengite and H_2O) calculated using Perple_X software (Connolly, 1990, 2005, 2009) for the bulk composition of CBas912m sample of Henry et al. (1996) considered as representative of most Liguro-Piemont calcschists. Calculated isopleths of Si a.p.f.u. in phengite are represented. The red line corresponds to a 8°C/km gradient. Calculated B) evolution of mineral modes and C) H_2O content and major dehydration reactions, along a 8°C/km gradient (from 300°C-1.25 GPa to 600°C-2.5GPa) for the pseudosection presented in A). Mineral abbreviations: Car: carpholite; Chl: Chlorite; Cld: chloritoid; Gln: glauchophane; Grt: grenat; Jd: jadeite; Ky: kyanite; Lws: lawsonite; Pg: paragonite; Ph: phengite; Qz: quartz; Zo: zoisite. Reaction abbreviations: Car-: carpholite-out; Chl-: chlorite-out; Cld+: chloritoid-in; Cld-chloritoid-out; Lws-: lawsonite-out. Mineral assemblages in A) 1: Car Jd Lws Stp; 2: Car Chl Jd Lws Stp; 3: Car Jd Lws Pg Stp; 4: Car Chl Jd Lws Pg; 5: Chl Cld Lws Pg Zo; 6: Car Gln Jd Lws; 7: Car Chl Gln Jd Lws; 8: Car Gln Grt Jd Lws; 9: Car Cld Gln Jd Lws; 10: Car Grt Jd Lws; 11: Cld Car Gln Lws Pg; 12: Cld Gln Lws Pg; 13: Car Chl Cld Jd Lws; 14: Car Grt Jd Lws Pg; 15: Car Gln Grt Lws Pg; 16: Gln Grt Ky Lws Pg; 17: Car Cld Grt Lws Jd; 18: Cld Gln Jd Lws Pg; 19: Gln Grt Jd Ky; 20: Cld Gln Grt Ky Pg; 21: Cld Gln Grt Pg; 22: Chl Cld Grt Pg.

et al., 2012b; Locatelli et al., 2018).

Individual slices were then plotted in a P-T space considering their mean RSCM temperature and their approximate mean peak pressure (Fig. 10a). For the slices where no pressure was determined by our study, the compiled P-T estimates from the literature of §3 were used. No pressure data is available, however, for the Avise-Tsaboc-Feluma, West-Sesia, Savoy Upper Unit, Venaus and Aigle slices, which are not shown in Fig. 10a. The slices were color-coded on the basis of the trimodal temperature distribution (Fig. 5b-e; §5.1). The different slices are also shown considering their peak pressure and age (see references in §3) in Fig. 10b.

Fig. 10a strengthens the existence of a trimodal distribution of tectonic slices with respect to peak burial conditions. The first cluster is characterized by mean peak conditions of 350-400°C and ~1.5-1.7 GPa. These slices (Calcschist unit, Lago Nero, Pelvas-Taillante and Puys) mosty consist of sediments (>90%; Table 1; Fig. 1a, 10a, b). Cornet unit has the same range of mean temperature (390°C; Table 2) but lower pressure (0.8-0.9 GPa; Manzotti et al., 2021). Some pressure estimates for the lower grade rocks of Lago Nero and Calcschist units (Agard et al., 2001a, 2001b; Tricart and Schwartz, 2006) are relatively close to those of Cornet unit, then considered to belongs to the same cluster. The second cluster shows mean peak conditions of 415-475°C and ~1.7-2.1 GPa. These units (Albergian, By, Cerogne-Ciantiplagna, Mirabouc-Bouchet, Savoy Middle Unit and Vin Vert) are also dominantly composed by sediments (Table 1, Fig. 1a, 10a). The third cluster is characterized by mean RSCM temperature of ~490-540°C and mean peak pressures of 2.2- ~2.6 GPa. These slices (Avic, Lago Superiore, Monviso, Savoy Lower Unit, Zermatt-Saas) are mostly composed by mafic and ultramafic rocks (~60%; Table 1; Fig. 1a, 10a) except for the Grivola-Urtier and Orsiera-Rocciavrè, which nevertheless show a higher ophiolitic content than all BS-facies slices.

7. Discussion

7.1. Correlations between tectonic slices, distribution, and revised structural sketchmap

Using the peak P-T conditions, lithostratigraphy, zoneography of index minerals and structural constraints, three groups of tectonic slices can be recognized in the L-P domain (Figs. 11,12a-d):

— the Liguro-Piemont Upper units (LPU):

These units, which make up ~18% of the Western Alps L-P surface (~440 km^2; Table 1), crop out in the west of the L-P domain (Figs. 11, 12a-d) and are dominated by metasediments (>90%, Table 1; Fig. 1a). They are largely exposed in the southern L-P domain (Queyras-Monviso and Cottian Alps, Fig. 11) while gradually disappearing from the Savoy-Susa to the Valais-Aosta region, where they are relatively rare (except for the Cornet slice; Fig. 11). From north to south, the LPU include the Cornet slice (Valais-Aosta), the Savoy Upper Unit with the Jovet, Grand Vallon, Upper Sana and Lamet klippen (Savoy-Susa region), the Lago Nero, Aigle and Puys slices (Cottian Alps) and the Calcschist and Pelvas-Taillante slices (Queyras-Monviso). Some of these slices exhibit an almost complete Chabrière-type stratigraphic succession (Lago Nero, Pelvas-Taillante, Cornet; Fig. 3b), whereas some only contain C4a-b calcschists-flyschs (Calcschist unit, Puys, Savoy Upper Unit; Fig. 3b). The lack of Lower-Cretaceous and Jurassic deposits in the latter units may indicates a more proximal origin (Fig. 3a) or reflects differences in décollement depth (see §7.4). These LPU units are characterized by low- to medium-temperature BS-facies peak metamorphism highlighted, in metasediments, by the presence of Fe-Mg carpholite and lawsonite (Fig. 1b). Chloritoid only appears in their higher-grade metasediments, in the eastern part of these units (Fig. 1b). Peak P-T conditions range mostly between 320-400°C and 1.2 to 1.9 GPa (Fig.4a-c, 5b-e, 10a; Table 2, 3, see §3). Mean and median RSCM temperatures for these units are ~373°C (86 samples; Fig. 13a), while mean/median values of $Si^{max}Ph$ are 3.40/3.42 a.p.f.u. (30 samples; Fig. 13b).

Some uncertainties remain on the exact distribution of the LPU slices. In Savoy-Aosta, the extent of the Cornet slice and the precise location of its contact with the underlying By slice (Manzotti et al., 2021) still need to be investigated to the east of the Dent Blanche Nappe (Fig. 11). In the Queyras-Monviso region, we have considered that Acceglio's half-window (Schwartz et al., 2000b) separates the Pelvas-Taillante (LPU) to the west from the Mirabouc-Bouchet to the east of Acceglio, the two samples closest to the contact nevertheless show temperatures <400°C, which is

Table 3
Maximum Si a.p.f.u. values of phengite ($Si^{max}Ph$) and estimated peak pressure for Liguro-Piemont slices. Peak pressures were estimated by crossing RSCM temperatures (see Table 1; Fig. 4a-c, 5a-e) with the calculated isopleths of Si a.p.f.u. in phengite for a representative rock composition (Fig. 9a). Selected $Si^{max}Ph$, RSCM temperature for the same samples and all estimated pressure values are presented in Sup. mat. 3.

Slice	$Si^{max}Ph$	Mean $Si^{max}Ph$	Med. $Si^{max}Ph$	sd	n samples	Relative pressure (GPa)	References for $Si^{max}Ph$
Lago Nero	3.27-3.5	3.39	3.42	0.082	19	~1.3 - ~1.9	This study; Agard et al. (2001a, 2001b); Liewig (1981)
Puys	3.46	/	/	/	1	1.7-1.8	This study
Vin Vert	3.55	/	/	/	1	2.1	This study
Cerogne-Ciantiplagna	3.4-3.57	3.49	3.49	0.113	2	1.7- ~2.2	This study; Agard et al. (2001a, 2001b)
Albergian	3.39-3.64	3.5	3.48	0.082	11	1.8- ~2.3	This study; Agard et al. (2001a, 2001b)
Orsiera-Rocciavrè	3.47-3.67	3.53	3.47	0.125	3	2.2- ~2.5	This study; Agard et al. (2001a, 2001b)
Calcschist unit	3.34-3.5	3.43	3.42	0.059	8	1.4-2	This study; Liewig (1981)
Pelvas-Taillante	3.31-3.42	3.37	3.37	0.077	2	1.4-1.7	This study; Bocquet (1974)
Mirirabouc-Bouchet	3.48-3.59	3.53	3.54	0.037	9	1.9- ~2.4	This study
Lago Superiore	3.61	/	/	/	1	> 2.4	Bonnet et al., 2022

significantly lower than most temperatures obtained for the Mirabouc-Bouchet slice (Fig. 4a-c) and may indicate that the Pelvas-Taillante slice is cropping out over a short distance to the east of Acceglio. Finally, only few temperature constraints are available for the Savoy Upper Unit (4 samples), Puys (1 sample) and Aigle (3 samples) slices, and almost no pressure constraints (only 1 sample for Puys). While their estimated RSCM temperatures are similar to LPU units (Table 2, Fig. 5b-e, 10a), more P-T estimates are needed to confirm this interpretation.

— *the Liguro-Piemont Middle units (LPM):*

These units make up ~42% of the L-P aeral exposure (~1050 km^2; Fig. 11, Table 1) and are also dominated by metasediments (generally >90%, Table 1; Fig. 1a). They crop out eastward of the LPU units (Fig. 11, 12a-d), except in Savoy-Susa where the LPU is found as klippen and in Valais-Aosta where the Cornet slice (LPU) forms a synformal stack atop the By slice (LPM; Fig. 12a). The Liguro-Piemont Middle units comprise the By slice (Valais-Aosta), the Savoy Middle Units (including Grande Sassière, Lower Sana and Chardonnet klippen) and the Venaus slice (Savoy-Susa), the Albergian, Cerogne-Ciantiplagna and Vin Vert slices (Cottian Alps) and the Mirabouc Bouchet slice (Queyras-Viso), and possibly the West-Sesia and Avise-Tsaboc-Feluma slices (see below). These slices generally exhibit a stratigraphic succession corresponding to an incomplete Chabrière-like series, commonly with a thick sequence of – and in places restricted to – Upper-Cretaceous C4a deposits (Fig. 3b). The LPM are characterized by a high-temperature blueschist-facies and up to transitional BS-eclogite-facies metamorphism highlighted in metasediments by the appearance of chloritoid in peak assemblages, the disappearance of Fe-Mg carpholite, the presence of lawsonite and the absence of garnet (Fig. 1b). Most P-T conditions range between 415-475°C and 1.7-2.2 GPa (Fig.4a-c, 5b-e, 10a; Table 2, 3, see §3). Mean/median RSCM temperatures for these units are 459°C/463°C (191 samples; Fig. 13a), while mean/median values of $Si^{max}Ph$ are 3.52/3.51 a.p.f.u. (23 samples; Fig. 13b).

Uncertainties on the spatial extent of the LPM concern slices with limited lithostratigraphic and P-T data. While the Venaus slice was already considered as an equivalent of the Savoy Middle Unit (Fudral, 1996) and shows a RSCM temperature of 485°C consistent with LPM, the attribution is less clear for the West-Sesia and Avise-Tsaboc-Feluma slices. The RSCM temperature for the West-Sesia slice (433°C; Fig. 4a-c; Table 2) fits LPM temperatures (no such low value was found in the eclogite-facies units; Table 2, Fig. 5b-e, 10a). It is furthermore largely dominated by metasediments (~93%; Table 1), in contrast with the LPL lithology (Table 1, Fig. 1a), and would be the only BS-facies slice eastward of eclogite-facies LPL (Fig. 11). We therefore suggest that this slice may be analogous to the other LPM units and reflect the doming of Savoy Middle Unit-like slices above the Gran Paradiso massif (Fig. 11). For the Avise-Tsaboc-Feluma slice(s), while the RSCM temperature of 522°C fits in the LPL temperature range (Table 2; Fig. 5b-e, 10a), its estimated sediment/mafic-ultramafic ratio does not fit with the LPL units (~99% of sediments; Table 1), notwithstanding the fact that a few temperatures are close to 500°C in the LPM Savoy Middle Unit, and even higher in the LPM By and Mirabouc-Bouchet slices. Further P-T constraints are needed to confirm these attributions.

— *the Liguro-Piemont Lower units (LPL)*

These units occupy ~40% of the L-P surface (~990 km^2) and contain much more mafic and ultramafic material than the LPU and LPM units (Table 1; Fig. 1a). Most LPL slices contain >60% of ophiolitic material (Avic, Zermatt-Saas, Savoy Lower Unit, Monviso, Lago Superiore; Table 1) and correspond to the MUM units of Agard (2021), while a few have ~40% of ophiolites (Grivola-Urtier, Orsiera-Rocciavrè; Table 1). The Liguro-Piemont Lower units comprise the Avic, Grivola-Urtier and Zermatt-Saas slices (Valais-Aosta), the Savoy Lower Unit (Savoy-Susa), the Orsiera-Rocciavrè slice (Cottian Alps) and the Monviso and Lago Superiore slices (Queyras-Monviso). The LPL units are characterized by a specific, incomplete Chabrière-type series, devoid of Upper Cretaceous deposits (Fig. 3b), which may reflect a distinct paleogeography and/or high topography on the seafloor or a tectonic removal of its sedimentary cover during the subduction/exhumation processes. These LPL slices were metamorphosed from BS-eclogite-facies to eclogite-facies as outlined by the presence of chloritoid-garnet assemblages in metasediments (Fig. 1b). Most P-T conditions range between 500 and 580°C and 2.2 to 2.8 GPa (Fig.4a-c, 5a-e, 10a; Table 2, 3, see §3). Mean/median RSCM temperatures for these units are 529°C/534°C (118 samples; Fig. 13a), while mean/median values of $Si^{max}Ph$ are 3.55/3.54 a.p.f.u. (4 samples; Fig. 13b). Note that some Alpine units fit the LPL in term of peak P-T conditions but appear slightly different in terms of lithology, containing either almost only ophiolitic material for the Lanzo massif (>90% of mafic and ultramafic rocks; Lagabrielle et al., 1990) or almost only metasediments for the small Lago di Cignana UHP slice (e.g., Compagnoni and Rolfo, 2003).

The LPL units are exposed on the eastern side of the domain and appear separated from the BS-facies LPM by a major extensional contact (Philippot, 1990; Ballèvre et al., 1990; Ballèvre and Merle, 1993; Fig. 2a-c, 11, 12a-d). One might further sub-divide the LPL between mafic-ultramafic-dominated (~60% mafic-ultramafic; Table 1) and sediment-dominated slices (~60% sediments; Table 1), with the latter potentially representing the former cover of the MUM units (Agard, 2021). Indeed, some of the described slices (Savoy Middle Unit, Orsiera-Rocciavrè; §3) contain large amount of sediments embedding mafic-ultramafic rocks in their western side and are almost devoid of sediments in their eastern side (Fig. 1a). This distribution may either be explained by the west-dipping foliation of the slices (i.e., with the oceanic basement at the base) or by the presence of tectonic contacts juxtaposing sedimentary dominated eclogite-facies slices on top of mafic-ultramafic dominant slices. The different peak burial age inferred for the Orsiera massif metasediments (61-53 Ma, Agard et al., 2001a; Fig. 10b; §3, 7.3) and the Rocciavrè metagabbros (46 Ma, Angiboust and Glodny, 2020; Fig. 10b; §3, 6.3) rather supports this distinction. The Grivola-Urtier slice, which is richer in metasediments than most LPL units, would be an analogous of these sediments-dominated eclogite-facies slices.

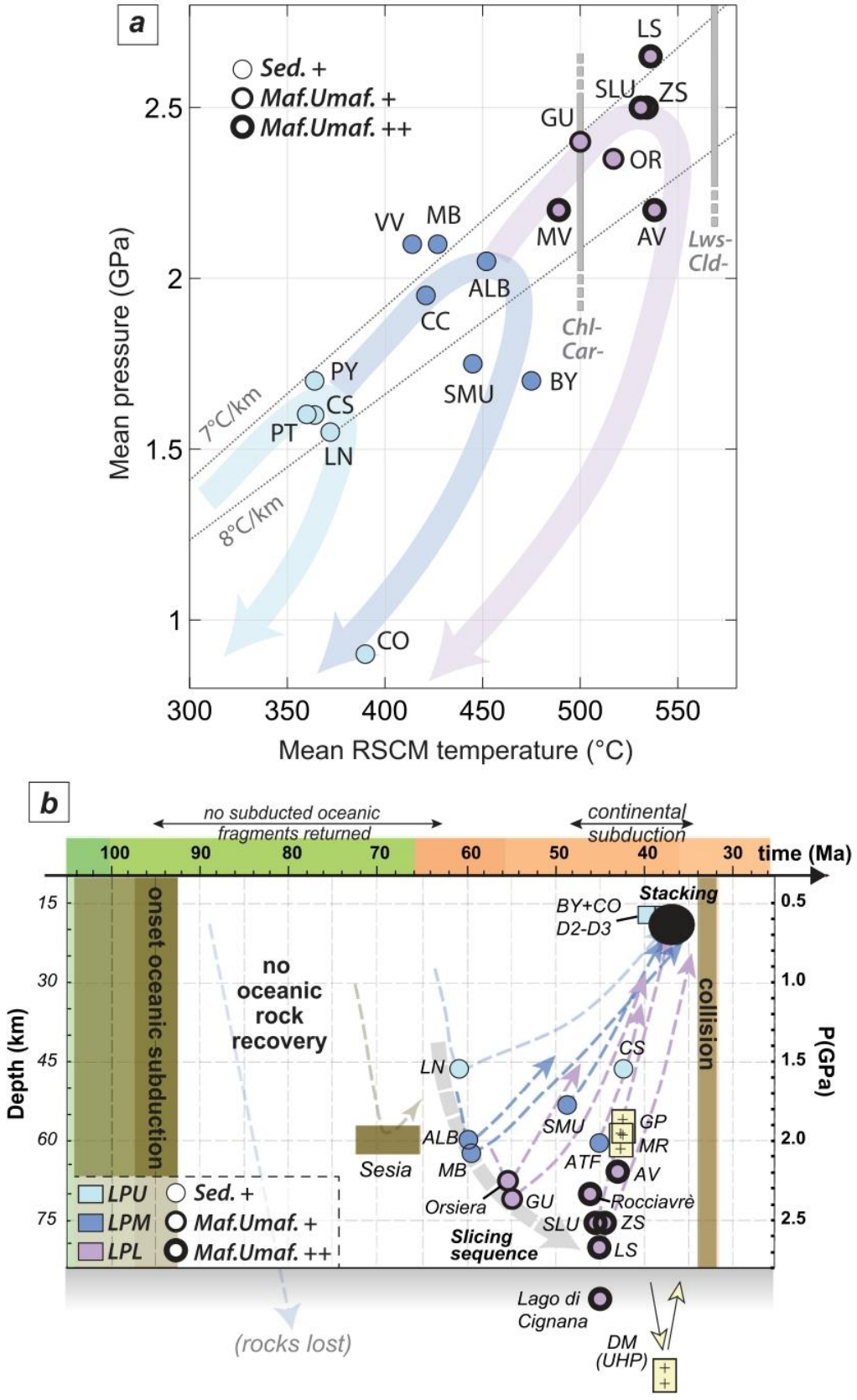

(caption on next page)

Fig. 10. A) Mean peak P-T conditions (circles) for the Liguro-Piemont slices. Slices were plotted in this P-T grid using their mean RSCM temperature and mean pressure retrieved from $Si^{max}Ph$ and the pseudosection (Fig. 9), or estimated in literature (§3). Increasing thickness of symbol contours represents increasing sediment/mafic-ultramafic ratio (table 1) in the slices: Sed.+: ≥ 90% of sediments; Maf.Umaf.+: ~60% of sediments. Maf.Umaf.++: ~40% of sediments (MUM units of Agard, 2021). The three major clusters of peak P-T conditions correspond to groups of slices with distinct sediment/mafic-ultramafic ratios. The major dehydration reactions of Fig. 9c are also reported. B) Subuction ages of Liguro-Piemont slices. Symbols correspond to the peak burial of the slices while dotted arrows depict their paths. This figure highlights the successive slicing of LPU, LPM, sediment-rich LPL and mafic-ultramafic-rich LPL from the downgoing slab and their stacking at ~36-35 Ma. Slices only composed by Upper Cretaceous deposits may be the last units sliced as highlighted by the peak burial age of CS. References for ages are in the text (§3; 7.2, 7.3). LPU: Liguro-piemont Upper units; LPM: Liguro-Piemont Middle units; LPL: Liguro-Piemont Lower units. Slice abbreviations: ALB: Albergian; ATF: Avise-Tsaboc-Feluma; AV: Avic; BY: By unit; CO: Cornet; CS: Calcschist unit; GU: Grivola-Urtier; LN: Lago Nero; LS: Lago Superiore; MB: Mirabouc-Bouchet; SLU: Savoy Lower Unit; SMU: Savoy Middle Unit; ZS: Zermatt-Saas. Abbreviations for continental units: DM: Dora-Maira; GP: Gran Paradiso; MR: Monte Rosa. Modified after Agard (2021).

7.2. *Diachronous burial and stacking, and possible paleogeographic origin*

The similar peak P-T conditions, structural position and lithological content among slices in each of the three L-P groups (§7.1) suggest that they may have recorded similar subduction histories and processes. The plot of RSCM temperatures versus longitude for each transect highlights the similarity of slice-stacking of LPU, LPM and LPL units across the L-P domain (Fig. 14a-e). The eastward-trend of temperature increase exposes the HP-LT subduction gradient, less conspicuous for the Valais-Aosta transect where a stronger collisional imprint on the nappe-stack (synformal-stack implying upper plate fragments) slightly erased this trend (Fig. 14e). Subtle differences in lithostratigraphy nevertheless point out to differences in their paleogeographic origin (Fig. 15a-c; see §7.3, 7.4), and all slices with similar P-T were probably not buried, sliced and juxtaposed at the same time. While the formation of deeply underplated nappe stacks suggests that the structurally lower units may have been buried, detached and underplated later (Kimura et al., 2007; Bachmann et al., 2009; Dumitru et al., 2010; Plunder et al., 2012), available metamorphic ages are here discussed to precise the slicing and underplating sequence of the LPU, LPM and LPL units (Fig. 10b, 14a, 15b).

Very few robust ages are available for the BS-facies LPU and LPM units (Fig. 10b; §3). The Lago Nero slice (LPU) was dated by in-situ Ar-Ar on phengite and gave 61-55 Ma, 51-43 Ma and 38-36 Ma ages for D1 (peak P-T), D2 and D3 fabrics respectively (Agard et al., 2002). Moreover, bulk Ar-Ar on separated generations of phengite from the Calcschist unit (LPU) gave a 42-40 Ma age for a peak P-T foliation (Lanari, 2012; Fig. 10b). These ages suggest a diachronous slicing of the LPU characterized by Chabrière-type series, which were buried and underplated earlier than the LPU units lacking deposits older than the Upper Cretaceous (Fig. 3b, 10b, 14a, 15a, b). The latter ones may have been originally located close to Piemont margin and been underplated on top of the L-P stack at the very end of oceanic subduction (Fig. 15b, 14a; see also Herviou et al., 2021, their Fig. 13 and §7.2.1).

In LPM (Albergian slice, Fig. 11), in situ Ar-Ar dating on phengite gave 64-49 Ma and ~50 Ma ages for D1 (peak P-T) and D2 fabrics (Agard et al., 2002; Fig. 10b). This method also gave 47-42 Ma and 40-36 Ma for S1(peak) and S2 (potentially equivalent to D3 of Agard et al., 2002; Fig. 10b) foliation in the Savoy Middle Unit (Ghignone et al., 2021b; Fig. 10b). Bulk Ar-Ar on isolated generation of phengite from the Mirabouc-Bouchet slices (LPM) gave 68-58 Ma for an early foliation (prograde to peak?), 45 Ma for a S2 (peak or early retrograde?) and an age younger than 30 Ma for a late S3 foliation (Lanari, 2012; Fig. 10b) while Rb-Sr on D3 phengite from the same slice gave ~35 Ma (Angiboust and Glodny, 2020; Fig. 10b). In the Valais-Aosta region, D2 to D3 exhumation-related episodes of By (LPM) and Cornet (LPU) slices were dated between 41 and 37 Ma (Reddy et al., 2003; Angiboust et al., 2014; Fig. 10b). These peak burial ages of the LPM units, either undistinguishable from or younger than those for the Lago Nero unit, are broadly consistent with a slicing and underplating somewhat later than the LPU Chabrière-serie slices (Fig. 10b, 14a, 15a, b) and with their present structural position (Fig. 12a-d).

Finally, for LPL mafic-ultramafic-dominated units, most of the peak burial ages (from various methods; see §3) range between 50 and 40 Ma (§3; Fig. 10b) and may represent the sampling of a mafic-rich zone close to the Piemont margin units (Fig. 14a, 15a), as pointed out by Agard (2021). Sediment-dominated units have older ages: 61-53 Ma, 46-42 Ma, 42-38 Ma in D1 (peak P-T), D2 and D3 fabrics of Orsiera massif sediments (in situ Ar-Ar in phengite; Agard et al., 2002; Fig. 10b) and 60-48 Ma for Grivola-Urtier slice (bulk Lu-Hf and Ar-Ar on phengite, Villa et al., 2014; Fig. 10b) suggesting that the few sediment-dominated eclogite-facies units may have been stripped from and underplated before the ophiolitic-dominated MUM LPL units (Fig. 14a, 15a). For each transect, the corresponding slices successively detached from the Alpine slab during a short-lived period prior to continental burial and were stacked together during exhumation around 40-35 Ma at ~20 km depth (Fig. 10b, 14a, 15a).

7.3. *Trimodal distribution of units: insights into subduction processes*

The three groups of L-P slices show peak P-T conditions comparable to those of subducted oceanic fragments recovered worldwide, for which two major recovery depths were recognized at 30-40 km and 80 ± 10 km, with a potential third cluster at 55-60 km (Fig. 16a-c; Agard et al., 2018; see also Plunder et al., 2015). The same distinct recovery depths were detected in continental-subduction slivers (Agard and Vitale-Brovarone, 2013; Soret et al., 2021). These rock clusters are thought to reflect major changes in mechanical coupling along the plate interface (Agard et al., 2018), which occur transiently (Monié and Agard, 2009) and in places coevally across-dip (Bonnet et al., 2018). While offscraping from the downgoing slab requires an increase in mechanical coupling (Agard et al., 2016, 2020), the stepping down of the plate interface décollement into the slab and strain localization into zones of weakness (Kimura et al., 1996; Kimura et al., 2007; Angiboust et al., 2012c; Ruh et al., 2015), mechanical processes controlling slicing are unknown. Similar depth clusters (35 ± 10 km and 60 ± 5 km) for the locus of interplate deformation bounding earthquakes were also recently identified by a mechanical analysis of the topography along the Chilean margin (Cubas et al., 2022; Fig. 16a). These depths are interpreted as zones of distributed deformation ultimately leading to slicing of the slab, underplating and topographic build-up (Menant et al., 2019, 2020), which are responsible for stress build-up eventually leading to the nucleation of earthquakes propagating across the domains B and C as defined by Lay et al., 2012; Cubas et al., 2022; see Fig. 16c). The LPU, LPM and LPL units, with their slicing depths of ~35-45 km, ~55-65 km and ~70-80 km, respectively, may therefore provide insights into the mechanisms that control strain localization and slicing along the plate interface (Fig. 16b).

— *Offscraping mechanisms in the LPU units*

The LPU ~35-45 km depth coincides with the downdip end of the seismogenic zone, where the transition from upper plate continental crust to mantle wedge likely induces a strong change in interplate coupling (Agard et al., 2018), and where ductile shear and dissolution-precipitation creep (DPC) may be the dominant deformation mechanisms (Wassmann and Stöckhert, 2013; Platt et al., 2018; Agard et al., 2018). Both geophysical and petrological data suggest the presence of

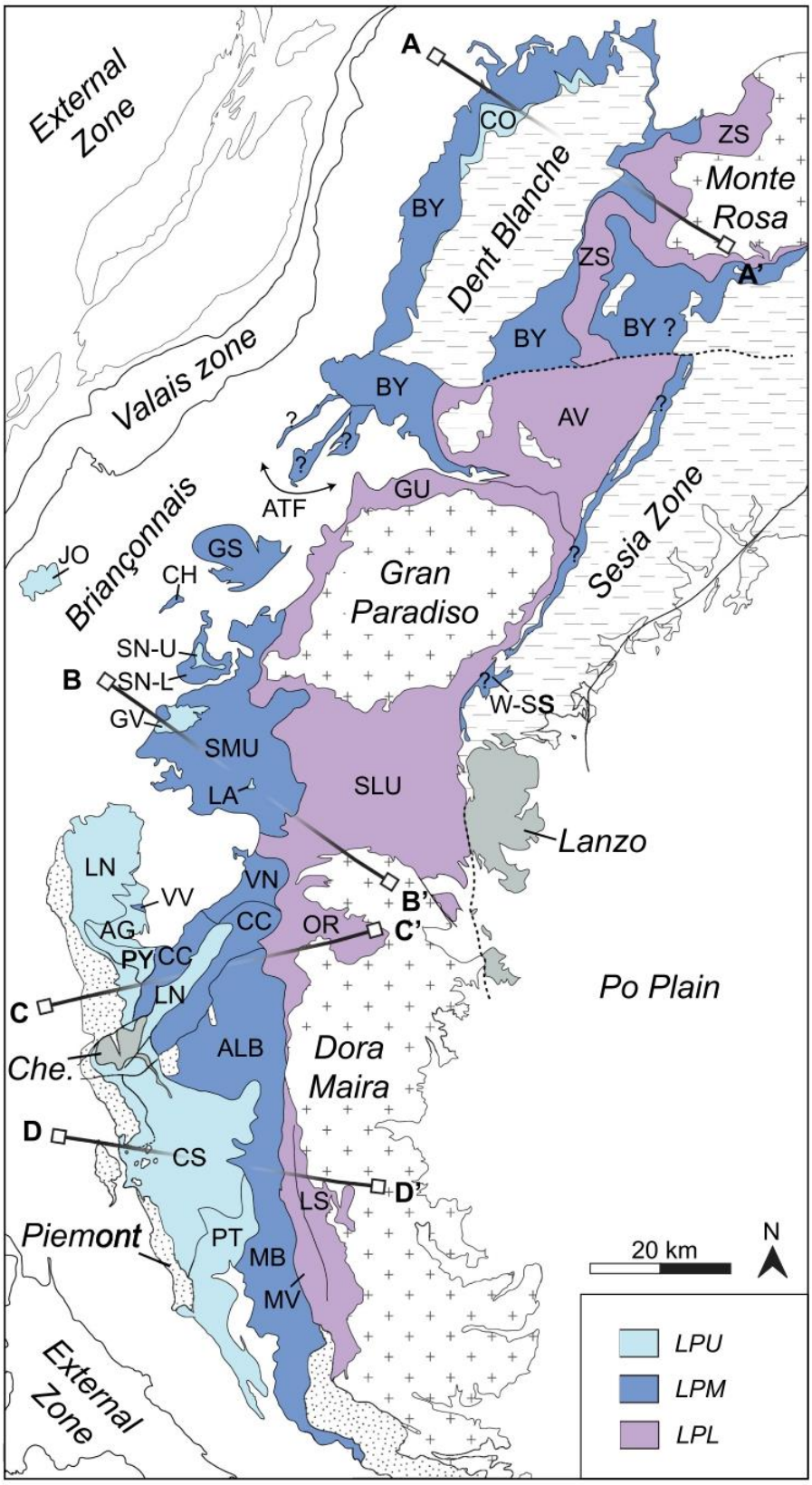

Fig. 11. Simplified map showing the distribution of the three Liguro-Piemont units across the Western Alps. Location of cross-sections shown in Fig. 12 is indicated (A-A'; B-B'; C-C'; D-D'). LPU: Liguro-Piemont Upper units; LPM: Liguro-Piemont Middle units; LPL: Liguro-Piemont Lower units.

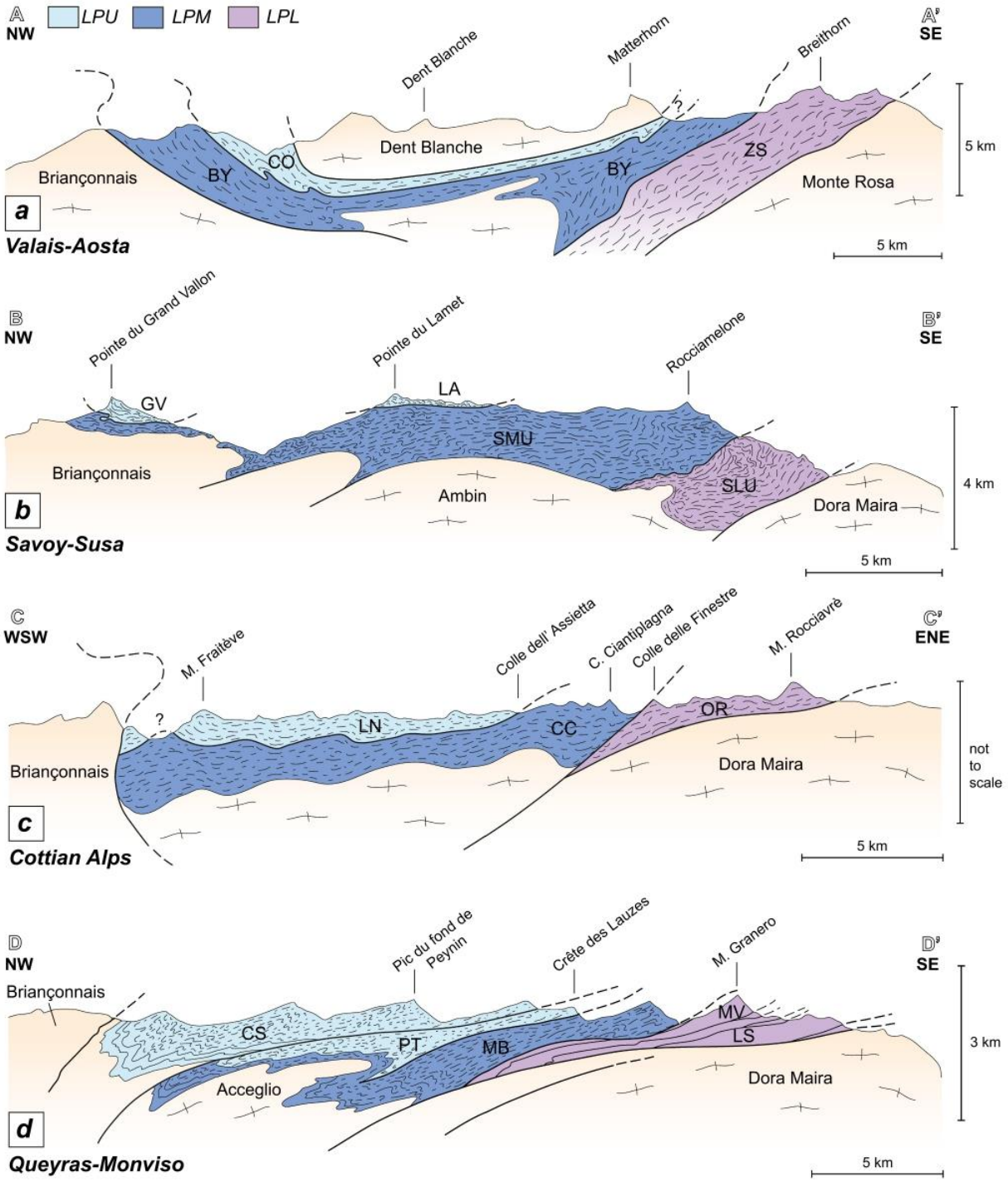

Fig. 12. Cross-sections of the four major Liguro-Piemont transects described in this study exposing the actual stacking of the different slices and units. Cross-section locations are indicated in Fig. 11. A) to D) were repectively modified after Negro et al. (2013); Plunder et al. (2012); Agard (2021); Lagabrielle (1987). LPU: Liguro-Piemont Upper units; LPM: Liguro-Piemont Middle units; LPL: Liguro-Piemont Lower units. Slice abbreviations: BY: By unit; CC: Cerogne-Ciantiplagna; CO: Cornet; CS: Calcschist unit; GV: Grand Vallon klippe; LA: Lamet klippe; LN: Lago Nero; LS: Lago Superiore; MB: Mirabouc-Bouchet; MV: Monviso; OR: Orsiera-Rocciavrè; PT: Pelvas-Taillante; SLU: Savoy Lower Unit; SMU: Savoy Middle Unit; ZS: Zermatt-Saas.

fluids and high pore fluid pressure (Audet et al., 2009; Saffer and Tobin, 2011; Behr and Bürgmann, 2021), which reduces shear strength and enhances strain localization in weak zones (Kimura and Ludden, 1995; Kimura et al., 2007; Saffer and Tobin, 2011; Kameda et al., 2017).

In the LPU units, the presence of fluids at peak burial conditions is attested by the large amount of hydrated phases in sediments and metamorphic veins (Goffé and Chopin, 1986; Lefeuvre et al., 2020; Herviou et al., 2021). The formation of lawsonite-bearing extensional cracks in these rocks reflects near-lithostatic fluid-pressure (Lefeuvre et al., 2020; Herviou et al., 2021). At these depths and for such a cold

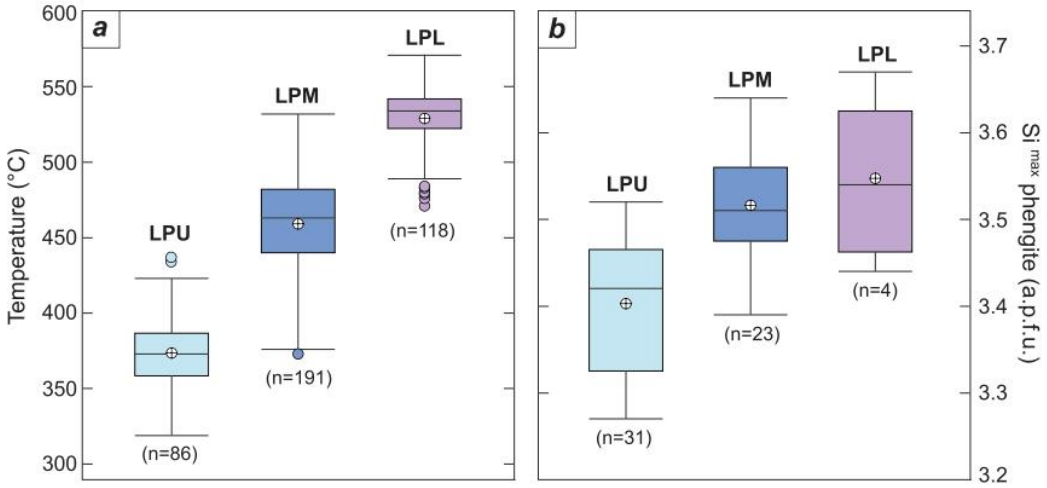

Fig. 13. Statistical distribution of RSCM temperatures in the Liguro-Piemont units. A) Boxplots of RSCM temperature for the three Liguro-Piemont units, both from this study and compiled from literature (see Fig. 4 caption). B) Boxplots of $Si^{max}Ph$ for the three Liguro-Piemont units, both from this study and compiled from literature (see Fig. 7 caption). inside boxes, lines and crossed circles correspond to median and mean values of each boxplot, given in the text (§7.1). LPU: Liguro-Piemont Upper units; LPM: Liguro-Piemont Middle units; LPL: Liguro-Piemont Lower units.

subduction gradient, however, no major dehydration reaction is predicted (Peacock, 1993; van Keken et al., 2011). Only the eastern samples contain chloritoid (Fig. 1b), showing that the progressive carpholite-out reaction is only crossed by the highest grade samples of LPU units, as predicted by our thermodynamic modelling (Fig. 9a-c; see also Agard et al., 2001a; Bebout et al., 2013; Herviou et al., 2021). Veins therefore likely formed by the local redistribution of material in the fluid through DPC-controlled deformation (Herviou et al., 2021). Slicing of the LPU units may then be related to inherited heterogeneities in the lithological succession and/or high fluid pressure rather than to embrittlement by major fluid release (e.g., Hacker et al., 2003).

In the LPU slices limited to Upper Cretaceous deposits (Fig. 3b, §4.1, 7.1, 7.2), strain may have localized between the Lower Cretaceous pelagic A3 and the more clastic Upper Cretaceous C4 calcschists-flyschs (Fig. 15c; see also Fig. 3b; §4.1), as observed between pelagic sediments and trench-filling turbidites in accretionary prisms (Karig and Sharman, 1975; Moore, 1975; Kimura et al., 2007). The Middle Cretaceous A3b shales would have served as a zone of rheological weakness (weaker than more siliceous hemipelagic sediments; Ikari et al., 2018) leading to deformation localization and slicing as in silty clays at slow aseismic creep conditions (Vannucchi et al., 2017).

In the LPU Chabrière-series slices (3b, 14; §4.1, 7.1, 7.2), which contain a dismembered ophiolitic basement (Table 1; Fig; 3b), slicing occurred deeper in the oceanic lithosphere (Fig. 15a, c), possibly along the numerous pre-Alpine structures identified in the L-P domain (e.g., oceanic-detachments; Manatschal et al., 2011; Lagabrielle et al., 2015; Balestro et al., 2018; Decrausaz et al., 2021; Agard, 2021). Fluid infiltration along theses structures, as notably attested by the strong hydrothermal alteration of the L-P oceanic fragments (Selverstone and Sharp, 2013; Busigny et al., 2011, 2018; see also Herviou et al., 2021), promoted strain localization (Fig. 15c). Strain localization in serpentinized horizons, in particular, is commonly considered for slicing in the slab (Angiboust et al., 2011; Agard et al., 2018; Tewksbury-Christle et al., 2021) and supported by modeling (e.g., Ruh et al., 2015).

— *Offscraping mechanisms in the LPM units*

At ~55-65 km, the slab is juxtaposed against the partly serpentinized and decoupled mantle wedge, explaining the lesser recovery of rocks for this range of subduction depths (Guillot et al., 2015; Agard et al., 2018; Fig. 16c). In the LPM units, fresh lawsonite is found in both metasediment matrix and veins (Fig. 1a; Herviou et al., 2021) and therefore considered to have remained stable during burial, as predicted by our pseudosection (Fig. 9a-c; 10a). In these slices, Fe-Mg carpholite is only found as micrometric needles in quartz crystals preserved from recrystallization (Agard et al., 2000, 2001a), whereas chloritoid is widespread in pelitic layers (Fig. 1a). The Fe-Mg carpholite (~12 wt% H_2O) to chloritoid (~7-8 wt% H_2O) reaction is therefore well under way. The carpholite-out reaction along a 8°C/km gradient is predicted at ~500°C-2 GPa (Fig. 9b, c, 10a), which fits the highest P-T conditions recorded by the LPM units (Fig. 5b-e; table 2, 3). However, no other major dehydration reaction releasing a large amount of water during a short P-T window is predicted for the LPM metasediments (Fig. 9b-c) or mafic-ultramafic rocks (Angiboust and Agard, 2010). The slicing of the LPM units may therefore be related to a combination of inherited lithological heterogeneities and fluid release (Fig. 15c, 16b). We therefore consider that strain localized in the Middle Cretaceous A3b shales for the Upper Cretaceous LPM slices (as for the LPU units; Fig. 3b, 15c) and around oceanic detachment faults for the Chabrière-like LPM (Fig. 3b, 16c).

— *Offscraping mechanisms in the LPL units*

The third cluster at ~70-80 km coincides with the depth beyond which rocks are generally not recovered, due to density and slab pull changes as well as to viscous recoupling (Wada and Wang, 2009; Syracuse et al., 2010, see also Kerswell et al., 2021; Fig. 16c) dragging down irreversibly the slab into the mantle once serpentinite is fully dehydrated (Agard et al., 2009, 2018; Duesterhoeft et al., 2014). A change in deformation mechanisms from fluid-assisted DPC to dislocation creep may drive this viscous coupling (Agard et al., 2020).

The transition from BS- to eclogite-facies is considered as a major dehydration-step for the downgoing plate (Peacock, 1993; Angiboust and Agard, 2010; van Keken et al., 2011; Paulatto et al., 2017). The boundary between these two facies coincides with the location of intermediate-depth earthquakes, suggesting that rocks undergo weakening and embrittlement during dehydration at eclogite-facies conditions (Hacker et al., 2003; Kita et al., 2006; Abers et al., 2006, 2013), especially for the coldest slabs (Abers et al., 2013). Dehydration reactions such as the lawsonite-out (~12 wt% H_2O) were suggested because crustal intermediate-depth seismicity coincide with the thermal stability of lawsonite (Abers et al., 2006), and because lawsonite dehydration may trigger brittle failure as unstable fault slip (Okazaki and Hirth, 2016; Incel et al., 2017). Brittle-deformation was furthermore evidenced in exhumed eclogites and may reflect an increase in fluid pressure induced by dehydration reactions (Angiboust et al., 2017; Hertgen et al., 2017; Behr et al., 2018).

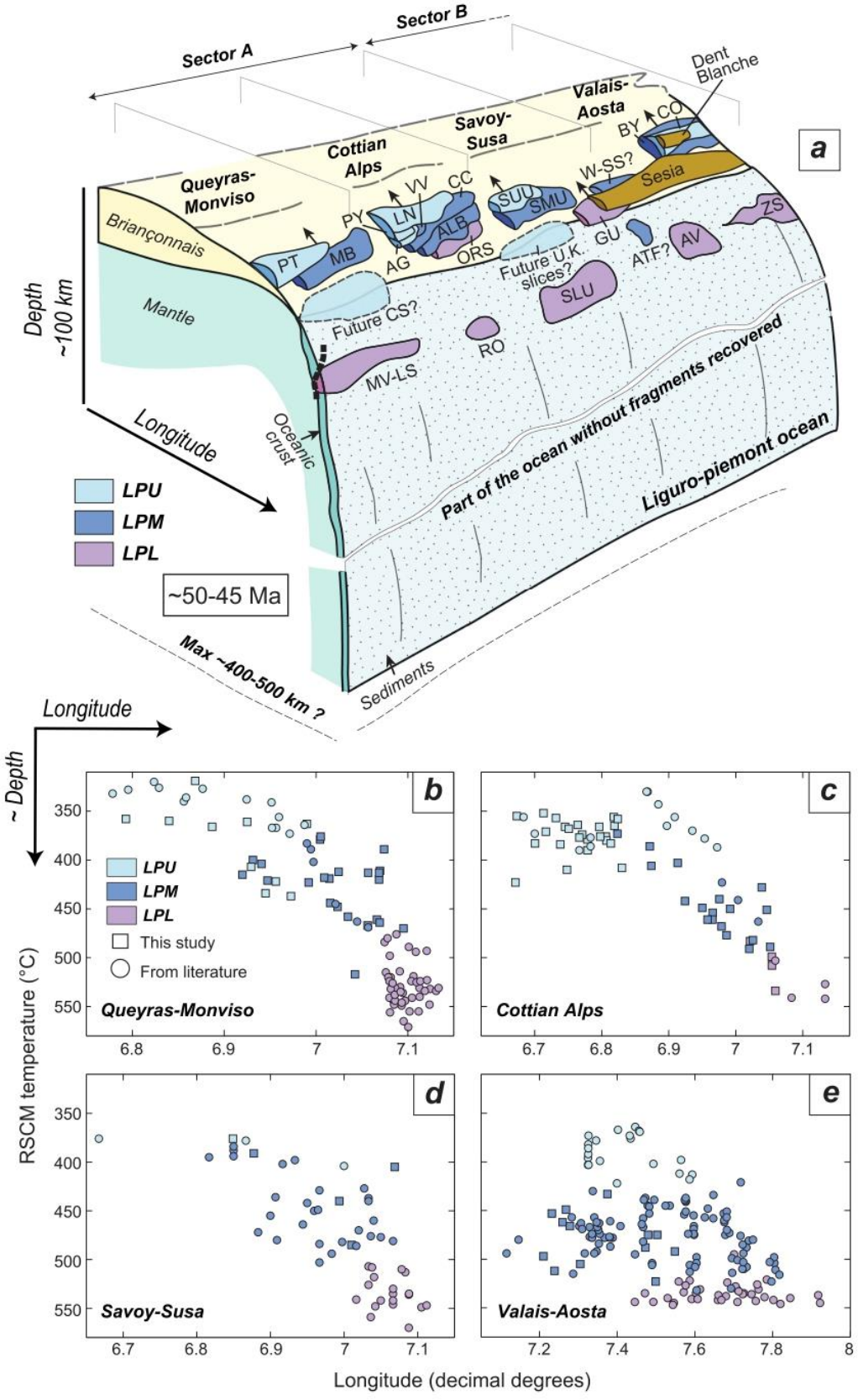

(caption on next page)

Fig. 14. Sketch of the slicing and stacking of Liguro-Piemont slices. A) Idealized view of the Alpine subduction zone at ~50-45 Ma, showing the relative location of the slices (for the four transects) discuted in the text. At this time, Chabrière-type LPU and LPM are already offscraped from the slab and are exhuming, as for the sedimentary-dominated LPL. Mafic-Ultramafic LPL, initially close to the continental margin are being sliced. Upper Cretaceous LPU and LPM will be the last to offscraped from the downgoing slab. Two different transects defined by Agard (2021) are represented (sectors A and B). Modified after Agard (2021). B) to E) RSCM temperature versus longitude for the four transects detailed in the text (see also Fig. 11, 12). These graphs show the increase of peak temperature from W to E and the current stacking of the L-P units, with LPU structurally at the top of LPM and LPL. Square/round symbols correspond to our samples/literature data respectively (see Fig. 4 caption). Abbreviations: LPU: Liguro-Piemont Upper units; LPM: Liguro-Piemont Middle units; LPL: Liguro-Piemont Lower units. AG: Aigle; ALB: Albergian; ATF: Avise-Tsaboc-Feluma; AV: Avic; BY: By unit; CC: Cerogne-Ciantiplagna; CO: Cornet; CS: Calcschist unit; GU: Grivola-Urtier; LN: Lago Nero; LS: Lago Superiore; MB: Mirabouc-Bouchet; MV: Monviso; OR: Orsiera-Rocciavrè; PT: Pelvas-Taillante; PY: Puys; SLU: Savoy Lower Unit; SMU: Savoy Middle Unit; SUU: Savoy Upper Unit; VV: Vin Vert; W-SS: West-Sesia unit; ZS: Zermatt-Saas. U.K. slices: slices mostly made by Upper Cretaceous sediments such as the Savoy Upper Unit at Grand Vallon or Lamet klippe.

In LPL units, eclogitic breccias and veins reveal rupture events along rheological contrasts and during fluid ingression at ~80 km (Angiboust et al., 2011, 2012a; Locatelli et al., 2018, 2019a, 2019b; Broadwell et al., 2019). Furthermore, pseudotachylites formed in the same depth range were reported in Lanzo massif, adjacent to the LPL units (Scambelluri et al., 2017; Pennacchioni et al., 2020). At peak P-T conditions, in LPL units mafic crust, lawsonite is supposedly still stable (Angiboust and Agard, 2010; Angiboust et al., 2011, 2012b; Locatelli et al., 2018) whereas chlorite (~12 wt% H_2O) is predicted to breakdown at the BS- to eclogite-facies transition (Angiboust and Agard, 2010). In the LPL ultramafic rocks, antigorite (~12 wt% H_2O) is still stable at peak P-T conditions (Angiboust and Agard, 2010; Schwartz et al., 2013). In the LPL mafics and ultramafics, the only reaction that may contribute to high fluid pressure and affect rheology is therefore chlorite breakdown. Dehydration reactions occurring deeper, such as antigorite breakdown, may also affect rocks at LPL units peak-burial depths (Angiboust et al., 2012a).

The P-T estimates for the LPL units lie close to predicted major dehydration reactions for metasediments (Fig. 9a-c; 10a), supporting the potential role of fluids in LPL slicing. While the chlorite and Fe-Mg carpholite breakdown in sediments is predicted at ~500°C-2 GPa (with a decrease in water content from ~3.5 wt% to ~2.8 wt% H_2O; Fig. 9b-c, 10a), another major step of dehydration (leading to a decrease from ~2.5 wt% to ~1.2 wt% H_2O) is predicted at ~575°C-2.4 GPa for

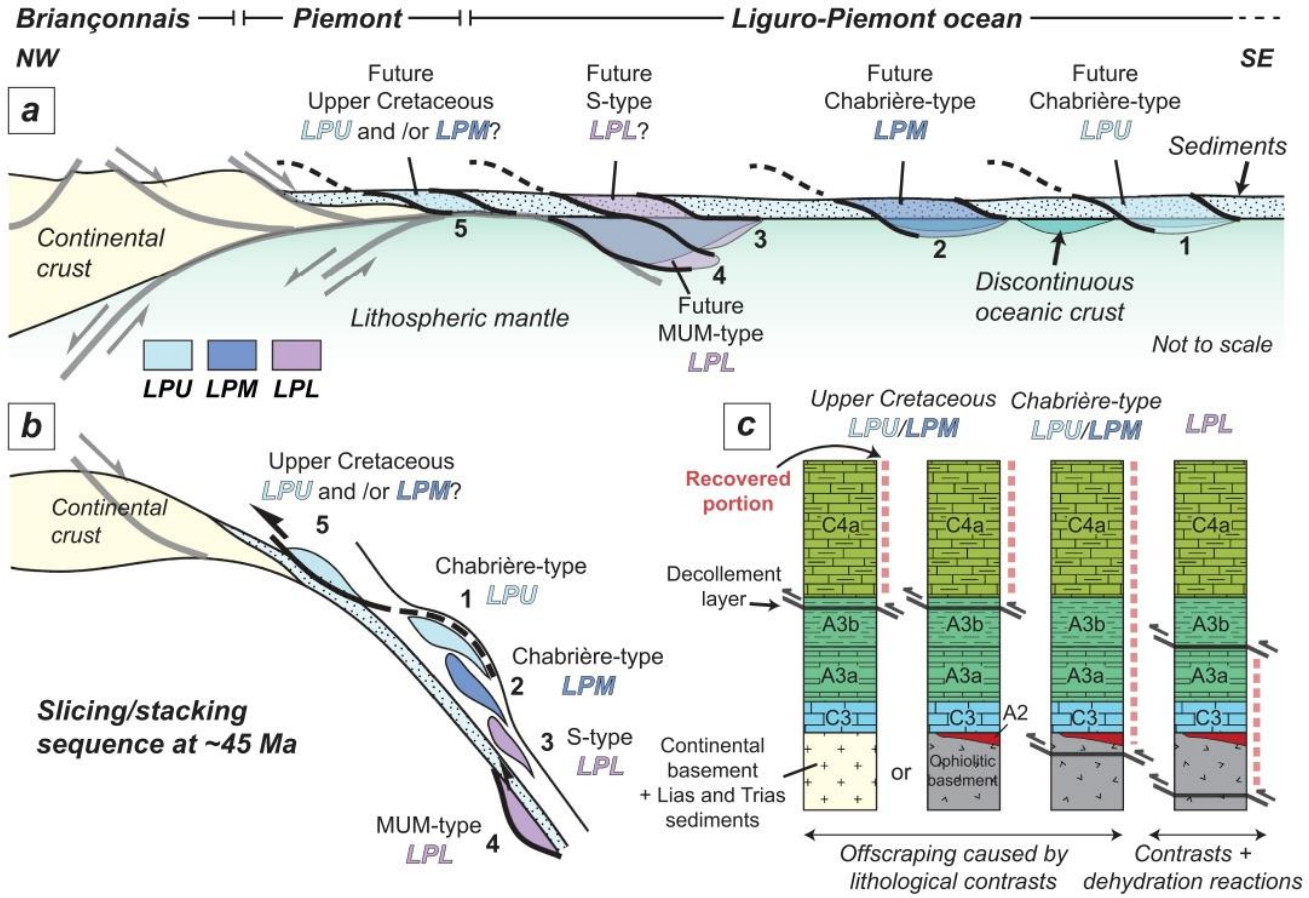

Fig. 15. A) Potential paleogeographic position of Liguro-Piemont units before subduction. B) Suggested slicing and stacking sequence of Liguro-Piemont units. C) Stratigraphic columns with recovered portion of the different Liguro-Piemont units and suggested decollement layers and offscraping mechanisms. For the Upper-Cretaceous LPU and LPM, the initial basement may either have been made of continental or oceanic rocks. We suggest that strain localization leading to LPU and LPM units' slicing mostly occurred due to major lithological contrasts in the pile, such as levels of pelagic sediments or serpentinized mantle acting as rheological weaknesses, possibly under high fluid pressure conditions. On the other side, LPL units slicing at eclogite facies conditions may be linked to major dehydration reactions (as lawsonite breakdown in sediments), under high fluid pressure conditions, responsible for rocks embrittlement. LPU: Liguro-Piemont Upper units; LPM: Liguro-Piemont Middle units; LPL: Liguro-Piemont Lower units.

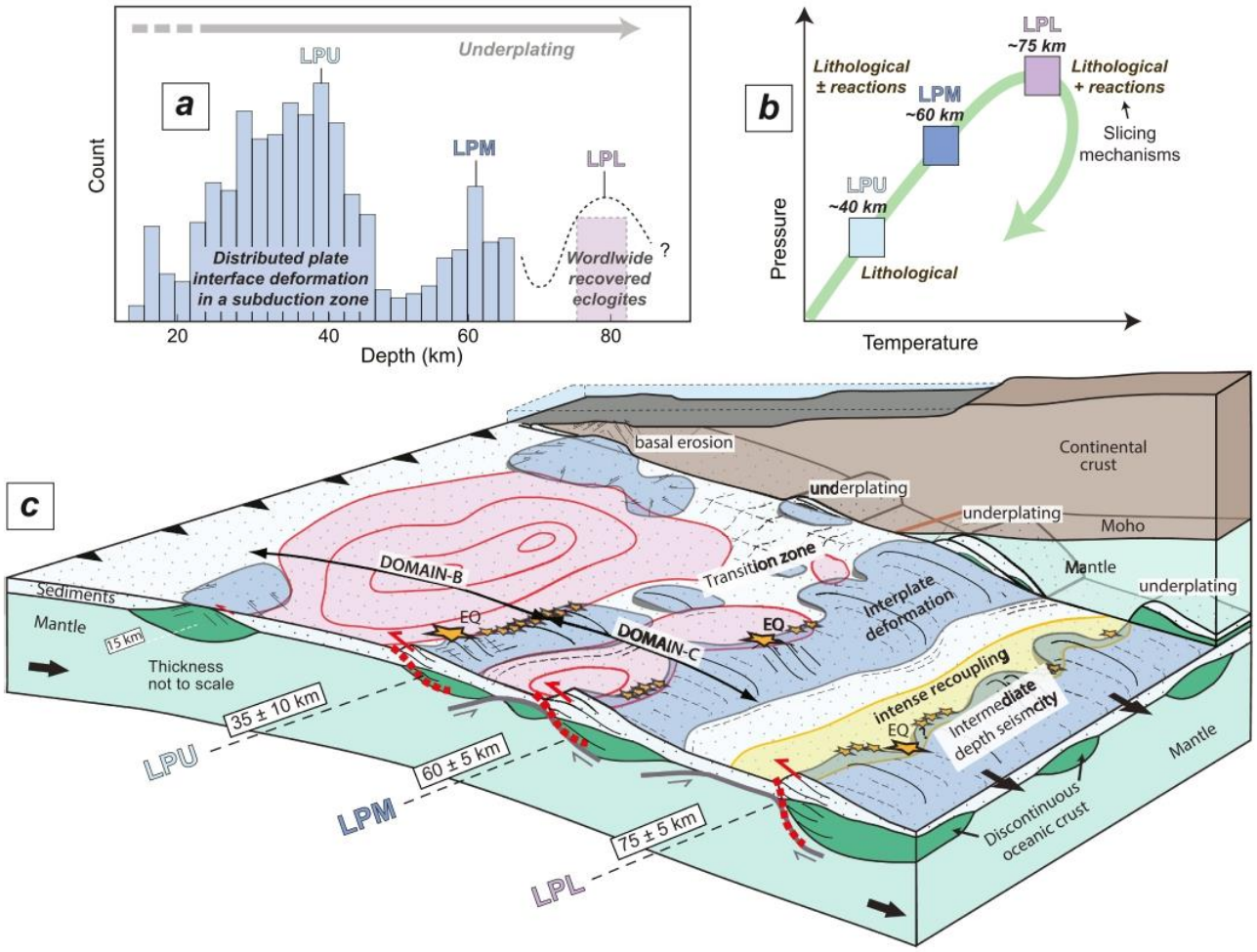

Fig. 16. Depth clusters and mechanisms of slicing in the Liguro-Piemont subduction zone. A) Bar chart of underplating depth (distributed deformation along the plate interface) along the Chilean margin (after Cubas et al., 2022). Mean peak burial depths estimated in this study for the Liguro-Piemont units LPU an LPM are in good agreement with the underplating depth clusters observed along the Chilean margin. The peak burial depth of the eclogite-facies LPL units is similar tot the estimated peak burial depth for most of worldwide recovered eclogites (after Agard et al., 2018). B) Schematic peak P-T depth conditions for the Liguro-Piemont units, and suggested major slicing mechanisms, i.e. major litholical heterogeneities for LPU and LPM and fluid release combined with lithological heterogeneities for LPL. C) Schematic view of a subducting slab with discontinuous oceanic crust, subjected to three main depths of slicing at ~35-45 km, 55-65 km and 70-80 km. The heterogeneously distributed deformation leads to slicing of the slab, underplating and topographic build-up responsible for the nucleation of earthquakes propagating across the B and C domains. Modified after Cubas et al. (2022). Abbreviations: LPU: Liguro-Piemont Upper units; LPM: Liguro-Piemont Middle units; LPL: Liguro-Piemont Lower units.

chloritoid (~7-8 wt% H_2O) and lawsonite breakdown (Fig. 9b-c, 10a). We note that this second step coincides with most of the maximum P-T conditions recorded in LPL units (Fig. 9c, 10a, see §3, 7.1), where lawsonite is no longer stable, and that large amounts of lawsonite, up to ~40 vol% of the host rocks, were present in metasediments (Lefeuvre et al., 2020). We therefore propose that the destabilization of these large amounts of lawsonite, accompanied by chloritoid-out reaction and/or chlorite breakdown (in mafic rocks), may have induced high fluid pressure and embrittlement able to slice LPL units from the downgoing slab (Fig. 15c, 16b; as supported by experiments; Okazaki and Hirth, 2016). These reactions would have helped localize strain deeper in the downgoing slab than for the LPU and LPM units, explaining the larger volume of mafic and ultramafic rocks in the present-day stack of LPL units (Fig. 1a, 10a, 15a, c; see §4, 7.1, 7.2). As for the LPU and LPM units, inherited detachment faults may have served as rheological weaknesses to localize the strain (Fig. 15a, 16c).

8. Conclusions

Through the compilation of petrological data (peak P-T estimations, zoneography of index minerals) and report of new RSCM temperatures, RSCM interpolation, maximum Si values of phengite (as a proxy for peak pressure) and thermodynamic modelling, this study provides a detailed framework of the peak P-T conditions recorded by the various Liguro-Piemont slices. A strong eastward increase in metamorphic grade through the Liguro-Piemont domain, as well as inside some slices, is notably highlighted by the distribution of RSCM temperatures and maximum Si values of phengite. In addition, the compilation of lithostratigraphic, structural and radiochronological data, together with the estimation of the sediment versus mafic-ultramafic content from aerial exposures, for each slice, allow refining the origin and evolution of these tectonometamorphic units/slices across the Liguro-Piemont domain. The revised structural organization of the various Liguro-Piemont units allows restoring the geometries of the Alpine subduction at peak burial conditions. Results point to a trimodal distribution of units with an

almost continuous increase in metamorphic conditions from the Liguro-Piemont Upper units (LPU; 320-400°C- 1.2-1.9 GPa) to the Liguro-Piemont Middle units (LPM; 415-475°C- 1.7-2.2 GPa) and to the Liguro-Piemont Lower units (LPL; 500-580°C- 2.2-2.8 GPa). The LPU and LPM units, metamorphosed under blueschist-facies conditions at peak P-T conditions, are dominated by sediments (>90%) whereas the LPL units, metamorphosed at eclogite-facies conditions at peak burial, are much richer in mafic-ultramafic rocks (>40%). These two types exhibit major differences in terms of initial paleogeography and/or mechanisms responsible for material-offscraping from the downgoing slab. Peak burial depths of the LPU, LPM and LPL units are similar to those deduced for the slicing and underplating of rocks in modern and fossil subduction zones, pointing to specific mechanisms controlling transient changes in interplate coupling at these depths. Combined petrological and lithostratigraphic data suggest that strain localization leading to the offscraping of the LPU and LPM units was mostly controlled by lithological contrasts across sedimentary packages, within the shales or along the contacts within the uppermost serpentinized mantle (some of which may have been inherited from former oceanic detachment faults), which acted as rheological weaknesses, possibly under high fluid pressure conditions. In contrast, major dehydration reactions (such as lawsonite breakdown in sediments and chlorite breakdown in mafics) likely controlled the offscraping of the LPL units at eclogite facies conditions, possibly through high fluid pressure conditions and rock embrittlement. In these units too, strain localization may have been guided by preexisting heterogeneities such as inherited oceanic detachment faults.

Supplementary data to this article can be found online at https://doi.org/10.1016/j.tecto.2022.229267.

Credit author statement

Conceptualization: *CH, PA*; Methodology and investigation: *CH, AP, DD, KM*; Writing – Original Draft and Visualization: *CH*; Review & Editing: *CH, PA, AP, KM, AV, DD, NC*.

Declaration of Competing Interest

The authors declare that they have no known competing financial interests or personal relationships that could have appeared to influence the work reported in this paper.

Acknowledgments

This study was funded by the BRGM in the frame of the RGF Alpes project. The authors thank S. Angiboust, O. Beyssac and T. Decrausaz for their help in locating samples of their articles. N. Rividi and M. Fialin are thanked for analytical support and E. Delairis for sample preparation. M. Ballèvre and an anonymous reviewer are thanked for their remarks and suggestions which have greatly helped to improve this work as Z.-X. Li for his editorial handling. We also thank G. Bonnet, B. Lefeuvre, S. Schwartz, L. Jolivet, H. Raimbourg, C. Chopin, B. Dubacq, T. Gyomlai and A. Lahfid for discussions.

References

Abers, G.A., van Keken, P.E., Kneller, E.A., Ferris, A., Stachnik, J.C., 2006. The thermal structure of subduction zones constrained by seismic imaging: Implications for slab dehydration and wedge flow. Earth Planet. Sci. Lett. 241, 387–397. https://doi.org/10.1016/j.epsl.2005.11.055.

Abers, G.A., Nakajima, J., van Keken, P.E., Kita, S., Hacker, B.R., 2013. Thermal–petrological controls on the location of earthquakes within subducting plates. Earth Planet. Sci. Lett. 369–370, 178–187. https://doi.org/10.1016/j.epsl.2013.03.022.

Agard, P., 1999. Evolution métamorphique et structurale des métapélites océaniques dans l'orogène Alpin : l'exemple des Schistes Lustrés des Alpes occidentales (Alpes Cottiennes). PhD thesis Université de Paris 6.

Agard, P., 2021. Subduction of oceanic lithosphere in the Alps: Selective and archetypal from (slow-spreading) oceans. Earth Sci. Rev. 214, 103517 https://doi.org/10.1016/j.earscirev.2021.103517.

Agard, P., Handy, M.R., 2021. Ocean Subduction Dynamics in the Alps. Elements 17, 9–16. https://doi.org/10.2138/gselements.17.1.9.

Agard, P., Vitale-Brovarone, A., 2013. Thermal regime of continental subduction: The record from exhumed HP–LT terranes (New Caledonia, Oman, Corsica). Tectonophysics 601, 206–215. https://doi.org/10.1016/j.tecto.2013.05.011.

Agard, P., Goffé, B., Touret, J.L.R., Vidal, O., 2000. Retrograde mineral and fluid evolution in high-pressure metapelites (Schistes lustrés unit, Western Alps). Contrib. Mineral. Petrol. 140, 296–315. https://doi.org/10.1007/s004100000190.

Agard, Philippe, Jolivet, L., Goffe, B., 2001a. Tectonometamorphic evolution of the Schistes Lustres Complex; implications for the exhumation of HP and UHP rocks in the Western Alps. Bulletin de la Société Géologique de France 172, 617–636. https://doi.org/10.2113/172.5.617.

Agard, P., Vidal, O., Goffé, B., 2001b. Interlayer and Si content of phengite in HP-LT carpholite-bearing metapelites. J. Metamorph. Geol. 19, 479–495. https://doi.org/10.1046/j.0263-4929.2001.00322.x.

Agard, P., Monie, P., Jolivet, L., Goffe, B., 2002. Exhumation of the Schistes Lustres complex: in situ laser probe 40Ar/39Ar constraints and implications for the Western Alps. J. Metamorph. Geol. 20, 599–618. https://doi.org/10.1046/j.1525-1314.2002.00391.x.

Agard, P., Yamato, P., Jolivet, L., Burov, E., 2009. Exhumation of oceanic blueschists and eclogites in subduction zones: Timing and mechanisms. Earth Sci. Rev. 92, 53–79. https://doi.org/10.1016/j.earscirev.2008.11.002.

Agard, P., Yamato, P., Soret, M., Prigent, C., Guillot, S., Plunder, A., Dubacq, B., Chauvet, A., Monié, P., 2016. Plate interface rheological switches during subduction infancy: Control on slab penetration and metamorphic sole formation. Earth Planet. Sci. Lett. 451, 208–220. https://doi.org/10.1016/j.epsl.2016.06.054.

Agard, P., Plunder, A., Angiboust, S., Bonnet, G., Ruh, J., 2018. The subduction plate interface: rock record and mechanical coupling (from long to short timescales). Lithos 320–321, 537–566. https://doi.org/10.1016/j.lithos.2018.09.029.

Agard, P., Prigent, C., Soret, M., Dubacq, B., Guillot, S., Deldicque, D., 2020. Slabitization: Mechanisms controlling subduction development and viscous coupling. Earth Sci. Rev. 208, 103259 https://doi.org/10.1016/j.earscirev.2020.103259.

Amato, J.M., Johnson, C.M., Baumgartner, L.P., Beard, B.L., 1999. Rapid exhumation of the Zermatt-Saas ophiolite deduced from high-precision SmNd and RbSr geochronology. Earth Planet. Sci. Lett. 171, 425–438. https://doi.org/10.1016/S0012-821X(99)00161-2.

Angiboust, S., Agard, P., 2010. Initial water budget: The key to detaching large volumes of eclogitized oceanic crust along the subduction channel?, 22.

Angiboust, S., Glodny, J., 2020. Exhumation of eclogitic ophiolitic nappes in the W. Alps: New age data and implications for crustal wedge dynamics. Lithos 356–357, 105374. https://doi.org/10.1016/j.lithos.2020.105374.

Angiboust, S., Agard, P., Jolivet, L., Beyssac, O., 2009. The Zermatt-Saas ophiolite: the largest (60-km wide) and deepest (c. 70-80 km) continuous slice of oceanic lithosphere detached from a subduction zone? Terra Nova 21, 171–180. https://doi.org/10.1111/j.1365-3121.2009.00870.x.

Angiboust, S., Agard, P., Raimbourg, H., Yamato, P., Huet, B., 2011. Subduction interface processes recorded by eclogite-facies shear zones (Monviso, W. Alps). Lithos 127, 222–238. https://doi.org/10.1016/j.lithos.2011.09.004.

Angiboust, S., Agard, P., Yamato, P., Raimbourg, H., 2012a. Eclogite breccias in a subducted ophiolite: A record of intermediate-depth earthquakes? Geology 40, 707–710. https://doi.org/10.1130/G32925.1.

Angiboust, S., Langdon, R., Agard, P., Waters, D., Chopin, C., 2012b. Eclogitization of the Monviso ophiolite (W. Alps) and implications on subduction dynamics. J. Metamorph. Geol. 30, 37–61. https://doi.org/10.1111/j.1525-1314.2011.00951.x.

Angiboust, S., Wolf, S., Burov, E., Agard, P., Yamato, P., 2012c. Effect of fluid circulation on subduction interface tectonic processes: Insights from thermo-mechanical numerical modelling. Earth Planet. Sci. Lett. 357–358, 238–248. https://doi.org/10.1016/j.epsl.2012.09.012.

Angiboust, S., Agard, P., De Hoog, J.C.M., Omrani, J., Plunder, A., 2013. Insights on deep, accretionary subduction processes from the Sistan ophiolitic "mélange" (Eastern Iran). Lithos 156–159, 139–158. https://doi.org/10.1016/j.lithos.2012.11.007.

Angiboust, S., Glodny, J., Oncken, O., Chopin, C., 2014. In search of transient subduction interfaces in the Dent Blanche–Sesia Tectonic System (W. Alps). Lithos 205, 298–321. https://doi.org/10.1016/j.lithos.2014.07.001.

Angiboust, S., Agard, P., Glodny, J., Omrani, J., Oncken, O., 2016. Zagros blueschists: Episodic underplating and long-lived cooling of a subduction zone. Earth Planet. Sci. Lett. 443, 48–58. https://doi.org/10.1016/j.epsl.2016.03.017.

Angiboust, S., Yamato, P., Hertgen, S., Hyppolito, T., Bebout, G.E., Morales, L., 2017. Fluid pathways and high- P metasomatism in a subducted continental slice (Mt. Emilius klippe, W. Alps). J. Metamorph. Geol. 35, 471–492. https://doi.org/10.1111/jmg.12241.

Angiboust, S., Cambeses, A., Hyppolito, T., Glodny, J., Monié, P., Calderón, M., Juliani, C., 2018. A 100-m.y.-long window onto mass-flow processes in the Patagonian Mesozoic subduction zone (Diego de Almagro Island, Chile). GSA Bull. 130, 1439–1456. https://doi.org/10.1130/B31891.1.

Audet, P., Bostock, M.G., Christensen, N.I., Peacock, S.M., 2009. Seismic evidence for overpressured subducted oceanic crust and megathrust fault sealing. Nature 457, 76–78.

Bachmann, R., Glodny, J., Oncken, O., Seifert, W., 2009. Abandonment of the South Penninic–Austroalpine palaeosubduction zone, Central Alps, and shift from

subduction erosion to accretion: constraints from Rb/Sr geochronology. J. Geol. Soc. 166, 217–231. https://doi.org/10.1144/0016-76492008-024.
Balestro, G., Festa, A., Borghi, A., Castelli, D., Gattiglio, M., Tartarotti, P., 2018. Role of Late Jurassic intra-oceanic structural inheritance in the Alpine tectonic evolution of the Monviso meta-ophiolite Complex (Western Alps). Geol. Mag. 155, 233–249. https://doi.org/10.1017/S0016756817000553.
Balestro, G., Festa, A., Dilek, Y., 2019. Structural architecture of the Western Alpine Ophiolites, and the Jurassic seafloor spreading tectonics of the Alpine Tethys. J. Geol. Soc. 176, 913–930. https://doi.org/10.1144/jgs2018-099.
Ballèvre, M., Lagabrielle, Y., 1994. Garnet in blueschist-facies marbles from the Queyras unit (Western Alps): its occurrence and its significance. Schweiz. Mineral. Petrogr. Mitt. 74, 203–212.
Ballèvre, M., Merle, O., 1993. The Combin Fault : compressional reactivation of a Late Cretaceous-Early Tertiary detachment fault in the Western Alps. Schweiz. Mineral. Petrogr. Mitt. 73, 205–227. https://doi.org/10.5169/SEALS-55570.
Ballèvre, M., Kienast, J.-R., Vuichard, J.-P., 1986. La "nappe de la Dent-Blanche" (Alpes occidentales) : deux unités austroalpines indépendantes. Eclogae Geol. Helv. 79, 57–74. https://doi.org/10.5169/SEALS-165826.
Ballèvre, M., Lagabrielle, Y., Merle, O., 1990. Tertiary ductile normal faulting as a consequence of lithospheric stacking in the western Alps. Mémoires de la Société géologique de France 156, 227–236.
Barféty, J.-C., Polino, R., Mercier, D., 2006. Notice explicative de la feuille Névache-Bardonecchia-Modane à 1/50000 (799) - Orléans : BRGM.
Bearth, P., 1959. Uber Eklogite, Glaukophanschiefer und metamorphe Pillowlaven. Schweiz. Mineral. Petrogr. Mitt. 39, 267–286.
Bearth, P., 1962. Versuch einer Gliederung alpinmetamorpher Serien der Westalpen. Schweiz. Mineral. Petrogr. Mitt. 42, 127–137.
Bearth, P., 1967. Die Ophiolite der Zone von Zermatt – Saas Fee. Beitr. Geol, Karte Schweiz, p. 132.
Bebout, G.E., Agard, P., Kobayashi, K., Moriguti, T., Nakamura, E., 2013. Devolatilization history and trace element mobility in deeply subducted sedimentary rocks: Evidence from Western Alps HP/UHP suites. Chem. Geol. 342, 1–20. https://doi.org/10.1016/j.chemgeo.2013.01.009.
Behr, W.M., Becker, T.W., 2018. Sediment control on subduction plate speeds. Earth Planet. Sci. Lett. 502, 166–173. https://doi.org/10.1016/j.epsl.2018.08.057.
Behr, W.M., Bürgmann, R., 2021. What's down there? The structures, materials and environment of deep-seated slow slip and tremor. Phil. Trans. R. Soc. A 379, 20200218. https://doi.org/10.1098/rsta.2020.0218.
Behr, W.M., Kotowski, A.J., Ashley, K.T., 2018. Dehydration-induced rheological heterogeneity and the deep tremor source in warm subduction zones. Geology 46, 475–478. https://doi.org/10.1130/G40105.1.
Bellahsen, N., Mouthereau, F., Boutoux, A., Bellanger, M., Lacombe, O., Jolivet, L., Rolland, Y., 2014. Collision kinematics in the western external Alps: Kinematics of the Alpine collision. Tectonics 33, 1055–1088. https://doi.org/10.1002/2013TC003453.
Berger, A., Bousquet, R., 2008. Subduction-related metamorphism in the Alps: review of isotopic ages based on petrology and their geodynamic consequences. Geol. Soc. Lond., Spec. Publ. 298, 117–144. https://doi.org/10.1144/SP298.7.
Beyssac, O., Goffé, B., Chopin, C., Rouzaud, J.N., 2002. Raman spectra of carbonaceous material in metasediments: a new geothermometer. J. Metamorph. Geol. 20, 859–871. https://doi.org/10.1046/j.1525-1314.2002.00408.x.
Beyssac, O., Goffé, B., Petitet, J.-P., Froigneux, E., Moreau, M., Rouzaud, J.-N., 2003. On the characterization of disordered and heterogeneous carbonaceous materials by Raman spectroscopy. Spectrochim. Acta A Mol. Biomol. Spectrosc. 59, 2267–2276. https://doi.org/10.1016/S1386-1425(03)00070-2.
Bocchio, R., Benciolini, L., Martin, S., Tartarotti, P., 2000. Geochemistry of eclogitised Fe-Ti-gabbros from various lithological settings (Aosta Valley ophiolites, Italian western Alps). Protolith composition and eclogitic paragenesis. Periodico di Mineralogia 69, 217–237.
Bocquet, J., 1974. Etudes minéralogiques et pétrologiques sur les métamorphismes d'âge alpin dans les alpes françaises. PhD thesis. Université de Grenoble.
Bodinier, J.-L., Menzies, M.A., Thirlwall, M.F., 1991. Continental to Oceanic Mantle Transition–REE and Sr-Nd Isotopic Geochemistry of the Lanzo Lherzolite Massif. J. Petrol. Special_Volume 191–210. https://doi.org/10.1093/petrology/Special_Volume.2.191.
Bonnet, G., Agard, P., Angiboust, S., Monié, P., Jentzer, M., Omrani, J., Whitechurch, H., Fournier, M., 2018. Tectonic slicing and mixing processes along the subduction interface: The Sistan example (Eastern Iran). Lithos 310–311, 269–287. https://doi.org/10.1016/j.lithos.2018.04.016.
Bonnet, G., Chopin, C., Locatelli, M., Kylander-Clark, A., R, C., Hacker, B.R., 2022. submitted Protracted subduction of the European hyperextended margin exposed in the Dora-Maira massif (W. Alps).
Bourbon, M., Caron, J.M., Lemoine, M., Tricart, P., 1979. Stratigraphie des schistes lustrés piémontais dans les Alpes cottiennes (Alpes occidentales franco-italiennes): nouvelle interprétation et conséquences géodynamiques. Bull. Soc. Geol. Fr. 180–2182.
Bousquet, R., 2008. Metamorphic heterogeneities within a single HP unit: Overprint effect or metamorphic mix? Lithos 103, 46–69. https://doi.org/10.1016/j.lithos.2007.09.010.
Bousquet, R., Oberhansli, R., Goffe, B., Jolivet, L., Vidal, O., 1998. High-pressure-low-temperature metamorphism and deformation in the Bundnerschiefer of the Engadine window: implications for the regional evolution of the eastern Central Alps. J. Metamorph. Geol. 16, 657–674. https://doi.org/10.1111/j.1525-1314.1998.00161.x.
Bousquet, R., Goffé, B., Vidal, O., Oberhänsli, R., Patriat, M., 2002. The tectono-metamorphic history of the Valaisan domain from the Western to the Central Alps: New constraints on the evolution of the Alps. Geol. Soc. Am. Bull. 114, 207–225. https://doi.org/10.1130/0016-7606(2002)114<0207:TTMHOT>2.0.CO;2.
Bousquet, R., Oberhänsli, R., Goffé, B., Wiederkehr, M., Koller, F., Schmid, S.M., Schuster, R., Engi, M., Berger, A., Martinotti, G., 2008. Metamorphism of metasediments at the scale of an orogen: a key to the Tertiary geodynamic evolution of the Alps. Geol. Soc. Lond., Spec. Publ. 298, 393–411. https://doi.org/10.1144/SP298.18.
Bowtell, S.A., Cliff, R.A., Barnicoat, A.C., 1994. Sm-Nd isotopic evidence on the age of eclogitization in the Zermatt-Saas ophiolite. J. Metamorph. Geol. 12, 187–196. https://doi.org/10.1111/j.1525-1314.1994.tb00013.x.
Broadwell, K.S., Locatelli, M., Verlaguet, A., Agard, P., Caddick, M.J., 2019. Transient and periodic brittle deformation of eclogites during intermediate-depth subduction. Earth Planet. Sci. Lett. 521, 91–102. https://doi.org/10.1016/j.epsl.2019.06.008.
Bucher, K., Grapes, R., 2009. The Eclogite-facies Allalin Gabbro of the Zermatt-Saas Ophiolite, Western Alps: a Record of Subduction Zone Hydration. J. Petrol. 50, 1405–1442. https://doi.org/10.1093/petrology/egp035.
Bucher, S., Schmid, S.M., Bousquet, R., Fugenschuh, B., 2003. Late-stage deformation in a collisional orogen (Western Alps): nappe refolding, back-thrusting or normal faulting? Terra Nova 15, 109–117. https://doi.org/10.1046/j.1365-3121.2003.00470.x.
Bucher, K., Fazis, Y., De Capitani, C., Grapes, R., 2005. Blueschists, eclogites, and decompression assemblages of the Zermatt-Saas ophiolite: High-pressure metamorphism of subducted Tethys lithosphere. Am. Mineral. 90, 821–835. https://doi.org/10.2138/am.2005.1718.
Busigny, V., Cartigny, P., Philippot, P., 2011. Nitrogen isotopes in ophiolitic metagabbros: A re-evaluation of modern nitrogen fluxes in subduction zones and implication for the early Earth atmosphere. Geochim. Cosmochim. Acta 75, 7502–7521. https://doi.org/10.1016/j.gca.2011.09.049.
Busigny, V., Chen, J., Philippot, P., Borensztajn, S., Moynier, F., 2018. Insight into hydrothermal and subduction processes from copper and nitrogen isotopes in oceanic metagabbros. Earth Planet. Sci. Lett. 498, 54–64. https://doi.org/10.1016/j.epsl.2018.06.030.
Caby, R., 1996. Low-angel extrusion of high-pressure rocks and the balance between outward and inward displacements of Middle Penninic units in the western Alps. Eclogae Geol. Helv. 89 (1), 229–267. https://doi.org/10.5169/SEALS-167901.
Caby, R., Kienast, J.R., Saliot, P., 1976. Modèle d'évolution structurale des Alpes occidentales. Colloque International CNRS, Ecologie et Géologie de l'Himalaya 85–92.
Caby, R., Kienast, J.-R., Saliot, P., 1978. Structure, métamorphisme et modèle d'évolution tectonique des Alpes occidentales. Revue de géographie physique et de géologie dynamique Paris 20, 307–322.
Cadoppi, P., Castelletto, M., Sacchi, R., Baggio, P., Carraro, F., Giraud, V., 2002. Note illustrative della carta geologica d'Italia alla scala 1:50000: foglio 154 Susa. ISPRA, Servizio Geologico d'Italia.
Caron, J.-M., 1974. Rapports entre diverses" generations" de lawsonite et les deformations dans les Schistes lustres des Alpes cottiennes septentrionales (France et Italie). Bulletin de la Société Géologique de France 7, 256–263.
Caron, J.M., 1977. Lithostratigraphie et tectonique des Schistes Lustrés dans les Alpes Cottiennes septentrionales et en Corse orientale. PhD thesis, université de Strasbourg.
Chopin, C., 1978. Les paragenèses réduites ou oxydées de concentrations manganésifères des «schistes lustrés» de Haute-Maurienne (Alpes françaises). Bull. Mineral. 101, 514–531.
Chopin, C., 1979. De la Vanoise au massif du Grand Paradis, Une approche pétrographique et radiochronologique de la signification géodynamique du métamorphisme de haute pression. PhD thesis. Université Pierre et Marie Curie, Paris 6.
Chopin, C., 1984. Coesite and pure pyrope in high-grade blueschists of the Western Alps: a first record and some consequences. Contrib. Mineral. Petrol. 86, 107–118. https://doi.org/10.1007/BF00381838.
Chopin, C., Maluski, H., 1980. 40Ar-39Ar dating of high pressure metamorphic micas from the Gran Paradiso area (Western Alps): Evidence against the blocking temperature concept. Contrib. Mineral. Petrol. 74, 109–122.
Compagnoni, R., Rolfo, F., 2003. UHPM units in the Western Alps. In: Papp, G., Weiszburg, T.G., Carswell, D.A., Compagnoni, R., Rolfo, F. (Eds.), Ultrahigh Pressure Metamorphism. Mineralogical Society of Great Britain and Ireland, Budapest, pp. 13–49. https://doi.org/10.1180/EMU-notes.5.2.
Connolly, J.A.D., 1990. Multivariable phase diagrams: an algorithm based on generalized thermodynamics. Am. J. Sci. 290, 666–718.
Connolly, J.A.D., 2005. Computation of phase equilibria by linear programming: A tool for geodynamic modeling and its application to subduction zone decarbonation. Earth Planet. Sci. Lett. 236, 524–541. https://doi.org/10.1016/j.epsl.2005.04.033.
Connolly, J.A.D., 2009. The geodynamic equation of state: What and how. Geochem. Geophys. Geosyst. 10, n/a-n/a. https://doi.org/10.1029/2009GC002540.
Corno, A., Mosca, P., Borghi, A., Gatteggio, M., 2019. Lithostratigraphy and petrography of the Monte Banchetta-Punta Rognosa oceanic succession (Troncea and Chisonetto Valleys, Western Alps). Ofioliti 44. https://doi.org/10.4454/ofioliti.v44i2.526.
Corno, A., Groppo, C., Mosca, P., Borghi, A., Gattiglio, M., 2021. Eclogitic metamorphism in the Alpine far-west: petrological constraints on the Banchetta-Rognosa tectonic unit (Val Troncea, Western Alps). Swiss J. Geosci. 114, 16. https://doi.org/10.1186/s00015-021-00393-7.
Cubas, N., Agard, P., Tissandier, R., 2022. submitted Predicting earthquake ruptures from topography.
Dal Piaz, G.V., 1974a. Le métamorphisme de haute pression et basse température dans l'évolution structurale du bassin ophiolitique alpino-apenninique. 1ère partie : Considérations paléogéographiques. Boll. Soc. Geol. Ital. 93, 437–467.

Dal Piaz, G.V., 1974b. Le métamorphisme de haute pression et basse température dans l'évolution structurale du bassin ophiolitique alpino-apenninique. Schweiz. Mineral. Petrogr. Mitt. 54, 399–424.
Dal Piaz, G.V., Cortiana, G., Del Moro, A., Martin, S., Pennachioni, G., Tartarotti, P., 2001. Tertiary age and paleostructural inferences of the eclogitic imprint in the Austroalpine outliers and Zermatt-Saas ophiolite, western Alps. Int. J. Earth Sci. (Geol Rundsch) 90, 668–684.
Dal Piaz, G.V., Gianotti, F., Monopoli, B., Pennachioni, G., Tartarotti, P., Schiavo, A., 2010. Note illustrative della carta geologica d'Italia alla scala 1:50000: foglio 091 Chatillon. ISPRA, Servizio Geologico d'Italia.
de Meyer, C.M.C., Baumgartner, L.P., Beard, B.L., Johnson, C.M., 2014. Rb–Sr ages from phengite inclusions in garnets from high pressure rocks of the Swiss Western Alps. Earth Planet. Sci. Lett. 395, 205–216. https://doi.org/10.1016/j.epsl.2014.03.050.
De Togni, M., Gattiglio, M., Ghignone, S., Festa, A., 2021. Pre-Alpine Tectono-Stratigraphic Reconstruction of the Jurassic Tethys in the High-Pressure Internal Piedmont Zone (Stura di Viù Valley, Western Alps). Minerals 11, 361. https://doi.org/10.3390/min11040361.
De Wever, P., Caby, R., 1981. Datation de la base des schistes lustrés postophiolitiques par des radiolaires (Oxfordien-Kimmeridgien moyen) dans les Alpes Cottiennes (Saint Véran, France). Comptes Rendus de l'Académie des Sciences de Paris 292, 467–472.
De Wever, P., Baumgartner, P.O., Polino, R., 1987a. Précision sur les datations de la base des Schistes Lustrés postophiolitiques dans les Alpes cottiennes. Comptes Rendus de l'Académie des Sciences de Paris 305, 487–491.
De Wever, P., Danelian, T., Durand-Delga, M., Cordey, M., Kito, N., 1987b. Datations des radiolarites post-ophiolitiques de Corse alpine à l'aide des Radiolaires. Comptes Rendus de l'Académie des Sciences de Paris 305, 893–900.
Debelmas, J., Caby, R., Desmons, J., 1991. Notice explicative de la feuille Sainte-Foy-Tarentaise à 1/50000 (728) - Orléans : BRGM.
Debret, B., Nicollet, C., Andreani, M., Schwartz, S., Godard, M., 2013. Three steps of serpentinization in an eclogitized oceanic serpentinization front (Lanzo Massif - Western Alps). J. Metamorph. Geol. 31, 165–186. https://doi.org/10.1111/jmg.12008.
Decandia, F.A., Elter, P., 1969. Riflessioni sul problema delle ofioliti nell'Appennino settentrionale (Nota preliminare). Atti Societa Toscana delle Science Naturali : memorie Serie A 76, 1–9.
Decandia, F.A., Elter, P., 1972. La" zona" ofiolitifera del Bracco nel settore compreso fra Levanto e la Val Gravena (Apennino ligure). Boll. Soc. Geol. Ital. 11, 37–64.
Decrausaz, T., Müntener, O., Manzotti, P., Lafay, R., Spandler, C., 2021. Fossil oceanic core complexes in the Alps. New field, geochemical and isotopic constraints from the Tethyan Aiguilles Rouges Ophiolite (Val d'Hérens, Western Alps, Switzerland). Swiss J. Geosci. 114, 3. https://doi.org/10.1186/s00015-020-00380-4.
Delaloye, M., Desmons, J., 1976. K-Ar Radiometric Age Determinations of White Micas from the Piemont Zone, French-Italian Western Alps. Contrib. Mineral. Petrol. 57, 297–303. https://doi.org/10.1007/BF03542939.
Deville, E., 1986. La klippe de la Pointe du Grand Vallon (Vanoise-Alpes occidentales) : un lambeau de métasédiments à foraminifères du Maastrichtien supérieur couronnant les nappes de « schistes lustrés ». Comptes rendus de l'Académie des sciences. Série 2. Mécanique, Physique, Chimie, Sciences de l'univers, Sciences de la Terre 303, 1221–1226.
Deville, E., 1987. Etude géologique en Vanoise orientale (Alpes occidentales, Savoie). De la naissance à la structuration d'un secteur de la paléo-marge européenne et de l'océan téthysien : aspects stratigraphiques, pétrographiques et tectoniques. PhD thesis. Université de Savoie.
Deville, E., Fudral, S., Lagabrielle, Y., Marthaler, M., Sartori, M., 1992. From oceanic closure to continental collision: A synthesis of the" Schistes lustrés" metamorphic complex of the Western Alps. Geol. Soc. Am. Bull. 104, 127–139.
Dragovic, B., Angiboust, S., Tappa, M.J., 2020. Petrochronological close-up on the thermal structure of a paleo-subduction zone (W. Alps). Earth Planet. Sci. Lett. 547, 116446 https://doi.org/10.1016/j.epsl.2020.116446.
Droop, G.T.R., Lombardo, B., Pognante, U., 1990. Formation and distribution of eclogite facies rocks in the Alps. In: Carswell, D.A. (Ed.), Eclogite Facies Rocks: Glasgow. Blackie, United Kingdom, pp. 225–259.
Duchêne, S., Blichert-Toft, J., Luais, B., Télouk, P., Lardeaux, J.-M., Albarède, F., 1997. The Lu–Hf dating of garnets and the ages of the Alpine high-pressure metamorphism. Nature 387, 586–589. https://doi.org/10.1038/42446.
Duesterhoeft, E., Quinteros, J., Oberhänsli, R., Bousquet, R., de Capitani, C., 2014. Relative impact of mantle densification and eclogitization of slabs on subduction dynamics: A numerical thermodynamic/thermokinematic investigation of metamorphic density evolution. Tectonophysics 637, 20–29. https://doi.org/10.1016/j.tecto.2014.09.009.
Dumitru, T.A., Wakabayashi, J., Wright, J.E., Wooden, J.L., 2010. Early Cretaceous transition from nonaccretionary behavior to strongly accretionary behavior within the Franciscan subduction complex: ACCRETION IN THE FRANCISCAN COMPLEX. Tectonics 29. https://doi.org/10.1029/2009TC002542.
Dumont, T., Lemoine, M., Tricart, P., 1984. Pérennité de la sédimentation pélagique du Jurassique supérieur jusque dans le crétacé supérieur au-dessus de la croûte océanique téthysienne ligure : la série supra-ophiolitique du lac des Cordes (zone piémontaise des Alpes occidentales au SE de Briançon). Comptes rendus de l'Académie des sciences. Série 2. Mécanique, Physique, Chimie, Sciences de l'univers, Sciences de la Terre 7, 921–933.
Ellero, A., Loprieno, A., 2018. Nappe stack of Piemonte–Ligurian units south of A osta V alley: New evidence from Urtier Valley (Western Alps). Geol. J. 53, 1665–1684. https://doi.org/10.1002/gj.2984.
Elter, G., 1971. Schistes lustrés et ophiolites de la zone piémontaise entre Orco et Doire Baltée (Alpes Graies). Hypothèses sur l'origine des ophiolites. Géologie Alpine 47, 147–169.
Frezzotti, M.L., Selverstone, J., Sharp, Z.D., Compagnoni, R., 2011. Carbonate dissolution during subduction revealed by diamond-bearing rocks from the Alps. Nat. Geosci. 4, 703–706. https://doi.org/10.1038/ngeo1246.
Fudral, S., 1996. Etude géologique de la suture tethysienne dans les Alpes franco-italiennes Nord-Occidentales de la Doire Ripaire (Italie) à la région de Bourg Saint-Maurice. PhD thesis. Université de Savoie.
Fudral, S., Deville, E., Marthaler, M., 1987. Distinction de trois ensembles d'unités dans les «Schistes lustrés» compris entre la Vanoise et le Val de Suse (Alpes franco-italiennes septentrionales): aspects lithostratigraphiques, paléogéographiques et géodynamiques. Comptes rendus de l'Académie des sciences. Série 2. Mécanique, Physique, Chimie, Sciences de l'univers, Sciences de la Terre 305, 467–472.
Gabalda, S., Beyssac, O., Jolivet, L., Agard, P., Chopin, C., 2009. Thermal structure of a fossil subduction wedge in the Western Alps. Terra Nova 21, 28–34. https://doi.org/10.1111/j.1365-3121.2008.00849.x.
Garber, J.M., Smye, A.J., Feineman, M.D., Kylander-Clark, A.R.C., Matthews, S., 2020a. Decoupling of zircon U–Pb and trace-element systematics driven by U diffusion in eclogite-facies zircon (Monviso meta-ophiolite, W. Alps). Contrib. Mineral. Petrol. 175, 55. https://doi.org/10.1007/s00410-020-01692-2.
Garber, J.M., Rioux, M., Kylander-Clark, A.R.C., Hacker, B.R., Vervoort, J.D., Searle, M. P., 2020b. Petrochronology of Wadi Tayin Metamorphic Sole Metasediment, With Implications for the Thermal and Tectonic Evolution of the Samail Ophiolite (Oman/UAE). Tectonics 39. https://doi.org/10.1029/2020TC006135.
Ghignone, S., Borghi, A., Balestro, G., Castelli, D., Gattiglio, M., Groppo, C., 2021a. HP tectono-metamorphic evolution of the Internal Piedmont Zone in Susa Valley (Western Alps): New petrologic insight from garnet+chloritoid-bearing micaschists and Fe–Ti metagabbro. J. Metamorph. Geol. 39, 391–416.
Ghignone, S., Sudo, M., Balestro, G., Borghi, A., Gattiglio, M., Ferrero, S., van Schijndel, V., 2021b. Timing of exhumation of meta-ophiolite units in the Western Alps: New tectonic implications from 40Ar/39Ar white mica ages from Piedmont Zone (Susa Valley). Lithos 404–405, 106443. https://doi.org/10.1016/j.lithos.2021.106443.
Goffé, B., Bousquet, R., 1997. Ferrocarpholite, chloritoid and lawsonite in metapelites of the Versoyen and Petit St Bernard units (Valais zone, Western Alps). Schweiz. Mineral. Petrogr. Mitt. 77, 137–147.
Goffé, B., Chopin, C., 1986. High-pressure metamorphism in the Western Alps : zoneography of metapelites, chronology and consequences. Schweiz. Mineral. Petrogr. Mitt. 66, 41–52. https://doi.org/10.5169/SEALS-50880.
Goffé, B., Schwartz, S., Lardeaux, J.-M., Bousquet, R., 2004. Explanatory notes of the map: metamorphic structure of the Alps Western and Ligurian Alps. MITT.ÖSTERR. MINER.GES. 125–144.
Gouzu, C., Itaya, T., Hyodo, H., Matsuda, T., 2006. Excess 40Ar-free phengite in ultrahigh-pressure metamorphic rocks from the Lago di Cignana area, Western Alps. Lithos 92, 418–430. https://doi.org/10.1016/j.lithos.2006.03.056.
Gouzu, C., Yagi, K., Thanh, N.X., Itaya, T., Compagnoni, R., 2016. White mica K–Ar geochronology of HP–UHP units in the Lago di Cignana area, western Alps, Italy: Tectonic implications for exhumation. Lithos 248–251, 109–118. https://doi.org/10.1016/j.lithos.2016.01.015.
Groppo, C., Castelli, D., 2010. Prograde P–T Evolution of a Lawsonite Eclogite from the Monviso Meta-ophiolite (Western Alps): Dehydration and Redox Reactions during Subduction of Oceanic FeTi-oxide Gabbro. J. Petrol. 51, 2489–2514. https://doi.org/10.1093/petrology/egq065.
Groppo, C., Beltrando, M., Compagnoni, R., 2009. The P-T path of the ultra-high pressure Lago Di Cignana and adjoining high-pressure meta-ophiolitic units: insights into the evolution of the subducting Tethyan slab. J. Metamorph. Geol. 27, 207–231. https://doi.org/10.1111/j.1525-1314.2009.00814.
Guillot, S., Hattori, K., Agard, P., Schwartz, S., Vidal, O., 2009. Exhumation Processes in Oceanic and Continental Subduction Contexts: A Review. In: Lallemand, S., Funiciello, F. (Eds.), Subduction Zone Geodynamics, Frontiers in Earth Sciences. Springer, Berlin Heidelberg, Berlin, Heidelberg, pp. 175–205. https://doi.org/10.1007/978-3-540-87974-9_10.
Guillot, S., Schwartz, S., Reynard, B., Agard, P., Prigent, C., 2015. Tectonic significance of serpentinites. Tectonophysics 646, 1–19. https://doi.org/10.1016/j.tecto.2015.01.020.
Hacker, B.R., Peacock, S.M., Abers, G.A., Holloway, S.D., 2003. Subduction factory 2. Are intermediate-depth earthquakes in subducting slabs linked to metamorphic dehydration reactions?: SUBDUCTION ZONE EARTHQUAKES AND DEHYDRATION. J. Geophys. Res. 108 https://doi.org/10.1029/2001JB001129.
Handy, M.R., 2010. Reconciling plate-tectonic reconstructions of Alpine Tethys with the geological–geophysical record of spreading and subduction in the Alps, p. 38.
Henry, C., Burkhard, M., Goffé, B., 1996. Evolution of synmetamorphic veins and their wallrocks through a Western Alps transect: no evidence for large-scale fluid flow. Stable isotope, major- and trace-element systematics. Chem. Geol. 127, 81–109. https://doi.org/10.1016/0009-2541(95)00106-9.
Hertgen, S., Yamato, P., Morales, L.F.G., Angiboust, S., 2017. Evidence for brittle deformation events at eclogite-facies P-T conditions (example of the Mt. Emilius klippe, Western Alps). Tectonophysics 706–707, 1–13. https://doi.org/10.1016/j.tecto.2017.03.028.
Herviou, C., Verlaguet, A., Agard, P., Locatelli, M., Raimbourg, H., Lefeuvre, B., Dubacq, B., 2021. Along-dip variations of subduction fluids: The 30–80 km depth traverse of the Schistes Lustrés complex (Queyras-Monviso, W. Alps). Lithos 394–395, 106168. https://doi.org/10.1016/j.lithos.2021.106168.
Holland, T.J.B., Powell, R., 1998. An internally consistent thermodynamic data set for phases of petrological interest: AN INTERNALLY CONSISTENT THERMODYNAMIC

DATA SET. J. Metamorph. Geol. 16, 309–343. https://doi.org/10.1111/j.1525-1314.1998.00140.x.
Holland, T., Baker, J., Powell, R., 1998. Mixing properties and activity-composition relationships of chlorites in the system MgO-FeO-Al2O3-SiO2-H2O. ejm, 10, pp. 395–406. https://doi.org/10.1127/ejm/10/3/0395.
Ikari, M.J., Kopf, A.J., Hüpers, A., Vogt, C., 2018. Lithologic control of frictional strength variations in subduction zone sediment inputs. Geosphere 14, 604–625. https://doi.org/10.1130/GES01546.1.
Incel, S., Hilairet, N., Labrousse, L., John, T., Deldicque, D., Ferrand, T., Wang, Y., Renner, J., Morales, L., Schubnel, A., 2017. Laboratory earthquakes triggered during eclogitization of lawsonite-bearing blueschist. Earth Planet. Sci. Lett. 459, 320–331. https://doi.org/10.1016/j.epsl.2016.11.047.
Jolivet, L., Goffé, B., Monié, P., Truffert-Luxey, C., Patriat, M., Bonneau, M., 1996. Miocene detachment in Crete and exhumation P-T-t paths of high-pressure metamorphic rocks. Tectonics 15, 1129–1153. https://doi.org/10.1029/96TC01417.
Jolivet, L., Faccenna, C., Goffé, B., Mattei, M., Rossetti, F., Brunet, C., Storti, F., Funiciello, R., Cadet, J.P., d'Agostino, N., Parra, T., 1998. Midcrustal shear zones in postorogenic extension: Example from the northern Tyrrhenian Sea. J. Geophys. Res. 103, 12123–12160. https://doi.org/10.1029/97JB03616.
Kameda, J., Inoue, S., Tanikawa, W., Yamaguchi, A., Hamada, Y., Hashimoto, Y., Kimura, G., 2017. Alteration and dehydration of subducting oceanic crust within subduction zones: implications for décollement step-down and plate-boundary seismogenesis. Earth Planets Space 69, 52. https://doi.org/10.1186/s40623-017-0635-1.
Karig, D.E., Sharman, G.F., 1975. Subduction and Accretion in Trenches. Geol. Soc. Am. Bull. 86, 377–389. https://doi.org/10.1130/0016-7606(1975)86<377:SAAIT>2.0.CO;2.
Kerswell, B.C., Kohn, M.J., Gerya, T.V., 2021. Backarc Lithospheric Thickness and Serpentine Stability Control Slab-Mantle Coupling Depths in Subduction Zones. Geochem. Geophys. Geosyst. 22 https://doi.org/10.1029/2020GC009304.
Kienast, J.R., 1973. Sur l'existence de deux séries différentes au sein de l'ensemble schistes lustrés-ophiolites du val d'Aoste ; quelques arguments fondés sur l'étude des roches métamorphiques. Comptes Rendus de l'Académie des Sciences de Paris 276, 2621–2624.
Kimura, G., Ludden, J., 1995. Peeling oceanic crust in subduction zones. Geol 23, 217–220. https://doi.org/10.1130/0091-7613(1995)023<0217:POCISZ>2.3.CO;2.
Kimura, G., Maruyama, S., Isozaki, Y., Terabayashi, M., 1996. Well-preserved underplating structure of the jadeitized Franciscan complex, Pacheco Pass. Calif. Geol. 24, 75. https://doi.org/10.1130/0091-7613(1996)024<0075:WPUSOT>2.3.CO;2.
Kimura, G., Kitamura, Y., Hashimoto, Y., Yamaguchi, A., Shibata, T., Ujiie, K., Okamoto, S., 2007. Transition of accretionary wedge structures around the up-dip limit of the seismogenic subduction zone. Earth Planet. Sci. Lett. 255, 471–484. https://doi.org/10.1016/j.epsl.2007.01.005.
Kita, S., Okada, T., Nakajima, J., Matsuzawa, T., Hasegawa, A., 2006. Existence of a seismic belt in the upper plane of the double seismic zone extending in the along-arc direction at depths of 70–100 km beneath NE Japan. Geophys. Res. Lett. 33, L24310. https://doi.org/10.1029/2006GL028239.
Kunz, P., 1988. Ophiolites penniques et sédiments associés dans la région d'Arolla (val d'Hérens, Valais, Suisse). Eclogae Geol. Helv. 81, 115–124. https://doi.org/10.5169/SEALS-166172.
Lagabrielle, Y., 1987. Les ophiolites : Marqueurs de l'histoire tectonique des domaines océaniques. PhD thesis Brest.
Lagabrielle, Y., Cannat, M., 1990. Alpine Jurassic ophiolites resemble the modern central Atlantic basement. Geology 18, 319–322.
Lagabrielle, Y., Polino, R., 1988. Un schéma structural du domaine des Schistes lustrés ophiolitifères au nord-ouest du massif du Mont Viso (Alpes Sud-Occidentales) et ses implications. Comptes rendus de l'Académie des sciences. Série 2. Mécanique, Physique, Chimie, Sciences de l'univers, Sciences de la Terre 306, 921–928.
Lagabrielle, Y., Fudral, S., Kienast, J.-R., 1990. La couverture océanique des ultrabasites de Lanzo (Alpes occidentales) : arguments lithostratigraphiques et pétrologiques. Geodin. Acta 4, 43–55. https://doi.org/10.1080/09853111.1990.11105199.
Lagabrielle, Y., Vitale Brovarone, A., Ildefonse, B., 2015. Fossil oceanic core complexes recognized in the blueschist metaophiolites of Western Alps and Corsica. Earth Sci. Rev. 141, 1–26. https://doi.org/10.1016/j.earscirev.2014.11.004.
Lahfid, A., Beyssac, O., Deville, E., Negro, F., Chopin, C., Goffé, B., 2010. Evolution of the Raman spectrum of carbonaceous material in low-grade metasediments of the Glarus Alps (Switzerland): RSCM in low-grade metasediments. Terra Nova 22, 354–360. https://doi.org/10.1111/j.1365-3121.2010.00956.x.
Lanari, P., 2012. Micro-cartographie P-T-ε dans les roches métamorphiques. Applications aux Alpes et à l'Himalaya. PhD thesis. Université de Grenoble.
Lapen, T.J., Johnson, C.M., Baumgartner, L.P., Mahlen, N.J., Beard, B.L., Amato, J.M., 2003. Burial rates during prograde metamorphism of an ultra-high-pressure terrane: an example from Lago di Cignana, western Alps, Italy. Earth Planet. Sci. Lett. 215, 57–72. https://doi.org/10.1016/S0012-821X(03)00455-2.
Lay, T., Kanamori, H., Ammon, C.J., Koper, K.D., Hutko, A.R., Ye, L., Yue, H., Rushing, T. M., 2012. Depth-varying rupture properties of subduction zone megathrust faults: MEGATHRUST RUPTURE DOMAINS. J. Geophys. Res. 117, n/a-n/a. https://doi.org/10.1029/2011JB009133.
Le Pichon, X., Bergerat, F., Roulet, M., 1988. Plate kinematics and tectonics leading to the Alpine belt formation: a new analysis. Geol. Soc. Am. Special Issue 218, 111–131.
Lefeuvre, B., Agard, P., Verlaguet, A., Dubacq, B., Plunder, A., 2020. Massive formation of lawsonite in subducted sediments from the Schistes Lustrés (W. Alps): Implications for mass transfer and decarbonation in cold subduction zones. Lithos 370–371, 105629. https://doi.org/10.1016/j.lithos.2020.105629.
Lemoine, M., 1959. Remarques a propos de quelques faits et hypotheses concernant l'age des Schistes lustres piemontais dans les Alpes cottiennes et brianconnaises. Bulletin de la Société Géologique de France 7, 90–92.
Lemoine, M., 1971. Données nouvelles sur la série du Gondran près Briançon (Alpes Cottiennes). Réflexions sur les problèmes stratigraphique et paléographique de la zone piémontaise. Géologie Alpine 47, 181–201.
Lemoine, M., 2003. Schistes lustrés from Corsica to Hungary : back to the original sediments and tentative dating of partly azoic metasediments. Bulletin de la Société Géologique de France 174, 197–209. https://doi.org/10.2113/174.3.197.
Lemoine, M., Tricart, P., 1986. Les Schistes lustrés piémontais des Alpes Occidentales : approche stratigraphique, structurales et sédimentologique. Eclogae Geol. Helv. 79, 271–294. https://doi.org/10.5169/SEALS-165835.
Lemoine, M., Steen, D.M., Vuagnat, M., 1970. Sur le problème stratigraphique des ophiolites piémontaises et des roches sédimentaires associées: observations dans le massif de Chabrière en Haute-Ubaye (Basses-Alpes, France). Compte rendu des séances de la Société de physique et d'histoire naturelle de Genève 5, 44–59.
Lemoine, M., Marthaler, M., Caron, M., Sartori, M., Amaudric du Chaffaut, S., 1984. Découverte de foraminifères planctoniques du Crétacé supérieur dans les schistes lustrés du Queyras (Alpes occidentales). Conséquences paléogéographiques et tectoniques. Comptes-rendus des séances de l'Académie des sciences. Série 2. Mécanique-physique, chimie, sciences de l'univers, sciences de la terre 299, 727–732.
Lemoine, M., Bas, T., Arnaud-Vanneau, A., Arnaud, H., Dumont, T., Gidon, M., Bourbon, M., de Graciansky, P.-C., Rudkiewicz, J.-L., Megard-Galli, J., Tricart, P., 1986. The continental margin of the Mesozoic Tethys in the Western Alps. Mar. Pet. Geol. 3, 179–199.
Liewig, N., 1981. Les phengites : marqueurs géométriques, chimiques et isotopiques de l'histoire des roches métamorphiques : application aux schistes lustres des Alpes cottiennes. PhD thesis, université de Strasbourg.
Locatelli, M., Verlaguet, A., Agard, P., Federico, L., Angiboust, S., 2018. Intermediate-depth brecciation along the subduction plate interface (Monviso eclogite, W. Alps). Lithos 320–321, 378–402. https://doi.org/10.1016/j.lithos.2018.09.028.
Locatelli, M., Federico, L., Agard, P., Verlaguet, A., 2019a. Geology of the southern Monviso metaophiolite complex (W-Alps, Italy). Journal of Maps 15, 283–297. https://doi.org/10.1080/17445647.2019.1592030.
Locatelli, M., Verlaguet, A., Agard, P., Pettke, T., Federico, L., 2019b. Fluid Pulses During Stepwise Brecciation at Intermediate Subduction Depths (Monviso Eclogites, W. Alps): First Internally Then Externally Sourced. Geochem. Geophys. Geosyst. 20, 5285–5318. https://doi.org/10.1029/2019GC008549.
Lombardo, B., Nervo, R., Compagnoni, R., Messiga, B., Kienast, J.R., Mevel, C., Fiora, L., Piccardo, G.B., Lanza, R., 1978. Osservazioni preliminari sulle ofioliti metamorfiche del Monviso (Alpi Occidentali). Rendiconti Della Soc. Ital. Mineral. E Petrol. 34, 235–305.
Malusà, M.G., Polino, R., Zattin, M., Bigazzi, G., Martin, S., Piana, F., 2005. Miocene to Present differential exhumation in the Western Alps: Insights from fission track thermochronology: EXHUMATION IN THE WESTERN ALPS. Tectonics 24, n/a-n/a. https://doi.org/10.1029/2004TC001782.
Manatschal, G., Sauter, D., Karpoff, A.M., Masini, E., Mohn, G., Lagabrielle, Y., 2011. The Chenaillet Ophiolite in the French/Italian Alps: An ancient analogue for an Oceanic Core Complex? Lithos 124, 169–184. https://doi.org/10.1016/j.lithos.2010.10.017.
Manzotti, P., Ballèvre, M., Pitra, P., Schiavi, F., 2021. Missing lawsonite and aragonite found: P–T and fluid composition in meta-marls from the Combin Zone (Western Alps). Contrib. Mineral. Petrol. 176, 60. https://doi.org/10.1007/s00410-021-01818-0.
Marthaler, M., 1984. Géologie des unités penniques entre le val d'Anniviers et le val de Tourtemagne (Valais, Suisse). Eclogae Geol. Helv. 77, 395–448. https://doi.org/10.5169/SEALS-165516.
Marthaler, M., Stampfli, G.M., 1989. Les Schistes lustrés à ophiolites de la nappe du Tsaté : un ancien prisme d'accrétion de la marge active apulienne? Schweiz. Mineral. Petrogr. Mitt. 69, 211–216. https://doi.org/10.5169/SEALS-52789.
Martin, S., Rebay, G., Kienast, J.-R., Mével, C., 2008. AN ECLOGITISED OCEANIC PALAEO-HYDROTHERMAL FIELD FROM THE ST. MARCEL VALLEY (ITALIAN WESTERN ALPS) 33, 16.
Massonne, H.J., 1992. Thermochemical determination of water activities relevant to eclogitic rocks. In: Kharaka, Y.K., Maest, A.S. (Eds.), Water-Rock Interaction. Balkema, Rotterdam, pp. 1523–1526.
Massonne, H.J., 1995. Experimental and petrogenetic study of UHPM. In: Coleman, R.G., Wang, X. (Eds.), 1995. Ultrahigh pressure metamorphism, Cambridge University Press, Cambridge, pp. 33–95.
Massonne, H.-J., Schreyer, W., 1987. Phengite geobarometry based on the limiting assemblage with K-feldspar, phlogopite, and quartz. Contrib. Mineral. Petrol. 96, 212–224. https://doi.org/10.1007/BF00375235.
Massonne, H.J., Schreyer, W., 1989. Stability field of the high-pressure assemblage, talc+phengite and two new phengite barometers. Eur. J. Mineral. 1, 391–410.
Menant, A., Angiboust, S., Gerya, T., 2019. Stress-driven fluid flow controls long-term megathrust strength and deep accretionary dynamics. Sci. Rep. 9, 9714. https://doi.org/10.1038/s41598-019-46191-y.
Menant, A., Angiboust, S., Gerya, T., Lacassin, R., Simoes, M., Grandin, R., 2020. Transient stripping of subducting slabs controls periodic forearc uplift. Nat. Commun. 11, 1823. https://doi.org/10.1038/s41467-020-15580-7.
Michard, A., Goffé, B., Chopin, C., Henry, C., 1996. Did the Western Alps develop through an Oman-type stage? The geotectonic setting of high-pressure metamorphism in two contrasting Tethyan transects. Eclogae Geol. Helv. 89, 43–80.
Michard, A., Avigad, D., Goffé, B., Chopin, C., 2004. The high-pressure metamorphic front of the south Western Alps (Ubaye-Maira transect, France, Italy). Schweiz. Mineral. Petrogr. Mitt. 84, 215–235.

Monié, P., Agard, P., 2009. Coeval blueschist exhumation along thousands of kilometers: Implications for subduction channel processes. Geochem. Geophys. Geosyst. 10, n/a-n/a. https://doi.org/10.1029/2009GC002428.
Moore, J.C., 1975. Selective subduction. Geol 3, 530. https://doi.org/10.1130/0091-7613(1975)3<530:SS>2.0.CO;2.
Müntener, O., Piccardo, G.B., Polino, R., Zanetti, A., 2005. REVISITING THE LANZO PERIDOTITE (NW-ITALY): 'ASTHENOSPHERIZATION' OF ANCIENT MANTLE LITHOSPHERE. Ofioliti 30, 111–124.
Negro, F., Bousquet, R., Vils, F., Pellet, C.-M., Hänggi-Schaub, J., 2013. Thermal structure and metamorphic evolution of the Piemont-Ligurian metasediments in the northern Western Alps. Swiss J. Geosci. 106, 63–78. https://doi.org/10.1007/s00015-013-0119-7.
Okazaki, K., Hirth, G., 2016. Dehydration of lawsonite could directly trigger earthquakes in subducting oceanic crust. Nature 530, 81–84. https://doi.org/10.1038/nature16501.
Paulatto, M., Laigle, M., Galve, A., Charvis, P., Sapin, M., Bayrakci, G., Evain, M., Kopp, H., 2017. Dehydration of subducting slow-spread oceanic lithosphere in the Lesser Antilles. Nat. Commun. 8, 15980. https://doi.org/10.1038/ncomms15980.
Peacock, S.M., 1993. The importance of blueschist → eclogite dehydration reactions in subducting oceanic crust. Geol. Soc. Am. Bull. 105, 684–694. https://doi.org/10.1130/0016-7606(1993)105<0684:TIOBED>2.3.CO;2.
Pelletier, L., Müntener, O., 2006. High-pressure metamorphism of the Lanzo peridotite and its oceanic cover, and some consequences for the Sesia–Lanzo zone (northwestern Italian Alps). Lithos 90, 111–130. https://doi.org/10.1016/j.lithos.2006.01.006.
Pennacchioni, G., Scambelluri, M., Bestmann, M., Notini, L., Nimis, P., Plümper, O., Faccenda, M., Nestola, F., 2020. Record of intermediate-depth subduction seismicity in a dry slab from an exhumed ophiolite. Earth Planet. Sci. Lett. 548, 116490 https://doi.org/10.1016/j.epsl.2020.116490.
Philippot, P., 1990. Opposite vergence of Nappes and crustal extension in the French-Italian western Alps. Tectonics 9, 1143–1164. https://doi.org/10.1029/TC009i005p01143.
Piccardo, G.B., Zanetti, A., Müntener, O., 2007. Melt/peridotite interaction in the Southern Lanzo peridotite: Field, textural and geochemical evidence. Lithos 94, 181–209. https://doi.org/10.1016/j.lithos.2006.07.002.
Platt, J.P., 1986. Dynamics of orogenic wedges and the uplift of high-pressure metamorphic rocks. Geol. Soc. Am. Bull. 97, 1037–1053. https://doi.org/10.1130/0016-7606(1986)97<1037:DOOWAT>2.0.CO;2.
Platt, J.P., 1988. The mechanics of frontal imbrication: a first-order analysis. Geol. Rundsch. 77, 577–589. https://doi.org/10.1007/BF01832399.
Platt, J.P., Xia, H., Schmidt, W.L., 2018. Rheology and stress in subduction zones around the aseismic/seismic transition. Prog Earth Planet Sci 5, 24. https://doi.org/10.1186/s40645-018-0183-8.
Plunder, A., Agard, P., Dubacq, B., Chopin, C., Bellanger, M., 2012. How continuous and precise is the record of P-T paths? Insights from combined thermobarometry and thermodynamic modelling into subduction dynamics (Schistes Lustrés, W. Alps): TOWARDS Continuous P-T PATHS? J. Metamorph. Geol. 30, 323–346. https://doi.org/10.1111/j.1525-1314.2011.00969.x.
Plunder, A., Agard, P., Chopin, C., Pourteau, A., Okay, A.I., 2015. Accretion, underplating and exhumation along a subduction interface: From subduction initiation to continental subduction (Tavşanlı zone, W. Turkey). Lithos 226, 233–254. https://doi.org/10.1016/j.lithos.2015.01.007.
Pognante, U., 1980. Preliminary data on the Piemonte ophiolite nappe in the lower Val Susa – Val Chisone area, Italian western Alps. Ofioliti 2, 221–240.
Pognante, U., 1984. Eclogitic versus blueschist metamorphism in the internal Western Alps along the Susa valley traverse. Sci. Géologiq., Bull. et Mémoires 37, 29–36.
Pognante, U., 1985. Coronitic reactions and ductile shear zones in eclogitised ophiolite metagabbro, Western Alps, North Italy. Chem. Geol. 50, 99–109. https://doi.org/10.1016/0009-2541(85)90114-7.
Pognante, U., 1991. Petrological constraints on the eclogite- and blueschistfacies metamorphism and P-T-t paths in the Western Alps. J. Metamorph. Geol. 9, 5–17. https://doi.org/10.1111/j.1525-1314.1991.tb00501.x.
Polino, R., Lemoine, M., 1984. Détritisme mixte d'origine continentale et océanique dans les sédiments jurassico-crétacés supra-ophiolitiques de la Téthys ligure: la série du Lago Nero (Alpes Occidentales franco-italiennes). Comptes rendus de l'Académie des sciences. Série 2. Mécanique, Physique, Chimie, Sciences de l'univers, Sciences de la Terre 298, 359–364.
Polino, R., Dela Pierre, F., Borghi, A., Carraro, F., Fioraso, G., Giardino, M., 2002. Note illustrative della carta geologica d'Italia alla scala 1:50000: foglio 132-152-153 Bardonecchia. ISPRA, Servizio Geologico d'Italia.
Polino, R., Malusà, M.G., Martin, S., Carraro, F., Gianotti, F., Bonetto, F., 2015. Note illustrative della carta geologica d'Italia alla scala 1:50000: foglio 090 Aosta. ISPRA, Servizio Geologico d'Italia.
Rebay, G., Zanoni, D., Langone, A., Luoni, P., Tiepolo, M., Spalla, M.I., 2018. Dating of ultramafic rocks from the Western Alps ophiolites discloses Late Cretaceous subduction ages in the Zermatt-Saas Zone. Geol. Mag. 155, 298–315. https://doi.org/10.1017/S0016756817000334.
Reddy, S.M., Wheeler, J., Butler, R.W.H., Cliff, R.A., Freeman, S., Inger, S., Pickles, C., Kelley, S.P., 2003. Kinematic reworking and exhumation within the convergent Alpine Orogen. Tectonophysics 365, 77–102. https://doi.org/10.1016/S0040-1951(03)00017-9.
Reinecke, T., 1991. Very-high-pressure metamorphism and uplift of coesite-bearing metasediments from the Zermatt-Saas zone. Western Alps. ejm 3, 7–18. https://doi.org/10.1127/ejm/3/1/0007.
Reinecke, T., 1998. Prograde high- to ultrahigh-pressure metamorphism and exhumation of oceanic sediments at Lago di Cignana, Zermatt-Saas Zone, western Alps. Lithos 42, 147–189. https://doi.org/10.1016/S0024-4937(97)00041-8.
Reynard, B., Ballèvre, M., 1988. Coexisting amphiboles in an eclogite from the Western Alps: new constraints on the miscibility gap between sodic and calcic amphiboles. J. Metamorph. Geol. 6, 333–350.
Robert, D., 1979. Contribution à l'étude géologique de la haute vallée de l'Arc-Région de Bonneval-Savoie. PhD thesis Université de Paris 6.
Rolland, Y., Lardeaux, J.-M., Guillot, S., Nicollet, C., 2000. Extension syn-convergence, poinçonnement vertical et unités métamorphiques contrastées en bordure ouest du Grand Paradis (Alpes Franco-Italiennes). Geodin. Acta 13, 133–148. https://doi.org/10.1080/09853111.2000.11105369.
Rubatto, D., Angiboust, S., 2015. Oxygen isotope record of oceanic and high-pressure metasomatism: a P–T–time–fluid path for the Monviso eclogites (Italy). Contrib. Mineral. Petrol. 170, 44. https://doi.org/10.1007/s00410-015-1198-4.
Rubatto, D., Hermann, J., 2001. Exhumation as fast as subduction? Geology 29, 3–6.
Rubatto, D., Hermann, J., 2003. Zircon formation during fluid circulation in eclogites (Monviso, Western Alps): implications for Zr and Hf budget in subduction zones. Geochim. Cosmochim. Acta 67, 2173–2187.
Rubatto, D., Gebauer, D., Fanning, M., 1998. Jurassic formation and Eocene subduction of the Zermatt-Saas-Fee ophiolites: implications for the geodynamic evolution of the Central and Western Alps. Contrib. Mineral. Petrol. 132, 269–287. https://doi.org/10.1007/s004100050421.
Ruff, L., Kanamori, H., 1980. Seismicity and the subduction process. Phys. Earth Planet. Inter. 23, 240–252. https://doi.org/10.1016/0031-9201(80)90117-X.
Ruh, J.B., Le Pourhiet, L., Agard, Ph., Burov, E., Gerya, T., 2015. Tectonic slicing of subducting oceanic crust along plate interfaces: Numerical modeling. Geochem. Geophys. Geosyst. 16, 3505–3531. https://doi.org/10.1002/2015GC005998.
Rüpke, L., 2004. Serpentine and the subduction zone water cycle. Earth Planet. Sci. Lett. 223, 17–34. https://doi.org/10.1016/j.epsl.2004.04.018.
Saffer, D.M., Tobin, H.J., 2011. Hydrogeology and Mechanics of Subduction Zone Forearcs: Fluid Flow and Pore Pressure. Annu. Rev. Earth Planet. Sci. 39, 157–186. https://doi.org/10.1146/annurev-earth-040610-133408.
Saliot, Pierre, 1978. Le métamorphisme dans les Alpes françaises. PhD thesis. Université Paris-Sud.
Saliot, P., Velde, B., 1982. Phengite compositions and post-nappe high-pressure metamorphism in the pennine zone of the French Alps. Earth Planet. Sci. Lett. 57, 133–138. https://doi.org/10.1016/0012-821X(82)90179-0.
Sartori, M., 1987. Structure de la zone du Combin entre les Diablons et Zermatt (Valais). Eclogae Geol. Helv. 80, 789–814. https://doi.org/10.5169/SEALS-166026.
Scambelluri, M., Pennacchioni, G., Gilio, M., Bestmann, M., Plümper, O., Nestola, F., 2017. Fossil intermediate-depth earthquakes in subducting slabs linked to differential stress release. Nat. Geosci. 10, 960–966. https://doi.org/10.1038/s41561-017-0010-7.
Schmid, S.M., Pfiffner, O.A., Froitzheim, N., Schönborn, G., Kissling, E., 1996. Geophysical-geological transect and tectonic evolution of the Swiss-Italian Alps. Tectonics 15, 1036–1064. https://doi.org/10.1029/96TC00433.
Schmid, S.M., Kissling, E., Diehl, T., van Hinsbergen, D.J.J., Molli, G., 2017. Ivrea mantle wedge, arc of the Western Alps, and kinematic evolution of the Alps–Apennines orogenic system. Swiss J. Geosci. 110, 581–612. https://doi.org/10.1007/s00015-016-0237-0.
Scholl, D.W., von Huene, R., Vallier, T.L., Howell, D.G., 1980. Sedimentary masses and concepts about tectonic processes at underthrust ocean margins. Geology 8, 564–568. https://doi.org/10.1130/0091-7613(1980)8<564:SMACAT>2.0.CO;2.
Schwartz, Stéphane, 2000. La zone Piémontaise des Alpes occidentales : un paléo-complexe de subduction. Arguments métamorphiques, géochronologiques et structuraux. PhD thesis. Université Claude Bernard-Lyon I.
Schwartz, S., Lardeaux, J.-M., Guillot, S., Tricart, P., 2000a. Diversité du métamorphisme éclogitique dans le massif ophiolitique du Monviso (Alpes occidentales, Italie). Geodin. Acta 13, 169–188. https://doi.org/10.1080/09853111.2000.11105371.
Schwartz, S., Lardeaux, J.-M., Tricart, P., 2000b. La zone d'Acceglio (Alpes cottiennes) : un nouvel exemple de croûte continentale éclogitisée dans les Alpes occidentales. C. R. Acad. Sci. Ser. IIA Earth Planet. Sci. 330, 859–866. https://doi.org/10.1016/S1251-8050(00)00218-4.
Schwartz, S., Lardeaux, J.M., Tricart, P., Guillot, S., Labrin, E., 2007. Diachronous exhumation of HP-LT metamorphic rocks from south-western Alps: evidence from fission-track analysis. Terra Nova 19, 133–140. https://doi.org/10.1111/j.1365-3121.2006.00728.x.
Schwartz, S., Guillot, S., Reynard, B., Lafay, R., Debret, B., Nicollet, C., Lanari, P., Auzende, A.L., 2013. Pressure–temperature estimates of the lizardite/antigorite transition in high pressure serpentinites. Lithos 178, 197–210. https://doi.org/10.1016/j.lithos.2012.11.023.
Schwartz, S., Gautheron, C., Ketcham, R.A., Brunet, F., Corre, M., Agranier, A., Pinna-Jamme, R., Haurine, F., Monvoin, G., Riel, N., 2020. Unraveling the exhumation history of high-pressure ophiolites using magnetite (U-Th-Sm)/He thermochronometry. Earth Planet. Sci. Lett. 543, 116359 https://doi.org/10.1016/j.epsl.2020.116359.
Selverstone, J., Sharp, Z.D., 2013. Chlorine isotope constraints on fluid-rock interactions during subduction and exhumation of the Zermatt-Saas ophiolite: CHLORINE ISOTOPES IN SUBDUCTED OPHIOLITE. Geochem. Geophys. Geosyst. 14, 4370–4391. https://doi.org/10.1002/ggge.20269.
Simon-Labric, T., Rolland, Y., Dumont, T., Heymes, T., Authemayou, C., Corsini, M., Fornari, M., 2009. 40 Ar/ 39 Ar dating of Penninic Front tectonic displacement (W Alps) during the Lower Oligocene (31-34 Ma). Terra Nova 21, 127–136. https://doi.org/10.1111/j.1365-3121.2009.00865.x.

Skora, S., Mahlen, N.J., Johnson, C.M., Baumgartner, L.P., Lapen, T.J., Beard, B.L., Szilvagyi, E.T., 2015. Evidence for protracted prograde metamorphism followed by rapid exhumation of the Zermatt-Saas Fee ophiolite. J. Metamorph. Geol. 33, 711–734. https://doi.org/10.1111/jmg.12148.

Soret, M., Larson, K.P., Cottle, J., Ali, A., 2021. How Himalayan collision stems from subduction. Geology 49, 894–898. https://doi.org/10.1130/G48803.1.

Stampfli, G.M., Marthaler, M., 1990. Divergent and convergent margins in the North-Western alps confrontation to actualistic models. Geodin. Acta 4, 159–184. https://doi.org/10.1080/09853111.1990.11105208.

Stampfli, G.M., Mosar, J., Marquer, D., Marchant, R., Baudin, T., Borel, G., 1998. Subduction and obduction processes in the Swiss Alps. Tectonophysics 296, 159–204. https://doi.org/10.1016/S0040-1951(98)00142-5.

Stern, R.J., 2002. SUBDUCTION ZONES. Rev. Geophys. 40 https://doi.org/10.1029/2001RG000108, 3-1-3–38.

Syracuse, E.M., van Keken, P.E., Abers, G.A., 2010. The global range of subduction zone thermal models. Phys. Earth Planet. Inter. 183, 73–90. https://doi.org/10.1016/j.pepi.2010.02.004.

Tartarotti, P., Martin, S., Festa, A., Balestro, G., 2021. Metasediments Covering Ophiolites in the HP Internal Belt of the Western Alps: Review of Tectono-Stratigraphic Successions and Constraints for the Alpine Evolution. Minerals 11, 411. https://doi.org/10.3390/min11040411.

Tatsumi, Y., 1986. Formation of the volcanic front in subduction zones. Geophys. Res. Lett. 13, 717–720. https://doi.org/10.1029/GL013i008p00717.

Tewksbury-Christle, C.M., Behr, W.M., Helper, M.A., 2021. Tracking Deep Sediment Underplating in a Fossil Subduction Margin: Implications for Interface Rheology and Mass and Volatile Recycling. Geochem. Geophys. Geosyst. 22 https://doi.org/10.1029/2020GC009463.

Tobin, H., Hirose, T., Ikari, M., Kanagawa, K., Kimura, G., Kinoshita, M., Kitajima, H., Saffer, D., Yamaguchi, A., Eguchi, N., Maeda, L., Toczko, S., 2019. Expedition 358 Preliminary Report: NanTroSEIZE Plate Boundary Deep Riser 4: Nankai Seismogenic/Slow Slip Megathrust. International Ocean Discovery Program Preliminary Report. International Ocean Discovery Program. https://doi.org/10.14379/iodp.pr.358.2019.

Tricart, P., 1974. Les Schistes lustrés du Haut-Cristillan (Alpes cottiennes, France) : litostratigraphie, architecture et tectogenèse. Géologie Alpine 50, 131–152.

Tricart, P., Schwartz, S., 2006. A north-south section across the Queyras Schistes lustrés (Piedmont zone, Western Alps): Syn-collision refolding of a subduction wedge. Eclogae Geol. Helv. 99, 429–442. https://doi.org/10.1007/s00015-006-1197-6.

van Keken, P.E., Hacker, B.R., Syracuse, E.M., Abers, G.A., 2011. Subduction factory: 4. Depth-dependent flux of H 2 O from subducting slabs worldwide. J. Geophys. Res. 116, B01401. https://doi.org/10.1029/2010JB007922.

Vannucchi, P., Spagnuolo, E., Aretusini, S., Di Toro, G., Ujiie, K., Tsutsumi, A., Nielsen, S., 2017. Past seismic slip-to-the-trench recorded in Central America megathrust. Nat. Geosci. 10, 935–940. https://doi.org/10.1038/s41561-017-0013-4.

Velde, B., 1967. Si+ 4 content of natural phengites. Contrib. Mineral. Petrol. 14, 250–258.

Villa, I.M., Bucher, S., Bousquet, R., Kleinhanns, I.C., Schmid, S.M., 2014. Dating Polygenetic Metamorphic Assemblages along a Transect across the Western Alps. J. Petrol. 55, 803–830. https://doi.org/10.1093/petrology/egu007.

Vitale Brovarone, A., Picatto, M., Beyssac, O., Lagabrielle, Y., Castelli, D., 2014. The blueschist–eclogite transition in the Alpine chain: P–T paths and the role of slow-spreading extensional structures in the evolution of HP–LT mountain belts. Tectonophysics 615–616, 96–121. https://doi.org/10.1016/j.tecto.2014.01.001.

Wada, I., Wang, K., 2009. Common depth of slab-mantle decoupling: Reconciling diversity and uniformity of subduction zones. Geochem. Geophys. Geosyst. 10, n/a-n/a. https://doi.org/10.1029/2009GC002570.

Wassmann, S., Stöckhert, B., 2013. Rheology of the plate interface — Dissolution precipitation creep in high pressure metamorphic rocks. Tectonophysics 608, 1–29. https://doi.org/10.1016/j.tecto.2013.09.030.

Weber, S., Sandmann, S., Miladinova, I., Fonseca, R.O.C., Froitzheim, N., Münker, C., Bucher, K., 2015. Dating the initiation of Piemonte-Liguria Ocean subduction: Lu–Hf garnet chronometry of eclogites from the Theodul Glacier Unit (Zermatt-Saas zone, Switzerland). Swiss J. Geosci. 108, 183–199. https://doi.org/10.1007/s00015-015-0180-5.

Wiederkehr, M., Bousquet, R., Ziemann, M.A., Berger, A., Schmid, S.M., 2011. 3-D assessment of peak-metamorphic conditions by Raman spectroscopy of carbonaceous material: an example from the margin of the Lepontine dome (Swiss Central Alps). Int. J. Earth sci. 100, 1029–1063.

Willner, A.P., 2005. Pressure–Temperature Evolution of a Late Palaeozoic Paired Metamorphic Belt in North–Central Chile (34°–35°30′S). J. Petrol. 46, 1805–1833. https://doi.org/10.1093/petrology/egi035.

Zanoni, D., Rebay, G., Spalla, M.I., 2016. Ocean floor and subduction record in the Zermatt-Saas rodingites, Valtournanche, Western Alps. J. Metamorph. Geol. 34, 941–961. https://doi.org/10.1111/jmg.12215.

Supplementary Material en annexe – 4

Chapitre IV – Distribution fractale de veines de type « crack-seal » formées en subduction : implications pour les processus de transfert de fluides et de rupture en base de zone simogénique

Mesures de distribution de veines dans les Schistes lustrés. Château-Queyras.

IV. Distribution fractale de veines de type « crack-seal » formées en subduction : implications pour les processus de transfert de fluides et de rupture en base de zone sismogénique

IV.1. Résumé du chapitre

Dans les écailles Liguro-Piémontaises de faciès schiste bleu, les sédiments, volumétriquement dominants, contiennent de grandes quantités de veines. Certaines veines, plissées par des phases précoces de déformation, contiennent des assemblages minéralogiques à lawsonite et à Fe-Mg carpholite attestant de leur formation à des conditions de haute pression, proches du pic d'enfouissement. A travers l'étude de transects le long de douze affleurements, nous montrons que les distributions des épaisseurs des veines approximent des lois de puissance. Dans ces mêmes affleurements, l'espacement et le regroupement des veines montrent des déviations significatives par rapport aux lois de puissance, interprétées comme le résultat d'artefacts liés au sous-échantillonnage. La distribution des veines à l'échelle de l'affleurement suggère que les fluides circulaient principalement de manière pervasive à travers les roches plutôt que de façon localisée dans le long de conduits majeurs. Grâce à l'étude macroscopique et microscopique des textures de veines, nous montrons que les veines se sont formées par des mécanismes incrémentaux de « crack-seal » et nous proposons une ouverture des veines, en extension et principalement entre des plans de cisaillement extrêmement faibles. Les espacements entre les « trails » et les bandes d'inclusions des « crack-seal » suivent des lois de puissance mais sur une gamme fractale restreinte. L'exposant fractal obtenu pour ces textures est similaire à celui calculé pour des données de glissements lents en subduction (durée des évènements, b-value). De plus, la valeur de relaxation de la contrainte de cisaillement estimée pour ces « crack-seal » est cohérente avec celles déduites pour les séismes lents. Cela suggère que nos veines formées aux profondeurs de la base de la zone sismogénique pourraient correspondre à l'enregistrement d'événements successifs de glissements lents pendant la subduction de l'océan Liguro-Piemontais.

IV.2. Ebauche d’article en preparation pour Journal of Structural Geology: Scaling laws for subduction-related crack-seal veins (Schistes Lustrés, W. Alps): fractal distribution and implications for rupture processes at the downdip end of the seismogenic zone.

Scaling laws for subduction-related crack-seal veins (Schistes Lustrés, W. Alps): fractal distribution and implications for rupture processes at the downdip end of the seismogenic zone

Clément Herviou[a], Philippe Agard[a], Anne Verlaguet[a], Thomas Gyomlai[a], Guillaume Bonnet[a], Kevin Mendes[a], Alexis Plunder[b]

[a] Sorbonne Université, CNRS-INSU, Institut des Sciences de la Terre de Paris, ISTeP UMR 7193, F 75005 Paris, France

[b] BRGM, F-45060, Orléans, France

* Corresponding author: clement.herviou@sorbonne-universite.fr (C. Herviou)

Abstract

Fragments of subducted oceanic lithosphere are exposed continuously in the Liguro-Piemont domain of Western Alps. In this nappe-stack, the Schistes Lustrés metasediments are volumetrically dominant and contain large amounts of veins. In the blueschist-facies Schistes Lustrés, lawsonite and Fe-Mg carpholite veins, formed close to peak burial conditions, abound. Vein thickness fit a power-law distribution while vein spacing and clustering show significant deviations from power laws interpreted as the result of truncation artefacts. Vein distribution at the outcrop scale suggests that fluids mostly circulated pervasively through the rock rather than along major localized conduits, in agreement with geochemical studies. Through the study of vein textures at macroscopic and microscopic scales we showed that veins formed by an incremental crack-seal mechanism under tensile and shear failure and possibly between extremely weak planes. The spacings between crack seal inclusion trails and bands fit a power law for a small fractal range with a fractal exponent similar to those estimated for slow slip event features. In addition, the shear stress drop estimated for our crack-seal veins is consistent with those inferred for slow slip and tremors. It suggests that our veins formed at the downdip end of the seismogenic zone may correspond to the record of successive slow slip events during subduction of the Liguro-Piemont ocean.

1. Introduction

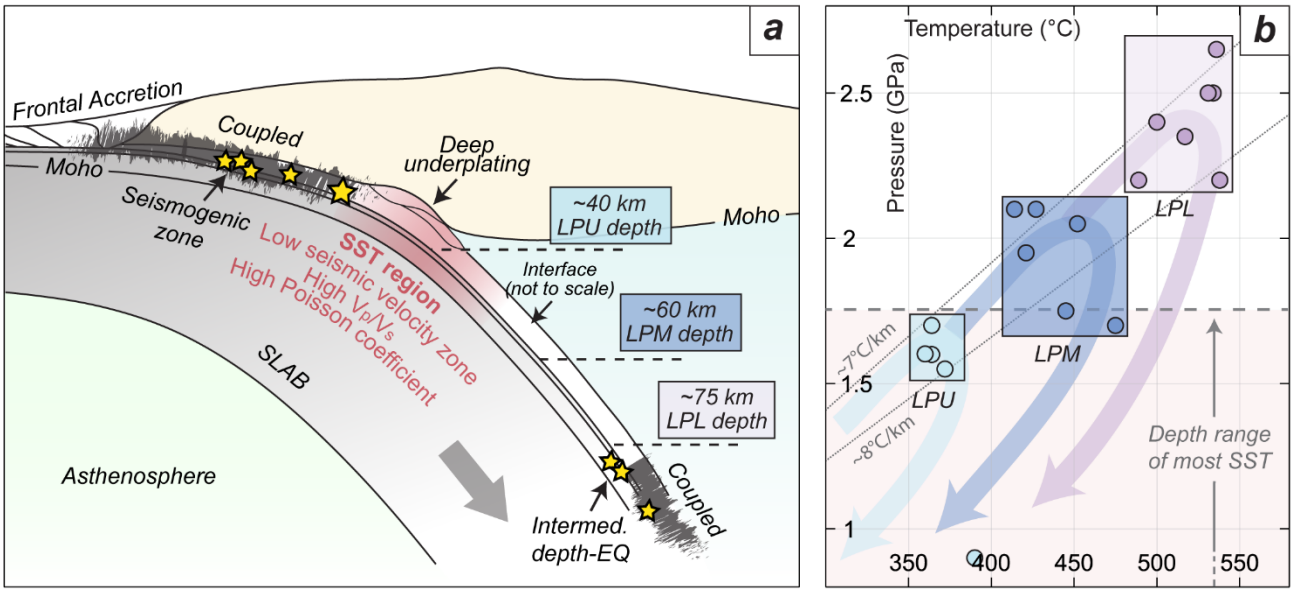

***Figure IV.1**: A) Major mechanical transitions in subduction zones and approximate peak burial depths of Liguro-Piemont units. Adapted from Agard et al. (2018). B) Pressure-Temperature conditions of Liguro-Piemont units after Herviou et al. (2022) and depth range of most slow slip and tremors after Behr and Bürgmann (2021). LPU: Liguro-Piemont Upper units; LPM: Liguro-Piemont Middle units; LPL: Liguro-Piemont Lower units; SST: slow slip and tremors; EQ: earthquakes.*

Immediately downdip of the seismogenic zone struck by subduction megathrust earthquakes (Lay et al., 2012), lies a major mechanical transition along the plate interface (e.g. Lay et al., 2012; Peacock et al., 1999; Agard et al., 2018; Fig. IV.1a). In this region, most subduction zones exhibit a few km-thick low velocity seismic layer characterized by high Poisson and V_P/V_s ratios, consistent with near-lithostatic pore fluid pressure (e.g. Audet et al., 2009; Peacock et al., 2011; Bostock, 2013; Audet and Bürgmann, 2014; Fig. IV.1a). This horizon is generally thought to originate from the presence of mafic crust and/or underplated sediments (Abers et al., 2009; Calvert et al., 2011; Hansen et al., 2012; Bostock, 2013; Paulatto et al., 2017; Delph et al., 2018, 2021; Behr and Bürgmann, 2021; Tewksbury-Christle and Behr, 2021). A wide array of seismic events, including transient slow slip events, low- and very-low-frequency earthquakes and episodic tremors (Dragert, 2001; Obara, 2002; Rogers and Dragert, 2003; Obara and Kato, 2016; referred to as slow slip and tremors, SST; Behr and Bürgmann, 2021), typifies this region, at depths and temperatures about 25-55 km and 350-550°C (Fig. IV.1a, b).

Although the role of fluids is generally invoked in the nucleation and recurrence of these events (Obara, 2002; Saffer and Tobin, 2011; Audet and Bürgmann, 2014), the preserved rock-record of SST

in exhumed subduction complexes remains highly debated (Kirkpatrick et al., 2021; Behr and Bürgmann, 2021; see also Oncken et al., 2021). While shear and dilatant crack-seal veins reflecting episodic fracturing, fluid infiltration and growth events are regularly invoked as a rock record of SST and/or earthquakes in exhumed subduction sediments (Fisher and Brantley, 1992, 2014; Fisher et al., 1995; Vannucchi et al., 2010; Fagereng et al., 2011; Fagereng and Harris, 2014; Ujiie et al., 2018; Muñoz-Montecinos et al., 2020; Cerchiari et al., 2020; Raimbourg et al., 2021; Giuntoli and Viola, 2021), only few studies have so far provided quantitative statistical support on the link between crack-seal veins and SST.

By measuring the spacing between crack-seal inclusion bands (generally a few micrometers), interpreted as one increment of displacement, and individual slip surfaces in the field, Fagereng et al. (2011) obtained potential stress drop estimates of ~30 kPa for the Chrystalls Beach Complex (New Zealand), similar to those of low-frequency earthquakes. For quartz veins of the Makamine mélange (Shimanto Belt, Japan), Ujiie et al. (2018) inferred a multi-year healing time, compatible with the recurrence intervals of SST, using the spacing of inclusion bands and a kinetic model of quartz precipitation. In these veins, the changes in band spacing are thought to reflect the temporal change in the recurrence intervals of SST during megathrust earthquake cycles (Nishiyama et al., 2021). Finally, Fisher et al. (1995) and Fisher and Brantley (2014), for en-échelon quartz veins of the Kodiak complex, calculated that salty fluids (7.5 wt% NaCl eq.) can seal fractures of a few microns at the scale of a week, compatible with the duration of slow earthquakes.

However, these studies concern subduction depths (~10-15 km depth; ~300°C, <0.55 GPa; 300-350°C, 0.3-0.5 GPa; 270°C, 0.22-0.3 GPa for the Chrystall Beach complex, Makamine mélange and Kodiak complex respectively; Toriumi and Teruya, 1988; Brantley et al., 1997; Fagereng and Cooper 2010; Palazzin et al., 2016) only compatible with the locus of some superficial SST (e.g. Araki et al., 2017, 4-10 km depth near the Nankai trench, Japan) and are shallower than most SST events (25-55 km; Behr and Bürgmann, 2021, and possibly down to 60-70 km depth: Brown et al., 2013). The description and statistical measurement of metamorphic veins therefore require further investigation to decipher the mechanisms of fluid transfer in the SST region, and to assess the potential relationships between the rock record and seismic processes.

Remnants of subducted slow-spreading oceanic lithosphere (Lagabrielle and Cannat, 1990) are exposed in the Liguro-Piemont domain of the Western Alps (Deville et al., 1992; Agard 2021; Agard and Handy, 2021; Herviou et al., 2022), one of the largest and better-preserved fossil subduction

complexes, which provides an access to subduction depths from ~30 to 80 km (Berger and Bousquet, 2008; Agard et al., 2002, 2018; Agard, 2021; Bebout et al., 2013; Herviou et al., 2021, 2022; Fig. IV.1a, b). Distinct subduction slices were recognized in the Western Alps, with a trimodal depth distribution (35-45 km, 55-65 km and 70-80 km; Herviou et al., 2022; Fig. IV.2a) marked by an increase in metamorphic conditions from the Upper (LPU; 320-400°C- 1.2-1.9 GPa) to the Middle (LPM; 415-475°C- 1.7-2.2 GPa) and to the Lower units (LPL; 500-580°C- 2.2-2.8 GPa). The metasedimentary fraction, known as the Schistes Lustrés (e.g. Agard et al., 2001) dominates in the blueschist-facies units LPU and LPM (>90%), whereas the eclogitic LPL units are far richer in mafic-ultramafic rocks (>40%; Herviou et al., 2022). The similarity between the peak burial depths of the LPU, LPM and LPL units and those inferred for tectonic slicing and underplating, in both modern and fossil subduction zones, points to specific mechanisms controlling transient changes in interplate coupling at these depths (Plunder et al., 2015; Agard et al., 2018; Herviou et al., 2022; Cubas et al., 2022).

In the LPU and LPM blueschist-facies units, which were sliced from the downgoing plate at depths similar to those considered as the locus of most SST (Behr and Bürgmann, 2021; Fig. IV.1a, b), there are abundant metamorphic veins hosting water-rich high pressure low temperature (HP-LT) minerals such as lawsonite and Fe-Mg carpholite (Agard et al., 2000, 2001; Lefeuvre et al., 2020; Herviou et al., 2021), thereby highlighting fluid transfer at the base of the seismogenic zone. The present work reports measurements of vein thickness, vein spacing, vein clustering and crack-seal band spacing, as well as their respective statistical distributions, across twelve outcrops of the LPU and LPM units, in order to clarify and quantify the relationships between the rock record and processes occurring at the subduction plate interface.

2. Distribution of hydrothermal/metamorphic veins in rocks

Hydrothermal/metamorphic veins reflecting crystal growth in cracks are almost ubiquitous in rocks and are considered as the best record of fluid circulation and fluid-rock interaction at depth (e.g. Fisher et al., 1995; Widmer and Thompson, 2001; Verlaguet et al., 2011). Most of these cracks are interpreted to form by tensile or shear brittle failure of the rocks under high fluid pressures and/or changes in the magnitude or orientation of the stresses (Oliver and Bons, 2001; Bons et al., 2012).

Characterization of fluid sources and fluid flow in rocks is central in the study of veins (e.g. Spandler et al., 2011; Locatelli et al., 2019; Muñoz-Montecinos et al., 2020; Herviou et al., 2021). Geochemical

methods, as fluid inclusions, trace elements and isotopes are generally used to provide clues on fluid compositions and sources (Roedder, 1984; Valley, 1986; Spandler and Pirard, 2013). Vein mineralization and microtextures inform about mineral precipitation and fluid supply mechanisms in veins, either by dominant local diffusive transport or larger scale advective transport (Oliver and Bons, 2001; Bons et al., 2012). Fluid flow patterns and distances over which fluids migrate are largely controlled by porosity and pore connectivity (i.e. permeability). Since the opening of cracks creates transient permeability changes amenable to fluid circulation, the study of vein thickness, vein spacing and their clustering in rocks sheds light on how the fluids pervade the rocks or localize in interconnected networks along major zones of weakness.

The statistical analysis of veins from various geological settings has shown that vein thickness generally follows a power-law distribution, where the number of objects N(a) of size a or larger satisfies the relationship $N(a) \propto a^{-D}$ (D being the fractal dimension; McCaffrey et al., 1993; Sanderson et al., 1994; Fisher et al., 1995; Clark et al., 1995; McCaffrey and Johnston, 1996; Gillespie et al., 1999; Roberts et al., 1999; Monecke et al., 2001; André-Mayer and Sausse, 2007; Sanderson et al., 2008; Fagereng, 2011; Mazzarini et al., 2011; Lahiri et al., 2020). Fractal theory and scale-invariant laws help linking small scale observations to large scale processes (Mandlebrot, 1982; Allègre et al., 1982; Turcotte, 1986, 1989; Pickering et al., 1995) such as the distribution of fracture spacing and apertures (La Pointe, 1988; Velde et al., 1990, 1991; Barton and Zoback, 1992; Ledésert et al., 1993; Hooker et al., 2013) and of fragmented material (Blenkinsop et al., 1991; Blenkinsop et al., 2000), as well as the scaling of faults and earthquakes (Gutenberg and Richter, 1954; Watterson, 1986; Jackson and Sanderson, 1992; Pickering et al., 1995, 1996).

Figure IV.2 *(next page): Geological setting of the Liguro-Piemont domain. A) Structural map of the Western Alps with focus on the Liguro-Piemont domain and showing the distribution of the three types of units throughout the complex. The studied area is outlined by the black dashed rectangle. Modified after Herviou et al. (2022). B) Simplified structural map of the studied area with location of the studied outcrops. Modified after Herviou et al. (2022). C) Schematic cross-section along the studied area highlighting the stacking of the Liguro-Piemont units and the eastward increase in metamorphic grade. Modified after Lagabrielle (1987) and Herviou et al. (2022). D), E), F) Main foliation planes, poles and lineations plotted on Schmidt net lower hesmisphere. Red planes and poles in D) and E) correspond to the studied outcrops. LPU: Liguro-Piemont Upper units; LPM: Liguro-Piemont Middle units; LPL: Liguro-Piemont Lower units; Che.: Chenaillet massif.*

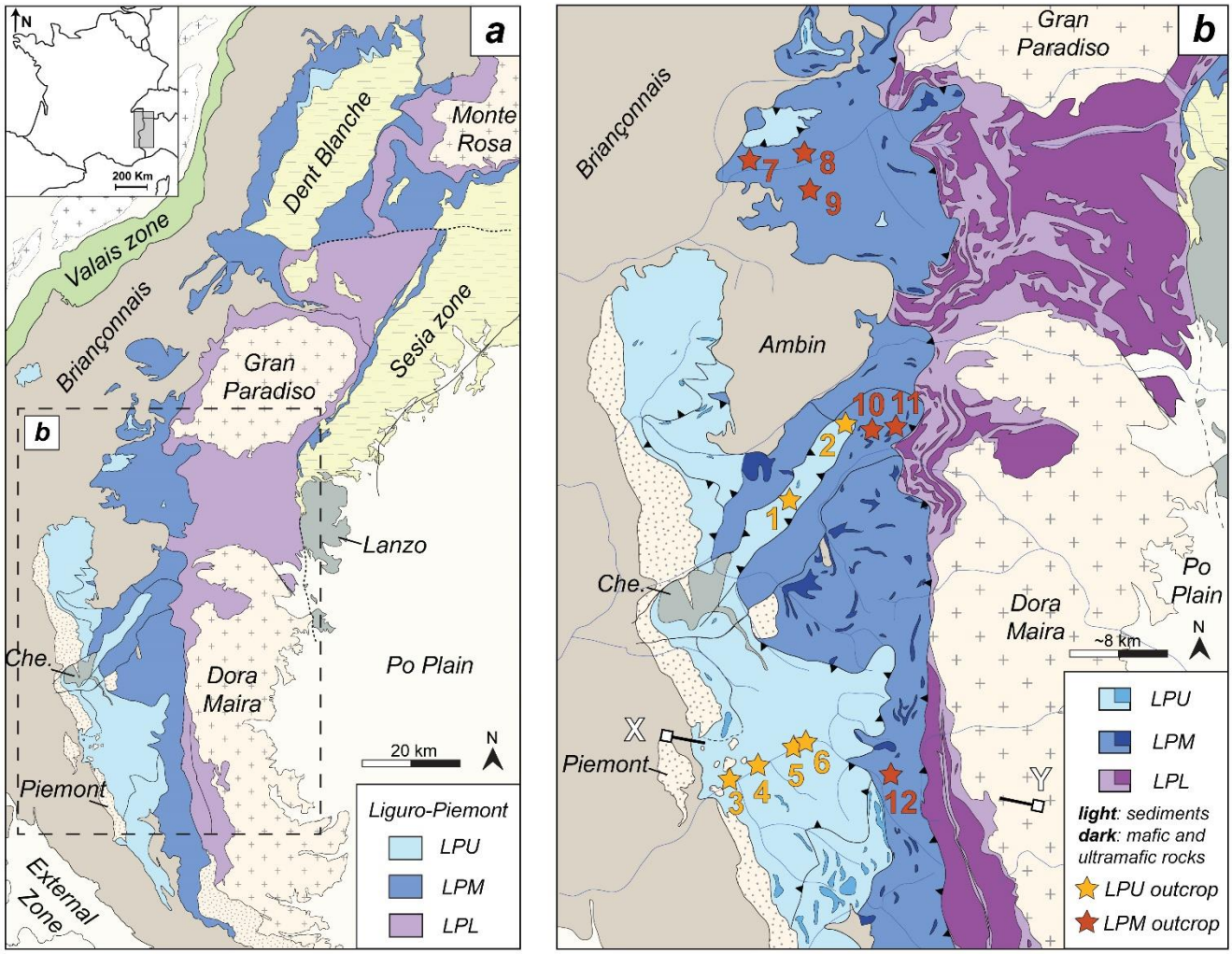
a
N
200 Km
Valais zone
Briançonnais
Dent Blanche
Monte Rosa
Gran Paradiso
Sesia zone
b
Lanzo
Che
Dora Maira
Po Plain
20 km
N
Piemont
External Zone
Liguro-Piemont
LPU
LPM
LPL
b
Gran Paradiso
Briançonnais
7
8
9
Ambin
10
11
2
1
Che
Dora Maira
Po Plain
~8 km
N
X
Piemont
5
6
4
3
12
Y
LPU
LPM
LPL
light: sediments
dark: mafic and ultramafic rocks
LPU outcrop
LPM outcrop

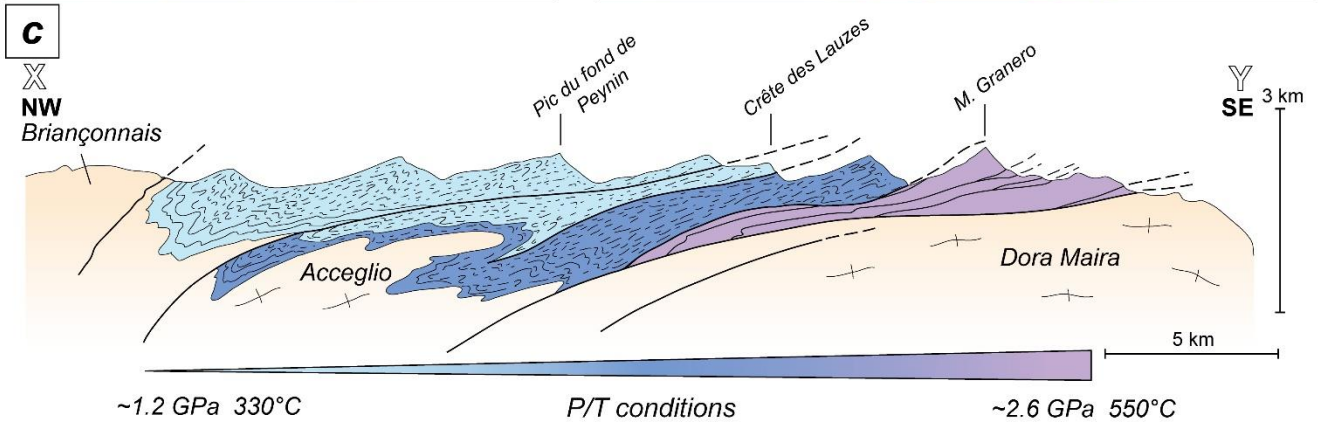
c
X
NW
Briançonnais
Pic du fond de Peynin
Crête des Lauzes
M. Granero
Y
SE
3 km
Acceglio
Dora Maira
5 km
~1.2 GPa 330°C
P/T conditions
~2.6 GPa 550°C

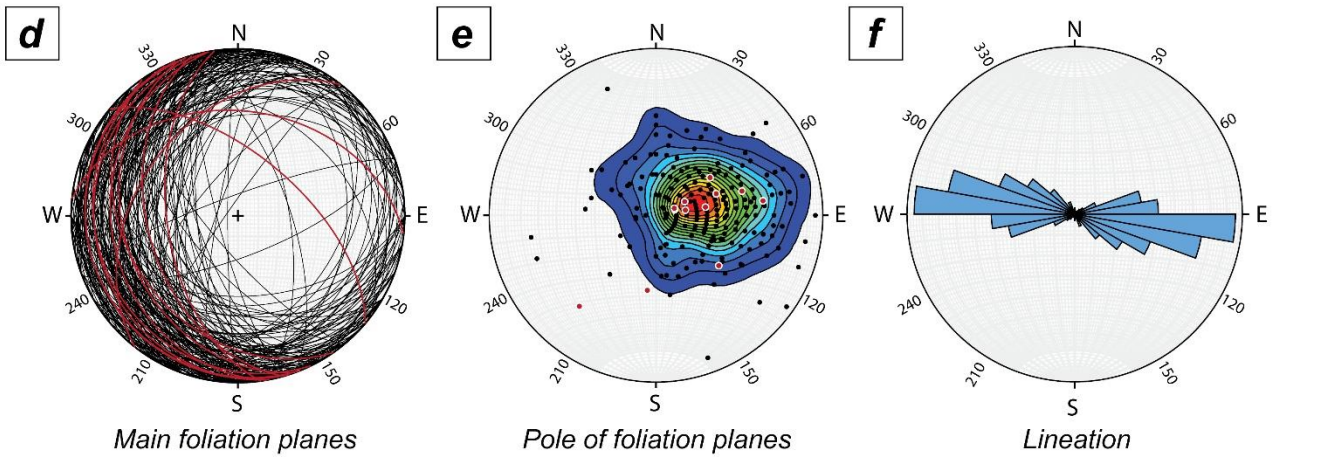
d
N
330
30
300
60
W
E
240
120
210
150
S
Main foliation planes
e
Pole of foliation planes
f
Lineation

The vein length-thickness ratio (McCaffrey et al., 1993; Johnston and McCaffrey, 1996; Stowell et al., 1999), as well as the vein clustering across outcrops (Manning et al., 1994; Barton, 1995; Madge et al., 1995; Holland and Urai, 2010; Fagereng, 2011), are also best described by a power-law distribution. In contrast, vein spacing either follows a power law (Fisher et al., 1995; Fagereng, 2011; Mazzarini et al., 2011) or a log-normal/negative exponential distribution (McCaffrey et al., 1993; Fisher et al., 1995; McCaffrey and Johnston, 1996; Johnston and McCaffrey, 1996; Gillespie et al., 1999; Simpson et al., 1999; André-Mayer and Sausse, 2007; Sanderson et al., 2008).

Most of these works are based on extension veins, for which D values allow estimating if the total extension was dominantly accommodated by growth in larger veins or opening of thinner veins (e.g. Fagereng, 2011). Using stochastic models, Clark et al. (1995) showed that a power-law distribution of extension vein thickness can be produced by incremental growth of existing veins and limited initiation of new fractures. Estimating the proportion of thick versus thin veins also informs about the localization of deformation and fluid transfer. Vein spacing distribution, as vein clustering, is considered to derive from the initial spacing of fractures and their D values also give clues on how the fluids pervaded the rocks or localized in specific zones (Manning et al., 1994; Simpson et al., 2000).

Most published works, however, have dealt with veins from mineralized ore deposits (McCaffrey et al., 1993; Sanderson et al., 1994; Barton, 1995; McCaffrey and Johnston, 1996; Johnston and McCaffrey, 1996; Gillespie et al., 1999; Roberts et al., 1999; Foxford et al., 2000; Monecke et al., 2001; André-Mayer and Sausse, 2007; Sanderson et al., 2008; Lahiri et al., 2020) or low-grade metamorphic rocks (Fisher et al., 1995; Clark et al., 1995; Simpson et al., 1999; Stowell et al., 1999; Holland and Urai, 2010; Fagereng, 2011). None has reported the statistical distribution of HP-LT metamorphic veins despite their large amounts in subduction complexes (Agard et al., 2000; Herviou et al., 2021; Muñoz-Montecinos et al., 2021), where the successive dehydration reactions during burial of the downgoing plate (Schmidt and Poli, 2014), and the low porosity/permeability of rocks (Ganzhorn et al., 2019), likely generate large fluid pressure variations as expected for the SST (Behr and Bürgmann, 2021).

3. Methodology

3.1 Deformation stages and vein distribution at ~35-60 km subduction depth (Schistes Lustrés metamorphic complex, Western Alps)

Remnants of the Liguro-Piemont oceanic lithosphere subducted below Adria/Apulia can be found in the Western Alps (Deville et al., 1992; Agard, 2021; Agard and Handy, 2021). These rocks were buried between ~30 and 80 km depth (Agard et al., 2001, 2002, 2009; Herviou et al., 2022) and were intensely folded, leading to significant thickening of the initial sedimentary pile to form a HP-LT nappe-stack known as the Schistes Lustrés complex (Caron, 1977; Tricart and Schwartz, 2006). After peak burial, these rocks were detached as tectonic slices from the subducting plate and exhumed from the Late Eocene to the Miocene (Agard et al., 2002; Schwartz et al., 2007, 2020; Angiboust and Glodny, 2020).

Several units corresponding to independent subduction slices were identified across the complex (Lagabrielle, 1987; Fudral, 1996). Herviou et al. (2022) showed the existence of a trimodal distribution of units, with an almost continuous eastward increase in peak burial conditions from the Upper units (LPU; 320-400°C; 1.2-1.9 GPa) to the Middle units (LPM; 415-475°C- 1.7-2.2 GPa) and to the Lower units (LPL; 500-580°C; 2.2-2.8 GPa; Fig. IV.2a, b, c). The LPU and LPM units, metamorphosed under blueschist-facies at peak P-T conditions, are dominated by sediments (>90%; Fig. IV.2a, b) whereas the LPL units, metamorphosed at eclogite-facies conditions at peak burial, are much richer in mafic-ultramafic rocks (>40% %; Fig. IV.2a, b).

Several deformation stages were identified and dated in the Schistes Lustrés complex of the Cottian Alps (Agard et al., 2001, 2002; Fig. IV.2d-f, IV.3a-h): the first episode (D1) relates to the development of an early foliation, EW trending folds and crystallization of peak metamorphic assemblages at ~62-55 Ma. A second phase (D2) at ~51-45 Ma corresponds to the ductile east-vergent deformation accompanying early exhumation under BS-facies conditions. The third fabric (D3), between ~38 and 35 Ma, is marked by top-to-the-west ductile to brittle deformation associated with greenschist-facies exhumation, and coincides with the final ductile exhumation of large mafic-ultramafic complexes such as Monviso (Angiboust and Glodny, 2020). Two late fabrics (D4 and D5; Tricart and Schwartz, 2006), marked by small-scale boudinage and west-dipping normal faulting, characterize the final ductile-brittle transition during late exhumation. All these tectonic patterns resulted in a flat to gently west-dipping foliation mostly formed by D1 to D2 patterns with stretching lineations trending N090 to N110 on average (Fig. IV.2d-f, IV.3a-h).

Figure IV.3 *(next page): A) to G) Schistes Lustrés outcrops with deformation stages, metamorphic veins and studied transects. Car: Fe-Mg carpholite; Lws: lawsonite.*

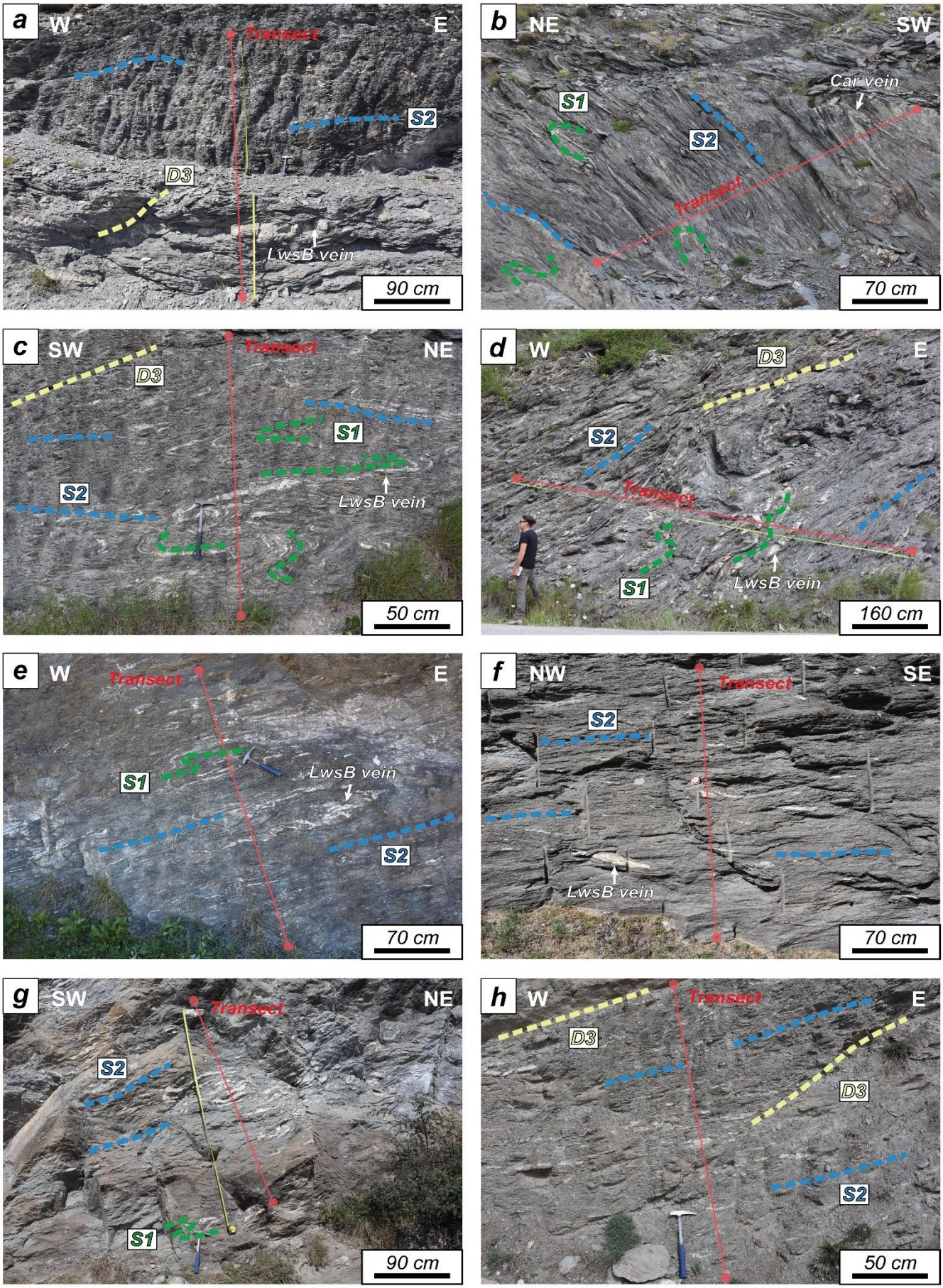
a
W
E
Transect
S2
D3
LwsB vein
90 cm
b
NE
SW
Car vein
S1
S2
Transect
70 cm
c
SW
NE
Transect
D3
S1
S2
LwsB vein
50 cm
d
W
E
D3
S2
Transect
S1
LwsB vein
160 cm
e
W
E
Transect
S1
LwsB vein
S2
70 cm
f
NW
SE
Transect
S2
LwsB vein
70 cm
g
SW
NE
Transect
S2
S1
90 cm
h
W
E
Transect
D3
D3
S2
50 cm

Metamorphic veins are ubiquitous in Schistes Lustrés LPU and LPM blueschist-facies metasediments. Some contain diagnostic HP-LT minerals: (i) lawsonite-bearing veins (Caron, 1974; Lefeuvre et al., 2020; Herviou et al., 2021) and (ii) Fe-Mg carpholite-bearing veins (Goffé and Chopin, 1986; Agard et al., 2000, 2001). Most of these veins relate to the D1 deformation stage and therefore record fluid circulation at prograde to peak burial of LPU and LPM units. These veins therefore allow studying fluid transfer at ~35-60 km depth in subduction zones (see Herviou et al., 2021).

3.2 Outcrop selection and sampling strategy

Twelve outcrops of blueschist-facies metasediments were selected (Fig. IV.2b; IV.3a-h) from both the LPU and the LPM units (#1-6 and #7-12, respectively; Fig. IV.2b). All outcrops are located in the Cottian Alps and in the Queyras region and contain rocks buried at SST depths (25-55 km; Fig. IV.1a-b; Table IV.1). The outcrop location and peak P-T estimates from neighbouring outcrops are given in Table IV.1. The selected outcrops contain slightly larger vein amounts than the average Schistes Lustrés outcrop but are representative of the veiny outcrops encountered across the complex.

Unit	Outcrop	Peak P-T	Latitude	Longitude	Main foliation dip	Transect length (cm)	n veins	Vein%
LPU	1. Triplex	343°C[(1)]/ ~1.5 Gpa[(2)]	44.99872222	6.883972222	N162 10°W	324.3	173	29.5
"	2. Assietta	378°C[(1)]/1.8-1.9 Gpa[(2,3)]	45.06581944	6.953452778	N130 60°E	334.3	95	22.0
"	3. Château-Queyras	332°C[(4)]/1.4 Gpa[(2)]	44.75793333	6.793083333	N145 33°W	355.8	65	32.4
"	4. Malafosse	360°C[(2)]/ 1.6 Gpa[(2)]	44.76747222	6.83125	N170 25°W	185.7	41	13.3
"	5. Gouret	366°C[(2)]/ 1.7 Gpa[(2)]	44.78751944	6.882408333	N172 55°W	708	111	17.9
"	6. Gouret	366°C[(2)]/ 1.7 Gpa[(2)]	44.78858333	6.887066	N164 45°W	897.9	149	20.6
LPM	7. Termignon	395°C[(5)]/~1.7 Gpa[(2)]	45.28455556	6.834305556	N038 40°N	151.7	37	12.1
"	8. Lanslevillard	480°C[(6)]/~1.6-1.9 Gpa[(6)]	45.28983333	6.906416667	N096 37°N	264.3	61	10.3
"	9. Mont-Cenis	435°C[(6)]/~1.6-1.9 Gpa[(6)]	45.25906389	6.903197222	N158 10°W	250.5	30	9.2
"	10. Cerogne	387°C[(1)]/~ 2 GPa[(2)]	44.05904167	6.984363889	N169 15°W	254	51	22.6
"	11. Balboutet	441°C[(1)]/ ~2.2 Gpa[(2)]	44.06230556	7.016666667	N154 16°W	191.8	66	14.7
"	12. Combe Morelle	388°C[(4)]/~2GPa[(2)]	44.76421389	6.996486111	N160 32°W	294.4	68	18.2

Table IV.1*: Studied outcrops, estimated P-T conditions, corresponding localities, estimated P-T conditions, and transect measurements. P-T conditions were estimated from host-rocks in: [(1)]Beyssac et al. (2002); [(2)]Herviou et al. (2022); [(3)]Agard et al. (2001); [(4)]Schwartz et al. (2013); [(5)]Gabalda et al. (2009); [(6)]Plunder et al. (2012).*

Vein distribution was quantified on 1D profiles for veins ≥1 mm-thick (Fig. IV.3a-h). For each outcrop, a representative linear transect, between ~150 cm- and ~900 cm-long, was selected perpendicular to the main S1-S2 schistosity (Fig. IV.3a-h, IV.2d-e; Table IV.1), avoiding late D3-to-D5 veins. Vein spacing was measured from vein center to vein center. Measurement accuracy is approximately 1-2 mm and spatial resolution ~1 mm. Transects that were not strictly perpendicular to the main schistosity were corrected for dip (outcrops #5, 6, 12). All measured veins are either clearly related to S1 or

located in the S1-S2 main schistosity, consistent with their HP-LT origin (Fig. IV.3a-g). Later folding of the D1 veins during D2 ± D3 deformation stages may however have affected their initial vein thickness and spacing (Fig. IV.3b, c), as discussed below.

For all studied outcrops, vein distribution is shown by plotting each vein as a single line (Fig. IV.4). Frequency-size plots are shown in figures IV.7-9. Due to undersampling of the thinnest structures and the rare presence of large ones across short transects (Barton and Zoback., 1992; Gillespie et al., 1993; Sanderson et al., 1994; Pickering et al.,1995; McCaffrey and Johnston, 1996; Roberts et al., 1999; Monecke et al., 2001; Ortega et al., 2006; André-Mayer and Sausse, 2007; Sanderson et al., 2008), datasets tend to follow a characteristic concave-shape rather than a perfectly linear trend as expected for power-law distributions (e.g. Blenkinsop et al., 1991; Barton and Zoback, 1992; Gillespie et al., 1993; Pickering et al., 1995; Braun and Kelemen, 2002; Ortega et al., 2006). These truncation effects, commonly observed in vein and fracture datasets, tend to degrade the power law into negative exponential or log-normal distribution (e.g. Gillespie et al., 1993; Fagereng, 2011). The D component is then estimated along the central, linear segment of the curve (e.g. Braun and Kelemen, 2002).

Vein clustering, and its potential relationship with deformation features, was evaluated using the interval-counting technique of Manning (1994): each transect is divided into equal segments of length r, and the number of segments N(r) that contain at least one vein is recorded. After repetition for a range in r, the fractal dimension of clustering D(c) correspond to: $D(c)=(d(\log N(r))/(d(\log 1/r))$. This method is an equivalent to the box-counting technique used for 2D datasets (Barton and Larsen, 1985; Gillespie et al., 1993; Barton, 1995). Vein clustering was also quantified using the ratio of the standard deviation of spacing over the mean spacing (coefficient of variation Cv; e.g. Gillespie et al., 1999; Foxford et al., 2000).

Finally, the distribution of spacing between inclusion bands and trails in crack-seal veins (Ramsay, 1980) was measured, in order to quantify the displacement of each crack increment and plotted in frequency-size graph to detect potential relationships with other statistical distributions. Previous works described exponential (Renard et al., 2005) and linear distributions (Fagereng et al., 2011) for spacing between inclusion bands in crack-seal veins. In inclusions trails, spacings measurements were conducted from core to core of the solid inclusions. These measurements were realized by optical microscope observations and the use of an image processing software. Accuracy of measurement is around 0.5-1 µm. Abbreviations and symbols used in the following are given in Table IV.2.

Symbol	Meaning
t	Vein thickness
N(t)	Number of objects size t or greater
D(t)	Fractal dimension of vein thickness
s	Vein spaging
N(s)	Number of objects size s or greater
D(s)	Fractal dimension of vein spacing
D(c)	Fractal dimension of vein clustering
Cv	Coefficient of variance
i	inclusion spacing
N(i)	Number of object size i or greater
D(i)	Fractal dimension of inclusion spacing

***Table IV.2**: List of symbols used in this study.*

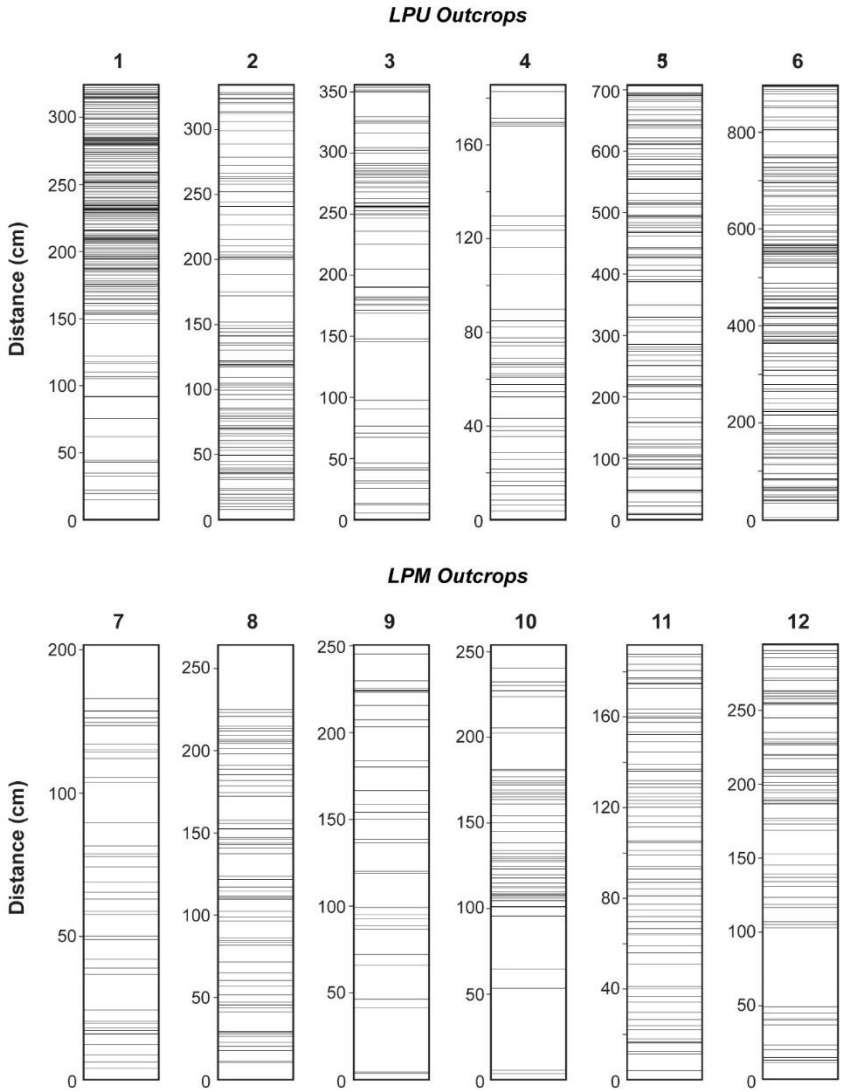

***Figure IV.4**: Vein distribution in the studied outcrops.*

4. Vein patterns and textures in the Schistes Lustrés

4.1 Field observations

Metamorphic veins were tracked across the entire Schistes Lustrés complex (Herviou et al., 2021). While blueschist-facies veins locally abund in both LPU and LPM units (Fig. IV.3a-h), larger amounts are observed in the LPU units than in the generally more carbonate-rich LPM metasediments. Across the twelve studied profiles, veins make up between 13-32% of the LPU and 9-23% of the LPM outcrops (Table IV.1). These calculations are consistent with estimations of Cartwright and Buick (2000) for the Schistes Lustrés of Alpine Corsica and those of Herviou et al. (2021) for the Western Alps. In their study, Cartwright and Buick (2000) estimated that veins can make up to 30% of individual outcrops but that volumes of 5-10% are the most common. Herviou et al. (2021) estimated that high pressure veins locally reach 20-25% of individual outcrops. A significant proportion of the quartz veins measured in the field also contain diagnostic high pressure minerals (i.e., lawsonite or Fe-Mg carpholite; Fig. IV.5a-f).

Lawsonite-bearing veins are by far the most abundant HP-LT veins in the Schistes Lustrés. Distinct types of lawsonite were described in the literature (Caron, 1974; Lefeuvre et al., 2020; Herviou et al., 2021) and the classification of Lefeuvre et al. (2020) is used in the following. In contrast to the dark, organic matter-rich crystals of lawsonite in the schist, two types of creamy-colored lawsonite-bearing quartz veins are observed: (i) pluri-cm- to m-long veins containing stretched crystals (in the sense of Bons et al., 2012) of lawsonite oriented parallel to the vein walls (LwsB) and to quartz crystals (± minor ankerite; Fig. IV.5a-d); (ii) mm- to cm-large tensional cracks containing lawsonite crystals, in textural equilibrium with ankerite and quartz, oriented perpendicular to the vein walls (LwsC; Fig. IV.5a, c). LwsB veins outline D1 folds in places, advocating for early formation during prograde-to peak burial (Fig. IV.5a, b, c), whereas LwsC cracks form during D1 and/or D2 (Fig. IV.5a).

Though more sensitive to retrogression than lawsonite and therefore scarcier, Fe-Mg carpholite-bearing veins with similar features to LwsB veins were also observed in the Schistes Lustrés metasediments (Fig. IV.5e, f). As for Lws-bearing veins, they markedly differ from the late-stage greenschist-facies D3/D4/D5 veins filled with quartz ± calcite, dolomite, albite and chlorite, that crosscut the main S1-S2 schistosity (Fig. IV.5g, h).

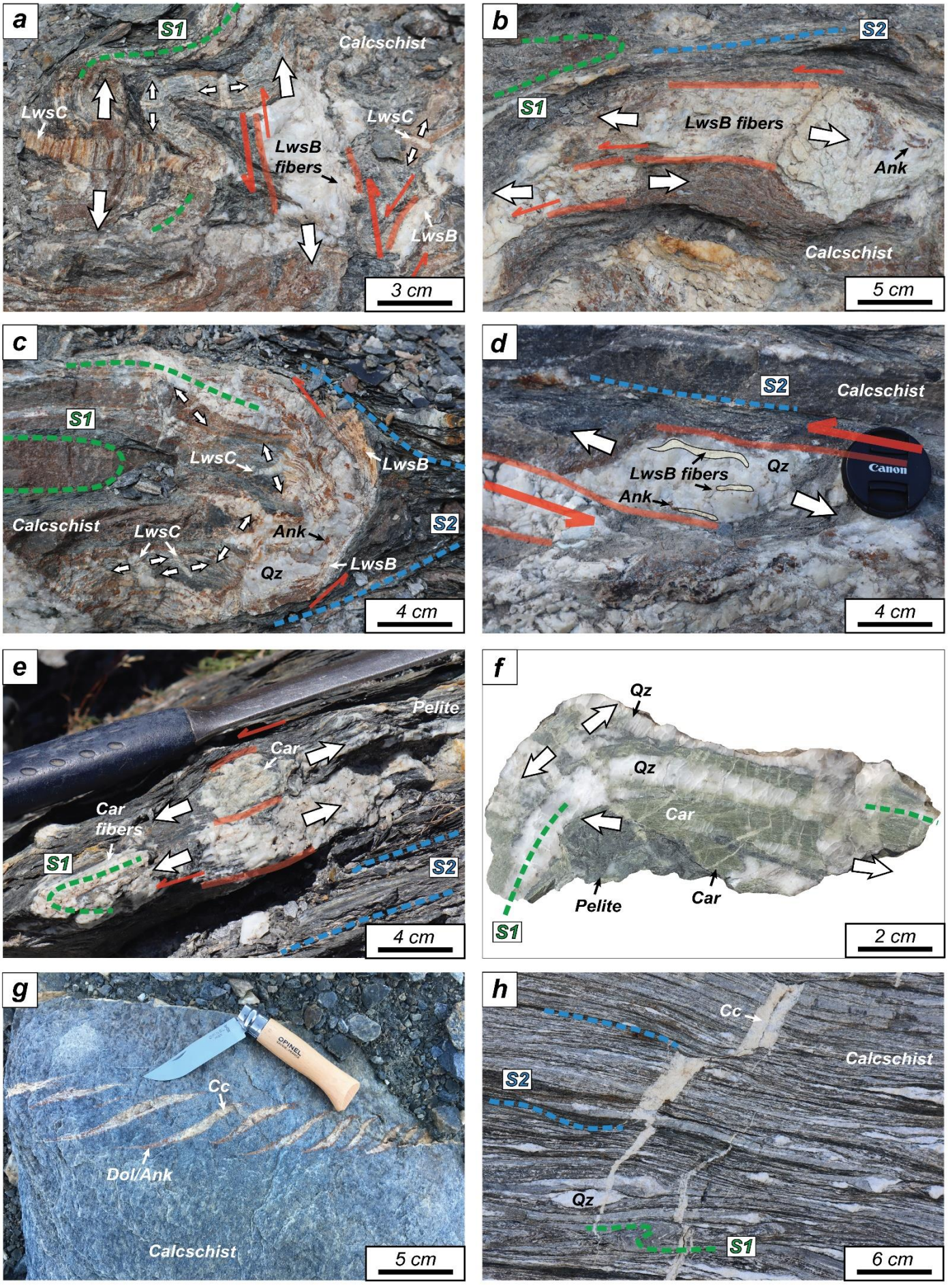
a
S1
Calcschist
LwsC
LwsC
LwsB fibers
LwsB
3 cm
b
S2
S1
LwsB fibers
Ank
Calcschist
5 cm
c
S1
LwsC
LwsB
Calcschist
LwsC
Ank
S2
Qz
LwsB
4 cm
d
S2
Calcschist
LwsB fibers
Qz
Ank
Canon
4 cm
e
Pelite
Car
Car fibers
S1
S2
4 cm
f
Qz
Qz
Car
Pelite
Car
S1
2 cm
g
Cc
Dol/Ank
Calcschist
5 cm
h
Cc
Calcschist
S2
Qz
S1
6 cm

Figure IV.5 *(previous page): Metamorphic veins in the Schistes Lustrés with opening directions. A) to D) Syn-D1-D2 lawsonite B- and lawsonite C-bearing veins. E), F) Syn-D1 Fe-Mg carpholite veins. G), H) Syn D3-D4-D5 veins* quartz ± calcite, dolomite, albite and chlorite. Ank: ankerite; Car: Fe-Mg carpholite; Cc: calcium carbonate; Dol: dolomite; Lws: lawsonite; Qz: quartz.

4.2 Microscope observations

At the microscopic-scale too, LwsB, LwsC and Fe-Mg carpholite-bearing veins contain stretched crystals of lawsonite or Fe-Mg carpholite in textural equilibrium with quartz ± ankerite crystals (Fig. IV.6a-h; see Lefeuvre et al., 2020 and Herviou et al., 2021 for more pictures on their textural relationships).

In LwsB and LwsC veins, quartz crystals preserved from dynamic recrystallization host successive trails of regularly spaced (micrometric) idiomorphic lawsonite crystals, with a similar aspect ratio among each trail. (Fig. IV.6a-d). These solid inclusions trails, oriented parallel to the stretched lawsonite crystals, are characteristic of vein opening by a crack-seal mechanism (Ramsay et al., 1980; Cox, 1987) through repeated fracturing and sealing events under high fluid pressure (Ramsay et al., 1980). Each crystal is considered to correspond to one increment of extensional opening and the thickness of quartz between each lawsonite crystal is interpreted as the amount of opening in one crack increment.

In crack-seal veins, ‘inclusion bands’ are planes of solid and/or fluid inclusions located perpendicular to the opening direction and interpreted as sealed microcracks (Ramsay, 1980; Fisher and Brantley, 1992, 2014; Fisher et al., 1995; Renard et al., 2005; Ujiie et al., 2018; Fagereng et al., 2011). Such bands were not observed in quartz crystals associated with LwsB and LwsC veins, probably due to removal during quartz recrystallization. Yet, lawsonite crystals better preserved from dynamic recrystallization than quartz contain successive trails of aqueous two-phase (liquid + vapor) fluid inclusions (Fig. IV.6e, f). Since they are oriented perpendicular to the stretched crystals and show a micrometer-sized spacing matching that of the lawsonite inclusion trails in quartz crystals (Fig. IV.6a-f), they are interpreted as crack-seal inclusion bands.

In Fe-Mg carpholite-bearing veins, successive inclusion bands, similar to those of LwsB and LwsC veins were observed in Fe-Mg carpholite (Fig. IV.6g) and in quartz crystals (Fig. IV.6h). These bands mostly contain aqueous biphase (liquid + vapor) fluid inclusions and are oriented perpendicular to stretched fibers and therefore to the opening direction.

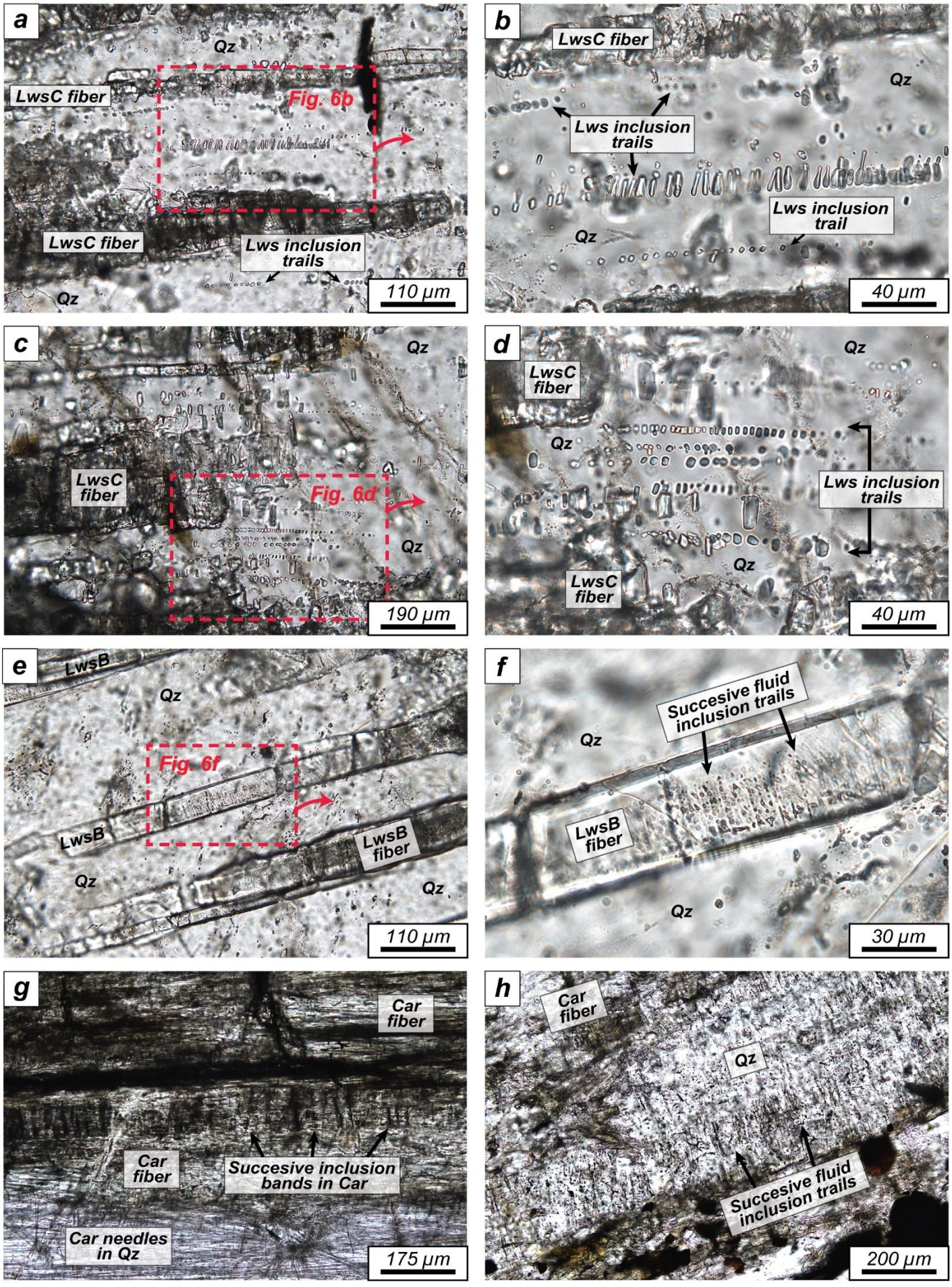
a
Qz
LwsC fiber
Fig. 6b
LwsC fiber
Lws inclusion trails
Qz
110 µm
b
LwsC fiber
Qz
Lws inclusion trails
Lws inclusion trail
Qz
40 µm
c
Qz
LwsC fiber
Fig. 6d
Qz
190 µm
d
Qz
LwsC fiber
Qz
Lws inclusion trails
Qz
LwsC fiber
40 µm
e
LwsB
Qz
Fig. 6f
LwsB
LwsB fiber
Qz
Qz
110 µm
f
Succesive fluid inclusion trails
Qz
LwsB fiber
Qz
30 µm
g
Car fiber
Car fiber
Succesive inclusion bands in Car
Car needles in Qz
175 µm
h
Car fiber
Qz
Succesive fluid inclusion trails
200 µm

Figure IV.6 *(previous page): Crack-seal textures in lawsonite- and Fe-Mg carpholite-bearing veins. A) to D) Successive lawsonite inclusion trails in quartz in textural equilibrium with Lawsonite C stretched crystals. E) and F) Successive trails of fluid inclusions in a lawsonite B fiber. These trails are considered as equivalents to Ramsay et al. (1980) crack-seal bands. G) Crack-seal bands made of fluid and solid inclusions in a Fe-Mg carpholite crystal. H) Successive fluid inclusions trails in quartz in textural equilibrium with Fe-Mg carpholite crystals. Car: Fe-Mg carpholite; Lws: lawsonite; Qz: quartz.*

5. Distribution of veins in the Schistes Lustrés

5.1 Vein thickness distribution

In the studied transects measured vein thicknesses vary between 0.1 cm and 24 cm. The mean and median vein thickness ranges are 0.4-1.2 cm and 0.2-0.5 cm, respectively (Table IV.3) highlighting the presence of many thin veins <1 cm. The mean/median thickness of veins from all outcrops, all LPU outcrops and all LPM outcrops are respectively 0.9/0.3 cm, 1/0.3 cm and 0.7/0.2 cm.

The statistical distribution of veins for a given outcrop, as well as for all outcrops, is not linear (Fig. IV.7a, b, Sup. mat. IV.1; for symbol descriptions see Table IV.2). Frequency-size plots in log-linear scale are characterized by a non-linear trend showing that vein thickness distributions are not well described by log-normal or exponential laws (Sup. mat. IV.1). Finally, most of the frequency-size plots in log-log scale exhibit linear trends with coefficients of determination greater than 0.91 (R^2; Fig. IV.7c-f; Sup. mat. IV.1), suggesting that vein thicknesses are well described by a power-law distribution. For some outcrops as for compiled datasets (all outcrops, all LPU outcrops and all LPM outcrops, the frequency-size plots in log-log scale show a relatively concave shape characteristic of truncated power-law distributions (Fig. IV.7c, e; e. g. Gillespie et al., 1993; see §3.2), reflecting the fact that very thin veins could not be measured and large ones may have been missed.

The range of fractal dimension for vein thickness D(t) is 0.74-1.05 in LPU outcrops and 0.58-1.21 in LPM outcrops (Table IV.3). Values of D(t) are 1.32, 0.97 and 0.93, when considering all outcrops, all LPU outcrops and all LPM outcrops, respectively (Table IV.3). Nearly all transects have D(t) values close to 1, suggesting comparable proportions of thick and thin veins between the different outcrops (Table IV.3). Outcrop 10 has a D(t) value of 0.58 showing the greatest proportion of thick veins in this outcrop, whereas outcrop 8 with a D(t) of 1.21 has the greatest proportion of thin veins (Table IV.3).

Outcrop	Mean thick. (cm)	Med. thick. (cm)	sd thick. (cm)	Mean spac. (cm)	Med. spac. (cm)	sd spac. (cm)	D(t)	R^2	D(s)	R^2	Cv spac.	D(c)	R^2
All outcrops	0.9	0.3	1.8	4.4	2.4	5.8	1.24-1.32	0.935-0.987	1.31	0.979	1.31	/	/
All LPU outcrops	1.0	0.3	2.1	4.4	2.3	5.6	1.15-0.97	0.934-0.975	1.58	0.992	1.27	/	/
All LPM outcrops	0.7	0.2	1.2	4.5	2.7	6.2	1.20-0.93	0.935-0.984	1.33	0.992	1.38	/	/
1	0.6	0.2	1.7	1.9	1.1	3.1	1.05	0.968	1.72	0.984	1.68	0.79	0.996
2	0.8	0.2	1.5	3.5	2.6	3.3	0.96	0.954	1.17	0.962	0.94	0.60	0.984
3	1.8	0.5	3.8	5.5	2.5	7.6	0.78	0.965	0.72	0.994	1.38	0.60	0.976
4	0.6	0.2	0.9	4.5	2.8	6.3	0.96	0.944	1.21	0.988	1.39	0.78	0.984
5	1.1	0.5	1.6	6.4	4.2	6.4	1.01-0.99	0.912-0.981	1.71	0.991	1.00	0.66	0.976
6	1.2	0.4	2.2	6.0	4.1	6.1	0.92-0.74	0.903-0.987	1.72	0.984	1.02	0.65	0.984
7	0.5	0.2	0.9	4.1	2.8	3.9	0.94	0.972	1.26	0.977	0.96	0.56	0.931
8	0.4	0.2	0.6	3.7	2.5	3.2	1.21	0.910	1.28	0.986	0.87	0.86	0.978
9	0.8	0.2	1.3	8.2	4.15	8.2	0.79	0.957	0.79	0.958	1.00	0.46	0.928
10	1.1	0.4	1.9	5.0	2.3	8.4	0.78-0.58	0.906-0.984	0.92	0.989	1.68	0.63	0.979
11	0.4	0.2	0.7	2.8	2.7	1.9	1.08	0.992	2.48	0.981	0.67	0.61	0.967
12	0.8	0.4	1.3	4.3	2.25	6.9	0.99	0.937	0.89	0.985	1.60	0.81	0.986

***Table IV.3**: Statistical data on vein distribution (vein thickness, vein spacing, and vein clustering). In some outcrops, vein thickness is affected by truncation artefacts (All outcrops, all LPU, all LPM, outcrops 5, 6, 10). For these outcrops D(t) and R^2 value are presented for all the dataset (left of the tick) and for the central linear section of the dataset (right of the tick).*

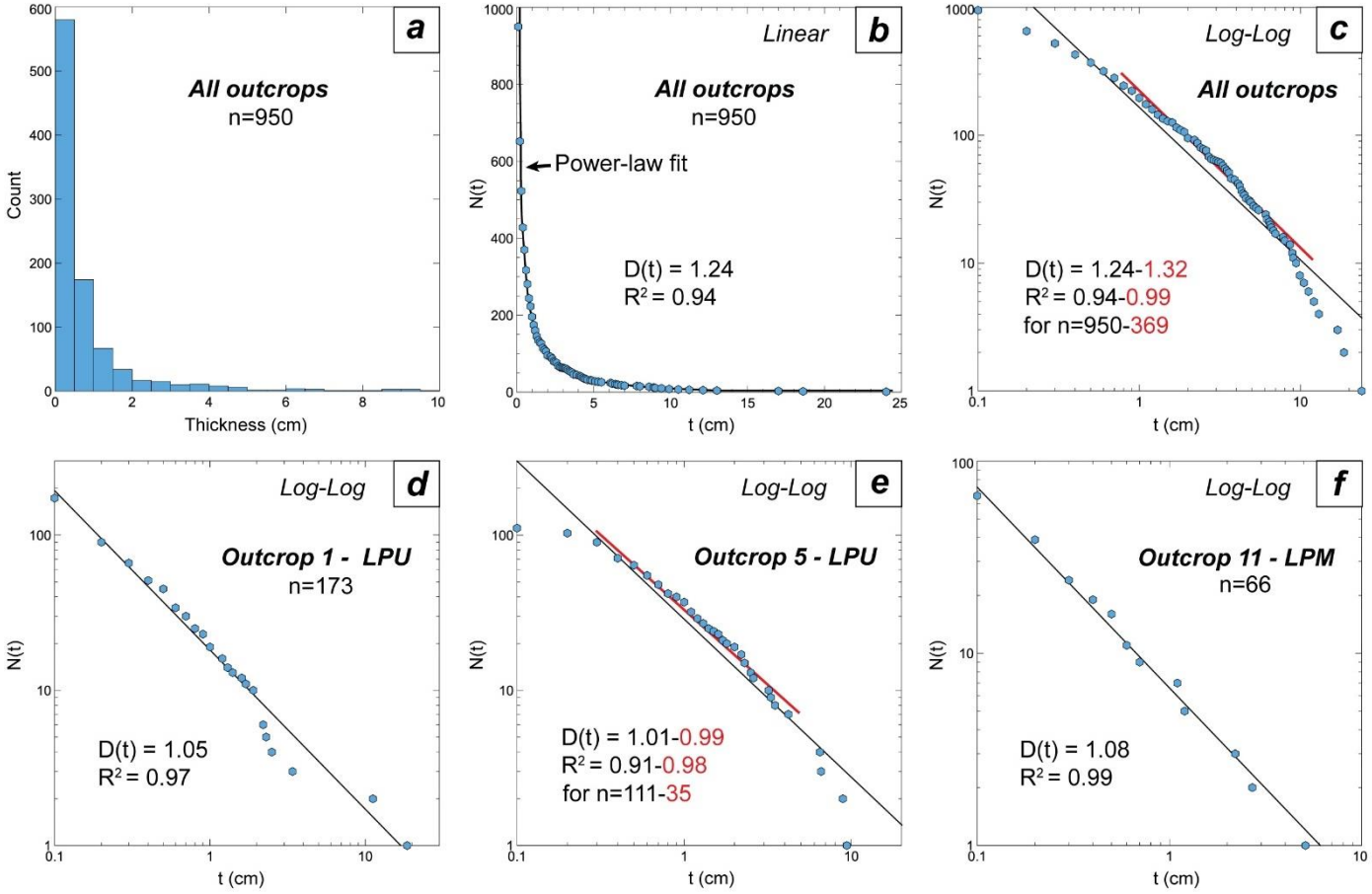

***Figure IV.7**: Vein thickness distribution. A) Histogram of all measured vein thicknesses. B) Frequency-size plot in linear scale of all measured vein thicknesses and fit with a power law (black curve). C) to F) Frequency-size plot in log-log scale of all thicknesses and representative outcrops. Lines correspond to linear regressions in log-log scale and therefore fits with power laws. Black lines correspond to power law fits for all measures while red lines correspond to power law fits for a range of values in truncated datasets.*

5.2 Vein spacing distribution

As for thicknesses, vein spacings vary largely, between 0.1 cm (resolution of the method, see §3.2) and 53.6 cm. The mean and median spacing ranges for outcrops are respectively 1.9-8.2 cm and 1.1-4.2 cm (Table IV.1). The mean/median spacings between veins from all outcrops, all LPU outcrops and all LPM outcrops are quite similar (4.4/2.4 cm, 4.4/2.3 cm and 4.5/2.7 cm, respectively).

The statistical distribution of spacings is not linear, as shown by cumulative histograms and frequency-size plot (Fig. IV.8a; Sup. mat. IV.2). These plots highlight the dominance of small spacings, yet with a lesser amount of spacings <0.5 cm (Fig. IV.8a), suggesting a poor fit via a power law. In log-linear scale, some frequency-size plots show a nice linear trend suggesting that vein spacings have a good fit with log-linear or exponential distributions (Fig. IV.8b). Conversely, some outcrop frequency-size plots rather have a concave-shape (Fig. IV.8c), demonstrating that the distribution of vein spacings does not correspond to log-linear or negative exponential distributions. The cumulative histogram of the Napierian logarithm of normalized vein spacing (each spacing divided by median spacing) for all outcrops has an almost symmetric shape, suggesting that spacings follow a log-normal distribution (Fig. IV.8d; Narr and Suppe, 1991) – contrary to single outcrops (Sup. mat. IV.2). Frequency-size plots of spacings in log-log scale have a concave shape with a central linear part (Fig. IV.8e, f) suggesting that, as for vein thickness, the distribution of spacings was affected by truncation of both small and large spacings (Barton and Zoback, 1992; Gillespie et al., 1993; Pickering et al., 1995; Fagereng, 2011).

The fractal dimension of vein spacing D(s) is thus calculated by linear regression on the central linear part of the curves (Fig. IV.8e, f). All coefficients of determination are greater than 0.96 (Table IV.3), and nearly always greater than those calculated in log-linear scale (Sup. mat. IV.2). The range of D(s) is 0.72-1.72 in LPU units and 0.79-2.48 in LPM units (Table IV.3), and 1.31, 1.58 and 1.33 for all, all LPU, and all LPM outcrops datasets, respectively (Table IV.3). Changes in D(s) values reflect differences in the proportions of thin and thick spacings, and greater D(s) value correspond to a greater proportion of thin veins. The variation of these fractal dimensions (0.72 to 2.48; Table IV.3) points to significant differences in vein spacing among outcrops. With D(s) values lower than 1, outcrops 3, 9, 10 and 12 have a much greater proportion of large spacings than the others where D(s) are greater than 1 (Table IV.3). Outcrops 2, 4, 7 and 8 showing D(s) around 1.2-1.3 have comparable proportion of small and large spacings (Table IV.3). With D(s) values around 1.7, outcrops 1, 5, 6 also have a comparable number of large and small spacings, yet with a greater proportion of thin spacings

than outcrops 2, 4, 7 and 8. Finally outcrop 11, with a D(s) value of 2.48, has the greatest proportion of small spacings amongst all studied outcrops.

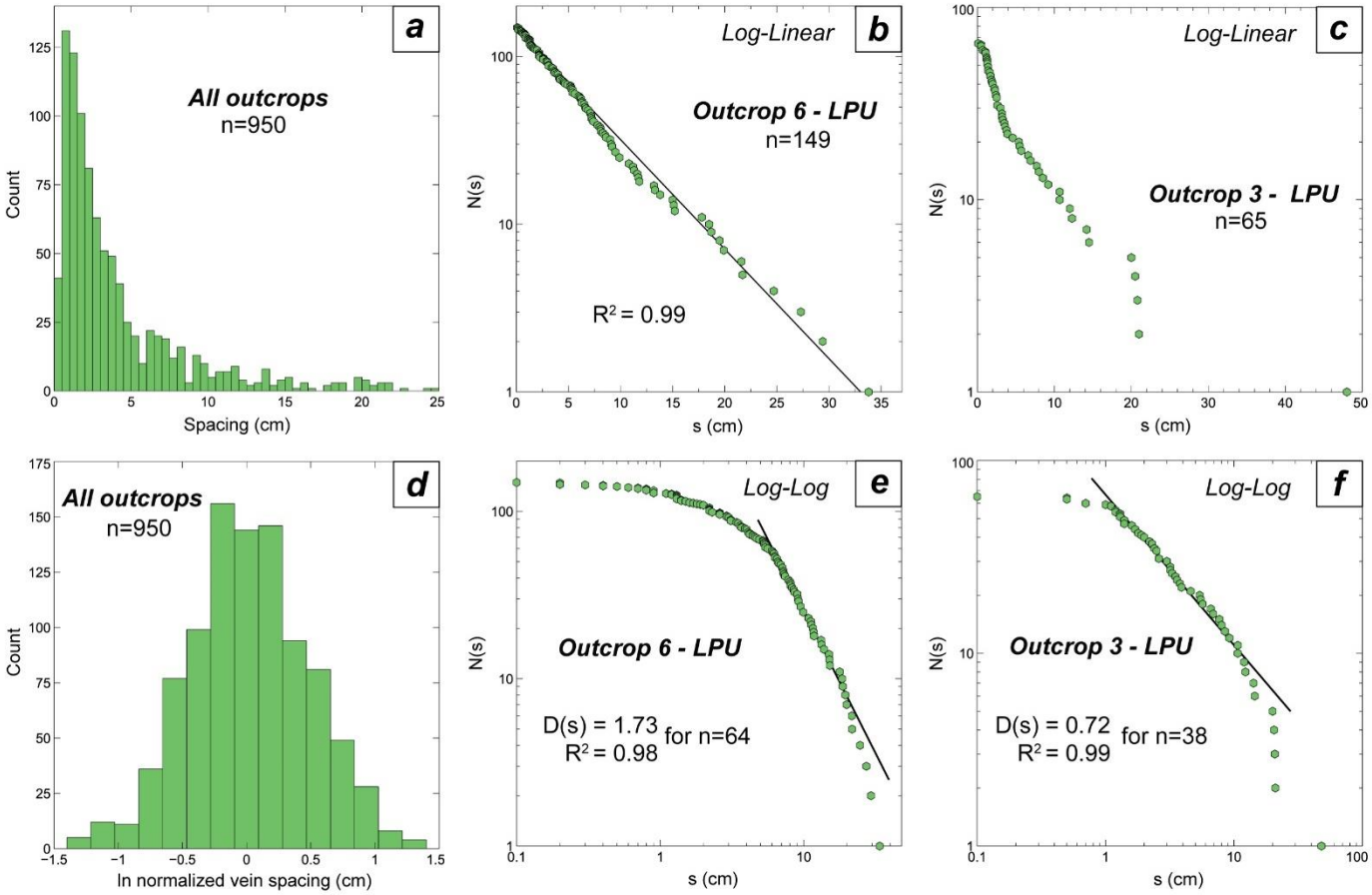

Figure IV.8*: Vein spacing distribution. A) Histogram of all measured vein spacings. B), C) Frequency-size plots of vein spacings in log-linear scale for two outcrops. The black line in B) correspond to a linear regression in log-linear scale and therefore to a fit with a log-normal or exponential law. D) Histogram of Napierian logarithm of normalized vein spacing (each spacing divided by median spacing). E), F) Frequency-size plots of vein spacings in log-log scale for two outcrops. Linear regressions correspond to fit with power laws for the central linear part of these truncated datasets.*

5.3 Vein clustering

Using the method of Manning (1994; see §3.2), frequency size plots of log N(r) versus log (1/r) show curved tendencies (Fig. IV.9a-c; Sup. mat. IV.3) as for vein spacing distributions and some vein thickness distributions (Fig. IV.8e, f, IV.7c, e). Most of the points of these plots show a linear trend up to a high log N(r) and high log (1/r) value where the slope changes to a concave shape (Fig. IV.9a-c). High log (1/r) values correspond to segments of small length r, the break in slope then occurs for a high number (high N(r)) of small divisions of the transects. This suggest that as the size of segments gets closer to the minimum vein spacing and thickness, the number of boxes containing at least one

vein stops increasing because of truncation of small veins and small spacings (Stowell et al., 1999). The fractal dimension of clustering D(c) can be calculated for the linear sections of the trends, for which coefficients of determination are greater than 0.93 (Table IV.3).

D(c) values provide a direct information on how veins cluster in outcrops, with an increase of D(c) reflecting an increasing filling of space by veins and a decreasing clustering (Manning, 1994; Barton, 1995; Madge et al., 1995; Fagereng, 2011). For intersection of veins with a transect, the distribution is fractal if 0<D(c)<1 (Manning, 1994). If D(c) is equal to 0.5, the spacing of veins is uncorrelated; from 0.5 to 0 the veins are increasingly clustered (Barton, 1995), whereas from 0.5 to 1 veins are less clustered and more evenly spaced (Barton, 1995). The mean D(c) for the LPU and LPM outcrops are 0.68 and 0.65 respectively, suggesting only low clustering and a relatively uniform spacing of veins. For single outcrops, D(c) values are in 0.60-0.79 and 0.46-0.86 range for LPU and LPM, respectively (Table IV.3), showing subtle variations of clustering. With a D(c) of 0.46, outcrop 9 shows the greatest clustering of all transects, whereas outcrops 1, 4, 8 and 12 are the least clustered (0.78-0.86; Table IV.3).

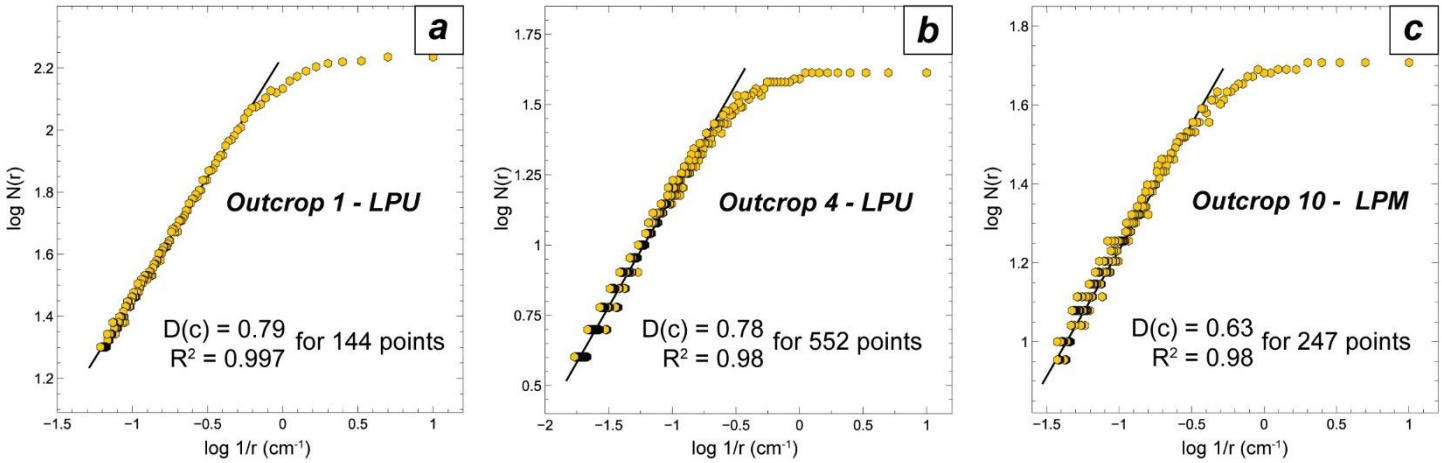

Figure IV.9: *A), B), C) Vein clustering following the methodology of Manning (1994). Black lines correspond to fits with power laws for the linear part of these truncated datasets.*

The coefficient of variation (ratio of standard variation to the mean) of vein spacing Cv (see table IV.2) provides an additional evaluation of clustering (Cox and Lewis, 1966; McCaffrey and Johnston, 1996; Gillespie et al., 1999; Foxford et al., 2000; Fagereng, 2011; Lahiri et al., 2011): Cv=0 if veins are equally spaced; Cv=1 for a random/independent distribution; Cv>1 if veins are clustered; Cv<1 if they are unclustered. Combined datasets yield 1.31, 1.27 and 1.38 for all, all LPU and all LPM outcrops,

respectively. Five over twelve transects (outcrops 1, 3, 4, 10, 11; Table IV.3) have Cv>1, indicating that veins are somewhat clustered. Three outcrops (5, 6 and 9; Table IV.3) have Cv spacing close to 1, indicating a random distribution, and the four remaining ones (2, 7, 8, 11; Table IV.3) have Cv<1, indicating anticlustered and regularly spaced veins.

Yet the evaluation of clustering obtained via D(c) and Cv only weakly correlates in the different outcrops (Table IV.3). This misfit was already observed (Fagereng, 2011) and is likely an artefact of the two different datasets considered for these calculations. Because of truncation artefacts, only a range of r was considered to obtain D(c), whereas Cv was obtained from the entire dataset, despite the fact that spacing distributions are also affected by truncation (see §3.2). We therefore consider that D(c) provides a better measure of clustering for our datasets.

5.4 Crack-seal inclusion trails and bands spacing

The spacing between lawsonite Inclusion trails was measured in one sample of LwsC vein and one sample of LwsB vein where crack-seal textures were particularly well preserved (Fig. IV.5a-d; §4.2). The spacing between fluid inclusions trails, interpreted as inclusions bands, was measured in lawsonite crystals of the same LwsB vein (Fig. IV.5e, f; §4.2). In these different trails and bands, the mean/median spacings are 6.3/5.5 µm 5.4/5.3 µm and 5.3/4.9 µm in lawsonite inclusion trails of the LwsC vein (n=432), lawsonite inclusion trails of the LwsB vein (n=139) and fluid inclusion bands of the same LwsB vein (n=100; Table IV.4), respectively. These very similar results for the three microstructures suggest that they may have formed through the same process.

As before, frequency-size plots and cumulative histograms are shown in Sup. mat. IV.4. No linear distribution was found (Fig. IV.10a, b), contrary to some previous studies (Fagereng et al., 2011). Some of the plots show fairly linear trends in log-linear scale, suggesting a possible good fit with log-normal or exponential distributions, as already shown in inclusion-bands from crack-seal veins (Renard et al., 2005), while some others don't (Fig. IV.10c). Frequency-size plots in log-log scale show concave trends, again with a fairly linear central section. Considering measurement issues (e.g., one cannot always tell if lawsonite inclusions are made of one of two crystals, so that some of the small inclusion spacings may have been missed), the central linear section of the log-log frequency-size plots was used to estimate the fractal distribution of inclusion spacings D(i) (see Table IV.2). Coefficients of determination are 0.99 for a significant part of the inclusion spacings (Fig. IV.10d-f). The D(i) value corresponds to the proportion of large versus small increments of displacement. D(i)

values are 2.72, 2.33 and 2.31 for lawsonite inclusion trails of the LwsC vein, lawsonite inclusion trails in the LwsB vein and fluid inclusion bands in the same LwsB vein, respectively (Table IV.3).

Vein type	Inclusion type	n measurements	Mean spac. (µm)	Med. spac. (µm)	sd spac. (µm)	D(i)	R^2
LwsC	Lws inclusion trails	432	6.3	5.5	3.9	2.72	0.989
LwsB	Lws inclusion trails	139	5.4	5.3	2.7	2.33	0.992
"	Fluid inclusions trails	100	5.3	4.9	2.5	2.31	0.987
"	Lws + fluid inclusions trails	239	5.4	5.0	2.6	2.67	0.993
LwsC + LwsB	Lws + fluid inclusions trails	671	6.0	5.3	3.5	2.82	0.993

***Table IV.4**: Statistical data on crack-seal inclusion bands and trails in lawsonite-bearing veins. Lws: lawsonite.*

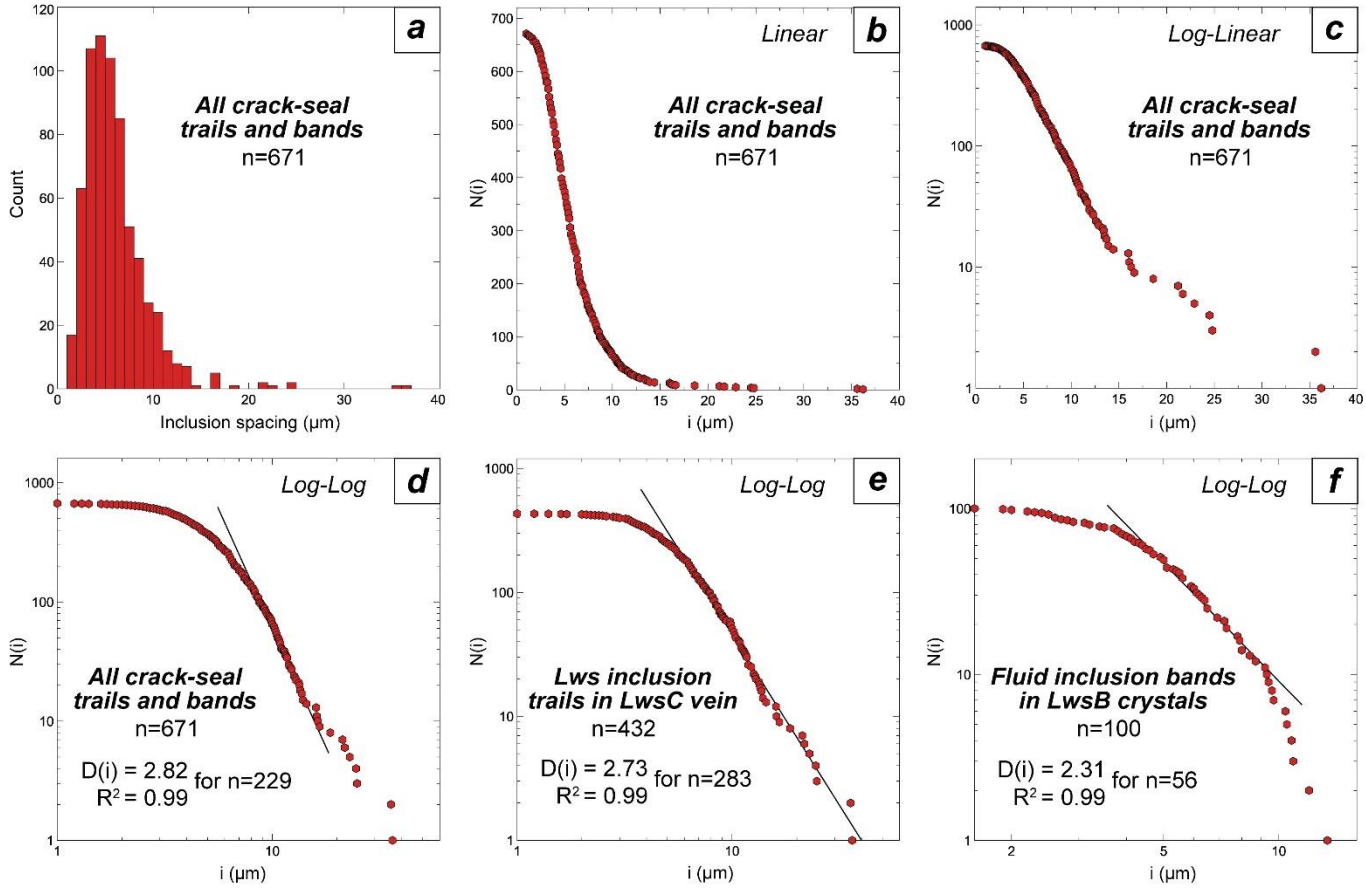

***Figure IV.10**: Spacings between crack-seal inclusion trails and bands. A) Histogram of all measured spacings between crack-seal bands and trails in lawsonite-bearing veins. B), C) Frequency-size plots of spacings between crack-seal bands and trails in lawsonite-bearing veins in linear and log-linear scales. D), E), F) Frequency-size plots of spacings between crack-seal bands and trails in lawsonite-bearing veins in log-log scale. Black lines correspond to fits with power laws on the linear part of these truncated datasets. Lws: lawsonite.*

6. Discussion

6.1 Mechanisms of vein formation in the Schistes Lustrés

High pressure veins of the Schistes Lustrés blueschist-facies metasediments contain lawsonite-bearing veins, either millimeter- to centimeter-long with mineral fibers perpendicular to the vein walls (LwsC veins), or decameter- to meter-long with mineral fibers parallel to the vein length (LwsB veins; part of the Fe-Mg carpholite-bearing veins; §4.1). While LwsC veins are readily interpreted as tension gashes formed by local extension through mode I fracturing, the formation of LwsB veins with lawsonite crystals parallel to the vein length is more enigmatic. Yet, in places where LwsB and LwsC coexist next to each other, LwsC veins are oriented at ~80-90° to LwsB veins (i.e., crystals oriented in the same direction), suggesting that these two types of veins may have formed under the same stress regime and possibly coevally (Fig. IV.5a-d). LwsB veins would thus form through incremental stretching and fiber growth during ductile deformation, in pressure shadows of rigid objects or by progressive opening under brittle failure.

This conclusion is strengthened by the existence of successive trails of lawsonite crystals parallel to the fibers in LwsB and LwsC veins, and by fluid inclusion bands perpendicular to crystal fibers in both lawsonite- and Fe-Mg carpholite-bearing veins (§4.2; Fig. IV.6). Collectively, these observations show that LwsB, LwsC and Fe-Mg carpholite-bearing veins formed as crack-seal veins (Ramsay, 1980; Cox, 1987) through repeated cycles of fracturing and mineral growth under high fluid pressure, with an opening direction parallel to the macroscopic fibers of lawsonite and Fe-Mg carpholite (Fig. IV.11). In the LwsB and elongate Fe-Mg carpholite-bearing veins best preserved from later folding of the S1 schistosity, the roof and ground walls are sharp (Fig. IV.5a, b, d) and shear senses can be observed at the contacts between the veins and the wall-rock. This suggests that fractures opened under mode II shear failure (Fig. IV.5d), and that these veins formed by local extension between faults or shear planes in cm-scale pull-aparts (Fig. IV.11), as suggested by Fagereng et al. (2010, 2011; see also Bons et al., 2012; Lemonnier et al., 2020).

The elongate high-pressure mineral-bearing veins studied here thus likely formed along weak cleavage/schistosity planes (similar to Fagereng et al., 2010; Fig. IV.11), during prograde to peak burial under the dominant subduction zone shear regime. Incremental crystal growth along the long axis of the vein reflects the strength ratio contrast between the matrix and the growing vein (e.g., LwsB vein), deformation being partitioned between distributed dissolution-precipitation creep in the matrix and brittle opening along the relatively stronger growing vein.

The similar spacings and D(i) values between the crack-seal textures (trails and bands) of LwsB and LwsC veins (Table IV.4; §5.4) indicate that some of the small veins classified as LwsC also formed incrementally along small pull-apart jogs, rather than as tension gashes (Fig. IV.11). LwsB pull-apart veins would therefore correspond to long-lived structures built through successive shear increments along or close to the subduction interface (Fig. IV.11). Such dilational shear veins showing incremental growth have been mentioned as a potential geological record of SST (Fagereng et al., 2011; Ujiie et al., 2018; Kirkpatrick et al., 2021; Behr and Bürgmann, 2021; Giuntoli and Viola, 2021). Similar 'dilational hydroshear' veins containing Fe-Mg carpholite were described in the Northern Apennines (Italy; Giuntoli and Viola, 2021).

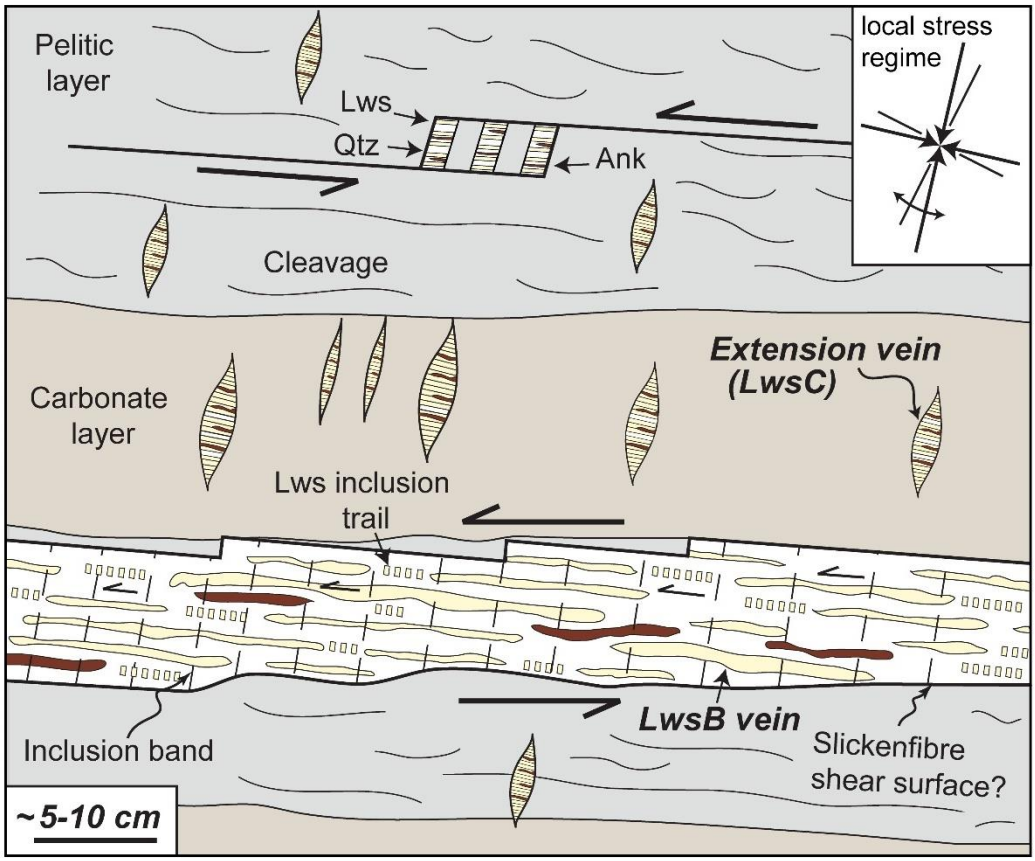

Figure IV.11*: Schematic drawing of the inferred mechanisms of vein formation and of the geometrical relationship between shear and extension veins. Inferred instantaneous local stress regime is in top right. Modified after Fagereng et al. (2010).*

6.2 Vein distribution in the Schistes Lustrés and implications for fluid flow

Vein thicknesses follow relatively well-defined power-law distributions, despite minor deviations in some outcrops (Fig. IV.7a-f; §5.1). Vein spacing, vein clustering and inclusion spacing show instead significant deviations from power-law distributions, as previously reported, commonly interpreted as

the result of truncation artefacts (e.g. Gillespie et al., 1999; Fig. IV.8a-h, IV.9a-h; §5.2, 5.3, 5.4). However, contrary to almost all previous studies of vein distribution (e.g. Sanderson et al., 1994; Fisher et al., 1995; Clark et al., 1995; see §2), the studied veins did not form by extension along the measured transects, but through schistosity-parallel incremental growth (§6.1). Therefore, the power-law distribution of vein thickness and vein spacing cannot be ascribed to the accommodation of general extension by nucleation and growth of veins (unlike Clark et al., 1995). A second consequence is that the extent to which the polyphase deformation of the Schistes Lustrés metasediments may have modified vein thickness/spacing and fractal dimensions must be assessed.

Folding and cumulative deformation may have 'multiplied' the number of veins along the measured transects, thereby affecting vein density and vein spacing. Thicknesses may also have been modified through folding and/or distributed pressure-solution processes (Gratier et al., 2013). Whether pressure-solution was distributed homogeneously or not, either across the outcrop, between the veins and host rocks or between the thin and thick veins, is unknown. It is likely, however, that dissolution along veins walls was less intense than along the schistosity, so that the distribution of vein thicknesses was probably not modified too significantly. This conclusion is even more valid for clustering. In contrast, the distribution of vein spacing is more uncertain, since it depends on the strain localization history. Despite these possible artefacts, it is in any case unlikely that later deformation generated the power-law distributions retrieved in our datasets. Furthermore, since all the studied transects were affected by the same deformation events, with veins lying along the composite D1-D2 main schistosity (§3.2), it is legitimate to compare their statistical distributions.

Calculated distributions for combined datasests show that the studied Schistes Lustrés outcrops have a great proportion of thin veins (power-law distributions with D(t) greater or close to 1 and mean thickness around 1 cm; Table IV.3) and thin spacings (power-law distributions with D(s) greater than 1; mean spacings around 4.5 cm; Table IV.3). This suggests that fluids mostly circulated pervasively through the rock rather than along major localized conduits. Moreover, the mean D(c) of 0.67 for all studied outcrops indicate a weak clustering of veins, in agreement with pervasive fluid flow. Fluid channelization, if any, must therefore be searched for at a greater scale (i.e., hm- to km-scale, where vein densities are higher), possibly along major tectonic contacts (Jaeckel et al., 2018). The conclusion that fluid flow was overall pervasive is also consistent with most geochemical studies on the Schistes Lustrés veins, which advocate for local fluid redistribution (e.g. Henry et al., 1996; Agard et al., 2000; Herviou et al., 2021).

For individual outcrops, 7/12 studied transects (group 1; outcrops 1, 4, 5, 6, 8, 11, 12) have a great proportion of thin veins (D(t) in the range 0.92-1.21 with most values greater than 1; see Table IV.3), a great proportion of small spacings (D(s) in the range 1.21-2.48) and a weak clustering of veins (D(c) in the range 0.61-0.86 with most values greater than 0.65-0.7). In contrast, 3/12 of the studied transects (group 2; outcrops 3, 9, 10) show a more localized distribution and connection of veins, with a greater proportion of thick veins (D(t)<1 and in the range 0.58-0.79), of thick spacings (D(s)<1 and in the range 0.72-0.92) and a greater clustering (D(c) in the range 0.46-0.63), suggesting a possibly more channelized fluid flow than for group 1. The two remaining transects (group 3; outcrops 2 and 7) show slightly different characteristics, with a greater proportion of thick veins than group 1 (D(t) ~0.94-0.96), a smaller proportion of thick spacings than group 2 but generally greater than group 1 (D(s) ~1.17-1.26) and a greater clustering than group 1 (D(c) ~0.56-0.60). Differences in vein distribution between the various outcrops do not correlate with the abundance of veins in a given outcrop (Fig. IV.4; 10.3-29.5 %, 9.2-32.4 %, 12.1-22 % in groups 1, 2 and 3 respectively; Table IV.1).

In the slightly more clustered vein systems of groups 2 and 3, 3/5 outcrops belong to the LPM units (outcrops 7, 9, 10) and the mean D(c) is similar in both LPM and LPU transects. The combined datasets of LPM outcrops have however a slightly greater proportion of thick veins, thick spacings (D(t)=0.93, D(s)=1.33) than LPU outcrops (D(t)=0.97, D(s)=1.58). This could suggest that fluid flow was somewhat more channelized in the LPM outcrops, which could tentatively be ascribed to greater porosity/permeability differences in the more carbonate-rich LPM protoliths (Herviou et al., 2022). Alternatively, local contrasts in vein spacing and/or vein distribution may essentially reflect strain partitioning, partly along inherited discontinuities (e.g., between the weaker early cleavage or fractures planes), and thereby provide an image of strain distribution. Stylolitic cleavage planes or joint/fracture planes indeed tend to follow power-law distributions too (La Pointe, 1988; Velde et al., 1990, 1991; Barton and Zoback, 1992; Ledésert et al., 1993; Hooker et al., 2013).

6.3 Implications for deformation and rupture processes at the downdip end of the seismogenic zone

Crack-seal lawsonite- and Fe-Mg carpholite-bearing veins formed by successive increments of fracturing, fluid infiltration and growth in the same depth range as most SST (25-55 km). The Schistes Lustrés metasediments contain large amounts of veins (9.2-32.4% in the studied outcrops; Table IV.1) and high-pressure hydrous minerals in host rocks (e.g. Lefeuvre et al., 2020) attesting to the ubiquitous presence of fluids at peak burial conditions. Tension gashes filled by high-pressure mineral

assemblages and crack-seal textures argue for high fluid pressure during vein formation. The Schistes Lustrés metasediments therefore represent a likely host for the low-velocity layer observed in modern subduction zones at SST depths (Audet et al., 2009; Calvert et al., 2011; Hansen et al., 2012; Bostock, 2013; Delph et al., 2021), and these crack-seal veins may represent the rock record of SST.

In LwsB and LwsC veins, the spacing between lawsonite inclusions in trails and inclusion bands, interpreted as displacement increments, is on the order of ~5 µm (Table IV.3; §5.4). We interpret the shear surfaces bounding the elongate LwsB and carpholite-bearing veins (and some of the LwsC veins; §6.1, Fig. IV.11) as extremely weak planes where preferential slip occurs (Fagereng et al., 2010, 2011; Fig. IV.5a-e, IV.11).

Considering a minimum rupture length L slightly longer than the vein length (~1 m) and up to the outcrop length (~10 m), the calculated shear stress drop $\Delta\tau$, based on slip increments d ~5 µm and a shear modulus µ ~3-30 GPa (for sediments; Geist and Bilek, 2001 and references therein), would be in the range 1.5-150 kPa (using $d/L=\Delta\tau/G$; Wells and Coppersmith, 1994; see also Fagereng et al., 2011). This value is consistent with shear stress drop estimates for slow-slip events, episodic tremor and slip and low-frequency earthquakes (1-100 kPa; Behr and Bürgmann and references therein).

The spacing between lawsonite inclusions in trails and inclusion bands is best described by power laws affected by truncation at small and large spacing values (§5.4; Fig. IV.10a-f). Fault planes geometry, as well as the relationship between the frequency and magnitude of regular earthquakes, follow power-law distributions (Gutenberg and Richter, 1954; Watterson, 1986; Jackson and Sanderson, 1992; Pickering et al., 1995, 1996). This is also the case for slow slip and tremors between the moment and duration, between the moment and the rupture area (or length), between the fault length and fault width, between the number of tremor swarms and their duration (Ide et al., 2007; Wech et al., 2010; Gao et al., 2012; Gomberg et al., 2016; Michel et al., 2019b; Dal Zilio et al., 2020). As for regular earthquakes, a power-law relationship between magnitude and frequency (Gutenberg-Richter law; Gutenberg and Richter, 1954) was suggested for slow slip events (Wech et al., 2010; Michel et al., 2019b; Chiba, 2019, 2020).

Since we interpret crack-seal spacing as individual slip increments, one may try to compare these data directly with SST data. Using a catalogue of 40 slow slip events from the Cascadia megathrust (Michel et al., 2019b), obtained by spatial inversion of surface deformation between 2007 and 2017 (Michel et al., 2019a), we show that the mean duration of slow slip events follows a power-law distribution with a fractal exponent D in the same range as for crack-seal texture spacings (D>2; Fig.

IV.12a). It is also possible to use the relationship $A= kd^2$ linking the rupture area A, the slip increment d, and the coefficient of proportionality k assumed for circular ruptures (e.g., Dal Zilio et al., 2020). For slip increments of ~5 µm on a 100 m^2 (outcrop scale) and 1 m^2 (vein scale), the magnitude of k lies between 10^{12} and 10^{10}, respectively. Using these assumptions, the moment magnitude for lawsonite inclusion spacings can be calculated, using $Mw=2/3 \log (\mu kd^3) - 6.07$ and a shear modulus µ ~30 GPa. The frequency-magnitude plot reveals a linear trend comparable to the classical Gutenberg-Richter law followed by earthquakes and slow slip events (Fig. IV.13b). The fractal exponent (~1.3; Fig. IV.12b) is similar to some high b-value estimated for slow slip events (Chiba, 2019, 2020), suggesting that our crack-seal textures formed at the downdip end of the seismogenic zone may correspond to the record of successive slow slip events during subduction of the Liguro-Piemont ocean.

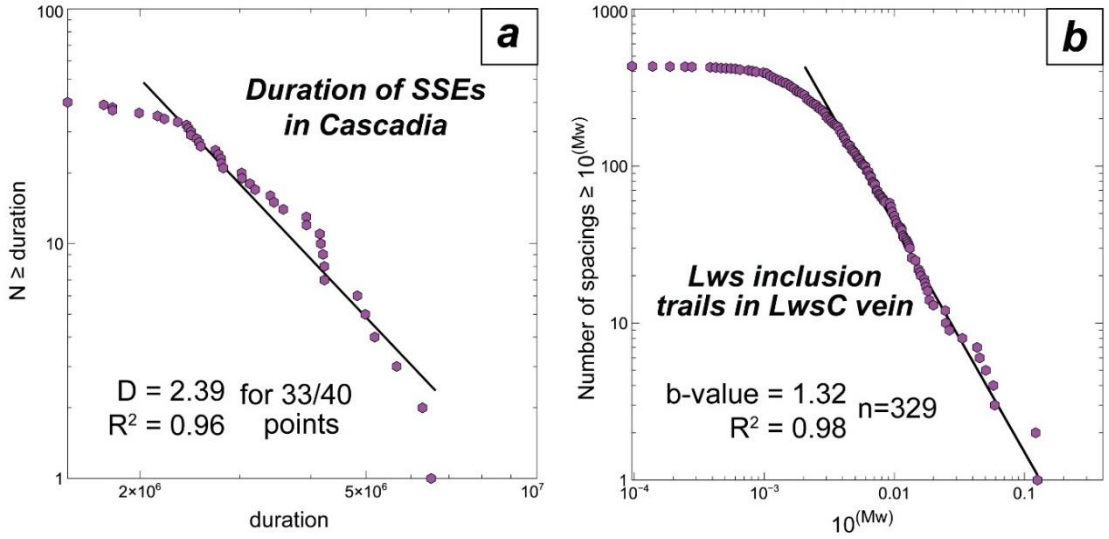

***Figure IV.12**: A) Frequency-duration plot for slow slip events in Cascadia using the catalogue of Michel et al. (2019a). B) Frequency-magnitude plot estimated from the spacing between lawsonite inclusion trails considered as slip increments. Black lies correspond to fit with power laws in the central linear part of these truncated datasets. SSEs: slow slip events; Lws: lawsonite.*

Conclusion

In the Liguro-Piemont domain of Western Alps, lawsonite and Fe-Mg carpholite veins abound, formed at blueschist-facies conditions in the Schistes Lustrés sediments, abound. This study provides insights about the mechanism that drive and control vein formation, deformation and fluid flow:

(1) Vein thickness fit a power-law distribution while vein spacing and clustering show significant deviations from power laws interpreted as the result of truncation artefacts. Vein distribution at the outcrop scale suggests that fluids mostly circulated pervasively through the rock rather than along major localized conduits, in agreement with geochemical studies.

(2) Through the study of vein textures at macroscopic and microscopic scale we showed that veins formed by incremental crack-seal mechanisms under tensile and shear failure and possibly between extremely weak planes.

(3) The spacings between crack seal inclusion trails and bands fit a power law for a small fractal range and have fractal exponents similar to those estimated for slow slip event features. In addition, the shear stress drop estimated for our crack-seal veins is consistent with those inferred for slow slip and tremors.

(4) The studied veins formed at the downdip end of the seismogenic zone may correspond to the record of successive slow slip events during subduction of the Liguro-Piemont ocean.

References

Abers, G.A., MacKenzie, L.S., Rondenay, S., Zhang, Z., Wech, A.G., Creager, K.C., 2009. Imaging the source region of Cascadia tremor and intermediate-depth earthquakes. Geology 37, 1119–1122. https://doi.org/10.1130/G30143A.1.

Agard, P., 2021. Subduction of oceanic lithosphere in the Alps: Selective and archetypal from (slow-spreading) oceans. Earth-Science Reviews 214, 103517. https://doi.org/10.1016/j.earscirev.2021.103517.

Agard, P., Goffé, B., Touret, J.L.R., Vidal, O., 2000. Retrograde mineral and fluid evolution in high-pressure metapelites (Schistes lustrés unit, Western Alps). Contributions to Mineralogy and Petrology 140, 296–315. https://doi.org/10.1007/s004100000190.

Agard, P., Handy, M.R., 2021. Ocean Subduction Dynamics in the Alps. Elements 17, 9–16. https://doi.org/10.2138/gselements.17.1.9.

Agard, P., Jolivet, L., Goffe, B., 2001. Tectonometamorphic evolution of the Schistes Lustres Complex; implications for the exhumation of HP and UHP rocks in the Western Alps. Bulletin de la Société Géologique de France 172, 617–636. https://doi.org/10.2113/172.5.617.

Agard, P., Monie, P., Jolivet, L., Goffe, B., 2002. Exhumation of the Schistes Lustres complex: in situ laser probe 40Ar/39Ar constraints and implications for the Western Alps. J Metamorph Geol 20, 599–618. https://doi.org/10.1046/j.1525-1314.2002.00391.x.

Agard, P., Plunder, A., Angiboust, S., Bonnet, G., Ruh, J., 2018. The subduction plate interface: rock record and mechanical coupling (from long to short timescales). Lithos 320–321, 537–566. https://doi.org/10.1016/j.lithos.2018.09.029.

Agard, P., Yamato, P., Jolivet, L., Burov, E., 2009. Exhumation of oceanic blueschists and eclogites in subduction zones: Timing and mechanisms. Earth-Science Reviews 92, 53–79. https://doi.org/10.1016/j.earscirev.2008.11.002.

Allègre, C.J., Le Mouel, J.L., Provost, A., 1982. Scaling rules in rock fracture and possible implications for earthquake prediction. Nature 297, 47–49. https://doi.org/10.1038/297047a0.

André-Mayer, A.-S., Sausse, J., 2007. Thickness and spatial distribution of veins in a porphyry copper deposit, Rosia Poieni, Romania. Journal of Structural Geology 29, 1695–1708. https://doi.org/10.1016/j.jsg.2007.06.010.

Angiboust, S., Glodny, J., 2020. Exhumation of eclogitic ophiolitic nappes in the W. Alps: New age data and implications for crustal wedge dynamics. Lithos 356–357, 105374. https://doi.org/10.1016/j.lithos.2020.105374.

Araki, E., Saffer, D. M., Kopf, A. J., Wallace, L. M., Kimura, T., Machida, Y., Ide, S., Davis, E., IODP expedition 365 shipboard scientists, 2017. Recurring and triggered slow-slip events near the trench at the Nankai Trough subduction megathrust. Science 356, 1157–1160.

Audet, P., Bostock, M.G., Christensen, N.I., Peacock, S.M., 2009. Seismic evidence for overpressured subducted oceanic crust and megathrust fault sealing. Nature 457, 76–78. https://doi.org/10.1038/nature07650.

Audet, P., Bürgmann, R., 2014. Possible control of subduction zone slow-earthquake periodicity by silica enrichment. Nature 510, 389–392. https://doi.org/10.1038/nature13391.

Barton, C. C, 1995. Fractal analysis of scaling and spatial clustering of fractures. In Fractals in the earth sciences, Springer, Boston, MA. 141–178.

Barton, C. C, Larsen, E, 1985. Fractal geometry of two-dimensional fracture networks at Yucca Mountain, southwest Nevada. Fundamentals of Rock Joints, Proceedings of the International Symposium on Fundamentals of Rock Joints, Bjorkliden, Lapland, Sweden (0. Stephannson, ed.).

Barton, C.A., Zoback, M.D., 1992. Self-similar distribution and properties of macroscopic fractures at depth in crystalline rock in the Cajon Pass Scientific Drill Hole. J. Geophys. Res. 97, 5181. https://doi.org/10.1029/91JB01674.

Bebout, G.E., Agard, P., Kobayashi, K., Moriguti, T., Nakamura, E., 2013. Devolatilization history and trace element mobility in deeply subducted sedimentary rocks: Evidence from Western Alps HP/UHP suites. Chemical Geology 342, 1–20. https://doi.org/10.1016/j.chemgeo.2013.01.009.

Behr, W.M., Bürgmann, R., 2021. What's down there? The structures, materials and environment of deep-seated slow slip and tremor. Phil. Trans. R. Soc. A. 379, 20200218. https://doi.org/10.1098/rsta.2020.0218.

Berger, A., Bousquet, R., 2008. Subduction-related metamorphism in the Alps: review of isotopic ages based on petrology and their geodynamic consequences. Geological Society, London, Special Publications 298, 117–144. https://doi.org/10.1144/SP298.7.

Beyssac, O., Goffé, B., Chopin, C., Rouzaud, J.N., 2002. Raman spectra of carbonaceous material in metasediments: a new geothermometer. Journal of Metamorphic Geology 20, 859–871. https://doi.org/10.1046/j.1525-1314.2002.00408.x.

Blenkinsop, T. G, 1991. Cataclasis and processes of particle size reduction. PAGEOPH 136, 59–86.

Blenkinsop, T.G., Fernandes, T.R.C., 2000. Fractal Characterization of Particle Size Distributions in Chromitites from the Great Dyke, Zimbabwe. Pure appl. geophys. 157, 505–521.

Bons, P.D., Elburg, M.A., Gomez-Rivas, E., 2012. A review of the formation of tectonic veins and their microstructures. Journal of Structural Geology 43, 33–62. https://doi.org/10.1016/j.jsg.2012.07.005.

Bostock, M.G., 2013. The Moho in subduction zones. Tectonophysics 609, 547–557. https://doi.org/10.1016/j.tecto.2012.07.007.

Brantley, S.L., Fisher, D.M., Deines, P., Clark, M.B., Myers, G., 1997. Segregation veins: Evidence for the deformation and dewatering of a low-grade metapelite, in: Deformation-Enhanced Fluid Transport in the Earth's Crust and Mantle. pp. 267–288.

Braun, M.G., Kelemen, P.B., 2002. Dunite distribution in the Oman Ophiolite: Implications for melt flux through porous dunite conduits. Geochem.-Geophys.-Geosyst. 3, 1–21. https://doi.org/10.1029/2001GC000289.

Calvert, A.J., Preston, L.A., Farahbod, A.M., 2011. Sedimentary underplating at the Cascadia mantle-wedge corner revealed by seismic imaging. Nature Geosci 4, 545–548. https://doi.org/10.1038/ngeo1195.

Caron, J.M., 1977. Lithostratigraphie et tectonique des Schistes Lustrés dans les Alpes Cottiennes septentrionales et en Corse orientale. PhD thesis, université de Strasbourg.

Caron, J.-M., 1974. Rapports entre diverses" generations" de lawsonite et les deformations dans les Schistes lustres des Alpes cottiennes septentrionales (France et Italie). Bulletin de la Société Géologique de France 7, 256–263.

Cartwright, I., Buick, I.S., 2000. Fluid generation, vein formation and the degree of fluid-rock interaction during decompression of high-pressure terranes: the Schistes Lustrés, Alpine Corsica, France. Journal of Metamorphic Geology 18, 607–624. https://doi.org/10.1046/j.1525-1314.2000.00280.x.

Cerchiari, A., Remitti, F., Mittempergher, S., Festa, A., Lugli, F., Cipriani, A., 2020. Cyclical variations of fluid sources and stress state in a shallow megathrust-zone mélange. Journal of the Geological Society 177, 647–659. https://doi.org/10.1144/jgs2019-072.

Chiba, K., 2020. Stress state along the western Nankai Trough subduction zone inferred from b-values, long-term slow-slip events, and low-frequency earthquakes. Earth Planets Space 72, 3. https://doi.org/10.1186/s40623-020-1130-7.

Chiba, K., 2019. Spatial and temporal distributions of b-values related to long-term slow-slip and low-frequency earthquakes in the Bungo Channel and Hyuga-nada regions, Japan. Tectonophysics 757, 1–9. https://doi.org/10.1016/j.tecto.2019.02.021.

Clark, M.B., Brantley, S.L., Fisher, D.M., 1995. Power-law vein-thickness distributions and positive feedback in vein growth. Geol 23, 975–978. https://doi.org/10.1130/0091-7613(1995)023<0975:PLVTDA>2.3.CO;2.

Cox, D. R, Lewis, P. A. W, 1966. The Statistical Analysis of Series of Events. Methuen, London.

Cox, S.F., 1987. Antitaxial crack-seal vein microstructures and their relationship to displacement paths. Journal of Structural Geology 9, 779–787. https://doi.org/10.1016/0191-8141(87)90079-4.

Cubas, N., Agard, P., Tissandier, R., 2022. submitted Predicting earthquake ruptures from topography.

Dal Zilio, L., Lapusta, N., Avouac, J., 2020. Unraveling Scaling Properties of Slow-Slip Events. Geophys. Res. Lett. 47. https://doi.org/10.1029/2020GL087477.

Delph, J.R., Levander, A., Niu, F., 2018. Fluid Controls on the Heterogeneous Seismic Characteristics of the Cascadia Margin. Geophys. Res. Lett. 45. https://doi.org/10.1029/2018GL079518.

Delph, J.R., Thomas, A.M., Levander, A., 2021. Subcretionary tectonics: Linking variability in the expression of subduction along the Cascadia forearc. Earth and Planetary Science Letters 556, 116724. https://doi.org/10.1016/j.epsl.2020.116724.

Deville, E., Fudral, S., Lagabrielle, Y., Marthaler, M., Sartori, M., 1992. From oceanic closure to continental collision: A synthesis of the" Schistes lustrés" metamorphic complex of the Western Alps. Geological Society of America Bulletin 104, 127–139.

Dragert, H., Wang, K., James, T.S., 2001. A Silent Slip Event on the Deeper Cascadia Subduction Interface. Science 292, 1525–1528. https://doi.org/10.1126/science.1060152.

Fagereng, Å., 2011. Fractal vein distributions within a fault-fracture mesh in an exhumed accretionary mélange, Chrystalls Beach Complex, New Zealand. Journal of Structural Geology 33, 918–927. https://doi.org/10.1016/j.jsg.2011.02.009.

Fagereng, Å., Cooper, A.F., 2010. The metamorphic history of rocks buried, accreted and exhumed in an accretionary prism: an example from the Otago Schist, New Zealand. Journal of Metamorphic Geology 28, 935–954. https://doi.org/10.1111/j.1525-1314.2010.00900.x.

Fagereng, Å., Harris, C., 2014. Interplay between fluid flow and fault–fracture mesh generation within underthrust sediments: geochemical evidence from the Chrystalls Beach Complex, New Zealand. Tectonophysics, 612, 147-157.

Fagereng, Å., Remitti, F., Sibson, R.H., 2010. Shear veins observed within anisotropic fabric at high angles to the maximum compressive stress. Nature Geosci 3, 482–485. https://doi.org/10.1038/ngeo898.

Fagereng, Å., Remitti, F., Sibson, R.H., 2011. Incrementally developed slickenfibers — Geological record of repeating low stress-drop seismic events? Tectonophysics 510, 381–386. https://doi.org/10.1016/j.tecto.2011.08.015.

Fisher, D.M., Brantley, S.L., 1992. Models of quartz overgrowth and vein formation: Deformation and episodic fluid flow in an ancient subduction zone. J. Geophys. Res. 97, 20043. https://doi.org/10.1029/92JB01582.

Fisher, D.M., Brantley, S.L., 2014. The role of silica redistribution in the evolution of slip instabilities along subduction interfaces: Constraints from the Kodiak accretionary complex, Alaska. Journal of Structural Geology 69, 395–414. https://doi.org/10.1016/j.jsg.2014.03.010.

Fisher, D.M., Brantley, S.L., Everett, M., Dzvonik, J., 1995. Cyclic fluid flow through a regionally extensive fracture network within the Kodiak accretionary prism. J. Geophys. Res. 100, 12881–12894. https://doi.org/10.1029/94JB02816.

Foxford, K.A., Nicholson, R., Polya, D.A., Hebblethwaite, R.P.B., 2000. Extensional failure and hydraulic valving at Minas da Panasqueira, Portugal: evidence from vein spatial distributions, displacements and geometries. Journal of Structural Geology 22, 1065–1086. https://doi.org/10.1016/S0191-8141(00)00029-8.

Fudral, S., 1996. Etude géologique de la suture tethysienne dans les Alpes franco-italiennes Nord-Occidentales de la Doire Ripaire (Italie) à la région de Bourg Saint-Maurice. PhD thesis Université de Savoie.

Gabalda, S., Beyssac, O., Jolivet, L., Agard, P., Chopin, C., 2009. Thermal structure of a fossil subduction wedge in the Western Alps. Terra Nova 21, 28–34. https://doi.org/10.1111/j.1365-3121.2008.00849.x.

Ganzhorn, A.C., Pilorgé, H., Reynard, B., 2019. Porosity of metamorphic rocks and fluid migration within subduction interfaces. Earth and Planetary Science Letters 522, 107–117. https://doi.org/10.1016/j.epsl.2019.06.030.

Gao, H., Schmidt, D.A., Weldon, R.J., 2012. Scaling Relationships of Source Parameters for Slow Slip Events. Bulletin of the Seismological Society of America 102, 352–360. https://doi.org/10.1785/0120110096.

Geist, E. L, Bilek, S. L, 2001. Effect of depth-dependent shear modulus on tsunami generation along subduction zones. Geophysical Research Letters 28, 1315–1318.

Gillespie, P.A., Howard, C.B., Walsh, J.J., Watterson, J., 1993. Measurement and characterisation of spatial distributions of fractures. Tectonophysics 226, 113-141.

Gillespie, P.A., Johnston, J.D., Loriga, M.A., McCaffrey, K.J.W., Walsh, J.J., Watterson, J., 1999. Influence of layering on vein systematics in line samples. Geological Society, London, Special Publications 155, 35–56. https://doi.org/10.1144/GSL.SP.1999.155.01.05.

Giuntoli, F., Viola, G., 2021. Cyclic Brittle-Ductile Oscillations Recorded in Exhumed High-Pressure Continental Units: A Record of Deep Episodic Tremor and Slow Slip Events in the Northern Apennines. Geochem Geophys Geosyst 22. https://doi.org/10.1029/2021GC009805.

Goffé, B., Chopin, C., 1986. High-pressure metamorphism in the Western Alps: zoneography of metapelites, chronology and consequences. Schweizerische Mineralogische Und Petrographische Mitteilungen 66, 41–52. https://doi.org/10.5169/SEALS-50880.

Gomberg, J., Wech, A., Creager, K., Obara, K., Agnew, D., 2016. Reconsidering earthquake scaling. Geophys. Res. Lett. 43, 6243–6251. https://doi.org/10.1002/2016GL069967.

Gratier, J. P., Dysthe, D. K., & Renard, F., 2013. The role of pressure solution creep in the ductility of the Earth's upper crust. Advances in geophysics, 54, 47-179.

Gutenberg, B, Richter, C. F, 1954. Seismicity of the Earth. Princeton University Press, Princeton.

Hansen, R.T.J., Bostock, M.G., Christensen, N.I., 2012. Nature of the low velocity zone in Cascadia from receiver function waveform inversion. Earth and Planetary Science Letters 337–338, 25–38. https://doi.org/10.1016/j.epsl.2012.05.031.

Henry, C., Burkhard, M., Goffé, B., 1996. Evolution of synmetamorphic veins and their wallrocks through a Western Alps transect: no evidence for large-scale fluid flow. Stable isotope, major- and trace-element systematics. Chemical Geology 127, 81–109. https://doi.org/10.1016/0009-2541(95)00106-9.

Herviou, C., Agard, P., Plunder, A., Mendes, K., Verlaguet, A., Deldicque, D., Cubas, N., 2022. Subducted fragments of the Liguro-Piemont ocean, Western Alps: spatial correlations and offscraping mechanisms during subduction. Tectonophysics 229267.

Herviou, C., Verlaguet, A., Agard, P., Locatelli, M., Raimbourg, H., Lefeuvre, B., Dubacq, B., 2021. Along-dip variations of subduction fluids: The 30–80 km depth traverse of the Schistes Lustrés complex (Queyras-Monviso, W. Alps). Lithos 394–395, 106168. https://doi.org/10.1016/j.lithos.2021.106168.

Holland, M., Urai, J.L., 2010. Evolution of anastomosing crack–seal vein networks in limestones: Insight from an exhumed high-pressure cell, Jabal Shams, Oman Mountains. Journal of Structural Geology 32, 1279–1290. https://doi.org/10.1016/j.jsg.2009.04.011.

Hooker, J.N., Laubach, S.E., Marrett, R., 2013. Fracture-aperture size—frequency, spatial distribution, and growth processes in strata-bounded and non-strata-bounded fractures, Cambrian Mesón Group, NW Argentina. Journal of Structural Geology 54, 54–71. https://doi.org/10.1016/j.jsg.2013.06.011.

Ide, S., Beroza, G.C., Shelly, D.R., Uchide, T., 2007. A scaling law for slow earthquakes. Nature 447, 76–79. https://doi.org/10.1038/nature05780.

Jackson, P, Sanderson, D. J, 1992. Scaling of fault displacements from the Badajoz-Cordoba shear zone, SW Spain. Tectonophysics 210, 189–190.

Jaeckel, K., Bebout, G.E., Angiboust, S., 2018. Deformation-enhanced fluid and mass transfer along Western and Central Alps paleo-subduction interfaces: Significance for carbon cycling models. Geosphere 14, 2355–2375. https://doi.org/10.1130/GES01587.1.

Johnston, J.D., McCaffrey, K.J.W., 1996. Fractal geometries of vein systems and the variation of scalingrelationships with mechanism. Journal of Structural Geology 18, 349–358. https://doi.org/10.1016/S0191-8141(96)80055-1.

Kirkpatrick, J.D., Fagereng, Å., Shelly, D.R., 2021. Geological constraints on the mechanisms of slow earthquakes. Nat Rev Earth Environ 2, 285–301. https://doi.org/10.1038/s43017-021-00148-w.

La Pointe, P.R., 1988. A method to characterize fracture density and connectivity through fractal geometry. International Journal of Rock Mechanics and Mining Sciences & Geomechanics Abstracts 25, 421–429. https://doi.org/10.1016/0148-9062(88)90982-5.

Lagabrielle, Y., 1987. Les ophiolites : Marqueurs de l'histoire tectonique des domaines océaniques. PhD thesis Brest.

Lagabrielle, Y., Cannat, M., 1990. Alpine Jurassic ophiolites resemble the modern central Atlantic basement. Geology 18, 319–322.

Lahiri, S., Rana, V., Bhatt, S., Mamtani, M.A., 2020. Paleostress and statistical analysis using quartz veins from mineralized and non-mineralized zones: Application for exploration targeting. Journal of Structural Geology 133, 104006. https://doi.org/10.1016/j.jsg.2020.104006.

Lay, T., Kanamori, H., Ammon, C.J., Koper, K.D., Hutko, A.R., Ye, L., Yue, H., Rushing, T.M., 2012. Depth-varying rupture properties of subduction zone megathrust faults. J. Geophys. Res. 117, n/a-n/a. https://doi.org/10.1029/2011JB009133.

Ledésert, B., Dubois, J., Genter, A., Meunier, A., 1993. Fractal analysis of fractures applied to Soultz-sous-Forets hot dry rock geothermal program. Journal of Volcanology and Geothermal Research 57, 1–17. https://doi.org/10.1016/0377-0273(93)90028-P.

Lefeuvre, B., Agard, P., Verlaguet, A., Dubacq, B., Plunder, A., 2020. Massive formation of lawsonite in subducted sediments from the Schistes Lustrés (W. Alps): Implications for mass transfer and decarbonation in cold subduction zones. Lithos 370–371, 105629. https://doi.org/10.1016/j.lithos.2020.105629.

Lemonnier, N., Homberg, C., Roche, V., Rocher, M., Boullier, A., Schnyder, J., 2020. Microstructures of bedding-parallel faults under multistage deformation: Examples from the Southeast Basin of France. Journal of Structural Geology 140, 104138. https://doi.org/10.1016/j.jsg.2020.104138.

Locatelli, M., Verlaguet, A., Agard, P., Pettke, T., Federico, L., 2019. Fluid Pulses During Stepwise Brecciation at Intermediate Subduction Depths (Monviso Eclogites, W. Alps): First Internally Then Externally Sourced. Geochem. Geophys. Geosyst. 20, 5285–5318. https://doi.org/10.1029/2019GC008549.

Magde, L.S., Dick, H.J.B., Hart, S.R., 1995. Tectonics, alteration and the fractal distribution of hydrothermal veins in the lower ocean crust. Earth and Planetary Science Letters 129, 103–119. https://doi.org/10.1016/0012-821X(94)00239-U.

Mandelbrot, B. B, 1982. The fractal geometry of nature (Vol. 1). New York : WH freeman.

Manning, C.E., 1994. Fractal clustering of metamorphic veins. Geology 22, 335–338. https://doi.org/10.1130/0091-7613(1994)022<0335:FCOMV>2.3.CO;2.

Mazzarini, F., Musumeci, G., Cruden, A.R., 2011. Vein development during folding in the upper brittle crust: The case of tourmaline-rich veins of eastern Elba Island, northern Tyrrhenian Sea, Italy. Journal of Structural Geology 33, 1509–1522. https://doi.org/10.1016/j.jsg.2011.07.001.

McCaffrey, K., Johnson, J.D., Feely, M., 1993. Use of Fractal Statistics in the Analysis of Mo-Cu Mineralisation at Mace Head, County Galway. Irish Journal of Earth Sciences 1, 139–148.

McCaffrey, K.J.W., Johnston, J.D., 1996. Fractal analysis of a mineralised vein deposit: Curraghinalt gold deposit, County Tyrone. Mineral. Deposita 31, 52–58.

Michel, S., Gualandi, A., Avouac, J.-P., 2019a. Interseismic Coupling and Slow Slip Events on the Cascadia Megathrust. Pure Appl. Geophys. 176, 3867–3891. https://doi.org/10.1007/s00024-018-1991-x.

Michel, S., Gualandi, A., Avouac, J.-P., 2019b. Similar scaling laws for earthquakes and Cascadia slow-slip events. Nature 574, 522–526. https://doi.org/10.1038/s41586-019-1673-6.

Monecke, T., Gemmell, J.B., Monecke, J., 2001. Fractal distributions of veins in drill core from the Hellyer VHMS deposit, Australia: constraints on the origin and evolution of the mineralising system. Min Dep 36, 406–415. https://doi.org/10.1007/s001260100161.

Muñoz-Montecinos, J., Angiboust, S., Cambeses, A., García-Casco, A., 2020. Multiple veining in a paleo–accretionary wedge: The metamorphic rock record of prograde dehydration and transient high pore-fluid pressures along the subduction interface (Western Series, central Chile). Geosphere 16, 765–786. https://doi.org/10.1130/GES02227.1.

Muñoz-Montecinos, J., Angiboust, S., Garcia-Casco, A., Glodny, J., Bebout, G., 2021. Episodic hydrofracturing and large-scale flushing along deep subduction interfaces: Implications for fluid transfer and carbon recycling (Zagros Orogen, southeastern Iran). Chemical Geology 571, 120173. https://doi.org/10.1016/j.chemgeo.2021.120173.

Narr, W., Suppe, J., 1991. Joint spacing in sedimentary rocks. Journal of Structural Geology, 13, 1037-1048.

Nishiyama, N., Ujiie, K., Kano, M., 2021. Spatial changes in inclusion band spacing as an indicator of temporal changes in slow slip and tremor recurrence intervals. Earth Planets Space 73, 126. https://doi.org/10.1186/s40623-021-01448-7.

Obara, K., 2002. Nonvolcanic Deep Tremor Associated with Subduction in Southwest Japan. Science 296, 1679–1681. https://doi.org/10.1126/science.1070378.

Obara, K., Kato, A., 2016. Connecting slow earthquakes to huge earthquakes. Science 353, 253–257. https://doi.org/10.1126/science.aaf1512.

Oliver, N.H.S., Bons, P.D., 2001. Mechanisms of fluid flow and fluid-rock interaction in fossil metamorphic hydrothermal systems inferred from vein-wallrock patterns, geometry and microstructure. Geofluids 1, 137–162. https://doi.org/10.1046/j.1468-8123.2001.00013.x.

Oncken, O., Angiboust, S., Dresen, G., 2021. Slow slip in subduction zones: Reconciling deformation fabrics with instrumental observations and laboratory results. Geosphere. https://doi.org/10.1130/GES02382.1.

Ortega, O.J., Marrett, R.A., Laubach, S.E., 2006. A scale-independent approach to fracture intensity and average spacing measurement. Bulletin 90, 193–208. https://doi.org/10.1306/08250505059.

Palazzin, G., Raimbourg, H., Famin, V., Jolivet, L., Kusaba, Y., Yamaguchi, A., 2016. Deformation processes at the down-dip limit of the seismogenic zone: The example of Shimanto accretionary complex. Tectonophysics 687, 28–43. https://doi.org/10.1016/j.tecto.2016.08.013.

Paulatto, M., Laigle, M., Galve, A., Charvis, P., Sapin, M., Bayrakci, G., Evain, M., Kopp, H., 2017. Dehydration of subducting slow-spread oceanic lithosphere in the Lesser Antilles. Nat Commun 8, 15980. https://doi.org/10.1038/ncomms15980.

Peacock, S.M., Hyndman, R.D., 1999. Hydrous minerals in the mantle wedge and the maximum depth of subduction thrust earthquakes. Geophys. Res. Lett. 26, 2517–2520. https://doi.org/10.1029/1999GL900558.

Peacock, S.M., Christensen, N.I., Bostock, M.G., Audet, P., 2011. High pore pressures and porosity at 35 km depth in the Cascadia subduction zone. Geology 39, 471–474. https://doi.org/10.1130/G31649.1.

Pickering, G., Bull, J.M., Sanderson, D.J., 1996. Scaling of fault displacements and implications for the estimation of sub-seismic strain. Geological Society, London, Special Publications 99, 11–26. https://doi.org/10.1144/GSL.SP.1996.099.01.03.

Pickering, G., Bull, J.M., Sanderson, D.J., 1995. Sampling power-law distributions. Tectonophysics 248, 1–20.

Plunder, A., Agard, P., Dubacq, B., Chopin, C., Bellanger, M., 2012. How continuous and precise is the record of P-T paths? Insights from combined thermobarometry and thermodynamic modelling into subduction dynamics (Schistes Lustrés, W. Alps). Journal of Metamorphic Geology 30, 323–346. https://doi.org/10.1111/j.1525-1314.2011.00969.x.

Plunder, A., Agard, P., Chopin, C., Pourteau, A., Okay, A.I., 2015. Accretion, underplating and exhumation along a subduction interface: From subduction initiation to continental subduction (Tavşanlı zone, W. Turkey). Lithos 226, 233–254. https://doi.org/10.1016/j.lithos.2015.01.007.

Raimbourg, H., Rajič, K., Moris-Muttoni, B., Famin, V., Palazzin, G., Fisher, D., Morell, K., Erdmann, S., Di Carlo, I., Montmartin, C., 2021. Quartz Vein Geochemistry Records Deformation Processes in Convergent Zones. Geochem Geophys Geosyst 22. https://doi.org/10.1029/2020GC009201.

Ramsay, J.G., 1980. The crack–seal mechanism of rock deformation. Nature 284, 135–139. https://doi.org/10.1038/284135a0.

Renard, F., Andréani, M., Boullier, A.-M., Labaume, P., 2005. Crack-seal patterns: records of uncorrelated stress release variations in crustal rocks. Geological Society, London, Special Publications 243, 67–79. https://doi.org/10.1144/GSL.SP.2005.243.01.07.

Roberts, S., Sanderson, D.J., Gumiel, P., 1999. Fractal analysis and percolation properties of veins. Geological Society, London, Special Publications 155, 7–16. https://doi.org/10.1144/GSL.SP.1999.155.01.03.

Roedder, E, 1984. Volume 12: fluid inclusions. Reviews in mineralogy 12.

Rogers, G., Dragert, H., 2003. Episodic Tremor and Slip on the Cascadia Subduction Zone: The Chatter of Silent Slip. Science 300, 1942–1943. https://doi.org/10.1126/science.1084783.

Saffer, D.M., Tobin, H.J., 2011. Hydrogeology and Mechanics of Subduction Zone Forearcs: Fluid Flow and Pore Pressure. Annu. Rev. Earth Planet. Sci. 39, 157–186. https://doi.org/10.1146/annurev-earth-040610-133408.

Sanderson, D.J., Roberts, S., Gumiel, P., 1994. A fractal relationship between vein thickness and gold grade in drill core from La Codosera, Spain. Economic Geology 89, 168–173. https://doi.org/10.2113/gsecongeo.89.1.168.

Sanderson, D.J., Roberts, S., Gumiel, P., Greenfield, C., 2008. Quantitative Analysis of Tin- and Tungsten-Bearing Sheeted Vein Systems. Economic Geology 103, 1043–1056. https://doi.org/10.2113/gsecongeo.103.5.1043.

Schmidt, M.W., Poli, S., 2014. Devolatilization During Subduction, in: Treatise on Geochemistry. Elsevier, pp. 669–701. https://doi.org/10.1016/B978-0-08-095975-7.00321-1.

Schwartz, S., Lardeaux, J.M., Tricart, P., Guillot, S., Labrin, E., 2007. Diachronous exhumation of HP-LT metamorphic rocks from south-western Alps: evidence from fission-track analysis. Terra Nova 19, 133–140. https://doi.org/10.1111/j.1365-3121.2006.00728.x.

Schwartz, S., Guillot, S., Reynard, B., Lafay, R., Debret, B., Nicollet, C., Lanari, P., Auzende, A.L., 2013. Pressure–temperature estimates of the lizardite/antigorite transition in high pressure serpentinites. Lithos 178, 197–210. https://doi.org/10.1016/j.lithos.2012.11.023.

Schwartz, S., Gautheron, C., Ketcham, R.A., Brunet, F., Corre, M., Agranier, A., Pinna-Jamme, R., Haurine, F., Monvoin, G., Riel, N., 2020. Unraveling the exhumation history of high-pressure ophiolites using magnetite (U-Th-Sm)/He thermochronometry. Earth and Planetary Science Letters 543, 116359. https://doi.org/10.1016/j.epsl.2020.116359.

Simpson, G.D.H., 2000. Synmetamorphic vein spacing distributions: characterisation and origin of a distribution of veins from NW Sardinia, Italy. Journal of Structural Geology 22, 335–348. https://doi.org/10.1016/S0191-8141(99)00161-3.

Spandler, C., Pirard, C., 2013. Element recycling from subducting slabs to arc crust: A review. Lithos 170–171, 208–223. https://doi.org/10.1016/j.lithos.2013.02.016.

Spandler, C., Pettke, T., Rubatto, D., 2011. Internal and External Fluid Sources for Eclogite-facies Veins in the Monviso Meta-ophiolite, Western Alps: Implications for Fluid Flow in Subduction Zones. Journal of Petrology 52, 1207–1236. https://doi.org/10.1093/petrology/egr025.

Stowell, J.F.W., Watson, A.P., Hudson, N.F.C., 1999. Geometry and population systematics of a quartz vein set, Holy Island, Anglesey, North Wales. Geological Society, London, Special Publications 155, 17–33. https://doi.org/10.1144/GSL.SP.1999.155.01.04.

Tewksbury-Christle, C.M., Behr, W.M., 2021. Constraints From Exhumed Rocks on the Seismic Signature of the Deep Subduction Interface. Geophysical Research Letters 48. https://doi.org/10.1029/2021GL093831.

Toriumi, A., Teruya, J., 1988. Tectono-metamorphism of the Shimanto Belt. Modern Geology 12, 303–324.

Tricart, P., Schwartz, S., 2006. A north-south section across the Queyras Schistes lustrés (Piedmont zone, Western Alps): Syn-collision refolding of a subduction wedge. Eclogae geol. Helv. 99, 429–442. https://doi.org/10.1007/s00015-006-1197-6.

Turcotte, D.L., 1989. Fractals in geology and geophysics. PAGEOPH 131, 26.

Turcotte, D.L., 1986. Fractals and fragmentation. J. Geophys. Res. 91, 1921. https://doi.org/10.1029/JB091iB02p01921.

Ujiie, K., Saishu, H., Fagereng, Å., Nishiyama, N., Otsubo, M., Masuyama, H., Kagi, H., 2018. An Explanation of Episodic Tremor and Slow Slip Constrained by Crack-Seal Veins and Viscous Shear in Subduction Mélange. Geophys. Res. Lett. 45, 5371–5379. https://doi.org/10.1029/2018GL078374.

Valley, J. W, 1986. Stable isotope geochemistry of metamorphic rocks. Stable isotopes in high temperature geological processes 445–490.

Vannucchi, P., Remitti, F., Bettelli, G., Boschi, C., Dallai, L., 2010. Fluid history related to the early Eocene-middle Miocene convergent system of the Northern Apennines (Italy): Constraints from structural and isotopic studies. J. Geophys. Res. 115, B05405. https://doi.org/10.1029/2009JB006590.

Velde, B, Dubois, J, Touchard, G, Badri, A, 1990. Fractal analysis of fractures in rocks: the Cantor's Dust method. Tectonophysics 179, 345–352.

Velde, B, Dubois, J, Moore, D, Touchard, G, 1991. Fractal patterns of fractures in granites. Earth and Planetary Science Letters 104, 25–35.

Verlaguet, A., Goffé, B., Brunet, F., Poinssot, C., Vidal, O., Findling, N., Menut, D., 2011. Metamorphic veining and mass transfer in a chemically closed system: a case study in Alpine metabauxites (western Vanoise). Journal of Metamorphic Geology 29, 275–300. https://doi.org/10.1111/j.1525-1314.2010.00918.x.

Watterson, J, 1986. Fault dimensions, displacements and growth. Pure and Applied Geophysics 124, 365–373.

Wech, A.G., Creager, K.C., Houston, H., Vidale, J.E., 2010. An earthquake-like magnitude-frequency distribution of slow slip in northern Cascadia. Geophys. Res. Lett. 37. https://doi.org/10.1029/2010GL044881.

Wells, D. L, Coppersmith, K. J, 1994. New empirical relationships among magnitude, rupture length, rupture width, rupture area, and surface displacement. Bulletin of the Seismological Society of America 84, 974–1002.

Widmer, T., Thompson, A. B, 2001. Local origin of high pressure vein material in eclogite facies rocks of the Zermatt-Saas-Zone, Switzerland. American Journal of Science 301, 627–656. https://doi.org/10.2475/ajs.301.7.627.

Supplementary Material en annexe – 5

Chapitre V – Carbonatation haute pression de serpentinites : une rétroaction positive entre déformation et infiltration de fluides responsable de l'écaillage en subduction ?

Talcschiste à dolomite. Crête de l'Eychassier.

V. Carbonatation haute pression de serpentinites : une rétroaction positive entre déformation et infiltration de fluides responsable de l'écaillage en subduction ?

V.1. Résumé du chapitre

Des horizons métriques à hectométriques de talcschistes riches en carbonates ont été observés le long ou à proximité des contacts délimitant les différentes écailles Liguro-Piémontaises. Grâce à des analyses géochimiques des minéraux et des roches totales, à des données d'inclusions fluides et à la géochronologie U-Pb de la titanite, cette étude met en évidence la formation de ces horizons par la transformation de serpentinites causée par l'infiltration de fluides externes provenant des sédiments environnants, lors du pic d'enfouissement. Ces roches, qui contiennent de grandes quantités de carbonates et de fortes concentrations en éléments généralement mobiles dans les fluides, pourraient contribuer au cycle profond du carbone et/ou affecter la composition du coin mantellique, lors de leur déstabilisation aux profondeurs sub-arc. Suite à l'infiltration de fluides, la formation de talc a probablement contrôlée la localisation de la déformation dans ces horizons, favorisant à son tour l'infiltration de fluides externes et créant une rétroaction positive entre déformation et infiltration de fluides. Nous proposons que ces roches aient pu jouer le rôle de niveaux de faiblesse rhéologique majeure responsables de l'écaillage de la plaque plongeante lors de la subduction alpine.

V.2. Ebauche d'article en préparation pour Earth and Planetary Science Letters:

Paleocene-Eocene high pressure carbonation of Western Alps serpentinites: a positive feedback between deformation and CO_2-CH_4 fluid ingression responsible for slab slicing?

Paleocene-Eocene high pressure carbonation of Western Alps serpentinites: a positive feedback between deformation and CO_2-CH_4 fluid ingression responsible for slab slicing?

Clément Herviou[a] & Guillaume Bonnet[a,b]

[a] Sorbonne Université, CNRS-INSU, Institut des Sciences de la Terre de Paris, ISTeP UMR 7193, F 75005 Paris, France

[b] Department of Earth Science, University of California, Santa Barbara, USA

* Corresponding author: clement.herviou@sorbonne-universite.fr (C. Herviou)

Abstract

Meter to hectometer-size horizons of carbonate-bearing talcschists were observed along or near the contacts delimiting the different Liguro-Piemont subduction slices. Through mineral and bulk-rock geochemical analyses, fluid inclusion data, and titanite U-Pb geochronology, this study highlights that these horizons formed by mineral transformation of initial serpentinites due to external fluid infiltration from the surrounding sediments, at peak burial. These rocks containing large amounts of carbonates and high concentrations of fluid-mobile element, may have contributed to carbon recycling and/or affected the composition of the mantle wedge, as they are stable up to high P-T conditions. Following fluid infiltration, the formation of talc likely controlled strain localization in these horizons, enhancing in turn the ingression of external fluids and creating a positive feedback between deformation and fluid infiltration. We suggest that these rocks may have acted as major rheological weaknesses responsible for material offscraping from the downgoing plate.

1. Introduction

Large amounts of fluids are released in subduction zones by the progressive dehydration of the downgoing lithosphere (Hacker, 2008; Schmidt and Poli, 2014). The release and migration of fluids at depth strongly impact rheology (i.e. fracturing and earthquake nucleation; e.g., Hacker et al., 2003) as well as the generation and geochemical signature of arc magmas (e.g., Stern, 2002). Characterization of the sources, amounts and pathways of fluids in subduction zones is therefore a prerequisite to assess their impact on subduction dynamics and global element recycling (e.g. Bebout and Penniston-Dorland, 2016).

In subduction zones, boundaries between dissimilar lithologies (i.e. sediments, mafic and ultramafic rocks) with contrasting mechanical behaviors tend to localize deformation and to act as important fluid pathways (Vitale Brovarone et al., 2014; Piccoli et al., 2018). Their contrasting chemical compositions, in the presence of fluids, enhance the formation of hybrid rocks enriched in fluid-mobile elements (Bebout and Barton, 1993, 2002; Spandler et al., 2008; Penniston-Dorland et al., 2012, 2014; Gyomlai et al., 2021). These hybrid rocks are generally made of high variance assemblages (generally talc or chlorite schists ± amphibole and carbonates) that may remain stable at high pressure-temperature conditions. Their destabilization at sub-arc depth may therefore have a crucial role in the deep transfer of volatiles and fluid-mobile elements to the mantle wedge (Spandler et al., 2008; Marschall and Schumacher, 2012; Bebout and Penniston-Dorland, 2016). In addition, considerable changes of rheology are imputed to the formation of hybrid rocks by metasomatic reactions in subduction environments (Moore and Lockner, 2007; Hirauchi et al., 2013; Tarling et al., 2019; Okamoto et al., 2021) that may control interplate coupling and strain localization (Peacock and Wang, 2021).

In the Western Alps, remnants of the Liguro-Piemont ocean recovered from the Alpine subduction zone are continuously exposed along the 200 km-long and up to 50-km wide Liguro-Piemont domain (Deville et al., 1992; Agard, 2021). This domain corresponds to a deep accretionary complex built by a stacking of subduction slices comprising variable amounts of mafic and ultramafic rocks embedded in oceanic metasediments (Herviou et al., 2022). Liguro-Piemont rocks span a range from ~30 to 80 km depth (Agard et al., 2018; Agard, 2021; Herviou et al., 2022), thereby providing an access to subduction processes across depths (Bebout et al., 2013; Herviou et al., 2021, 2022).

Isotopic, trace elements and fluid inclusion studies on the metasediments suggest the dominance of a rock-buffered system during subduction, with only limited external fluid infiltration (e.g. Henry et al., 1996; Bebout et al., 2013; Herviou et al., 2021) except along major tectonic contacts (Jaeckel et al., 2018; Epstein et al., 2021) and along lithological boundaries with mafic (Debret et al., 2016; Inglis et al., 2019; Vitale Brovarone et al., 2020; Herviou et al., 2021) and ultramafic rocks (Lafay et al., 2013; Debret et al., 2018; Tartarotti et al., 2019; Vitale Brovarone et al., 2020; Rotondo et al., 2021).

This study reports on the existence of m- to hm-scale carbonate-bearing talcschist horizons in metasediments located along or close to the tectonic contacts between the Liguro-Piemont subduction slices. Understanding whether these horizons correspond to metasomatic interactions between ultramafic rocks and sediments and if they formed during subduction is here addressed using mineral and bulk-rock geochemical analyses, fluid inclusion data and titanite U-Pb geochronology.

Results shed light on the mechanisms responsible for the formation of these rocks, as well as on their importance for mass transfer and offscraping mechanisms in a cold subduction zone.

2. The Western Alps Liguro-Piemont domain: a deep accretionary complex

The Western Alps formed as a result of an east- to south-east-dipping and slow (~1 cm/yr) subduction of the 100-1000 km wide Valais and Liguro-Piemont oceans below Adria/Apulia (Le Pichon et al., 1988; Schmid et al., 1996, 2017; Lapen et al., 2003; Handy et al., 2010; Agard and Handy, 2021). Subduction of these slow-spreading oceanic domains (Lagabrielle and Cannat, 1990) started in the Late Cretaceous and was over by ~35 Ma (Stampfli et al., 1998; Schmid et al., 2017).

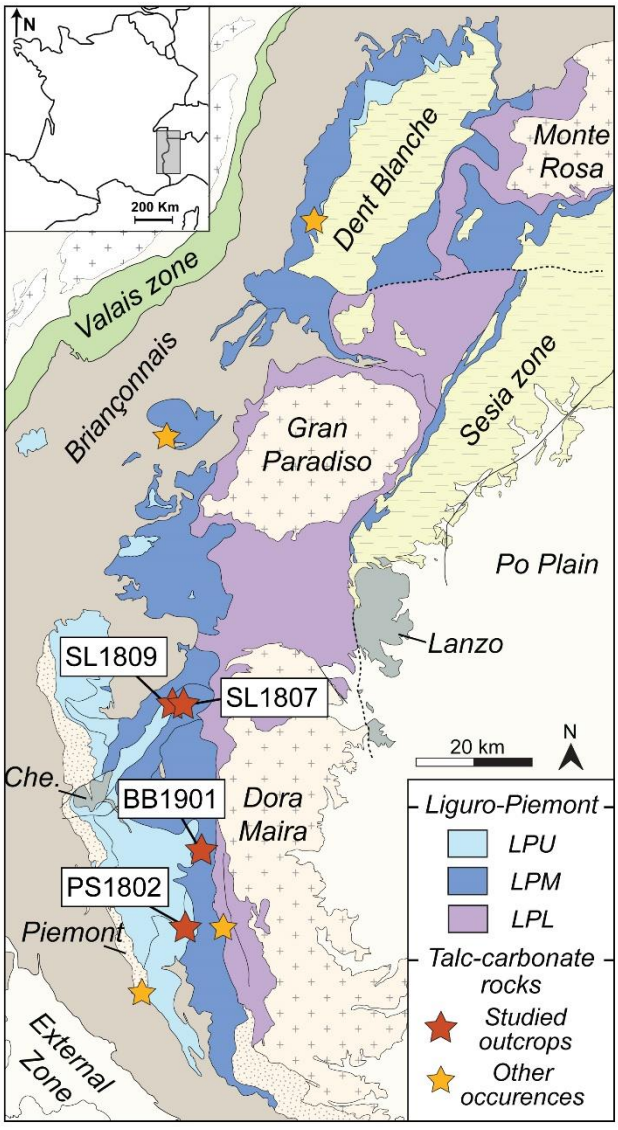

***Figure V.1**: Structural map of the Western Alps focused on the Liguro-Piemont domain. Occurrences and studied samples of carbonate-bearing talcschists are reported. Abbreviations: LPU: Liguro-Piemont Upper units; LPM: Liguro-Piemont Middle units; LPL: Liguro-Piemont Lower units.*

Remnants of subducted Liguro-Piemont oceanic lithosphere are now exposed in the internal domain of the Western Alps and form a nappe-stack known as the Liguro-Piemont domain (Deville et al., 1992; Agard, 2021) or Schistes Lustrés complex (owing to their characteristic sedimentary features; Agard et al., 2001, 2009). Metasediments (Schistes Lustrés s.s.) are volumetrically dominant in this complex and range from the Late Jurassic (De Wever and Caby, 1981) to the Late Cretaceous (Lemoine et al., 1984). They correspond to an initial ~200-400 m thick sequence of pelagic and hemipelagic seafloor deposits (marls, shales and limestones metamorphosed as calcschists, metapelites and marbles; Lemoine et al., 1984; Lemoine and Tricart, 1986; Deville et al., 1992) embedding variable amounts of mafic and ultramafic rocks (Herviou et al., 2022).

During subduction, these rocks were buried between ~30 and 80 km depth (Agard et al., 2002, 2009; Herviou et al., 2022) and intensely folded, leading to a significant thickening of the initial sedimentary pile (Agard et al., 2002; Tricart and Schwartz, 2006). Agard et al. (2009) roughly estimated that approximatively 30% to 50% of the sedimentary deposits were scraped off from the downgoing plate and exhumed, as opposed to only ~5% of the oceanic crust and serpentinized mantle. After a peak burial between 60 and ~40 Ma (e.g. Agard et al., 2002; Rubatto and Hermann, 2003), these rocks were successively scraped off from the subducting plate as tectonic slices and were exhumed from the Late Eocene to the Miocene (Agard et al., 2002, 2009; Schwartz et al., 2007, 2020; Angiboust and Glodny, 2020). This complex stack of slices therefore formed as a deep accretionary complex, built through progressive underplating (Platt, 1986; Marthaler and Stampfli, 1989; Agard et al., 2009, 2018; Agard, 2021; Herviou et al., 2022).

Several independent subduction slices were identified in transects across the complex (Lagabrielle, 1987; Fudral, 1996; Agard, 2021; see Herviou et al., 2022 for a compilation). Recently, through the compilation of metamorphic, structural, lithostratigraphic and radiochronogical data, Herviou et al. (2022) reappraised the overall structure of the complex, highlighting the existence of a trimodal distribution of units with an almost continuous eastward increase in peak burial conditions from the Liguro-Piemont Upper (LPU; 320-400°C; 1.2-1.9 GPa) to the Middle (LPM; 415-475°C- 1.7-2.2 GPa) and Lower units (LPL; 500-580°C; 2.2-2.8 GPa; Fig. V.1). The LPU and LPM units, metamorphosed under blueschist-facies conditions at peak P-T conditions, are dominated by sediments (>90%) whereas the LPL units, metamorphosed at eclogite-facies conditions at peak burial, are much richer in mafic-ultramafic rocks (>40%; Herviou et al., 2022). Petrological and lithostratigraphic data suggest that the offscraping of the LPU and LPM units was mostly controlled by lithological contrasts, within pelagic shales or along contacts within the uppermost serpentinized mantle and possibly enhanced

by high fluid pressure (Herviou et al., 2022). In contrast, major dehydration reactions (such as lawsonite breakdown in sediments) likely controlled the offscraping of the LPL units at eclogite-facies conditions, possibly through high fluid pressure conditions and rocks embrittlement (Herviou et al., 2022).

So far unreported carbonate-bearing talcschists were observed in or nearby the tectonic contacts between the Liguro-Piemont slices and/or the Briançonnais domain (Fig. V.1) and are described below.

3. Observation of carbonate-bearing talcschists in the Liguro-Piemont domain

Ten centimeter to several meter-thick and up to hundred meters-long horizons of carbonate-bearing talcschists can be observed in the Liguro-Piemont metasediments (Fig. V.2a-f). These zones are intensively sheared and often folded by a D1 deformation stage (D1 stage of Agard et al., 2001 in the Schistes Lustrés) showing their early formation. Field observations suggest that talc is the dominant mineral in these rocks and is always associated to large amounts of a reddish carbonate interpreted as dolomite (Fig. V.2d-e). Dolomite crystals are idiomorphic and commonly centimeter-sized (Fig. V.2e). Quartz layers were also observed in these talcschists (Fig. V.2d). At the boundaries between calcschists and the carbonate-bearing talcschists, the proportion of dolomite increases in place to form almost pure carbonate horizons with minor quartz (Fig. V.2c). These contacts also contain chlorite schists and early-formed, D1-related quartz veins in the metasediments (Fig. V.2c). Crystals of fuchsite (i.e. Cr-bearing muscovite) are observed in the calcschists nearby the talcschist zones (Fig. V.2f).

All of the carbonate-bearing talcschists are located along or near the contacts delimiting the different Liguro-Piemont slices or at the contact between Liguro-Piemont slices and the Briançonnais domain (Fig. V.1). Similar rocks were reported at the contact between Liguro-Piemont slices and upper plate fragments (Dent Blanche; Jaeckel et al., 2018; Epstein et al., 2021).

In order to understand the origin of these rocks and their potential implication during the Alpine subduction, they were sampled from four outcrops (Fig. V.1). The two northernmost outcrops are located on each side of the tectonic contact delimiting the Lago Nero LPU and Cerogne-Ciantiplagna LPM units in the Cottian Alps (samples SL1809 and SL1807 respectively: Fig. V.1; Colle dell Assietta locality; see Herviou et al., 2022 for the different Liguro-Piemont slices). Sample BB1901 was

collected in the Mirabouc-Bouchet LPM unit near the contact with the Calcschist LPU unit (Fig. V.1; Bric Bouchet locality). Sample PS1802 was collected in the Pelvas-Taillante LPU unit near the contact with the Calcschist LPU unit (Fig. V.1; Crête de l'Eychassier locality).

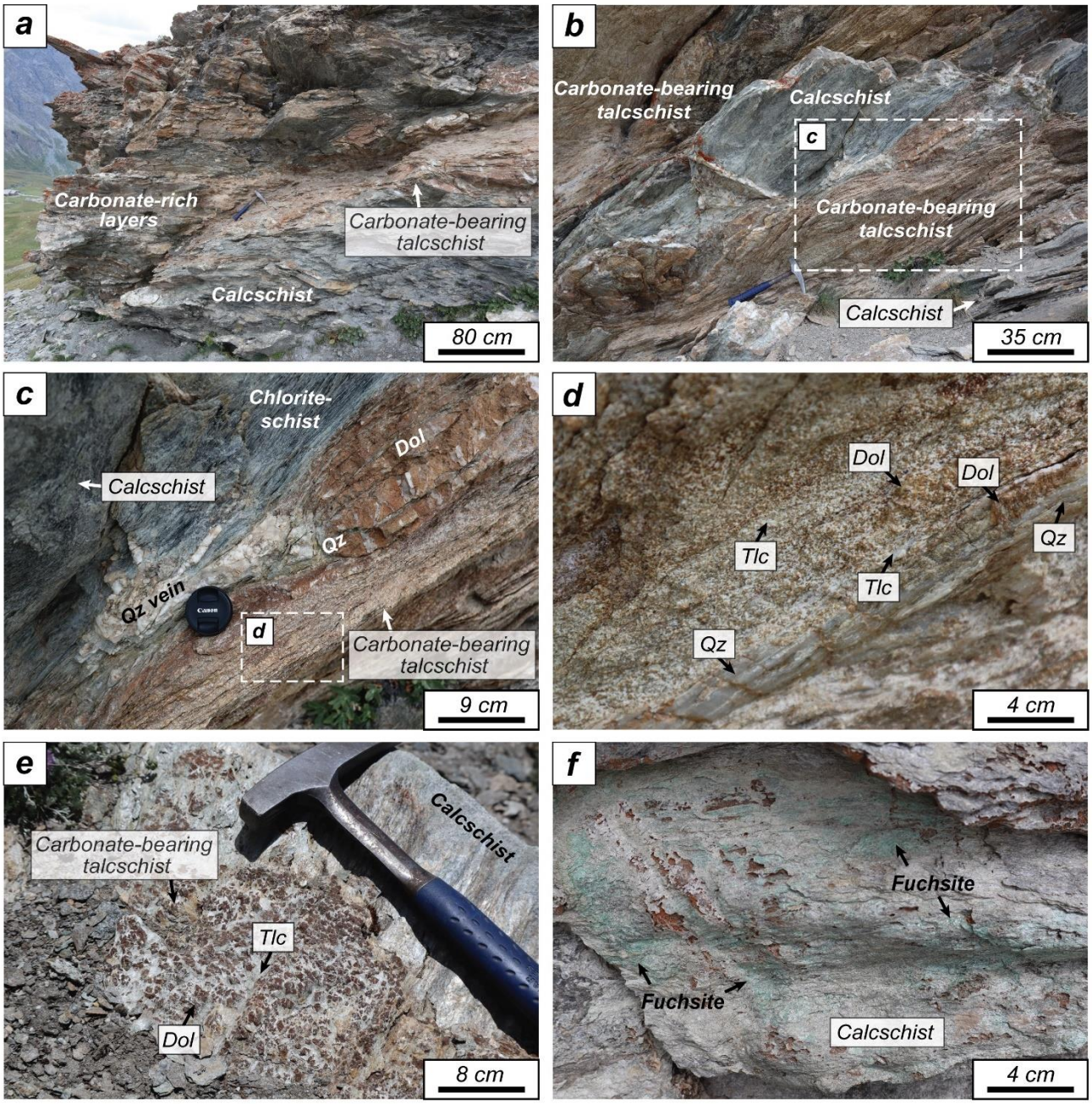

***Figure V.2**: Field observations. A), B) Large view of carbonate-bearing talcschist outcrops embedded inside the Schistes Lustrés métasediments. C) Closer view of B) showing the presence of an early quartz vein, chlorite schists and an almost pure dolomite horizon with minor quartz at the contact between the talcschists and the calcschists. D) Closer view of C) showing talc, dolomite and quartz crystals in the talcschist horizons. E) Centimeter-size dolomite in a talcschist. F) Fuchsite crystals in the calschists at 1-2 meters away from the talcschist horizons. Abbreviations: Dol: dolomite; Qz: quartz; Tlc: talc.*

4. Analytical Methods

4.1.Characterization of mineralogy and mineral chemistry

Mineral assemblages were characterized using both optical microscopy and Scanning Electron Microscopy (SEM; Zeiss Supra 55VP equipped with a SSD detector PTG Sahara for EDS analysis; ISTeP).

Mineral chemical compositions were obtained by Electron Probe Microanalyses (EPMA) at Camparis (Sorbonne Université, Paris) using a Cameca SX-100 instrument. Point measurements were made in classical analytical conditions (15 kV acceleration voltage, 10 nA beam current allowing ~2 µm beam size in wavelength-dispersive spectroscopy mode) using diopside (Ca, Mg, Si), $MnTiO_3$ (Mn, Ti), orthoclase (K, Al), Fe_2O_3 (Fe), albite (Na) and Cr_2O_3 (Cr) as standards for calibration of elements in parentheses. WDS-mode compositional maps were obtained in the same conditions with 100 ms counting time and a step size of 2 µm. Representative mineral analyses are in Sup. mat. V.1.

4.2. Bulk-rock chemistry

Samples were finely crushed in an agate mortar. Powders were dissolved at 80°C in closed cups with HNO_3 and HF. For major elements, $B(OH)_3$ was introduced after opening of the cups to avoid SiO_2 loss. Further dilution was carried out with 2% HNO_3 solution before analysis. Major, minor and trace element compositions were analyses at ALIPP6 (Sorbonne Université, Paris) using an ICP-OES spectrometer (Agilent 5100 HVDV) for major and minor elements (Si, Ti, Al, Fe, Mn, Na, K, P, Mg, Ca, Ni, Zn) and an ICP-MS-MS (Agilent 8900) for minor and trace elements (Li, Co, Cu, Cr, As, Mo, Sb, Rb, Sr, Y, Zr, Nb, Cs, Ba, La, Ce, Pr, Nd, Sm, Eu, Gd, Tb, Dy, Ho, Er, Tm, Yb, Lu, Hf, Ta, Pb, Th, U, Sc, V, Be, Ga). All analyses can be found in Table V.1 with all ICP-OES analyses in oxide weight% except for Ni and Zn (in µg/g) and all ICP-MS-MS analyses in µg/g. Mo, Rb and Hf were below detection limits for the four studied samples and are consequently not presented here.

Table V.1 *(next page):* Whole-rock major, minor and trace element analyses. Major oxides reported in wt.%, minor and trace elements reported in µg/g. Average Schistes-Lustrés metasediment and average Liguro-Piemont serpentinites were calculated using Bebout et al. (2013)[1]; Lafay et al. (2013)[2] and Gilio et al. (2013)[3] whole rock analyses.

	BB1901	PS1801	SL1807	SL1809	Average metasediment[1,2]	Average serpentinite[2,3]
SiO_2	38.3	34.67	34.95	32.17	52.45	40.18
Al_2O_3	2.11	2.37	1.31	3.43	15.52	1.68
Fe_2O_3	5.11	5.85	4.89	5.87	6.82	7.80
MnO	0.26	0.13	0.13	0.38	0.17	0.09
MgO	18.17	22.24	22.40	14.70	2.63	37.38
CaO	14.02	12.63	13.19	17.50	7.82	0.42
Na_2O	0.00	0.01	0.01	0.01	0.92	0.01
K_2O	0.19	0.18	0.18	0.17	2.87	0.00
TiO_2	0.05	0.05	0.02	0.25	0.65	0.04
P_2O_5	0.04	0.04	0.03	0.06	0.11	0.00
L.O.I.	21.6	21.19	22.61	25.30	9.59	12.12
Total	100.44	100.05	100.56	100.27	99.57	99.63
Li	6.93	14.30	9.66	14.18	51.28	0.54
Co	36.82	75.13	69.35	26.97	21.96	93.01
Ni	974.4	1490.5	1490.7	724.3	71.96	1800.3
Cu	9.64	13.80	16.53	22.39	55.75	16.15
Zn	46.33	36.17	31.36	47.05	111.00	48.00
As	8.22	2.62	180.13	4.95	5.57	0.54
Sb	0.15	0.14	1.58	0.12	0.75	0.11
Sr	102.77	89.03	104.87	113.37	183.38	2.58
Y	6.66	2.20	1.23	13.70	25.74	1.19
Zr	5.81	6.77	6.19	7.84	103.34	1.56
Nb	b.d.l.	b.d.l.	b.d.l.	0.85	14.51	0.08
Cs	b.d.l.	0.01	b.d.l.	b.d.l.	6.97	0.26
Ba	6.62	6.19	7.43	6.11	378.79	2.36
La	2.08	0.40	0.62	3.85	34.55	0.10
Ce	5.13	2.13	2.50	10.25	72.46	0.28
Pr	0.52	0.07	0.11	1.25	7.74	0.05
Nd	2.59	0.56	0.71	5.96	29.82	0.25
Sm	0.68	0.25	0.18	1.57	5.55	0.08
Eu	0.19	0.02	0.05	0.31	1.12	0.02
Gd	0.88	0.19	0.17	1.86	5.17	0.13
Tb	0.15	0.05	0.03	0.32	0.80	0.02
Dy	1.00	0.38	0.24	2.10	4.70	0.17
Ho	0.22	0.11	0.03	0.49	0.96	0.04
Er	0.67	0.28	0.11	1.51	2.66	0.13
Tm	0.10	0.06	0.03	0.22	0.39	0.02
Yb	0.64	0.32	0.14	1.55	2.45	0.16
Lu	0.11	0.07	0.03	0.28	0.35	0.03
Ta	b.d.l.	b.d.l.	b.d.l.	0.05	1.07	0.01
Pb	6.67	1.82	2.42	24.99	18.66	1.41
Th	0.76	0.82	0.76	1.46	10.14	0.02
U	b.d.l.	0.15	b.d.l.	0.01	1.83	0.01
Cr	1386.50	1666.47	2124.82	926.65	195.83	2325.56
Sc	6.66	11.42	5.72	11.54	17.42	12.13
V	32.14	49.77	33.23	52.36	128.67	52.90
Be	0.15	0.14	0.15	0.14	3.55	0.08
Ga	3.11	2.78	2.21	5.29	20.92	2.21

4.3. Characterization of fluid inclusion generations and composition

Fluid inclusion (FI) analyses were performed on 100 µm thick double-polished sections. FI were observed using optical microscopy, in order to characterize their morphology, gas/liquid ratios and textural location within crystals. To characterize the pristine fluids present during crystal growth, only FI showing good textural evidences of primary entrapment were selected (i.e. fluid inclusions either isolated or in non-planar clusters inside mineral grains; Roedder, 1994; Van den Kerkhof and Hein, 2001). FI were carefully examined and we selected inclusions with the most regular shapes in order

to avoid as much as possible post-entrapment modification of their chemistry. FI aligned on trails crosscutting several mineral grains, considered as secondary inclusions in recrystallized fractures, were not considered in this study.

Salinity and gas content of the 101 studied FI were determined by Raman spectroscopy, by focusing the laser on the liquid phase and gas bubble respectively. Raman measurements were performed at GeoRessources laboratory (Université de Lorraine, Nancy) using LabRAM HR and LabRAM spectrometers (Horiba Jobin-Yvon®) equipped with a liquid nitrogen-cooled CCD detector, a 600 groove.mm^{-1} grating for salinity measurements and a 1800 groove.mm^{-1} grating for gas analysis. The excitation light was provided by an Ar^+ laser (Stabilite 2017, Newport Spectra-Physics) at 514.532 nm at a power of 200, 160 or 120 mW, focused on the sample using a 100x objective (Olympus).

Salinities were determined using the method described in Caumon et al. (2013). Raman spectra of water in the studied FI were acquired with the very same spectrometers used for calibration in the work above and salinity was determined using the intensity ratio of two defined positions (3260 and 3425 cm^{-1}) after subtraction of a linear baseline. This method has an accuracy of ±0.4 wt.% NaCl eq. and is well suited and accurate for the characterization of FI salinity in high-pressure rocks (Herviou et al., 2021).

For gas analysis, Raman spectra were corrected using an ICS function (Intensity Correction System) to normalize the instrument response with wavelength. Gas spectra were identified using peak positions compiled by Frezzotti et al. (2012). CO_2 was detected by the presence of the Fermi diad (Fermi, 1931; 1285 and 1388 cm^{-1} peaks) and CH_4 its major band at 2917 cm^{-1}. For CO_2-CH_4 mixtures, peak areas were computed after substraction of a linear baseline. Molar proportions of each gas in the mixtures were determined using the respective peak areas and the corresponding relative Raman scattering cross-sections (RRSCS; Wopenka and Pasteris, 1987). We choose to use the recent values of Le et al. (2019, 2020) for RRSCS of CO_2 (1.40 ± 0.03 for the 1388 cm^{-1} peak and 0.89 ± 0.02 for the 1285 cm^{-1} peak) and CH_4 (7.73 ± 0.16 for the major band at 2917 cm^{-1}).

4.4. U-Pb geochronology on titanite

Titanite and rutile were analyzed by LASS (laser ablation split-stream) at the University of California, Santa Barbara). After ablation, the U-Pb isotopes and trace elements were analyzed simultaneously on a multicollector and a quadrupole mass spectrometer. Samples were ablated using a Photon Machine 193 nm ArF ultraviolet laser with a HelEx ablation cell, coupled to an Agilent 7700X quadrupole ICP-MS system for trace element measurements and a Plasma 3D muticollector ICP-MS

for U-Pb measurements. We systematically used a 35 µm spot size and a laser fluence of ~1 J.cm^{-2}. Pre-ablation shots were fired on the samples at 50% laser power to remove surface contamination, and the material was allowed to wash out for ~15 s. Material was then ablated at 4 Hz during ~25 s. Analyses of unknowns were bracketed by analyses of titanite reference material MKED (1517.3 ± 0.3 Ma ^{238}U/^{206}Pb date; Spandler et al., 2016).

Secondary U-Pb standards were included in each run as a monitor of accuracy. During the course of this study, we obtained common-Pb corrected (Stacey-Kramers iterative correction in IsoplotR after Stacey and Kramers, 1975; Vermeesch, 2018) dates of 1039.7 ± 3.6 Ma (2σ, n = 24) for BLR (1047.1 ± 1.4 Ma Concordia date; Aleinikoff et al., 2007), 385.6 ± 2.2 Ma (2σ, n = 12) for Y1710C5 (388.6 ± 0.5 Ma TIMS date; Spencer et al., 2013), and 28.03 ± 0.08 Ma (2σ, n = 12) for FC (28.4 ± 0.05 MA TIMS date; Schmitz and Bowring, 2001). These dates are accurate to within 0.7% (BLR), 0.8% (Y1710C5), 1.3% (FC).

All unknowns were additionally bracketed by analyses of glass standard NIST SRM 610 (Jochum et al., 2011) that was used as primary reference materials for trace elements. Measured peaks were ^{29}Si, ^{44}Ca, ^{49}Ti, ^{51}V, ^{52}Cr, ^{56}Fe, ^{89}Y, ^{90}Zr, ^{93}Nb, ^{178}Hf, ^{181}Ta, ^{139}La, ^{140}Ce, ^{141}Pr, ^{146}Nd, ^{147}Sm, ^{153}Eu, ^{157}Gd, ^{159}Tb, ^{163}Dy, ^{165}Ho, ^{166}Er, ^{169}Tm, ^{172}Yb, ^{175}Lu, ^{178}Hf, ^{181}Ta. Internal standardization of trace elements was done on Ca, assuming 19.25 wt.% Ca.

The Iolite plug-in (Paton et al., 2011) for the Wavemetrics Igor Pro Software was used to correct measured isotopic ratios for baselines, time-dependent laser-induced fractionation, and instrument drift. Baseline intensities were determined prior to each analysis. Uncertainties on isotopic measurements were extracted from Iolite. The error correlation between the ^{238}U/^{206}Pb and ^{207}Pb/^{206}Pb ratios was recalculated following the method of Schmitz and Schoene (2007). A quadratic uncertainty was added to isotopic ratios to account for analytical uncertainty so that the MSWD of the weighted means of ^{238}U/^{206}Pb and ^{207}Pb/^{206}Pb of secondary reference material BLR equals to 1 for each run. This correction adds relative uncertainties of 1.4-2.25% (for ^{238}U/^{206}Pb) and 1.5-2.5% (for ^{207}Pb/^{206}Pb) on the ratios.

In all calculations, spots with values of Zr, P, Ti and Si inconsistent with titanite analyses were not considered in date calculation in order to avoid the contamination by inclusions of zircon, apatite/monazite/xenotime, rutile or allanite, respectively.

Analyses were sorted to extract populations with homogeneous trace-element patterns, and isochron dates were calculated from the Tera-Wasserburg projection using the “spine” robust regression by

Powell et al. (2020). Contrary to the traditional least-squares regression by York (1967), this method does not assume a Gaussian uncertainty on the scatter of the individual analyses, and hence is less sensitive to outliers. This method optimizes error calculation, and yields isochrons (with errors) when spines pass a 95% confidence test, and less probable errorchrons (without errors) when they fail the test.

5. Results

5.1. Petrographic observations of minerals

Optical and SEM observations reveal the ubiquity of talc in the four studied samples (Fig. V.3a-e). Chlorite crystals are finely interstratified and in textural equilibrium with talc (Fig. V.3a-e). Large amounts of titanite and quartz were observed in textural equilibrium with both talc and chlorite (Fig. V.3b, c, e). Titanite crystals are idiomorphic and often contain inclusions of chlorite and talc. Most carbonate crystals are dolomite, with only rare calcite (Fig. V.3a-f). Dolomite crystals are idiomorphic too, with sharp contacts with talc and chlorite and contain inclusions of talc, chlorite and titanite advocating for their co-crystallization (Fig. V.3a-e). Calcite is essentially overgrowing dolomite and therefore retrograde. The main mineral assemblage of the four studied samples corresponds to a talc-dolomite-chlorite-quartz-titanite paragenesis (in decreasing modal proportion).

In the four samples, SEM observations reveal the presence of sulfide crystals (Fig. V.3e, f), generally iron sulfide, with variable Co content, with common inclusions of pentlandite and Cr-rich chlorite, and rare chalcopyrite, nickel sulfide, copper sulfide and native platinum. Sulfide minerals are systematically replaced by Fe-oxide/oxyhydroxide crystals (Fig. V.3e, f). These tend to have high Co, Ni and As contents (Fig. V.3f).

Other minor phases include rare Ti-oxide, zircon, apatite, fuchsite and magnetite. Allanite crystals were observed in sample SL1809.

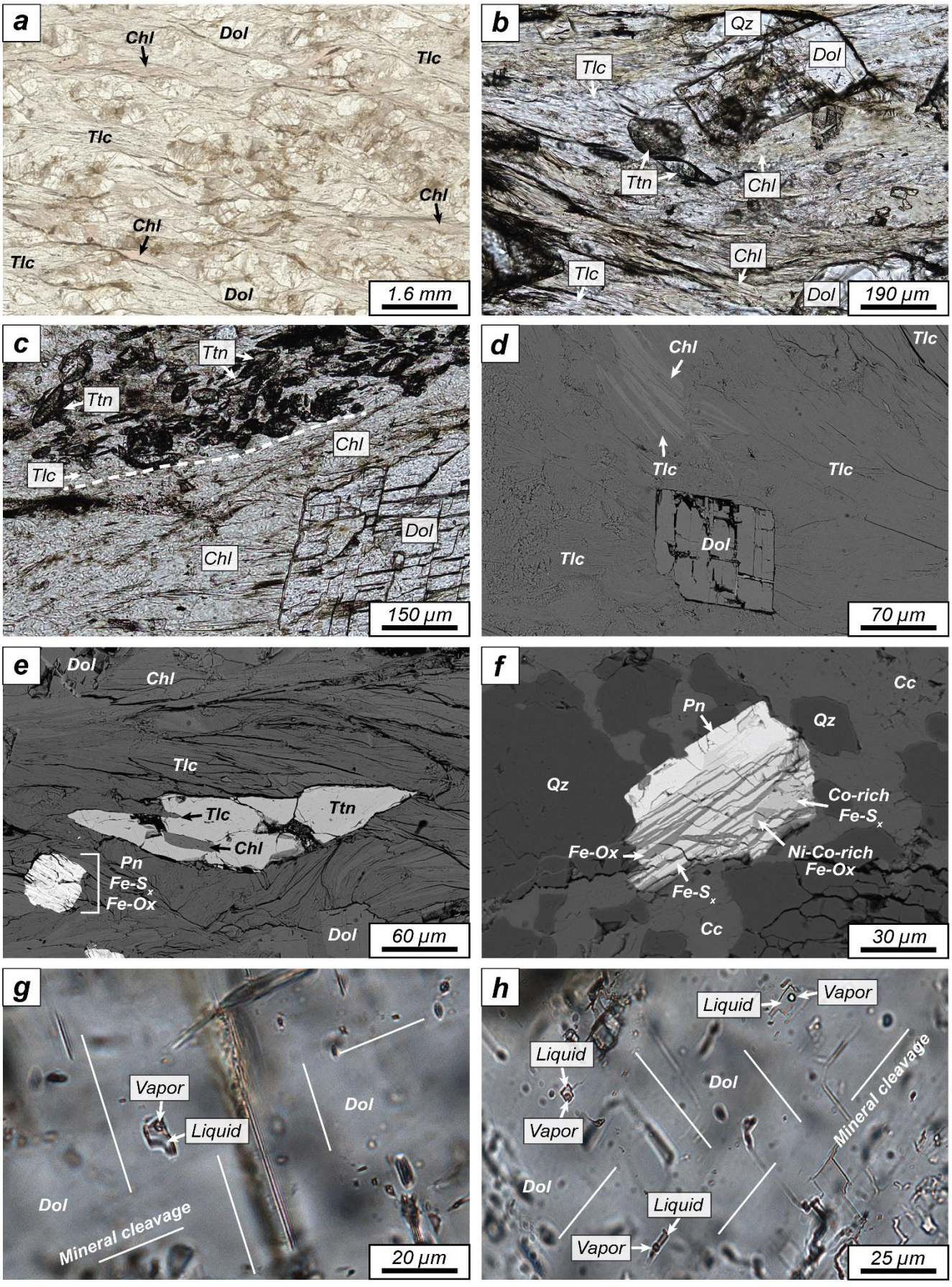
a
Chl
Dol
Tlc
Tlc
Chl
Chl
Tlc
Dol
1.6 mm
b
Qz
Tlc
Dol
Ttn
Chl
Chl
Tlc
Dol
190 µm
c
Ttn
Ttn
Chl
Tlc
Dol
Chl
150 µm
d
Chl
Tlc
Tlc
Tlc
Dol
Tlc
70 µm
e
Dol
Chl
Tlc
Tlc
Ttn
Chl
Pn
Fe-Sx
Fe-Ox
Dol
60 µm
f
Cc
Pn
Qz
Qz
Co-rich
Fe-Sx
Fe-Ox
Ni-Co-rich
Fe-Ox
Fe-Sx
Cc
30 µm
g
Vapor
Liquid
Dol
Dol
Mineral cleavage
20 µm
h
Liquid
Vapor
Liquid
Vapor
Dol
Mineral cleavage
Dol
Liquid
Vapor
25 µm

Figure V.3 *(previous page)**: Microphotographs and backscattered electron images of the carbonate-bearing talcschists. A), B), C), D) Evidences of apparent equilibrium of talc, dolomite, chlorite, quartz and titanite in the talcschists. E) Titanite containing inclusions of chlorite and talc and presence of pentlandite-Fe-sulfide + Fe-oxide/oxyhydroxide mineral aggregates in the talcschists. Closer view of a sulfide-oxide mineral aggregate showing the presence of pentlandite core with Fe-sulfide and Fe-oxide/oxyhydroxide overgrowth. Fe-sulfide and Fe-oxide/oxyhydroxide contain variable amounts of Co and Ni. G), H) Primary two-phase fluid inclusions in dolomite. Inclusions are oriented parallel to the main mineral cleavages of dolomite. Abbreviations: Cc: calcium carbonate; Chl: chlorite; Dol: dolomite; Fe-Ox: Fe-oxide/oxyhydroxide; Qz: quartz; Pn: pentlandite; FeS_x: Fe-sulfide; Tlc: talc; Ttn: titanite*

5.2. Petrographic observations of fluid inclusions

FI were mostly characterized in dolomite crystals, where they occur as isolated inclusions or in non-planar clusters (Fig. V.3g, h). They are rectangular-tubular shaped, typically 5-15 µm large and systematically oriented parallel to the principal mineral cleavages of dolomite, suggesting a primary entrapment (Roedder, 1994; Van den Kerkhof and Hein, 2001; Fig. V.3g, h). All these inclusions are two-phase (liquid + vapor) with a bubble occupying ~10% of the total inclusion volume (Fig. V.3g, h).

A few quartz-hosted FI were also characterized in sample PS1802. These inclusions are 4-7 µm large, two-phase (liquid + vapor), and occur as isolated inclusions which suggests a primary entrapment. Vapor bubbles typically occupy ~10% of the total inclusion volume.

5.3. Mineral chemical compositions

Talc has an almost homogeneous composition over the four samples, with X_{Mg} in the range 0.90-0.93 and therefore elevated iron concentrations (FeO up to 7 wt.%; Sup. mat. V.1). Talc also contains a significant amount of chromium (Cr_2O_3 up to 0.1 wt.%; Sup. mat. V.1).

Dolomite has a similar composition in the four studied samples with a large iron content (mean X_{Mg}=0.87; Fig. V.4a; Sup. mat. V.1). These dolomite crystals have a significantly lower iron content than high-pressure ankerite co-crystallized at high pressure with lawsonite in the Schistes Lustrés metasediments (Lefeuvre et al., 2020). Dolomite shows a slight enrichment in magnesium and depletion in manganese from core to rim.

Chlorite from our samples correspond to clinochlore with a mean X_{Mg} of 0.80 (Fig. V.4b, c; Sup. mat. V.1). Like for dolomite, the composition of chlorite crystals differs from that of the usual high pressure chlorite of the Schistes Lustrés metasediments (Fig. V.4b; Plunder et al., 2012; Lefeuvre et al., 2020). In our samples, chlorite is a chromium-rich clinochlore (kämmererite; Lapham, 1958; McCormick,

1975) with up to 7 wt.% Cr_2O_3 (Fig. V.4d; V.5a-b; Sup. mat. V.1). Cr is substituting for Al in octahedral sites (as shown by the linear trend in Fig. V.4d) and chlorite is generally zoned with chromium-richer cores (Fig. V.5a, b).

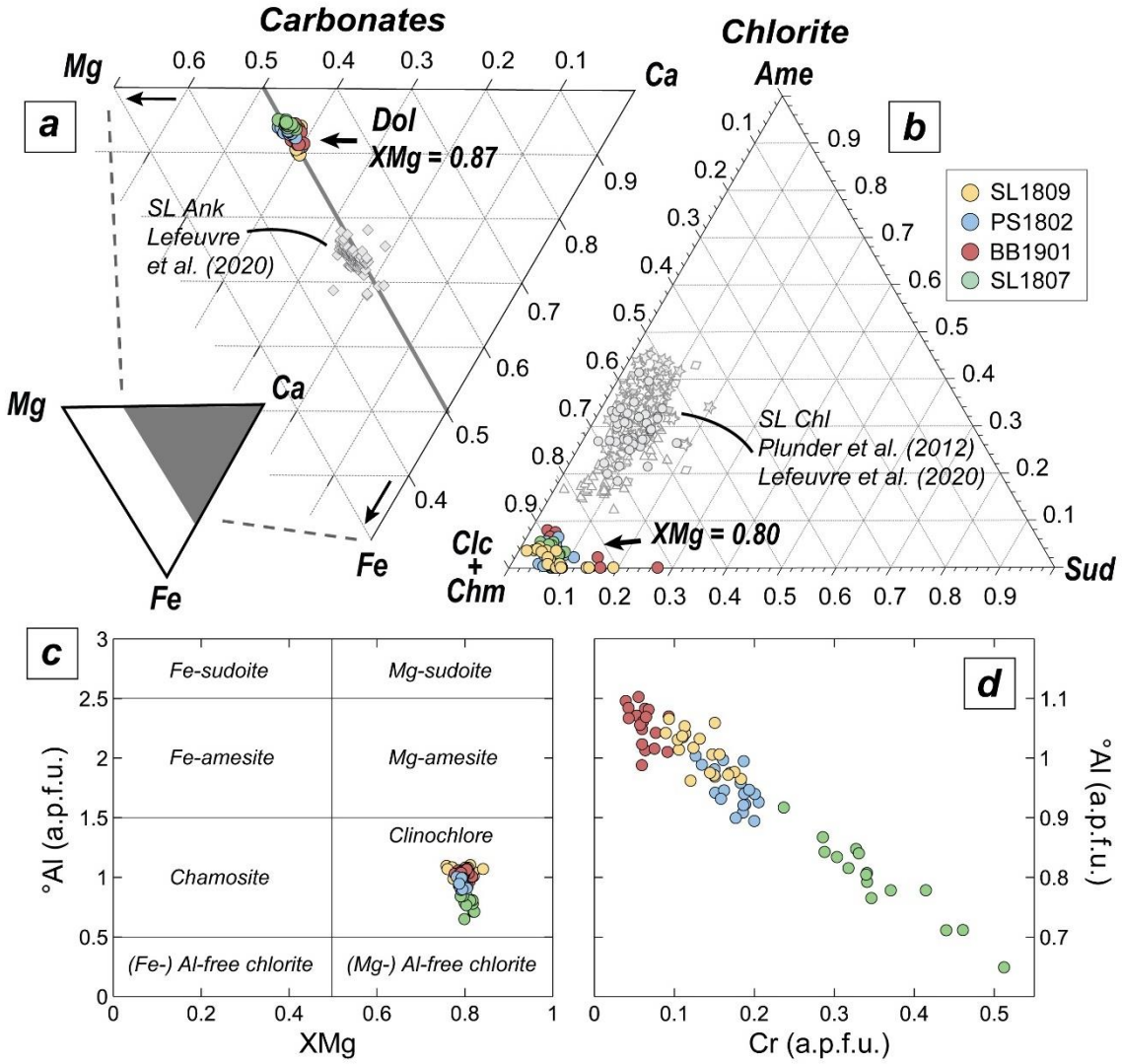

***Figure V.4**: Chemistry of carbonate-bearing talcschist minerals. A) Ternary diagram of carbonates showing the systematic difference between dolomite in the talcschists and high pressure ankerite compositions of the Schistes Lustrés from Lefeuvre et al. (2020). Ternary diagram of chlorite showing the differences in composition between chlorite from the talcschists and high pressure chlorite analyses in the Schistes Lustrés metasediments from Plunder et al. (2012) and Lefeuvre et al. (2020). C) Al in octahedral sites versus XMg in chlorite. D) Linear trend for Al in octahedral sites versus Cr in chlorite. Abbreviations: Ame: amesite; Ank: ankerite; Chl: chlorite; Chm: chamosite; Clc: clinochlore; Dol: dolomite; Sud: sudoite.*

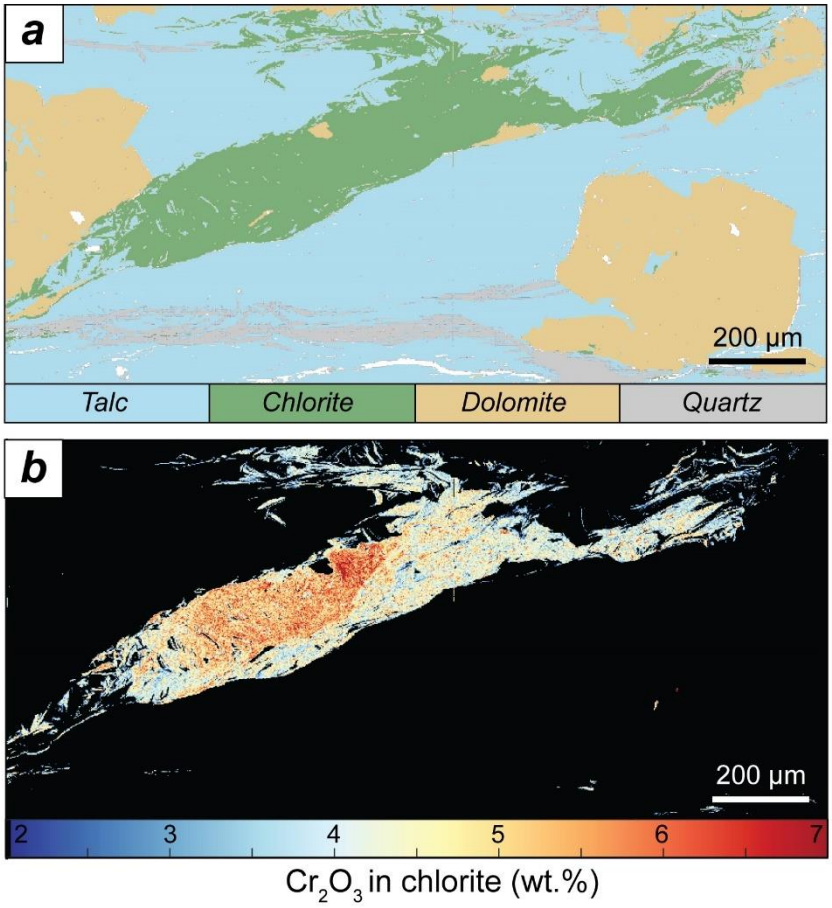

Figure V.5*: Electron microprobe compositional map. A) Mask by phase. B) Cr_2O_3 zoning in chlorite.*

5.4. Bulk-rock geochemistry

Bulk-rock compositions were compared with previously published geochemical compositions of Schistes Lustrés metasediments (Bebout et al., 2013; Lafay et al., 2013) and Liguro-Piemont serpentinites (Lafay et al., 2013; Gilio et al., 2020). Our talcschist samples have important Ni (724-1490 µg/g) and Cr (925-2125 µg/g) concentrations, much greater that all considered Schistes Lustrés metasediments while serpentinites have slightly greater concentrations in these elements (Fig. V.6a, b; Table V.1). For Ni and Cr, as for CaO, our samples show intermediate concentrations between typical Schistes Lustrés metasediments and Liguro-Piemont serpentinites (Fig. V.6a, b; Table V.1).

Another comparison to Schistes Lustrés metasediments and Liguro-Piemont serpentinites (Table V.1) is based on average compositions calculated after Bebout et al. (2013), Lafay et al. (2013) and Gilio et al. (2020). Sample compositions were normalized over the average metasediment and serpentinite compositions to detect relative enrichment or depletion (Fig. V.6c-f). The four talcschist samples appear to be enriched in Cr, Ni, Co and MgO compared to sediments, and slightly depleted in these elements compared to serpentinites (Fig. V.6c-f; Table V.1). In contrast, some LILE (K_2O, Ba, Sr), as for most REE (La, Ce, Pr, Nd, Sm, Gd, Tb, Dy, Tm, Lu, Ta) and Th, Zr, Li, Be, P_2O_5 are enriched in talcschists compared to serpentinites and depleted compared to sediments (Fig. V.6c-f; Table V.1). For the remaining REE, the same feature was observed except for slight depletions compared to sediments in SL1807 (for Yb, Er, Ho) and in PS1802 (For Eu; Fig. V.6c-f; Table V.1). Na_2O, Pb, Sb, MnO and As tend to have a similar behavior compared to sediments, with only minor differences (Na_2O depletion in SL1807; As and MnO enrichment in BB1901; Sb and As enrichment in SL1807; Pb and MnO enrichment in SL1809 Fig. V.6c-f; Table V.1). Ca is enriched in talcschists compared to both sediments and serpentinites in the four samples (Fig. V.6c-f; Table V.1). Fe_2O_3, SiO_2, Al_2O_3, TiO_2, Sc, V, Cu, Zn are depleted compared to the average sediment composition in the four samples, and also slightly depleted compared to serpentinites (yet close to the vertical line; Fig. V.6c-f; Table V.1).

Figure V.6 *(next page): Whole rock geochemistry. A) Cr vs Ni. B) CaO vs Ni. C) to E) Talcschist compositions normalized to an average Schistes Lustrés (SL) sediment and an average Liguro-Piemont (L-P) serpentinite compositions. Sediment and serpentinites compositions as average caluclations are after Bebout et al. (2013); Lafay et al. (2013) and Gilio et al. (2020) data. Whole rock element compositions are in Table V.1.*

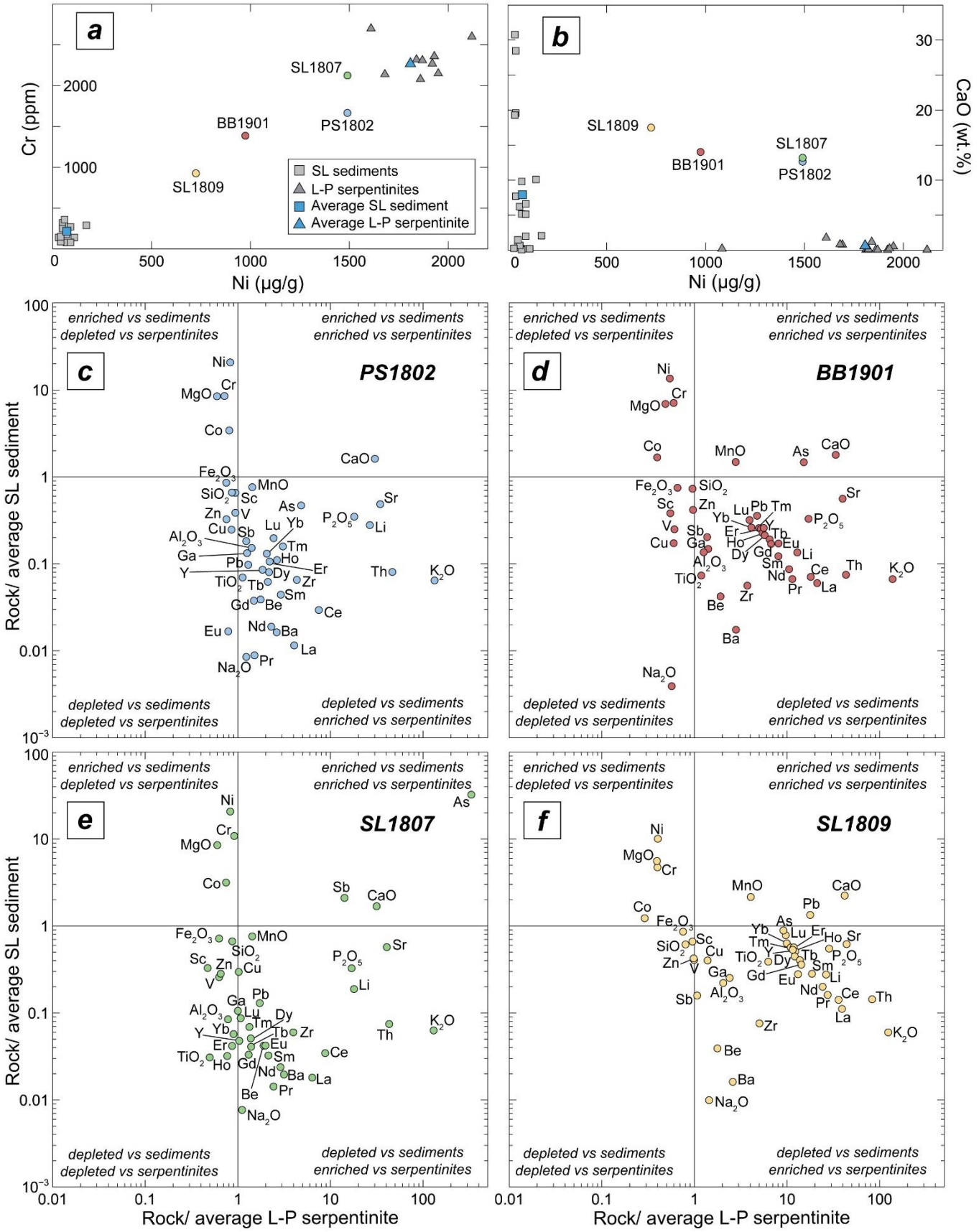
a
Cr (ppm)
Ni (µg/g)
SL1807
BB1901
PS1802
SL1809
SL sediments
L-P serpentinites
Average SL sediment
Average L-P serpentinite
b
CaO (wt.%)
Ni (µg/g)
SL1809
BB1901
SL1807
PS1802
c
PS1802
d
BB1901
e
SL1807
f
SL1809
enriched vs sediments
depleted vs serpentinites
enriched vs sediments
enriched vs serpentinites
depleted vs sediments
depleted vs serpentinites
depleted vs sediments
enriched vs serpentinites
Rock/ average SL sediment
Rock/ average L-P serpentinite

5.5. Fluid inclusion salinity and gas content

Fluid salinity estimated in the primary FI of the four talcschist samples generally shows low to intermediate salt concentrations (mean: 3.7 wt.% NaCl eq.; median: 3.6 wt.% NaCl eq.; for n = 101; Fig. V.7a) and fairly variable values (range of 0-9.3 wt.% NaCl eq. and standard deviation sd: 2.3). Detailed salinity values are the following for the different samples (with mean; median; sd; in wt.% NaCl eq. and FI numbers): PS1802 (0.7 wt.%; 0.4 wt.%; 0.8; n = 18); SL1809 (3.7 wt.%; 3.3 wt.%; 1.8; n = 30); SL1807 (4.4 wt.%; 4.8 wt.%; 2.1; n = 27) and BB1901 (5.1 wt.%; 5.0 wt.%; 2.0; n = 26). Compared to Early Cretaceous seawater salinity (~3.2-3.7 wt.%; Hay et al., 2006), PS1802 has lower values, SL1809 has comparable values and SL1807 and BB1901 have slightly higher values (Fig. V.7a). In PS1802 sample, quartz-hosted FI in quartz have salinity values similar to those of dolomite-hosted inclusions (Fig. V.7a).

The two peaks constituting the Fermi diad of CO_2 (1285 cm^{-1} and 1388 cm^{-1}) and/or the 2907 cm^{-1} peak of CH_4 were identified in most FI bubbles, and 39 FI had a Raman signal strong enough to enable quantification of gas relative proportions. The molar proportion of each gas in the CO_2-CH_4 gas mixtures is shown as a function of FI salinity (Fig. V.7b). The studied inclusions generally contain a dominant proportion of CO_2 (mean: 72%; median: 81%) except for few inclusions only containing CH_4, especially for 3 over 4 of PS1802 inclusions (Fig. V.7b). Proportions of CO_2 for the different samples are the following (mean; median; fluid inclusion numbers): PS1802 (15%; 0%; n = 4); SL1809 (69%; 86% n = 12); SL1807 (87%; 90% n = 8); BB1901 (77%; 81%; n = 15).

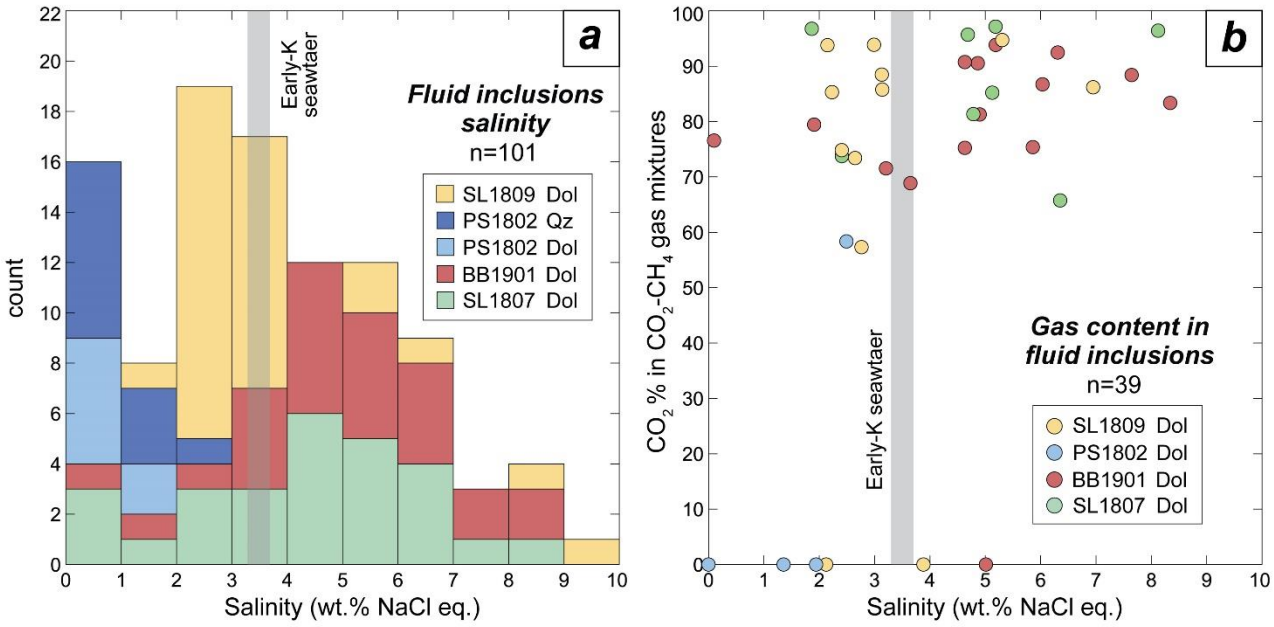

Figure V.7 *(previous page)**:** Fluid inclusion chemistry. A) Salinity of fluid inclusions. B) Gas content in fluid inclusions. Abbrevations: Early-K: Early Cretaceous; Dol: dolomite Qz: quartz*.

5.6. U-Pb geochronology

U-Pb analyses on titanite for PS1802 sample gave a well constrained isochron of 58.9 ± 4.5 Ma (2σ) for 64 spots (Fig. V.8a). In this sample, all titanite crystals have a similar REE pattern with a strong positive europium anomaly compared to CI chondrite (McDonough and Sun, 1995; Fig. V.8a), suggesting that they belong to a unique titanite generation.

SL1809 analyses gave a 61.0 ± 10.6 Ma (2σ) isochron for 69 spots (Fig. V.8b). For this sample too, a similar REE pattern was observed in all titanite crystals, but with a negative europium anomaly (Fig. V.8b).

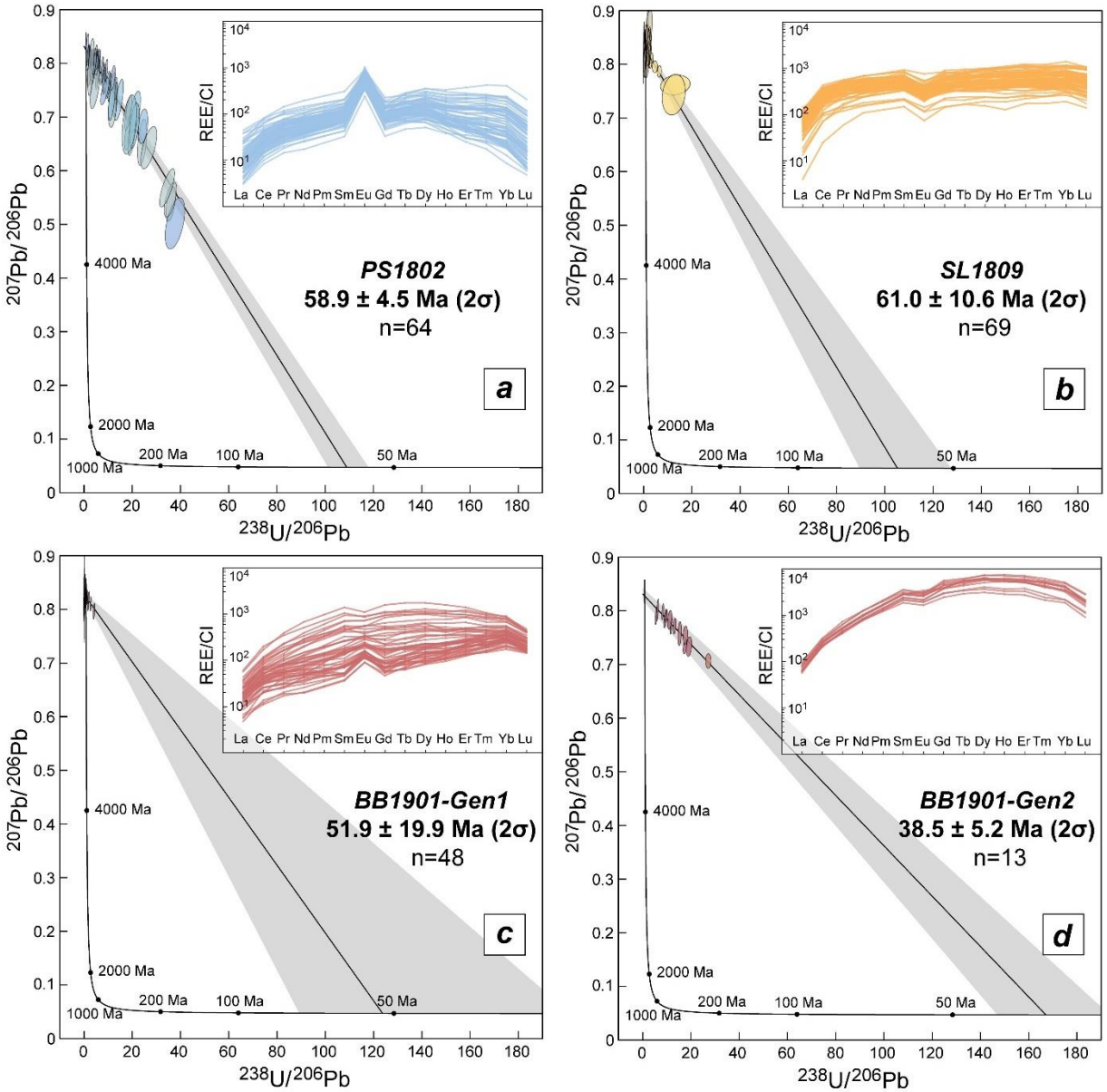

Figure V.8 *(previous page): Titanite U-Pb geochronology and REE compositions. A) PS1802; B) SL1809; C) BB1901, first generation. D) BB1901, second generation. Titanite REE compositions are normalized over CI chondrite (McDonough and Sun, 1995).*

Conversely to the two samples described above, in BB1901, two generations of titanite were distinguished by their distinct REE patterns (Fig. V.8c, d). The first generation shows a slightly positive or inexistent europium anomaly, and a much lower enrichment in REE compared to chondrite I than the second generation (Fig. V.8c, d). The second generation has a slightly negative anomaly in europium (Fig. V.8c, d) and generally corresponds to the rims of titanite crystals. Generation 1 gave a poorly constrained isochron of 51.9 ± 19.9 Ma (2σ) for 48 spots while the second generation gave a well constrained isochron of 38.5 ± 5.2 Ma (2σ) (Fig. V.8c, d).

SL1807 sample did not contain enough titanite for U-Pb geochronology.

6. Discussion

6.1. Protoliths and fluid sources

The four studied talcschist samples have large Cr, Ni, Co and MgO contents, almost equal to those of Liguro-Piemont serpentinites (Fig. V.6a-f; Table V.1). Chlorite is the main host for Cr and contains up to 7 wt.% Cr_2O_3 (Fig. V.4d; V.5a, b). Such Cr-rich clinochlore (kämmererite) was so far, to our knowledge, only described in ultramafic rocks (Lapham, 1958; McCormick, 1975). Ni and Co are hosted by sulfides as pentlandite and associated oxides (Fig. V.3e, f). Moreover, platinum-group mineralization was observed and is frequently described in ultramafic rocks as well as pentlandite (e.g. Escayola et al., 2011; Penniston-Dorland et al., 2014; Menzel et al., 2018). Finally, talc is almost ubiquitous in altered serpentinites (Spandler et al., 2008; Beinlich et al., 2012; Gyomlai et al., 2021; Austrheim et al., 2021). All these observations testify that our talcschists are derived from an ultramafic protolith.

The four studied samples are overall enriched in LILE (K_2O, Ba, Sr, Na, Pb, Eu), REE, Li, As, Sb, Th and Ca compared to Liguro-Piemont serpentinites (Fig. V.6a-h), consistent with some contribution from metasediments, which contain important concentrations of these elements (Bebout et al., 2013, Fig. V.6c-f; Table V.1). The presence of fluid-mobile elements such as LILE, Li, As, Sb in hybrid rocks is commonly interpreted as resulting from the infiltration of sediment-derived fluids (Bebout and Barton, 1993; Bebout, 2007; Penniston-Dorland et al., 2012; Angiboust et al., 2014; Gyomlai et al.,

2021). Likewise, the enrichment of Li, As, Sb in Liguro-Piemont serpentinites and metamafics was interpreted as reflecting the ingression of fluids from the Schistes Lustrés metasediments during prograde devolatilization (Lafay et al., 2013; Debret et al., 2016; 2018). In addition to Ni and Co, As, Sb, Pb, Cu are likely hosted by the sulfide-oxide/oxyhydroxide mineralization in our talcschist samples (see §5.1). The higher As concentrations in Fe-oxide/oxyhydroxide than in the primary pentlandite (± Fe-rich sulfides with variable Co, Ni and Cu content) suggest that this element was provided by the fluid (Fig. V.6a-f; Table V.1). We interpret the presence of Cr-richer chlorite cores (Fig. V.5a, b) as reflecting the direct replacement of the primary chromite from the original serpentinites. Minor fuchsite crystals are also hosting part of the Cr content. The REE, Y, Zr, TiO_2, P_2O_5 concentrations are accounted for by the presence of minor phases such as rutile, zircon, apatite, and by the presence of allanite in the more REE-enriched sample SL1809 (Fig. V.6c-f).

A contribution from sediments is supported by the CO_2-CH_4-bearing, low- to moderately saline fluids found in FI, which are similar to those reported in high pressure veins of the Schistes Lustrés metasediments (Herviou et al., 2021; Fig. V.7a, b).

These carbonate-bearing talcschist horizons are therefore similar to the carbonate-talc-bearing soapstones commonly associated to listvenites (quartz-magnesite-fuchsite rocks; Halls and Zhao, 1995) and formed through the carbonation of ultramafic rocks by CO_2-rich fluids derived from sediments (Beinlich et al., 2012; Falk and Kelemen, 2015; Menzel et al., 2018; Austrheim et al., 2021; Godard et al., 2021). These rocks are interpreted to form in various settings, e.g. during ophiolite obduction (Beinlich et al., 2012, Austrheim et al., 2021) or infiltration of slab fluids in the upper plate mantle during subduction (Falk and Kelemen, 2015; Menzel et al., 2018). The timing of formation of the talcschist samples is addressed below, to understand the mechanisms responsible for their presence in the Schistes Lustrés metasediments.

6.2. Timing of formation and implications for fluid transfer in subduction

Titanite in samples PS1802 and SL1809, which is in textural equilibrium with the main mineral assemblage (§5.1), gave well constrained isochrones at 58.9 ± 4.5 Ma (2σ, n = 64) and 61.0 ± 10.6 Ma (2σ, n = 69) respectively (Fig. V.8a, b). The few available ages for the different deformation stages identified in the LPU units of the Cottian Alps are in the range 61-55 Ma, 51-43 Ma and 38-36 Ma for D1, D2 and D3 respectively (Agard et al., 2002, Ar-Ar on phengite). The oldest stage D1, which is responsible for the development of an early fabric, corresponds to the crystallization of peak metamorphic assemblages in the Schistes Lustrés metasediments (Agard et al., 2001, 2002). The

talc + dolomite + chlorite + quartz + titanite mineral assemblage in PS1802 and SL1809 therefore formed during subduction at/or close to the peak burial conditions of the LPU units (1.7-1.9 GPa and 370-390°C for these two localities, Herviou et al., 2022).

Sample BB1901 from the LPM units contains two generations of titanite yielding respectively: (i) a poorly constrained isochron at 51.9 ± 19.9 Ma (2σ, n = 48; Fig. V.8c) and (ii) a well constrained isochron at 38.5 ± 5.2 Ma (2σ, n = 13; Fig. V.8d). Peak-burial related D1 deformation stage of the LPM units from Cottian Alps-Queyras region was dated at 64-49 Ma (Agard et al., 2002, Ar-Ar on phengite) while D3 deformation coeval with the late stacking of Liguro-Piemont slices was dated at ~35 Ma (Angiboust and Glodny, 2020, Rb-Sr on phengite). The first generation may therefore have recorded the formation of talcschists at/or close to peak burial of the LPM units (~2.1 GPa and 418°C for this locality, Herviou et al., 2022), as for the LPU samples PS1802 and SL1809, whereas the second titanite generation fits well the age of D3, for which greenschist-facies fluid circulations are documented during exhumation (e.g. Agard et al., 2000).

Results therefore indicate that these carbonate-bearing talcschists formed at depth during subduction, and that a significant part of the metasomatic transformation occurred at or close to peak burial conditions. These horizons are embedded within metasediments, thereby representing former lithological contacts between sediments and serpentinites transformed by CO_2-CH_4-bearing fluids (as indicated by FI data and the large amounts of dolomite; Fig. V.2a-e). These fluids were likely liberated by surrounding sediments, devolatilizing during burial, as highlighted by both the strong enrichment in LILE and other fluid-mobile elements compared to Liguro-Piemont serpentinites, and by the composition of fluids trapped in inclusions (§6.1; Fig. V.6c-f, V.7a, b). The mean-median CO_2 proportions (over CH_4) of 70%-81% in the gas phase of our talcschist FI are furthermore equivalent to those estimated for decimeter-to-meter large lawsonite- and Fe-Mg carpholite- bearing high pressure veins of the surrounding sediments (mean-median: 64-80%; Herviou et al., 2021; Fig. V.7b). Samples PS1802 and SL1809 also belong to the eastern part of the LPU units, where lawsonite-bearing high pressure veins in sediments recorded salinity close to seawater values (Herviou et al., 2021). Sample PS1802 has salinity values significantly lower than Early Cretaceous seawater salinity, whereas those of sample SL1809 are similar (~3.2-3.7 wt.%; Hay et al., 2006; Fig. V.7a). Samples SL1807 and BB1901, from the LPM units where high-pressure veins in sediments recorded salinity below seawater values (Herviou et al., 2021), have salinity values slightly greater than seawater (Fig. V.7a). Serpentinites, and notably Alpine ones, often contain high chlorine concentrations (e.g. Scambelluri et al., 1997; Kendrick et al., 2011) and the redistribution of their high chlorine content in

the fluid during the infiltration of sediment-derived fluids in serpentinites may account for the salinity greater than seawater in samples SL1807 and BB1901.

In the Queyras region, the sediment-derived fluids result from the devolatilization of metapelites that are rich in carbonaceous-material (CH_4-bearing) at or close to peak-burial conditions (Herviou et al., 2021). This fluid might have interacted with carbonate-layers close to the serpentinite horizons (Fig. V.2a, b, e) explaining the enrichment in CO_2, CaO, Sr and precipitation of large amounts of dolomite in the talcschists. Consistently with the low-salinity of sample PS1802 FI and the relatively low salinity of the other samples (§6.1, Fig. V.7a), the low-saline fluids of the eastern-LPU and the LPM units are interpreted to be related to fresh-fluids released by Fe-Mg carpholite-dehydration in metasediments (Herviou et al., 2021, 2022).

It was previously suggested by isotopic, trace elements and FI studies that the Schistes Lustrés metasediments mostly acted as a rock-buffered system during subduction with only limited external fluid infiltration (e.g. Henry et al., 1996; Bebout et al., 2013; Herviou et al., 2021). This study highlights that, along lithological boundaries, external fluids from sediments may affect serpentinites as already suggested in some sediment-mafic (Debret et al., 2016; Inglis et al., 2019; Vitale Brovarone et al., 2020; Herviou et al., 2021) and sediment-ultramafic contacts (Lafay et al., 2013; Debret et al., 2018; Tartarotti et al., 2019; Vitale Brovarone et al., 2020; Rotondo et al., 2021). Due to its (ultra-) slow-spreading character, a large part of the Liguro-Piemont oceanic seafloor was in fact made of serpentinites (Lagabrielle and Cannat, 1990; Lagabrielle et al., 2015) and serpentinite-sediment contacts might have been ubiquitous in the lithostratigraphy (Herviou et al., 2022). During subduction, the formation of carbonate-bearing talcschists may therefore have been extensive and volumetrically significant. These rocks, which are stable up to high P-T conditions (Spandler et al., 2008; Bebout and Penniston-Dorland, 2016), contain large amounts of carbonates and high concentrations of fluid-mobile elements that may have contributed to carbon recycling and/or affected the composition of the mantle wedge during their destabilization at sub-arc depths (Stern, 2002; Kelley and Cottrell, 2009; Kelemen and Manning, 2015; Cannao et al., 2020).

6.3. Offscraping of oceanic lithosphere led by a positive feedback between deformation and fluid infiltration?

One question remains: since carbonate-bearing talcschists mark initial boundaries between serpentinites and sediments, why are they only found inside or close to subduction-related tectonic contacts? (i.e. contact between subduction slices; §3, Fig. V.1).

Most of the Liguro-Piemont slices expose an almost complete lithostratigraphic succession, with a preserved serpentinite basement often dismembered by exhumation processes (Herviou et al., 2022). For the LPU and LPM units, which contain this complete succession, the décollement layer was therefore necessarily in the serpentinites. The tectonic slicing is interpreted to have occurred in weak zones along lithological contacts, along a slightly more serpentinized mantle and/or along former oceanic detachments, possibly under high fluid pressure (Herviou et al., 2022). This is also attested by the presence of serpentinites in numerous tectonic contacts between the Liguro-Piemont slices (Angiboust et Agard, 2010; Angiboust et al., 2011; Herviou et al., 2022).

Our results show that lithological boundaries between serpentinites and sediments acted as major pathways for the ingression of sediments-derived fluids (§6.1, 6.2), locally hybridizing the former serpentinite horizons. Since the contact between these two rock types represents a rheological contrast, we propose that deformation along these boundaries during prograde metamorphism focused external fluids derived from metasediments. As an external out-of-equilibrium fluid percolated the rocks, it reacted with the serpentinites and the talc-dolomite-chlorite-quartz-titanite assemblages started forming (Fig. V.9a). Serpentinites are often considered as weak rocks, where deformation might localize in subduction zones (Hermann et al., 2000; Hilairet et al., 2017; Angiboust et al., 2011; Ruh et al., 2015; Agard et al., 2018; Tewksbury-Christle et al., 2021). However, since talc has a much lower shear strength than serpentine minerals (lizardite, antigorite, chrysotile; Moore and Lockner, 2007; Moore and Rymer, 2007), the presence of even small amounts of talc in serpentine-talc or quartz-talc assemblages must have drastically reduced the overall strength of these ultramafic horizons (Moore and Lockner, 2011; Hirauchi et al., 2013). As the talcschists started forming, strain did localize along the metasomatic horizon (Fig. V.2a, b, c), enhancing in turn the infiltration of external fluids and creating a positive feedback between deformation and fluid infiltration (Fig. V.9b).

We propose that this positive feedback may have ultimately led to the slicing of tectonic slivers from the downgoing plate along these very weak horizons (Fig. V.9b), thereby explaining their presence only along tectonic contacts bounding the Liguro-Piemont units. After offscraping, the talcschist horizons would represent the edges of the Liguro-Piemont slices directly exposed to the fluids released by the dehydrating slab (Fig. V.9c). Likewise, the later greenschist-facies fluids likely reacted with the talcschists, explaining the syn-D3 ages retrieved in the second generation of titanite from BB1901 (Fig. V.9c, d, e).

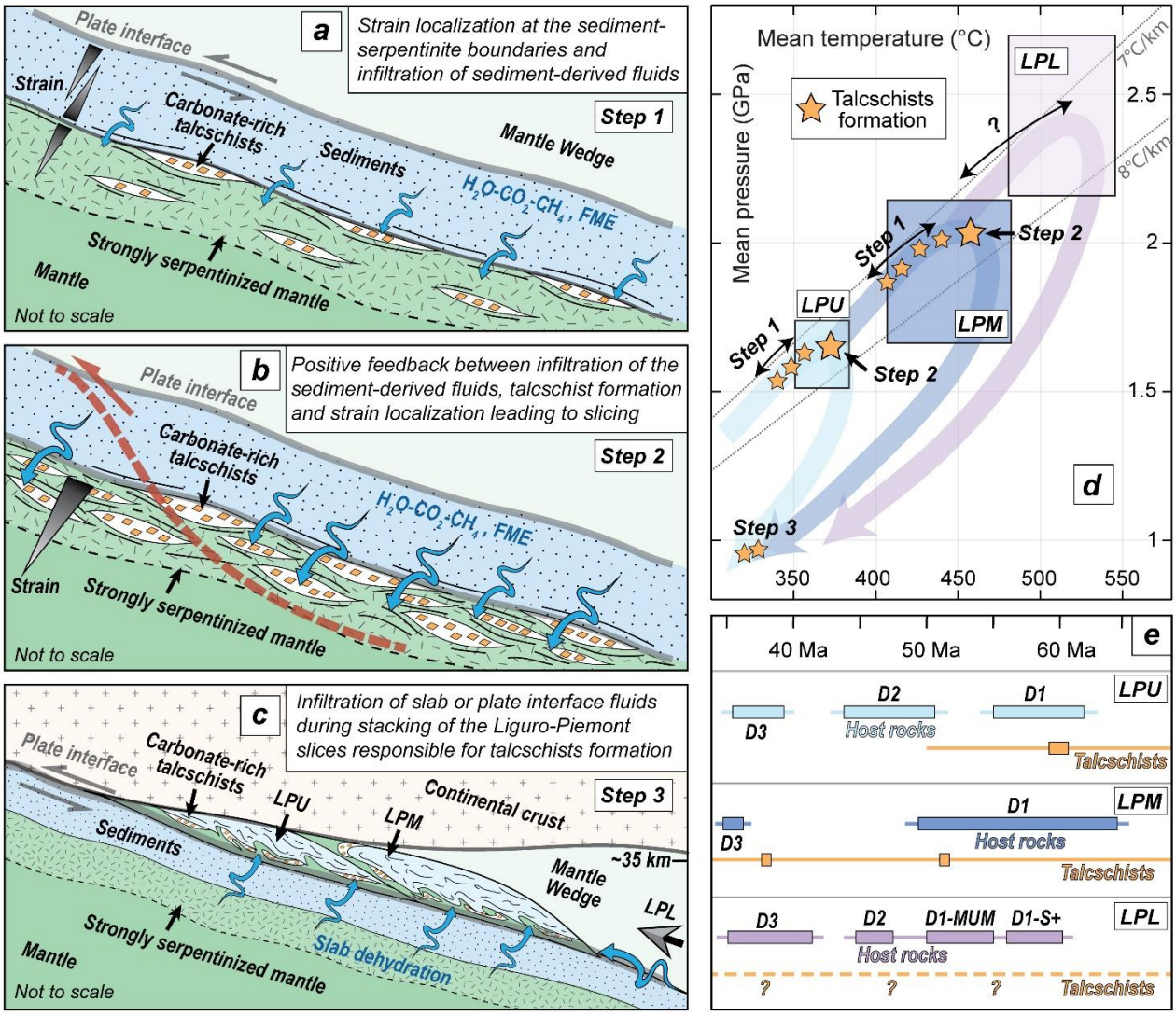

***Figure V.9**: A) sketch representing the successive steps of talcschist formation: step 1: strain localization at the sediment-serpentinite boundaries and infiltration of sediment-derived fluids leading to talcschist formation. Step 2: Positive feedback beteen infiltration of fluids and strain localization in talcschists leading to slicing at peak burial. Step 3: infiltration of fluids from the dehydrating slab during exhumation responsible for talcschist formation. B) Steps of talcschist formation reported on the pressure temperature paths of the Liguro-Piemont units. P-T paths are after Herviou et al. (2022) C) Timing of talcschist formation compared to the major deformation events dated in the Liguro-Piemont units. Ages for the deformation events are after Agard et al. (2002) and Angiboust and Glodny (2020). Abbreviations: LPU: Liguro-Piemont Upper units; LPM: Liguro-Piemont Middle Units; LPL: Liguro-Piemont Lower units. MUM: Mafic-ultramafic dominated units; S+: sediment dominated units.*

Conclusion

Carbonate-bearing talcschists horizons have been discovered near subduction-related tectonic contacts in the Liguro-Piemont domain. These rocks are rich in Ni, Co, Cr and Mg, and contain significant amounts of fluid-mobile elements. Fluid inclusions in dolomite and quartz revealed the

presence of an aqueous, low saline and CO_2-CH_4-bearing fluid during their formation. The talcschists are interpreted as hybrid rocks formed by the metasomatism of ultramafic rocks by external, sediment-derived fluids. Titanite U-Pb geochronology constrains the timing of formation of theses rocks, coeval with high-pressure metamorphism in the Liguro-Piemont domain. Large amounts of carbonates and concentrations of fluid-mobile elements in these rocks (stable over a wide range of P-T conditions) suggest that these rocks are a significant carrier of carbon to depth and might exist in the mantle wedge. The formation of rheologically weak talc in response to external fluid infiltration likely controlled a positive feedback between fluid ingression and deformation. This suggests that these rocks played a major role to localize strain within the downgoing plate prior to slicing and exhumation.

References

Agard, P., 2021. Subduction of oceanic lithosphere in the Alps: Selective and archetypal from (slow-spreading) oceans. Earth-Science Reviews 214, 103517. https://doi.org/10.1016/j.earscirev.2021.103517.

Agard, P., Goffé, B., Touret, J.L.R., Vidal, O., 2000. Retrograde mineral and fluid evolution in high-pressure metapelites (Schistes lustrés unit, Western Alps). Contributions to Mineralogy and Petrology 140, 296–315. https://doi.org/10.1007/s004100000190.

Agard, P., Handy, M.R., 2021. Ocean Subduction Dynamics in the Alps. Elements 17, 9–16. https://doi.org/10.2138/gselements.17.1.9.

Agard, P., Jolivet, L., Goffe, B., 2001. Tectonometamorphic evolution of the Schistes Lustres Complex; implications for the exhumation of HP and UHP rocks in the Western Alps. Bulletin de la Société Géologique de France 172, 617–636. https://doi.org/10.2113/172.5.617.

Agard, P., Monie, P., Jolivet, L., Goffe, B., 2002. Exhumation of the Schistes Lustres complex: in situ laser probe 40Ar/39Ar constraints and implications for the Western Alps. J Metamorph Geol 20, 599–618. https://doi.org/10.1046/j.1525-1314.2002.00391.x.

Agard, P., Plunder, A., Angiboust, S., Bonnet, G., Ruh, J., 2018. The subduction plate interface: rock record and mechanical coupling (from long to short timescales). Lithos 320–321, 537–566. https://doi.org/10.1016/j.lithos.2018.09.029.

Agard, P., Yamato, P., Jolivet, L., Burov, E., 2009. Exhumation of oceanic blueschists and eclogites in subduction zones: Timing and mechanisms. Earth-Science Reviews 92, 53–79. https://doi.org/10.1016/j.earscirev.2008.11.002.

Aleinikoff, J. N., Wintsch, R. P., Tollo, R. P., Unruh, D. M., Fanning, C. M., Schmitz, M. D., 2007. Ages and origins of rocks of the Killingworth dome, south-central Connecticut: Implications for the tectonic evolution of southern New England. American Journal of Science, 307, 63-118.

Angiboust, S., Agard, P, 2010. Initial water budget: The key to detaching large volumes of eclogitized oceanic crust along the subduction channel? 22.

Angiboust, S., Agard, P., Raimbourg, H., Yamato, P., Huet, B., 2011. Subduction interface processes recorded by eclogite-facies shear zones (Monviso, W. Alps). Lithos 127, 222–238. https://doi.org/10.1016/j.lithos.2011.09.004.

Angiboust, S., Glodny, J., 2020. Exhumation of eclogitic ophiolitic nappes in the W. Alps: New age data and implications for crustal wedge dynamics. Lithos 356–357, 105374. https://doi.org/10.1016/j.lithos.2020.105374.

Angiboust, S., Pettke, T., De Hoog, J.C.M., Caron, B., Oncken, O., 2014. Channelized Fluid Flow and Eclogite-facies Metasomatism along the Subduction Shear Zone. Journal of Petrology 55, 883–916. https://doi.org/10.1093/petrology/egu010.

Austrheim, H., Corfu, F., Renggli, C.J., 2021. From peridotite to fuchsite bearing quartzite via carbonation and weathering: with implications for the Pb budget of continental crust. Contrib Mineral Petrol 176, 94. https://doi.org/10.1007/s00410-021-01851-z.

Bebout, G.E., 2007. Metamorphic chemical geodynamics of subduction zones. Earth and Planetary Science Letters 260, 373–393. https://doi.org/10.1016/j.epsl.2007.05.050.

Bebout, G.E., Barton, M.D., 1993. Metasomatism during subduction: products and possible paths in the Catalina Schist, California. Chemical Geology 108, 61–92. https://doi.org/10.1016/0009-2541(93)90318-D.

Bebout, G.E., Barton, M.D., 2002. Tectonic and metasomatic mixing in a high-T, subduction-zone mélange—insights into the geochemical evolution of the slab–mantle interface. Chemical Geology 187, 79–106. https://doi.org/10.1016/S0009-2541(02)00019-0.

Bebout, G.E., Penniston-Dorland, S.C., 2016. Fluid and mass transfer at subduction interfaces—The field metamorphic record. Lithos 240–243, 228–258. https://doi.org/10.1016/j.lithos.2015.10.007.

Bebout, G.E., Agard, P., Kobayashi, K., Moriguti, T., Nakamura, E., 2013. Devolatilization history and trace element mobility in deeply subducted sedimentary rocks: Evidence from Western Alps HP/UHP suites. Chemical Geology 342, 1–20. https://doi.org/10.1016/j.chemgeo.2013.01.009.

Beinlich, A., Plümper, O., Hövelmann, J., Austrheim, H., Jamtveit, B., 2012. Massive serpentinite carbonation at Linnajavri, N-Norway: Massive serpentinite carbonation at Linnajavri, N-Norway. Terra Nova 24, 446–455. https://doi.org/10.1111/j.1365-3121.2012.01083.x.

Cannaò, E., Scambelluri, M., Bebout, G.E., Agostini, S., Pettke, T., Godard, M., Crispini, L., 2020. Ophicarbonate evolution from seafloor to subduction and implications for deep-Earth C cycling. Chemical Geology 546, 119626. https://doi.org/10.1016/j.chemgeo.2020.119626.

Caumon, M.-C., Dubessy, J., Robert, P., Tarantola, A., 2013. Fused-silica capillary capsules (FSCCs) as reference synthetic aqueous fluid inclusions to determine chlorinity by Raman spectroscopy. ejm 25, 755–763. https://doi.org/10.1127/0935-1221/2013/0025-2280.

De Wever, P., Caby, R., 1981. Datation de la base des schistes lustrés postophiolitiques par des radiolaires (Oxfordien-Kimmeridgien moyen) dans les Alpes Cottiennes (Saint Véran, France). Comptes Rendus de l'Académie des Sciences de Paris 292, 467–472.

Debret, B., Koga, K.T., Cattani, F., Nicollet, C., Van den Bleeken, G., Schwartz, S., 2016. Volatile (Li, B, F and Cl) mobility during amphibole breakdown in subduction zones. Lithos 244, 165–181. https://doi.org/10.1016/j.lithos.2015.12.004.

Debret, B., Bouilhol, P., Pons, M.L., Williams, H., 2018. Carbonate Transfer during the Onset of Slab Devolatilization: New Insights from Fe and Zn Stable Isotopes. Journal of Petrology 59, 1145–1166. https://doi.org/10.1093/petrology/egy057.

Deville, E., Fudral, S., Lagabrielle, Y., Marthaler, M., Sartori, M., 1992. From oceanic closure to continental collision: A synthesis of the" Schistes lustrés" metamorphic complex of the Western Alps. Geological Society of America Bulletin 104, 127–139.

Epstein, G.S., Bebout, G.E., Angiboust, S., 2021. Fluid and mass transfer along transient subduction interfaces in a deep paleo-accretionary wedge (Western Alps). Chemical Geology 559, 119920. https://doi.org/10.1016/j.chemgeo.2020.119920.

Escayola, M., Garuti, G., Zaccarini, F., Proenza, J.A., Bedard, J.H., Van Staal, C., 2011. Chromitite and platinum-group-element mineralization at middle arm brook, Central Advocate ophiolite complex, Baie Verte peninsula, Newfoundland, Canada. The Canadian Mineralogist 49, 1523–1547. https://doi.org/10.3749/canmin.49.6.1523.

Falk, E.S., Kelemen, P.B., 2015. Geochemistry and petrology of listvenite in the Samail ophiolite, Sultanate of Oman: Complete carbonation of peridotite during ophiolite emplacement. Geochimica et Cosmochimica Acta 160, 70–90. https://doi.org/10.1016/j.gca.2015.03.014.

Fermi, E., 1931. Über den ramaneffekt des kohlendioxyds. Zeitschrift für Physik 71, 250–259.

Frezzotti, M.L., Tecce, F., Casagli, A., 2012. Raman spectroscopy for fluid inclusion analysis. Journal of Geochemical Exploration 112, 1–20. https://doi.org/10.1016/j.gexplo.2011.09.009.

Fudral, S., 1996. Etude géologique de la suture tethysienne dans les Alpes franco-italiennes Nord-Occidentales de la Doire Ripaire (Italie) à la région de Bourg Saint-Maurice. PhD thesis Université de Savoie.

Gilio, M., 2020. Fingerprinting and relocating tectonic slices along the plate interface: Evidence from the Lago Superiore unit at Monviso (Western Alps). Lithos, 105308.

Godard, M., Carter, E.J., Decrausaz, T., Lafay, R., Bennett, E., Kourim, F., Obeso, J. -C., Michibayashi, K., Harris, M., Coggon, J.A., Teagle, D.A.H., Kelemen, P.B., the Oman Drilling Project Phase 1 Science Party, 2021. Geochemical Profiles Across the Listvenite-Metamorphic Transition in the Basal Megathrust of the Semail Ophiolite: Results From Drilling at OmanDP Hole BT1B. JGR Solid Earth 126. https://doi.org/10.1029/2021JB022733.

Gyomlai, T., Agard, P., Marschall, H.R., Jolivet, L., Gerdes, A., 2021. Metasomatism and deformation of block-in-matrix structures in Syros: The role of inheritance and fluid-rock interactions along the subduction interface. Lithos 386–387, 105996. https://doi.org/10.1016/j.lithos.2021.105996.

Hacker, B.R., 2008. H 2 O subduction beyond arcs. Geochem. Geophys. Geosyst. 9. https://doi.org/10.1029/2007GC001707.

Hacker, B.R., Peacock, S.M., Abers, G.A., Holloway, S.D., 2003. Subduction factory 2. Are intermediate-depth earthquakes in subducting slabs linked to metamorphic dehydration reactions?. J. Geophys. Res. 108. https://doi.org/10.1029/2001JB001129.

Halls, C., Zhao, R., 1995. Listvenite and related rocks: perspectives on terminology and mineralogy with reference to an occurrence at Cregganbaun, Co. Mayo, Republic of Ireland. Mineral. Deposita 30, 303–313. https://doi.org/10.1007/BF00196366.

Handy, M.R., 2010. Reconciling plate-tectonic reconstructions of Alpine Tethys with the geological–geophysical record of spreading and subduction in the Alps. Earth-Science Reviews 102, 121-158.

Hay, W.W., Migdisov, A., Balukhovsky, A.N., Wold, C.N., Flögel, S., Söding, E., 2006. Evaporites and the salinity of the ocean during the Phanerozoic: Implications for climate, ocean circulation and life. Palaeogeography, Palaeoclimatology, Palaeoecology 240, 3–46. https://doi.org/10.1016/j.palaeo.2006.03.044.

Henry, C., Burkhard, M., Goffé, B., 1996. Evolution of synmetamorphic veins and their wallrocks through a Western Alps transect: no evidence for large-scale fluid flow. Stable isotope, major- and trace-element systematics. Chemical Geology 127, 81–109. https://doi.org/10.1016/0009-2541(95)00106-9.

Hermann, J., Müntener, O., Scambelluri, M., 2000. The importance of serpentinite mylonites for subduction and exhumation of oceanic crust. Tectonophysics 327, 225–238. https://doi.org/10.1016/S0040-1951(00)00171-2.

Herviou, C., Verlaguet, A., Agard, P., Locatelli, M., Raimbourg, H., Lefeuvre, B., Dubacq, B., 2021. Along-dip variations of subduction fluids: The 30–80 km depth traverse of the Schistes Lustrés complex (Queyras-Monviso, W. Alps). Lithos 394–395, 106168. https://doi.org/10.1016/j.lithos.2021.106168.

Herviou, C., Agard, P., Plunder, A., Mendes, K., Verlaguet, A., Deldicque, D., Cubas, N., 2022. Subducted fragments of the Liguro-Piemont ocean, Western Alps: spatial correlations and offscraping mechanisms during subduction. Tectonophysics 827, 229267. https://doi.org/10.1016/j.tecto.2022.229267.

Hilairet, N., Reynard, B., Wang, Y., Daniel, I., Merkel, S., Nishiyama, N., Petitgirard, S., 2007. High-Pressure Creep of Serpentine, Interseismic Deformation, and Initiation of Subduction. Science 318, 1910–1913. https://doi.org/10.1126/science.1148494.

Inglis, E.C., Debret, B., Burton, K.W., Millet, M.-A., Pons, M.-L., Dale, C.W., Bouilhol, P., Cooper, M., Nowell, G.M., McCoy-West, A.J., Williams, H.M., 2017. The behavior of iron and zinc stable isotopes accompanying the subduction of mafic oceanic crust: A case study from Western Alpine ophiolites. Geochem. Geophys. Geosyst. 18, 2562–2579. https://doi.org/10.1002/2016GC006735.

Jaeckel, K., Bebout, G.E., Angiboust, S., 2018. Deformation-enhanced fluid and mass transfer along Western and Central Alps paleo-subduction interfaces: Significance for carbon cycling models. Geosphere 14, 2355–2375. https://doi.org/10.1130/GES01587.1.

Jochum, K. P., Weis, U., Stoll, B., Kuzmin, D., Yang, Q., Raczek, I., Jacob, D.E., Stracke, A., Birbaum, K., Frick, D.A., Günther, D., Enzweiler, J., 2011. Determination of reference values for NIST SRM 610–617 glasses following ISO guidelines. Geostandards and Geoanalytical Research, 35(4), 397-429.

Kelemen, P.B., Manning, C.E., 2015. Reevaluating carbon fluxes in subduction zones, what goes down, mostly comes up. Proc Natl Acad Sci USA 112, E3997–E4006. https://doi.org/10.1073/pnas.1507889112.

Kelley, K.A., Cottrell, E., 2009. Water and the Oxidation State of Subduction Zone Magmas. Science 325, 605–607. https://doi.org/10.1126/science.1174156.

Kendrick, M.A., Scambelluri, M., Honda, M., Phillips, D., 2011. High abundances of noble gas and chlorine delivered to the mantle by serpentinite subduction. Nature Geoscience 4, 807–812. https://doi.org/10.1038/ngeo1270.

Lafay, R., Deschamps, F., Schwartz, S., Guillot, S., Godard, M., Debret, B., Nicollet, C., 2013. High-pressure serpentinites, a trap-and-release system controlled by metamorphic conditions: Example from the Piedmont zone of the western Alps. Chemical Geology 343, 38–54. https://doi.org/10.1016/j.chemgeo.2013.02.008.

Lagabrielle, Y., 1987. Les ophiolites : Marqueurs de l'histoire tectonique des domaines océaniques. PhD thesis Brest.

Lagabrielle, Y., Cannat, M., 1990. Alpine Jurassic ophiolites resemble the modern central Atlantic basement. Geology 18, 319–322.

Lagabrielle, Y., Vitale Brovarone, A., Ildefonse, B., 2015. Fossil oceanic core complexes recognized in the blueschist metaophiolites of Western Alps and Corsica. Earth-Science Reviews 141, 1–26. https://doi.org/10.1016/j.earscirev.2014.11.004

Lapen, T.J., Johnson, C.M., Baumgartner, L.P., Mahlen, N.J., Beard, B.L., Amato, J.M., 2003. Burial rates during prograde metamorphism of an ultra-high-pressure terrane: an example from Lago di Cignana, western Alps, Italy. Earth and Planetary Science Letters 215, 57–72. https://doi.org/10.1016/S0012-821X(03)00455-2.

Lapham, D.M., 1958. Structural and chemical variation in chromium chlorite. American Mineralogist: Journal of Earth and Planetary Material 43, 921–956.

Le Pichon, X., Bergerat, F., Roulet, M., 1988. Plate kinematics and tectonics leading to the Alpine belt formation: a new analysis. Geological Society of America Special Issue 218, 111–131.

Le, V.-H., Caumon, M.-C., Tarantola, A., Randi, A., Robert, P., Mullis, J., 2020. Calibration data for simultaneous determination of P-V-X properties of binary and ternary CO2 - CH4 - N2 gas mixtures by Raman spectroscopy over 5–600 bar: Application to natural fluid inclusions. Chemical Geology 552, 119783. https://doi.org/10.1016/j.chemgeo.2020.119783.

Le, V.-H., Caumon, M.-C., Tarantola, A., Randi, A., Robert, P., Mullis, J., 2019. Quantitative Measurements of Composition, Pressure, and Density of Microvolumes of CO 2 –N 2 Gas Mixtures by Raman Spectroscopy. Anal. Chem. 91, 14359–14367. https://doi.org/10.1021/acs.analchem.9b02803.

Lefeuvre, B., Agard, P., Verlaguet, A., Dubacq, B., Plunder, A., 2020. Massive formation of lawsonite in subducted sediments from the Schistes Lustrés (W. Alps): Implications for mass transfer and decarbonation in cold subduction zones. Lithos 370–371, 105629. https://doi.org/10.1016/j.lithos.2020.105629.

Lemoine, M., Marthaler, M., Caron, M., Sartori, M., Amaudric du Chaffaut, S., 1984. Découverte de foraminifères planctoniques du Crétacé supérieur dans les schistes lustrés du Queyras (Alpes occidentales). Conséquences paléogéographiques et tectoniques. Comptes-rendus des séances de l'Académie des sciences. Série 2, Mécanique-physique, chimie, sciences de l'univers, sciences de la terre 299, 727–732.

Lemoine, M., Tricart, P., 1986. Les Schistes lustrés piémontais des Alpes Occidentales : approche stratigraphique, structurales et sédimentologique. Eclogae Geologicae Helvetiae 79, 271–294. https://doi.org/10.5169/SEALS-165835.

Marschall, H.R., Schumacher, J.C., 2012. Arc magmas sourced from mélange diapirs in subduction zones. Nature Geosci 5, 862–867. https://doi.org/10.1038/ngeo1634.

Marthaler, M., Stampfli, G.M., 1989. Les Schistes lustrés à ophiolites de la nappe du Tsaté : un ancien prisme d'accrétion de la marge active apulienne? Schweizerische Mineralogische und Petrographische Mitteilunge 69, 211–216. https://doi.org/10.5169/SEALS-52789

McCormick, G. R, 1975. A chemical study of kämmererite, Day Book Body, Yancey County, North Carolina. American Mineralogist: Journal of Earth and Planetary Material 60, 924–927.

McDonough, W.F., Sun, S.-S., 1995. The composition of the Earth'. Chemical Geology 120, 223–253.

Menzel, M.D., Garrido, C.J., López Sánchez-Vizcaíno, V., Marchesi, C., Hidas, K., Escayola, M.P., Delgado Huertas, A., 2018. Carbonation of mantle peridotite by CO2-rich fluids: the formation of listvenites in the Advocate ophiolite complex (Newfoundland, Canada). Lithos 323, 238–261. https://doi.org/10.1016/j.lithos.2018.06.001.

Moore, D.E., Lockner, D.A., 2007. Comparative Deformation Behavior of Minerals in Serpentinized Ultramafic Rock: Application to the Slab-Mantle Interface in Subduction Zones. International Geology Review 49, 401–415. https://doi.org/10.2747/0020-6814.49.5.401.

Moore, D.E., Lockner, D.A., 2011. Frictional strengths of talc-serpentine and talc-quartz mixtures. J. Geophys. Res. 116, B01403. https://doi.org/10.1029/2010JB007881.

Moore, D.E., Rymer, M.J., 2007. Talc-bearing serpentinite and the creeping section of the San Andreas fault. Nature 448, 795–797. https://doi.org/10.1038/nature06064.

Okamoto, A., Oyanagi, R., Yoshida, K., Uno, M., Shimizu, H., Satish-Kumar, M., 2021. Rupture of wet mantle wedge by self-promoting carbonation. Commun Earth Environ 2, 151. https://doi.org/10.1038/s43247-021-00224-5.

Paton, C., Hellstrom, J., Paul, B., Woodhead, J., & Hergt, J., 2011. Visualization Iolite: Freeware for the visualisation and processing of mass spectrometric data. Journal of Analytical Atomic Spectrometry, 26(12), 2508-2518.

Peacock, S.M., Wang, K., 2021. On the stability of talc in subduction zones: a possible control on the maximum depth of decoupling between the subducting plate and mantle wedge. Geophysical Research Letters, 48, e2021GL094889.

Penniston-Dorland, S.C., Bebout, G.E., Pogge von Strandmann, P.A.E., Elliott, T., Sorensen, S.S., 2012. Lithium and its isotopes as tracers of subduction zone fluids and metasomatic processes: Evidence from the

Catalina Schist, California, USA. Geochimica et Cosmochimica Acta 77, 530–545. https://doi.org/10.1016/j.gca.2011.10.038.

Penniston-Dorland, S.C., Gorman, J.K., Bebout, G.E., Piccoli, P.M., Walker, R.J., 2014. Reaction rind formation in the Catalina Schist: Deciphering a history of mechanical mixing and metasomatic alteration. Chemical Geology 384, 47–61. https://doi.org/10.1016/j.chemgeo.2014.06.024.

Piccoli, F., Vitale Brovarone, A., Ague, J.J., 2018. Field and petrological study of metasomatism and high-pressure carbonation from lawsonite eclogite-facies terrains, Alpine Corsica. Lithos 304–307, 16–37. https://doi.org/10.1016/j.lithos.2018.01.026.

Platt, J.P., 1986. Dynamics of orogenic wedges and the uplift of high-pressure metamorphic rocks. Geol Soc America Bull 97, 1037–1053. https://doi.org/10.1130/0016-7606(1986)97<1037:DOOWAT>2.0.CO;2.

Powell, R., Green, E. C., Marillo Sialer, E., & Woodhead, J., 2020. Robust isochron calculation. Geochronology, 2(2), 325-342.

Roedder, E, 1984. Fluid Inclusions. Reviews in Mineralogy, Vol. 12, Mineralogical Society of America, 644 p.

Rotondo, F.C., Tartarotti, P., Guerini, S., Della Porta, G., Campomenosi, N., 2021. Metasomatic horizon sealing serpentinite-metasediments pair in the Zermatt-Saas metaophiolite (Northwestern Alps): record of a channel for focussed fluid flow during subduction. Ofioliti 46, 1–25. https://doi.org/10.4454/ofioliti.v46i1.535.

Rubatto, D., Hermann, J., 2003. Zircon formation during fluid circulation in eclogites (Monviso, Western Alps): implications for Zr and Hf budget in subduction zones. Geochimica et Cosmochimica Acta 67, 2173–2187.

Ruh, J.B., Le Pourhiet, L., Agard, Ph., Burov, E., Gerya, T., 2015. Tectonic slicing of subducting oceanic crust along plate interfaces: Numerical modeling. Geochem. Geophys. Geosyst. 16, 3505–3531. https://doi.org/10.1002/2015GC005998.

Scambelluri, M., Piccardo, G., Philippot, P., Robbiano, A., Negretti, L., 1997. High salinity fluid inclusions formed from recycled seawater in deeply subducted alpine serpentinite. Earth and Planetary Science Letters 148, 485–499. https://doi.org/10.1016/S0012-821X(97)00043-5.

Schmid, S.M., Pfiffner, O.A., Froitzheim, N., Schönborn, G., Kissling, E., 1996. Geophysical-geological transect and tectonic evolution of the Swiss-Italian Alps. Tectonics 15, 1036–1064. https://doi.org/10.1029/96TC00433.

Schmid, S.M., Kissling, E., Diehl, T., van Hinsbergen, D.J.J., Molli, G., 2017. Ivrea mantle wedge, arc of the Western Alps, and kinematic evolution of the Alps–Apennines orogenic system. Swiss J Geosci 110, 581–612. https://doi.org/10.1007/s00015-016-0237-0.

Schmidt, M.W., Poli, S., 2014. Devolatilization During Subduction, in: Treatise on Geochemistry. Elsevier, pp. 669–701. https://doi.org/10.1016/B978-0-08-095975-7.00321-1.

Schmitz, M. D., Bowring, S. A., 2001. U-Pb zircon and titanite systematics of the Fish Canyon Tuff: an assessment of high-precision U-Pb geochronology and its application to young volcanic rocks. Geochimica et Cosmochimica Acta, 65, 2571-2587.

Schmitz, M. D., Schoene, B., 2007. Derivation of isotope ratios, errors, and error correlations for U-Pb geochronology using 205Pb-235U-(233U)-spiked isotope dilution thermal ionization mass spectrometric data. Geochemistry, Geophysics, Geosystems, 8.

Schwartz, S., Lardeaux, J.M., Tricart, P., Guillot, S., Labrin, E., 2007. Diachronous exhumation of HP-LT metamorphic rocks from south-western Alps: evidence from fission-track analysis. Terra Nova 19, 133–140. https://doi.org/10.1111/j.1365-3121.2006.00728.x.

Schwartz, S., Gautheron, C., Ketcham, R.A., Brunet, F., Corre, M., Agranier, A., Pinna-Jamme, R., Haurine, F., Monvoin, G., Riel, N., 2020. Unraveling the exhumation history of high-pressure ophiolites using

magnetite (U-Th-Sm)/He thermochronometry. Earth and Planetary Science Letters 543, 116359. https://doi.org/10.1016/j.epsl.2020.116359.

Spandler, C., Hermann, J., Faure, K., Mavrogenes, J.A., Arculus, R.J., 2008. The importance of talc and chlorite "hybrid" rocks for volatile recycling through subduction zones; evidence from the high-pressure subduction mélange of New Caledonia. Contrib Mineral Petrol 155, 181–198. https://doi.org/10.1007/s00410-007-0236-2.

Spandler, C., Hammerli, J., Sha, P., Hilbert-Wolf, H., Hu, Y., Roberts, E., & Schmitz, M., 2016. MKED1: a new titanite standard for in situ analysis of Sm–Nd isotopes and U–Pb geochronology. Chemical Geology, 425, 110-126.

Spencer, K. J., Hacker, B. R., Kylander-Clark, A. R. C., Andersen, T. B., Cottle, J. M., Stearns, M. A., Poletti, J.E., Seward, G. G. E., 2013. Campaign-style titanite U–Pb dating by laser-ablation ICP: Implications for crustal flow, phase transformations and titanite closure. Chemical Geology, 341, 84-101.

Stacey, J. S., & Kramers, J.D., 1975. Approximation of terrestrial lead isotope evolution by a two-stage model. Earth and Planetary Science Letters, 26, 207-221.

Stampfli, G.M., Mosar, J., Marquer, D., Marchant, R., Baudin, T., Borel, G., 1998. Subduction and obduction processes in the Swiss Alps. Tectonophysics 296, 159–204. https://doi.org/10.1016/S0040-1951(98)00142-5.

Stern, R.J., 2002. Subduction zones. Rev. Geophys. 40, 3-1-3–38. https://doi.org/10.1029/2001RG000108.

Tarling, M.S., Smith, S.A.F., Scott, J.M., 2019. Fluid overpressure from chemical reactions in serpentinite within the source region of deep episodic tremor. Nat. Geosci. 12, 1034–1042. https://doi.org/10.1038/s41561-019-0470-z.

Tartarotti, P., Martin, S., Meyzen, C.M., Benciolini, L., Toffolo, L., 2019. Structural Evolution and Metasomatism of Subducted Metaophiolites in the Northwestern Alps. Tectonics 38, 4185–4206. https://doi.org/10.1029/2019TC005626.

Tewksbury-Christle, C.M., Behr, W.M., Helper, M.A., 2021. Tracking Deep Sediment Underplating in a Fossil Subduction Margin: Implications for Interface Rheology and Mass and Volatile Recycling. Geochem Geophys Geosyst 22. https://doi.org/10.1029/2020GC009463.

Tricart, P., Schwartz, S., 2006. A north-south section across the Queyras Schistes lustrés (Piedmont zone, Western Alps): Syn-collision refolding of a subduction wedge. Eclogae geol. Helv. 99, 429–442. https://doi.org/10.1007/s00015-006-1197-6.

Van den Kerkhof, A. M., Hein, U. F., 2001. Fluid inclusion petrography. Lithos 55, 27–47.

Vermeesch, P., 2018. IsoplotR: A free and open toolbox for geochronology. Geoscience Frontiers, 9, 1479-1493.

Vitale Brovarone, A., Alard, O., Beyssac, O., Martin, L., Picatto, M., 2014. Lawsonite metasomatism and trace element recycling in subduction zones. J. Meta. Geol. 32, 489–514. https://doi.org/10.1111/jmg.12074.

Vitale Brovarone, A., Tumiati, S., Piccoli, F., Ague, J.J., Connolly, J.A.D., Beyssac, O., 2020. Fluid-mediated selective dissolution of subducting carbonaceous material: Implications for carbon recycling and fluid fluxes at forearc depths. Chemical Geology 549, 119682. https://doi.org/10.1016/j.chemgeo.2020.119682.

Wopenka, B., Pasteris, J. D., 1987. Raman intensities and detection limits of geochemically relevant gas mixtures for a laser Raman microprobe. Analytical Chemistry 59, 2165–2170.

York, D., 1967. The best isochron. Earth and Planetary Science Letters, 2, 479-482.

Acknowledgments

The authors thank P. Agard, A. Verlaguet and B. Lefeuvre for stimulating discussions, suggestions and help on the field during the initiation of this work. A.R.C. Kylander-Clark is thanked for his assistance with LASS analyses. B. Dubacq and T. Gyomlai are also thanked for helpful discussions. The authors are grateful to N. Rividi, O. Boudouma, M. Fialin, M.-C. Caumon, J. Noël, E. Delairis and M. Moroni for analytical support and sample preparation. This study was partly found by the BRGM in the frame of the RGF-Alpes project. GB was financially supported by the NSF partnership for international research and education EFIRE (OIA 1545903), with additional funding from UCSB and NSF for LASS analyses. B.R. Hacker is warmly thanked for his overall support.

Supplementary Material en annexe – 6

Chapitre VI – Evolution de la composition des fluides en zone de subduction en fonction de la profondeur : étude des inclusions fluides à l'échelle du domaine Liguro-Piémontais des Alpes occidentales

Veines à lawsonite C dans les Schistes lustrés. Punta Bagna

VI. Evolution de la composition des fluides en zone de subduction en fonction de la profondeur : étude des inclusions fluides à l'échelle du domaine Liguro-Piémontais des Alpes occidentales

VI.1. Objectifs de cette étude

L'étude des inclusions fluides le long d'un transect majeur des Schistes Lustrés Liguro-Piémontais (transect Queyras-Monviso, ~30-80 km de profondeur) a permis de caractériser la présence de fluides aqueux faiblement à moyennement salés, contenant de faibles quantités de CO_2 et de CH_4 dans la phase vapeur, dans les veines de haute pression des méta-sédiments (Herviou et al., 2021 ; **chapitre II**). Dans ces veines une décroissance des salinités avec l'augmentation du grade métamorphique a été détectée et interprétée comme reflétant la dilution progressive des fluides de pores initiaux (salinités proches de celle de l'eau de mer) par l'eau libérée par les réactions de déshydratation (déstabilisation de la Fe-Mg carpholite notamment). Malgré l'échantillonnage important de cette première étude caractérisant l'évolution en profondeur des compositions de fluides le long du panneau plongeant alpin (445 inclusions fluides analysées dans 22 échantillons), cette tendance de décroissance des salinités reste à confirmer en densifiant la quantités d'échantillons/inclusions étudiés et en comparant avec d'autres transects le long du complexe des Schistes Lustrés. De plus, les veines provenant des méta-sédiments des unités inférieures éclogitiques etaient sous-représentées dans cette première étude. En effet, aucune veine contenant des minéraux index attestant de leur formation dans des conditions de haute pression n'avait pu être analysée. La composition des fluides présents dans les sédiments à ces profondeurs lors de la subduction de l'océan Liguro-Piémontais reste donc à déterminer.

Afin de densifier les observations et de confirmer ou bien d'infirmer les résultats à l'échelle de la coupe Queyras-Monviso (**chapitre II**), deux autres coupes majeures plus au Nord sont étudiées dans ce chapitre : la coupe Savoy-Susa et la coupe des Alpes Cottiennes (Fig. VI.1a, b, VI.2a-c ; voir également **chapitre III**, Herviou et al., 2022). Le long de ces trois transects, une augmentation vers l'Est du grade métamorphique allant de ~1.3 GPa- 330°C dans les unités Liguro-Piémontaises supérieures (LPU) à ~2.5 GPa-550°C dans les unités Liguro-Piémontaises inférieures (LPL) a été documentée (Agard et al., 2001a ; Gabalda et al., 2009 ; Plunder et al., 2012 ; Schwartz et al., 2013 ; Herviou et al., 2022), ce qui permet donc l'étude d'unités écaillées entre ~30 et 80 km de profondeur

(**chapitre II**, Herviou et al., 2021). Ce chapitre a donc pour objectif de déterminer l'évolution de la composition des fluides en profondeur le long d'une subduction froide à travers l'acquisition de la plus grande base de données d'inclusions fluides en subduction (1585 inclusions fluides et plus de 70 échantillons analysés).

***Figure VI.1** : A) Carte tectonométamorphique du domaine Liguro-Piémontais, localisation des trois zones d'études principales étudiées. B) Localisation et nature des échantillons étudiés. Abréviations : LPU = Liguro-Piemont Upper units ; LPM = Liguro-Piemont Middle units ; LPL = Liguro-Piemont Lower units.*

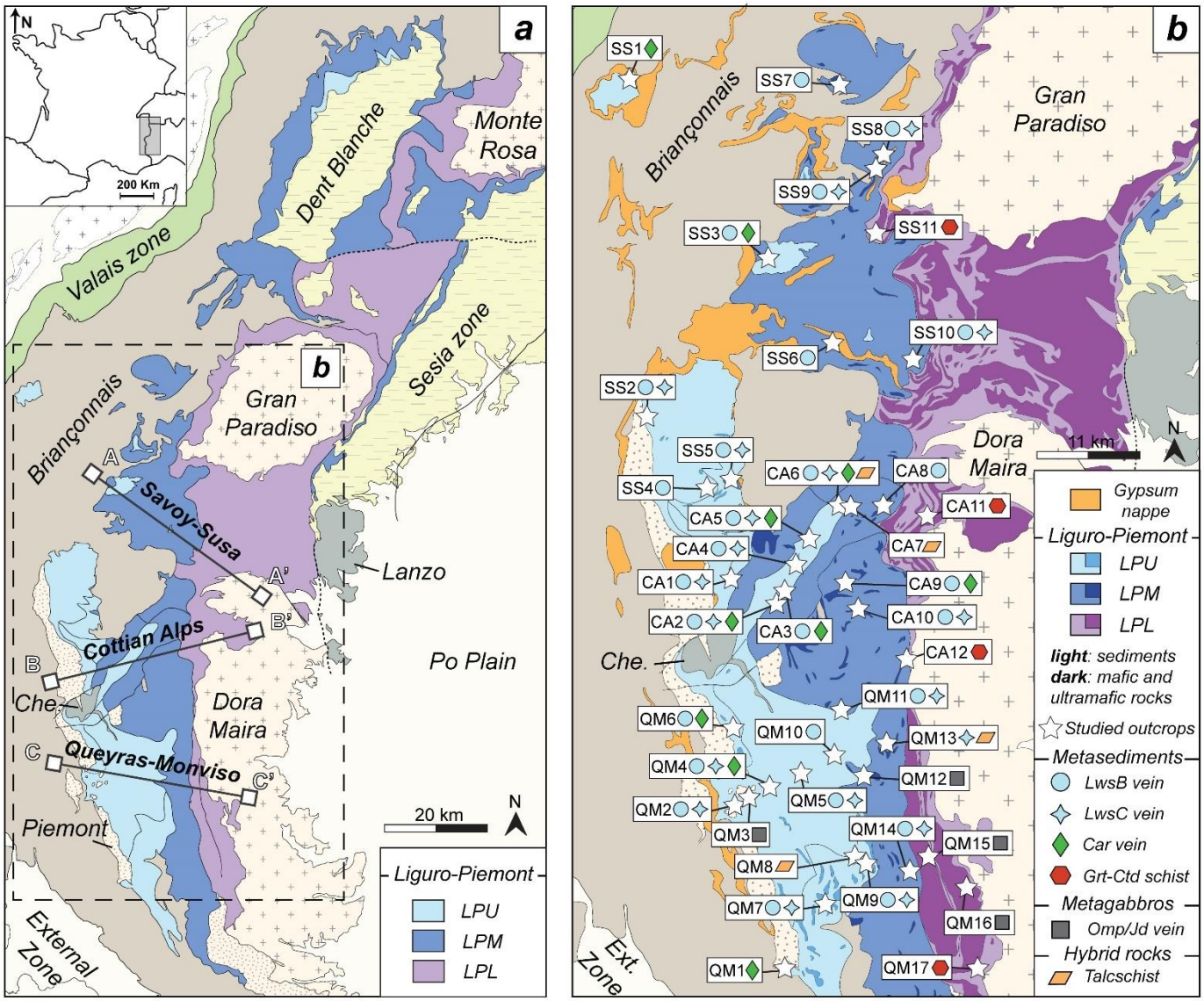

VI.2. Observations de terrain et échantillonnage

Le long de ces deux nouveaux transects (Savoy-Susa et Alpes Cottiennes, Fig. VI.1a, VI.2a, b), les veines porteuses de minéraux index furent longuement traquées et échantillonnées dans les méta-

sédiments afin de pouvoir analyser la composition des inclusions fluides avec l'augmentation des conditions pression-température (P-T) vers l'Est. L'échantillonnage le long de la coupe Queyras-Monviso fût également densifié afin de conforter la tendance de décroissance des salinités observée dans le **chapitre II**.

Le long de ces trois coupes les mêmes types de veines à LwsB, LwsC, et Fe-Mg carpholite ont été observés et échantillonnés (Fig. VI.3a-f). La lawsonite est stable au pic des unités supérieures et médianes (**chapitre III**, Herviou et al., 2022) et les veines de LwsB sont souvent prises dans des plis D1 (**chapitre IV** ; Fig. VI.3a) suggérant leur formation aux conditions du pic pression-température de ces unités. La plupart des veines à Fe-Mg carpholite sont également plissées par la phase de déformation D1 dans les unités supérieures (**chapitre IV** ; Agard et al., 2000) et donc vraisemblablement reliées au pic d'enfouissement. La Fe-Mg carpholite commence à se déstabiliser à l'Est des unités supérieures et est entièrement remplacée par le chloritoïde dans les unités médianes (**chapitre III**, Herviou et al., 2022). L'échantillon CA3car échantillonné dans les unités médianes correspond donc à une relique prograde de veine à Fe-Mg carpholite.

Afin d'avoir un signal de composition des fluides dans les réservoirs mafiques, les veines à jadéite dans les méta-gabbros de faciès schiste bleu ainsi que les veines et matrices de brèches à omphacite des méta-gabbros de faciès éclogite étudiées dans le **chapitre II** (Fig. VI.3g) sont à nouveaux utilisées dans ce volet. Les quatre échantillons de talcschistes à dolomite du **chapitre V**, formés par métasomatisme de serpentinites par l'infiltration de fluides sédimentaires dans des conditions de haute pression sont également utilisés dans ce chapitre. Pour finir, comme aucune veine de haute pression n'a pu être observée dans les unités Liguro-Piémontaises inférieures (LPL), des méta-pélites préservant l'assemblage à grenat-chloritoïde caractéristique du pic de pression (Agard et al., 2001a ; Plunder et al., 2012 ; Herviou et al., 2022) furent collectées pour cette étude. Les 70 échantillons étudiés dans ce chapitre sont reportés sur la carte en figure VI.1b et la localisation des affleurements et les conditions P-T des roches de ces derniers figurent en table VI.1.

Figure VI.2 *(page suivante) : Coupes géologiques des transects étudiés. A) Savoy-Susa. Modifié d'après Negro et al. (2013). B) Cottian Alps. Modifié d'après Agard (2021). C) Queyras-Monviso. Modifié d'après Lagabrielle (1987). Abréviations : LPU = Liguro-Piemont Upper units ; LPM = Liguro-Piemont Middle units ; LPL = Liguro-Piemont Lower units ; GV = klippe du Grand Vallon ; LA = klippe du Lamet ; SMU = Savoy Middle Unit ; SLU = Savoy Lower Unit ; LN = unité du Lago Nero ; CC = unité de Cerogne-Ciantiplagna ; OR = unité d'Orsiera-Rocciavrè ; CS = unité des calcschistes ; PT = unité de Pelvas-Taillante ; MB = unité de Mirabouc-Bouchet ; MV = unité du Monviso ; LS = unité du Lago Superiore.*

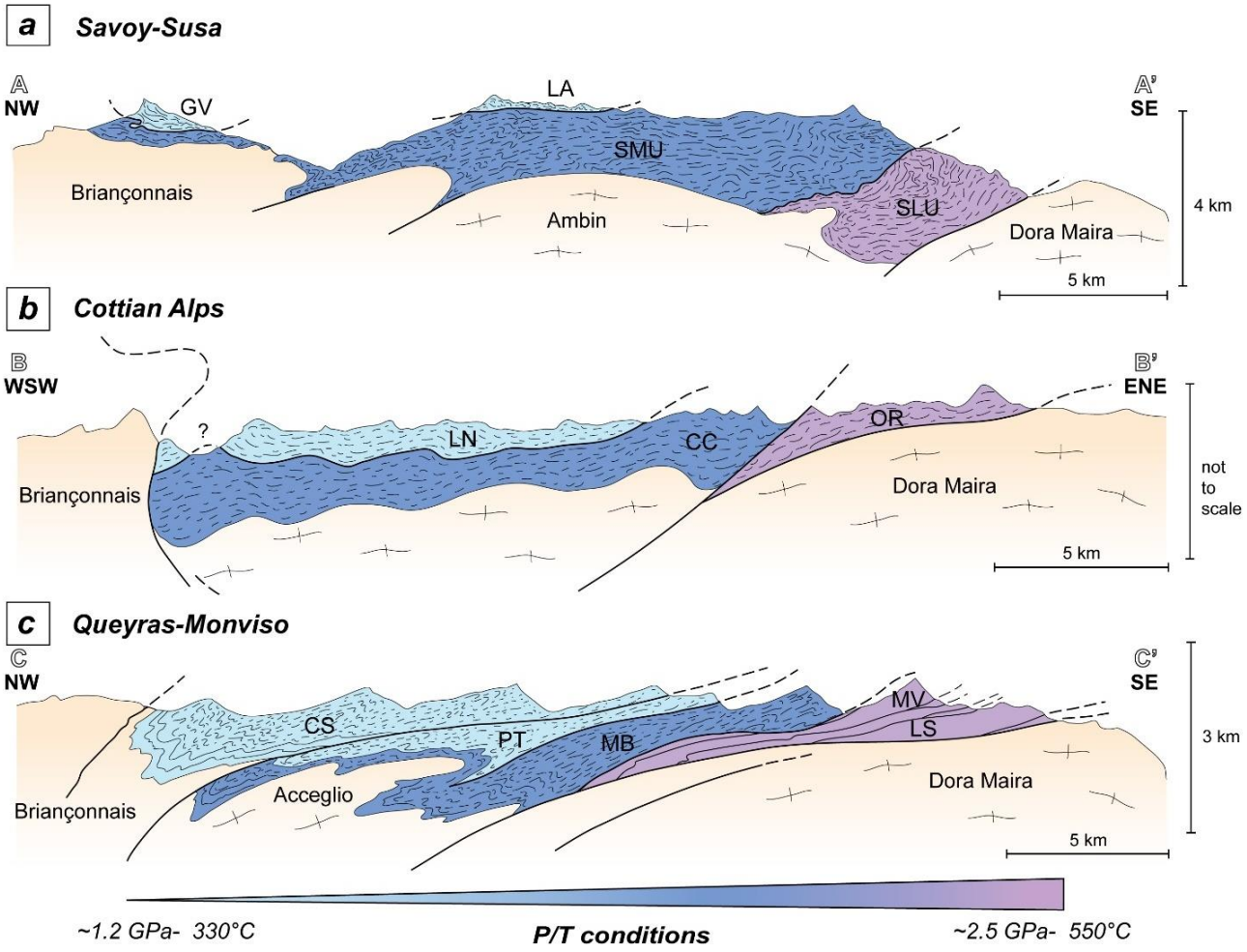

Figure VI.3 *(page suivante) : Observations de terrain des marqueurs géologiques de circulations de fluides dans le domaine Liguro-Piémontais. A) Pli D1 d'une veine contenant du quartz, de l'ankérite et des fibres de LwsB avec de petites fentes de tension à LwsC-ankérite-quartz au bord de la veine. B) Vue rapprochées de fibres de LwsB de couleur crème associées à de l'ankérite et du quartz. C) Fente de tension à LwsC dans un calcschiste. D) Fentes en échelon à LwsC. E) Veine centimétrique à quartz et fibres vertes de Fe-Mg carpholite recoupée par une microfaille tardive. F) Photo de détail de fibres pluri-centimétriques de Fe-Mg carpholite dans une veine. G) Veine à omphacite dans un méta-gabbro de faciès éclogite. H) talcschiste riche en dolomite provenant d'un contact tectonique entre unités Liguro-Piémontaises. Abréviations : Ank = ankérite ; Lws = lawsonite ; Qz = quartz ; Car = Fe-Mg carpholite ; Omp = omphacite.*

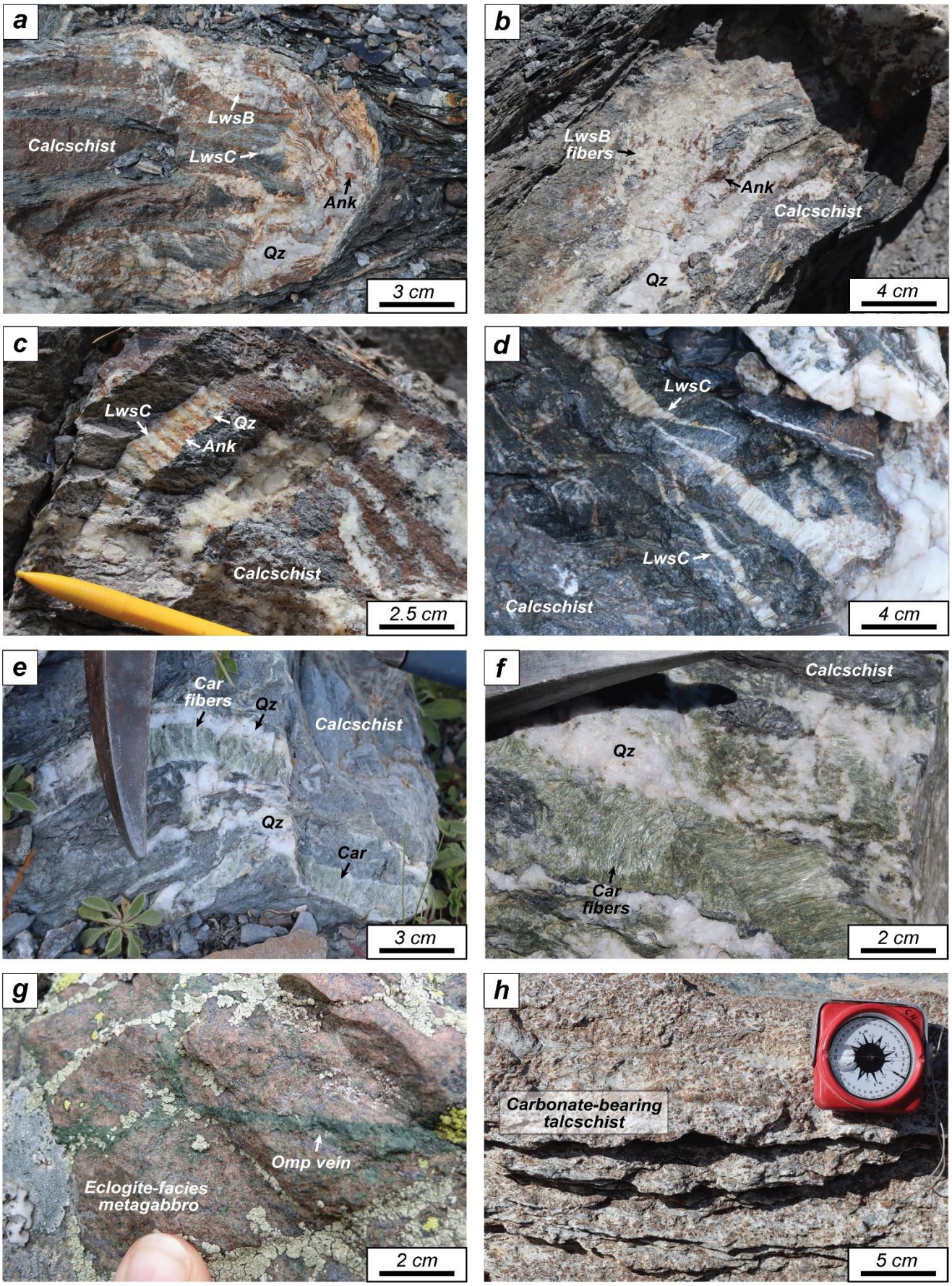
a
LwsB
Calcschist
LwsC
Ank
Qz
3 cm
b
LwsB
fibers
Ank
Calcschist
Qz
4 cm
c
LwsC
Qz
Ank
Calcschist
2.5 cm
d
LwsC
LwsC
Calcschist
4 cm
e
Car
fibers
Qz
Calcschist
Qz
Car
3 cm
f
Calcschist
Qz
Car
fibers
2 cm
g
Omp vein
Eclogite-facies
metagabbro
2 cm
h
Carbonate-bearing
talcschist
5 cm

Transect	Outcrop	Unit	Locality	Host rocks P/T	Samples	longitude	latitude
Savoy-Susa	SS1	LPU Jovet klippe	Mont Jovet	376°C[1]/~1.4 GPa[2]	SS1Car	6.666389	45.507500
"	SS2	LPU Lago Nero	Punta Bagna	355°C[2]/~1.4 GPa[2]	SS2LwsB	6.673333	45.144806
"	"	"	"	"	SS2LwsC	"	"
"	SS3	LPU Grand Vallon klippe	Col de Lanseria	378°C[2]/~1.6 GPa[2]	SS3LwsB	6.849194	45.324556
"	"	"	"	"	SS3Car	"	"
"	SS4	LPU Lago Nero	Monte Jafferau	374°C[2]/~1.6 GPa[2]	SS4LwsB	6.770861	45.085194
"	SS5	LPM Vin Vert	Monte Vin Vert	413°C[2]/2.1 GPa[2]	SS5LwsB	6.805361	45.081833
"	"	"	"	"	SS5LwsC	"	"
"	SS6	LPM Savoy Middle Unit	Mont-Cenis	450°C[1]/~1.6-1.9 GPa[1]	SS6LwsB	6.959444	45.233667
"	SS7	"	Grande Sassière	449°C[1]/~1.6-1.9 GPa[1]	SS7LwsB	6.966333	45.496778
"	SS8	"	Col de l'Iseran	427°C[2]/~1.6-1.9 GPa[1]	SS8LwsB	7.027050	45.416189
"	"	"	"	"	SS8LwsC	"	"
"	SS9	"	Col de la Calabourdane	427°C[2]/~1.6-1.9 GPa[1]	SS9LwsB	7.015850	45.406450
"	"	"	"	"	SS9LwsC	"	"
"	SS10	"	Rocciamelone	405°C[2]/~1.6-1.9 GPa[1]	SS10LwsB	7.074817	45.204550
"	"	"	"	"	SS10LwsC	"	"
"	SS11	LPL Savoy Lower Unit	Le Vilaron	541°C[1]/2.4 GPa[1]	SS11Grt	7.012222	45.335556
Cottian Alps	CA1	LPU Lago Nero	Desertes	376°C[2]/~1.5 GPa[2]	CA1LwsB	6.806167	44.994333
"	"	"	"	"	CA1LwsC	"	"
"	CA2	"	Sestrières	330°C[3]/1.3-1.4 GPa[2,4]	CA2LwsB	6.864306	44.959833
"	"	"	"	"	CA2LwsC	"	"
"	"	"	"	"	CA2Car	"	"
"	CA3	"	Fraitève-Colle Basset	330°C[3]/1.3-1.4 Gpa[2,4]	CA3LwsB	6.877361	44.978694
"	"	"	"	"	CA3Car	"	"
"	CA4	"	Triplex	343°C[3]/1.7 GPa[2]	CA4LwsB	6.880361	44.997194
"	"	"	"	"	CA4LwsC	"	"
"	CA5	"	Genevris	365°C[3]/1.8 GPa[2]	CA5LwsB	6.905564	45.032889
"	"	"	"	"	CA5LwsC	"	"
"	"	"	"	"	CA5Car	"	"
"	CA6	"	Assietta	378°C[3]/1.9 GPa[2, 4]	CA6LwsB	6.949694	45.063611
"	"	"	"	"	CA6LwsC	"	"
"	"	"	"	"	CA6Car	"	"
"	"	"	"	"	CA6Tlc	"	"
"	CA7	LPM Cerone-Ciantiplagna	Gran Serin	387°C[3]/1.9 GPa[2, 4]	CA7Tlc	6.966167	45.061667
"	CA8	"	Serret Durmilleus	441°C[3]/2.2 GPa[2,4]	CA8LwsB	7.020083	45.063083
"	CA9	LPM Albergian	Colle del Pis	454°C[2]/2.1 GPa[2, 4]	CA9LwsB	6.975567	44.492667
"	"	"	"	"	CA9Car	"	"
"	CA10	"	Laghi del Beth	468°C[2]/2.1 GPa[2]	CA10LwsB	6.986183	44.958417
"	"	"	"	"	CA10LwsC	"	"
"	CA11	LPL Orsiera-Rocciavrè	Fontana Chesalet	508°C[2]/2.2 GPa[2, 4]	CA11Grt	7.075700	45.052983
"	CA12	"	Prali Villa	534°C[2]/2.4 GPa[2]	CA12Grt	7.051361	44.907972
Queyras-Monviso	QM1	LPU Pelvas-Taillante	Plan de Paroir	319°C[2]/1.4 GPa[2]	QM1Car	6.871556	44.606636
"	QM2	LPU Calcschist unit	Château-Queyras	332°C[5]/1.4 GPa[2]	QM2LwsB	6.793083	44.757933
"	"	"	"	"	QM2LwsC	"	"
"	QM3	"	Ville-Vieille	328°C[5]/~1.4 GPa[2]	QM3Jd	6.817350	44.761550
"	QM4	"	Malafosse	336°C[5]/~1.5 GPa[2]	QM4LwsB	6.840083	44.771133
"	"	"	"	"	QM4LwsC	"	"
"	"	"	"	"	QM4Car	"	"
"	QM5	"	Gouret	366°C[2]/1.8 GPa[2]	QM5LwsB	6.887067	44.788583
"	"	"	"	"	QM5LwsC	"	
"	QM6	LPU Lago Nero?	Lac des Cordes	380°C[2]/1.7 GPa[2]	QM6LwsB	6.792722	44.840472
"	"	"	"	"	QM6Car	"	"
"	QM7	LPU Pelvas-Taillante	Lac de la Blanche	361°C[2]/1.7 GPa[2]	QM7LwsB	6.925017	44.662983
"	"	"	"	"	QM7LwsC	"	"
"	QM8	"	Crête de l'Eychassier	373°C[5]/1.7 GPa[2]	QM8Tlc	6.978694	44.695861
"	QM9	"	Pain de Sucre	"	QM9LwsB	6.990050	44.693683
"	"	"	"	"	QM9LwsC	"	"
"	QM10	LPU Calcschists unit	Abriès	407°C[2]/2 GPa[2]	QM10LwsB	6.929361	44.805361
"	QM11	LPM Albergian	Bric Froid	404°C[2]/2 GPa[2]	QM11LwsB	6.940639	44.858111
"	"	"	"	"	QM11LwsC	"	"
"	QM12	LPM Mirabouc-Bouchet	Pelvas	402°C[5]/~2 GPa[2]	QM12Jd	6.995667	44.796806
"	QM13	"	Bric Bouchet	444°C[2]/~2.1 GPa[2]	QM13LwsC	7.015417	44.811850
"	"	"	"	"	QM13Tlc	"	"
"	QM14	"	Refuge du Viso	464°C[2]/2.2 GPa[2]	QM14LwsB	7.063700	44.683667
"	"	"	"	"	QM14LwsC	"	"
"	QM15	LPL Lago Superiore	Intermediate shear zone	580°C[6]/2.8 GPa[6]	QM15OmpV1	7.087500	44.693889
"	"	"	"	560°C[6]/2.4 GPa[6]	QM15OmpV2	"	"
"	"	"	"	"	QM15OmpM2	"	"
"	QM16	"	Lower shear zone	580°C[6]/2.8 GPa[6]	QM16OmpM1	7.134167	44.670000
"	QM17	"	Pian Fourengh	493°C[5]/2.4 GPa[2]	QM17Grt	7.156572	44.593592

Table VI.1 *(page précédente) : Nature des échantillons étudiés, localisation des affleurements et conditions pression-température. Conditions pression-température d'après : Plunder et al. (2012)[1] ; Herviou et al. (2022)[2] ; Beyssac et al. (2002)[3] ; Agard et al. (2001a)[4] ; Schwartz et al. (2013)[5] et Locatelli et al. (2018)[6]. Abréviations : LwsB = veine de lawsonite B ; LwsC = veine de lawsonite C ; Car = veine de Fe-Mg carpholite ; Grt = meta-pélite à grenat-chloritoïde ; Tlc = talcschiste à dolomite ; Jd = veine de jadeite ; OmpV1 = veine d'omphacite V1 ; OmpV2 = veine d'omphacite V2 ; OmpM1 = matrice M1 à omphacite ; OmpM2 = matrice M2 à omphacite. LPU = Liguro-Piemont Upper units ; LPM = Liguro-Piemont Middle units ; LPL = Liguro-Piemont Lower units.*

VI.3. Stratégie analytique et méthodes

VI.3.1. Analyse micro-texturale des inclusions fluides et sélection

L'analyse des inclusions fluides a été réalisée sur des lames épaisses de 100 µm, polies sur les deux faces. Les inclusions fluides furent observées au microscope optique afin de caractériser leur morphologie, leur rapport volume de bulle de gaz/volume total de l'inclusion et leur position texturale à l'intérieur des cristaux. Afin de caractériser les fluides présents durant la cristallisation des phases de haute pression, seules les inclusions montrant de bonnes preuves texturales de piégeage primaire furent sélectionnées (i.e., les inclusions fluides isolées ou présentes dans des groupes d'inclusions non planaires à l'intérieur des cristaux ; Roedder, 1984 ; Van den Kerkhof et Hein, 2001). Les inclusions fluides ont été examinées avec attention et seulement celles avec les formes les plus régulières ont été sélectionnées dans le but d'éviter autant que possible les modifications chimiques qui pourrait intervenir lors de fuites après leur piégeage. Les inclusions fluides alignées dans des « trails » recoupant plusieurs grains, considérées comme des inclusions secondaires piégées dans des fractures recristallisées, ne furent pas sélectionnées pour cette étude.

VI.3.2. Analyses par spectroscopie Raman des salinités, du contenu en gaz et des solides dans les inclusions fluides

La plupart des inclusions étudiées sont biphasées (liquide et vapeur) et seulement quelques rares inclusions sont triphasées (liquide, vapeur et solide(s)). La salinité, le contenu en gaz et la nature des « daughter minerals » des 1585 inclusions fluides étudiées ont été déterminés par spectroscopie Raman en focalisant le laser monochromatique sur la phase liquide, la bulle de gaz et les minéraux respectivement. Les analyses Raman furent réalisées au laboratoire GéoRessources (Université de Lorraine, Nancy) à l'aide de spectromètres LabRAM HR et LabRam (Horiba Jobin-Yvon®) équipés d'un détecteur CCD refroidi à l'azote liquide, d'un réseau de diffraction à 600 traits.mm^{-1} pour la

mesure des salinités et des solides et d'un réseau de diffraction à 1800 traits.mm^{-1} pour l'analyse des gaz. La lumière d'excitation est produite par un laser Ar^+ (Stabilite 2017, Newport Spectra-Physics) à 514.532 nm et à une puissance de 200, 160 ou 120 mW, focalisé sur l'échantillon à l'aide d'un objectif x100 (Olympus).

Les salinités furent déterminées en utilisant la méthode décrite dans Caumon et al. (2013, 2015) et Tarantola et Caumon (2015). L'acquisition de spectres Raman de l'eau dans les inclusions étudiées a été réalisée sur exactement les mêmes spectromètres que ceux utilisés pour la calibration de la méthode des travaux ci-dessus. Cette méthode permet de déterminer la salinité de fluides aqueux en faisant le rapport des intensités de spectres Raman de l'eau à deux nombres d'ondes définis (3260 et 3425 cm^{-1}) après soustraction d'une ligne de base linéaire. Cette méthode a une précision de ± 0.4 wt.% eq. NaCl et est particulièrement adaptée et précise pour une approche statistique de la caractérisation des salinités dans les inclusions fluides des roches de haute pression (Herviou et al., 2021, **chapitre II**).

Pour l'analyse des gaz, les spectres Raman ont été corrigés à l'aide d'une fonction ICS (Intensity Correction System) afin de normaliser la réponse instrumentale en fonction de la longueur d'onde. La présence de gaz dans les spectres Raman fut détectée à l'aide des positions de pics de gaz compilés par Frezzotti et al. (2012). Le CO_2 fut identifié par la présence du doublet de Fermi (Fermi, 1931, pics à 1285 and 1388 cm^{-1}), le CH_4 par sa bande majeure à 2917 cm^{-1} et le N_2 par sa bande majeure à 2331 cm^{-1}. La présence de N_2 dans les inclusions fut ensuite confirmée par soustraction du pic de N_2 atmosphérique à la bande principale de N_2 détectée dans l'inclusion (signal du N_2 dans le cristal à côté de l'inclusion). Pour les mélanges gazeux à CO_2-CH_4, les aires des pics furent calculées après soustraction d'une ligne de base linéaire. Les proportions molaires de chaque gaz dans ces mélanges furent déterminées à l'aide de leurs aires respectives et des surfaces spécifiques correspondant aux pics de ces gaz (RRSCS ; Wopenka et Pasteris, 1987). Nous avons choisi d'utiliser les valeurs récentes de Le et al. (2019, 2020) pour les surfaces spécifiques du CO_2 (1.40 ± 0.03 pour le pic à 1388 cm^{-1} et 0.89 ± 0.02 pour le pic à 1285 cm^{-1}) et du CH_4 (7.73 ± 0.16 pour le pic principal à 2917 cm^{-1}).

Les phases solides présentes dans les inclusions fluides ont été identifiées à l'aide de la compilation de données Raman de Frezzotti et al. (2012).

VI.4. Pétrographie et analyse micro-texturale des inclusions fluides

VI.4.1. Veines à lawsonite (unités LPU et LPM)

Le long des trois transects d'étude, tous les échantillons observés de veines à LwsB contiennent des cristaux automorphes et fibreux de lawsonite. Ces fibres sont généralement longues de plusieurs centimètres et épaisses de plusieurs millimètres et sont toujours associées et à l'équilibre textural avec des cristaux de quartz et souvent avec des fibres d'ankérite (Fig. VI.4a-d). Les mêmes observations ont été faites dans les veines à LwsC (Fig. VI.4e, f).

Dans ces veines à lawsonite, les inclusions fluides étudiées étaient systématiquement dans des cristaux de quartz co-cristallisant avec les fibres de lawsonite ± ankérite (Fig. VI.4a-f). Ces inclusions sont soit isolées soit dans des clusters non-planaires indiquant leur piégeage primaire. La taille de ces inclusions est généralement comprise entre 5 et 15 µm et atteint rarement une vingtaine de microns. La plupart de ces inclusions sont biphasées (liquide + vapeur ; Fig. VI.4b, c, d, f) avec une bulle de vapeur qui occupe ~10-20% du volume total de l'inclusion. Ces inclusions ont généralement une forme allongée régulière (Fig. VI.4c, d, f) même si certaines, plus rares, ont des formes un peu plus irrégulières liés à des modifications post-piégeage des inclusions (Fig. VI.4b). Sur les 998 inclusions fluides analysées dans les veines à lawsonite, seulement quatre (toutes de l'échantillon QM2LwsB) sont triphasées (liquide + vapeur + solide) avec deux d'entre elles contenant un cristal de forme cubique (**chapitre II**, Herviou et al., 2021).

VI.4.2. Veines à Fe-Mg carpholite (unités LPU ± LPM)

Dans les veines à Fe-Mg carpholite, presque toute la carpholite est remplacée par de la chlorite retrograde et la majorité de la carpholite fraiche préservée de la rétromorphose est présente sous la forme d'aiguilles dans des cristaux de quartz (Fig. VI.4g, h) suggérant leur co-cristallisation.

Sur les 229 inclusions fluides étudiées dans ces veines, 195 furent observées dans le quartz co-cristallisant avec les aiguilles de carpholite et 34 dans des cristaux de Fe-Mg carpholite préservés de la rétromorphose.

Dans le quartz, les inclusions fluides observées étaient isolées ou présentes dans des clusters non planaires indiquant leur piégeage primaire. La taille de ces inclusions varie pour la plupart entre 5 et 15 µm et atteint rarement 20 microns. Ces inclusions sont biphasées (liquide + vapeur ; Fig. VI.4g, h), avec une bulle qui occupe ~10-20% du volume total de l'inclusion, et sont généralement de forme régulière. Dans les cristaux de Fe-Mg carpholite, les inclusions examinées étaient isolées ou en

clusters, et alignées salon l'axe-c des cristaux indiquant un piégeage primaire (Fig. VI.4i). Sur les 34 inclusions étudiées dans la carpholite, 6 inclusions de l'échantillon Ca3Car sont triphasées (liquide + vapeur + solide ; Fig. VI.4i) et les 28 restantes sont biphasées. Toutes ces inclusions ont une bulle qui occupe ~10-20 % du volume total de l'inclusion, ont une forme tubulaire et une taille généralement comprise entre 5 et 20 µm.

VI.4.3. Méta-pélites à grenat-chloritoïde (unités LPL)

Afin d'obtenir un signal de la composition des fluides présents dans les sédiments aux profondeurs du pic d'enfouissement des unités inférieures, des méta-pélites ayant préservées la paragénèse du pic furent collectées. Ces échantillons contiennent principalement des assemblages à grenat-chloritoïde-phengite-quartz (Fig. VI.4j). Les grenats sont généralement millimétriques et zonés avec une bordure formée au pic de pression des unités inférieures (Plunder et al., 2012).

Dans ces bordures, des inclusions fluides furent observées (Fig. VI.4k, l). Ces inclusions sont isolées ou situées dans des trails limités à la bordure du grenat montrant leur piégeage primaire ou pseudo-secondaire lors de la formation du grenat. Les inclusions ont une forme légèrement tubulaire et une taille généralement comprise entre quelques microns et 10 µm. Sur les 88 inclusions étudiées dans ces échantillons, 62 sont biphasées (liquide + vapeur) et 26 triphasées (liquide + vapeur + solide) avec une bulle de vapeur occupant généralement ~10-20% du volume total de l'inclusion (Fig. VI.4k, l).

Figure VI.4 *(page suivante) : Photos microscopiques d'inclusions fluides. A) Equilibre textural entre quartz et fibres de LwsB. B) Vue rapprochée de A) montrant la présence d'une inclusion fluide primaire biphasée dans le quartz. C) Inclusion fluide primaire biphasée dans un cristal de quartz à l'équilibre textural avec une fibre de LwsB. D) Cluster d'inclusions fluides primaires biphasées dans le quartz d'une veine à LwsB. E) Equilibre textural entre quartz et fibres de LwsC. F) Vue rapprochée de E) montrant une inclusion fluide primaire biphasée dans le quartz. G) Inclusion fluide primaire isolée et biphasée dans le quartz co-cristallisant avec des aiguilles de Fe-Mg carpholite. H) Inclusion fluide primaire isolée et biphasée dans le quartz co-cristallisant avec des aiguilles de Fe-Mg carpholite. I) Inclusion fluide primaire isolée et triphasée dans un cristal de Fe-Mg carpholite. J) Méta-pélite à grenat-chloritoïde. K) Vue rapprochée de J) montrant une inclusion fluide primaire isolée et biphasée dans le grenat. I) Trail d'inclusions fluides pseudo-secondaires biphasées dans un grenat. M) Cluster d'inclusions fluides primaires biphasées dans un cristal de dolomite d'un talcschiste. Ces inclusions fluides sont orientées parallèlement aux clivages principaux de la dolomite. N) Cristal zoné d'omphacite d'une veine V2 avec un cœur sombre riche en inclusions fluides. O) Inclusion fluide triphasée d'une veine V2. Cette inclusion est orientée parallèlement à l'axe c de l'omphacite. Abréviations : Car = Fe-Mg carpholite ; Ctd = chloritoïde ; Dol = dolomite ; Grt = grenat ; Lws = lawsonite ; Omp = omphacite ; Ph = phengite ; Qz = quartz.*

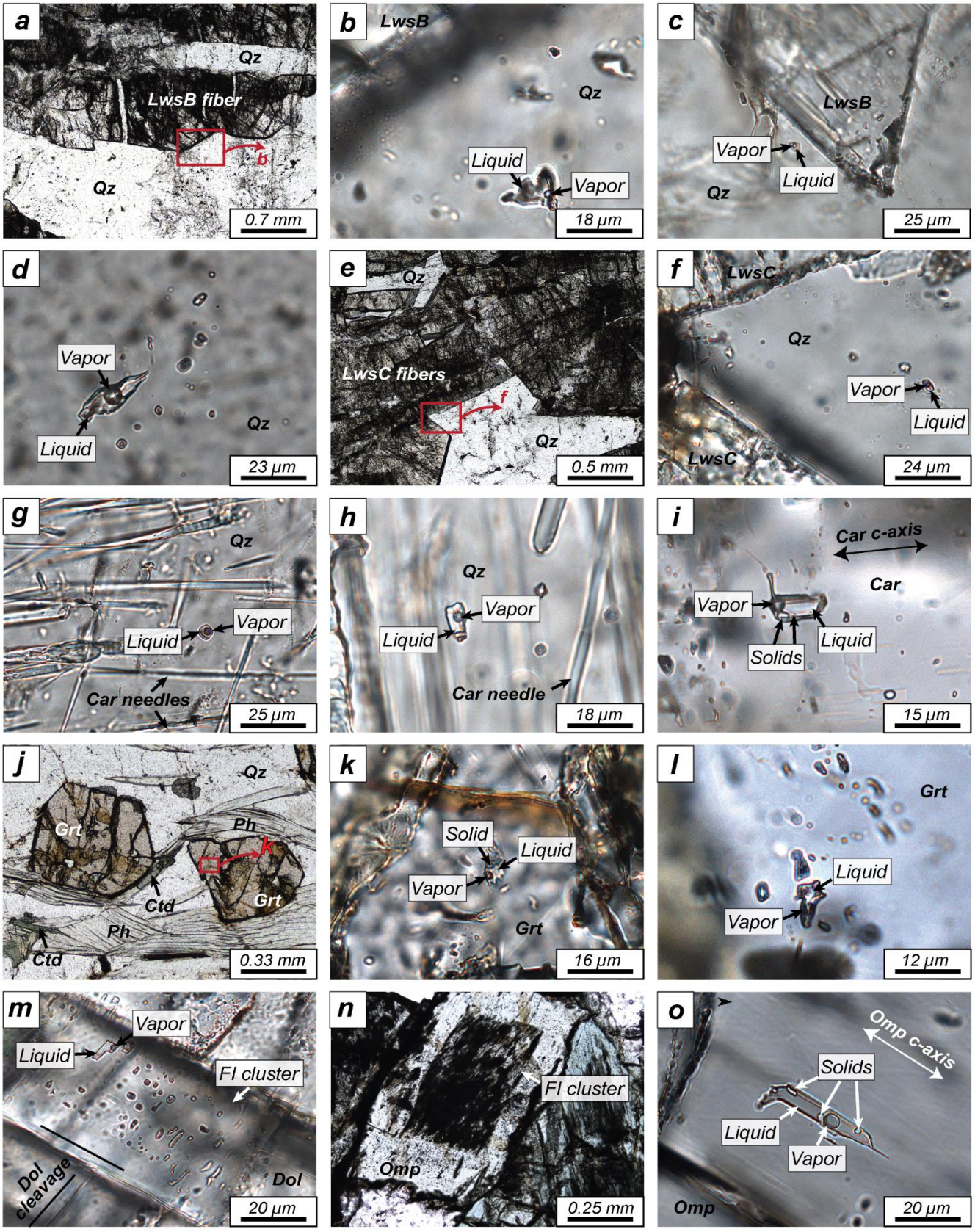
a
Qz
LwsB fiber
b
Qz
0.7 mm
b
LwsB
Qz
Liquid
Vapor
18 µm
c
LwsB
Vapor
Liquid
Qz
25 µm
d
Vapor
Liquid
Qz
23 µm
e
Qz
LwsC fibers
f
Qz
0.5 mm
f
LwsC
Qz
Vapor
Liquid
LwsC
24 µm
g
Qz
Liquid
Vapor
Car needles
25 µm
h
Qz
Vapor
Liquid
Car needle
18 µm
i
Car c-axis
Car
Vapor
Solids
Liquid
15 µm
j
Qz
Grt
Ph
k
Ctd
Grt
Ph
Ctd
0.33 mm
k
Solid
Liquid
Vapor
Grt
16 µm
l
Grt
Liquid
Vapor
12 µm
m
Vapor
Liquid
FI cluster
Dol cleavage
Dol
20 µm
n
FI cluster
Omp
0.25 mm
o
Omp c-axis
Solids
Liquid
Vapor
Omp
20 µm

VI.4.4. Talcschistes à dolomite (contacts tectoniques entre unités LPU et LPM)

Des talcschistes riches en dolomite furent échantillonnés dans les unités supérieures et médianes à proximité des contacts tectoniques entre les écailles Liguro-Piémontaises. Ces échantillons formés par transformation de serpentinites via l'action de fluides sédimentaires en subduction (**chapitre V**) contiennent des paragénèses à talc-dolomite-chlorite-quartz-sphène.

Les inclusions fluides furent majoritairement observées dans les cristaux de dolomite, à l'exception de 11 des 18 inclusions de l'échantillon QM8Tlc qui furent caractérisées dans des cristaux de quartz. Dans les cristaux de dolomite, les inclusions fluides sont isolées ou dans des clusters non planaires (Fig. VI.4m). Ces inclusions sont de forme rectangulaire, typiquement de taille 5-15 µm et toujours orientées parallèlement aux clivages principaux de la dolomite suggérant un piégeage primaire (Fig. VI.4m). Toutes ces inclusions sont biphasées (liquide + vapeur) avec une bulle occupant ~10% du volume totale des inclusions. Dans les cristaux de quartz de QM8Tlc, les inclusions sont isolées, de taille 4-7 µm et de forme régulière. Ces inclusions sont également biphasées avec une bulle de vapeur occupant ~10% du volume total des inclusions.

VI.4.5. Veines à jadéite (unités LPU et LPM)

Les veines à jadéite des méta-gabbros de faciès schiste bleu sont composées de cristaux verts automorphes de jadéite avec de multiples orientations (**chapitre II**, Herviou et al., 2021) et de rares cristaux de glaucophane remplissant généralement des fractures.

Les inclusions fluides furent observées dans les cristaux de jadéite. Ces inclusions ont des formes tubulaires de taille variable généralement comprises entre quelques microns et 20-25 µm. Ces inclusions sont généralement orientées parallèlement à l'axe-c des cristaux de jadéite et sont soit isolées, soit dans des clusters non planaires suggérant leur piégeage primaire. La plupart de ces inclusions sont biphasées (liquide + vapeur) même si de rares monophasées (liquide), biphasées (liquide + solide ; 2/23 dans QM3Jd) et triphasées (liquide + vapeur + solide ; 2/23 dans QM2Jd) furent observées. La bulle de vapeur occupe généralement ~5-10 % du volume total de l'inclusion dans l'échantillon QM3Jd et ~20% dans l'échantillon QM12Jd.

VI.4.6. Veines à omphacite V1 et V2 (unités LPL)

Les veines V1 sont presque parallèles à la foliation éclogitique de l'unité inférieure du Lago Superiore. Ces veines sont remplies par des cristaux longs de plusieurs millimètres et automorphes d'omphacite. Ces cristaux sont orientés perpendiculairement aux épontes des veines et montrent une zonation

concentrique. Les veines V2 sont remplies par des assemblages de grenat et d'omphacite. Les grenats sont automorphes, de taille millimétrique tandis que les cristaux d'omphacite sont légèrement plus petits que ceux des veines V1.

Dans ces deux types de veines, la plupart des inclusions primaires sont concentrées dans le cœur des cristaux d'omphacite. La forte densité d'inclusions confère une couleur sombre à ces cœurs d'omphacite (Fig. VI.4n). Ces inclusions sont de forme tubulaire, soit isolées, soit dans des clusters non planaires. La taille de ces inclusions est typiquement de 10-20 µm et peut atteindre ~40 µm et elles sont orientées parallèlement à l'axe-c des cristaux d'omphacite. Il y autant d'inclusions biphasées (liquide + vapeur) que triphasées (liquide + vapeur + solide ; Fig. VI.4o) et la bulle occupe généralement 15-20% du volume totale de l'inclusion. Les inclusions triphasées contiennent généralement un ou plus solides translucides et anisotropes et un cristal cubique de couleur sombre.

VI.4.7. Matrices de brèches éclogitiques M1 et M2 (unités LPL)

Les matrices M1 des brèches éclogitiques du massif du Monviso sont presque entièrement faite de cristaux automorphes verts clairs d'omphacite avec de rares cristaux d'apatite, tandis que les matrices M2 sont majoritairement composées de cristaux automorphes d'omphacite accompagnés de cristaux de grenat.

Dans les matrices M1, les inclusions fluides sont isolées ou dans des clusters non planaires et orientées parallèlement à l'axe-c des cristaux d'omphacite suggérant un piégeage primaire. La plupart des inclusions ont une taille de 5 à 10 µm, sont généralement biphasées (liquide + vapeur) et rarement triphasées (liquide + vapeur + solide) contenant un solide incolore (5/24 inclusions). La bulle de vapeur occupe généralement 10-15% du volume total des inclusions.

Dans les matrices M2, les inclusions fluides primaires sont relativement similaires à celles des matrices M1 : de taille 5-15 µm et jusqu'à 20 µm et orientées parallèlement à l'axe-c des cristaux d'omphacite. Ces inclusions sont biphasées (liquide + vapeur) et seulement deux inclusions triphasées (sur 19 inclusions ; liquide + vapeur + solide) furent observées : une avec un solide opaque et l'autre avec un solide incolore. La bulle de vapeur occupe généralement ~10% du volume totale de l'inclusion.

Transect	Outcrop	Unit type	sample	Host mineral	mean salinity (wt% NaCl eq.)	med.salinity (wt% NaCl eq.)	sd salinity	n FI salinity data	solid identified (number of FI)	Gas detected	mean CO_2%	med. CO_2%	n FI CO_2-CH_4 data
Savoy-Susa	SS1	LPU	SS1Car	Qz	9.7	7.0	6.2	21	/	CO_2-CH_4	86.9	87.3	11
"	SS2	"	SS2LwsB	"	6.4	6.2	2.1	20	/	"	79.3	88.8	10
"	"	"	SS2LwsC	"	5.8	6.7	2.8	20	/	"	83.5	82.6	5
"	SS3	"	SS3LwsB	"	8.3	8.9	4.5	20	/	"	81.1	96.2	7
"	"	"	SS3Car	"	1.7	1.7	1.4	20	/	"	80.9	84.8	7
"	SS4	"	SS4LwsB	"	13.3	14.8	7.5	14	/	"	72.8	81.3	7
"	SS5	LPM	SS5LwsB	"	4.0	3.0	4.0	20	/	"	81.4	84.7	8
"	"	"	SS5LwsC	"	7.3	5.6	7.0	20	/	"	52.9	51.7	13
"	SS6	"	SS6LwsB	"	8.6	5.2	8.3	20	/	"	30.3	27.7	12
"	SS7	"	SS7LwsB	"	6.4	6.1	1.3	20	/	"	53.3	53.2	9
"	SS8	"	SS8LwsB	"	3.1	1.5	5.4	20	/	"	52.9	56.0	10
"	"	"	SS8LwsC	"	1.0	0.3	1.1	20	/	"	71.6	77.6	12
"	SS9	"	SS9LwsB	"	23.3	24.1	3.8	18	/	"	22.4	15.1	8
"	"	"	SS9LwsC	"	9.1	10.5	5.4	20	/	"	68.2	71.7	10
"	SS10	"	SS10LwsB	"	4.8	3.9	3.2	21	/	"	76.4	78.2	13
"	"	"	SS10LwsC	"	1.3	1.1	1.3	20	/	"	84.5	89.3	11
"	SS11	LPL	SS11Grt	Grt	11.3	10.5	4.0	38	WM (14)	"	91.3	97.6	10
Cottian Alps	CA1	LPU	CA1LwsB	Qz	11.7	9.4	8.4	22	/	"	78.0	89.0	13
"		"	CA1LwsC	"	6.5	5.2	4.5	22	/	"	69.1	71.0	12
"	CA2	"	CA2LwsB	"	1.8	1.6	1.4	20	/	"	62.4	58.7	6
"		"	CA2LwsC	"	4.1	3.7	2.2	18	/	"	73.6	72.8	6
"		"	CA2Car	Qz and Car	5.5	5.2	2.7	21	/	"	80.8	84.2	9
"	CA3	"	CA3LwsB	Qz	2.9	3.2	1.1	20	/	"	53.6	56.9	11
"		"	CA3Car	Qz and Car	5.6	4.9	4.5	35	Qz (3), Chl (2), WM (1)	"	88.7	89.6	22
"	CA4	"	CA4LwsB	Qz	3.6	3.7	1.5	107	/	"	84.3	88.0	15
"		"	CA4LwsC	"	5.5	5.4	1.4	32	/	"	91.2	92.0	5
"	CA5	"	CA5LwsB	"	9.4	9.6	4.8	20	/	"	78.0	78.5	12
"		"	CA5LwsC	"	3.9	3.8	3.2	20	/	"	80.5	85.1	8
"		"	CA5Car	Qz and Car	4.2	4.5	1.7	20	/	"	82.6	87.9	9
"	CA6	"	CA6LwsB	Qz	2.9	2.5	2.8	20	/	"	64.4	73.8	12
"		"	CA6LwsC	"	4.0	3.9	1.9	24	/	"	83.5	85.5	18
"		"	CA6Car	"	9.2	10.0	4.0	20	/	"	87.7	95.0	10
"		"	CA6Tlc	Dol	3.7	3.1	1.8	30	/	"	69.5	85.5	12
"	CA7	LPM	CA7Tlc	"	4.4	4.8	2.1	27	/	"	86.5	90.5	8
"	CA8	"	CA8LwsB	Qz	3.2	2.0	5.2	18	/	"	44.0	44.0	1
"	CA9	"	CA9LwsB	"	1.5	0.2	2.3	17	/	"	66.6	81.8	10
"		"	CA9Car	"	6.7	6.3	3.1	24	/	"	93.1	94.7	8
"	CA10	"	CA10LwsB	"	2.0	1.5	1.8	22	/	"	53.1	56.4	11
"		"	CA10LwsC	"	0.3	0.0	0.8	22	/	"	89.4	92.1	5
"	CA11	LPL	CA11Grt	Grt	7.8	7.5	1.9	19	WM (1)	"	48.0	50.8	16
"	CA12	"	CA12Grt	"	23.2	23.3	4.7	16	WM (8 FI)	"	30.8	28.7	9
Queyras-Monviso	QM1	LPU	QM1Car	Qz and Car	6.6	5.2	5.4	23	/	"	79.4	80.7	12
"	QM2	"	QM2LwsB	Qz	10.7	7.8	8.5	12	Cal (2), salts (2)	"	94.8	96.0	5
"		"	QM2LwsC	"	11.1	7.8	8.1	12	/	"	27.8	28.7	9
"	QM3	"	QM3Jd	Jd	9.1	9.1	2.8	23	Cal (2), WM (2)	none	/	/	/
"	QM4	"	QM4LwsB	Qz	2.5	2.3	1.0	17	/	CO_2-CH_4	95.1	95.8	5
"		"	QM4LwsC	"	1.1	0.0	1.5	16	/	"	33.8	16.2	7
"		"	QM4Car	"	2.4	2.7	1.5	22	/	"	88.1	90.4	9
"	QM5	"	QM5LwsB	"	7.6	7.3	2.0	22	/	"	75.0	77.3	18
"		"	QM5LwsC	"	5.2	4.3	3.7	22	/	"	34.8	39.0	13
"	QM6	"	QM6LwsB	"	3.5	3.7	2.4	20	/	"	83.1	83.7	10
"		"	QM6Car	"	4.7	3.8	4.4	23	/	"	78.4	85.3	10
"	QM7	"	QM7LwsB	"	6.1	2.5	7.2	22	/	"	38.6	10.1	16
"		"	QM7LwsC	"	6.0	5.1	4.1	22	/	"	16.5	0.0	5
"	QM8	"	QM8Tlc	Dol and Qz	0.7	0.4	0.8	18	/	"	14.6	0.0	4
"	QM9	"	QM9LwsB	Qz	1.1	0.8	1.2	20	/	"	51.7	51.7	2
"		"	QM9LwsC	"	4.3	4.2	2.1	24	/	"	67.4	75.6	4
"	QM10	"	QM10LwsB	"	1.4	1.3	1.6	17	/	"	86.3	89.7	7
"	QM11	LPM	QM11LwsB	"	3.3	2.6	3.8	20	/	"	95.7	96.8	10
"		"	QM11LwsC	"	3.4	3.0	2.3	20	/	"	44.4	42.9	8
"	QM12	"	QM12Jd	Jd	24.6	28.4	7.1	20	/	none	/	/	/
"	QM13	"	QM13LwsC	Qz	4.3	3.2	4.1	14	/	CO_2-CH_4	0.0	0.0	2
"		"	QM13Tlc	Dol	5.1	5.0	2.0	26	/	"	77.0	81.3	15
"	QM14	"	QM14LwsB	Qz	0.7	0.1	1.0	26	/	"	72.4	84.2	11
"		"	QM14LwsC	"	2.1	2.2	1.1	15	/	"	0.0	0.0	4
"	QM15	LPL	QM15OmpV1	Omp	14.6	13.7	5.5	37	Cal (12), WM (2), opaque (6)	N_2	/	/	/
"		"	QM15OmpV2	"	14.6	14.8	4.1	46	Cal (7), WM (1), opaque (1)	"	/	/	/
"		"	QM15OmpM2	"	18.9	17.4	4.6	19	opaque (1)	"	/	/	/
"	QM16	"	QM16OmpM1	"	26.4	27.2	2.6	24	Cal (2)	none	/	/	/
"	QM17	"	QM17Grt	Grt	13.5	13.1	6.2	15	WM (3)	"	/	/	/

Table VI.2 *: Salinités, solides et contenu en gaz des inclusions fluides dans nos échantillons. Abréviations : LwsB = veine de lawsonite B ; LwsC = veine de lawsonite C ; Car = veine de Fe-Mg carpholite ; Grt = meta-pélite à grenat-chloritoïde ; Tlc = talcschiste à dolomite ; Jd = veine de jadeite ; OmpV1 = veine d'omphacite V1 ; OmpV2 = veine d'omphacite V2 ; OmpM1 = matrice M1 à omphacite ; OmpM2 = matrice M2 à omphacite. LPU = Liguro-Piemont Upper units ; LPM = Liguro-Piemont Middle units ; LPL = Liguro-Piemont Lower units.*

VI.5. Géochimie des inclusions fluides

Nous avons analysé 1585 inclusions : 810 dans les méta-sédiments des unités supérieures, 397 dans les méta-sédiments des unités médianes (dont 24 dans des veines à Fe-Mg carpholite prograde), 88 dans des sédiments des unités inférieures, 101 dans des talcschistes à dolomite des contacts

tectoniques et 169 dans les méta-gabbros des unités supérieures, médianes et inférieures. Toutes ces inclusions furent analysées par spectroscopie Raman pour déterminer leur salinité, leur contenu en gaz et la nature des solides. Le détail de toutes les analyses faites dans les échantillons est présenté en table VI.2 et dans les histogrammes de la figure VI.5a-I. Des données statistiques pour des groupes d'échantillons sont présentées en table VI.3.

VI.5.1. Salinité des inclusions fluides

Veines à lawsonite B, à lawsonite C et à Fe-Mg carpholite (unités LPU et LPM)

Le long des trois transects d'étude, la salinité estimée dans le quartz des veines à lawsonite est généralement faible à intermédiaire (Table VI.2, VI.3) :

- pour les veines à lawsonite B (salinité moyenne ; médiane ; écart-type en wt.% eq. NaCl et nombre d'inclusions) : Savoy-Susa (8.3 wt.% ; 6.1 wt % ; 7.4 ; n = 173) ; Alpes Cottiennes (4.2 wt.% ; 3.4 wt.% ; 4.4 ; n = 266) ; Queyras-Monviso (3.8 wt.% ; 2.3 wt.% ; 4.8 ; n = 176) ; tous les transects (5.2 wt.% ; 3.5 wt.% ; 5.9 ; n = 615).

- comme pour les veines à lawsonite C (Table VI.2, VI.3) : Savoy-Susa (4.9 wt.% ; 2.8 wt.% ; 5.3 ; n = 100) ; Alpes Cottiennes (4.1 wt.% ; 4.2 wt.% ; 3.2 ; n = 138) ; Queyras-Monviso (5.0 wt.% ; 3.6 wt.% ; 4.9 ; n = 145) ; tous les transects (4.7 wt.% ; 3.8 wt.% ; 4.5 ; n = 383).

Aucune différence majeure ou systématique de salinités entre les veines à LwsB et les veines à LwsC n'est observable (Table VI.2, VI.3 ; Fig. VI.5a, b, d, e, g, h, j, k).

Dans les veines à Fe-Mg carpholite, aucune différence majeure de salinité ne fut observée entre les inclusions fluides contenues dans la carpholite et dans le quartz, et ces données sont donc présentées ensemble afin de simplifier l'information déjà complexe de ce travail. Dans ces veines, les salinités estimées sont également, de façon générale, faibles à intermédiaires le long des transects d'étude (Table VI.1, VI.2 ; Fig. VI.5a, d, e, g, j, k) : Savoy-Susa (5.8 wt.% ; 4.4 wt.% ; 6.0 ; n = 41) ; Alpes Cottiennes (6.2 wt.% ; 5.6 wt.% ; 3.8 ; n = 120) ; Queyras-Monviso (4.6 wt.% ; 3.4 wt.% ; 4.4 ; n = 68) ; tous les transects (5.6 wt.% ; 4.8 wt.% ; 4.5 ; n = 229). Aucune différence majeure ou systématique entre les valeurs de salinités des veines à Fe-Mg carpholite avec celles des veines à lawsonite des mêmes affleurements n'a pu être établie (Table VI.1, VI.2 ; Fig. VI.5a, d, e, g, j, k). La seule veine à carpholite des unités médianes, formée lors du chemin prograde, a une salinité plus forte que les veines à lawsonite formées au pic dans le même affleurement (CA9 ; Table VI.2 ; Fig. VI.5e).

Pour chaque affleurement, la dispersion forte des données est illustrée par les écarts types élevés (Table VI.2, VI.3) dont les valeurs sont généralement plus importantes pour les veines à LwsB (tous les transects = 5.9) que pour les veines à LwsC (tous les transects = 4.5) et à Fe-Mg carpholite (tous les transsects = 4.5)

Pour les trois transects d'étude, les salinités des veines à LwsB, LwsC et Fe-Mg carpholite sont inférieures dans les unités médianes que dans les unités supérieures (Table VI.2, Table VI.3 ; Fig. VI.5a, b, d, e, g, h, j, k) : Savoy Susa LPU (7.3 wt.% ; 6.7 wt.% ; 5.5 ; n = 115) ; Savoy Susa LPM (6.7 wt.% ; 3.7 wt.% ; 7.5 ; n = 199) ; Alpes Cottiennes LPU (5.1 wt.% ; 4.2 wt.% ; 4 ; n = 421) ; Alpes Cottiennes LPM (1.7 wt.% ; 0.7 wt.% ; 3.0 ; n = 79) ; Queyras-Monviso LPU (5.0 wt.% ; 3.5 wt.% ; 5.1 ; n = 294) ; Queyras-Monviso LPM (2.6 wt.% ; 1.9 wt.% 2.9 ; n = 95) ; tous les transects LPU (5.3 wt.% ; 3.5 wt.% ; 5.1 ; n = 830) ; tous les transects LPM (4.6 wt.% ; 2.4 wt.% ; 6.2 ; n = 373). Généralement, les veines de haute pression de l'unité supérieure ont des salinités supérieures ou égales à celle de l'eau de mer au crétacé inférieur (~ 3.2-3.7 wt.% ; Hay et al., 2006) alors que les veines des unités médianes ont des salinités inférieures à celle de l'eau de mer (Fig. VI.5 a, b, d, e, g, h, j, k). En représentant les valeurs médianes de salinité de chaque type de veines et pour chaque affleurement en fonction de la longitude (augmentation du grade métamorphique vers l'Est) ou bien de la température du pic de chaque affleurement, une décroissance progressive des salinités vers l'Est, et avec le grade est clairement identifiable à travers les unités supérieures et médianes des trois transects d'étude (Fig. VI.6a-c).

Pour finir certains affleurements plus rares ont des salinités médianes fortes proches de 10 wt.% eq. NaCl ou même encore supérieures et se situent soient à l'Ouest des unités supérieures (SS1, SS4, CA1, QM2, QM5 ; Table VI.2), soit dans l'unité médiane du transect Savoy-Susa (SS9 principalement). D'autres échantillons des unités médianes du même transect ont également des salinités significativement supérieures à celle de l'eau de mer (SS5, SS6, SS7 ; Table VI.2).

Table VI.3 *(page suivante) : Calculs statistiques des salinités et contenu en gaz des inclusions fluides dans nos échantillons. Abréviations : LwsB = veine de lawsonite B ; LwsC = veine de lawsonite C ; Car = veine de Fe-Mg carpholite ; Grt = meta-pélite à grenat-chloritoïde ; Tlc : talcschiste à dolomite ; Jd : veine de jadeite ; OmpV1 = veine d'omphacite V1 ; OmpV2 = veine d'omphacite V2 ; OmpM1 = matrice M1 à omphacite ; OmpM2 = matrice M2 à omphacite. LPU = Liguro-Piemont Upper units ; LPM = Liguro-Piemont Middle units ; LPL : Liguro-Piemont Lower units.*

Transect	datasets	mean salinity (wt% NaCl eq.)	med.salinity (wt% NaCl eq.)	sd salinity	n FI salinity data	mean CO_2%	med. CO_2%	n FI CO_2-CH_4 data
Savoy-Susa	All LPU LwsB	8.9	8.1	5.5	54	77.9	88.8	24
"	All LPM LwsB	8.1	5.1	8.2	119	53.3	63.3	60
"	All LPU + LPM LwsB	8.3	6.1	7.4	173	60.3	73.9	84
"	All LPU LwsC	5.8	6.7	2.8	20	83.5	82.6	5
"	All LPM LwsC	4.7	2.2	5.7	80	67.9	76.7	46
"	All LPU + LPM LwsC	4.9	2.8	5.3	100	70.1	78.3	51
"	All Car	5.8	4.4	6.0	41	84.6	87.2	18
"	All LPU metasediments	7.3	6.7	5.5	115	81.1	87.3	47
"	All LPM metasediments	6.7	3.7	7.5	199	59.9	69.5	106
"	All LPL metasediments	11.3	10.5	4.0	38	91.3	97.6	10
Cottian Alps	All LPU LwsB	4.7	3.7	4.5	209	71.8	77.3	69
"	All LPM LwsB	2.3	1.5	3.4	57	58.8	65.3	22
"	All LPU + LPM LwsB	4.2	3.4	4.4	266	68.6	77.3	91
"	All LPU LwsC	4.9	4.8	2.9	116	79.0	84.0	49
"	All LPM LwsC	0.3	0.0	0.8	22	89.4	92.1	5
"	All LPU + LPM LwsC	4.1	4.2	3.2	138	80.0	84.9	54
"	All Car	6.2	5.6	3.8	120	87.0	90.6	58
"	All LPU metasediments	5.1	4.2	4.0	421	78.1	84.1	168
"	All LPM metasediments	1.7	0.7	3.0	79	64.5	79.2	27
"	All LPL metasediments	14.9	10.8	8.5	35	41.7	40.9	27
Queyras-Monviso	All LPU LwsB	4.5	2.7	5.1	130	70.7	82.1	63
"	All LPM LwsB	1.8	1.1	2.9	46	83.5	92.8	21
"	All LPU + LPM LwsB	3.8	2.3	4.8	176	73.9	83.8	84
"	All LPU LwsC	5.8	4.6	5.5	96	34.0	39.7	38
"	All LPM LwsC	3.2	2.8	2.8	49	25.4	11.4	14
"	All LPU + LPM LwsC	5.0	3.6	4.9	145	31.7	37.1	52
"	All Car	4.6	3.4	4.4	68	81.6	87.6	31
"	All LPU metasediments	5.0	3.5	5.1	294	62.7	76.9	132
"	All LPM metasediments	2.6	1.9	2.9	95	60.3	82.6	35
"	All LPL metasediments	13.5	13.1	6.2	15	/	/	/
All transects	All LPU LwsB	5.2	3.7	5.1	393	72.3	81.8	156
"	All LPM LwsB	5.3	2.7	7.0	222	60.6	74.3	103
"	All LPU + LPM LwsB	5.2	3.5	5.9	615	67.7	78.2	259
"	All LPU LwsC	5.3	4.8	4.3	232	60.7	72.6	92
"	All LPM LwsC	3.6	1.7	5.0	151	61.0	72.0	65
"	All LPU + LPM LwsC	4.7	3.8	4.5	383	60.8	72.0	157
"	All Car	5.6	4.8	4.5	229	85.0	88.4	107
"	All LPU metasediments	5.3	3.5	5.1	830	72.7	83.2	347
"	All LPM metasediments	4.6	2.4	6.2	373	60.7	73.9	168
"	All LPL metasediments	13.1	11.0	6.6	88	55.9	52.1	37
"	All units metamafics	17.2	16.0	7.2	169	/	/	/
"	All units talcschists	3.7	3.6	2.3	101	70.2	81.3	32

Figure VI.5 *(page suivante) : Histogrammes des salinités des inclusions fluides des trois transects d'étude. A) Unités supérieures du transect Savoy-Susa. B) Unités médianes du transect Savoy-Susa. C) Unités inférieures du transect Savoy-Susa. D) Unités supérieures du transect des Alpes Cottiennes ; E) Unités médianes du transect des Alpes Cottiennes. F) Unités inférieures du transect des Alpes Cottiennes. G) Unités supérieures du transect Queyras-Monviso. H) Unités médianes du transect Queyras-Monviso. I) Unités inférieures du transect Queyras- Monviso. J) Unités supérieures des trois transects. K) Unités médianes des trois transects. L) Unités Inférieures des trois transects. Abréviations : LwsB = veine de lawsonite B ; LwsC = veine de lawsonite C ; Car = veine de Fe-Mg carpholite ; Grt = meta-pélite à grenat-chloritoïde ; Tlc = talcschiste à dolomite ; Jd = veine de jadeite ; OmpV1 = veine d'omphacite V1 ; OmpV2 = veine d'omphacite V2 ; OmpM1 = matrice M1 à omphacite ; OmpM2 = matrice M2 à omphacite. LPU = Liguro-Piemont Upper units ; LPM = Liguro-Piemont Middle units ; LPL = Liguro-Piemont Lower units.*

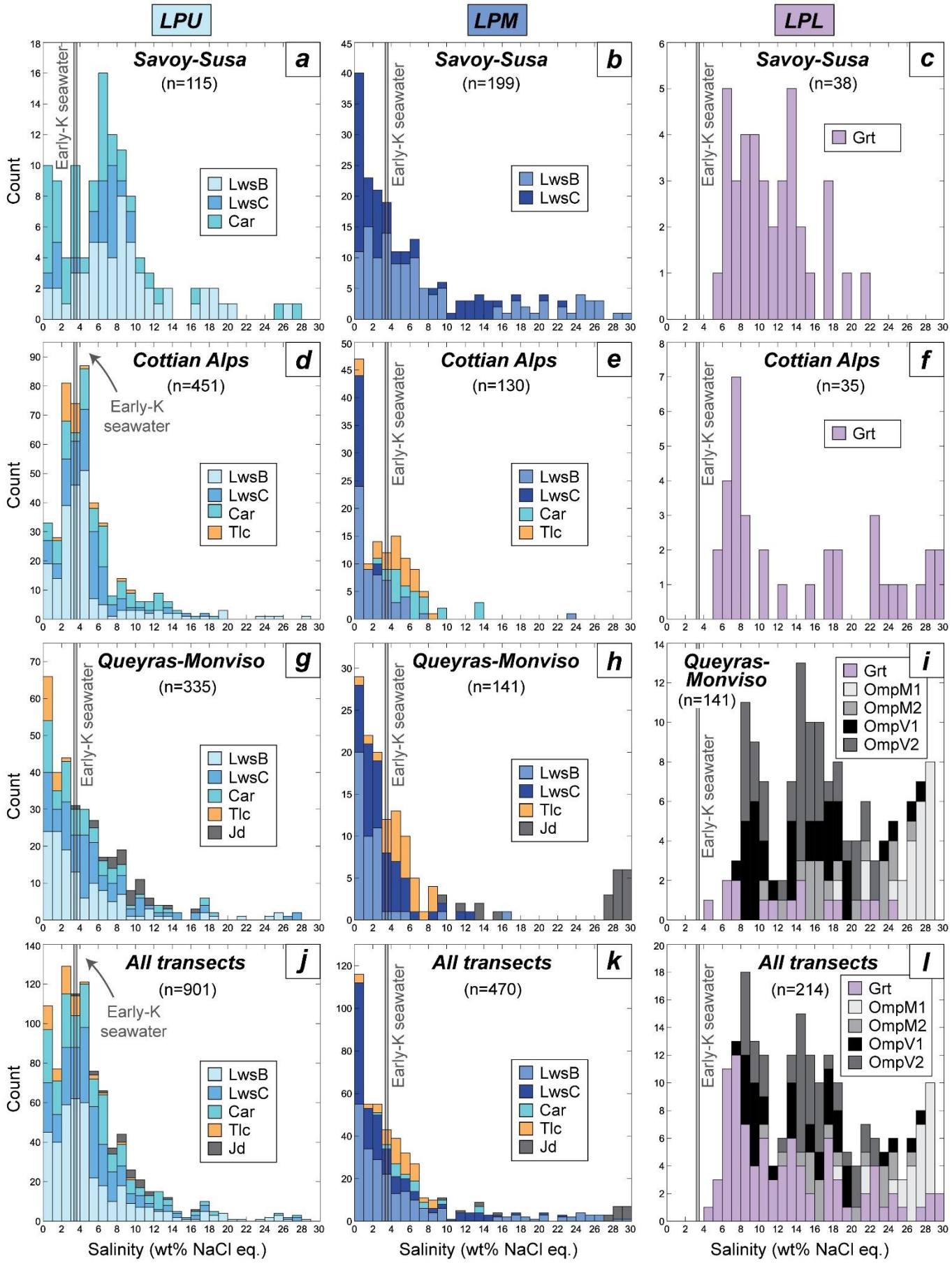
LPU
LPM
LPL
a
Savoy-Susa
(n=115)
Early-K seawater
LwsB
LwsC
Car
b
Savoy-Susa
(n=199)
Early-K seawater
LwsB
LwsC
c
Savoy-Susa
(n=38)
Early-K seawater
Grt
d
Cottian Alps
(n=451)
Early-K seawater
LwsB
LwsC
Car
Tlc
e
Cottian Alps
(n=130)
Early-K seawater
LwsB
LwsC
Car
Tlc
f
Cottian Alps
(n=35)
Early-K seawater
Grt
g
Queyras-Monviso
(n=335)
Early-K seawater
LwsB
LwsC
Car
Tlc
Jd
h
Queyras-Monviso
(n=141)
Early-K seawater
LwsB
LwsC
Tlc
Jd
i
Queyras-Monviso
(n=141)
Early-K seawater
Grt
OmpM1
OmpM2
OmpV1
OmpV2
j
All transects
(n=901)
Early-K seawater
LwsB
LwsC
Car
Tlc
Jd
k
All transects
(n=470)
Early-K seawater
LwsB
LwsC
Car
Tlc
Jd
l
All transects
(n=214)
Early-K seawater
Grt
OmpM1
OmpM2
OmpV1
OmpV2
Count
Salinity (wt% NaCl eq.)

Méta-pélites à grenat-chloritoïde (unités LPL)

Dans les grenats des méta-pélites des unités inférieures, les salinités sont assez fortes (Table VI.2, VI.3 ; Fig. VI.5c, f, i, l) : Savoy-Susa (11.3 wt.% ; 10.3 wt.% ; 4.0 ; n =38) ; Alpes Cottiennes (14.9 wt.% ; 10.8 wt.% ; 8.5 ; n = 35) ; Queyras-Monviso (13.5 wt.% ; 13.1 wt.% ; 6.2 ; n = 15) ; tous les transects (13.1 wt.% ; 11.0 wt.% ; 6.6 ; n = 88).

Ces salinités sont significativement supérieures à celle de l'eau de mer au Crétacé inférieur (~ 3.2-3.7 wt.% ; Hay et al., 2006) ainsi qu'à celles des veines des unités supérieures et médianes (Fig. VI.5a-l). Alors qu'une décroissance progressive des salinités est observée dans les sédiments des unités supérieures et médianes, une forte augmentation des salinités est observée à plus haut grade dans les unités inférieures (Fig. VI.6a-c).

Talcschistes à dolomite (contacts tectoniques entre unités LPU et LPM)

Dans les inclusions fluides primaires des talcschistes à dolomite, les salinités sont assez faibles (3.7 wt.% ; 3.6 wt.% ; 2.3 ; n = 101 ; Table VI.3 ; Fig. VI.5j, k) avec en détails pour les différents échantillons (Table VI.2 ; Fig. VI.5d, e, g, h, j, k) : CA6Tlc (3.7 wt.% ; 3.3 wt.% ; 1.8 : n = 30) ; CA7Tlc (4.4 wt.% ; 4.8 wt.% ; 2.1 ; n = 27) ; QM8Tlc (0.7 wt.% ; 0.4 wt.% ; 0.8 ; n = 18) ; QM13Tlc (5.1 wt.% ; 5.0 wt.% ; 2.0 ; n = 26). Ces salinités sont donc proches ou légèrement supérieures à la valeur de l'eau de mer au Crétacé inférieur (~ 3.2-3.7 wt.% ; Hay et al., 2006), à part pour l'échantillon QM8Tlc pour lequel les salinités sont bien plus faibles. Aucune différence ne fut détectée entre les inclusions fluides du quartz et de la dolomite de cet échantillon.

Les salinités des échantillons CA6Tlc et QM8Tlc sont comparables à celles estimées dans les veines des méta-sédiments provenant d'affleurements à proximité de ces échantillons, dans les unités supérieures (Fig. VI.5d, g, j ; VI.6a-c). Les échantillons CA7Tlc et QM13Tlc ont par contre des salinités significativement supérieures à celles des méta-sédiments des unités médianes collectés à proximité (Fig. VI.5e, h, k ; VI.6a-c).

Veines à Jadéite, omphacite et matrices de brèches à omphacite (unités LPU, LPM, LPL)

Dans tous les échantillons des méta-gabbros des unités LPU, LPM et LPM les salinités sont intermédiaires à fortes et généralement bien supérieures à celles des sédiments autour (Table VI.2, VI.3 ; Fig. VI.5g-l ; VI.6a-c) : veine de jadéite LPU (9.1 wt.% ; 9.1 wt.% ; 2.8 ; n = 23) ; veine de jadéite LPM (24.6 wt.% ; 28.4 wt.% ; 7.1 ; n = 20) ; veines d'omphacite V1 LPL (14.6 wt.% ; 13.7 wt.% ; 5.5 ; n = 37) ; veines d'omphacite V2 LPL (14.6 wt.% ; 14.8 wt.% ; 4.1 ; n = 46) ; matrice d'omphacite M1

LPL (26.4 wt.% ; 27.2 wt.% ; 2.6 ; n = 24) ; matrice d'omphacite M2 LPL (18.9 wt.% ; 17.4 wt.% ; 4.6 ; n = 19) ; tous les échantillons méta-mafiques (17.2 wt.% ; 16.0 wt.% ; 7.2 ; n = 169). Des valeurs d'eutectiques entre -22°C et -24.3°C mesurées dans les veines V1 suggèrent la présence majoritaire de NaCl et KCl et la potentielle présence minoritaire de $MgCl_2$ et/ou de $CaCl_2$ (Herviou et al., 2021 ; **chapitre II**).

Les salinités sont plus faibles pour la veine à jadéite des unités supérieures et pour une partie des inclusions de la veine à jadéite des unités médianes que pour la plupart des inclusions des veines et matrices à omphacite des unités inférieures.

Figure VI.6 *(page suivante) : Evolution des valeurs médianes de salinités des inclusions fluides en fonction de la longitude et de la température du pic d'enfouissement. A) Evolution de la salinité médiane en fonction de la longitude pour chaque type d'échantillons et le long des 3 transects d'étude. Les flèches grises montrent la décroissance progressive des salinités en fonction de la longitude et donc du grade dans les méta-sédiments des unités supérieures à médianes et l'augmentation des salinités dans les méta-sédiments des unités inférieures. B) Evolution de la salinité médiane en fonction de la longitude pour chaque affleurement et le long des 3 transects d'étude. C) Evolution de la salinité médiane en fonction de la température du pic d'enfouissement pour chaque affleurement et le long des 3 transects d'étude. Les flèches noires pointent les échantillons situés à moins d'un kilomètre de la Nappe des Gypses, caractérisés par des salinités plus fortes. Abréviations : LwsB = veine de lawsonite B ; LwsC = veine de lawsonite C ; Car = veine de Fe-Mg carpholite ; Grt = meta-pélite à grenat-chloritoïde ; Tlc = talcschiste à dolomite ; Jd/Omp = veines à jadéite ou omphacite et matrices de brèches à omphacite dans les méta-gabbros. LPU = Liguro-Piemont Upper units ; LPM = Liguro-Piemont Middle units ; LPL = Liguro-Piemont Lower units.*

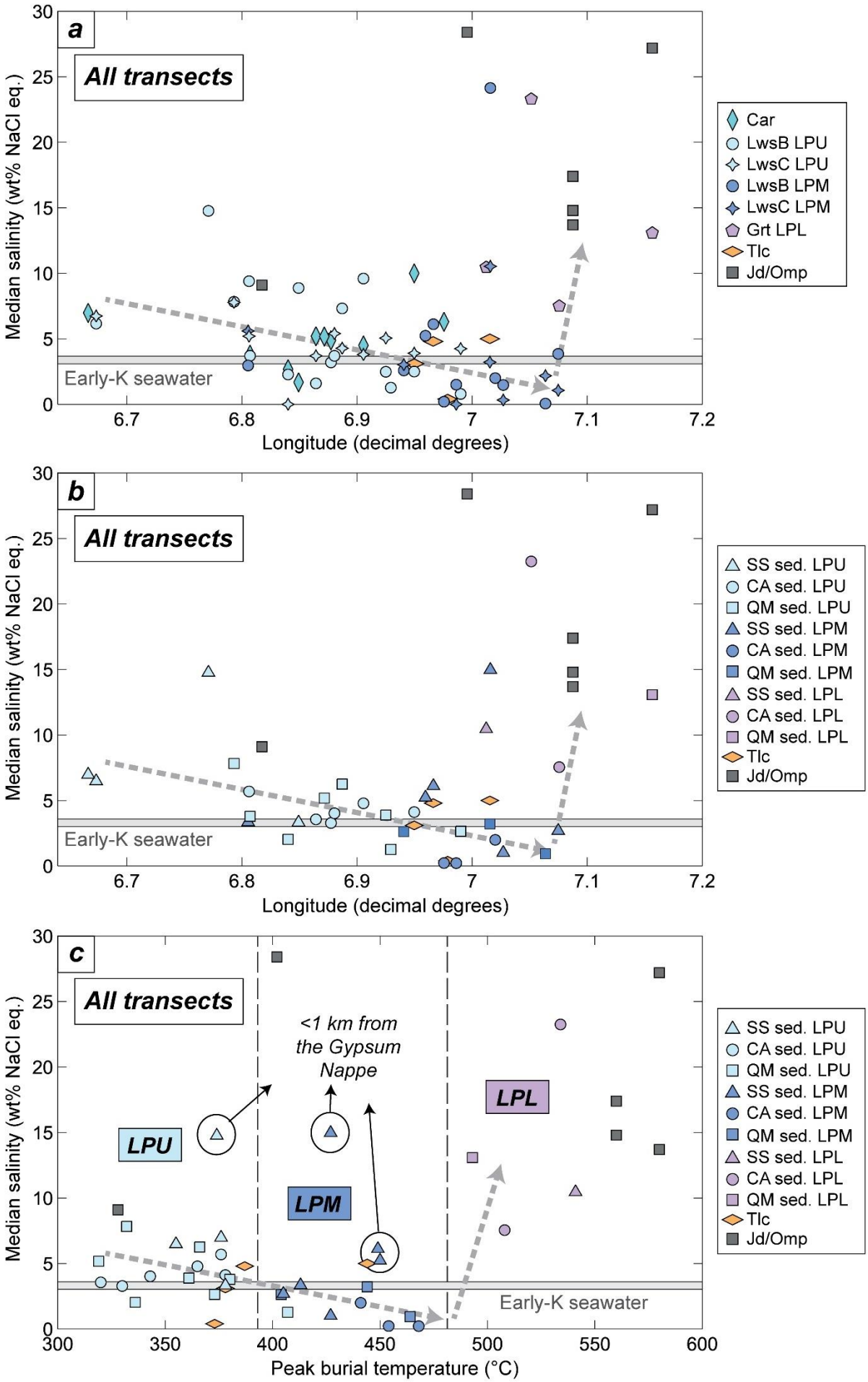
a
All transects
Median salinity (wt% NaCl eq.)
Longitude (decimal degrees)
Early-K seawater
Car
LwsB LPU
LwsC LPU
LwsB LPM
LwsC LPM
Grt LPL
Tlc
Jd/Omp
b
All transects
Median salinity (wt% NaCl eq.)
Longitude (decimal degrees)
Early-K seawater
SS sed. LPU
CA sed. LPU
QM sed. LPU
SS sed. LPM
CA sed. LPM
QM sed. LPM
SS sed. LPL
CA sed. LPL
QM sed. LPL
Tlc
Jd/Omp
c
All transects
<1 km from the Gypsum Nappe
LPU
LPM
LPL
Median salinity (wt% NaCl eq.)
Peak burial temperature (°C)
Early-K seawater
SS sed. LPU
CA sed. LPU
QM sed. LPU
SS sed. LPM
CA sed. LPM
QM sed. LPM
SS sed. LPL
CA sed. LPL
QM sed. LPL
Tlc
Jd/Omp

VI.5.2. Contenu en gaz des inclusions fluides

Veines à lawsonite B, à lawsonite C et à Fe-Mg carpholite (unités LPU et LPM)

Les deux pics formant le doublet de Fermi du CO_2 (1285 cm^{-1} et 1388 cm^{-1}) ainsi que le pic principal à 2907 cm^{-1} du CH_4 furent observés dans la plupart des bulles de vapeur des veines méta-sédimentaires de faciès schiste bleu et le signal Raman fut suffisamment fort pour faire des mesures quantitatives du contenu en gaz dans 515 inclusions (Table VI.2, VI.3). La proportion molaire de CO_2 dans les mélanges CO_2-CH_4 est présentée en fonction de la salinité dans la figure VI.7a-f et les valeurs moyennes et médianes de pourcentage de CO_2 sont présentées en table VI.2 et VI.3.

Les proportions de CO_2 dans ces mélanges sont largement variables mais le CO_2 est généralement dominant dans les veines à lawsonite B (Table VI.2, VI.3 ; Fig. VI.7a, b, c, d ; XCO_2 moyen ; XCO_2 médian ; nombre d'inclusions) : Savoy-Susa (60.3 ; 73.9 ; n = 84) ; Alpes Cottiennes (68 .6 ; 77.3 ; n = 91) ; Queyras-Monviso (73.9 ; 83.8 ; n = 84) ; tous les transects (67.7 ; 78.2 ; n = 259) et pour les veines à Fe-Mg carpholite (Table VI.2, VI.3 ; Fig. VI.7a, b, c, f): Savoy-Susa (84.6 ; 87.2 ; n = 18) ; Alpes Cottiennes (87.0 ; 90.6 ; n = 58) ; Queyras-Monviso (81.6 ; 87.6 ; n = 31) ; tous les transects (85.0 ; 88.4 ; n = 107). Pour les veines à lawsonite C, les inclusions contiennent également plus de CO_2 (Table VI.2, VI.3 ; Fig. VI.7a, b, c, e) : Savoy-Susa (70.1 ; 78.3 ; n = 51) ; Alpes Cottiennes (80.0 ; 84.9 ; n = 54) sauf pour le transect Queyras-Monviso pour lequel les inclusions contiennent globalement plus de CH_4 (34.0 ; 39.7 ; n = 38). Cette distinction de contenu en CO_2-CH_4, entre veines à lawsonite B et à Fe-Mg carpholite d'un côté et veines à lawsonite C de l'autre, le long du transect Queyras-Monviso fut déjà signalé (Herviou et al., 2021 ; **chapitre II**). A l'exception de ce transect, aucune différence systématique entre veines à lawsonite B, lawsonite C et Fe-Mg carpholite ne fut observée. Notons toutefois la teneur importante en CH_4 dans certains échantillons à salinités fortes du transect Savoy-Susa (lawsonite B ± lawsonite C ; Fig. VI.7a). Malgré une dispersion forte des ratios CO_2-CH_4 dans les échantillons étudiés notons le contenu relativement constant entre 80 et 90% de CO_2 dans les veines à Fe-Mg carpholite (Table VI.2, VI.3 ; Fig. VI.7f).

En représentant l'évolution du contenu moyen en CO_2 en fonction de la longitude et de la température du pic d'enfouissement, pour chaque type d'échantillon, la forte dispersion des rapports CO_2-CH_4 est mise en évidence (Fig. VI.8a). Une potentielle tendance d'augmentation de la proportion de CH_4 semble cependant apparaitre des unités supérieures à médianes en faisant le calcul des valeurs moyennes par affleurement (Fig. VI.8b, c). Cette différence est notamment illustrée par les moyennes du pourcentage de CO_2 dans tous les méta-sédiments de ces unités : Savoy-Susa LPU (81.1% ; n =

47) ; Savoy-Susa LPM (59.9% ; n = 106) ; Alpes Cottiennes LPU (78.1% ; n =168) ; Alpes Cottiennes LPM (64.5% ; n = 27 ; en excluant les valeurs des veines à carpholite non formées au pic) ; Queyras-Monviso LPU (62.7 ; n = 132) ; Queyras-Monviso LPM (60.3 ; n = 35) ; tous les transects LPU (72.7 ; n = 347) ; tous les transects LPM (60.7 ; n = 168).

De rares potentiels hydrocarbures furent également observés dans les veines à lawsonite B et C (voir **chapitre II**, Herviou et al., 2021 pour plus de détails).

Méta-pélites à grenat-chloritoïde (unités LPL)

Dans les grenats des méta-pélites des unités inférieures, les pics caractéristiques du CO_2 et du CH_4 furent également détectés sauf dans l'échantillon QM17Grt ou les inclusions étaient trop petites pour réussir à analyser les gaz. Le CO_2 et le CH_4 étaient présents en quantités suffisantes pour faire des analyses quantitatives dans 37 inclusions. La proportion de CO_2 dans les mélanges à CO_2-CH_4 est très variable (Table VI.2, VI.3 ; Fig. VI.7a, b, f ; XCO_2 moyen ; XCO_2 médian ; nombre d'inclusions) : avec le CO_2 largement dominant dans l'échantillon du transect Savoy-Susa (91.3 ; 97.6 ; n = 10) et généralement inférieur dans les échantillons du transect des Alpes Cottiennes (41.7 ; 40.9, n = 27). En prenant en compte ces deux transects, le rapport obtenu est équilibré entre CO_2 et CH_4 (55.9 ; 52. 1 n = 37) et s'intègre bien dans la tendance de décroissance de la proportion en CO_2 observée avec l'augmentation du grade métamorphique (Fig. VI.8a-c).

Figure VI.7 *(page suivante) : Salinités en fonction de la proportion de CO_2 dans les mélanges CO_2-CH_4 des inclusions fluides étudiées. La salinité et la quantité de CO_2 dans les inclusions furent déterminés par spectroscopie Raman. Une incertitude de 0.4 wt.% eq. NaCl pour les valeurs de salinités est reportée d'après Caumon et al. (2013). A) Savoy-Susa B) Alpes cottiennes C) Queyras-Monviso D) Veines à lawsonite B de tous les transects E) Veines à lawsonite C de tous les transects F) Veines à Fe-Mg carpholite ; talcschistes à dolomite et méta-pélites à grenat-chloritoïde.*

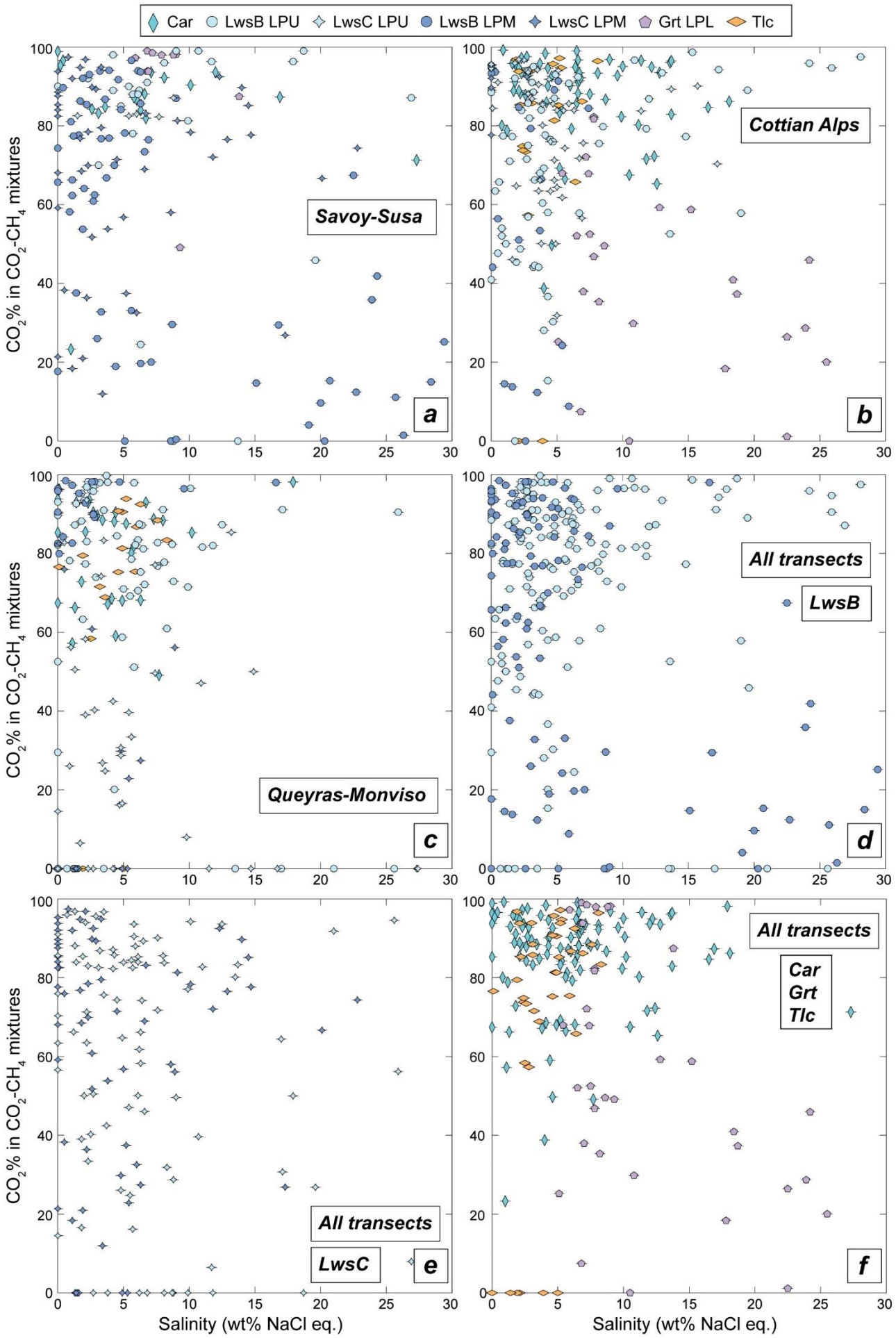
Car
LwsB LPU
LwsC LPU
LwsB LPM
LwsC LPM
Grt LPL
Tlc
CO2 % in CO2-CH4 mixtures
Salinity (wt% NaCl eq.)
Savoy-Susa
a
Cottian Alps
b
Queyras-Monviso
c
All transects
LwsB
d
All transects
LwsC
e
All transects
Car
Grt
Tlc
f

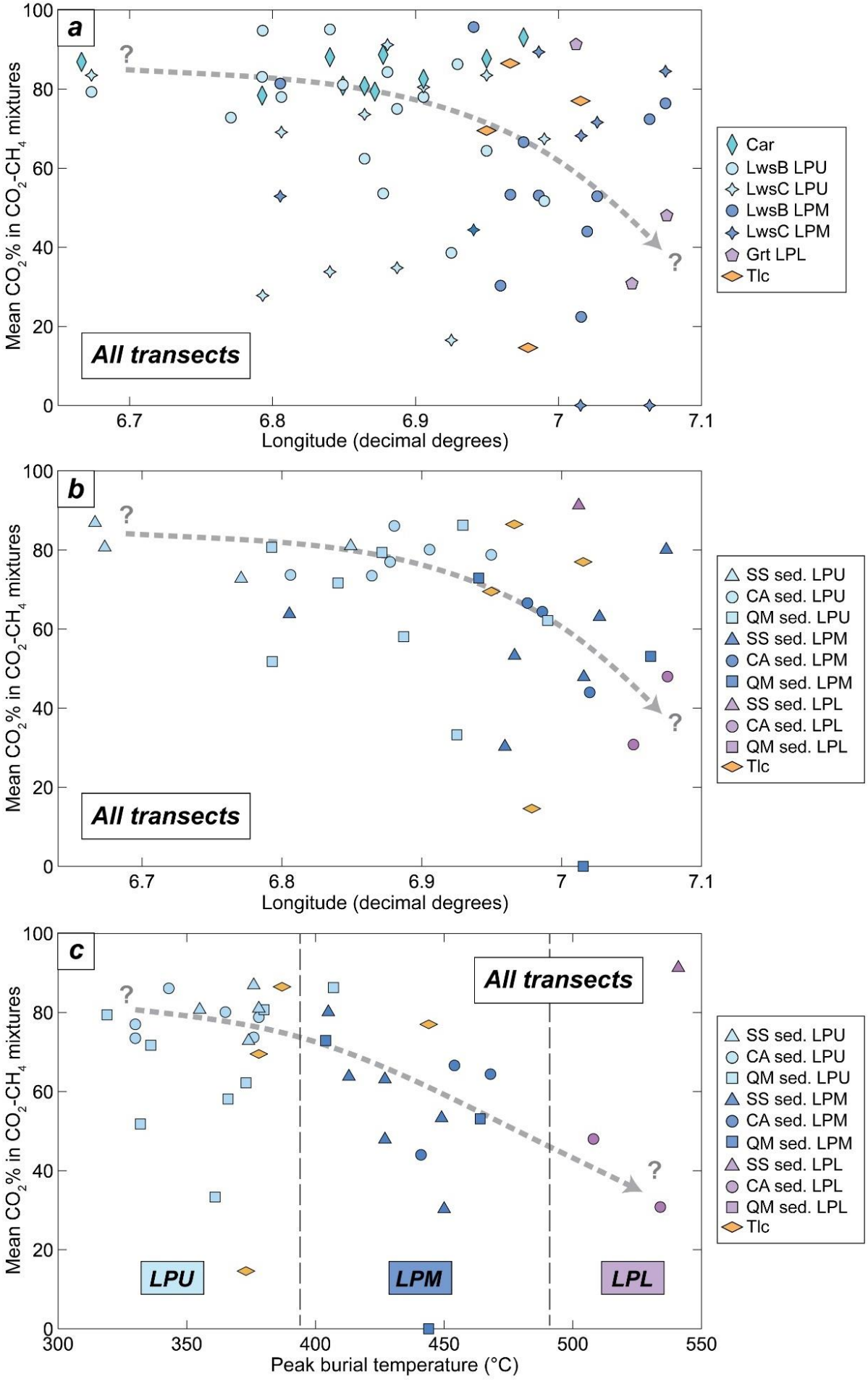
a
All transects
Mean CO2% in CO2-CH4 mixtures
Longitude (decimal degrees)
Car
LwsB LPU
LwsC LPU
LwsB LPM
LwsC LPM
Grt LPL
Tlc
b
All transects
Mean CO2% in CO2-CH4 mixtures
Longitude (decimal degrees)
SS sed. LPU
CA sed. LPU
QM sed. LPU
SS sed. LPM
CA sed. LPM
QM sed. LPM
SS sed. LPL
CA sed. LPL
QM sed. LPL
Tlc
c
All transects
LPU
LPM
LPL
Mean CO2% in CO2-CH4 mixtures
Peak burial temperature (°C)
SS sed. LPU
CA sed. LPU
QM sed. LPU
SS sed. LPM
CA sed. LPM
QM sed. LPM
SS sed. LPL
CA sed. LPL
QM sed. LPL
Tlc

Figure VI.8 *(page précédente) : Evolution de la proportion de CO_2 dans les mélanges CO_2-CH_4 des inclusions fluides étudiées en fonction de la longitude et de la température du pic d'enfouissement. A) Evolution de la teneur en CO_2 en fonction de la longitude pour chaque type d'échantillons et le long des 3 transects d'étude. La flèche montre la potentielle tendance de décroissance progressive du contenu en CO_2 fonction de la longitude et donc du grade dans les méta-sédiments des unités supérieures à inférieures B) Evolution de la teneur en CO_2 en fonction de la longitude pour chaque affleurement et le long des 3 transects d'étude. C) Evolution de la teneur en CO_2 en fonction de la température du pic d'enfouissement pour chaque affleurement et le long des 3 transects d'étude. Abréviations : LwsB = veine de lawsonite B ; LwsC = veine de lawsonite C ; Car = veine de Fe-Mg carpholite ; Grt = meta-pélite à grenat-chloritoïde ; Tlc = talcschiste à dolomite ; Jd/Omp = veines à jadéite ou omphacite et matrices de brèches à omphacite dans les méta-gabbros. LPU = Liguro-Piemont Upper units ; LPM = Liguro-Piemont Middle units ; LPL = Liguro-Piemont Lower units.*

Talcschistes à dolomite (contacts tectoniques entre unités LPU et LPM)

Dans les inclusions des talcschistes à dolomite, du CO_2 et du CH_4 furent également détectés et présents en quantité suffisante dans 39 inclusions pour faire de mesures quantitatives. Les inclusions étudiées contiennent généralement plus de CO_2 que de CH_4 (Table VI.2, VI.3 ; Fig. VI.7b, c, f ; XCO_2 moyen ; XCO_2 médian ; nombre d'inclusions) : tous les échantillons (70.2% ; 81.3% ; n = 32) CA6Tlc (69% ; 86 % ; n = 12) ; CA7Tlc (87% ; 90% ; n = 8) ; QM13Tlc (77% ; 81% ; n = 15) à l'exception de QM8Tlc, plus riche en CH_4 (15% ; 0% ; n = 4). A part cet échantillon, les valeurs de CO_2% des talcschistes à carbonate sont proches de celles des sédiments autour de ces affleurements (Fig. VI.8a-c).

Veines à jadéite, omphacite et matrices de brèches à omphacite (unités LPU, LPM, LPL)

Aucun gaz (autre que la vapeur d'eau) ne fut détecté dans les inclusions aqueuses des veines à jadéite et des matrices de brèches M1. Du N_2 fut détecté régulièrement (Table VI.2) dans les inclusions des veines V1 (dans 10/17 des inclusions), V2 (dans 18/29 des inclusions) et dans les matrices de brèches M2 (dans 5/13 inclusions) et surtout dans les inclusions triphasées (liquide + vapeur + solide) et dans quelques biphasées (liquide + vapeur).

De rares potentiels hydrocarbures furent également observés dans les deux échantillons de veines à jadéite (voir Herviou et al., 2021, **chapitre II** pour plus de détails).

VI.5.3. Solides dans les inclusions fluides

Dans les veines à lawsonite, seulement quatre inclusions, toutes de l'échantillon QM2LwsB et toutes à salinités fortes (i.e. salinité excédant la valeur de saturation du NaCl dans l'eau à température ambiante) contiennent des solides. Le spectre Raman de la calcite fut détecté dans deux de ces

inclusions et les deux autres contiennent un solide incolore non détectable par spectroscopie Raman et avec un habitus cubique rappelant celui des cristaux de sels (Table VI.2). Nous faisons l'hypothèse que ces solides sont des « daughter minerals » formés par sursaturation du fluide en sels lors de l'exhumation des roches. L'absence de cristaux similaires dans les autres inclusions fluides très salés est certainement lié à des phénomènes de méta-stabilité (Bodnar, 1994, 2003a) ou à la présence de systèmes de sels complexes ($NaCl \pm KCl \pm CaCl_2 \pm MgCl_2$).

Dans les veines à Fe-Mg carpholite, seulement six inclusions fluides analysées dans les cristaux de carpholite de l'échantillon CA3Car sont triphasées. Deux de ces inclusions contiennent du quartz, deux contiennent de la chlorite. La dernière inclusion contient un cristal de mica blanc (Table VI.2).

Les 26/62 inclusions fluides triphasées des méta-pélites à grenat-chloritoïde contiennent des cristaux de mica blanc (Table VI.2).

Dans la veine de jadéite QM12Jd, sur les quatre solides observés dans les inclusions fluides, deux sont de la calcite et deux sont des micas blancs (Table VI.2).

Finalement la calcite fut observée dans 12 inclusions des veines à omphacite V1, 7 inclusions des veines à omphacite V2 (Table VI.2). La forte présence de calcite dans les inclusions de ces veines ainsi que le rapport constant observé entre les différentes phases (liquide/gaz/solide) laissent suggérer qu'il s'agit d'un « daughter mineral » formé par sursaturation lors de la diminution des conditions P-T (Herviou et al., 2021, **chapitre II**). De la calcite fut également détectée dans deux inclusions des matrices de brèches M1 (Table VI.2). Des micas blancs furent détectés dans trois des inclusions à calcite des veines et pourraient s'être formées par des réactions avec le minéral hôte après piégeage (Table VI.2 ; Herviou et al., 2021, **chapitre II**). Les solides opaques (7 occurrences dans les inclusions à calcite ; Table VI.2) ne purent pas être détectés par Raman car trop mobiles sous l'action du faisceau. Ces solides opaques se seraient formés soit pas des réactions entre le fluide et le minéral hôte ou bien auraient été piégées accidentellement dans ces inclusions (Herviou et al., 2021, **chapitre II**). Un de ces solides opaques fut également détecté dans une inclusion des matrices M2 (Table VI.2). Finalement, dans 12 inclusions fluides, des solides incolores sont restés non-détectées par Raman. La plupart de ces solides sont présents dans des inclusions très salées des matrices et veines d'omphacite et pourraient être des cristaux de sels (Herviou et al., 2021, **chapitre II**).

VI.6. Discussion de ce chapitre

VI.6.1. Sources des fluides : localement produits par les roches ou infiltration externe depuis d'autres réservoirs ?

Veines à Jadéite, omphacite et matrices de brèches à omphacite (unités LPU, LPM, LPL)

Dans les échantillons de méta-gabbros de faciès schiste bleu et éclogite, les salinités sont bien plus fortes que dans les méta-sédiments de grade équivalent (Table VI.2, VI.3 ; Fig. VI.5g, h, i, j, k, l). Ces salinités fortes sont interprétées comme au moins partiellement héritées de l'altération hydrothermale subie sur les fonds océaniques (Nadeau et al., 1993 ; Philippot et al., 1998 ; voir Herviou et al., 2021, **chapitre II** pour plus de détails). En effet, l'altération hydrothermale à haute-température des gabbros dans les zones de réactions proches des rides océaniques est classiquement accompagnée d'une séparation des phases entrainant la formation de saumures (avec des salinités atteignant ~40-50 wt. % eq. NaCl) et de phases vapeurs (e.g., Alt et al., 2010 ; Castelain et al., 2014 ; Delaney et al., 1987 ; Kelley et al., 1992 ; Kelley et Delaney, 1987 ; Nehlig, 1991 ; Vanko, 1988 ; Verlaguet et al., 2020). Alors que les phases vapeurs peu denses s'échappent rapidement des roches, les saumures denses peuvent être piégés dans les inclusions fluides des gabbros et enrichir en chlore les amphiboles hydrothermales (amphiboles hydrothermales contenant 0.3 wt.% Cl au Chenaillet, Debret et al., 2016 ; et jusqu'à 4 wt.% Cl en domaine océanique, Vanko, 1986). La déstabilisation des amphiboles hydrothermales (+ plagioclase) dans les conditions du faciès schiste bleu produit la formation de glaucophane et lawsonite (+ jadéite) moins riches en chlore (Debret et al., 2016) : les faibles quantités de fluides libérées (la lawsonite étant très hydratée) seront donc relativement riches en Cl, expliquant les fortes salinités des IF piégées dans les veines de jadéite (Herviou et al., 2021, **chapitre II**).

La déstabilisation de ces glaucophanes et lawsonites, moins riches en chlore, en grenat et omphacite lors de l'éclogitisation libèrera a priori un fluide relativement moins salé, qui aura tendance à diluer progressivement le fluide issu de la phase schiste bleu, ce qui peut expliquer les salinités un peu plus faibles mesurées dans certaines veines et brèches à omphacite formées dans le faciès éclogite (moyenne-médiane : 14.6-13.7 wt.% eq. NaCl ; Herviou et al., 2021, **chapitre II**). La présence de N_2 dans de nombreuses inclusions des veines et matrices de brèches éclogitiques est interprétée comme héritée de la déstabilisation des minéraux contenant du NH_4^+ comme le glaucophane (Busigny et al., 2011). Les veines V1 et matrices M1 sont en effet interprétées comme synchrones de la formation du grenat dans les méta-gabbros de composition intermédiaire (entre Fe-Ti et Mg-Al) à

des conditions P-T (~510°C- 2.5 GPa ; Locatelli et al., 2019b) proches de celles du pic d'enfouissement des unités inférieures (500-580°C 2.2-2.8 GPa ; Herviou et al., 2022, **chapitre III**).

Pour finir, la présence de rares potentielles inclusions d'hydrocarbures associée à des inclusions moins salées dans les veines de jadéite suggère une faible infiltration de fluide provenant des sédiments dans les unités de faciès schiste bleu où les sédiments sont volumétriquement dominants par rapport aux roches mafiques et ultramafiques (Herviou et al., 2021).

Veines à lawsonite B, à lawsonite C et à Fe-Mg carpholite (unités LPU et LPM)

L'étude d'inclusions fluides dans les roches de haute pression le long de trois transects majeurs des Alpes occidentales montre que la composition des fluides dans les méta-sédiment de faciès schiste bleu (veines à lawsonite B, à lawsonite C, à Fe-Mg carpholite) est caractéristique et similaire à celle déjà décrite le long du transect Queyras-Monviso (Herviou et al., 2021, **chapitre II**) : les valeurs de salinité sont faibles à intermédiaires et les bulles des inclusions contiennent des mélanges de CO_2 et de CH_4 (Fig. VI.5a, b, d, e, g, h, j, k ; Fig. VI.6a-f ; Table VI.2, VI.3). Ces salinités faibles souvent proches ou inférieures à celle de l'eau de mer sont classiquement observées dans les sédiments des prismes d'accrétion et sont souvent interprétées comme reflétant un mélange entre l'eau de mer piégée initialement dans les pores et des fluides de salinité faible libérés par les réactions de déshydratation prograde (Brantley et al., 1997 ; Smith et Yardley, 1999 ; Yardley et Graham, 2002 ; Sadofsky et Bebout, 2004 ; Rossetti et al., 2006 ; Raimbourg et al., 2014, 2015, 2018). Le CH_4 est l'espèce gazeuse dominante dans les méta-sédiments de basse température des prismes d'accrétion (Raimbourg et al., 2014, 2015, 2018 ; Vrolijk, 1987 ; Vrolijk et al., 1988 ; Sadofsky et Bebout, 2004) tandis que le contenu en CO_2 à tendance à augmenter au-dessus de 270°C et à devenir dominant par rapport au CH_4 en-dessous de la transition cassant-ductile (Raimbourg et al., 2018). Des fluides faiblement salés à CH_4 ont d'ailleurs été identifiés dans les flysch à Helminthoïdes (Raimbourg et al., 2018), sédiments non subduits analogues aux Schistes Lustrés. Ces informations mises en parallèle avec nos données semblent indiquer que nos veines se sont principalement formées par une alimentation locale de fluide comme souligné dans le **chapitre II** (Herviou et al., 2021).

Cependant, certains de nos affleurements, plus rares, ont des salinités plus fortes proches de 10 wt.% eq. NaCl ou même supérieures, et se situent soit à l'Ouest des unités supérieures (SS1, SS4, CA1, QM2, QM5 ; Table VI.2) soit dans l'unité médiane du transect Savoy-Susa (SS9 principalement). D'autres échantillons des unités médianes du transect Savoy-Susa ont également des salinités significativement plus importantes que celles (généralement inférieures à l'eau de mer) de ces unités

(SS5, SS6, SS7 ; Table VI.2). Puisque les échantillons de roches méta-mafiques (veines à jadéite, veines et brèches à omphacite) ont des salinités plus fortes que celles des méta-sédiments encaissants (Fig. VI.5g, h, i, j, k, l ; Table VI.2, VI.3), une infiltration de fluides provenant de ces méta-gabbros dans les sédiments pourrait augmenter localement la salinité des inclusions fluides des sédiments. Cependant, l'assemblage de faciès schiste bleu dans les roches mafiques (lawsonite ou zoïsite + glaucophane + jadéite) reste très hydraté, limitant la quantité de fluides libérés dans ces conditions. De plus, la plupart des affleurements méta-sédimentaires à salinités fortes sont situés loin (plusieurs kilomètres) de roches mafiques (Fig. VI.1b), ce qui exclut cette hypothèse. Ces échantillons sont par contre tous proches soit (i) des unités de marge du Piémontais riches en dépôts triasiques contenant des évaporites (voir Herviou et al., 2021 pour plus de détail ; Fig. VI.1b) soit (ii) à proximité directe (de 100 m à 2 km) de la Nappe des Gypses, une unité d'évaporites pincée entre domaines Liguro-piémontais et Briançonnais (Barré et al., 2020) et particulièrement présente sur le transect Savoy-Susa (Fig. VI.1b). Dans cette nappe, l'étude des inclusions fluides dans le quartz, la fluorite et l'anhydrite a permis de montrer la présence de saumures ayant une salinité proche de 25 wt.% eq. NaCl (Barré et al., 2017). Les veines de nos affleurements ont donc vraisemblablement été alimentées, au moins en partie, par des saumures provenant de ces évaporites. Comme la plupart de ces veines se sont formées lors de la phase de déformation D1 aux (ou proche des) conditions du pic P-T, ce résultat à un impact paléogéographique important : les écailles Liguro-piémontaises concernées étaient nécessairement proches de la marge continentale lors de leur enfouissement. La nature proximale de l'unité supérieure des Calcschistes (QM2, QM5), de l'unité océanique supérieure de Savoy (SS1), de l'unité du Vin Vert (SS5) et de l'unité médiane de Savoy (SS6, SS7, SS9) fut d'ailleurs précédemment suggérée à travers l'étude de leur lithostratigraphie singulière limitée au Crétacé supérieur ou bien avec un Crétacé supérieur très développé (Herviou et al., 2022, **chapitre III**). De plus, pour la Nappe des Gypses, l'estimation des conditions P-T du pic d'enfouissement sont très proches de celles des unités Liguro-Piémontaises, ce qui amena Barré et al. (2020) à suggérer une structuration pré-subduction entre ces unités. Cette affinité précoce entre unités Liguro-Piémontaise et Nappe des Gypses est donc confirmée dans notre étude.

La plus forte dispersion des salinités dans les veines à lawsonite B (sd = 5.9) que dans les veines à lawsonite C (sd = 4.5) pourrait s'expliquer par les différences de mécanismes d'ouverture entre ces deux objets (**chapitre IV**). En effet, les veines à lawsonite B se sont formées par de plus nombreux incréments d'ouverture que les fentes de tension à lawsonite C. Avec leur ouverture plus étalée dans

le temps et dans l'espace, les veines à lawsonite B seraient plus propices à enregistrer une variation spatiotemporelle de compositions des fluides.

Méta-pélites à grenat-chloritoïde (unités LPL)

Dans les méta-pélites à grenat-chloritoïde des unités inférieures de faciès éclogite, des mélanges gazeux à CO_2-CH_4 (Fig. VI.6a, b, f ; Table VI.2, VI.3) ont également été identifiés. Comme pour les veines à lawsonite et à Fe-Mg carpholite, le CO_2 et le CH_4 ont largement pu être produits par interactions locales entre le fluide et les sédiments. Par contre, les salinités estimées dans les inclusions fluides (médiane = 11.0 wt.% eq. NaCl) sont significativement supérieures aux valeurs de l'eau de mer du Crétacé inférieur (~ 3.2-3.7 wt.% ; Hay et al., 2006) et à celles des veines des méta-sédiments des unités LPU et LPM de faciès schiste bleu (Fig. VI.5a-l ; Table VI.2, VI.3). A notre connaissance cette étude est la première à apporter des données de compositions d'inclusions fluides dans des méta-sédiments océaniques de faciès éclogite, les points de comparaison manquent donc pour déterminer avec certitude la source de ces fluides. Ces fortes salinités peuvent résulter soit de l'infiltration de fluides externes plus salés, soit de processus locaux permettant une concentration en sel du fluide. Dans ces conditions éclogitiques, les réactions de déshydratation formant notamment le grenat devraient plutôt diluer le fluide local. Cependant, la déstabilisation de la chlorite (et potentiellement de la lawsonite), susceptible de contenir des quantités non négligeables de chlore (en moyenne 400 µg/g de Cl dans les chlorites des unités supérieures et médianes, transect des Alpes Cottiennes, Barnes et al., 2019), pourrait contribuer à augmenter la salinité du fluide libéré.

D'autre part, la contribution de fluide salé provenant des roches mafiques (et/ou ultramafiques) est clairement plausible. En effet, dans les unités Liguro-Piémontaises inférieures, la proportion de roches mafiques et ultramafiques est beaucoup plus importante que dans les unités supérieures et médianes (>40 % de roches mafiques-ultramafiques dans les unités LPL contre <10% dans les unités LPU et LPM ; Herviou et al., 2022, **chapitre III**) et tous les échantillons étudiés sont situés proches d'affleurements de roches mafiques (de quelques centaines de mètres à 1.8 km ; Fig. VI.1b). Dans les unités de faciès schiste bleu, la salinité des inclusions fluides est bien supérieure dans les échantillons de méta-gabbros (moyenne-médiane : 16.4-28.4 wt.% eq. NaCl) que dans les méta-sédiments (moyenne-médiane : 5.1-3.8 wt.% eq. NaCl), et la salinité des méta-gabbros éclogitiques reste forte (moyenne-médiane : 17.5-16.6 wt.% eq. NaCl). Les salinités intermédiaires des méta-pélites à grenat (moyenne-médiane : 13.1-11.0 wt.% eq. NaCl) pourraient donc refléter un mélange de fluides à salinité faible produits dans les sédiments par les réactions de déshydratation formant le

grenat, et de fluides à salinité forte libérés par les roches mafiques et/ou ultramafiques. Comme mentionné plus haut, à des conditions P-T proches de celles du pic d'enfouissement des unités inférieures (500-580°C 2.2-2.8 GPa ; Herviou et al., 2022, **chapitre III**), les réactions de formation du grenat dans les gabbros intermédiaires ont provoqué la déstabilisation progressive de la lawsonite, de la chlorite et du glaucophane et de déstabilisation du glaucophane (Locatelli et al., 2019b), des minéraux riches en chlore (Debret et al., 2016), libérant des fluides relativement salés dans les veines d'omphacite V1 (moyenne-médiane : 14.6-13.7 wt.% eq. NaCl ; Herviou et al., 2021). Enfin, dans les roches ultramafiques, la réaction de déstabilisation de la brucite, autour de 500°C pourrait contribuer à l'augmentation des salinités en libérant le chlore contenu dans les réactifs (brucite et antigorite ; Scambelluri et al., 1997).

Cette hypothèse d'infiltration de fluides provenant des roches mafiques et/ou ultramafiques est en accord avec les concentrations et signatures isotopiques du chlore obtenues par Barnes et al. (2019) dans les méta-sédiments le long du transect des Alpes Cottiennes. Dans cette étude, les sédiments des unités inférieures présentent les concentrations moyennes en chlore les plus élevées (9-13 µg/g) et sont parmi les seuls à avoir des valeurs positives de $\delta^{37}Cl$ (jusqu'à 0.9 ; Barnes et al., 2019). Ces valeurs de $\delta^{37}Cl$ sont comparables à celles de la croûte océanique hydrothermalisée (Barnes et Cisneros, 2012) et à celles de fragments de serpentinite et de croûte océanique hydrothermalisée métamorphisés à haute pression dans le domaine Liguro-Piémontais (Selverstone et Sharp, 2013) alors que les sédiments et méta-sédiments océaniques ont généralement des valeurs négatives de $\delta^{37}Cl$ (Barnes et al., 2008, 2009 ; Selverstone et Sharp, 2013, 2015). Une infiltration de fluides provenant des roches mafiques et/ou ultramafiques pourrait donc expliquer les concentrations et valeurs isotopiques du chlore obtenues par Barnes et al. (2019) dans les méta-sédiments des unités inférieures. Comme le chlore est un élément généralement mobile dans le fluide dont il contrôle directement la salinité, les salinités fortes estimées dans ces sédiments pourraient donc s'expliquer par une contribution de roches mafiques ou ultramafiques.

Pour finir, des micas blancs ont été détectés dans 26/88 inclusions dans ces échantillons. La cristallisation de ces minéraux hydroxylés lors de la décompression pourrait avoir impacté la composition du fluide et provoqué une augmentation des salinités (Frezzotti et Ferrando, 2015).

Talcschistes à dolomite (contacts tectoniques entre unités LPU et LPM)

Sur différents critères géochimiques et pétrologiques nous avons déjà montré (**chapitre V**) que ces échantillons s'étaient formés par infiltration de fluides des méta-sédiments dans des serpentinites au

pic de pression-température des unités Liguro-Piémontaises. Les salinités relativement faibles ainsi que la présence de CO_2 et de CH_4 dans des proportions similaires aux veines des méta-sédiments (Fig. VI.7b, c, f ; Table VI.2, VI.3) va effectivement dans ce sens. Les fluides globalement plus salés que l'eau de mer dans les échantillons de talcschistes à dolomite des unités médianes pourraient montrer une contribution des fluides locaux des serpentinites, à priori plus salés (Scambelluri et al., 1997 ; Sharp et Barnes, 2004) se mélangeant aux fluides externes provenant des méta-sédiments. En effet, les minéraux des serpentinites Liguro-Piémontaises ont des concentrations fortes en chlore et un partitionnement du chlore dans la phase fluide (e.g., Scambelluri et al., 1997 ; Kendrick et al., 2011) lors du remplacement de l'assemblage de la serpentinite par celui des talcschistes pourrait augmenter les salinités des fluides provenant des sédiments.

VI.6.2. Evolution progressive de la composition des fluides dans les méta-sédiments avec l'augmentation du grade

Evolution des salinités avec le grade

Dans les méta-sédiments le long des trois transects d'étude, les salinités sont plus faibles dans les unités médianes que dans les unités supérieures (Fig. VI.5a-l ; VI.6a-c ; VI.9a). Malgré une certaine dispersion liée aux hétérogénéités lithologiques entre affleurements (contenu en Cl différents selon la distance avec les fronts d'altération hydrothermale ?), et à l'infiltration de fluides provenant d'évaporites des unités de marge du Piémontais et de la Nappe des Gypses dans certains affleurements, une décroissance générale des salinités avec l'augmentation du grade métamorphique est observable dans les méta-sédiments des unités supérieures et médianes (Fig. VI.6a-c ; VI.9a) : tous les transects LPU (5.3 wt.% ; 3.5 wt.% ; 5.1 ; n = 830) ; tous les transects LPM (4.6 wt.% ; 2.4 wt.% ; 6.2 ; n = 373). Nous interprétons cette tendance par une contribution plus importante de fluides libérés par les réactions métamorphiques de déshydratation en profondeur, diluant les salinités des fluides de pores initiaux. La seule réaction majeure de déshydratation prédite dans les méta-sédiments Liguro-piémontais à ces profondeurs est le remplacement progressif de la Fe-Mg carpholite par le chloritoïde (Herviou et al., 2022, **chapitre III**). Comme signalé précédemment, l'augmentation des salinités des unités médianes à inférieures ne serait par contre pas liée à un changement de composition de fluides lié au grade métamorphique mais plutôt à un contraste lithostratigraphique avec la présence de volumes de roches mafiques et ultramafiques bien plus

importants dans les unités inférieures. Ces roches seraient susceptibles d'avoir libérés des fluides salés infiltrant les sédiments lors de leur déshydratation en subduction.

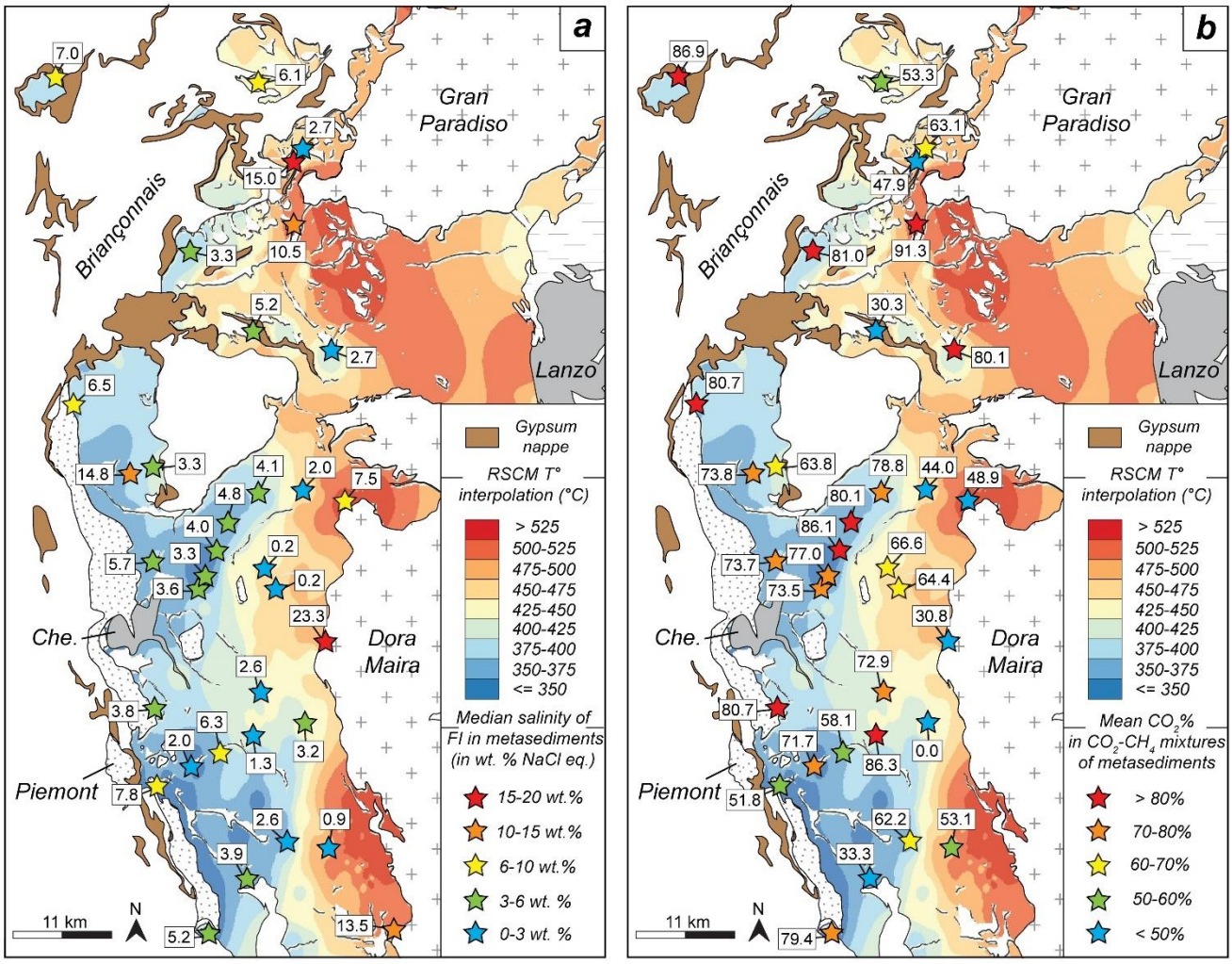

Figure VI.9 *: Evolution de la composition des inclusions fluides, dans les méta-sédiments, à travers le domaine Liguro-Piémontais et en fonction de la température maximum. A) Evolution de la salinité dans les méta-sédiments en fonction de la température maximum. B) Evolution de la proportion de CO_2 dans les mélanges CO_2-CH_4 des méta-sédiments en fonction de la température maximum. RSCM T° = Raman Spectra of Carbonaceous Material Temperature. L'interpolation de température provient de Herviou et al. (2022, chapitre III).*

Evolution des contenus en gaz avec le grade

De fortes variations du ratio CO_2/CH_4 sont observées dans les sédiments (Fig. VI.7a-f ; VI.8a-c ; VI.9b). Bien que le CO_2 ait tendance à être dominant dans les mélanges gazeux, aucune tendance systématique n'a pu être observée entre les différents types d'échantillons (Fig. VI.7a-f ; VI.8a). Des variations du ratio entre ces deux gaz pourraient s'expliquer par des interactions plus ou moins

marquées entre le fluide et les bancs carbonatés d'une part, et avec les zones plus pélitiques riches en matière organique d'autre part. Des variations de réactivité de la matière organique et de son équilibration avec le fluide pourraient être à l'origine de l'hétérogénéité des rapport CO_2-CH_4 le long du domaine Liguro-Piémontais (Fig. VI.9b). Le CO_2 peut également se former par oxydation du CH_4 et les variations de ce ratio pourraient également révéler des variations locales des conditions d'oxydo-réduction (Tarantola et al., 2007, 2009). La potentielle tendance de diminution des proportions de CO_2 avec l'augmentation du grade métamorphique (Fig. VI.8b, c ; VI.9b) reste à explorer.

Chapitre VII – Synthèse des données et discussion générale

Cristaux de lawsonite dans des méta-basites. Laghi del Beth.

VII. Synthèse des données et discussion générale

Dans ce chapitre, je présente une synthèse des résultats obtenus dans les différents volets de cette thèse et reprends les principaux points de discussion des différents chapitres pour tenter d'apporter un modèle conceptuel de circulation des fluides et de déformation dans les zones de subduction. Un schéma bilan imageant les différents points de discussion est présenté sur la dernière page de ce chapitre (Fig. VII.4).

VII.1. Révision du cadre tectonométamorphique Liguro-Piémontais

Dans le but d'étudier les processus de subduction le long du domaine Liguro-Piémontais des Alpes occidentales, une révision du contexte tectonométamorphique était nécessaire. A travers la compilation des données pétrologiques de la littérature et l'acquisition de nouvelles données de température Raman sur matière carbonée et de leur interpolation en carte, de données de Si dans les phengites et de modélisation thermodynamique, cette étude présentée dans le **chapitre III** a permis d'obtenir un cadre détaillé des conditions du pic métamorphique à travers le domaine. Une augmentation générale du grade métamorphique vers l'Est à travers le domaine et à l'intérieur de chaque écaille a donc pu être imagé grâce à cette cartographie haute résolution des conditions du pic métamorphique. La compilation des données lithostratigraphiques, structurales et radiochronologiques de chaque écaille du domaine a quant à elle permis de déterminer la position initiale de ces unités dans le domaine océanique. Tous ces résultats permettent de mettre en évidence la présence d'une distribution trimodale d'unités avec une augmentation des conditions métamorphiques des unités Liguro-Piémontaises supérieures (LPU ; 320-400°C- 1.2-1.9 GPa), aux unités médianes (LPM ; 415-475°C- 1.7-2.2 GPa) et aux unités inférieures (LPL ; 500-580°C- 2.2-2.8 GPa ; Fig. VII.1a, b). Les unités supérieures et médianes, métamorphisées dans le faciès schiste bleu sont dominées par les sédiments (>90%) et sont séparées des unités inférieures de faciès éclogite, bien plus riches en roches mafiques et ultramafiques (>40% ; Fig. VII.1a), par un contact extensif majeur (Philippot, 1990 ; Ballèvre et al., 1990 ; Ballèvre et Merle, 1993).

Dans les unités supérieures et médianes, certaines écailles ont des successions lithostratigraphiques singulièrement différentes (Herviou et al., 2022, **chapitre III** ; Fig. VII.1c). Tandis que certaines, dites de Chabrière (Lemoine et al., 1970 ; Tricart, 1974 ; Lemoine, 2003), sont caractérisées par une série Liguro-Piémontaise complète (ou presque) s'étalant du Jurassique supérieur au Crétacé supérieur,

d'autres sont quasiment limitées à des calcschistes d'âge Crétacé supérieur. Alors que dans les séries de type Chabrière les fragments de socle océanique démembré sont courants, les séries limitées au Crétacé supérieur sont presque entièrement dénuées de roches mafiques et ultramafiques. L'absence de dépôts d'âge Jurassique et Crétacé inférieur ainsi que d'un socle océanique dans ces dernières pourrait indiquer une origine plus proximale et/ou refléter des différences de niveaux de décollement entre ces unités et celles de type Chabrière (Fig. VII.1c). Cette différence paléogéographique entre certaines unités, déjà soulevée par Lagabrielle (1987) et Deville et al. (1992) est également suggérée par l'âge du pic P-T à 42-40 Ma obtenu par Lanari (2012) pour l'unité des Calcschistes du transect du Queyras (Ar-Ar sur phengites), soit significativement plus jeune que les âges métamorphiques disponibles dans les autres unités supérieures (~61-55 Ma ; Agard et al., 2002 ; Ar-Ar sur phengites ; Fig. VII.1d).

Toutes les données lithostratigraphiques des unités inférieures indiquent qu'elles contiennent une série de type Chabrière incomplète, sans Crétacé supérieur et donc limitée à des dépôts d'âge Jurassique et Crétacé inférieur (Fig. VII.1c). Des différences paléogéographiques, des variations de bathymétrie ou bien une perte de certaines formations lors des processus d'écaillage et d'exhumation pourraient expliquer ce contraste avec les unités supérieures et médianes. Dans les unités inférieures, une subdivision entre des unités dominées par les roches mafiques et ultramafiques (~60% ; unités MUM de Agard, 2021) et des unités dominées par les sédiments (~60% ; unités S de Agard, 2021) peut être faite, les unités S pouvant correspondre à la couverture initiale des unités MUM (Agard, 2021). En effet, certaines de ces unités inférieures, (unité inférieure de Savoie, Orsiera-Rocciavrè) contiennent d'importantes quantités de sédiments emballant des roches mafiques et ultramafiques dans leur partie ouest et sont presque entièrement dépourvues de sédiments dans leur partie Est (Fig. VII.1a). Cette répartition de roches pourrait être expliquée par le pendage général vers l'Ouest des écailles (avec le socle océanique à la base de l'écaille), ou par la présence de contacts tectoniques juxtaposant les unités inférieures dominés par les sédiments au-dessus de celles où les roches mafiques et ultramafiques sont dominantes. Cette deuxième hypothèse est notamment supportée par l'âge du pic à 46 Ma obtenu pour les méta-gabbros de Rocciavrè (Angiboust et Glodny, 2020 ; Rb-Sr sur phengites), similaires à ceux des unités inférieures de type MUM (généralement entre 40 et 50 Ma, e.g., Rubatto et Hermann, 2003 ; Dragovic et al., 2020 ; Garber et al., 2020a ; méthodes multiples) et sensiblement plus jeunes que ceux obtenus pour les sédiments du massif d'Orsiera, affleurant juste à l'Ouest (61-53 Ma ; Agard et al., 2002, Ar-Ar sur phengites).

La formation d'un complexe d'accrétion profond suggère généralement que les écailles inférieures ont été enfouies, détachées et sous-plaquées en dernier (Bachmann et al., 2009 ; Dumitru et al., 2010 ; Angiboust et al., 2022). La compilation des âges de subduction disponibles pour les différentes écailles suggère une séquence d'écaillages successifs des unités supérieures de type Chabrière, des unités médianes de type Chabrière, des unités inférieures de type S et des Unités inférieures de type MUM, entre ~60 et 45 Ma, suivi d'un empilement de ces unités autour de 38-35 Ma (Fig. VII.1d, e). Les unités supérieures et médianes contenant uniquement des dépôts d'âge Crétacé supérieur correspondraient quant à elles à des fragments proximaux potentiellement déposés sur un socle continental et directement empilés au-dessus des unités supérieures de type Chabrière, comme le suggère l'empilement actuel et les âges de subduction plus jeunes (Fig. VII.1d, e). Malgré ces interprétations, les données radiochronologiques disponibles pour les âges du pic d'enfouissement des unités de faciès schiste bleu sont très réduites et quasiment limitées aux Alpes Cottiennes (e.g., Agard et al., 2002). Une analyse géochronologique fine des âges de subduction dans les différentes écailles du domaine reste indispensable pour confirmer et affiner ce scénario d'écaillage et d'empilement.

Figure VII.1 *(page suivante) : Contexte tectonométamorphique révisé du domaine Liguro-Piémontais des Alpes occidentales. A) Schéma structural montrant la distribution des trois principaux types d'unités Liguro-Piémontaises. B) Conditions pression-température moyennes des différentes unités Liguro-Piémontaises. C) Portions de colonne lithostratigraphique Liguro-Piémontaise complète (Chabrière) retrouvées dans les différentes unités. D) Ages de subduction des différentes écailles Liguro-Piémontaises. E) Séquence d'écaillage et d'empilement suggérée pour les différentes unités Liguro-Piémontaises. Abréviations : LPU = Liguro-Piemont Upper units ; LPM = Liguro-Piemont Middle units ; LPL = Liguro-Piemont Lower units ; AG = Aigle ; ALB = Albergian ; ATF = Avise-Tsaboc-Feluma ; AV = Avic ; BY = By unit ; CC = Cerogne-Ciantiplagna ; CH = Chardonnet klippe ; CO = Cornet ; CS = Calcschist unit ; GU = Grivola-Urtier ; GS = Grande-Sassière klippe ; GV = Grand Vallon klippe ; JO = Jovet klippe ; LA = Lamet klippe ; LN = Lago Nero ; LS = Lago Superiore ; MB = Mirabouc-Bouchet; MV = Monviso unit ; OR = Orsiera-Rocciavrè ; PT = Pelvas-Taillante ; PY = Puys ; SLU = Savoy Lower Unit ; SMU = Savoy Middle Unit ; SN-L = Lower Sana klippe ; SN-U = Upper Sana klippe ; VN = Venaus ; VV = Vin Vert ; W-SS = West-Sesia unit ; ZS = Zermatt-Saas. Figures modifiées d'après Herviou et al. (2022, chapitre III).*

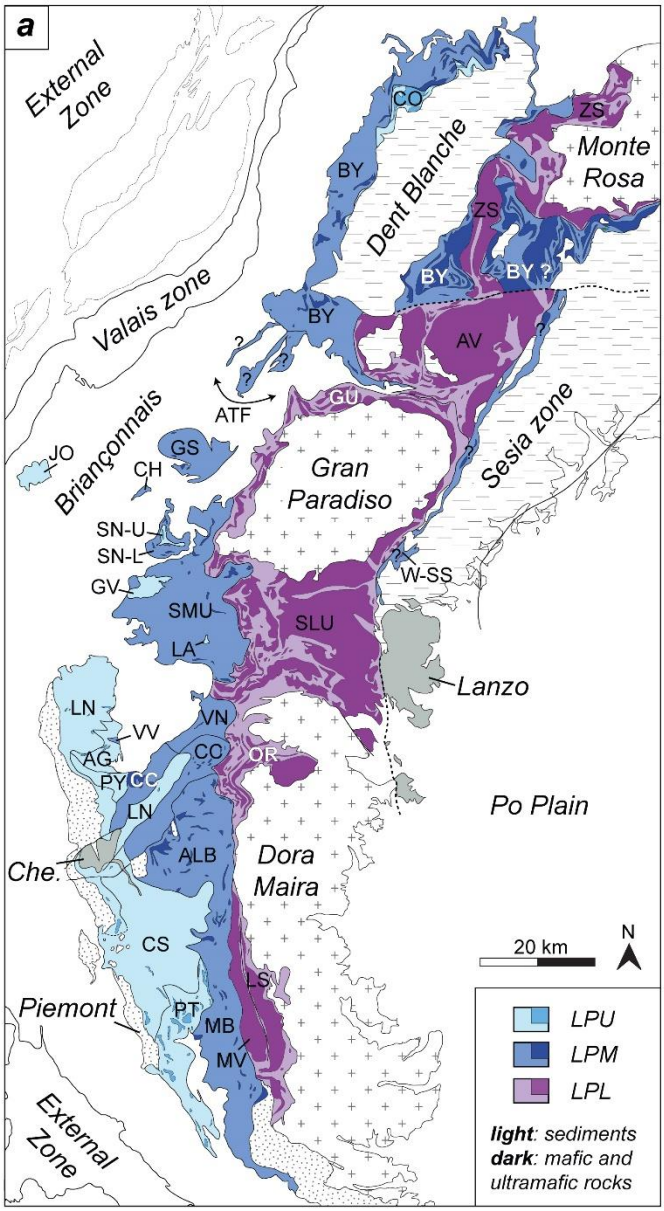
a
External Zone
Valais zone
Briançonnais
Dent Blanche
Monte Rosa
Gran Paradiso
Sesia zone
Lanzo
Po Plain
Dora Maira
Che.
Piemont
External Zone
CO
ZS
BY
BY ?
AV
GU
ATF
JO
GS
CH
SN-U
SN-L
GV
W-SS
SMU
SLU
LA
LN
VV
VN
AG
CC
OR
PY
ALB
CS
LS
PT
MB
MV
20 km
N
LPU
LPM
LPL
light: sediments
dark: mafic and ultramafic rocks

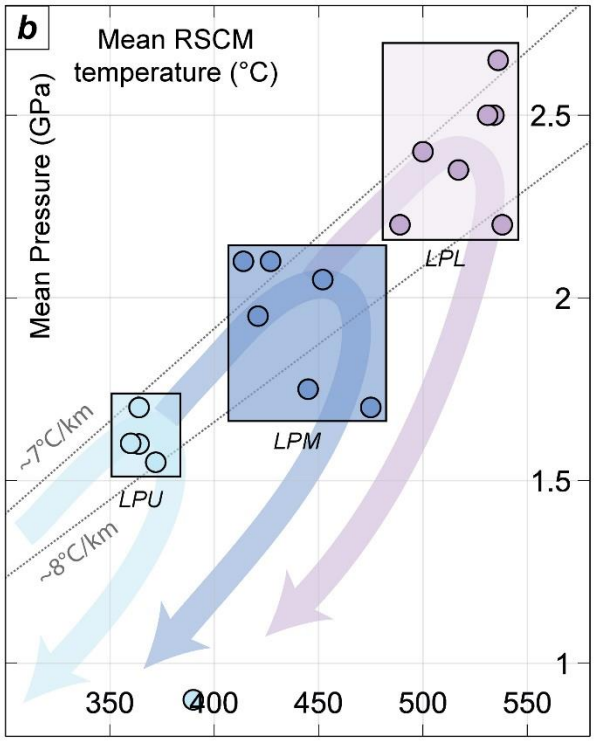
b
Mean RSCM temperature (°C)
Mean Pressure (GPa)
2.5
2
1.5
1
350
400
450
500
550
LPL
LPM
LPU
~7°C/km
~8°C/km

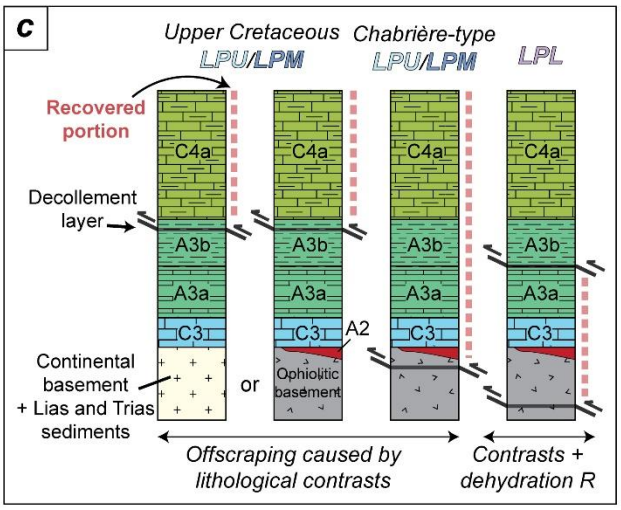
c
Upper Cretaceous
LPU/LPM
Chabrière-type
LPU/LPM
LPL
Recovered portion
Decollement layer
C4a
A3b
A3a
C3
A2
Continental basement + Lias and Trias sediments
or
Ophiolitic basement
Offscraping caused by lithological contrasts
Contrasts + dehydration R

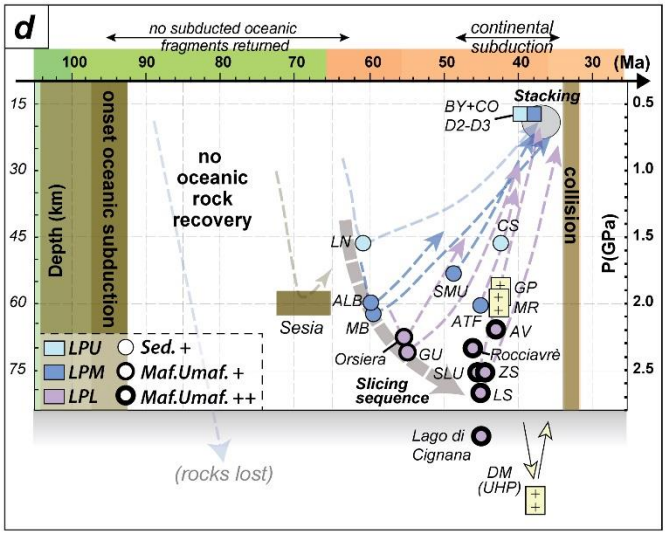
d
no subducted oceanic fragments returned
continental subduction
100
90
80
70
60
50
40
30
(Ma)
onset oceanic subduction
collision
Depth (km)
P(GPa)
no oceanic rock recovery
Stacking
BY+CO
D2-D3
LN
CS
ALB
SMU
GP
MR
ATF
AV
Sesia
MB
Orsiera
GU
Rocciavrè
SLU
ZS
LS
Slicing sequence
Lago di Cignana
DM (UHP)
(rocks lost)
LPU
LPM
LPL
Sed. +
Maf.Umaf. +
Maf.Umaf. ++

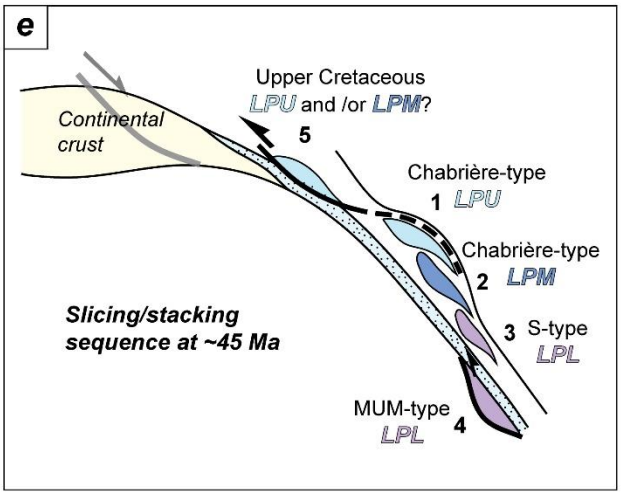
e
Continental crust
Upper Cretaceous
LPU and /or LPM?
5
Chabrière-type
1 LPU
Chabrière-type
2 LPM
3 S-type
LPL
MUM-type
4
LPL
Slicing/stacking sequence at ~45 Ma

Quelques inconnues ou incertitudes demeurent dans la distribution générale des unités au sein de ce modèle trimodal comme : (i) l'extension des unités supérieures le long du transect Valais-Aosta et l'identification de leur présence ou absence à l'Est de la Dent Blanche, (ii) le passage des unités supérieures à médianes autour de la bande d'Acceglio, (iii) l'identification précise des conditions du pic d'enfouissement dans les unités West-Sesia, Avise-Tsaboc-Feluma, Puys et Aigle afin de les relier avec certitude à ce modèle.

VII.2. Circulation de fluides durant la subduction du domaine Liguro-Piémontais

VII.2.1. Veines de haute pression dans le domaine Liguro-Piémontais

Un long travail de traque systématique sur le terrain des veines contenant des assemblages minéralogiques de haute pression, dans le domaine Liguro-Piémontais, a été réalisé durant cette thèse (Fig. VII.1a). Ces veines sont les marqueurs directs de la circulation de fluides et des interactions fluides-roches qui ont eu lieu lors de la subduction Alpine. Dans le domaine Liguro-Piémontais des Alpes occidentales, les méta-sédiments sont dominants par rapport aux roches mafiques et ultramafiques (~70% ; Herviou et al., 2022, **chapitre III**) et affleurent de façon continue entre les différentes écailles à travers le domaine (Fig. VII.1a). Dans les sédiments, les veines métamorphiques sont ubiquistes, et bien plus nombreuses que dans les roches mafiques et ultramafiques de ces mêmes unités. Des veines contenant des assemblages attestant de leur formation à haute pression ont été décrites (veines à lawsonite, Fe-Mg carpholite ; Goffé et Chopin, 1986 ; Agard et al., 2000 ; Lefeuvre et al., 2020), mais seulement sur quelques affleurements restreints aux unités supérieures et principalement dans les Alpes Cottiennes. Une attention particulière a donc été apportée à la recherche de veines de haute pression dans les sédiments le long de plusieurs transects, afin d'étendre les observations disponibles dans la littérature.

Sur le terrain, de nombreuses veines ont été observées dans les méta-sédiments de faciès schiste bleu des unités supérieures et médianes (entre 12 et 32% de veines dans des affleurements ciblés, **chapitre IV**). Parmi les veines de haute pression, les veines à lawsonite, sont de loin les plus abondantes que j'ai pu observer dans les Schistes Lustrés (Fig. VII.2a). Dans ces veines, la lawsonite est présente sous forme de fibres de couleur crème associées au quartz et à l'ankérite dans de grandes veines généralement pluri-décimétriques (veines à lawsonite B de Lefeuvre et al., 2020) et dans des fentes de tension, parfois en échelon, de taille centimétrique (veines à lawsonite C de

Lefeuvre et al., 2020 ; Fig. VII.2a-c). Dans les calcschistes entourant ces veines, la lawsonite est généralement présente sous forme de cristaux prismatiques noirs remplis de matériel carboné (lawsonite A de Lefeuvre et al., 2020).

L'abondance de la lawsonite dans les veines et roches hôtes semble largement contrôlée par la lithologie : elles sont généralement bien plus présentes dans des calcschistes qui contiennent des proportions comparables de méta-pélites et de bancs de carbonates en alternances fines, plutôt que dans des méta-pélites ou marbres purs. Les veines de lawsonite B sont souvent plissées par des déformations précoces (plis D1 de Agard et al., 2001a) suggérant leur formation à des conditions proches du pic d'enfouissement (**chapitre IV**). Alors que les fentes de tension à lawsonite C, contenant des fibres perpendiculaires au épontes (Fig. VII.2c), montrent un mécanisme d'ouverture classique par extension en mode I, le mode de formation des veines à lawsonite B était plus énigmatique (**chapitre IV**). Ces veines contiennent de longues fibres parallèles aux épontes supérieures et inférieures des veines (Fig. VII.2b) indiquant une ouverture dans la direction d'allongement de ces veines. Au sein d'un même affleurement, les fibres des veines à lawsonite B sont souvent orientées parallèlement à celles des lawsonite C, suggérant une formation compatible, dans un même champ de contraintes. Nous proposons que les veines à lawsonite B se sont formées par une extension locale entre deux plans de cisaillement comme déjà décrit dans des sédiments non métamorphiques à faiblement métamorphisés (Fagereng et al., 2010, 2011 ; Bons et al., 2012 ; Lemonnier et al., 2020). Les fentes de tension à lawsonite C s'ouvrent perpendiculairement à la contrainte compressive la plus forte (σ1). Leur orientation à ~80-90° des lawsonites B implique une orientation inhabituelle des plans de cisaillement bordant les veines à lawsonite B par rapport à σ1, suggérant leur très faible résistance (Fagereng et al., 2010). Dans ces veines, la présence de trails successifs de cristaux de lawsonite dans le quartz, mais aussi de plans d'inclusions fluides perpendiculaires à l'orientation des fibres de lawsonite (bandes d'inclusions de Ramsay, 1980) indiquent leur formation par des mécanismes de crack-seal (Ramsay, 1980 ; Cox, 1987). Ce type de veines est généralement interprété comme représentant l'enregistrement d'incréments successifs de fracturation et de cristallisation sous des pressions de fluide fortes (Ramsay, 1980). L'étude statistique de ces textures permet de proposer un lien avec des glissements lents en subduction.

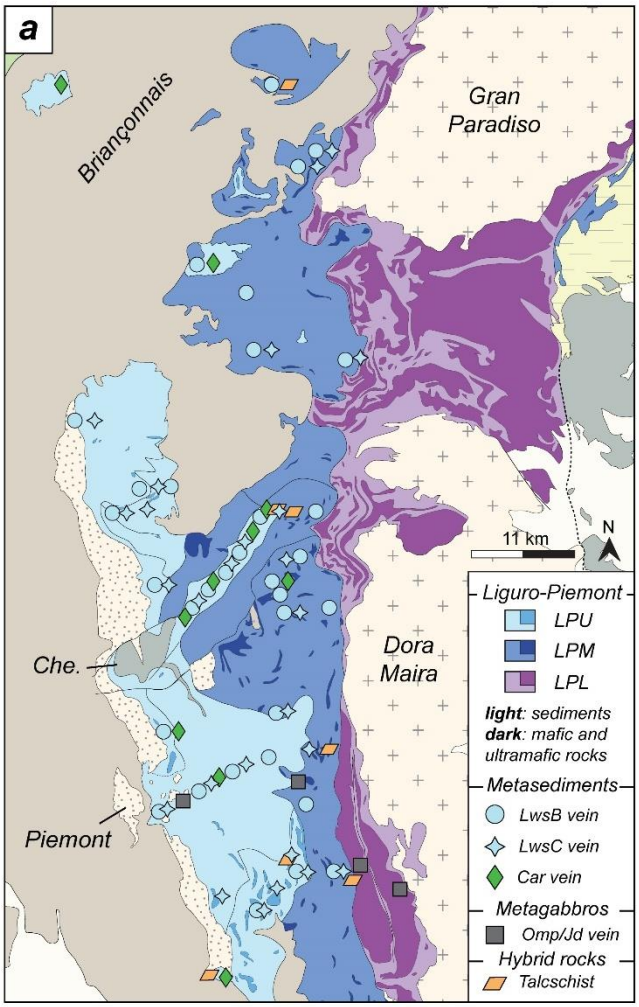
a
Briançonnais
Gran Paradiso
Dora Maira
Che.
Piemont
11 km
N
Liguro-Piemont
LPU
LPM
LPL
light: sediments
dark: mafic and ultramafic rocks
Metasediments
LwsB vein
LwsC vein
Car vein
Metagabbros
Omp/Jd vein
Hybrid rocks
Talcschist

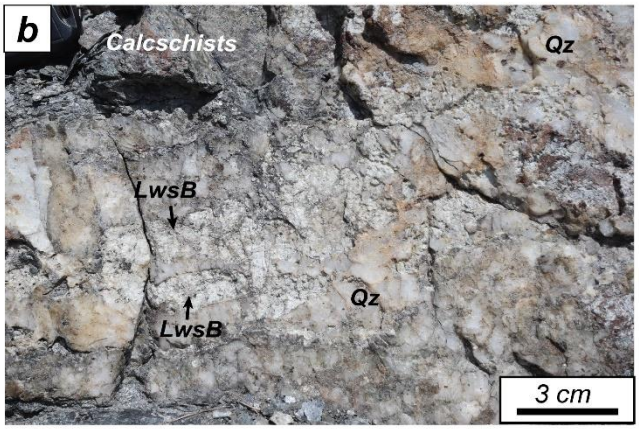
b
Calcschists
Qz
LwsB
LwsB
Qz
3 cm

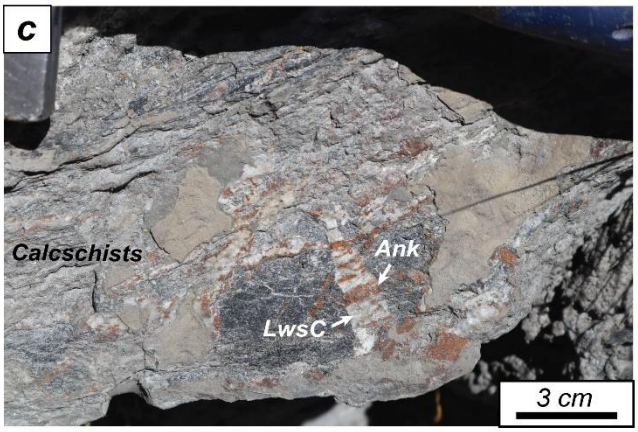
c
Calcschists
Ank
LwsC
3 cm

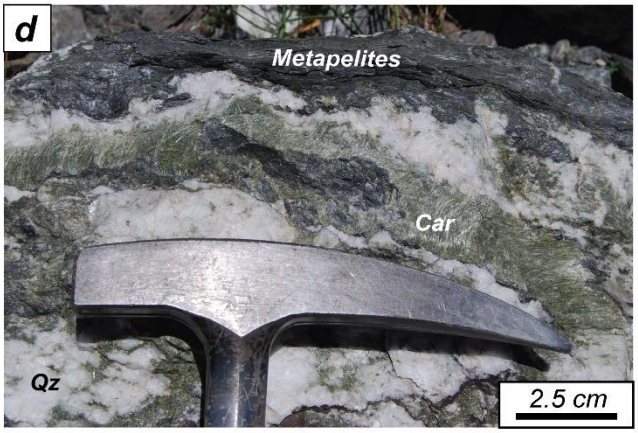
d
Metapelites
Car
Qz
2.5 cm

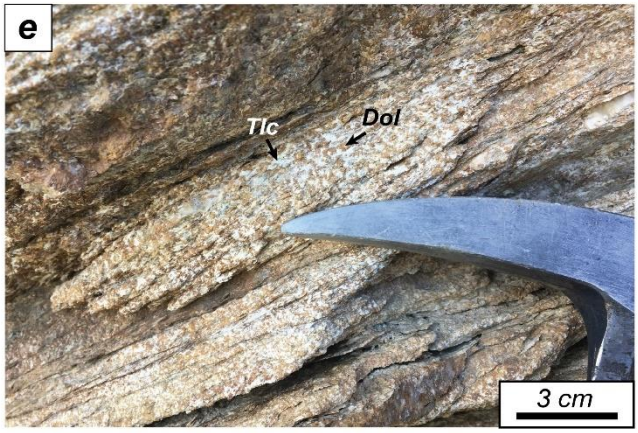
e
Tlc
Dol
3 cm


f
Jd
Blueschist-facies metagebbros
4 cm

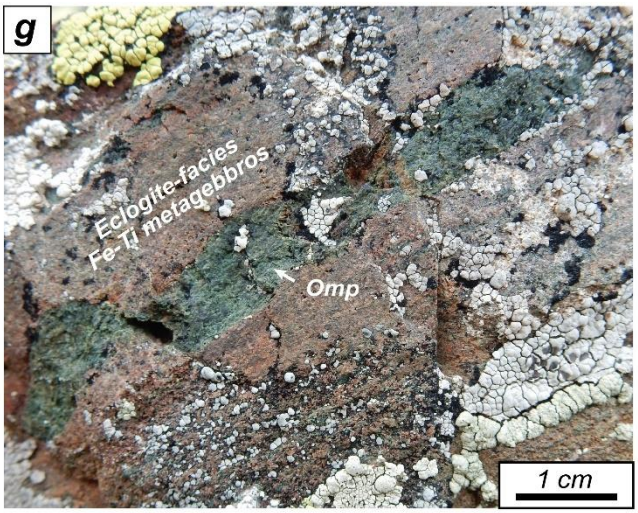
g
Eclogite-facies Fe-Ti metagebbros
Omp
1 cm

Figure VII.2 *(page précédente) : Veines métamorphiques dans le domaine Liguro-Piémontais. A) Distribution des types de veines métamorphiques observées durant cette thèse. B) Veine de lawsonite B, triplex, Alpes Cottiennes. C) Veine de lawsonite C, Aiguilles, Queyras. D) Veine de Fe-Mg carpholite, Plan de paroir, Haute-Ubaye. E) Horizon de talcschistes à dolomite, Crête de l'Eychassier, Queyras. F) Veine de jadéite dans un méta-gabbro de faciès schiste bleu, Ville-Vieille, Queyras. G) Veine d'omphacite dans un gabbro Fe-Ti éclogitique, Lago Superiore, Monviso. Abréviations : LPU = Liguro-Piemont Upper units ; LPM = Liguro-Piemont Middle units ; LPL = Liguro-Piemont Lower units ; Lws = lawsonite ; Qz = quartz ; Ank = ankérite ; Talc = talc ; Dol = dolomite ; Car = Fe-Mg carpholite ; Jd = jadéite ; Omp = omphacite.*

En plus des nombreuses veines à lawsonite, de plus rares veines à Fe-Mg carpholite ont été observées dans les Schistes Lustrés Liguro-Piémontais (Fig. VII.2a, d). Ces veines sont généralement pluri-décimétriques, le plus souvent observées dans des affleurements avec une proportion forte de pélites, et la carpholite est systématiquement accompagnée de quartz. La Fe-Mg carpholite commence à se déstabiliser à l'Est des unités supérieures et est entièrement remplacée par le chloritoïde dans les unités médianes (**chapitre III**, Herviou et al., 2022 ; Agard et al., 2001a). Ainsi, les veines observées dans les unités médianes correspondent à des reliques prograde, où la carpholite très sensible à la rétromorphose est uniquement préservée sous la forme d'aiguilles dans des cristaux de quartz. Dans les unités supérieures où les veines à Fe-Mg carpholite sont plus nombreuses, ces dernières sont généralement plissées par la phase de déformation D1 (plis D1 de Agard et al., 2001a), comme les veines à lawsonite B, suggérant leur formation à des conditions proches du pic d'enfouissement (Agard et al., 2000 ; **chapitre IV**). L'orientation des fibres, qui sont le plus souvent parallèles aux épontes supérieures et inférieures des veines, ainsi que la présence de trails successifs d'inclusions fluides (bandes d'inclusions de Ramsay, 1980) orientés perpendiculairement aux cristaux étirés de carpholite et de quartz, suggèrent des mécanismes de formation par cycles incrémentaux de cisaillement dilatant comme dans les veines de lawsonite B.

A proximité des contacts entre écailles Liguro-Piémontaises ou avec les unités Briançonnaises, des horizons de talcschistes d'épaisseur généralement métrique, très cisaillés, et contenant d'importantes quantités de carbonates ont également été observés dans les sédiments Liguro-Piémontais (Fig. VII.2e). Dans ces roches, le talc et la dolomite sont à l'équilibre textural avec la chlorite, le quartz et le sphène et les âges obtenus par datations U-Pb sur titanite (~ 60-50 Ma) attestent de la formation de ces roches à des conditions proches des pics d'enfouissement des unités supérieures et médianes

(**chapitre V**). Un âge (2e génération de sphènes) similaire à celui de D3 dans les Schistes Lustrés (~38 Ma) montre quant à lui une recristallisation des sphènes lors de l'exhumation.

Les sédiments des unités inférieures contiennent beaucoup moins de veines que les unités supérieures et médianes et aucune veine contenant des minéraux du pic métamorphique n'a été observée dans ces roches.

Afin d'étudier les potentielles infiltrations de fluides entre roches mafiques et méta-sédiments, des veines formées à haute pression ont également été recherchées dans les méta-gabbros Liguro-Piémontais (Fig. VII.2a, f, g), mais s'avèrent bien plus rares que dans les sédiments. Les seuls exemples de veines de haute pression correspondent à des veines à jadéite dans les méta-gabbros des unités inférieures et médianes de faciès schiste bleu, et à des veines à omphacite ± grenat dans ceux des unités inférieures éclogitiques (Fig. VII.2a, f, g ; **chapitres I, VI**). Dans les deux cas, les veines contiennent l'assemblage métamorphique stable aux conditions des pics de P-T de ces roches. Des échantillons de brèches éclogitiques des zones de cisaillement du massif du Monviso, témoins de phases de fracturation et d'infiltration de fluides dans le faciès éclogite, ont également été collectés (**chapitres I, VI**).

VII.2.2. Evolution de la composition des fluides en subduction

L'étude des inclusions fluides dans les veines de haute pression a permis l'acquisition du plus grand set de données d'inclusions fluides dans des roches HP-BT (1585 inclusions, plus de 70 échantillons). Cette étude, principalement présentée dans les **chapitres II et VI**, permet de caractériser la composition des fluides qui circulaient en profondeur lors de la subduction de l'océan Liguro-Piémontais.

Les fluides des veines à lawsonite et à Fe-Mg carpholite des unités supérieures et médianes, de faciès schiste bleu, sont majoritairement aqueux, faiblement salés et contiennent du CO_2 et du CH_4 (Fig. VII.3a-c) indiquant une alimentation des veines par les fluides produits localement par les réactions de déshydratation prograde, et s'équilibrant avec les sédiments hôtes (carbonates et matière organique des niveaux pélitiques). Dans quelques rares affleurements proches des unités de marges (Piémontais, Nappe des Gypses ; Fig. VII.3a), les inclusions fluides plus salées suggèrent une infiltration de fluides provenant des dépôts évaporitiques de ces unités lors de la subduction, ce qui implique une origine proximale des écailles Liguro-Piémontaises concernées. Cette pré-structuration entre unités Liguro-Piémontaises et Nappe des Gypses avait déjà été avancée par Barré et al. (2020) sur la base des conditions P-T similaires de leurs pics d'enfouissement. Malgré une forte

dispersion des valeurs de salinité liée à ces infiltrations de fluides des marges et aux hétérogénéités lithologiques, on observe une décroissance générale des salinités de l'Ouest des unités supérieures jusqu'à l'Est des unités médianes, et donc avec l'augmentation du grade métamorphique (Fig. VII.3a). Cette baisse progressive de la salinité des fluides au cours de l'enfouissement est interprétée comme reflétant la dilution progressive des fluides de pores initiaux par la déstabilisation des minéraux hydratés. La seule réaction majeure de déshydratation dans les Schistes Lustrés prédite à ces profondeurs est la transformation graduelle de la Fe-Mg carpholite en chloritoïde (**chapitre III**) qui est donc suggérée comme responsable de ces changements de salinité en profondeur. De rares inclusions contenant de potentiels hydrocarbures plus lourds que le CH_4 ont également été identifiées dans ces veines.

Dans les méta-sédiments des unités inférieures, en l'absence de veine métamorphique formée au pic P-T, l'étude des inclusions fluides dans les grenats de l'assemblage du pic d'enfouissement a permis de mettre en évidence la présence de fluides aqueux contenant des mélanges de CO_2-CH_4 mais sensiblement plus salés que ceux des veines des unités supérieures et médianes (Fig. VII.3a, b). Ces salinités plus fortes pourraient notamment s'expliquer par une contribution de fluides externes provenant des roches mafiques et ultramafiques particulièrement abondantes dans ces unités (**chapitre VI**).

A travers les méta-sédiments des unités supérieures à inférieures, les variations des proportions de CO_2 dans les mélanges à CO_2-CH_4 ne montrent pas de tendance systématique (Fig. VII.3b) et sont interprétées comme reflétant des interactions et équilibres plus ou moins marqués entre le fluide et les roches (bancs carbonatés et pélites riches en matériel carboné de nature et maturité variable).

Dans les contacts tectoniques, les niveaux à talc-dolomite-chlorite-quartz-titanite contiennent de fortes concentrations en nickel, chrome, cobalt et magnésium, et les rares minéraux reliques hérités d'une paragénèse antérieure (pentlandite, chalcopyrite et platine natif) sont diagnostiques des serpentinites, ce qui montre que le protolithe de ces roches est ultramafique. Les inclusions fluides aqueuses faiblement salées et à CO_2-CH_4 des cristaux de dolomite et de quartz de ces roches, ainsi que les fortes concentrations en éléments généralement mobiles dans le fluide et concentrés dans les sédiments (LILE notamment) suggèrent la transformation des serpentinites initiales par l'infiltration de fluides issus des sédiments lors de l'enfouissement en subduction (**chapitre V**).

Enfin, dans les roches mafiques, les inclusions fluides sont généralement bien plus salées que dans les méta-sédiments (Fig. VII.3c) et semblent héritées d'une phase d'altération hydrothermale des

gabbros à haute température, ayant provoqué la formation de saumures (séparation de phases). Durant la déstabilisation progressive des amphiboles hydrothermales, riches en chlore, en glaucophane (faciès schiste bleu) puis en omphacite (faciès éclogite), le partitionnement préférentiel du chlore dans le fluide, associé au recyclage des saumures piégées dans les inclusions fluides pourrait être à l'origine de ces salinités fortes. Les inclusions fluides des veines et matrices de brèches à clinopyroxène (jadéite ou omphacite) contiennent une grande variété de « daughter minerals », suggérant des systèmes chimiques complexes. Les salinités (sursaturation en NaCl sans cristal de sel exprimé) et températures d'eutectiques confirment des mélanges à NaCl ± KCl ± $CaCl_2$ ± $MgCl_2$. Les faibles quantités de N_2 dans les éclogites semblent héritées de la déstabilisation des minéraux porteurs de NH_4^+ (glaucophane notamment). Pour finir, la présence de rares inclusions de potentiels hydrocarbures dans les veines de jadéite des méta-gabbros de faciès schiste bleu, similaires à celles trouvées dans les veines de lawsonite B et C, suggère l'infiltration de faibles quantités de fluides externes des méta-sédiments encaissants.

Figure VII.3 *(page suivante) : Composition des inclusions fluides dans les roches HP-BT. A) Evolution de la salinité dans les méta-sédiments Liguro-Piémontais en fonction de la température maximum. B) Evolution de la proportion de CO_2 dans les mélanges CO_2-CH_4 des méta-sédiments Liguro-Piémontais en fonction de la température maximum. RSCM T° = Température déterminée par spectroscopie Raman sur matière organique. L'interpolation de température provient de Herviou et al. (2022, chapitre III). C) Compilation des salinités des inclusions fluides dans les roches des subductions océaniques exhumées et comparaison avec nos données du trasnsect Queyras-Monviso. Les données de salinités sont représentées sous la forme de boîtes à moustaches positionnées en fonction des pressions estimées pour le pic d'enfouissement dans les roches encaissantes. Un graphique simplifié montre la salinité moyenne en fonction de la pression du pic d'enfouissement en haut de la figure. Les références des études utilisées sont présentées dans la table 1 du chapitre II.*

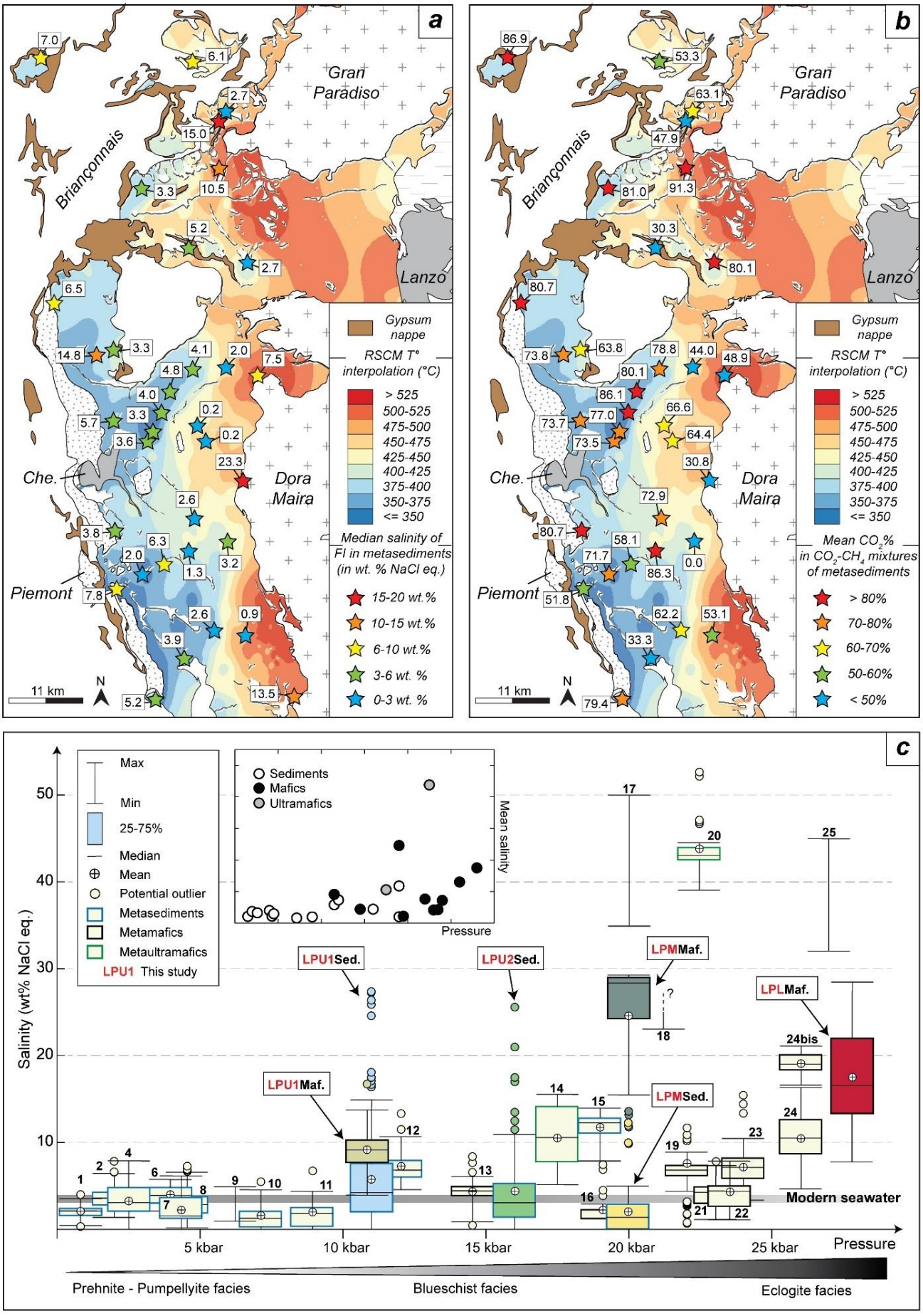
a
b
c
Gran Paradiso
Lanzo
Briançonnais
Che.
Dora Maira
Piemont
Gypsum nappe
RSCM T° interpolation (°C)
> 525
500-525
475-500
450-475
425-450
400-425
375-400
350-375
<= 350
Median salinity of FI in metasediments (in wt. % NaCl eq.)
15-20 wt.%
10-15 wt.%
6-10 wt.%
3-6 wt. %
0-3 wt. %
Mean CO2% in CO2-CH4 mixtures of metasediments
> 80%
70-80%
60-70%
50-60%
< 50%
11 km
N
Max
Min
25-75%
Median
Mean
Potential outlier
Metasediments
Metamafics
Metaultramafics
LPU1 This study
Sediments
Mafics
Ultramafics
Mean salinity
Pressure
Salinity (wt% NaCl eq.)
LPU1Sed.
LPU2Sed.
LPMMaf.
LPLMaf.
LPU1Maf.
LPMSed.
Modern seawater
5 kbar
10 kbar
15 kbar
20 kbar
25 kbar
Pressure
Prehnite - Pumpellyite facies
Blueschist facies
Eclogite facies

Avant ce travail, les données disponibles d'inclusions fluides dans les roches HP-BT exhumées d'anciennes zones de subduction océanique concernaient principalement des sédiments des prismes d'accrétion peu profonds et des roches mafiques et ultramafiques de faciès éclogite. Ces nouvelles données permettent d'apporter des contraintes sur des profondeurs très peu étudiées en subduction (**chapitre II**, Fig. VII.3c). La compilation exhaustive des données des roches exhumées des subductions océaniques (Fig. VII.3c) montre que les méta-sédiments peu profonds jusqu'aux conditions du faciès schiste bleu possèdent des fluides aqueux peu salés contenant de faibles quantités de $CH_4 \pm CO_2$ (Brantley et al., 1997 ; Smith et Yardley, 1999 ; Agard et al., 2000 ; Sadofsky et Bebout, 2004 ; Rossetti et al., 2006 ; Raimbourg et al., 2015, 2018 ; Herviou et al., 2021, **chapitres II, VI**). Une dilution progressive des salinités des fluides de pores par les réactions de déshydratation est observée dans les prismes d'accrétion peu profonds et dans les sédiments de faciès schiste bleu (Sadofsky et Bebout, 2004 ; Raimbourg et al., 2015 ; Herviou et al., 2021, **chapitres II, VI**).

Les roches mafiques de faciès éclogite contiennent généralement des inclusions de saumures moyennement à fortement salées (Philippot et Selverstone, 1991 ; Selverstone et al., 1992 ; Vallis et Scambelluri, 1996 ; Philippot, 1998 ; Yoshida et al., 2015 ; Herviou et al., 2021, **chapitres II, VI**) parfois cogénétiques avec des inclusions gazeuses (N_2-$CO_2 \pm CH_4$; Selverstone et al., 1992), suggérant une potentielle immiscibilité de fluides aux conditions du pic d'enfouissement. Des observations similaires ont été faites dans les éclogites des zones de subduction continentales (Andersen et al., 1990, 1993 ; Klemd et al., 1992 ; Scambelluri et al., 1998 ; Mukherjee et Sachan, 2009). Les inclusions de saumures contiennent généralement de nombreuses inclusions solides attestant de systèmes chimiques complexes ($NaCl \pm KCl \pm CaCl_2 \pm FeCl_2 \pm MgCl_2$) et peuvent contenir de faibles quantités de N_2 et/ou de CO_2-CH_4 dans leur bulle de vapeur (e.g., Philippot et Selverstone, 1991 ; Selverstone et al., 1992 ; Yoshida et al., 2015 ; Herviou et al., 2021). La plupart de ces études ont été conduites dans des méta-gabbros d'écailles cohérentes de la subduction alpine aujourd'hui exhumées. Elles enregistrent les salinités les plus fortes (10-45 wt. % eq. NaCl ; Nadeau et al., 1993 ; Philippot et Selverstone, 1991 ; Selverstone et al., 1992 ; Philippot et al., 1998 ; Herviou et al., 2021, **chapitres II, VI**). Ces unités reflètent un héritage au moins partiel de l'altération hydrothermale à haute température des gabbros (Nadeau et al., 1998 ; Philippot et al., 1998). Dans les roches ultramafiques du massif de Voltri (Alpes ligures), les minéraux de veines à olivine contiennent des inclusions de saumures également interprétées comme issues de l'altération hydrothermale : le chlore initialement incorporé dans les serpentinites lors de l'altération hydrothermale (dans les

minéraux et/ou aux joints de grains ; Sharp et Barnes, 2004) aurait tendance à se partitionner dans le fluide aqueux libéré en faible quantité (2 wt.% H_2O ; Kendrick et al., 2011) lors de la réaction de déstabilisation de la brucite (Scambelluri et al., 1997). En comparaison, lors de la déstabilisation de l'antigorite (réaction finale de dé-serpentinisation), le chlore est dilué dans la forte quantité d'eau libérée (6-10 wt.% H_2O ; Kendrick et al., 2011), ce qui explique les faibles salinités des inclusions fluides (Scambelluri et al., 2001, 2004, 2015 ; Kendrick et al., 2011).

En dehors des Alpes (Tianshan, République dominicaine, Syros, Complexe Franciscain ; Barr, 1990 ; Giaramita et Sorensen ; Gao et Klemd, 1991 ; Kawamoto et al., 2018), les salinités des roches mafiques sont significativement plus faibles (~2-7 wt.% eq. NaCl ; Fig. VII.3c) mais malgré tout supérieures à celles généralement trouvées dans les méta-sédiments. Ces salinités plus faibles pourraient s'expliquer par les circulations de fluides plus fortes au sein des mélanges de subduction et/ou par un héritage hydrothermal moins marqué. En effet, les roches de ces contextes correspondent à des roches méta-volcaniques et l'altération hydrothermale des basaltes à plus faible température que celle des gabbros ne provoque pas une séparation de phases et la formation de saumures (**chapitre II**).

VII.2.3. Mécanismes et échelles de circulation des fluides lors de la subduction Alpine

Les études isotopiques et d'éléments traces dans les méta-sédiments Liguro-Piémontais de faciès schiste bleu suggèrent la prédominance d'un système relativement « fermé », dans lequel le fluide est tamponné par les roches, avec une infiltration limitée de fluides externes (Henry et al., 1996 ; Busigny et al., 2003 ; Bebout et al., 2013 ; Cook-Kollars et al., 2014 ; Epstein et al., 2020) à l'exception des zones proches des contacts tectoniques (Jaeckel et al., 2018 ; Epstein et al., 2021) qui localisent des circulations de fluides externes à plus grande échelle. La composition des inclusions fluides des méta-sédiments, faiblement salées et à CO_2-CH_4, semble confirmer ce modèle de veines de haute pression alimentées par les réactions locales de déshydratation et contenant un fluide à l'équilibre avec les roches hôtes. Tout cela suggère une échelle de migration des fluides limitée, probablement d'échelle décimétrique à pluri-métrique (hectométrique au maximum). Ces résultats sont en accord avec des flux de fluide globalement pervasifs et faiblement chenalisés, comme le suggèrent les mesures statistiques sur les veines de haute pression des Schistes Lustrés des unités supérieures et médianes (**chapitre IV**). Dans certains affleurement, l'infiltration de fluides externes salés provenant des unités de marge continentale montre une échelle de migration maximum des fluides d'échelle hectométrique à kilométrique. Dans les méta-sédiments des unités inférieures, les salinités plus fortes

suggèrent une infiltration de fluides provenant des roches mafiques et/ou ultramafiques lors de leur déshydratation, ce qui implique également une échelle de circulation des fluides d'échelle hectométrique à kilométrique.

Dans les roches mafiques et ultramafiques du domaine Liguro-Piémontais, les études isotopiques et des éléments traces montrent une re-distribution locale des fluides lors des réactions successives de déshydratation au sein de chaque écaille. La composition des inclusions fluides dans les roches mafiques du transect Queyras-Monviso suggère également une alimentation des veines par des fluides locaux et partiellement hérités de l'altération hydrothermale, donc une circulation restreinte et transitoire de fluides (échelle hectométrique au maximum ?). La présence de rares potentielles inclusions d'hydrocarbures légers dans les veines de jadéite des schistes bleus, associée à la présence d'inclusions fluides moins salées dans ces mêmes échantillons, suggère une faible infiltration de fluide provenant des sédiments encaissants dans les unités de faciès schiste bleu où les sédiments sont volumétriquement dominants par rapport aux roches mafiques et ultramafiques (Herviou et al., 2021, **chapitre II**).

Finalement, le long des contacts lithologiques entre serpentinites et sédiments, l'infiltration de fluides externes des sédiments transforme entièrement les serpentinites en talcschistes à dolomite lors des conditions du pic d'enfouissement.

Les différentes écailles du domaine Liguro-Piémontais subissent donc peu d'infiltration de fluides externes, et les fluides produits localement par les réactions de déshydratation circulent de manière diffuse, à petite échelle, restant tamponnés par les roches encaissantes. Il n'y a pas d'évidence de variation d'échelle de circulation avec l'augmentation du grade métamorphique vers l'Est. A l'inverse, les contrastes lithologiques (et donc rhéologiques, cf contacts serpentinites-sédiments, métabasites-sédiments ; Vitale Brovarone et al., 2020b) et les contacts tectoniques, limitant les différentes écailles, localisent des circulations de fluides externes à grande échelle, comme le montrent les signatures élémentaires et isotopiques (Lafay et al., 2013 ; Angiboust et al., 2014a ; Debret et al., 2016, 2018 ; Locatelli et al., 2019b ; Tartarotti et al., 2019 ; Rotondo et al., 2021).

VII.3. Mécanismes d'écaillage en subduction

Les trois groupes d'écailles identifiés dans le domaine Liguro-Piémontais sont caractérisées par des conditions pression-température du pic comparables à celles des fragments de lithosphère océanique

métamorphisés dans des conditions HP-BT à travers le monde, pour lesquels deux profondeurs caractéristiques d'écaillage ont été reconnus à 30-40 km et 80 ± 10 km, avec un potentiel troisième groupe à 55-60 km de profondeur (Plunder et al., 2015 ; Agard et al., 2018). Les mêmes profondeurs d'écaillages ont également été reconnues dans des unités exhumées de zones de subduction continentale (Agard et Vitale Brovarone, 2013 ; Soret et al., 2021). Il a été suggéré que ces gammes de profondeurs reflètent des changements majeurs du couplage mécanique le long de l'interface des plaques. Alors que l'arrachement de matériel au panneau plongeant nécessite une augmentation du couplage mécanique (Agard et al., 2016, 2020), le déplacement vers le bas du décollement de l'interface et la localisation de la déformation dans des zones de faiblesses (Kimura et Ludden, 1996 ; Kimura et al., 2007 ; Angiboust et al., 2012c ; Ruh et al., 2015), les processus mécaniques qui contrôlent l'écaillage sont inconnus. Des zones de déformation interplaques bordant les séismes ont également été identifiées aux mêmes profondeurs (35 ± 10 km et 60 ± 5 km) par une analyse mécanique de la topographie le long de la marge chilienne (Cubas et al., soumis). Ces profondeurs sont interprétées comme des zones de déformation distribuée où des fragments de panneau plongeant s'écaillent et se sous-plaquent à la plaque supérieure, et peuvent être responsables de l'accumulation des contraintes et potentiellement de la nucléation de séismes (Cubas et al., soumis). Les unités Liguro-Piémontaises supérieures (LPU), médianes (LPM) et inférieures (LPL) avec leurs profondeurs d'écaillage à ~35-45 km, ~55-65 km et ~70-80 km, respectivement peuvent nous aider à apporter des contraintes sur les mécanismes contrôlant la localisation de la déformation et l'écaillage le long de l'interface des plaques.

La profondeur d'écaillage des unités supérieures (LPU) coïncide avec celle de la base de la zone sismogénique, où le panneau plongeant passe d'une juxtaposition avec la croûte continentale de la plaque supérieure à une juxtaposition avec le coin mantellique, induisant un probable changement majeur dans le couplage mécanique entre les plaques (Agard et al., 2018) et où le fluage dissolution-précipitation devient le principal mécanisme de déformation (Wassmann et Stöckhert, 2013; Platt et al., 2018). Les modèles géophysiques comme pétrologiques suggèrent la présence de fluide ainsi que de fortes pression de fluide à ces profondeurs, qui pourraient réduire la résistance des roches et favoriser la localisation de la déformation dans des zones de faiblesses (Kimura et Ludden, 1995 ; Kimura et al., 2007 ; Saffer et Tobin, 2011 ; Kameda et al., 2017). Dans ces unités (LPU), la présence de fluides aux conditions du pic d'enfouissement est attestée par les grandes quantités de minéraux hydratés dans les sédiments et les veines métamorphiques (Goffé et Chopin, 1986 ; Agard et al., 2000 ; Lefeuvre et al., 2020 ; Herviou et al., 2021, **chapitres II, IV, VI**). Ce type de sédiments riches

en veines métamorphiques serait caractérisé par des vitesses sismiques comparables à celle de l'horizon de faibles vitesses (Low Velocity Zone) observé à ces profondeurs dans les zones de subduction actives et cohérent avec la présence de fluides à des pressions lithostatiques (Tewksbury-Christle et Behr, 2021). Les textures de veines en crack-seal ainsi que les mécanismes d'ouvertures proposés, le long de plans très faibles, témoignent de la pression de fluide forte à ces profondeurs dans les Schistes Lustrés. Comme aucune réaction de déshydratation majeure n'est franchie aux gammes P-T du pic d'enfouissement de ces unités (**chapitre III**), l'écaillage de ces unités serait plutôt lié à des hétérogénéités lithostratigraphiques sous des conditions de fortes pressions de fluide plutôt qu'à de la fracturation causée par une libération majeure de fluides ('dehydration embrittlement' e.g., Hacker et al., 2003). Dans les unités supérieures limitées à des dépôts d'âge Crétacé supérieur, la localisation de la déformation aurait eu lieu à la base de ces dépôts de calcschistes-flysch, dans des pélites comme observé entre les sédiments pélagiques et les turbidites de fosse dans les prismes d'accrétion actifs (Karig et Sharman, 1975 ; Moore, 1975 ; Kimura et al., 2007). Dans les unités de type Chabrière qui contiennent un socle océanique démembré, l'écaillage s'est fait plus profondément dans la lithosphère océanique, potentiellement le long de structures héritées comme les nombreux détachements océaniques observés dans le domaine Liguro-piémontais (Manatschal et al., 2011 ; Lagabrielle et al., 2015 ; Balestro et al., 2018 ; Decrausaz et al., 2021). La localisation de la déformation dans des horizons de serpentinites est communément évoquée pour expliquer l'écaillage du panneau plongeant (Angiboust et al., 2011 ; Agard et al., 2018 ; Tewksbury-Christle et al., 2021) et l'infiltration de fluides dans ces structures est susceptible d'avoir favorisé l'altération hydrothermale du manteau lithosphérique (serpentinisation).

Pour finir, au niveau des contacts lithologiques entre les sédiments et les serpentinites, la localisation de la déformation aurait focalisé l'infiltration de fluides externes provenant des méta-sédiments et la formation de talcschistes au pic d'enfouissement des unités supérieures (**chapitre V**). Le talc à une résistance beaucoup plus faible que la serpentine (lizardite, chrysotile, antigorite ; Moore et Lockner, 2007 ; Moore et Rymer, 2007) et la présence de faibles quantités de talc réduit drastiquement la résistance de mélanges à serpentine-talc et quartz-talc (Moore et Lockner, 2011). Je propose donc que suite à la formation de talc, la déformation se localise le long de ces horizons métasomatiques, favorisant en retour la formation de talcschistes par rétroaction positive entre la localisation de la déformation et des infiltrations de fluides. Cette rétroaction pourrait être responsable de l'écaillage de fragments du panneau plongeant ce qui pourrait expliquer qu'on retrouve ces talcschistes uniquement le long de contacts entre écailles.

Aux profondeurs du pic d'enfouissement des unités médianes (55-65 km), le panneau plongeant est juxtaposé avec le coin mantellique partiellement serpentinisé et mécaniquement découplé, expliquant la plus faible quantité de roches HP-BT écaillées à ces profondeurs à travers le monde (Agard et al., 2018). A ces profondeurs, dans les unités médianes, la seule réaction de déshydratation prédite est la déstabilisation progressive de la Fe-Mg carpholite (~12 wt.% H_2O) en chloritoïde (~7-8 wt.% H_2O ; Herviou et al., 2022, **chapitre III**) qui explique la décroissance progressive des salinités dans les sédiments par dilution (Herviou et al., 2021, **chapitres II, VI**). Aucune autre réaction majeure libérant de grandes quantités d'eau sur une gamme restreinte de conditions P-T n'est prédite dans les sédiments ou les roches mafiques et ultramafiques (Angiboust et Agard, 2010 ; Herviou et al., 2022, **chapitre III**). L'écaillage des unités médianes serait donc relié, comme pour les unités supérieures, à des contrastes lithologiques/lithostratigraphiques et à la présence de fluides à fortes pressions. Les pélites du Crétacé moyen, comme les détachements océaniques, sont donc considérées comme des zones majeures de faiblesse comme pour les unités supérieures. Des talcschistes potentiellement formés aux conditions du pic d'enfouissement ont également été trouvés aux bordures des unités médianes et pourraient également être reliés à l'écaillage de ces unités.

La troisième gamme de profondeur à ~70-80 km coïncide à la profondeur limite, en-dessous de laquelle les roches ne sont généralement pas exhumées du fait de leur densité, de la traction du panneau plongeant ('slab pull') et du re-couplage visqueux (Wada et Wang, 2009 ; Syracuse et al., 2010). La transition du faciès schiste bleu au faciès éclogite est considérée comme un palier majeur de déshydratation du panneau plongeant (Peacock, 1993 ; Angiboust et Agard, 2010 ; Van Keken et al., 2011 ; Paulatto et al., 2017). La frontière entre ces deux faciès coïncide avec la localisation des séismes de profondeurs intermédiaires suggérant un affaiblissement et une fracturation des roches lors de la déshydratation aux conditions du faciès éclogite ('dehydration embrittlement' Hacker et al., 2003 ; Kita et al., 2006 ; Abers et al., 2006, 2013) et particulièrement pour les zones de subduction à gradients thermiques froids (Abers et al., 2013). Certaines réactions de déshydratation comme la déstabilisation de la lawsonite (~12 wt.% H_2O) ont été particulièrement étudiées car la limite de stabilité thermique de la lawsonite coïncide avec la profondeur de localisation des séismes intermédiaires dans la croûte (Abers et al., 2006) et parce que la déshydratation de la lawsonite pourrait entraîner de la déformation cassante et du glissement frictionnel ('stick-slip' ; Okazaki et Hirth, 2016 ; Incel et al., 2017). Dans les unités inférieures, la présence de brèches et de veines formées aux conditions éclogitiques révèle des épisodes de fracturation le long de contrastes rhéologiques et l'infiltration de fluide à ~80 km de profondeur (Angiboust et al., 2011, 2012a ; Locatelli et al., 2018,

2019a, b ; Broadwell et al., 2019). Aux conditions du pic d'enfouissement des unités inférieures, la lawsonite est supposée stable dans la croûte océanique (Angiboust et Agard, 2010 ; Angiboust et al., 2011, 2012b ; Locatelli et al., 2018) tandis que la déstabilisation de la chlorite (~12 wt.% H_2O) est prédite à la transition entre faciès schiste bleu et éclogite (Angiboust et Agard, 2010). Dans les roches ultamafiques, l'antigorite (~12 wt.% H_2O) est toujours stable aux conditions du pic d'enfouissement (Angiboust et Agard, 2010; Schwartz et al., 2013). Dans les roches mafiques et ultramafiques des unités inférieures, la seule réaction susceptible de contribuer à une pression de fluide forte et d'affecter la rhéologie des roches est donc la déstabilisation de la chlorite. Les conditions estimées pour le pic d'enfouissement des unités inférieures coïncident par contre avec celles estimées pour des réactions de déshydratation majeures dans les méta-sédiments (Fe-Mg carpholite, chlorite, lawsonite, chloritoïde). La déstabilisation de la lawsonite à ~575°C – 2.4 GPa coïncide avec la plupart des conditions P-T du pic enregistrées par les unités inférieures. D'ailleurs, alors que les unités supérieures et médianes contiennent de grandes quantités de lawsonite (jusqu'à 40 vol% des sédiments ; Lefeuvre et al., 2020), les unités inférieures n'en contiennent plus. Il est donc proposé que la déstabilisation de ces grandes quantités de lawsonite dans les sédiments, associée à la déstabilisation de la chlorite dans les roches mafiques, pourrait avoir induit des pressions de fluide très fortes et une fracturation des roches susceptible d'être responsable de l'écaillage des unités inférieures. Ces réactions auraient permis de localiser la déformation plus profondémment dans le panneau plongeant que pour les unités supérieures et médianes, expliquant les volumes plus importants de roches mafiques et ulramafiques dans ces unités. Comme pour les unités supérieures et médianes, des détachements océaniques hérités pourraient avoir servi de zones de faiblesses rhéologiques permettant la localisation de la déformation.

Figure VII.4 *(page suivante) : Schéma bilan de cette thèse illustrant les transferts de fluides et les déformations associées à 4 profondeurs/étapes distinctes d'une zone de subduction océanique en prenant appui sur les données obtenues dans le domaine Liguro-Piémontais des Alpes occidentales.*

La première étape (1) montre l'altération hydrothermale sur le plancher océanique dans un contexte de dorsale lente ou le manteau est exhumé à la faveur de détachements océaniques. Cette phase d'altération à haute température, pour les gabbros, entraîne la formation de saumures et le stockage de grandes concentrations de Cl dans les minéraux.

La deuxième étape (2) montre la formation de veines de lawsonite et de Fe-Mg carpholite à ~35-45 km de profondeur. Ces veines sont alimentées par les réactions locales de déshydratation et pour certaines par l'infiltration de fluides provenant des évaporites des unités de marge continentale. Dans les veines de jadéite des méta-gabbros, la libération du Cl des minéraux dans le fluide et le recyclage des saumures piégées dans les inclusions fluides provoquent la préservation de salinités fortes. De faibles quantités de fluides des sédiments peuvent également s'infiltrer dans ces méta-gabbros. Enfin, l'infiltration de fluides libérés par les sédiments dans les serpentinites entraîne la formation de talcschistes riches en carbonates. La localisation de la déformation dans ces horizons pourrait entrainer l'écaillage de fragments du panneau plongeant à ces profondeurs. D'autres niveaux de faiblesse comme des horizons particulièrement argileux ou la partie supérieure du manteau lithosphérique, plus serpentinisée et présentant un héritage structural marqué (détachement océanique) pourraient localiser la déformation et entrainer l'arrachement de fragments de lithosphère océanique.

La troisième étape (3) se déroule à ~55-65 km de profondeur. Alors que les veines de lawsonite continuent de se former, la déstabilisation de la Fe-Mg carpholite en chloritoïde permet de libérer des fluides peu salés qui vont baisser les salinités de pores initiales enregistrées dans les inclusions fluides des veines à lawsonite. A ces profondeurs encore, la signature hydrothermale des gabbros est préservée. L'écaillage du panneau plongeant se ferait également par le biais d'hétérogénéités lithostratigraphiques/lithologiques et par la formation de talcschistes aux contacts sédiments/serpentinites.

La quatrième et dernière étape (4) a lieu à ~70-80 km de profondeur, dans le faciès éclogite. La formation de grenat et d'omphacite dans les méta-gabbros va permettre de libérer des fluides qui vont légèrement baisser les salinités retrouvées dans les inclusions fluides des veines d'omphacite et par contre augmenter les salinités des fluides des sédiments. Les nombreuses réactions de déshydratation et notamment la déstabilisation des grandes quantités de lawsonite des sédiments pourraient induire des pressions de fluide très fortes, la fracturation des roches et entrainer l'écaillage dans des niveaux de faiblesse comme des détachements océaniques hérités. Ces réactions pourraient permettre de localiser la déformation bien plus profondément à l'intérieur du panneau plongeant.

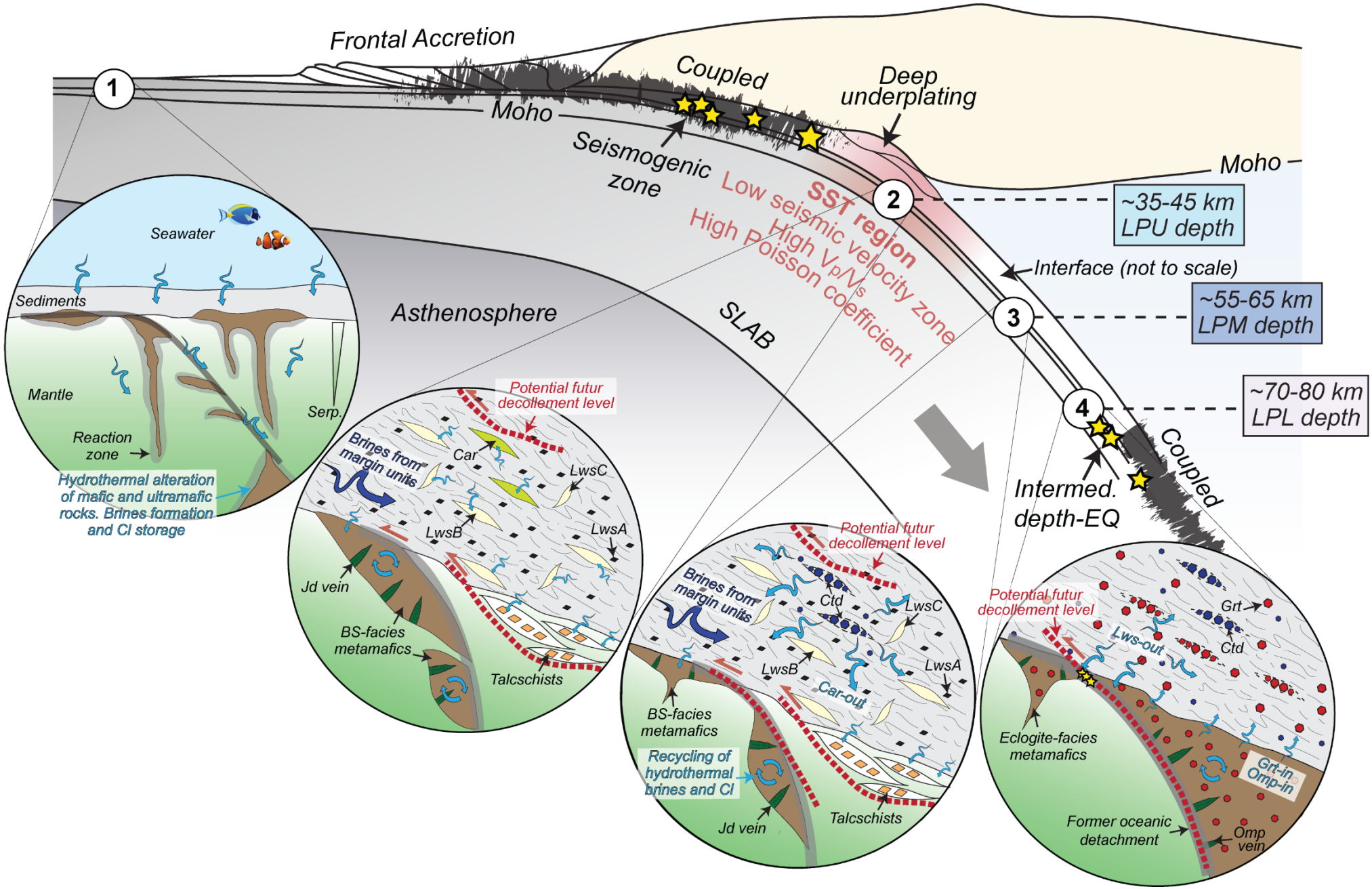
Frontal Accretion
Coupled
Deep underplating
Moho
Seismogenic zone
Low seismic velocity zone
High Vp/Vs
High Poisson coefficient
SST region
Moho
~35-45 km LPU depth
Interface (not to scale)
~55-65 km LPM depth
~70-80 km LPL depth
Asthenosphere
SLAB
Coupled
Intermed. depth-EQ
1
2
3
4
Seawater
Sediments
Mantle
Serp.
Reaction zone
Hydrothermal alteration of mafic and ultramafic rocks. Brines formation and Cl storage
Potential futur decollement level
Brines from margin units
Car
LwsC
LwsB
LwsA
Jd vein
BS-facies metamafics
Talcschists
Ctd
Car-out
Recycling of hydrothermal brines and Cl
Lws-out
Grt
Eclogite-facies metamafics
Grt-in
Omp-in
Former oceanic detachment
Omp vein

Chapitre VIII – Conclusions et perspectives

Massif de l'Albaron. Haute-Maurienne.

VIII. Conclusions et perspectives

VIII.1. Conclusions

A travers la compilation et l'acquisition de nouvelles données pétrologiques, cette thèse fournit un cadre détaillé des conditions métamorphiques enregistrées le long des différentes écailles Liguro-Piémontaises, confirmant la présence d'une augmentation forte du grade métamorphique vers l'Est, à travers le domaine comme à l'intérieur des écailles. La compilation des données lithostratigraphiques, structurales et radiochronologiques ainsi que l'estimation des rapports volumétriques entre sédiments et roches mafiques et ultramafiques pour chaque écaille permet d'affiner l'origine paléogéographique de ces unités à l'intérieur du domaine océanique initial. Toutes ces données permettent de mettre en évidence la présence d'une distribution trimodale d'unités avec une augmentation des conditions métamorphiques des unités Liguro-Piémontaises supérieures (LPU ; 320-400°C- 1.2-1.9 GPa), aux unités médianes (LPM ; 415-475°C- 1.7-2.2 GPa) et aux unités inférieures (LPL ; 500-580°C- 2.2-2.8 GPa). Les unités supérieures et médianes métamorphisées dans le faciès schiste bleu sont dominées par les sédiments (>90%) tandis que les unités inférieures de faciès éclogite sont bien plus riches en roches mafiques et ultramafiques (>40%). Ces caractéristiques, accompagnées de distinctions lithostratigraphiques subtiles, reflètent des différences initiales de paléogéographie et/ou des mécanismes responsables de l'arrachement de matériel au panneau plongeant.

Dans les unités supérieures et médianes, de nombreuses veines métamorphiques constituant jusqu'à 32% des affleurement ont été observées. Parmi ces veines, certaines contenant des minéraux caractéristiques de conditions de haute pression (lawsonite et Fe-Mg carpholite) sont des témoins directs de la circulation de fluides lors de la subduction alpine, dans des conditions proches de celles du pic d'enfouissement. L'étude statistique des textures de ces veines permet de mettre en évidence leur formation par des mécanismes incrémentaux de fracturation en dilatation et généralement entre des plans de cisaillement particulièrement faibles et de proposer un lien avec des glissements lents en subduction. Les inclusions fluides piégées dans ces veines contiennent des salinités modérées avec de faibles quantités de CO_2 et de CH_4, suggérant une alimentation locale par des fluides libérés par les réactions de déshydratation, à l'équilibre avec les roches, et circulant de manière pervasive dans les roches comme suggéré par l'étude statistique de distribution des veines. Certaines veines, proches des unités de marge continentale, contiennent des salinités plus fortes suggérant une infiltration de fluides provenant des évaporites de ces marges. Ces salinités fortes montrent donc une

ouverture du système jusqu'à l'échelle hectométrique à kilométrique et impliquent une position proximale des écailles Liguro-Piémontaises concernées. La tendance générale de décroissance des salinités avec l'augmentation du grade métamorphique dans les Schistes Lustrés (unités supérieures et médianes) est interprétée comme reflétant la dilution progressive des salinités des fluides de pores initiaux par les fluides libérés par les réactions métamorphiques. Dans les sédiments des unités inférieures où les veines métamorphiques sont quasiment absentes, l'étude des inclusions fluides dans les grenats, formés au pic d'enfouissement, a permis de mettre en évidence la présence d'un fluide aqueux à CO_2-CH_4 dans les conditions du faciès éclogite. Les salinités plus fortes que dans les unités supérieures et médianes suggèrent un mélange entre le fluide produit localement par les sédiments et une infiltration de fluides externes provenant des roches mafiques et/ou ultramafiques, volumétriquement importantes dans ces unités. En effet, les roches mafiques des unités supérieures à inférieures contiennent des inclusions fluides bien plus salées que celles des sédiments affleurant autour. Les salinités retrouvés dans des veines et brèches métamorphiques contenant les assemblages minéralogiques du pic d'enfouissement de ces unités sont bien plus fortes que dans les sédiments affleurant autour. Les fortes salinités mesurées dans des veines à jadéite (assemblage du pic de faciès schiste bleu, unités supérieures et médianes) et veines/matrices de brèches à omphacite ± grenat (assemblage du pic éclogitique, unités inférieures) sont interprétées comme héritées de la phase d'altération hydrothermale des gabbros océaniques à haute température, qui engendre la formation de saumures (stockées dans les inclusions fluides) et enrichi les amphiboles hydrothermales en chlore.

Dans les contacts tectoniques entre écailles Liguro-Piémontaises, des talcschistes à dolomite ont été découverts. L'étude des compositions des minéraux, de la géochimie des roches totales, des inclusions fluides et les datations U-Pb sur titanite ont permis de montrer que ces roches se sont formées par la transformation de serpentinites via l'infiltration de fluides des sédiments, au pic d'enfouissement des unités. Ces roches riches en carbonates et en éléments mobiles dans le fluide pourraient avoir un impact sur le cycle profond du carbone et la composition du coin mantellique lors de leur déstabilisation aux conditions sub-arc.

Pour finir, les profondeurs du pic d'enfouissement des unités supérieures (LPU ; ~35-45 km), médianes (LPM ; ~55-65 km) et inférieures (LPL ; ~70-80 km) sont similaires à celles déduites pour l'écaillage et le sous-plaquage dans les zones de subduction modernes et fossiles, reflétant des changements majeurs du couplage mécanique à l'interface des plaques. Toutes les données pétrologiques et lithostratigraphiques compilées et obtenues dans ce travail de thèse permettent de

proposer que l'écaillage des unités LPU et LPM a principalement été contrôlé par des contrastes lithostratigraphiques majeurs comme des niveaux très pélitiques ou la partie supérieure du manteau serpentinisé et sous de fortes pressions de fluide. En revanche, des réactions de déshydratation majeures comme la déstabilisation des grandes quantités de lawsonite dans les méta-sédiments pourraient être à l'origine de l'écaillage de unités inférieures éclogitiques, également sous de fortes pressions de fluide engendrant une fragilisation des roches. Enfin, une rétroaction positive entre déformation et infiltration de fluides (formation de talc) dans les contacts lithologiques entre serpentinites et sédiments pourrait également avoir contribué à l'écaillage des unités Liguro-Piémontaises, ce qui expliquerait la position structurale présente des talcschistes à dolomite identifiés dans ce travail.

VIII.2. Perspectives

De nombreuses interrogations ont été soulevées dans cette thèse. Quelques perspectives de travail, permettant d'apporter des éléments de réponse à ces nouveaux questionnements et aux problématiques non résolues, sont présentées ci-dessous.

Affinage du cadre tectonométamorphique régional et de la distribution trimodale d'unités

La révision du contexte tectonométamorphique Liguro-Piémontais a permis de proposer un modèle simple de distribution des unités en trois groupes. Plusieurs inconnues ou incertitudes demeurent concernant l'étendue et la distribution des unités en certains points du complexe. Très peu de données pétrologiques et lithostratigraphiques sont disponibles pour les unités Liguro-Piémontaises à l'Est du Grand Paradis (écaille West-Sesia), dans le méga-pli du Valsavaranche (écailles Avise-Tsaboc-Feluma) et au Nord-Ouest des Alpes Cottiennes (écailles de Puys et de l'Aigle). De nouvelles estimations des conditions P-T du pic d'enfouissement dans ces écailles permettraient de préciser leur relation avec les trois groupes d'unités. L'extension des limites des unités supérieures et médianes autour de la bande d'Acceglio et de la Dent Blanche permettrait également d'affiner ce cadre tectonométamorphique. Enfin, l'identification de sauts métamorphiques et de contacts entre les unités inférieures riches en sédiments (Unités S) et celles riches en roches mafiques-ultramafiques (unités MUM) permettrait de confirmer la distinction entre ces unités proposée dans cette thèse.

Chronologie de l'écaillage et de l'empilement des unités Liguro-Piémontaises

Très peu de données radiochronologiques sont disponibles pour les âges de subduction des unités supérieures et médianes ainsi que pour les unités inférieures riches en sédiments. Ce manque de données empêche de préciser avec certitude la paléogéographie des Unités Liguro-Piémontaises et leur séquence d'écaillage et de sous-plaquage. Une collaboration est en cours avec Thomas Gyomlai (Sorbonne Université, ISTeP) pour la datation in-situ Rb-Sr et Ar-Ar sur phengites dans les unités supérieures à inférieures. Une autre collaboration est en cours avec Joshua Garber (Penn State) pour la datation U-Pb sur zircon (± sur sphènes et rutiles) dans les unités inférieures.

Révision grande échelle du cadre tectonométamorphique Liguro-Piémontais et processus de formation de veines métamorphiques lors de la subduction océanique alpine : comparaison avec les Alpes centrales, orientales et corses

Différentes unités tectoniques Liguro-Piémontaises (et Valaisannes) ont été identifiées dans les Alpes centrales, orientales et corses (Berger and Bousquet, 2008 ; Vitale Brovarone et al., 2013, 2014a ; Agard, 2021 ; Fig. VIII.1). Une comparaison de ces écailles (données pétrologiques, litostratigraphiques et structurales) avec le modèle de distribution proposé dans cette thèse pour les Alpes occidentales permettrait d'étendre les observations à l'échelle de toute la chaine alpine et de fournir des informations clés sur les profondeurs et mécanismes d'écaillages lors de la subduction océanique alpine. L'observation systématique des veines métamorphiques de haute pression préservées dans ces différentes écailles de subduction permettrait d'évaluer le caractère représentatif des objets décrits dans cette thèse et de caractériser avec précision les marqueurs des interactions fluides-roches. La comparaison des compositions d'inclusions fluides piégées aux pics P-T dans les différentes coupes permettrait également de caractériser de manière plus globale l'évolution de la composition des fluides en subduction.

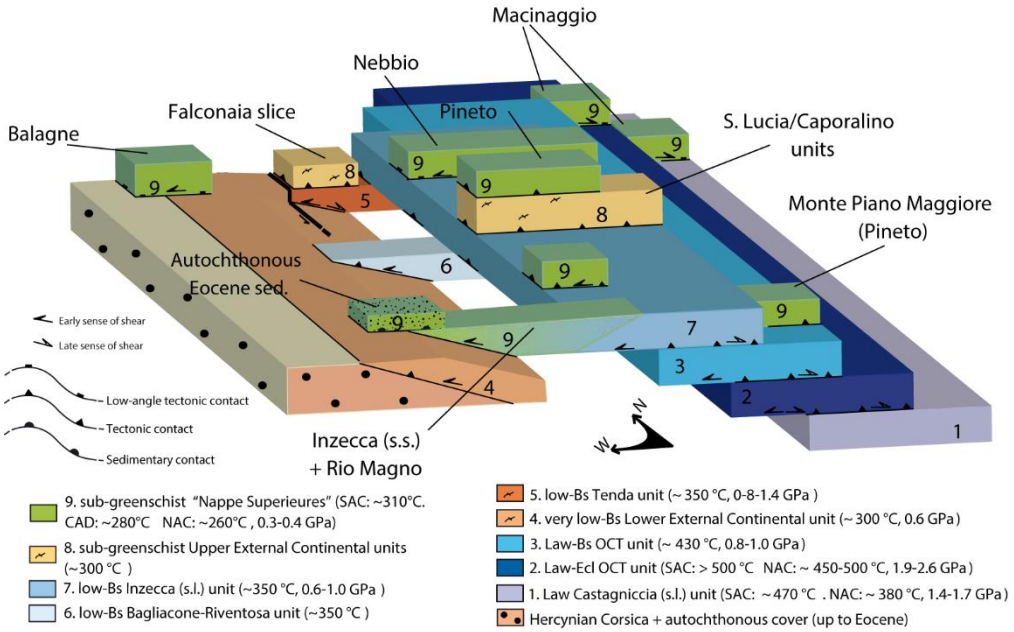

***Figure VIII.1** : Reconstruction schématique de l'empilement des unités de Corse alpine. D'après Vitale Brovarone et al. (2013).*

Origine des salinités fortes dans les méta-gabbros et lien avec l'altération hydrothermale

Dans cette thèse, les salinités fortes des inclusions fluides dans les méta-gabbros de faciès schiste bleu et éclogite ont été interprétées comme héritées de l'altération hydrothermale des gabbros à haute température, qui provoque la formation de saumures par séparation de phases et l'incorporation de grandes quantités de Cl dans les minéraux. Cette interprétation est notamment en accord avec les études des éléments traces et isotopiques qui montrent que, jusque dans le faciès des éclogites les méta-gabbros alpins préservent un signal hydrothermal fort (Nadeau et al., 1993 ; Philippot et al., 1998 ; Selverstone et al., 2013 ; Debret et al., 2016 ; Busigny et al., 2011, 2018). Une étude plus statistique des inclusions fluides dans les méta-gabbros, sur un set d'échantillons plus large des différentes unités, permettrait de déterminer l'ampleur locale de ces zones à salinités fortes (anciennes zones de réaction), et de détecter de potentielles variations avec l'augmentation des conditions P-T. L'altération hydrothermale des basaltes, à plus basse température, n'entraine pas la formation de saumures. L'analyse de la composition des inclusions fluides des méta-basaltes des unités Liguro-piémontaises permettrait de déterminer si les salinités sont en effet plus faibles, appuyant ainsi l'hypothèse de recyclage de fluides hydrothermaux. L'étude des inclusions fluides dans les assemblages hydrothermaux des roches mafiques (gabbros et basaltes) du massif non-subduit du Chenaillet permettrait également d'apporter des clés sur l'ampleur des réactions

d'altération hydrothermale sur le plancher océanique Liguro-Piémontais et donc sur la possibilité de conserver ensuite des signatures océaniques lors du métamorphisme HP-BT de ces roches. Enfin, l'étude du contenu en chlore et de ses isotopes dans les roches mafiques (subduites ou non) permettrait de confirmer la préservation d'un signal hydrothermal fort lors de la formation des veines à jadéite et à omphacite des méta-gabbros de faciès schiste bleu et éclogite.

Evolution de la composition des fluides en fonction de la profondeur en subduction et redistribution des fluides lors de l'exhumation : comparaison de différents contextes de subduction

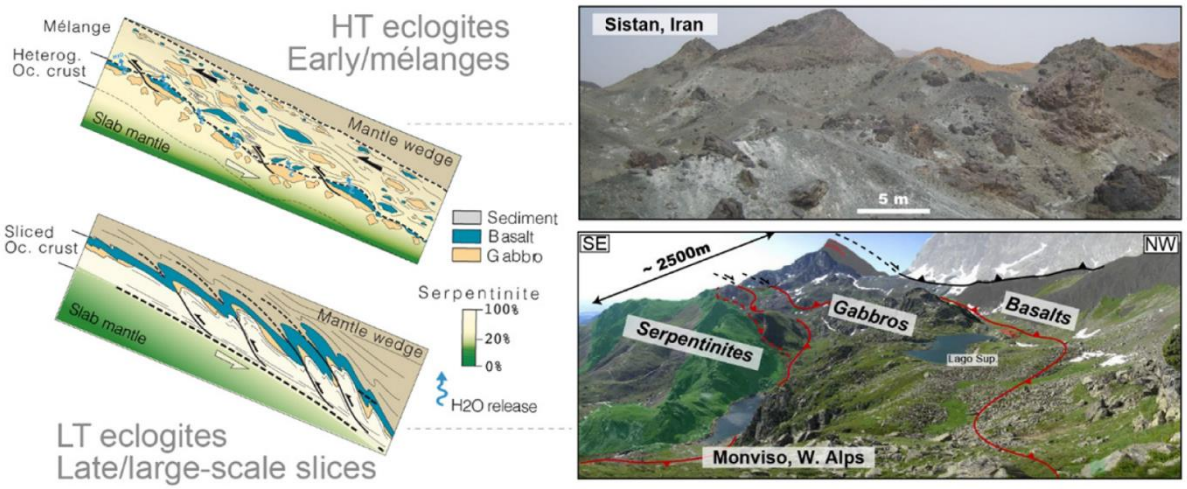

***Figure VIII.2** : Distinctions entre éclogites de haute température des mélanges de subduction et éclogites de basse température d'écailles cohérentes. D'après Guillot et al., 2015 et Agard et al., 2018.*

Le **chapitre II** de cette thèse a permis de montrer les différences significatives entre les salinités des roches mafiques des Alpes et celles d'autres complexes HP-BT (Franciscain, République Dominicaine, Syros, etc…). Ces différences pourraient être liées à des circulations de fluides bien plus intenses dans les mélanges de subduction. La comparaison des compositions d'inclusions fluides et des signatures, isotopiques et en éléments traces, de veines métamorphiques formées à des profondeurs comparables (faciès éclogite) mais dans des contextes de subduction différents (fragments cohérents vs blocs de mélanges de subduction ; Fig. VIII.2) permettrait d'identifier

d’éventuelles différences systématiques entre ces types majeurs de complexes HP-BT. Enfin, l’étude de veines formées durant les étapes successives d’exhumation (faciès schiste bleu et schiste vert) permettrait d’identifier comment les fluides piégés aux conditions du pic métamorphique sont préservés et redistribués lors du chemin rétrograde. Ce projet a été soumis et sélectionné pour un financement post-doctoral de deux ans à UNC Chapel Hill et sera réalisé en collaboration avec Kennet E. Flores.

Enfin, l’analyse de la composition des fluides circulant à haute température lors de l’initiation de la subduction Omanaise a fait l’objet de nombreuses analyses (Raman, MEB et microsonde électronique sur inclusions fluides et solides polyphasées ; Fig. VIII.3) en collaboration avec Mathieu Soret lors de cette thèse. L’étude de ces roches permet d’identifier les sources de fluides et les mécanismes de transfert de matière dans un régime thermique comparable aux conditions des profondeurs sub-arc. Presque aucune roche métamorphique n’est exhumée des profondeurs sub-arc tandis que les libérations de fluides dans ces conditions ont des conséquences directes sur la dynamique de subduction : fusion partielle du coin mantellique, formation (et signature géochimique) des magmas d’arcs, couplage-découplage mécanique à l’interface des plaques. Un article, sur cette thématique, est en préparation pour la revue Geology.

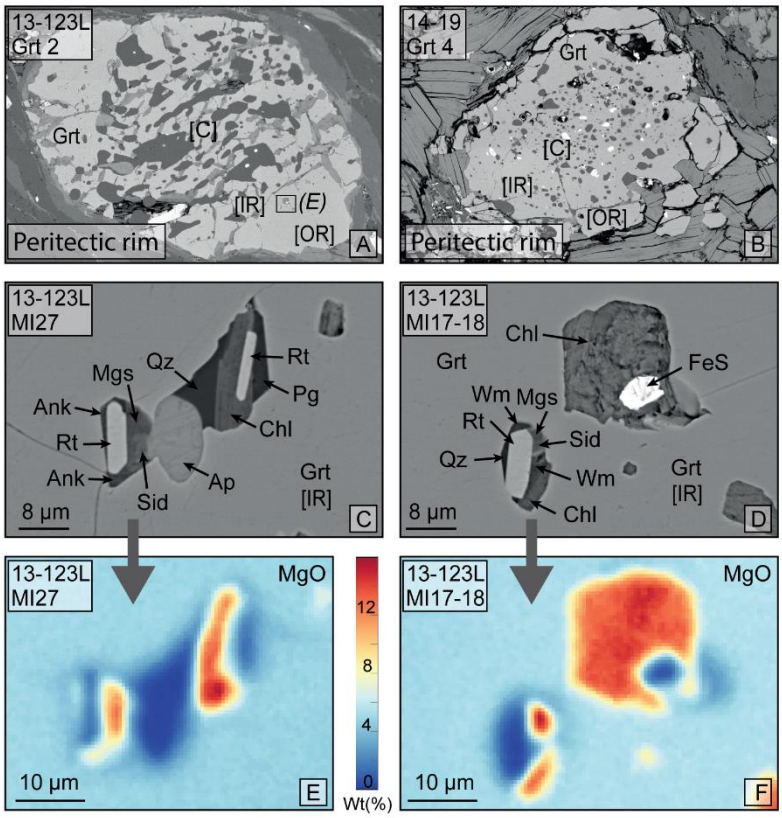

Figure VIII.3 *(page précédente) : Nanogranitoïdes dans les grenats de la semelle métamorphique d'Oman. A) et B) grenats de méta-pélites de la semelle d'Oman. C) et D) Inclusions solides multiphasées dans les grenats de A) et B). E) et F) Cartographie de microsonde électronique du MgO dans les inclusions de B) et C). Abréviations : [C] = core ; [IR] = inner rim ; [OR] = outer rim ; Ank = ankérite ; Ap = apatite ; Chl = chlorite ; FeS = sulfure de fer ; Grt = grenat ; Mgs = magnésite ; Qz = quartz ; Pg = paragonite ; Sid = sidérite ; Rt = rutile ; WM = white mica.*

Références bibliographiques

Abers, G.A., van Keken, P.E., Kneller, E.A., Ferris, A., Stachnik, J.C., 2006. The thermal structure of subduction zones constrained by seismic imaging: Implications for slab dehydration and wedge flow. Earth Planet. Sci. Lett. 241, 387–397. https://doi.org/10.1016/j.epsl.2005.11.055.

Abers, G.A., MacKenzie, L.S., Rondenay, S., Zhang, Z., Wech, A.G., Creager, K.C., 2009. Imaging the source region of Cascadia tremor and intermediate-depth earthquakes. Geology 37, 1119–1122. https://doi.org/10.1130/G30143A.1

Abers, G.A., Nakajima, J., van Keken, P.E., Kita, S., Hacker, B.R., 2013. Thermal–petrological controls on the location of earthquakes within subducting plates. Earth Planet. Sci. Lett. 369–370, 178–187. https://doi.org/10.1016/j.epsl.2013.03.022.

Agard, P., 1999. Evolution métamorphique et structurale des métapélites océaniques dans l'orogène Alpin : l'exemple des Schistes Lustrés des Alpes occidentales (Alpes Cottiennes). PhD thesis Université de Paris 6.

Agard, P., 2021. Subduction of oceanic lithosphere in the Alps: Selective and archetypal from (slow-spreading) oceans. Earth Sci. Rev. 214, 103517 https://doi.org/10.1016/j.earscirev.2021.103517.

Agard, P., Handy, M.R., 2021. Ocean Subduction Dynamics in the Alps. Elements 17, 9–16. https://doi.org/10.2138/gselements.17.1.9.

Agard, P., Vitale-Brovarone, A., 2013. Thermal regime of continental subduction: The record from exhumed HP–LT terranes (New Caledonia, Oman, Corsica). Tectonophysics 601, 206–215. https://doi.org/10.1016/j.tecto.2013.05.011.

Agard, P., Goffé, B., Touret, J.L.R., Vidal, O., 2000. Retrograde mineral and fluid evolution in high-pressure metapelites (Schistes lustr´es unit, Western Alps). Contrib. Mineral. Petrol. 140, 296–315. https://doi.org/10.1007/s004100000190.

Agard, Philippe, Jolivet, L., Goffé, B., 2001a. Tectonometamorphic evolution of the Schistes Lustres Complex; implications for the exhumation of HP and UHP rocks in the Western Alps. Bulletin de la Soci´et´e G´eologique de France 172, 617–636. https://doi.org/10.2113/172.5.617.

Agard, P., Vidal, O., Goffé, B., 2001b. Interlayer and Si content of phengite in HP-LT carpholite-bearing metapelites. J. Metamorph. Geol. 19, 479–495. https://doi.org/10.1046/j.0263-4929.2001.00322.x.

Agard, P., Monie, P., Jolivet, L., Goffé, B., 2002. Exhumation of the Schistes Lustres complex: in situ laser probe 40Ar/39Ar constraints and implications for the Western Alps. J. Metamorph. Geol. 20, 599–618. https://doi.org/10.1046/j.1525-1314.2002.00391.x.

Agard, P., Yamato, P., Jolivet, L., Burov, E., 2009. Exhumation of oceanic blueschists and eclogites in subduction zones: Timing and mechanisms. Earth Sci. Rev. 92, 53–79. https://doi.org/10.1016/j.earscirev.2008.11.002.

Agard, P., Yamato, P., Soret, M., Prigent, C., Guillot, S., Plunder, A., Dubacq, B., Chauvet, A., Moni´e, P., 2016. Plate interface rheological switches during subduction infancy: Control on slab penetration and metamorphic sole formation. Earth Planet. Sci. Lett. 451, 208–220. https://doi.org/10.1016/j.epsl.2016.06.054.

Agard, P., Plunder, A., Angiboust, S., Bonnet, G., Ruh, J., 2018. The subduction plate interface: rock record and mechanical coupling (from long to short timescales). Lithos 320–321, 537–566. https://doi.org/10.1016/j.lithos.2018.09.029.

Agard, P., Prigent, C., Soret, M., Dubacq, B., Guillot, S., Deldicque, D., 2020. Slabitization: Mechanisms controlling subduction development and viscous coupling. Earth Sci. Rev. 208, 103259 https://doi.org/10.1016/j.earscirev.2020.103259.

Aleinikoff, J. N., Wintsch, R. P., Tollo, R. P., Unruh, D. M., Fanning, C. M., Schmitz, M. D., 2007. Ages and origins of rocks of the Killingworth dome, south-central Connecticut: Implications for the tectonic evolution of southern New England. American Journal of Science, 307, 63-118.

Allègre, C.J., Le Mouel, J.L., Provost, A., 1982. Scaling rules in rock fracture and possible implications for earthquake prediction. Nature 297, 47–49. https://doi.org/10.1038/297047a0

Alt, J. C., Laverne, C., Vanko, D. A., Tartarotti, P., Teagle, D. A., Bach, W., Zuleger, E., Erzinger, J., Honnorez, J., Pezard, P.A., Becker, K., Salisbury, M.H., Wilkens, R.H., 1996. 34. Hydrothermal alteration of a section of upper oceanic crust in the Eastern Equatorial Pacific: a synthesis of results from site 504 (DSDP LEGS 69, 70, and 83, and ODP LEGS 111, 137,140, and 148). In Proceedings of the Ocean Drilling Program, scientific results Vol. 148, 417-434.

Alt, J.C., Laverne, C., Coggon, R.M., Teagle, D.A.H., Banerjee, N.R., Morgan, S., Smith-Duque, C.E., Harris, M., Galli, L., 2010. Subsurface structure of a submarine hydrothermal system in ocean crust formed at the East Pacific Rise, ODP/IODP Site 1256. Geochem. Geophys. Geosyst. 11. https://doi.org/10.1029/2010GC003144.

Amato, J.M., Johnson, C.M., Baumgartner, L.P., Beard, B.L., 1999. Rapid exhumation of the Zermatt-Saas ophiolite deduced from high-precision Sm-Nd and Rb-Sr geochronology. Earth Planet. Sci. Lett. 171, 425–438. https://doi.org/10.1016/S0012-821X(99)00161-2.

Andersen, T., Burke, E.A.J., Austrheim, H., 1989. Nitrogen-bearing, aqueous fluid inclusions in some eclogites from the Western Gneiss Region of the Norwegian Caledonides. Contrib. Mineral. Petrol. 103, 153–165. https://doi.org/10.1007/BF00378501.

Andersen, T., Austrheim, H., Burke, E.A.J., 1990. Fluid inclusions in granulites and eclogites from the Bergen Arcs, Caledonides ofW. Norway. Mineral. Mag. 54, 145–158. https://doi.org/10.1180/minmag.1990.054.375.02.

Andersen, T., Austrheim, H., Burke, E.A.J., Elvevold, S., 1993. N2 and CO2 in deep crustal fluids: evidence from the Caledonides of Norway. Chem. Geol. 108, 113–132. https://doi.org/10.1016/0009-2541(93)90320-I.

André-Mayer, A.-S., Sausse, J., 2007. Thickness and spatial distribution of veins in a porphyry copper deposit, Rosia Poieni, Romania. Journal of Structural Geology 29, 1695–1708. https://doi.org/10.1016/j.jsg.2007.06.010

Angiboust, S., Agard, P., 2010. Initial water budget: The key to detaching large volumes of eclogitized oceanic crust along the subduction channel? Lithos 120, 453-474.

Angiboust, S., Glodny, J., 2020. Exhumation of eclogitic ophiolitic nappes in the W. Alps: New age data and implications for crustal wedge dynamics. Lithos 356–357, 105374. https://doi.org/10.1016/j.lithos.2020.105374.

Angiboust, S., Agard, P., Jolivet, L., Beyssac, O., 2009. The Zermatt-Saas ophiolite: the largest (60-km wide) and deepest (c. 70-80 km) continuous slice of oceanic lithosphere detached from a subduction zone? Terra Nova 21, 171–180. https://doi.org/10.1111/j.1365-3121.2009.00870.x.

Angiboust, S., Agard, P., Raimbourg, H., Yamato, P., Huet, B., 2011. Subduction interface processes recorded by eclogite-facies shear zones (Monviso, W. Alps). Lithos 127, 222–238. https://doi.org/10.1016/j.lithos.2011.09.004.

Angiboust, S., Agard, P., Yamato, P., Raimbourg, H., 2012a. Eclogite breccias in a subducted ophiolite: A record of intermediate-depth earthquakes? Geology 40, 707–710. https://doi.org/10.1130/G32925.1.

Angiboust, S., Langdon, R., Agard, P., Waters, D., Chopin, C., 2012b. Eclogitization of the Monviso ophiolite (W. Alps) and implications on subduction dynamics. J. Metamorph. Geol. 30, 37–61. https://doi.org/10.1111/j.1525-1314.2011.00951.x.

Angiboust, S., Wolf, S., Burov, E., Agard, P., Yamato, P., 2012c. Effect of fluid circulation on subduction interface tectonic processes: Insights from thermo-mechanical numerical modelling. Earth Planet. Sci. Lett. 357–358, 238–248. https://doi.org/10.1016/j.epsl.2012.09.012.

Angiboust, S., Agard, P., De Hoog, J.C.M., Omrani, J., Plunder, A., 2013. Insights on deep, accretionary subduction processes from the Sistan ophiolitic "Mélange" (Eastern Iran). Lithos 156–159, 139–158. https://doi.org/10.1016/j.lithos.2012.11.007.

Angiboust, S., Pettke, T., De Hoog, J.C.M., Caron, B., Oncken, O., 2014a. Channelized Fluid Flow and Eclogite-facies Metasomatism along the Subduction Shear Zone. Journal of Petrology 55, 883–916. https://doi.org/10.1093/petrology/egu010.

Angiboust, S., Glodny, J., Oncken, O., Chopin, C., 2014b. In search of transient subduction interfaces in the Dent Blanche–Sesia Tectonic System (W. Alps). Lithos 205, 298–321. https://doi.org/10.1016/j.lithos.2014.07.001.

Angiboust, S., Agard, P., Glodny, J., Omrani, J., Oncken, O., 2016. Zagros blueschists: Episodic underplating and long-lived cooling of a subduction zone. Earth Planet. Sci. Lett. 443, 48–58. https://doi.org/10.1016/j.epsl.2016.03.017.

Angiboust, S., Yamato, P., Hertgen, S., Hyppolito, T., Bebout, G.E., Morales, L., 2017. Fluid pathways and high-P metasomatism in a subducted continental slice (Mt. Emilius klippe, W. Alps). J. Metamorph. Geol. 35, 471–492. https://doi.org/10.1111/jmg.12241.

Angiboust, S., Cambeses, A., Hyppolito, T., Glodny, J., Monié, P., Calderon, M.,Juliani, C., 2018. A 100-m.y.-long window onto mass-flow processes in the Patagonian Mesozoic subduction zone (Diego de Almagro Island, Chile). GSA Bull. 130, 1439–1456. https://doi.org/10.1130/B31891.1.

Angiboust, S., Menant, A., Gerya, T., Oncken, O., 2022. The rise and demise of deep accretionary wedges: A long-term field and numerical modeling perspective. Geosphere 18, 69-103.

Araki, E., Saffer, D. M., Kopf, A. J., Wallace, L. M., Kimura, T., Machida, Y., Ide, S., Davis, E., IODP expedition 365 shipboard scientists, 2017. Recurring and triggered slow-slip events near the trench at the Nankai Trough subduction megathrust. Science 356, 1157–1160.

Audet, P., Bürgmann, R., 2014. Possible control of subduction zone slow-earthquake periodicity by silica enrichment. Nature 510, 389–392. https://doi.org/10.1038/nature13391

Audet, P., Bostock, M.G., Christensen, N.I., Peacock, S.M., 2009. Seismic evidence for overpressured subducted oceanic crust and megathrust fault sealing. Nature 457, 76–78.

Austrheim, H., Corfu, F., Renggli, C.J., 2021. From peridotite to fuchsite bearing quartzite via carbonation and weathering: with implications for the Pb budget of continental crust. Contrib Mineral Petrol 176, 94. https://doi.org/10.1007/s00410-021-01851-z.

Bachmann, R., Glodny, J., Oncken, O., Seifert, W., 2009. Abandonment of the South Penninic–Austroalpine palaeosubduction zone, Central Alps, and shift from subduction erosion to accretion: constraints from Rb/Sr geochronology. J. Geol. Soc. 166, 217–231. https://doi.org/10.1144/0016-76492008-024.

Bakker, R.J., Jansen, J.B.H., 1990. Preferential water leakage from fluid inclusions by means of mobile dislocations. Nature 345, 58–60.

Bakker, R.J., Jansen, J.B.H., 1991. Experimental post-entrapment water loss from synthetic CO2-H2O inclusions in natural quartz. Geochim. Cosmochim. Acta 55, 2215–2230.

Bakker, R.J., Jansen, J.B.H., 1994. A mechanism for preferential H2O leakage from fluid inclusions in quartz, based on TEM observations. Contrib. Mineral. Petrol. 116, 7–20.

Balestro, G., Festa, A., Borghi, A., Castelli, D., Gattiglio, M., Tartarotti, P., 2018. Role of Late Jurassic intra-oceanic structural inheritance in the Alpine tectonic evolution of the Monviso meta-ophiolite Complex (Western Alps). Geol. Mag. 155, 233–249. https://doi.org/10.1017/S0016756817000553.

Balestro, G., Festa, A., Dilek, Y., 2019. Structural architecture of the Western Alpine Ophiolites, and the Jurassic seafloor spreading tectonics of the Alpine Tethys. J. Geol. Soc. 176, 913–930. https://doi.org/10.1144/jgs2018-099.

Ballèvre, M., Lagabrielle, Y., 1994. Garnet in blueschist-facies marbles from the Queyras unit (Western Alps): its occurrence and its significance. Schweiz. Mineral. Petrogr. Mitt. 74, 203–212.

Ballèvre, M., Merle, O., 1993. The Combin Fault: compressional reactivation of a Late Cretaceous-Early Tertiary detachment fault in the Western Alps. Schweiz. Mineral. Petrogr. Mitt. 73, 205–227. https://doi.org/10.5169/SEALS-55570.

Ballèvre, M., Kienast, J.-R., Vuichard, J.-P., 1986. La “nappe de la Dent-Blanche” (Alpes occidentales) : deux unités austroalpines indépendantes. Eclogae Geol. Helv. 79, 57–74. https://doi.org/10.5169/SEALS-165826.

Ballèvre, M., Lagabrielle, Y., Merle, O., 1990. Tertiary ductile normal faulting as a consequence of lithospheric stacking in the western Alps. Mémoires de la Société Géologique de France 156, 227–236.

Barféty, J.-C., Polino, R., Mercier, D., 2006. Notice explicative de la feuille Névache-Bardonecchia-Modane à 1/50000 (799) - Orléans : BRGM.

Barnes, J.D., Cisneros, M., 2012. Mineralogical control on the chlorine isotope composition of altered oceanic crust. Chemical Geology 326, 51-60.

Barnes, J.D., Sharp, Z.D., Fischer, T.P., 2008. Chlorine isotope variations across the Izu-Bonin-Mariana arc. Geology 36, 883-886.

Barnes, J.D., Sharp, Z.D., Fischer, T.P., Hilton, D.R., Carr, M.J., 2009. Chlorine isotope variations along the Central American volcanic front and back arc. Geochemistry, Geophysics, Geosystems 10.

Barnes, J.D., Penniston-Dorland, S.C., Bebout, G.E., Hoover, W., Beaudoin, G.M., Agard, P., 2019. Chlorine and lithium behavior in metasedimentary rocks during prograde metamorphism: a comparative study of exhumed subduction complexes (Catalina Schist and Schistes Lustrés). Lithos 336–337, 40–53. https://doi.org/10.1016/j.lithos.2019.03.028.

Barr, H., 1990. Preliminary fluid inclusion studies in a high-grade blueschist terrain, Syros, Greece. Mineral. Mag. 54, 159–168. https://doi.org/10.1180/minmag.1990.054.375.03.

Barré, G., Truche, L., Bazarkina, E.F., Michels, R., Dubessy, J., 2017. First evidence of the trisulfur radical ion S3− and other sulfur polymers in natural fluid inclusions. Chemical Geology 462, 1-14.

Barré, G., Strzerzynski, P., Michels, R., Guillot, S., Cartigny, P., Thomassot, E., Lorgeoux, C., Assayag, N., Truche, L., 2020. Tectono-metamorphic evolution of an evaporitic décollement as recorded by mineral and fluid geochemistry: The “Nappe des Gypses” (Western Alps) case study. Lithos 358, 105419.

Barton, C. C, 1995. Fractal analysis of scaling and spatial clustering of fractures. In Fractals in the earth sciences, Springer, Boston, MA. 141–178.

Barton, C. C, Larsen, E, 1985. Fractal geometry of two-dimensional fracture networks at Yucca Mountain, southwest Nevada. Fundamentals of Rock Joints, Proceedings of the International Symposium on Fundamentals of Rock Joints, Bjorkliden, Lapland, Sweden (0. Stephannson, ed.).

Barton, C.A., Zoback, M.D., 1992. Self-similar distribution and properties of macroscopic fractures at depth in crystalline rock in the Cajon Pass Scientific Drill Hole. J. Geophys. Res. 97, 5181. https://doi.org/10.1029/91JB01674

Bearth, P., 1959. Uber Eklogite, Glaukophanschiefer und metamorphe Pillowlaven. Schweiz. Mineral. Petrogr. Mitt. 39, 267–286.

Bearth, P., 1962. Versuch einer Gliederung alpinmetamorpher Serien der Westalpen.Schweiz. Mineral. Petrogr. Mitt. 42, 127–137.

Bearth, P., 1967. Die Ophiolite der Zone von Zermatt – Saas Fee. Beitr. Geol, Karte Schweiz, p. 132.

Bebout, G.E., 2007. Metamorphic chemical geodynamics of subduction zones. Earth and Planetary Science Letters 260, 373–393. https://doi.org/10.1016/j.epsl.2007.05.050.

Bebout, G.E., Barton, M.D., 1993. Metasomatism during subduction: products and possible paths in the Catalina Schist, California. Chemical Geology 108, 61–92. https://doi.org/10.1016/0009-2541(93)90318-D.

Bebout, G.E., Barton, M.D., 2002. Tectonic and metasomatic mixing in a high-T, subduction-zone mélange—insights into the geochemical evolution of the slab–mantle interface. Chemical Geology 187, 79–106. https://doi.org/10.1016/S0009-2541(02)00019-0.

Bebout, G.E., Penniston-Dorland, S.C., 2016. Fluid and mass transfer at subduction interfaces—The field metamorphic record. Lithos 240–243, 228–258. https://doi.org/10.1016/j.lithos.2015.10.007.

Bebout, G.E., Agard, P., Kobayashi, K., Moriguti, T., Nakamura, E., 2013. Devolatilization history and trace element mobility in deeply subducted sedimentary rocks: Evidence from Western Alps HP/UHP suites. Chem. Geol. 342, 1–20. https://doi.org/10.1016/j.chemgeo.2013.01.009.

Behr, W.M., Becker, T.W., 2018. Sediment control on subduction plate speeds. Earth Planet. Sci. Lett. 502, 166–173. https://doi.org/10.1016/j.epsl.2018.08.057.

Behr, W.M., Bürgmann, R., 2021. What's down there? The structures, materials and environment of deep-seated slow slip and tremor. Phil. Trans. R. Soc. A 379, 20200218. https://doi.org/10.1098/rsta.2020.0218.

Behr, W.M., Kotowski, A.J., Ashley, K.T., 2018. Dehydration-induced rheological heterogeneity and the deep tremor source in warm subduction zones. Geology 46, 475–478. https://doi.org/10.1130/G40105.1.

Beinlich, A., Plümper, O., Hövelmann, J., Austrheim, H., Jamtveit, B., 2012. Massive serpentinite carbonation at Linnajavri, N-Norway: Massive serpentinite carbonation at Linnajavri, N-Norway. Terra Nova 24, 446–455. https://doi.org/10.1111/j.1365-3121.2012.01083.x.

Bellahsen, N., Mouthereau, F., Boutoux, A., Bellanger, M., Lacombe, O., Jolivet, L., Rolland, Y., 2014. Collision kinematics in the western external Alps: Kinematics of the Alpine collision. Tectonics 33, 1055–1088. https://doi.org/10.1002/2013TC003453.

Berger, A., Bousquet, R., 2008. Subduction-related metamorphism in the Alps: review of isotopic ages based on petrology and their geodynamic consequences. Geol. Soc. Lond., Spec. Publ. 298, 117–144. https://doi.org/10.1144/SP298.7.

Beyssac, O., Goffé, B., Chopin, C., Rouzaud, J.N., 2002. Raman spectra of carbonaceous material in metasediments: a new geothermometer. J. Metamorph. Geol. 20, 859–871. https://doi.org/10.1046/j.1525-1314.2002.00408.x.

Beyssac, O., Goffé, B., Petitet, J.-P., Froigneux, E., Moreau, M., Rouzaud, J.-N., 2003. On the characterization of disordered and heterogeneous carbonaceous materials by Raman spectroscopy. Spectrochim. Acta A Mol. Biomol. Spectrosc. 59, 2267–2276. https://doi.org/10.1016/S1386-1425(03)00070-2.

Blake Jr., M.C., 1988. Metamorphic and tectonic evolution of the Franciscan complex, northern California. Metamorphism and Crustal Evolution of the Western United States, pp. 1035–1060.Blenkinsop, T. G, 1991. Cataclasis and processes of particle size reduction. PAGEOPH 136, 59–86.

Blenkinsop, T.G., Fernandes, T.R.C., 2000. Fractal Characterization of Particle Size Distributions in Chromitites from the Great Dyke, Zimbabwe. Pure appl. geophys. 157, 505–521.

Bocchio, R., Benciolini, L., Martin, S., Tartarotti, P., 2000. Geochemistry of eclogitised Fe-Ti-gabbros from various lithological settings (Aosta Valley ophiolites, Italian western Alps). Protolith composition and eclogitic paragenesis. Periodico di Mineralogia 69, 217–237.

Bocquet, J., 1974. Etudes min´eralogiques et p´etrologiques sur les m´etamorphismes d'age alpin dans les alpes françaises. PhD thesis. Université de Grenoble.

Bodinier, J.-L., Menzies, M.A., Thirlwall, M.F., 1991. Continental to Oceanic Mantle Transition–REE and Sr-Nd Isotopic Geochemistry of the Lanzo Lherzolite Massif. J. Petrol. Special_Volume 191–210. https://doi.org/10.1093/petrology/Special_Volume.2.191.

Bodnar, R.J., 1993. Revised equation and table for determining the freezing point depression of H2O-NaCl solutions. Geochim. Cosmochim. Acta 57, 683–684.

Bodnar, R.J., 1994. Synthetic fluid inclusions: XII. The systemH2O-NaCl. Experimental determination of the halite liquidus and isochores for a 40 wt% NaCl solution. Geochim. Cosmochim. Acta 58, 1053–1063.

Bodnar, R.J., 2003a. Introduction to aqueous-elecrolyte fluid inclusions. In: Samson, I., Anderson, A., Marshall, D. (Eds.), Fluid Inclusions: Analysis and Interpretation. 32. Mineral Association of Canada, Short Course, pp. 81–100.

Bodnar, R.J., 2003b. Re-equilibration of fluid inclusions. In: Samson, I., Anderson, A., Marshall, D. (Eds.), Fluid Inclusions: Analysis and Interpretation. 32. Mineral Association of Canada, Short Course, pp. 213–230.

Bonnet, G., Agard, P., Angiboust, S., Moni´e, P., Jentzer, M., Omrani, J., Whitechurch, H., Fournier, M., 2018. Tectonic slicing and mixing processes along the subduction interface: The Sistan example (Eastern Iran). Lithos 310–311, 269–287. https://doi.org/10.1016/j.lithos.2018.04.016.

Bonnet, G., Chopin, C., Locatelli, M., Kylander-Clark, A., R, C., Hacker, B.R., 2022. Submitted. Protracted subduction of the European hyperextended margin exposed in the Dora-Maira massif (W. Alps).

Bons, P.D., Elburg, M.A., Gomez-Rivas, E., 2012. A review of the formation of tectonic veins and their microstructures. Journal of Structural Geology 43, 33–62. https://doi.org/10.1016/j.jsg.2012.07.005

Bostock, M.G., 2013. The Moho in subduction zones. Tectonophysics 609, 547–557. https://doi.org/10.1016/j.tecto.2012.07.007

Bourbon, M., Caron, J.M., Lemoine, M., Tricart, P., 1979. Stratigraphie des schistes lustrés piémontais dans les Alpes cottiennes (Alpes occidentales franco-italiennes): nouvelle interprétation et conséquences géodynamiques. Bull. Soc. Geol. Fr.180–2182.

Bousquet, R., 2008. Metamorphic heterogeneities within a single HP unit: Overprint effect or metamorphic mix? Lithos 103, 46–69. https://doi.org/10.1016/j.lithos.2007.09.010.

Bousquet, R., Oberhansli, R., Goffe, B., Jolivet, L., Vidal, O., 1998. High-pressure-low temperature metamorphism and deformation in the Bundnerschiefer of the Engadine window: implications for the regional evolution of the eastern Central Alps. J. Metamorph. Geol. 16, 657–674. https://doi.org/10.1111/j.1525-1314.1998.00161.x.

Bousquet, R., Goffé, B., Vidal, O., Oberhänsli, R., Patriat, M., 2002. The tectonometamorphic history of the Valaisan domain from the Western to the Central Alps: New constraints on the evolution of the Alps. Geol. Soc. Am. Bull. 114, 207–225. https://doi.org/10.1130/0016-7606(2002)114<0207:TTMHOT>2.0.CO;2.

Bousquet, R., Oberhänsli, R., Goffé, B., Wiederkehr, M., Koller, F., Schmid, S.M., Schuster, R., Engi, M., Berger, A., Martinotti, G., 2008. Metamorphism of metasediments at the scale of an orogen: a key to the Tertiary geodynamic evolution of the Alps. Geol. Soc. Lond., Spec. Publ. 298, 393–411. https://doi.org/10.1144/SP298.18.

Bowtell, S.A., Cliff, R.A., Barnicoat, A.C., 1994. Sm-Nd isotopic evidence on the age of eclogitization in the Zermatt-Saas ophiolite. J. Metamorph. Geol. 12, 187–196. https://doi.org/10.1111/j.1525-1314.1994.tb00013.x.

Brantley, S.L., Fisher, D.M., Deines, P., Clark, M.B., Myers, G., 1997. Segregation veins: Evidence for the deformation and dewatering of a low-grade metapelite, in: Deformation-Enhanced Fluid Transport in the Earth's Crust and Mantle. pp. 267–288.

Braun, M.G., Kelemen, P.B., 2002. Dunite distribution in the Oman Ophiolite: Implications for melt flux through porous dunite conduits. Geochem.-Geophys.-Geosyst. 3, 1–21. https://doi.org/10.1029/2001GC000289

Broadwell, K.S., Locatelli, M., Verlaguet, A., Agard, P., Caddick, M.J., 2019. Transient and periodic brittle deformation of eclogites during intermediate-depth subduction. Earth Planet. Sci. Lett. 521, 91–102. https://doi.org/10.1016/j.epsl.2019.06.008.

Brooks, H.L., Dragovic, B., Lamadrid, H.M., Caddick, M.J., Bodnar, R.J., 2019. Fluid capture during exhumation of subducted lithologies: a fluid inclusion study from Sifnos, Greece. Lithos 332, 120–134.

Bucher, K., Grapes, R., 2009. The Eclogite-facies Allalin Gabbro of the Zermatt-Saas Ophiolite, Western Alps: a Record of Subduction Zone Hydration. J. Petrol. 50, 1405–1442. https://doi.org/10.1093/petrology/egp035.

Bucher, S., Schmid, S.M., Bousquet, R., Fugenschuh, B., 2003. Late-stage deformation in a collisional orogen (Western Alps): nappe refolding, back-thrusting or normal faulting? Terra Nova 15, 109–117. https://doi.org/10.1046/j.1365-3121.2003.00470.x.

Bucher, K., Fazis, Y., De Capitani, C., Grapes, R., 2005. Blueschists, eclogites, and decompression assemblages of the Zermatt-Saas ophiolite: High-pressure metamorphism of subducted Tethys lithosphere. Am. Mineral. 90, 821–835. https://doi.org/10.2138/am.2005.1718.

Busigny, V., Cartigny, P., Philippot, P., Ader, M., Javoy,M., 2003.Massive recycling of nitrogen and other fluid-mobile elements (K, Rb, Cs, H) in a cold slab environment: evidence from HP to UHP oceanic metasediments of the Schistes Lustrés nappe (western Alps, Europe). Earth Planet. Sci. Lett. 215, 27–42. https://doi.org/10.1016/S0012-821X(03)00453-9.

Busigny, V., Cartigny, P., Philippot, P., 2011. Nitrogen isotopes in ophiolitic metagabbros: A re-evaluation of modern nitrogen fluxes in subduction zones and implication for the early Earth atmosphere. Geochim. Cosmochim. Acta 75, 7502–7521. https://doi.org/10.1016/j.gca.2011.09.049.

Busigny, V., Chen, J., Philippot, P., Borensztajn, S., Moynier, F., 2018. Insight into hydrothermal and subduction processes from copper and nitrogen isotopes in oceanic metagabbros. Earth Planet. Sci. Lett. 498, 54–64. https://doi.org/10.1016/j.epsl.2018.06.030.

Caby, R., 1996. Low-angel extrusion of high-pressure rocks and the balance between outward and inward displacements of Middle Penninic units in the western Alps. Eclogae Geol. Helv. 89 (1), 229–267. https://doi.org/10.5169/SEALS-167901.

Caby, R., Kienast, J.R., Saliot, P., 1976. Modèle d'évolution structurale des Alpes occidentales. Colloque International CNRS, Ecologie et Géologie de l'Himalaya 85–92.

Caby, R., Kienast, J.-R., Saliot, P., 1978. Structure, métamorphisme et modèle d'évolution tectonique des Alpes occidentales. Revue de géographie physique et de géologie dynamique Paris 20, 307–322.

Cadoppi, P., Castelletto, M., Sacchi, R., Baggio, P., Carraro, F., Giraud, V., 2002. Note illustrative della carta geologica d'Italia alla scala 1:50000: foglio 154 Susa. ISPRA, Servizio Geologico d'Italia.

Calvert, A.J., Preston, L.A., Farahbod, A.M., 2011. Sedimentary underplating at the Cascadia mantle-wedge corner revealed by seismic imaging. Nature Geosci 4, 545–548. https://doi.org/10.1038/ngeo1195

Cannaò, E., Malaspina, N., 2018. From oceanic to continental subduction: Implications for the geochemical and redox evolution of the supra-subduction mantle. Geosphere 14, 2311–2336. https://doi.org/10.1130/GES01597.1.

Cannaò, E., Scambelluri, M., Bebout, G.E., Agostini, S., Pettke, T., Godard, M., Crispini, L., 2020. Ophicarbonate evolution from seafloor to subduction and implications for deep-Earth C cycling. Chemical Geology 546, 119626. https://doi.org/10.1016/j.chemgeo.2020.119626.

Caron, J.-M., 1974. Rapports entre diverses" generations" de lawsonite et les deformations dans les Schistes lustres des Alpes cottiennes septentrionales (France et Italie). Bulletin de la Société Géologique de France 7, 256–263.

Caron, J.M., 1977. Lithostratigraphie et tectonique des Schistes Lustrés dans les Alpes Cottiennes septentrionales et en Corse orientale. PhD thesis, université de Strasbourg.

Cartwright, I., Buick, I.S., 2000. Fluid generation, vein formation and the degree of fluid-rock interaction during decompression of high-pressure terranes: the Schistes Lustrés, Alpine Corsica, France. Journal of Metamorphic Geology 18, 607–624. https://doi.org/10.1046/j.1525-1314.2000.00280.x

Castelain, T., McCaig, A.M., Cliff, R.A., 2014. Fluid evolution in an Oceanic Core Complex: a fluid inclusion study from IODP hole U1309 D—Atlantis Massif, 30°N, Mid-Atlantic Ridge. Geochem. Geophys. Geosyst. 15, 1193–1214. https://doi.org/10.1002/2013GC004975.

Caumon, M.-C., Dubessy, J., Robert, P., Tarantola, A., 2013. Fused-silica capillary capsules (FSCCs) as reference synthetic aqueous fluid inclusions to determine chlorinity by Raman spectroscopy. ejm 25, 755–763. https://doi.org/10.1127/0935-1221/2013/0025-2280.

Caumon,M.-C., Tarantola, A.,Mosser-Ruck, R., 2015. Raman spectra of water in fluid inclusions: I. Effect of host mineral birefringence on salinity measurement: effect of mineral birefringence on salinity measured by Raman spectroscopy. J. Raman Spectrosc.46, 969–976. https://doi.org/10.1002/jrs.4708.

Cerchiari, A., Remitti, F., Mittempergher, S., Festa, A., Lugli, F., Cipriani, A., 2020. Cyclical variations of fluid sources and stress state in a shallow megathrust-zone mélange. Journal of the Geological Society 177, 647–659. https://doi.org/10.1144/jgs2019-072

Chiba, K., 2020. Stress state along the western Nankai Trough subduction zone inferred from b-values, long-term slow-slip events, and low-frequency earthquakes. Earth Planets Space 72, 3. https://doi.org/10.1186/s40623-020-1130-7

Chiba, K., 2019. Spatial and temporal distributions of b-values related to long-term slow-slip and low-frequency earthquakes in the Bungo Channel and Hyuga-nada regions, Japan. Tectonophysics 757, 1–9. https://doi.org/10.1016/j.tecto.2019.02.021

Chopin, C., 1978. Les paragenèses réduites ou oxydées de concentrations manganésifères des «schistes lustrés» de Haute-Maurienne (Alpes françaises). Bull. Mineral. 101, 514–531.

Chopin, C., 1979. De la Vanoise au massif du Grand Paradis, Une approche pétrographique et radiochronologique de la signification géodynamique du métamorphisme de haute pression. PhD thesis. Université Pierre et Marie Curie, Paris 6.

Chopin, C., 1984. Coesite and pure pyrope in high-grade blueschists of the Western Alps: a first record and some consequences. Contrib. Mineral. Petrol. 86, 107–118. https://doi.org/10.1007/BF00381838.

Chopin, C., Maluski, H., 1980. 40Ar-39Ar dating of high pressure metamorphic micas from the Gran Paradiso area (Western Alps): Evidence against the blocking temperature concept. Contrib. Mineral. Petrol. 74, 109–122.

Clark, M.B., Brantley, S.L., Fisher, D.M., 1995. Power-law vein-thickness distributions and positive feedback in vein growth. Geol 23, 975–978. https://doi.org/10.1130/0091-7613(1995)023<0975:PLVTDA>2.3.CO;2

Coleman, R.G., 1971. Plate tectonic emplacement of upper mantle peridotites along continental edges. Journal of Geophysical Research 76, 1212-1222.

Compagnoni, R., Rolfo, F., 2003. UHPM units in the Western Alps. In: Papp, G., Weiszburg, T.G., Carswell, D.A., Compagnoni, R., Rolfo, F. (Eds.), Ultrahigh Pressure Metamorphism. Mineralogical Society of Great Britain and Ireland, Budapest, pp. 13–49. https://doi.org/10.1180/EMU-notes.5.2.

Connolly, J.A.D., 1990. Multivariable phase diagrams: an algorithm based on generalized thermodynamics. Am. J. Sci. 290, 666–718.

Connolly, J.A.D., 2005. Computation of phase equilibria by linear programming: A tool for geodynamic modeling and its application to subduction zone decarbonation. Earth Planet. Sci. Lett. 236, 524–541. https://doi.org/10.1016/j.epsl.2005.04.033.

Connolly, J.A.D., 2009. The geodynamic equation of state: What and how. Geochem. Geophys. Geosyst. 10, n/a-n/a. https://doi.org/10.1029/2009GC002540.

Cook-Kollars, J., Bebout, G.E., Collins, N.C., Angiboust, S., Agard, P., 2014. Subduction zone metamorphic pathway for deep carbon cycling: I. Evidence from HP/UHP metasedimentary rocks, Italian Alps. Chem. Geol. 386, 31–48. https://doi.org/10.1016/j.chemgeo.2014.07.013.

Corno, A., Mosca, P., Borghi, A., Gatteggio, M., 2019. Lithostratigraphy and petrography of the Monte Banchetta-Punta Rognosa oceanic succession (Troncea and Chisonetto Valleys, Western Alps). Ofioliti 44. https://doi.org/10.4454/ofioliti.v44i2.526.

Corno, A., Groppo, C., Mosca, P., Borghi, A., Gattiglio, M., 2021. Eclogitic metamorphism in the Alpine far-west: petrological constraints on the Banchetta-Rognosa tectonic unit (Val Troncea, Western Alps). Swiss J. Geosci. 114, 16. https://doi.org/10.1186/s00015-021-00393-7.

Cox, D. R, Lewis, P. A. W, 1966. The Statistical Analysis of Series of Events. Methuen, London.

Cox, S.F., 1987. Antitaxial crack-seal vein microstructures and their relationship to displacement paths. Journal of Structural Geology 9, 779–787. https://doi.org/10.1016/0191-8141(87)90079-4

Cubas, N., Agard, P., Tissandier, R., 2022. Submitted. Predicting earthquake ruptures from topography.

Dal Piaz, G.V., 1974a. Le métamorphisme de haute pression et basse température dans l'évolution structurale du bassin ophiolitique alpino-apenninique. 1ère partie : Considérations paléogéographiques. Boll. Soc. Geol. Ital. 93, 437–467.

Dal Piaz, G.V., 1974b. Le métamorphisme de haute pression et basse température dansl'évolution structurale du bassin ophiolitique alpino-apenninique. Schweiz. Mineral. Petrogr. Mitt. 54, 399–424.

Dal Piaz, G.V., Cortiana, G., Del Moro, A., Martin, S., Pennachioni, G., Tartarotti, P., 2001. Tertiary age and paleostructural inferences of the eclogitic imprint in the Austroalpine outliers and Zermatt-Saas ophiolite, western Alps. Int. J. Earth Sci. (Geol Rundsch) 90, 668–684.

Dal Piaz, G.V., Gianotti, F., Monopoli, B., Pennachioni, G., Tartarotti, P., Schiavo, A., 2010. Note illustrative della carta geologica d'Italia alla scala 1:50000: foglio 091 Chatillon. ISPRA, Servizio Geologico d'Italia.

Dal Zilio, L., Lapusta, N., Avouac, J., 2020. Unraveling Scaling Properties of Slow-Slip Events. Geophys. Res. Lett. 47. https://doi.org/10.1029/2020GL087477

Davis, D.W., Lowenstein, T.K., Spencer, R.J., 1990. Melting behavior of fluid inclusions in laboratory-grown halite crystals in the systems NaCl-H2O, NaCl-KCl-H2O, NaCl-MgCl2-H2O, and NaCl-CaCl2-H2O. Geochim. Cosmochim. Acta 54, 591–601.

de Meyer, C.M.C., Baumgartner, L.P., Beard, B.L., Johnson, C.M., 2014. Rb–Sr ages from phengite inclusions in garnets from high pressure rocks of the Swiss Western Alps. Earth Planet. Sci. Lett. 395, 205–216. https://doi.org/10.1016/j.epsl.2014.03.050.

De Togni, M., Gattiglio, M., Ghignone, S., Festa, A., 2021. Pre-Alpine Tectono-Stratigraphic Reconstruction of the Jurassic Tethys in the High-Pressure Internal Piedmont Zone (Stura di Viù Valley, Western Alps). Minerals 11, 361. https://doi.org/10.3390/min11040361.

De Wever, P., Caby, R., 1981. Datation de la base des schistes lustrés postophiolitiques par des radiolaires (Oxfordien-Kimmeridgien moyen) dans les Alpes Cottiennes (Saint Véran, France). Comptes Rendus de l'Académie des Sciences de Paris 292, 467–472.

De Wever, P., Baumgartner, P.O., Polino, R., 1987a. Précision sur les datations de la base des Schistes Lustrés postophiolitiques dans les Alpes cottiennes. Comptes Rendus de l'Académie des Sciences de Paris 305, 487–491.

De Wever, P., Danelian, T., Durand-Delga, M., Cordey, M., Kito, N., 1987b. Datations des radiolarites post-ophiolitiques de Corse alpine à l'aide des Radiolaires. Comptes Rendus de l'Académie des Sciences de Paris 305, 893–900.

Debelmas, J., Caby, R., Desmons, J., 1991. Notice explicative de la feuille Sainte-Foy-Tarentaise à 1/50000 (728) - Orléans : BRGM.

Debret, B., Nicollet, C., Andreani, M., Schwartz, S., Godard, M., 2013. Three steps of serpentinization in an eclogitized oceanic serpentinization front (Lanzo Massif - Western Alps). J. Metamorph. Geol. 31, 165–186. https://doi.org/10.1111/jmg.12008.

Debret, B., Koga, K.T., Cattani, F., Nicollet, C., Van den Bleeken, G., Schwartz, S., 2016. Volatile (Li, B, F and Cl) mobility during amphibole breakdown in subduction zones. Lithos 244, 165–181. https://doi.org/10.1016/j.lithos.2015.12.004.

Debret, B., Bouilhol, P., Pons, M.L., Williams, H., 2018. Carbonate Transfer during the Onset of Slab Devolatilization: New Insights from Fe and Zn Stable Isotopes. Journal of Petrology 59, 1145–1166. https://doi.org/10.1093/petrology/egy057.

Decandia, F.A., Elter, P., 1969. Riflessioni sul problema delle ofioliti nell'Appennino settentrionale (Nota preliminare). Atti Societa Toscana delle Science Naturali: memorie Serie A 76, 1–9.

Decandia, F.A., Elter, P., 1972. La" zona" ofiolitifera del Bracco nel settore compreso fra Levanto e la Val Gravena (Apennino ligure). Boll. Soc. Geol. Ital. 11, 37–64.

Decrausaz, T., Müntener, O., Manzotti, P., Lafay, R., Spandler, C., 2021. Fossil oceanic core complexes in the Alps. New field, geochemical and isotopic constraints from the Tethyan Aiguilles Rouges Ophiolite (Val d'H´erens, Western Alps, Switzerland). Swiss J. Geosci. 114, 3. https://doi.org/10.1186/s00015-020-00380-4.

Delaloye, M., Desmons, J., 1976. K-Ar Radiometric Age Determinations of White Micas from the Piemont Zone, French-Italian Western Alps. Contrib. Mineral. Petrol. 57, 297–303. https://doi.org/10.1007/BF03542939.

Delaney, J.R., Mogk, D.W., Mottl, M., 1987. Quartz-cemented breccias from the Mid-Atlantic Ridge: Samples of a high-salinity hydrothermal upflow zone. J. Geophys. Res. 92, 9175–9192.

Delph, J.R., Levander, A., Niu, F., 2018. Fluid Controls on the Heterogeneous Seismic Characteristics of the Cascadia Margin. Geophys. Res. Lett. 45. https://doi.org/10.1029/2018GL079518

Delph, J.R., Thomas, A.M., Levander, A., 2021. Subcretionary tectonics: Linking variability in the expression of subduction along the Cascadia forearc. Earth and Planetary Science Letters 556, 116724. https://doi.org/10.1016/j.epsl.2020.116724

Deville, E., 1986. La klippe de la Pointe du Grand Vallon (Vanoise-Alpes occidentales) : un lambeau de métasédiments à foraminifères du Maastrichtien supérieur couronnant les nappes de « schistes lustrés ». Comptes rendus de l'Acad´emie des sciences. Série 2. Mécanique, Physique, Chimie, Sciences de l'univers, Sciences de la Terre 303, 1221–1226.

Deville, E., 1987. Etude géologique en Vanoise orientale (Alpes occidentales, Savoie). De la naissance à la structuration d'un secteur de la paléo-marge européenne et de l'océan téthysien : aspects stratigraphiques, pétrographiques et tectoniques. PhD thesis. Université de Savoie.

Deville, E., Fudral, S., Lagabrielle, Y., Marthaler, M., Sartori, M., 1992. From oceanic closure to continental collision: A synthesis of the" Schistes lustrés" metamorphic complex of the Western Alps. Geol. Soc. Am. Bull. 104, 127–139.

Dewey, J.F., Bird, J.M., 1971. Origin and emplacement of the ophiolite suite: Appalachian ophiolites in Newfoundland. Journal of Geophysical Research 76, 3179-3206.

Diamond, L.W., 2003. Introduction to gas-bearing, aqueous fluid inclusions. In: Samson, I., Anderson, A., Marshall, D. (Eds.), Fluid inclusions: Analysis and Interpretation. 32. Mineral Association of Canada, Short Course, pp. 101–158.

Diamond, L.W., Tarantola, A., 2015. Interpretation of fluid inclusions in quartz deformed by weak ductile shearing: Reconstruction of differential stress magnitudes and predeformation fluid properties. Earth Planet. Sci. Lett. 417, 107–119. https://doi.org/10.1016/j.epsl.2015.02.019.

Diamond, L.W., Tarantola, A., Stünitz, H., 2010. Modification of fluid inclusions in quartz by deviatoric stress. II: experimentally induced changes in inclusion volume and composition. Contrib. Mineral. Petrol. 160, 845–864. https://doi.org/10.1007/s00410-010-0510-6.

Dilek, Y., Furnes, H., 2011. Ophiolite genesis and global tectonics: Geochemical and tectonic fingerprinting of ancient oceanic lithosphere. Bulletin 123, 387-411.

Dragert, H., Wang, K., James, T.S., 2001. A Silent Slip Event on the Deeper Cascadia Subduction Interface. Science 292, 1525–1528. https://doi.org/10.1126/science.1060152

Dragovic, B., Angiboust, S., Tappa, M.J., 2020. Petrochronological close-up on the thermal structure of a paleo-subduction zone (W. Alps). Earth Planet. Sci. Lett. 547, 116446 https://doi.org/10.1016/j.epsl.2020.116446.

Droop, G.T.R., Lombardo, B., Pognante, U., 1990. Formation and distribution of eclogite facies rocks in the Alps. In: Carswell, D.A. (Ed.), Eclogite Facies Rocks: Glasgow. Blackie, United Kingdom, pp. 225–259.

Duchène, S., Blichert-Toft, J., Luais, B., Télouk, P., Lardeaux, J.-M., Albar`ede, F., 1997. The Lu–Hf dating of garnets and the ages of the Alpine high-pressure metamorphism. Nature 387, 586–589. https://doi.org/10.1038/42446.

Duesterhoeft, E., Quinteros, J., Oberhänsli, R., Bousquet, R., de Capitani, C., 2014. Relative impact of mantle densification and eclogitization of slabs on subduction dynamics: A numerical thermodynamic/thermokinematic investigation of metamorphic density evolution. Tectonophysics 637, 20–29. https://doi.org/10.1016/j.tecto.2014.09.009.

Dumitru, T.A., Wakabayashi, J., Wright, J.E., Wooden, J.L., 2010. Early Cretaceous transition from nonaccretionary behavior to strongly accretionary behavior within the Franciscan subduction complex. Tectonics 29. https://doi.org/10.1029/2009TC002542.

Dumont, T., Lemoine, M., Tricart, P., 1984. Pérennité de la sédimentation pélagique du Jurassique supérieur jusque dans le crétacé supérieur au-dessus de la croûte océanique téthysienne ligure : la série supra-ophiolitique du lac des Cordes (zone piémontaise des Alpes occidentales au SE de Briançon). Comptes rendus de l'Académie des sciences. Série 2. Mécanique, Physique, Chimie, Sciences de l'univers, Sciences de la Terre 7, 921–933.

El-Shazly, A.K., Sisson, V.B., 1999. Retrograde evolution of eclogite facies rocks from NE Oman: evidence from fluid inclusions and petrological data. Chem. Geol. 154, 193–223. https://doi.org/10.1016/S0009-2541(98)00132-6.

El-Shazly, A.K., Sisson, V.B., 2004. Fluid inclusions in carpholite-bearing metasediments and blueschists from NE Oman: Constraints on P-T evolution. Eur. J. Mineral. 16, 221–233. https://doi.org/10.1127/0935-1221/2004/0016-0221.

Ellero, A., Loprieno, A., 2018. Nappe stack of Piemonte–Ligurian units south of Aosta Valley: New evidence from Urtier Valley (Western Alps). Geol. J. 53, 1665–1684. https://doi.org/10.1002/gj.2984.

Elter, G., 1971. Schistes lustrés et ophiolites de la zone piémontaise entre Orco et Doire Baltée (Alpes Graies). Hypoth`eses sur l'origine des ophiolites. Géologie Alpine 47,147–169.

Endo, S., 2010. Pressure-temperature history of titanite-bearing eclogite from the Western Iratsu body, Sanbagawa Metamorphic Belt, Japan: Titanite eclogite from Sanbagawa Belt. Island Arc 19, 313–335. https://doi.org/10.1111/j.1440-1738.2010.00708.x.

Epstein, G.S., Bebout, G.E., Angiboust, S., Agard, P., 2020. Scales of fluid-rock interaction and carbon mobility in the deeply underplated and HP-Metamorphosed Schistes Lustrés, Western Alps. Lithos 354–355, 105229. https://doi.org/10.1016/j.lithos.2019.105229.

Epstein, G.S., Bebout, G.E., Angiboust, S., 2021. Fluid and mass transfer along transient subduction interfaces in a deep paleo-accretionary wedge (Western Alps). Chemical Geology 559, 119920. https://doi.org/10.1016/j.chemgeo.2020.119920.

Ernst, W.G., 1988. Tectonic history of subduction zones inferred from retrograde blueschist PT paths. Geology 16, 1081-1084.

Ernst, W.G., 1993. Metamorphism of Franciscan tectonostratigraphic assemblage, Pacheco Pass area, east-central Diablo Range, California coast ranges. Geol. Soc. Am. Bull. 105, 618–636.

Escayola, M., Garuti, G., Zaccarini, F., Proenza, J.A., Bedard, J.H., Van Staal, C., 2011. Chromitite and platinum-group-element mineralization at middle arm brook, Central Advocate ophiolite complex, Baie Verte peninsula, Newfoundland, Canada. The Canadian Mineralogist 49, 1523–1547. https://doi.org/10.3749/canmin.49.6.1523.

Escuder-Viruete, J., Pérez-Estaún, A., 2006. Subduction-related P–T path for eclogites and garnet glaucophanites from the Samaná Peninsula basement complex, northern Hispaniola. Int. J. Earth Sci. (Geol Rundsch) 95, 995–1017. https://doi.org/10.1007/s00531-006-0079-5.

Fagereng, Å., 2011. Fractal vein distributions within a fault-fracture mesh in an exhumed accretionary mélange, Chrystalls Beach Complex, New Zealand. Journal of Structural Geology 33, 918–927. https://doi.org/10.1016/j.jsg.2011.02.009

Fagereng, Å., Cooper, A.F., 2010. The metamorphic history of rocks buried, accreted and exhumed in an accretionary prism: an example from the Otago Schist, New Zealand. Journal of Metamorphic Geology 28, 935–954. https://doi.org/10.1111/j.1525-1314.2010.00900.x

Fagereng, Å., Harris, C., 2014. Interplay between fluid flow and fault–fracture mesh generation within underthrust sediments: geochemical evidence from the Chrystalls Beach Complex, New Zealand. Tectonophysics, 612, 147-157.

Fagereng, Å., Remitti, F., Sibson, R.H., 2010. Shear veins observed within anisotropic fabric at high angles to the maximum compressive stress. Nature Geosci 3, 482–485. https://doi.org/10.1038/ngeo898

Fagereng, Å., Remitti, F., Sibson, R.H., 2011. Incrementally developed slickenfibers — Geological record of repeating low stress-drop seismic events? Tectonophysics 510, 381–386. https://doi.org/10.1016/j.tecto.2011.08.015

Falk, E.S., Kelemen, P.B., 2015. Geochemistry and petrology of listvenite in the Samail ophiolite, Sultanate of Oman: Complete carbonation of peridotite during ophiolite emplacement. Geochimica et Cosmochimica Acta 160, 70–90. https://doi.org/10.1016/j.gca.2015.03.014.

Fermi, E., 1931. Über den ramaneffekt des kohlendioxyds. Zeitschrift für Physik 71, 250–259.

Fisher, D.M., Brantley, S.L., 1992. Models of quartz overgrowth and vein formation: Deformation and episodic fluid flow in an ancient subduction zone. J. Geophys. Res. 97, 20043. https://doi.org/10.1029/92JB01582

Fisher, D.M., Brantley, S.L., 2014. The role of silica redistribution in the evolution of slip instabilities along subduction interfaces: Constraints from the Kodiak accretionary complex, Alaska. Journal of Structural Geology 69, 395–414. https://doi.org/10.1016/j.jsg.2014.03.010

Fisher, D., Byrne, T., 1990. The character and distribution of mineralized fractures in the Kodiak Formation, Alaska: Implications for fluid flow in an underthrust sequence. J. Geophys. Res. 95, 9069. https://doi.org/10.1029/JB095iB06p09069.

Fisher, D.M., Brantley, S.L., Everett, M., Dzvonik, J., 1995. Cyclic fluid flow through a regionally extensive fracture network within the Kodiak accretionary prism. J. Geophys. Res. 100, 12881–12894. https://doi.org/10.1029/94JB02816

Fontaine, F.J., Wilcock, W.S.D., 2006. Dynamics and storage of brine in mid-ocean ridge hydrothermal systems. J. Geophys. Res. 111. https://doi.org/10.1029/2005JB003866.

Fontaine, F.J., Wilcock, W.S.D., Butterfield, D.A., 2007. Physical controls on the salinity of mid-ocean ridge hydrothermal vent fluids. Earth Planet. Sci. Lett. 257, 132–145. https://doi.org/10.1016/j.epsl.2007.02.027.

Foxford, K.A., Nicholson, R., Polya, D.A., Hebblethwaite, R.P.B., 2000. Extensional failure and hydraulic valving at Minas da Panasqueira, Portugal: evidence from vein spatial distributions, displacements and geometries. Journal of Structural Geology 22, 1065–1086. https://doi.org/10.1016/S0191-8141(00)00029-8

Frezzotti, M.L., 2019. Diamond growth from organic compounds in hydrous fluids deep within the Earth. Nat. Commun. 10, 4952. https://doi.org/10.1038/s41467-019-12984-y.

Frezzotti, M.L., Ferrando, S., 2015. The chemical behavior of fluids released during deep subduction based on fluid inclusions. Am. Mineral. 100, 352–377. https://doi.org/10.2138/am-2015-4933.

Frezzotti, M.L., Selverstone, J., Sharp, Z.D., Compagnoni, R., 2011. Carbonate dissolution during subduction revealed by diamond-bearing rocks from the Alps. Nat. Geosci. 4, 703–706. https://doi.org/10.1038/ngeo1246.

Frezzotti, M.L., Tecce, F., Casagli, A., 2012. Raman spectroscopy for fluid inclusion analysis. Journal of Geochemical Exploration 112, 1–20. https://doi.org/10.1016/j.gexplo.2011.09.009.

Frezzotti, M.-L., Huizenga, J.-M., Compagnoni, R., Selverstone, J., 2014. Diamond formation by carbon saturation in C–O–H fluids during cold subduction of oceanic lithosphere. Geochim. Cosmochim. Acta 143, 68–86. https://doi.org/10.1016/j.gca.2013.12.022.

Fry, N., Barnicoat, A.C., 1987. The tectonic implications of high-pressure metamorphism in the western Alps. J. Geol. Soc. 144, 653–659. https://doi.org/10.1144/gsjgs.144.4.0653.

Fudral, S., 1996. Etude géologique de la suture tethysienne dans les Alpes francoitaliennes Nord-Occidentales de la Doire Ripaire (Italie) `a la région de Bourg Saint-Maurice. PhD thesis. Université de Savoie.

Fudral, S., Deville, E., Marthaler, M., 1987. Distinction de trois ensembles d'unités dans les «Schistes lustrés» compris entre la Vanoise et le Val de Suse (Alpes franco-italiennes septentrionales): aspects lithostratigraphiques, paléogéographiques et géodynamiques. Comptes rendus de l'Académie des sciences. Série 2. Mécanique, Physique, Chimie, Sciences de l'univers, Sciences de la Terre 305, 467–472.

Gabalda, S., Beyssac, O., Jolivet, L., Agard, P., Chopin, C., 2009. Thermal structure of a fossil subduction wedge in the Western Alps. Terra Nova 21, 28–34. https://doi.org/10.1111/j.1365-3121.2008.00849.x.

Ganzhorn, A.C., Pilorgé, H., Reynard, B., 2019. Porosity of metamorphic rocks and fluid migration within subduction interfaces. Earth and Planetary Science Letters 522, 107–117. https://doi.org/10.1016/j.epsl.2019.06.030

Gao, J., Klemd, R., 2000. Eclogite occurrences in the Southern Tianshan high-pressure belt, Xinjiang, Western China. Gondwana Res. 3, 33–38.

Gao, J., Klemd, R., 2001. Primary fluids entrapped at blueschist to eclogite transition: evidence from the Tianshan meta-subduction complex in northwestern China. Contrib. Mineral. Petrol. 142, 1–14.

Gao, J., Klemd, R., Zhang, L., Wang, Z., Xiao, X., 1999. P-T path of high-pressure/low-temperature rocks and tectonic implications in the western Tianshan Mountains, NW China. J. Metamorph. Geol. 17, 621–636. https://doi.org/10.1046/j.1525-1314.1999.00219.x.

Gao, H., Schmidt, D.A., Weldon, R.J., 2012. Scaling Relationships of Source Parameters for Slow Slip Events. Bulletin of the Seismological Society of America 102, 352–360. https://doi.org/10.1785/0120110096

Garber, J.M., Smye, A.J., Feineman, M.D., Kylander-Clark, A.R.C., Matthews, S., 2020a. Decoupling of zircon U–Pb and trace-element systematics driven by U diffusion in eclogite-facies zircon (Monviso meta-ophiolite, W. Alps). Contrib. Mineral. Petrol.175, 55. https://doi.org/10.1007/s00410-020-01692-2.

Garber, J.M., Rioux, M., Kylander-Clark, A.R.C., Hacker, B.R., Vervoort, J.D., Searle, M.P., 2020b. Petrochronology of Wadi Tayin Metamorphic Sole Metasediment, With Implications for the Thermal and Tectonic Evolution of the Samail Ophiolite (Oman/UAE). Tectonics 39. https://doi.org/10.1029/2020TC006135.

Geist, E. L, Bilek, S. L, 2001. Effect of depth-dependent shear modulus on tsunami generation along subduction zones. Geophysical Research Letters 28, 1315–1318.

Ghignone, S., Borghi, A., Balestro, G., Castelli, D., Gattiglio, M., Groppo, C., 2021a. HP tectono-metamorphic evolution of the Internal Piedmont Zone in Susa Valley (Western Alps): New petrologic insight from garnet+chloritoid-bearing micaschists and Fe–Ti metagabbro. J. Metamorph. Geol. 39, 391–416.

Ghignone, S., Sudo, M., Balestro, G., Borghi, A., Gattiglio, M., Ferrero, S., van Schijndel, V., 2021b. Timing of exhumation of meta-ophiolite units in the Western Alps: New tectonic implications from 40Ar/39Ar white mica ages from Piedmont Zone (Susa Valley). Lithos 404–405, 106443. https://doi.org/10.1016/j.lithos.2021.106443.

Giaramita, M.J., Sorensen, S.S., 1994. Primary fluids in low-temperature eclogites: evidence from two subduction complexes (Dominican Republic, and California, USA). Contrib. Mineral. Petrol. 117, 279–292. https://doi.org/10.1007/BF00310869.

Gilio, M., 2020. Fingerprinting and relocating tectonic slices along the plate interface: Evidence from the Lago Superiore unit at Monviso (Western Alps). Lithos, 105308.

Gillespie, P.A., Howard, C.B., Walsh, J.J., Watterson, J., 1993. Measurement and characterisation of spatial distributions of fractures. Tectonophysics 226, 113-141.

Gillespie, P.A., Johnston, J.D., Loriga, M.A., McCaffrey, K.J.W., Walsh, J.J., Watterson, J., 1999. Influence of layering on vein systematics in line samples. Geological Society, London, Special Publications 155, 35–56. https://doi.org/10.1144/GSL.SP.1999.155.01.05

Giuntoli, F., Viola, G., 2021. Cyclic Brittle-Ductile Oscillations Recorded in Exhumed High-Pressure Continental Units: A Record of Deep Episodic Tremor and Slow Slip Events in the Northern Apennines. Geochem Geophys Geosyst 22. https://doi.org/10.1029/2021GC009805

Godard, M., Carter, E.J., Decrausaz, T., Lafay, R., Bennett, E., Kourim, F., Obeso, J. -C., Michibayashi, K., Harris, M., Coggon, J.A., Teagle, D.A.H., Kelemen, P.B., the Oman Drilling Project Phase 1 Science Party, 2021. Geochemical Profiles Across the Listvenite-Metamorphic Transition in the Basal Megathrust of the Semail Ophiolite: Results From Drilling at OmanDP Hole BT1B. JGR Solid Earth 126. https://doi.org/10.1029/2021JB022733.

Goffé, B., 1982. Définition du faciès A Fe Mg carpholite-chloritoïde, un marqueur du métamorphisme de HP-BT dans les métasédiments alumineux. PhD thesis Université Pierre et Marie Curie-Paris VI.

Goffé, B., Bousquet, R., 1997. Ferrocarpholite, chloritoid and lawsonite in metapelites of the Versoyen and Petit St Bernard units (Valais zone, Western Alps). Schweiz. Mineral. Petrogr. Mitt. 77, 137–147.

Goffé, B., Chopin, C., 1986. High-pressure metamorphism in the Western Alps : zoneography of metapelites, chronology and consequences. Schweiz. Mineral. Petrogr. Mitt. 66, 41–52. https://doi.org/10.5169/SEALS-50880.

Goffé, B., Velde, B., 1984. Contrasted metamorphic evolutions in thrusted cover units of the Briançonnais zone (French Alps): a model for the conservation of HP-LT metamorphic mineral assemblages. Earth Planet. Sci. Lett. 68, 351–360.

Goffé, B., Villey, M., 1984. Texture d'un matériel carboné impliqué dans un métamorphisme haute pression-basse température (Alpes françaises). Les hautes pressions influencent-elles la carbonification ? Bull. Mineral. 107, 81–91. https://doi.org/10.3406/bulmi.1984.7795.

Goffé, B., Schwartz, S., Lardeaux, J.-M., Bousquet, R., 2004. Explanatory notes of the map: metamorphic structure of the Alps Western and Ligurian Alps. Mitt. Österr. Miner. Ges. 125–144.

Gomberg, J., Wech, A., Creager, K., Obara, K., Agnew, D., 2016. Reconsidering earthquake scaling. Geophys. Res. Lett. 43, 6243–6251. https://doi.org/10.1002/2016GL069967

Gouzu, C., Itaya, T., Hyodo, H., Matsuda, T., 2006. Excess 40Ar-free phengite in ultrahigh-pressure metamorphic rocks from the Lago di Cignana area, Western Alps. Lithos 92, 418–430. https://doi.org/10.1016/j.lithos.2006.03.056.

Gouzu, C., Yagi, K., Thanh, N.X., Itaya, T., Compagnoni, R., 2016. White mica K–Ar geochronology of HP–UHP units in the Lago di Cignana area, western Alps, Italy: Tectonic implications for exhumation. Lithos 248–251, 109–118. https://doi.org/10.1016/j.lithos.2016.01.015.

Gratier, J. P., Dysthe, D. K., & Renard, F., 2013. The role of pressure solution creep in the ductility of the Earth's upper crust. Advances in geophysics, 54, 47-179.

Groppo, C., Castelli, D., 2010. Prograde P–T Evolution of a Lawsonite Eclogite from the Monviso Meta-ophiolite (Western Alps): Dehydration and Redox Reactions during Subduction of Oceanic FeTi-oxide Gabbro. J. Petrol. 51, 2489–2514. https://doi.org/10.1093/petrology/egq065.

Groppo, C., Beltrando, M., Compagnoni, R., 2009. The P-T path of the ultra-high pressure Lago Di Cignana and adjoining high-pressure meta-ophiolitic units: insights into the evolution of the subducting Tethyan slab. J. Metamorph. Geol. 27, 207–231. https://doi.org/10.1111/j.1525-1314.2009.00814.

Groppo, C., Rolfo, F., Sachan, H.K., Rai, S.K., 2016. Petrology of blueschist from the Western Himalaya (Ladakh, NW India): Exploring the complex behavior of a lawsonite bearing system in a paleo-accretionary setting. Lithos 252–253, 41–56. https://doi.org/10.1016/j.lithos.2016.02.014.

Guillot, S., Hattori, K., Agard, P., Schwartz, S., Vidal, O., 2009. Exhumation Processes in Oceanic and Continental Subduction Contexts: A Review. In: Lallemand, S., Funiciello, F. (Eds.), Subduction Zone Geodynamics, Frontiers in Earth Sciences. Springer, Berlin Heidelberg, Berlin, Heidelberg, pp. 175–205. https://doi.org/10.1007/978-3-540-87974-9_10.

Guillot, S., Schwartz, S., Reynard, B., Agard, P., Prigent, C., 2015. Tectonic significance of serpentinites. Tectonophysics 646, 1–19. https://doi.org/10.1016/j.tecto.2015.01.020.

Gutenberg, B, Richter, C. F, 1954. Seismicity of the Earth. Princeton University Press, Princeton.

Gyomlai, T., Agard, P., Marschall, H.R., Jolivet, L., Gerdes, A., 2021. Metasomatism and deformation of block-in-matrix structures in Syros: The role of inheritance and fluid-rock interactions along the subduction interface. Lithos 386–387, 105996. https://doi.org/10.1016/j.lithos.2021.105996.

Hacker, B.R., 2008. H 2 O subduction beyond arcs. Geochem. Geophys. Geosyst. 9. https://doi.org/10.1029/2007GC001707.

Hacker, B.R., Peacock, S.M., Abers, G.A., Holloway, S.D., 2003. Subduction factory 2. Are intermediate-depth earthquakes in subducting slabs linked to metamorphic dehydration reactions? J. Geophys. Res. 108 https://doi.org/10.1029/2001JB001129.

Hall, D.L., Sterner, S.M., 1993. Preferential water loss from synthetic fluid inclusions. Contrib. Mineral. Petrol. 114, 489–500. https://doi.org/10.1007/BF00321753.

Halls, C., Zhao, R., 1995. Listvenite and related rocks: perspectives on terminology and mineralogy with reference to an occurrence at Cregganbaun, Co. Mayo, Republic of Ireland. Mineral. Deposita 30, 303–313. https://doi.org/10.1007/BF00196366.

Handy, M.R., 2010. Reconciling plate-tectonic reconstructions of Alpine Tethys with the geological–geophysical record of spreading and subduction in the Alps, Earth-Science Reviews 102, 121-158.

Hansen, R.T.J., Bostock, M.G., Christensen, N.I., 2012. Nature of the low velocity zone in Cascadia from receiver function waveform inversion. Earth and Planetary Science Letters 337–338, 25–38. https://doi.org/10.1016/j.epsl.2012.05.031

Hay, W.W., Migdisov, A., Balukhovsky, A.N., Wold, C.N., Flögel, S., Söding, E., 2006. Evaporites and the salinity of the ocean during the Phanerozoic: Implications for climate, ocean circulation and life. Palaeogeography, Palaeoclimatology, Palaeoecology 240, 3–46. https://doi.org/10.1016/j.palaeo.2006.03.044.

Henry, C., Burkhard, M., Goffé, B., 1996. Evolution of synmetamorphic veins and their wallrocks through a Western Alps transect: no evidence for large-scale fluid flow. Stable isotope, major- and trace-element systematics. Chem. Geol. 127, 81–109. https://doi.org/10.1016/0009-2541(95)00106-9.

Hermann, J., Müntener, O., Scambelluri, M., 2000. The importance of serpentinite mylonites for subduction and exhumation of oceanic crust. Tectonophysics 327, 225–238. https://doi.org/10.1016/S0040-1951(00)00171-2.

Hertgen, S., Yamato, P., Morales, L.F.G., Angiboust, S., 2017. Evidence for brittle deformation events at eclogite-facies P-T conditions (example of the Mt. Emilius klippe, Western Alps). Tectonophysics 706–707, 1–13. https://doi.org/10.1016/j.tecto.2017.03.028.

Hertwig, A., McClelland, W.C., Kitajima, K., Schertl, H.-P., Maresch, W.V., Stanek, K., Valley, J.W., Sergeev, S.A., 2016. Inherited igneous zircons in jadeitite predate high-pressure metamorphism and jadeitite formation in the Jagua Clara serpentinite mélange of the Rio San Juan complex (Dominican Republic). Contrib.Mineral. Petrol. 171, 48. https://doi.org/10.1007/s00410-016-1256-6.

Herviou, C., Verlaguet, A., Agard, P., Locatelli, M., Raimbourg, H., Lefeuvre, B., Dubacq, B., 2021. Along-dip variations of subduction fluids: The 30–80 km depth traverse of the Schistes Lustrés complex (Queyras-Monviso, W. Alps). Lithos 394–395, 106168. https://doi.org/10.1016/j.lithos.2021.106168.

Herviou, C., Agard, P., Plunder, A., Mendes, K., Verlaguet, A., Deldicque, D., Cubas, N., 2022. Subducted fragments of the Liguro-Piemont ocean, Western Alps: spatial correlations and offscraping mechanisms during subduction. Tectonophysics 229267. https://doi.org/10.1016/j.tecto.2022.229267.

Hilairet, N., Reynard, B., Wang, Y., Daniel, I., Merkel, S., Nishiyama, N., Petitgirard, S., 2007. High-Pressure Creep of Serpentine, Interseismic Deformation, and Initiation of Subduction. Science 318, 1910–1913. https://doi.org/10.1126/science.1148494.

Holland, T.J.B., 1979. High water activities in the generation of high pressure kyanite eclogites of the Tauern Window, Austria. J. Geol. 87, 1–27. https://doi.org/10.1086/628388.

Holland, T.J.B., Powell, R., 1998. An internally consistent thermodynamic data set for phases of petrological interest. J. Metamorph. Geol. 16, 309–343. https://doi.org/10.1111/j.1525-1314.1998.00140.x.

Holland, M., Urai, J.L., 2010. Evolution of anastomosing crack–seal vein networks in limestones: Insight from an exhumed high-pressure cell, Jabal Shams, Oman Mountains. Journal of Structural Geology 32, 1279–1290. https://doi.org/10.1016/j.jsg.2009.04.011

Holland, T., Baker, J., Powell, R., 1998. Mixing properties and activity-composition relationships of chlorites in the system MgO-FeO-Al2O3-SiO2-H2O. ejm, 10, pp. 395–406. https://doi.org/10.1127/ejm/10/3/0395.

Hooker, J.N., Laubach, S.E., Marrett, R., 2013. Fracture-aperture size—frequency, spatial distribution, and growth processes in strata-bounded and non-strata-bounded fractures, Cambrian Mesón Group, NW Argentina. Journal of Structural Geology 54, 54–71. https://doi.org/10.1016/j.jsg.2013.06.011

Huang, F., Daniel, I., Cardon, H., Montagnac, G., Sverjensky, D.A., 2017. Immiscible hydrocarbon fluids in the deep carbon cycle. Nat. Commun. 8, 15798. https://doi.org/10.1038/ncomms15798.

Hyndman, R.D., McCrory, P.A., Wech, A., Kao, H., Ague, J., 2015. Cascadia subducting plate fluids channelled to fore-arc mantle corner: ETS and silica deposition. J. Geophys. Res. Solid Earth 120, 4344–4358. https://doi.org/10.1002/2015JB011920.

Ide, S., Beroza, G.C., Shelly, D.R., Uchide, T., 2007. A scaling law for slow earthquakes. Nature 447, 76–79. https://doi.org/10.1038/nature05780

Ikari, M.J., Kopf, A.J., Hüpers, A., Vogt, C., 2018. Lithologic control of frictional strength variations in subduction zone sediment inputs. Geosphere 14, 604–625. https://doi.org/10.1130/GES01546.1.

Incel, S., Hilairet, N., Labrousse, L., John, T., Deldicque, D., Ferrand, T., Wang, Y., Renner, J., Morales, L., Schubnel, A., 2017. Laboratory earthquakes triggered during eclogitization of lawsonite-bearing blueschist. Earth Planet. Sci. Lett. 459, 320–331. https://doi.org/10.1016/j.epsl.2016.11.047.

Inglis, E.C., Debret, B., Burton, K.W., Millet, M.-A., Pons, M.-L., Dale, C.W., Bouilhol, P., Cooper, M., Nowell, G.M., McCoy-West, A.J., Williams, H.M., 2017. The behavior of iron and zinc stable isotopes accompanying the subduction of mafic oceanic crust: A case study from Western Alpine ophiolites. Geochem. Geophys. Geosyst. 18, 2562–2579. https://doi.org/10.1002/2016GC006735.

Invernizzi, C., Bigazzi, G., Corrado, S., Leo, P.D., Schiattarella, M., Zattin, M., 2008. New thermobaric constraints on the exhumation history of the Liguride accretionary wedge, southern Italy. Ofioliti 33, 21–32.

Ito, E., Anderson, A.T., 1983. Submarine metamorphism of gabbros from the Mid-Cayman rise: Petrographic and mineralogic constraints on hydrothermal processes at slow spreading ridges. Contrib. Mineral. Petrol. 82, 371–388. https://doi.org/10.1007/BF00399714.

Jackson, P, Sanderson, D. J, 1992. Scaling of fault displacements from the Badajoz-Cordoba shear zone, SW Spain. Tectonophysics 210, 189–190.

Jaeckel, K., Bebout, G.E., Angiboust, S., 2018. Deformation-enhanced fluid and mass transfer along Western and Central Alps paleo-subduction interfaces: Significance for carbon cycling models. Geosphere 14, 2355–2375. https://doi.org/10.1130/GES01587.1

Jamieson, R.A., Craw, D., 1987. Sphalerite geobarometry in metamorphic terranes: an appraisal with implications for metamorphic pressure in the Otago Schist.J. Metamorph. Geol. 5, 87–99. https://doi.org/10.1111/j.1525-1314.1987.tb00371.x.

Jochum, K. P., Weis, U., Stoll, B., Kuzmin, D., Yang, Q., Raczek, I., Jacob, D.E., Stracke, A., Birbaum, K., Frick, D.A., Günther, D., Enzweiler, J., 2011. Determination of reference values for NIST SRM 610–617 glasses following ISO guidelines. Geostandards and Geoanalytical Research, 35(4), 397-429.

John, T., Klemd, R., Gao, J., Garbe-Schönberg, C.D., 2008. Trace-element mobilization in slabs due to non steady-state fluid–rock interaction: constraints from an eclogite-facies transport vein in blueschist (Tianshan, China). Lithos 103, 1-24.

Johnston, J.D., McCaffrey, K.J.W., 1996. Fractal geometries of vein systems and the variation of scalingrelationships with mechanism. Journal of Structural Geology 18, 349–358. https://doi.org/10.1016/S0191-8141(96)80055-1

Jolivet, L., Goffé, B., Monié, P., Truffert-Luxey, C., Patriat, M., Bonneau, M., 1996. Miocene detachment in Crete and exhumation P-T-t paths of high-pressure metamorphic rocks. Tectonics 15, 1129–1153. https://doi.org/10.1029/96TC01417.

Jolivet, L., Faccenna, C., Goff´e, B., Mattei, M., Rossetti, F., Brunet, C., Storti, F., Funiciello, R., Cadet, J.P., d'Agostino, N., Parra, T., 1998. Midcrustal shear zones in postorogenic extension: Example from the northern Tyrrhenian Sea. J. Geophys. Res. 103, 12123–12160. https://doi.org/10.1029/97JB03616.

Kameda, J., Inoue, S., Tanikawa, W., Yamaguchi, A., Hamada, Y., Hashimoto, Y., Kimura, G., 2017. Alteration and dehydration of subducting oceanic crust within subduction zones: implications for d´ecollement step-down and plate-boundary seismogenesis. Earth Planets Space 69, 52. https://doi.org/10.1186/s40623-017-0635-1.

Karig, D.E., Sharman, G.F., 1975. Subduction and Accretion in Trenches. Geol. Soc. Am. Bull. 86, 377–389. https://doi.org/10.1130/0016-7606(1975)86<377:SAAIT>2.0.CO;2.

Kastner, M., Elderfield, H., Martin, J. B., 1991. Fluids in convergent margins: What do we know about their composition, origin, role in diagenesis and importance for oceanic chemical fluxes?. Philosophical Transactions of the Royal Society of London. Series A: Physical and Engineering Sciences 335, 243-259.

Kawamoto, T., Hertwig, A., Shertl, H.-P., Maresch, W.V., 2018. Fluid inclusions in jadeitite and jadeite-rich rock from serpentinite mélanges in northern Hispaniola: Trapped ambient fluids in a cold subduction channel. Lithos 308-309, 227–241.

Kelemen, P.B., Manning, C.E., 2015. Reevaluating carbon fluxes in subduction zones, what goes down, mostly comes up. Proc Natl Acad Sci USA 112, E3997–E4006. https://doi.org/10.1073/pnas.1507889112.

Kelley, K.A., Cottrell, E., 2009. Water and the Oxidation State of Subduction Zone Magmas. Science 325, 605–607. https://doi.org/10.1126/science.1174156.

Kelley, D.S., Delaney, J.R., 1987. Two-phase separation and fracturing in mid-ocean ridge gabbros at temperatures greater than 700°C. Earth Planet. Sci. Lett. 83, 53–66. https://doi.org/10.1016/0012-821X(87)90050-1.

Kelley, D.S., Robinson, P.T., Malpas, J.G., 1992. Processes of brine generation and circulation in the oceanic crust: Fluid inclusion evidence from the Troodos Ophiolite, Cyprus. J. Geophys. Res. 97, 9307. https://doi.org/10.1029/92JB00520.

Kendrick, M.A., Scambelluri, M., Honda, M., Phillips, D., 2011. High abundances of noble gas and chlorine delivered to the mantle by serpentinite subduction. Nature Geoscience 4, 807–812. https://doi.org/10.1038/ngeo1270.

Kerswell, B.C., Kohn, M.J., Gerya, T.V., 2021. Backarc Lithospheric Thickness and Serpentine Stability Control Slab-Mantle Coupling Depths in Subduction Zones. Geochem. Geophys. Geosyst. 22 https://doi.org/10.1029/2020GC009304.

Kienast, J.R., 1973. Sur l'existence de deux séries différentes au sein de l'ensemble schistes lustrés-ophiolites du val d'Aoste ; quelques arguments fondés sur l'étude des roches métamorphiques. Comptes Rendus de l'Académie des Sciences de Paris 276, 2621–2624.

Kimura, G., Ludden, J., 1995. Peeling oceanic crust in subduction zones. Geol 23, 217–220. https://doi.org/10.1130/0091-7613(1995)023<0217:POCISZ>2.3.CO;2.

Kimura, G., Maruyama, S., Isozaki, Y., Terabayashi, M., 1996. Well-preserved underplating structure of the jadeitized Franciscan complex, Pacheco Pass. Calif. Geol. 24, 75. https://doi.org/10.1130/0091-7613(1996)024<0075:WPUSOT>2.3.CO;2.

Kimura, G., Kitamura, Y., Hashimoto, Y., Yamaguchi, A., Shibata, T., Ujiie, K., Okamoto, S., 2007. Transition of accretionary wedge structures around the up-dip limit of the seismogenic subduction zone. Earth Planet. Sci. Lett. 255, 471–484. https://doi.org/10.1016/j.epsl.2007.01.005.

Kirkpatrick, J.D., Fagereng, Å., Shelly, D.R., 2021. Geological constraints on the mechanisms of slow earthquakes. Nat Rev Earth Environ 2, 285–301. https://doi.org/10.1038/s43017-021-00148-w

Kita, S., Okada, T., Nakajima, J., Matsuzawa, T., Hasegawa, A., 2006. Existence of a seismic belt in the upper plane of the double seismic zone extending in the along-arc direction at depths of 70–100 km beneath NE Japan. Geophys. Res. Lett. 33, L24310. https://doi.org/10.1029/2006GL028239.

Klemd, R., Van den Kerkhof, A.M., Horn, E.E., 1992. High-density CO 2 -N 2 inclusions in eclogite-facies metasediments of the Mfinchberg gneiss complex, SE Germany. Contrib. Mineral. Petrol. 111, 409–419.

Kolesnikov, A., Kutcherov, V.G., Goncharov, A.F., 2009. Methane-derived hydrocarbons produced under upper-mantle conditions. Nat. Geosci. 2, 566–570. https://doi.org/10.1038/ngeo591.

Kotowski, A.J., Behr, W.M., 2019. Length scales and types of heterogeneities along the deep subduction interface: Insights from exhumed rocks on Syros Island, Greece. Geosphere 15, 1038-1065.

Kunz, P., 1988. Ophiolites penniques et s´sédiments associés dans la région d'Arolla (val d'Hérens, Valais, Suisse). Eclogae Geol. Helv. 81, 115–124. https://doi.org/10.5169/SEALS-166172.

Küster, M., Stöckhert, B., 1997. Density changes of fluid inclusions in high-pressure low temperature metamorphic rocks from Crete: a thermobarometric approach based on the creep strength of the host minerals. Lithos 41, 151–167. https://doi.org/10.1016/S0024-4937(97)82010-5.

La Pointe, P.R., 1988. A method to characterize fracture density and connectivity through fractal geometry. International Journal of Rock Mechanics and Mining Sciences & Geomechanics Abstracts 25, 421–429. https://doi.org/10.1016/0148-9062(88)90982-5

Lafay, R., Deschamps, F., Schwartz, S., Guillot, S., Godard, M., Debret, B., Nicollet, C., 2013. High-pressure serpentinites, a trap-and-release system controlled by metamorphic conditions: Example from the Piedmont zone of the western Alps. Chemical Geology 343, 38–54. https://doi.org/10.1016/j.chemgeo.2013.02.008.

Lagabrielle, Y., 1987. Les ophiolites : Marqueurs de l'histoire tectonique des domaines océaniques. PhD thesis, Brest.

Lagabrielle, Y., Cannat, M., 1990. Alpine Jurassic ophiolites resemble the modern central Atlantic basement. Geology 18, 319–322.

Lagabrielle, Y., Polino, R., 1988. Un schéma structural du domaine des Schistes lustrés ophiolitifères au nord-ouest du massif du Mont Viso (Alpes Sud-Occidentales) et ses implications. Comptes rendus de l'Acad´emie des sciences. Série 2. Mécanique, Physique, Chimie, Sciences de l'univers, Sciences de la Terre 306, 921–928.

Lagabrielle, Y., Fudral, S., Kienast, J.-R., 1990. La couverture océanique des ultrabasites de Lanzo (Alpes occidentales) : arguments lithostratigraphiques et pétrologiques. Geodin. Acta 4, 43–55. https://doi.org/10.1080/09853111.1990.11105199.

Lagabrielle, Y., Vitale Brovarone, A., Ildefonse, B., 2015. Fossil oceanic core complexes recognized in the blueschist metaophiolites of Western Alps and Corsica. Earth Sci. Rev. 141, 1–26. https://doi.org/10.1016/j.earscirev.2014.11.004.

Lahfid, A., Beyssac, O., Deville, E., Negro, F., Chopin, C., Goffé, B., 2010. Evolution of the Raman spectrum of carbonaceous material in low-grade metasediments of the Glarus Alps (Switzerland): RSCM in low-grade metasediments. Terra Nova 22, 354–360. https://doi.org/10.1111/j.1365-3121.2010.00956.x.

Lahiri, S., Rana, V., Bhatt, S., Mamtani, M.A., 2020. Paleostress and statistical analysis using quartz veins from mineralized and non-mineralized zones: Application for exploration targeting. Journal of Structural Geology 133, 104006. https://doi.org/10.1016/j.jsg.2020.104006

Lallemand, S., 1999. La subduction océanique. Pour la Science 108.

Lanari, P., 2012. Micro-cartographie P-T-ε dans les roches m´métamorphiques. Applications aux Alpes et à l'Himalaya. PhD thesis. Université de Grenoble.

Lapen, T.J., Johnson, C.M., Baumgartner, L.P., Mahlen, N.J., Beard, B.L., Amato, J.M., 2003. Burial rates during prograde metamorphism of an ultra-high-pressure terrane: an example from Lago di Cignana, western Alps, Italy. Earth Planet. Sci. Lett. 215, 57–72. https://doi.org/10.1016/S0012-821X(03)00455-2.

Lapham, D.M., 1958. Structural and chemical variation in chromium chlorite. American Mineralogist: Journal of Earth and Planetary Material 43, 921–956.

Laurent, V., Lanari, P., Naïr, I., Augier, R., Lahfid, A., Jolivet, L., 2018. Exhumation of eclogite and blueschist (Cyclades, Greece): Pressure-temperature evolution determined by thermobarometry and garnet equilibrium modelling. J. Metamorph. Geol. 36, 769–798.

Lay, T., Kanamori, H., Ammon, C.J., Koper, K.D., Hutko, A.R., Ye, L., Yue, H., Rushing, T. M., 2012. Depth-varying rupture properties of subduction zone megathrust faults. J. Geophys. Res. 117, n/a-n/a. https://doi.org/10.1029/2011JB009133.

Le Pichon, X., Bergerat, F., Roulet, M., 1988. Plate kinematics and tectonics leading to the Alpine belt formation: a new analysis. Geol. Soc. Am. Special Issue 218, 111–131.

Le, V.-H., Caumon, M.-C., Tarantola, A., Randi, A., Robert, P., Mullis, J., 2020. Calibration data for simultaneous determination of P-V-X properties of binary and ternary CO2 - CH4 - N2 gas mixtures by Raman

spectroscopy over 5–600 bar: Application to natural fluid inclusions. Chemical Geology 552, 119783. https://doi.org/10.1016/j.chemgeo.2020.119783.

Le, V.-H., Caumon, M.-C., Tarantola, A., Randi, A., Robert, P., Mullis, J., 2019. Quantitative Measurements of Composition, Pressure, and Density of Microvolumes of CO 2 –N 2 Gas Mixtures by Raman Spectroscopy. Anal. Chem. 91, 14359–14367. https://doi.org/10.1021/acs.analchem.9b02803.

Ledésert, B., Dubois, J., Genter, A., Meunier, A., 1993. Fractal analysis of fractures applied to Soultz-sous-Forets hot dry rock geothermal program. Journal of Volcanology and Geothermal Research 57, 1–17. https://doi.org/10.1016/0377-0273(93)90028-P

Lefeuvre, B., 2020. La lawsonite dans les métasédiments en base de zone sismogénique : géochimie, échelles de migration des fluides et rôle de la déformation dans les Schistes Lustrés. PhD thesis. Sorbonne Université, Paris.

Lefeuvre, B., Agard, P., Verlaguet, A., Dubacq, B., Plunder, A., 2020. Massive formation of lawsonite in subducted sediments from the Schistes Lustrés (W. Alps): Implications for mass transfer and decarbonation in cold subduction zones. Lithos 370–371, 105629. https://doi.org/10.1016/j.lithos.2020.105629.

Lemonnier, N., Homberg, C., Roche, V., Rocher, M., Boullier, A., Schnyder, J., 2020. Microstructures of bedding-parallel faults under multistage deformation: Examples from the Southeast Basin of France. Journal of Structural Geology 140, 104138. https://doi.org/10.1016/j.jsg.2020.104138

Lemoine, M., 1959. Remarques à propos de quelques faits et hypothèses concernant l'âge des Schistes lustres piémontais dans les Alpes cottiennes et brianconnaises. Bulletin de la Société Géologique de France 7, 90–92.

Lemoine, M., 1971. Données nouvelles sur la série du Gondran près Briançon (Alpes Cottiennes). Réflexions sur les problèmes stratigraphique et paléographique de la zone piémontaise. Géologie Alpine 47, 181–201.

Lemoine, M., 2003. Schistes lustrés from Corsica to Hungary: back to the original sediments and tentative dating of partly azoic metasediments. Bulletin de la Société Géologique de France 174, 197–209. https://doi.org/10.2113/174.3.197.

Lemoine, M., Tricart, P., 1986. Les Schistes lustrés piémontais des Alpes Occidentales : approche stratigraphique, structurales et sédimentologique. Eclogae Geol. Helv. 79, 271–294. https://doi.org/10.5169/SEALS-165835.

Lemoine, M., Steen, D.M., Vuagnat, M., 1970. Sur le problème stratigraphique des ophiolites piémontaises et des roches sédimentaires associées : observations dans le massif de Chabrière en Haute-Ubaye (Basses-Alpes, France). Compte rendu des séances de la Société de physique et d'histoire naturelle de Gen`eve 5, 44–59.

Lemoine, M., Marthaler, M., Caron, M., Sartori, M., Amaudric du Chaffaut, S., 1984. Découverte de foraminifères planctoniques du Crétacé supérieur dans les schistes lustrés du Queyras (Alpes occidentales). Conséquences paléogéographiques et tectoniques. Comptes-rendus des séances de l'Académie des sciences. Série 2. Mécanique-physique, chimie, sciences de l'univers, sciences de la terre 299, 727–732.

Lemoine, M., Bas, T., Arnaud-Vanneau, A., Arnaud, H., Dumont, T., Gidon, M., Bourbon, M., de Graciansky, P.-C., Rudkiewicz, J.-L., Megard-Galli, J., Tricart, P., 1986. The continental margin of the Mesozoic Tethys in the Western Alps. Mar. Pet. Geol. 3, 179–199.

Li, Y., 2017. Immiscible C-H-O fluids formed at subduction zone conditions. Geochem. Perspect. Lett. 3, 12–21. https://doi.org/10.7185/geochemlet.1702.

Liewig, N., 1981. Les phengites : marqueurs géométriques, chimiques et isotopiques de l'histoire des roches m´métamorphiques : application aux schistes lustres des Alpes cottiennes. PhD thesis, université de Strasbourg.

Locatelli, M., Verlaguet, A., Agard, P., Federico, L., Angiboust, S., 2018. Intermediate depth brecciation along the subduction plate interface (Monviso eclogite, W. Alps). Lithos 320–321, 378–402. https://doi.org/10.1016/j.lithos.2018.09.028.

Locatelli, M., Federico, L., Agard, P., Verlaguet, A., 2019a. Geology of the southern Monviso metaophiolite complex (W-Alps, Italy). Journal of Maps 15, 283–297. https://doi.org/10.1080/17445647.2019.1592030.

Locatelli, M., Verlaguet, A., Agard, P., Pettke, T., Federico, L., 2019b. Fluid Pulses During Stepwise Brecciation at Intermediate Subduction Depths (Monviso Eclogites, W. Alps): First Internally Then Externally Sourced. Geochem. Geophys. Geosyst. 20, 5285–5318. https://doi.org/10.1029/2019GC008549.

Lombardo, B., Nervo, R., Compagnoni, R., Messiga, B., Kienast, J.R., Mevel, C., Fiora, L., Piccardo, G.B., Lanza, R., 1978. Osservazioni preliminari sulle ofioliti metamorfiche del Monviso (Alpi Occidentali). Rendiconti Della Soc. Ital. Mineral. E Petrol. 34, 235–305.

Luckscheiter, B., Morteani, G., 1980. The fluid phase in eclogites, glaucophane-bearing rocks and amphibolites from the central tauern window as deduced from fluid inclusion studies. TMPM Tschermaks Petr. Mitt. 27, 99–111. https://doi.org/10.1007/BF01082401.

Magde, L.S., Dick, H.J.B., Hart, S.R., 1995. Tectonics, alteration and the fractal distribution of hydrothermal veins in the lower ocean crust. Earth and Planetary Science Letters 129, 103–119. https://doi.org/10.1016/0012-821X(94)00239-U

Malusà, M.G., Polino, R., Zattin, M., Bigazzi, G., Martin, S., Piana, F., 2005. Miocene to Present differential exhumation in the Western Alps: Insights from fission track thermochronology. Tectonics 24. https://doi.org/10.1029/2004TC001782.

Manatschal, G., Sauter, D., Karpoff, A.M., Masini, E., Mohn, G., Lagabrielle, Y., 2011. The Chenaillet Ophiolite in the French/Italian Alps: An ancient analogue for an Oceanic Core Complex? Lithos 124, 169–184. https://doi.org/10.1016/j.lithos.2010.10.017.

Mandelbrot, B. B, 1982. The fractal geometry of nature (Vol. 1). New York: WH freeman.

Mangenot, X., Tarantola, A., Mullis, J., Girard, J.P., Le, V.H., Eiler, J.M., 2021. Geochemistry of clumped isotopologues of CH4 within fluid inclusions in Alpine tectonic quartz fissures. Earth Planet. Sci. Lett. 561, 116792.Manning, C.E., 1994. Fractal clustering of metamorphic veins. Geology 22, 335–338. https://doi.org/10.1130/0091-7613(1994)022<0335:FCOMV>2.3.CO;2

Manzotti, P., Ballèvre, M., Pitra, P., Schiavi, F., 2021. Missing lawsonite and aragonite found: P–T and fluid composition in meta-marls from the Combin Zone (Western Alps). Contrib. Mineral. Petrol. 176, 60. https://doi.org/10.1007/s00410-021-01818-0.

Marschall, H.R., Schumacher, J.C., 2012. Arc magmas sourced from mélange diapirs in subduction zones. Nature Geosci 5, 862–867. https://doi.org/10.1038/ngeo1634.

Marthaler, M., 1984. Géologie des unités penniques entre le val d'Anniviers et le val de Tourtemagne (Valais, Suisse). Eclogae Geol. Helv. 77, 395–448. https://doi.org/10.5169/SEALS-165516.

Marthaler, M., Stampfli, G.M., 1989. Les Schistes lustrés à ophiolites de la nappe du Tsaté : un ancien prisme d'accrétion de la marge active apulienne? Schweiz. Mineral. Petrogr. Mitt. 69, 211–216. https://doi.org/10.5169/SEALS-52789.

Martin, S., Rebay, G., Kienast, J.-R., Mével, C., 2008. An eclogitised oceanic palaeo-hydrothermal field from the St. Marcel valley (Italian Western Alps) 33, 16.

Maruyama, S., Liou, J.G., Terabayashi, M., 1996. Blueschists and eclogites of the world and their exhumation. International geology review 38, 485-594.

Massonne, H.J., 1992. Thermochemical determination of water activities relevant to eclogitic rocks. In: Kharaka, Y.K., Maest, A.S. (Eds.), Water-Rock Interaction. Balkema, Rotterdam, pp. 1523–1526.

Massonne, H.J., 1995. Experimental and petrogenetic study of UHPM. In: Coleman, R.G., Wang, X. (Eds.), 1995. Ultrahigh pressure metamorphism, Cambridge University Press, Cambridge, pp. 33–95.

Massonne, H.-J., Schreyer, W., 1987. Phengite geobarometry based on the limiting assemblage with K-feldspar, phlogopite, and quartz. Contrib. Mineral. Petrol. 96, 212–224. https://doi.org/10.1007/BF00375235.

Massonne, H.J., Schreyer, W., 1989. Stability field of the high-pressure assemblage, talc+phengite and two new phengite barometers. Eur. J. Mineral. 1, 391–410.

Mazzarini, F., Musumeci, G., Cruden, A.R., 2011. Vein development during folding in the upper brittle crust: The case of tourmaline-rich veins of eastern Elba Island, northern Tyrrhenian Sea, Italy. Journal of Structural Geology 33, 1509–1522. https://doi.org/10.1016/j.jsg.2011.07.001

McCaffrey, K., Johnson, J.D., Feely, M., 1993. Use of Fractal Statistics in the Analysis of Mo-Cu Mineralisation at Mace Head, County Galway. Irish Journal of Earth Sciences 1, 139–148.

McCaffrey, K.J.W., Johnston, J.D., 1996. Fractal analysis of a mineralised vein deposit: Curraghinalt gold deposit, County Tyrone. Mineral. Deposita 31, 52–58.

McCollom, T.M., 2013. Laboratory simulations of abiotic hydrocarbon formation in earth's deep subsurface. Rev. Mineral. Geochem. 75, 467–494. https://doi.org/10.2138/rmg.2013.75.15.

McCormick, G. R, 1975. A chemical study of kämmererite, Day Book Body, Yancey County, North Carolina. American Mineralogist: Journal of Earth and Planetary Material 60, 924–927.

McDonough, W.F., Sun, S.-S., 1995. The composition of the Earth'. Chemical Geology 120, 223–253.

Menant, A., Angiboust, S., Gerya, T., 2019. Stress-driven fluid flow controls long-term megathrust strength and deep accretionary dynamics. Sci. Rep. 9, 9714. https://doi.org/10.1038/s41598-019-46191-y.

Menant, A., Angiboust, S., Gerya, T., Lacassin, R., Simoes, M., Grandin, R., 2020. Transient stripping of subducting slabs controls periodic forearc uplift. Nat. Commun. 11, 1823. https://doi.org/10.1038/s41467-020-15580-7.

Meneghini, F., Marroni, M., Moore, J.C., Pandolfi, L., Rowe, C.D., 2009. The processes of underthrusting and underplating in the geologic record: structural diversity between the Franciscan complex (California), the Kodiak complex (Alaska) and the Internal Ligurian units (Italy). Geol. J. 44, 126–152. https://doi.org/10.1002/gj.1144.

Menzel, M.D., Garrido, C.J., López Sánchez-Vizcaíno, V., Marchesi, C., Hidas, K., Escayola, M.P., Delgado Huertas, A., 2018. Carbonation of mantle peridotite by CO2-rich fluids: the formation of listvenites in the Advocate ophiolite complex (Newfoundland, Canada). Lithos 323, 238–261. https://doi.org/10.1016/j.lithos.2018.06.001.

Messiga, B., Scambelluri, M., Piccardo, G.B., 1995. Chloritoid-bearing assemblages in mafic systems and eclogite-facies hydration of alpine Mg-Al metagabbros (Erro-Tobbio Unit, Ligurian Western Alps). Eur. J. Mineral. 7, 1149–1168. https://doi.org/10.1127/ejm/7/5/1149.

Michard, A., Goffé, B., Chopin, C., Henry, C., 1996. Did the Western Alps develop through an Oman-type stage? The geotectonic setting of high-pressure metamorphism in two contrasting Tethyan transects. Eclogae Geol. Helv. 89, 43–80.

Michard, A., Avigad, D., Goff´e, B., Chopin, C., 2004. The high-pressure metamorphic front of the south Western Alps (Ubaye-Maira transect, France, Italy). Schweiz. Mineral. Petrogr. Mitt. 84, 215–235.

Michel, S., Gualandi, A., Avouac, J.-P., 2019a. Interseismic Coupling and Slow Slip Events on the Cascadia Megathrust. Pure Appl. Geophys. 176, 3867–3891. https://doi.org/10.1007/s00024-018-1991-x

Michel, S., Gualandi, A., Avouac, J.-P., 2019b. Similar scaling laws for earthquakes and Cascadia slow-slip events. Nature 574, 522–526. https://doi.org/10.1038/s41586-019-1673-6

Monaco, C., Tortorici, L., 1995. Tectonic role of ophiolite-bearing terranes in the development of the Southern Apennines orogenic belt. Terra Nova 7, 153–160. https://doi.org/10.1111/j.1365-3121.1995.tb00684.x.

Monecke, T., Gemmell, J.B., Monecke, J., 2001. Fractal distributions of veins in drill core from the Hellyer VHMS deposit, Australia: constraints on the origin and evolution of the mineralising system. Min Dep 36, 406–415. https://doi.org/10.1007/s001260100161

Monié, P., Agard, P., 2009. Coeval blueschist exhumation along thousands of kilometers: Implications for subduction channel processes. Geochem. Geophys. Geosyst. 10. https://doi.org/10.1029/2009GC002428.

Moody, J. B., 1976. Serpentinization: a review. Lithos, 9, 125-138.

Moore, J.C., 1975. Selective subduction. Geol 3, 530. https://doi.org/10.1130/0091-7613(1975)3<530:SS>2.0.CO;2.

Moore, D.E., Lockner, D.A., 2007. Comparative Deformation Behavior of Minerals in Serpentinized Ultramafic Rock: Application to the Slab-Mantle Interface in Subduction Zones. International Geology Review 49, 401–415. https://doi.org/10.2747/0020-6814.49.5.401.

Moore, D.E., Lockner, D.A., 2011. Frictional strengths of talc-serpentine and talc-quartz mixtures. J. Geophys. Res. 116, B01403. https://doi.org/10.1029/2010JB007881.

Moore, D.E., Rymer, M.J., 2007. Talc-bearing serpentinite and the creeping section of the San Andreas fault. Nature 448, 795–797. https://doi.org/10.1038/nature06064.

Mukherjee, B.K., Sachan, H.K., 2009. Fluids in coesite-bearing rocks of the Tso Morari complex, NWHimalaya: evidence for entrapment during peak metamorphism and subsequent uplift. Geol. Mag. 146, 876–889. https://doi.org/10.1017/S0016756809990069.

Mullis, J., 1979. The system methane-water as a geologic thermometer and barometer from the external part of the Central Alps. Bull. Mineral. 102, 526–536. https://doi.org/10.3406/bulmi.1979.7301.

Mullis, J., Dubessy, J., Poty, B., O'Neil, J., 1994. Fluid regimes during late stages of a continental collision: physical, chemical, and stable isotope measurements of fluid inclusions in fissure quartz from a geotraverse through the Central Alps, Switzerland. Geochim. Cosmochim. Acta 58, 2239–2267. https://doi.org/10.1016/0016-7037(94)90008-6.

Muñoz-Montecinos, J., Angiboust, S., Cambeses, A., García-Casco, A., 2020. Multiple veining in a paleo–accretionary wedge: The metamorphic rock record of prograde dehydration and transient high pore-fluid pressures along the subduction interface (Western Series, central Chile). Geosphere 16, 765–786. https://doi.org/10.1130/GES02227.1

Muñoz-Montecinos, J., Angiboust, S., Garcia-Casco, A., Glodny, J., Bebout, G., 2021. Episodic hydrofracturing and large-scale flushing along deep subduction interfaces: Implications for fluid transfer and carbon recycling (Zagros Orogen, southeastern Iran). Chemical Geology 571, 120173. https://doi.org/10.1016/j.chemgeo.2021.120173

Müntener, O., Piccardo, G.B., Polino, R., Zanetti, A., 2005. Revisiting the Lanzo peridotite (NW-Italy): 'asthenospherization' of ancient mantle lithosphere. Ofioliti 30, 111–124.

Nadeau, S., Philippot, P., Pineau, F., 1993. Fluid inclusion and mineral isotopic compositions (HCO) in eclogitic rocks as tracers of local fluid migration during high pressure metamorphism. Earth Planet. Sci. Lett. 114, 431–448. https://doi.org/10.1016/0012-821X(93)90074-J.

Narr, W., Suppe, J., 1991. Joint spacing in sedimentary rocks. Journal of Structural Geology, 13, 1037-1048.

Negro, F., Bousquet, R., Vils, F., Pellet, C.-M., H¨anggi-Schaub, J., 2013. Thermal structure and metamorphic evolution of the Piemont-Ligurian metasediments in the northern Western Alps. Swiss J. Geosci. 106, 63–78. https://doi.org/10.1007/s00015-013-0119-7.

Nehlig, P., 1991. Salinity of oceanic hydrothermal fluids: a fluid inclusion study. Earth Planet. Sci. Lett. 102, 310–325. https://doi.org/10.1016/0012-821X(91)90026-E.

Nishiyama, N., Ujiie, K., Kano, M., 2021. Spatial changes in inclusion band spacing as an indicator of temporal changes in slow slip and tremor recurrence intervals. Earth Planets Space 73, 126. https://doi.org/10.1186/s40623-021-01448-7

Obara, K., 2002. Nonvolcanic Deep Tremor Associated with Subduction in Southwest Japan. Science 296, 1679–1681. https://doi.org/10.1126/science.1070378

Obara, K., Kato, A., 2016. Connecting slow earthquakes to huge earthquakes. Science 353, 253–257. https://doi.org/10.1126/science.aaf1512

Okazaki, K., Hirth, G., 2016. Dehydration of lawsonite could directly trigger earthquakes in subducting oceanic crust. Nature 530, 81–84. https://doi.org/10.1038/nature16501.

Okamoto, A., Oyanagi, R., Yoshida, K., Uno, M., Shimizu, H., Satish-Kumar, M., 2021. Rupture of wet mantle wedge by self-promoting carbonation. Commun Earth Environ 2, 151. https://doi.org/10.1038/s43247-021-00224-5.

Oliver, N.H.S., Bons, P.D., 2001. Mechanisms of fluid flow and fluid-rock interaction in fossil metamorphic hydrothermal systems inferred from vein-wallrock patterns, geometry and microstructure. Geofluids 1, 137–162. https://doi.org/10.1046/j.1468-8123.2001.00013.x

Oncken, O., Angiboust, S., Dresen, G., 2021. Slow slip in subduction zones: Reconciling deformation fabrics with instrumental observations and laboratory results. Geosphere. https://doi.org/10.1130/GES02382.1

Ortega, O.J., Marrett, R.A., Laubach, S.E., 2006. A scale-independent approach to fracture intensity and average spacing measurement. Bulletin 90, 193–208. https://doi.org/10.1306/08250505059

Padrón-Navarta, J.A., Hermann, J., Garrido, C.J., López Sánchez-Vizcaíno, V., Gómez-Pugnaire, M.T., 2010. An experimental investigation of antigorite dehydration in natural silica-enriched serpentinite. Contrib. Mineral. Petrol. 159, 25–42. https://doi.org/10.1007/s00410-009-0414-5.

Palazzin, G., Raimbourg, H., Famin, V., Jolivet, L., Kusaba, Y., Yamaguchi, A., 2016. Deformation processes at the down-dip limit of the seismogenic zone: The example of Shimanto accretionary complex. Tectonophysics 687, 28–43. https://doi.org/10.1016/j.tecto.2016.08.013

Paton, C., Hellstrom, J., Paul, B., Woodhead, J., & Hergt, J., 2011. Visualization Iolite: Freeware for the visualisation and processing of mass spectrometric data. Journal of Analytical Atomic Spectrometry, 26(12), 2508-2518.

Paulatto, M., Laigle, M., Galve, A., Charvis, P., Sapin, M., Bayrakci, G., Evain, M., Kopp, H., 2017. Dehydration of subducting slow-spread oceanic lithosphere in the Lesser Antilles. Nat. Commun. 8, 15980. https://doi.org/10.1038/ncomms15980.

Peacock, S.M., 1993. The importance of blueschist → eclogite dehydration reactions in subducting oceanic crust. Geol. Soc. Am. Bull. 105, 684–694. https://doi.org/10.1130/0016-7606(1993)105<0684:TIOBED>2.3.CO;2.

Peacock, S.M., Hyndman, R.D., 1999. Hydrous minerals in the mantle wedge and the maximum depth of subduction thrust earthquakes. Geophys. Res. Lett. 26, 2517–2520. https://doi.org/10.1029/1999GL900558

Peacock, S.M., Wang, K., 2021. On the stability of talc in subduction zones: a possible control on the maximum depth of decoupling between the subducting plate and mantle wedge. Geophysical Research Letters, 48, e2021GL094889.

Peacock, S.M., Christensen, N.I., Bostock, M.G., Audet, P., 2011. High pore pressures and porosity at 35 km depth in the Cascadia subduction zone. Geology 39, 471–474. https://doi.org/10.1130/G31649.1

Pelletier, L., Müntener, O., 2006. High-pressure metamorphism of the Lanzo peridotite and its oceanic cover, and some consequences for the Sesia–Lanzo zone (northwestern Italian Alps). Lithos 90, 111–130. https://doi.org/10.1016/j.lithos.2006.01.006.

Pennacchioni, G., Scambelluri, M., Bestmann, M., Notini, L., Nimis, P., Plümper, O., Faccenda, M., Nestola, F., 2020. Record of intermediate-depth subduction seismicity in a dry slab from an exhumed ophiolite. Earth Planet. Sci. Lett. 548, 116490 https://doi.org/10.1016/j.epsl.2020.116490.

Penniston-Dorland, S.C., Bebout, G.E., Pogge von Strandmann, P.A.E., Elliott, T., Sorensen, S.S., 2012. Lithium and its isotopes as tracers of subduction zone fluids and metasomatic processes: Evidence from the Catalina Schist, California, USA. Geochimica et Cosmochimica Acta 77, 530–545. https://doi.org/10.1016/j.gca.2011.10.038.

Penniston-Dorland, S.C., Gorman, J.K., Bebout, G.E., Piccoli, P.M., Walker, R.J., 2014. Reaction rind formation in the Catalina Schist: Deciphering a history of mechanical mixing and metasomatic alteration. Chemical Geology 384, 47–61. https://doi.org/10.1016/j.chemgeo.2014.06.024.

Philippot, P., 1987. “Crack seal” vein geometry in eclogitic rocks. Geodin. Acta 1, 171–181.

Philippot, P., 1990. Opposite vergence of Nappes and crustal extension in the French-Italian western Alps. Tectonics 9, 1143–1164. https://doi.org/10.1029/TC009i005p01143.

Philippot, P., Kienast, J.-R., 1989. Chemical-microstructural changes in eclogite-facies shear zones (Monviso, Western Alps, North Italy) as indicators of strain history and the mechanism and scale of mass transfer. Lithos 23, 179–200. https://doi.org/10.1016/0024-4937(89)90004-2.

Philippot, P., Selverstone, J., 1991. Trace-element-rich brines in eclogitic veins: implications for fluid composition and transport during subduction. Contrib. Mineral. Petrol. 106, 417–430. https://doi.org/10.1007/BF00321985.

Philippot, P., Agrinier, P., Scambelluri, M., 1998. Chlorine cycling during subduction of altered oceanic crust. Earth Planet. Sci. Lett. 12.

Piccardo, G.B., Zanetti, A., Müntener, O., 2007. Melt/peridotite interaction in the Southern Lanzo peridotite: Field, textural and geochemical evidence. Lithos 94, 181–209. https://doi.org/10.1016/j.lithos.2006.07.002.

Piccoli, F., Vitale Brovarone, A., Ague, J.J., 2018. Field and petrological study of metasomatism and high-pressure carbonation from lawsonite eclogite-facies terrains, Alpine Corsica. Lithos 304–307, 16–37. https://doi.org/10.1016/j.lithos.2018.01.026.

Pickering, G., Bull, J.M., Sanderson, D.J., 1995. Sampling power-law distributions. Tectonophysics 248, 1–20.

Platt, J.P., 1986. Dynamics of orogenic wedges and the uplift of high-pressure metamorphic rocks. Geol. Soc. Am. Bull. 97, 1037–1053. https://doi.org/10.1130/0016-7606(1986)97<1037:DOOWAT>2.0.CO;2.

Platt, J.P., 1988. The mechanics of frontal imbrication: a first-order analysis. Geol. Rundsch. 77, 577–589. https://doi.org/10.1007/BF01832399.

Platt, J.P., Xia, H., Schmidt, W.L., 2018. Rheology and stress in subduction zones around the aseismic/seismic transition. Prog Earth Planet Sci 5, 24. https://doi.org/10.1186/s40645-018-0183-8.

Plunder, A., Agard, P., Dubacq, B., Chopin, C., Bellanger, M., 2012. How continuous and precise is the record of P-T paths? Insights from combined thermobarometry and thermodynamic modelling into subduction dynamics (Schistes Lustr´es, W. Alps). J. Metamorph. Geol. 30, 323–346. https://doi.org/10.1111/j.1525-1314.2011.00969.x.

Plunder, A., Agard, P., Chopin, C., Pourteau, A., Okay, A.I., 2015. Accretion, underplating and exhumation along a subduction interface: From subduction initiation to continental subduction (Tavs¸anlı zone, W. Turkey). Lithos 226, 233–254. https://doi.org/10.1016/j.lithos.2015.01.007.

Pognante, U., 1980. Preliminary data on the Piemonte ophiolite nappe in the lower Val Susa – Val Chisone area, Italian western Alps. Ofioliti 2, 221–240.

Pognante, U., 1984. Eclogitic versus blueschist metamorphism in the internal Western Alps along the Susa valley traverse. Sci. Géologiq., Bull. et Mémoires 37, 29–36.

Pognante, U., 1985. Coronitic reactions and ductile shear zones in eclogitised ophiolite metagabbro, Western Alps, North Italy. Chem. Geol. 50, 99–109. https://doi.org/10.1016/0009-2541(85)90114-7.

Pognante, U., 1991. Petrological constraints on the eclogite- and blueschist facies metamorphism and P-T-t paths in the Western Alps. J. Metamorph. Geol. 9, 5–17. https://doi.org/10.1111/j.1525-1314.1991.tb00501.x.

Polino, R., Lemoine, M., 1984. Détritisme mixte d'origine continentale et océanique dans les sédiments jurassico-crétacés supra-ophiolitiques de la Téthys ligure : la série du Lago Nero (Alpes Occidentales franco-italiennes). Comptes rendus de l'Académie des sciences. Série 2. Mécanique, Physique, Chimie, Sciences de l'univers, Sciences de la Terre 298, 359–364.

Polino, R., Dela Pierre, F., Borghi, A., Carraro, F., Fioraso, G., Giardino, M., 2002. Note illustrative della carta geologica d'Italia alla scala 1:50000: foglio 132-152-153 Bardonecchia. ISPRA, Servizio Geologico d'Italia.

Polino, R., Malusà, M.G., Martin, S., Carraro, F., Gianotti, F., Bonetto, F., 2015. Note illustrative della carta geologica d'Italia alla scala 1:50000: foglio 090 Aosta. ISPRA, Servizio Geologico d'Italia.

Pourteau, A., Bousquet, R., Vidal, O., Plunder, A., Duesterhoeft, E., Candan, O., Oberhänsli, R., 2014. Multistage growth of Fe–Mg–carpholite and Fe–Mg–chloritoid, from field evidence to thermodynamic modelling. Contrib. Mineral. Petrol. 168, 1090.

Powell, R., Green, E. C., Marillo Sialer, E., & Woodhead, J., 2020. Robust isochron calculation. Geochronology, 2(2), 325-342.

Raimbourg, H., Thiéry, R., Vacelet, M., Ramboz, C., Cluzel, N., Le Trong, E., Yamaguchi, A., Kimura, G., 2014. A new method of reconstituting the P–T conditions of fluid circulation in an accretionary prism (Shimanto, Japan) from microthermometry of methane-bearing aqueous inclusions. Geochim. Cosmochim. Acta 125, 96–109.https://doi.org/10.1016/j.gca.2013.09.025.

Raimbourg, H., Vacelet, M., Ramboz, C., Famin, V., Augier, R., Palazzin, G., Yamaguchi, A., Kimura, G., 2015. Fluid circulation in the depths of accretionary prisms: an example of the Shimanto Belt, Kyushu, Japan. Tectonophysics 655, 161–176. https://doi.org/10.1016/j.tecto.2015.05.023.

Raimbourg, H., Famin, V., Palazzin, G., Mayoux, M., Jolivet, L., Ramboz, C., Yamaguchi, A., 2018. Fluid properties and dynamics along the seismogenic plate interface. Geosphere 14, 469–491. https://doi.org/10.1130/GES01504.1.

Raimbourg, H., Rajič, K., Moris-Muttoni, B., Famin, V., Palazzin, G., Fisher, D., Morell, K., Erdmann, S., Di Carlo, I., Montmartin, C., 2021. Quartz Vein Geochemistry Records Deformation Processes in Convergent Zones. Geochem Geophys Geosyst 22. https://doi.org/10.1029/2020GC009201

Ramsay, J.G., 1980. The crack–seal mechanism of rock deformation. Nature 284, 135–139. https://doi.org/10.1038/284135a0

Rebay, G., Zanoni, D., Langone, A., Luoni, P., Tiepolo, M., Spalla, M.I., 2018. Dating of ultramafic rocks from the Western Alps ophiolites discloses Late Cretaceous subduction ages in the Zermatt-Saas Zone. Geol. Mag. 155, 298–315. https://doi.org/10.1017/S0016756817000334.

Reddy, S.M., Wheeler, J., Butler, R.W.H., Cliff, R.A., Freeman, S., Inger, S., Pickles, C., Kelley, S.P., 2003. Kinematic reworking and exhumation within the convergent Alpine Orogen. Tectonophysics 365, 77–102. https://doi.org/10.1016/S0040-1951(03)00017-9.

Reinecke, T., 1991. Very-high-pressure metamorphism and uplift of coesite-bearing metasediments from the Zermatt-Saas zone. Western Alps. ejm 3, 7–18. https://doi.org/10.1127/ejm/3/1/0007.

Reinecke, T., 1998. Prograde high- to ultrahigh-pressure metamorphism and exhumation of oceanic sediments at Lago di Cignana, Zermatt-Saas Zone, western Alps. Lithos 42, 147–189. https://doi.org/10.1016/S0024-4937(97)00041-8.

Renard, F., Andréani, M., Boullier, A.-M., Labaume, P., 2005. Crack-seal patterns: records of uncorrelated stress release variations in crustal rocks. Geological Society, London, Special Publications 243, 67–79. https://doi.org/10.1144/GSL.SP.2005.243.01.07

Reynard, B., Ballèvre, M., 1988. Coexisting amphiboles in an eclogite from the Western Alps: new constraints on the miscibility gap between sodic and calcic amphiboles. J. Metamorph. Geol. 6, 333–350.

Robert, D., 1979. Contribution à l'étude géologique de la haute vallée de l'Arc-Région de Bonneval-Savoie. PhD thesis Université de Paris 6.

Roberts, S., Sanderson, D.J., Gumiel, P., 1999. Fractal analysis and percolation properties of veins. Geological Society, London, Special Publications 155, 7–16. https://doi.org/10.1144/GSL.SP.1999.155.01.03

Roedder, E, 1984. Volume 12: fluid inclusions. Reviews in mineralogy 12.

Rogers, G., Dragert, H., 2003. Episodic Tremor and Slip on the Cascadia Subduction Zone: The Chatter of Silent Slip. Science 300, 1942–1943. https://doi.org/10.1126/science.1084783

Rolland, Y., Lardeaux, J.-M., Guillot, S., Nicollet, C., 2000. Extension syn-convergence, poinçonnement vertical et unités métamorphiques contrastées en bordure ouest du Grand Paradis (Alpes Franco-Italiennes). Geodin. Acta 13, 133–148. https://doi.org/10.1080/09853111.2000.11105369.

Rossetti, F., Tecce, F., Aldega, L., Brilli, M., Faccenna, C., 2006. Deformation and fluid flow during orogeny at the palaeo-Pacific active margin of Gondwana: the early Palaeozoic Robertson Bay accretionary complex (North Victoria Land, Antarctica). J. Metamorph. Geol. 24, 33–53. https://doi.org/10.1111/j.1525-1314.2005.00620.x.

Rotondo, F.C., Tartarotti, P., Guerini, S., Della Porta, G., Campomenosi, N., 2021. Metasomatic horizon sealing serpentinite-metasediments pair in the Zermatt-Saas metaophiolite (Northwestern Alps): record of a channel for focussed fluid flow during subduction. Ofioliti 46, 1–25. https://doi.org/10.4454/ofioliti.v46i1.535.

Rubatto, D., Angiboust, S., 2015. Oxygen isotope record of oceanic and high-pressure metasomatism: a P–T–time–fluid path for the Monviso eclogites (Italy). Contrib. Mineral. Petrol. 170, 44. https://doi.org/10.1007/s00410-015-1198-4.

Rubatto, D., Hermann, J., 2001. Exhumation as fast as subduction? Geology 29, 3–6.

Rubatto, D., Hermann, J., 2003. Zircon formation during fluid circulation in eclogites (Monviso, Western Alps): implications for Zr and Hf budget in subduction zones. Geochim. Cosmochim. Acta 67, 2173–2187.

Rubatto, D., Gebauer, D., Fanning, M., 1998. Jurassic formation and Eocene subduction of the Zermatt-Saas-Fee ophiolites: implications for the geodynamic evolution of the Central and Western Alps. Contrib. Mineral. Petrol. 132, 269–287. https://doi.org/10.1007/s004100050421.

Ruff, L., Kanamori, H., 1980. Seismicity and the subduction process. Phys. Earth Planet. Inter. 23, 240–252. https://doi.org/10.1016/0031-9201(80)90117-X.

Ruh, J.B., Le Pourhiet, L., Agard, Ph., Burov, E., Gerya, T., 2015. Tectonic slicing of subducting oceanic crust along plate interfaces: Numerical modeling. Geochem. Geophys. Geosyst. 16, 3505–3531. https://doi.org/10.1002/2015GC005998.

Rüpke, L., 2004. Serpentine and the subduction zone water cycle. Earth Planet. Sci. Lett. 223, 17–34. https://doi.org/10.1016/j.epsl.2004.04.018.

Sachan, H.K., Kharya, A., Singh, P.C., Rolfo, F., Groppo, C., Tiwari, S.K., 2017. A fluid inclusion study of blueschist-facies lithologies from the Indus suture zone, Ladakh (India): Implications for the exhumation

of the subduction related Sapi-Shergol ophiolitic mélange. J. Asian Earth Sci. 146, 185–195. https://doi.org/10.1016/j.jseaes.2017.05.025.

Sadofsky, S.J., Bebout, G.E., 2004. Field and isotopic evidence for fluid mobility in the Franciscan complex: forearc paleohydrogeology to depths of 30 kilometers. Int. Geol. Rev. 46, 1053–1088. https://doi.org/10.2747/0020-6814.46.12.1053.

Saffer, D.M., Tobin, H.J., 2011. Hydrogeology and Mechanics of Subduction Zone Forearcs: Fluid Flow and Pore Pressure. Annu. Rev. Earth Planet. Sci. 39, 157–186. https://doi.org/10.1146/annurev-earth-040610-133408.

Saliot, P., 1978. Le métamorphisme dans les Alpes françaises. PhD thesis. Université Paris-Sud.

Saliot, P., 1979. La jadéite dans les Alpes françaises. Bull. Mineral. 102, 391–401. https://doi.org/10.3406/bulmi.1979.7335.

Saliot, P., Velde, B., 1982. Phengite compositions and post-nappe high-pressure metamorphism in the pennine zone of the French Alps. Earth Planet. Sci. Lett. 57, 133–138. https://doi.org/10.1016/0012-821X(82)90179-0.

Sanderson, D.J., Roberts, S., Gumiel, P., 1994. A fractal relationship between vein thickness and gold grade in drill core from La Codosera, Spain. Economic Geology 89, 168–173. https://doi.org/10.2113/gsecongeo.89.1.168

Sanderson, D.J., Roberts, S., Gumiel, P., Greenfield, C., 2008. Quantitative Analysis of Tin- and Tungsten-Bearing Sheeted Vein Systems. Economic Geology 103, 1043–1056. https://doi.org/10.2113/gsecongeo.103.5.1043

Sartori, M., 1987. Structure de la zone du Combin entre les Diablons et Zermatt (Valais). Eclogae Geol. Helv. 80, 789–814. https://doi.org/10.5169/SEALS-166026.

Scambelluri, M., Philippot, P., 2001. Deep fluids in subduction zones. Lithos 55, 213–227. https://doi.org/10.1016/S0024-4937(00)00046-3.

Scambelluri, M., Piccardo, G., Philippot, P., Robbiano, A., Negretti, L., 1997. High salinity fluid inclusions formed from recycled seawater in deeply subducted alpine serpentinite. Earth and Planetary Science Letters 148, 485–499. https://doi.org/10.1016/S0012-821X(97)00043-5.

Scambelluri, M., Pennacchioni, G., Philippot, P., 1998. Salt-rich aqueous fluids formed during eclogitization of metabasites in the Alpine continental crust (Austroalpine Mt. Emilius unit, Italian western Alps). Lithos 43, 151-167.

Scambelluri, M., Bottazzi, P., Trommsdorff, V., Vannucci, R., Hermann, J., Gomez-Pugnaire, M.T., Lopez-Sanchez, V., 2001. Incompatible element-rich fluids released by antigorite breakdown in deeply subducted mantle. Earth Planet. Sci. Lett. 192, 457–470.

Scambelluri, M., Fiebig, J., Malaspina, N., Müntener, O., Pettke, T., 2004. Serpentinite subduction: implications for fluid processes and trace-element recycling. International Geology Review 46, 595-613.

Scambelluri, M., Pettke, T., Cannaò, E., 2015. Fluid-related inclusions in Alpine high-pressure peridotite reveal trace element recycling during subduction-zone dehydration of serpentinized mantle (Cima di Gagnone, Swiss Alps). Earth and Planetary Science Letters 429, 45-59.

Scambelluri, M., Pennacchioni, G., Gilio, M., Bestmann, M., Plümper, O., Nestola, F., 2017. Fossil intermediate-depth earthquakes in subducting slabs linked to differential stress release. Nat. Geosci. 10, 960–966. https://doi.org/10.1038/s41561-017-0010-7.

Schertl, H.-P., Maresch, W.V., Stanek, K.P., Hertwig, A., Krebs, M., Baese, R., Sergeev, S.S., 2012. New occurrences of jadeitite, jadeite quartzite and jadeite-lawsonite quartzite in the Dominican Republic, Hispaniola: petrological and geochronological overview. Eur. J. Mineral. 24, 199–216. https://doi.org/10.1127/0935-1221/2012/0024-2201.

Schmid, S.M., Pfiffner, O.A., Froitzheim, N., Sch¨onborn, G., Kissling, E., 1996. Geophysical-geological transect and tectonic evolution of the Swiss-Italian Alps. Tectonics 15, 1036–1064. https://doi.org/10.1029/96TC00433.

Schmid, S.M., Kissling, E., Diehl, T., van Hinsbergen, D.J.J., Molli, G., 2017. Ivrea mantle wedge, arc of the Western Alps, and kinematic evolution of the Alps–Apennines orogenic system. Swiss J. Geosci. 110, 581–612. https://doi.org/10.1007/s00015-016-0237-0.

Schmidt, M.W., Poli, S., 2014. Devolatilization During Subduction, in: Treatise on Geochemistry. Elsevier, pp. 669–701. https://doi.org/10.1016/B978-0-08-095975-7.00321-1

Schmitz, M. D., Bowring, S. A., 2001. U-Pb zircon and titanite systematics of the Fish Canyon Tuff: an assessment of high-precision U-Pb geochronology and its application to young volcanic rocks. Geochimica et Cosmochimica Acta, 65, 2571-2587.

Schmitz, M. D., Schoene, B., 2007. Derivation of isotope ratios, errors, and error correlations for U-Pb geochronology using 205Pb-235U-(233U)-spiked isotope dilution thermal ionization mass spectrometric data. Geochemistry, Geophysics, Geosystems, 8.

Scholl, D.W., von Huene, R., Vallier, T.L., Howell, D.G., 1980. Sedimentary masses and concepts about tectonic processes at underthrust ocean margins. Geology 8, 564–568. https://doi.org/10.1130/0091-7613(1980)8<564:SMACAT>2.0.CO;2.

Schwartz, Stéphane, 2000. La zone Piémontaise des Alpes occidentales : un paléocomplexe de subduction. Arguments métamorphiques, géochronologiques et structuraux. PhD thesis. Université Claude Bernard-Lyon I.

Schwartz, S., Lardeaux, J.-M., Guillot, S., Tricart, P., 2000a. Diversité du métamorphisme éclogitique dans le massif ophiolitique du Monviso (Alpes occidentales, Italie). Geodin. Acta 13, 169–188. https://doi.org/10.1080/09853111.2000.11105371.

Schwartz, S., Lardeaux, J.-M., Tricart, P., 2000b. La zone d'Acceglio (Alpes cottiennes) : un nouvel exemple de croûte continentale éclogitisée dans les Alpes occidentales. C. R. Acad. Sci. Ser. IIA Earth Planet. Sci. 330, 859–866. https://doi.org/10.1016/S1251-8050(00)00218-4.

Schwartz, S., Lardeaux, J.M., Tricart, P., Guillot, S., Labrin, E., 2007. Diachronous exhumation of HP-LT metamorphic rocks from south-western Alps: evidence from fission-track analysis. Terra Nova 19, 133–140. https://doi.org/10.1111/j.1365-3121.2006.00728.x.

Schwartz, S., Guillot, S., Reynard, B., Lafay, R., Debret, B., Nicollet, C., Lanari, P., Auzende, A.L., 2013. Pressure–temperature estimates of the lizardite/antigorite transition in high pressure serpentinites. Lithos 178, 197–210. https://doi.org/10.1016/j.lithos.2012.11.023.

Schwartz, S., Gautheron, C., Ketcham, R.A., Brunet, F., Corre, M., Agranier, A., Pinna-Jamme, R., Haurine, F., Monvoin, G., Riel, N., 2020. Unraveling the exhumation history of high-pressure ophiolites using magnetite (U-Th-Sm)/He thermochronometry. Earth Planet. Sci. Lett. 543, 116359 https://doi.org/10.1016/j.epsl.2020.116359.

Selverstone, J., Sharp, Z.D., 2013. Chlorine isotope constraints on fluid-rock interactions during subduction and exhumation of the Zermatt-Saas ophiolite. Geochem. Geophys. Geosyst. 14, 4370–4391. https://doi.org/10.1002/ggge.20269.

Selverstone, J., Sharp, Z.D., 2015. Chlorine isotope behavior during prograde metamorphism of sedimentary rocks. Earth and Planetary Science Letters 417, 120-131.

Selverstone, J., Franz, G., Thomas, S., Getty, S., 1992. Fluid variability in 2 GPa eclogites as an indicator of fluid behavior during subduction. Contrib. Mineral. Petrol. 112, 341–357. https://doi.org/10.1007/BF00310465.

Sharp, Z.D., Barnes, J.D., 2004. Water-soluble chlorides in massive seafloor serpentinites: a source of chloride in subduction zones. Earth and Planetary Science Letters 226, 243-254.

Sicard-Lochon, E., 1987. La Lawsonite et Ses Pseudomorphoses. PhD thesis, Université Claude Bernard-Lyon I.

Simon-Labric, T., Rolland, Y., Dumont, T., Heymes, T., Authemayou, C., Corsini, M., Fornari, M., 2009. 40 Ar/ 39 Ar dating of Penninic Front tectonic displacement (W Alps) during the Lower Oligocene (31-34 Ma). Terra Nova 21, 127–136. https://doi.org/10.1111/j.1365-3121.2009.00865.x.

Simpson, G.D.H., 2000. Synmetamorphic vein spacing distributions: characterisation and origin of a distribution of veins from NW Sardinia, Italy. Journal of Structural Geology 22, 335–348. https://doi.org/10.1016/S0191-8141(99)00161-3

Sisson, V.B., Hollister, L.S., Onstott, T.C., 1989. Petrologic and age constraints on the origin of a low-pressure/high-temperature metamorphic complex, southern Alaska. J. Geophys. Res. 94, 4392–4410. https://doi.org/10.1029/JB094iB04p04392.

Skora, S., Mahlen, N.J., Johnson, C.M., Baumgartner, L.P., Lapen, T.J., Beard, B.L., Szilvagyi, E.T., 2015. Evidence for protracted prograde metamorphism followed by rapid exhumation of the Zermatt-Saas Fee ophiolite. J. Metamorph. Geol. 33, 711–734. https://doi.org/10.1111/jmg.12148.

Smith, M.P., Yardley, B.W.D., 1999. Fluid evolution during metamorphism of the Otago Schist, New Zealand: (I) evidence from fluid inclusions. J. Metamorph. Geol. 17, 173–186. https://doi.org/10.1046/j.1525-1314.1999.00189.x.

Soret, M., Larson, K.P., Cottle, J., Ali, A., 2021. How Himalayan collision stems from subduction. Geology 49, 894–898. https://doi.org/10.1130/G48803.1.

Spandler, C., Hermann, J., 2006. High-pressure veins in eclogite from New Caledonia and their significance for fluid migration in subduction zones. Lithos 89, 135-153.

Spandler, C., Pirard, C., 2013. Element recycling from subducting slabs to arc crust: A review. Lithos 170–171, 208–223. https://doi.org/10.1016/j.lithos.2013.02.016

Spandler, C., Hermann, J., Faure, K., Mavrogenes, J.A., Arculus, R.J., 2008. The importance of talc and chlorite “hybrid” rocks for volatile recycling through subduction zones; evidence from the high-pressure subduction mélange of New Caledonia. Contrib Mineral Petrol 155, 181–198. https://doi.org/10.1007/s00410-007-0236-2.

Spandler, C., Pettke, T., Rubatto, D., 2011. Internal and External Fluid Sources for Eclogite-facies Veins in the Monviso Meta-ophiolite, Western Alps: Implications for Fluid Flow in Subduction Zones. Journal of Petrology 52, 1207–1236. https://doi.org/10.1093/petrology/egr025

Spandler, C., Hammerli, J., Sha, P., Hilbert-Wolf, H., Hu, Y., Roberts, E., & Schmitz, M., 2016. MKED1: a new titanite standard for in situ analysis of Sm–Nd isotopes and U–Pb geochronology. Chemical Geology, 425, 110-126.

Spear, F.S., Franz, G., 1986. P-T evolution of metasediments from the Eclogite Zone, southcentral Tauern Window, Austria. Lithos 19, 219–234. https://doi.org/10.1016/0024-4937(86)90024-1.

Spencer, K. J., Hacker, B. R., Kylander-Clark, A. R. C., Andersen, T. B., Cottle, J. M., Stearns, M. A., Poletti, J.E., Seward, G. G. E., 2013. Campaign-style titanite U–Pb dating by laser-ablation ICP: Implications for crustal flow, phase transformations and titanite closure. Chemical Geology, 341, 84-101.

Stacey, J. S., & Kramers, J.D., 1975. Approximation of terrestrial lead isotope evolution by a two-stage model. Earth and Planetary Science Letters, 26, 207-221.

Stampfli, G.M., Marthaler, M., 1990. Divergent and convergent margins in the North-Western alps confrontation to actualistic models. Geodin. Acta 4, 159–184. https://doi.org/10.1080/09853111.1990.11105208.

Stampfli, G.M., Mosar, J., Marquer, D., Marchant, R., Baudin, T., Borel, G., 1998. Subduction and obduction processes in the Swiss Alps. Tectonophysics 296, 159–204. https://doi.org/10.1016/S0040-1951(98)00142-5.

Starr, P.G., Broadwell, K.S., Dragovic, B., Scambelluri, M., Haws, A.A., Caddick, M.J., Smye, A.J., Baxter, E.F., 2020. The subduction and exhumation history of the Voltri Ophiolite, Italy: evaluating exhumation mechanisms for high-pressure metamorphic massifs. Lithos 376-377, 105767.

Sterin, K.E., Aleksanyan, V.T., Zhizhin, G.N., 1980. Raman Spectra of Hydrocarbons (Pergamon. ed).

Stern, R.J., 2002. Subduction Zones. Rev. Geophys. 40 https://doi.org/10.1029/2001RG000108, 3-1-3–38.

Sterner, S.M., Bodnar, R.J., 1989. Synthetic fluid inclusions - VII. Re-equilibration of fluid inclusions in quartz during laboratory-simulated metamorphic burial and uplift. J. Metamorph. Geol. 7, 243–260. https://doi.org/10.1111/j.1525-1314.1989.tb00587.x.

Stowell, J.F.W., Watson, A.P., Hudson, N.F.C., 1999. Geometry and population systematics of a quartz vein set, Holy Island, Anglesey, North Wales. Geological Society, London, Special Publications 155, 17–33. https://doi.org/10.1144/GSL.SP.1999.155.01.04

Sverjensky, D., Daniel, I., Brovarone, A.V., 2020. The changing character of carbon in fluids with pressure: organic geochemistry of Earth's uppermantle fluids. In: Manning, C.E., Lin, J., Mao, W.L. (Eds.), Geophysical Monograph Series. Wiley, pp. 259–269 https://doi.org/10.1002/9781119508229.ch22.

Syracuse, E.M., van Keken, P.E., Abers, G.A., 2010. The global range of subduction zone thermal models. Phys. Earth Planet. Inter. 183, 73–90. https://doi.org/10.1016/j.pepi.2010.02.004.

Taetz, S., John, T., Bröcker, M., Spandler, C., Stracke, A., 2018. Fast intraslab fluid-flow events linked to pulses of high pore fluid pressure at the subducted plate interface. Earth and Planetary Science Letters 482, 33-43.

Tao, R., Zhang, L., Tian, M., Zhu, J., Liu, X., Liu, J., Höfer, H.E., Stagno, V., Fei, Y., 2018. Formation of abiotic hydrocarbon from reduction of carbonate in subduction zones: constraints from petrological observation and experimental simulation. Geochim. Cosmochim. Acta 239, 390–408. https://doi.org/10.1016/j.gca.2018.08.008.

Tarantola, A., Caumon, M.-C., 2015. Raman spectra of water in fluid inclusions: II. Effect of negative pressure on salinity measurement: Effect of negative pressure on salinity measured by Raman spectroscopy. J. Raman Spectrosc. 46, 977–982. https://doi.org/10.1002/jrs.4668.

Tarantola, A., Mullis, J., Vennemann, T., Dubessy, J., de Capitani, C., 2007. Oxidation of methane at the CH4/H2O–(CO2) transition zone in the external part of the Central Alps, Switzerland: evidence from stable isotope investigations. Chem. Geol. 237, 329–357. https://doi.org/10.1016/j.chemgeo.2006.07.007.

Tarantola, A., Mullis, J., Guillaume, D., Dubessy, J., de Capitani, C., Abdelmoula, M., 2009. Oxidation of CH4 to CO2 and H2O by chloritization of detrital biotite at 270±5 °C in the external part of the Central Alps, Switzerland. Lithos 112, 497–510. https://doi.org/10.1016/j.lithos.2009.04.008.

Tarantola, A., Diamond, L.W., Stünitz, H., Thust, A., Pec, M., 2012. Modification of fluid inclusions in quartz by deviatoric stress. III: Influence of principal stresses on inclusion density and orientation. Contrib. Mineral. Petrol. 164, 537–550. https://doi.org/10.1007/s00410-012-0749-1.

Tarling, M.S., Smith, S.A.F., Scott, J.M., 2019. Fluid overpressure from chemical reactions in serpentinite within the source region of deep episodic tremor. Nat. Geosci. 12, 1034–1042. https://doi.org/10.1038/s41561-019-0470-z.

Tartarotti, P., Martin, S., Meyzen, C.M., Benciolini, L., Toffolo, L., 2019. Structural Evolution and Metasomatism of Subducted Metaophiolites in the Northwestern Alps. Tectonics 38, 4185–4206. https://doi.org/10.1029/2019TC005626.

Tartarotti, P., Martin, S., Festa, A., Balestro, G., 2021. Metasediments Covering Ophiolites in the HP Internal Belt of the Western Alps: Review of Tectono-Stratigraphic Successions and Constraints for the Alpine Evolution. Minerals 11, 411. https://doi.org/10.3390/min11040411.

Tatsumi, Y., 1986. Formation of the volcanic front in subduction zones. Geophys. Res. Lett. 13, 717–720. https://doi.org/10.1029/GL013i008p00717.

Tatsumi, Y., 1989. Migration of fluid phases and genesis of basalt magmas in subduction zones. Journal of Geophysical Research: Solid Earth, 94, 4697-4707.

Terabayashi, M., Maruyama, S., 1998. Large pressure gap between the Coastal and Central Franciscan belts, northern and Central California. Tectonophysics 285, 87–101. https://doi.org/10.1016/S0040-1951(97)00194-7.

Tewksbury-Christle, C.M., Behr, W.M., 2021. Constraints From Exhumed Rocks on the Seismic Signature of the Deep Subduction Interface. Geophysical Research Letters 48. https://doi.org/10.1029/2021GL093831

Tewksbury-Christle, C.M., Behr, W.M., Helper, M.A., 2021. Tracking Deep Sediment Underplating in a Fossil Subduction Margin: Implications for Interface Rheology and Mass and Volatile Recycling. Geochem. Geophys. Geosyst. 22 https://doi.org/10.1029/2020GC009463.

Tobin, H., Hirose, T., Ikari, M., Kanagawa, K., Kimura, G., Kinoshita, M., Kitajima, H., Saffer, D., Yamaguchi, A., Eguchi, N., Maeda, L., Toczko, S., 2019. Expedition 358 Preliminary Report: NanTroSEIZE Plate Boundary Deep Riser 4: Nankai Seismogenic/Slow Slip Megathrust. International Ocean Discovery Program Preliminary Report. International Ocean Discovery Program. https://doi.org/10.14379/iodp.pr.358.2019.

Toriumi, A., Teruya, J., 1988. Tectono-metamorphism of the Shimanto Belt. Modern Geology 12, 303–324.

Touret, J.L.R., Frezzotti, M.-L., 2003. Fluid inclusions in high pressure and ultrahigh pressure metamorphic rocks. In: Papp, G., Weiszburg, T.G., Carswell, D.A., Compagnoni, R., Rolfo, F. (Eds.), Ultrahigh Pressure Metamorphism. Mineralogical Society of Great Britain and Ireland, Budapest, pp. 467–487 https://doi.org/10.1180/EMUnotes. 5.15.

Tricart, P., 1974. Les Schistes lustrés du Haut-Cristillan (Alpes cottiennes, France) : lithostratigraphie, architecture et tectogenèse. Géologie Alpine 50, 131–152.

Tricart, P., Schwartz, S., 2006. A north-south section across the Queyras Schistes lustrés (Piedmont zone, Western Alps): Syn-collision refolding of a subduction wedge. Eclogae Geol. Helv. 99, 429–442. https://doi.org/10.1007/s00015-006-1197-6.

Tsujimori, T., Matsumoto, K., Wakabayashi, J., Liou, J.G., 2006a. Franciscan eclogite revisited: Reevaluation of the P–T evolution of tectonic blocks from Tiburon Peninsula, California, U.S.a. Mineral. Petrol. 88, 243–267. https://doi.org/10.1007/s00710-006-0157-1.

Tsujimori, T., Sisson, V.B., Liou, J.G., Harlow, G.E., & Sorensen, S.S., 2006b. Very-low-temperature record of the subduction process: A review of worldwide lawsonite eclogites. Lithos 92, 609-624.

Turcotte, D.L., 1989. Fractals in geology and geophysics. PAGEOPH 131, 26.

Turcotte, D.L., 1986. Fractals and fragmentation. J. Geophys. Res. 91, 1921. https://doi.org/10.1029/JB091iB02p01921

Ujiie, K., Saishu, H., Fagereng, Å., Nishiyama, N., Otsubo, M., Masuyama, H., Kagi, H., 2018. An Explanation of Episodic Tremor and Slow Slip Constrained by Crack-Seal Veins and Viscous Shear in Subduction Mélange. Geophys. Res. Lett. 45, 5371–5379. https://doi.org/10.1029/2018GL078374

Valley, J. W, 1986. Stable isotope geochemistry of metamorphic rocks. Stable isotopes in high temperature geological processes 445–490.

Vallis, F., Scambelluri, M., 1996. Redistribution of high-pressure fluids during retrograde metamorphism of eclogite-facies rocks (Voltri Massif, Italian Western Alps). Lithos 39, 81–92. https://doi.org/10.1016/S0024-4937(96)00012-6.

Van den Kerkhof, A. M., Hein, U. F., 2001. Fluid inclusion petrography. Lithos 55, 27–47.

van Keken, P.E., Hacker, B.R., Syracuse, E.M., Abers, G.A., 2011. Subduction factory: 4. Depth-dependent flux of H 2 O from subducting slabs worldwide. J. Geophys. Res. 116, B01401. https://doi.org/10.1029/2010JB007922.

Vanko, D.A., 1986. High-chlorine amphiboles fromoceanic rocks: product of highly-saline hydrothermal fluids? Am. Mineral. 71, 51–59.

Vanko, D.A., 1988. Temperature, pressure, and composition of hydrothermal fluids, with their bearing on the magnitude of tectonic uplift at mid-ocean ridges, inferred from fluid inclusions in oceanic layer 3 rocks. J. Geophys. Res. 93, 4595–4611.

Vannucchi, P., 2001. Monitoring paleo-fluid pressure through vein microstructures. J. Geodyn. 32, 567–581. https://doi.org/10.1016/S0264-3707(01)00048-5.

Vannucchi, P., Remitti, F., Bettelli, G., Boschi, C., Dallai, L., 2010. Fluid history related to the early Eocene-middle Miocene convergent system of the Northern Apennines (Italy): Constraints from structural and isotopic studies. J. Geophys. Res. 115, B05405. https://doi.org/10.1029/2009JB006590

Vannucchi, P., Spagnuolo, E., Aretusini, S., Di Toro, G., Ujiie, K., Tsutsumi, A., Nielsen, S., 2017. Past seismic slip-to-the-trench recorded in Central America megathrust. Nat. Geosci. 10, 935–940. https://doi.org/10.1038/s41561-017-0013-4.

Velde, B., 1967. Si+ 4 content of natural phengites. Contrib. Mineral. Petrol. 14, 250–258.

Velde, B, Dubois, J, Touchard, G, Badri, A, 1990. Fractal analysis of fractures in rocks: the Cantor's Dust method. Tectonophysics 179, 345–352.

Velde, B, Dubois, J, Moore, D, Touchard, G, 1991. Fractal patterns of fractures in granites. Earth and Planetary Science Letters 104, 25–35.

Verlaguet, A., Goffé, B., Brunet, F., Poinssot, C., Vidal, O., Findling, N., Menut, D., 2011. Metamorphic veining and mass transfer in a chemically closed system: a case study in Alpine metabauxites (western Vanoise). Journal of Metamorphic Geology 29, 275–300. https://doi.org/10.1111/j.1525-1314.2010.00918.x

Verlaguet, A., Bonnemains, D., Mével, C., Escartín, J., Andreani, M., Bourdelle, F., Boiron, M.-C., Chavagnac, V., 2020. Fluid circulation along an oceanic detachment fault: insights from fluid inclusions in silicified brecciated fault rocks (Mid-Atlantic Ridge at 13°20′N). Geochem. Geophys. Geosyst. https://doi.org/10.1029/2020GC009235.

Vermeesch, P., 2018. IsoplotR: A free and open toolbox for geochronology. Geoscience Frontiers, 9, 1479-1493.

Villa, I.M., Bucher, S., Bousquet, R., Kleinhanns, I.C., Schmid, S.M., 2014. Dating Polygenetic Metamorphic Assemblages along a Transect across the Western Alps. J. Petrol. 55, 803–830. https://doi.org/10.1093/petrology/egu007.

Vitale Brovarone, A., Beyssac, O., Malavieille, J., Molli, G., Beltrando, M., Compagnoni, R., 2013. Stacking and metamorphism of continuous segments of subducted lithosphere in a high-pressure wedge: the example of Alpine Corsica (France). Earth-Science Reviews 116, 35-56.

Vitale Brovarone, A., Picatto, M., Beyssac, O., Lagabrielle, Y., Castelli, D., 2014a. The blueschist–eclogite transition in the Alpine chain: P–T paths and the role of slowspreading extensional structures in the evolution of HP–LT mountain belts. Tectonophysics 615–616, 96–121. https://doi.org/10.1016/j.tecto.2014.01.001.

Vitale Brovarone, A., Alard, O., Beyssac, O., Martin, L., Picatto, M., 2014b. Lawsonite metasomatism and trace element recycling in subduction zones. J. Meta. Geol. 32, 489–514. https://doi.org/10.1111/jmg.12074.

Vitale Brovarone, A., Martinez, I., Elmaleh, A., Compagnoni, R., Chaduteau, C., Ferraris, C., Esteve, I., 2017. Massive production of abiotic methane during subduction evidenced in metamorphosed ophicarbonates from the Italian Alps. Nat. Commun. 8, 14134. https://doi.org/10.1038/ncomms14134.

Vitale Brovarone, A., Sverjensky, D.A., Piccoli, F., Ressico, F., Giovannelli, D., Daniel, I., 2020a. Subduction hides high-pressure sources of energy that may feed the deep subsurface biosphere. Nat. Commun. 11, 3880. https://doi.org/10.1038/s41467-020-17342-x.

Vitale Brovarone, A., Tumiati, S., Piccoli, F., Ague, J.J., Connolly, J.A.D., Beyssac, O., 2020b. Fluid-mediated selective dissolution of subducting carbonaceous material: implications for carbon recycling and fluid fluxes at forearc depths. Chem. Geol. 549, 119682. https://doi.org/10.1016/j.chemgeo.2020.119682.

Vityk, M.O., Bodnar, R.J., 1995a. Do fluid inclusions in high-grade metamorphic terranes preserve peakmetamorphic density during retrograde decompression? Am. Mineral. 80, 641–644.

Vityk, M.O., Bodnar, R.J., 1995b. Textural evolution of synthetic fluid inclusions in quartz during reequilibration, with applications to tectonic reconstruction. Contrib. Mineral. Petrol. 121, 309–323. https://doi.org/10.1007/BF02688246.

Von Huene, R., Scholl, D.W., 1991. Observations at convergent margins concerning sediment subduction, subduction erosion, and the growth of continental crust. Reviews of Geophysics 29, 279-316.

Vrolijk, P., 1987. Tectonically driven fluid flowin the Kodiak accretionary complex, Alaska. Geology 15, 466–469.

Vrolijk, P., Myers, G., Moore, J.C., 1988. Warm fluid migration along tectonic melanges in the Kodiak Accretionary complex, Alaska. J. Geophys. Res. 93, 10313–10324. https://doi.org/10.1029/JB093iB09p10313.

Wada, I., Wang, K., 2009. Common depth of slab-mantle decoupling: Reconciling diversity and uniformity of subduction zones. Geochem. Geophys. Geosyst. 10. https://doi.org/10.1029/2009GC002570.

Wassmann, S., St¨ockhert, B., 2013. Rheology of the plate interface — Dissolution precipitation creep in high pressure metamorphic rocks. Tectonophysics 608, 1–29. https://doi.org/10.1016/j.tecto.2013.09.030.

Watterson, J, 1986. Fault dimensions, displacements and growth. Pure and Applied Geophysics 124, 365–373.

Weber, S., Sandmann, S., Miladinova, I., Fonseca, R.O.C., Froitzheim, N., Münker, C., Bucher, K., 2015. Dating the initiation of Piemonte-Liguria Ocean subduction: Lu–Hf garnet chronometry of eclogites from the Theodul Glacier Unit (Zermatt-Saas zone, Switzerland). Swiss J. Geosci. 108, 183–199. https://doi.org/10.1007/s00015-015-0180-5.

Wech, A.G., Creager, K.C., Houston, H., Vidale, J.E., 2010. An earthquake-like magnitude-frequency distribution of slow slip in northern Cascadia. Geophys. Res. Lett. 37. https://doi.org/10.1029/2010GL044881

Wells, D. L, Coppersmith, K. J, 1994. New empirical relationships among magnitude, rupture length, rupture width, rupture area, and surface displacement. Bulletin of the Seismological Society of America 84, 974–1002.

Widmer, T., Thompson, A. B, 2001. Local origin of high pressure vein material in eclogite facies rocks of the Zermatt-Saas-Zone, Switzerland. American Journal of Science 301, 627–656. https://doi.org/10.2475/ajs.301.7.627

Wiederkehr, M., Bousquet, R., Ziemann, M.A., Berger, A., Schmid, S.M., 2011. 3-D assessment of peak-metamorphic conditions by Raman spectroscopy of carbonaceous material: an example from the margin of the Lepontine dome (Swiss Central Alps). Int. J. Earth sci. 100, 1029–1063.

Willner, A.P., 2005. Pressure–Temperature Evolution of a Late Palaeozoic Paired Metamorphic Belt in North–Central Chile (34◦–35◦30′ S). J. Petrol. 46, 1805–1833. https://doi.org/10.1093/petrology/egi035.

Wopenka, B., Pasteris, J. D., 1987. Raman intensities and detection limits of geochemically relevant gas mixtures for a laser Raman microprobe. Analytical Chemistry 59, 2165–2170.

Yardley, B.W.D., 1982. The early metamorphic history of the Haast Schists and related rocks of New Zealand. Contrib. Mineral. Petrol. 81, 317–327. https://doi.org/10.1007/BF00371686.

Yardley, B.W.D., Graham, J.T., 2002. The origins of salinity in metamorphic fluids: origins of salinity in metamorphic fluids. Geofluids 2, 249–256. https://doi.org/10.1046/j.1468-8123.2002.00042.x.

York, D., 1967. The best isochron. Earth and Planetary Science Letters, 2, 479-482.

Yoshida, K., Hirajima, T., Ohsawa, S., Kobayashi, T., Mishima, T., Sengen, Y., 2015. Geochemical features and relative B–Li–Cl compositions of deep-origin fluids trapped in high-pressure metamorphic rocks. Lithos 226, 50–64. https://doi.org/10.1016/j.lithos.2015.03.002.

Zanoni, D., Rebay, G., Spalla, M.I., 2016. Ocean floor and subduction record in the Zermatt-Saas rodingites, Valtournanche, Western Alps. J. Metamorph. Geol. 34, 941–961. https://doi.org/10.1111/jmg.12215.

Annexes

Grand Roc Noir et lac de Lanserlia. Haute-Maurienne.

American Mineralogist, Volume 104, pages 403–417, 2019

A XANES and EPMA study of Fe^{3+} in chlorite: Importance of oxychlorite and implications for cation site distribution and thermobarometry

Lorella Masci[1,*], Benoît Dubacq[1], Anne Verlaguet[1], Christian Chopin[2], Vincent De Andrade[3], and Clément Herviou[1]

[1]Sorbonne Université, CNRS-INSU, Institut des Sciences de la Terre Paris, ISTeP UMR 7193, 75005 Paris, France
[2]Laboratoire de Géologie, Ecole normale supérieure, CNRS, UMR8538, PSL Research University, 24 rue Lhomond, 75005 Paris, France
[3]Advanced Photon Source, Argonne National Laboratory, Argonne, Illinois 60439, U.S.A.

Abstract

Chlorite is a ubiquitous product of metamorphism, alteration of magmatic rocks and hydrothermal processes owing to its large stability field and wide compositional range. Its composition is governed by several substitutions and has been used as a geothermometer, on the basis of empirical, semi-empirical, and thermodynamic models. As in some other phyllosilicates of petrological interest, the oxidation state of iron in chlorite may differ from the usually assumed divalent state. However, the crystal chemistry of trivalent iron in chlorite remains poorly known, and the thermodynamic properties of ferric chlorite are missing from databases used for petrological modeling. As part of an attempt to fill this gap, we present results from in situ, micrometer-scale measurements of the oxidation state of iron in various chlorite-bearing samples. X-ray absorption near-edge spectroscopy (XANES) was combined with electron probe microanalysis (EPMA) on the same crystals. Results show iron oxidation states varying from ferrous to ferric; iron is in octahedral coordination in all ferromagnesian chlorites but to ~25% tetrahedral in the lithian chlorite cookeite (1.0 wt% $Fe_2O_{3(total)}$). Absolute amounts of ferric iron cover an unprecedented range (0 to ~30 wt% Fe_2O_3). For highly magnesian, ferric chlorite, Fe concentrations are low and can be accounted for by $Al = Fe^{3+}$ substitution. In Fe-rich samples, Fe^{3+} may exceed 2 atoms per formula unit (pfu, 18 oxygen basis). When structural formulas are normalized to 28 charges corresponding to the standard $O_{10}(OH)_8$ anionic basis, these measurements define the exchange vector of a di-trioctahedral-type substitution: $3\ ^{VI}(Mg, Fe^{2+}) = {}^{VI}\square + 2\ ^{VI}Fe^{3+}$, as described in earlier studies. However, structural formulas calculated on the basis of the oxygen contents actually measured by EPMA show that this trend is an artifact, due to the neglect of variations in the number of protons in the structure. Our measurements indicate increasing hydrogen deficiency with increasing Fe^{3+} content, up to ~ 2 H^+ pfu in the Fe^{3+}-rich chlorite samples, corresponding to a net exchange vector of the type $R^{2+} + H^+ = Fe^{3+}$. These results do not support substitutions toward di-trioctahedral ferric end-members, and highlight the need for considering substitution toward an "oxychlorite" (i.e., H-deficient) ferric component, close to tri-trioctahedral, with an $O_{12}(OH)_6$ anionic basis, even in green, pristine-looking chlorite. The effects of iron oxidation and H deficiency on chlorite geothermometers were explored. They are deterring if H deficiency is ignored but, given the sensitivity of most thermometers to octahedral vacancy, the assumption $Fe_{total} = Fe^{2+}$ is still safer than using high measured Fe^{3+} contents *and* the standard 28 charge basis, which artificially increases vacancies. In such ferric chlorites, EPMA measurement of oxygen allows a fair estimate of H content if Fe^{3+}/Fe^{2+} is known; it should be more systematically implemented. For the same reasons, literature data reporting Fe^{3+}-rich chlorite with vacancy content along the possibly artificial di-trioctahedral-type substitution should be verified. With the help of constraints from thermodynamic models, charge balance, crystal symmetry, and proton loss, a new cation site distribution is proposed for di-tri- to tri-trioctahedral chlorites in the Fe^{2+}-Fe^{3+}-Mg-Al-Si-O-H system, allowing a more realistic thermodynamic handling of their solid solutions.

Keywords: Chlorite, oxychlorite, hydrogen deficiency, XANES, EPMA, ferric iron incorporation, geothermometry, solid solution, cation site distribution

Introduction

Chlorite is a ubiquitous phyllosilicate characterized by a 14 Å *c* cell-parameter that is found in a wide range of geological environments and crystallizes from diagenesis conditions up to blueschist- and amphibolite-facies metamorphic conditions. This 14 Å value reflects the combination of a TOT mica-like layer (a partially hydroxylated octahedral sheet between two opposing tetrahedral sheets) with an interlayer hydroxide sheet ("brucitic" octahedral sheet) in which each oxygen atom is part of a hydroxyl group involved in hydrogen bonding to the facing 2:1 layer (Fig. 1). Both octahedral sheets may be fully or partly occupied, leading to tri-tri-, di-tri-, and di-di-octahedral chlorite end-members. Zazzi et al. (2006) and Beaufort et al. (2015) offered extensive reviews of the structure and crystal chemistry of chlorite. The usual site assignment of cations in the chlorite structure is recalled in Table 1, together with a list of the potential end-members referred to in this and previous studies.

* E-mail: lorella.masci@sorbonne-universite.fr

0003-004X/19/0003–403$05.00/DOI: https://doi.org/10.2138/am-2019-6766

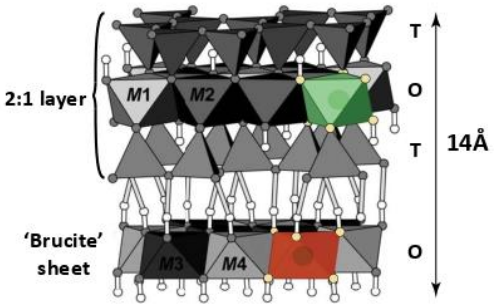

FIGURE 1. Structure of chlorite, after Zazzi et al. (2006). Gray (or yellow) spheres are oxygen atoms; white spheres are H atoms. An M1 site (in the TOT layer) and an M3 site (in the hydroxide interlayer, "brucite sheet") are highlighted in color.

Chlorite is used as a geothermometer because its composition varies with its crystallization temperature via several solid solutions. Empirical and semi-empirical equations establish a link between temperature and the amount of, e.g., tetrahedral Al (Cathelineau 1988), octahedral vacancies (Hillier and Velde 1991) or, in addition, Mg contents (Inoue et al. 2009; Bourdelle et al. 2013a). Thermodynamic models are also available (e.g., Walshe 1986; Holland et al. 1998; Vidal et al. 2001; Lanari et al. 2014); they use end-members (of which some are fictive) with fixed thermodynamic properties and activity models for solid solutions, some considering ordering and reciprocal solid solutions. These models are based on the structure and composition of chamosite (a tri-trioctahedral chlorite solid solution among the clinochlore, Mg-amesite, and "daphnite" end-members, e.g., Holland and Powell 1998) extended to the end-members "Al-free chlorite" (e.g., Holland et al. 1998), sudoite [the di-trioctahedral chlorite $\square Mg_2Al_3(Si_3Al)O_{10}(OH)_8$, Vidal et al. 2001], and Fe-amesite (Vidal et al. 2005). These models account for three main substitutions observed in chlorite: (1) homovalent Fe-Mg substitution Fe = Mg; (2) the di-trioctahedral substitution $^{VI}\square + 2\ ^{VI}Al = 3\ ^{VI}(Mg, Fe^{2+})$ where $^{VI}\square$ is an octahedral vacancy, and (3) the Tschermak substitution $^{IV}Si + {}^{VI}(Mg, Fe^{2+}) = {}^{IV}Al + {}^{VI}Al$ (e.g., Zane et al. 1998). The Al-free chlorite end-member is used to account for compositions with Si/Al ratio greater than that of clinochlore (3/1). The need for a di-dioctahedral "pyrophyllite-gibbsite" end-member has been mentioned (Inoue et al. 2009), yet its thermodynamic properties remain unknown.

TABLE 1. Cation site distribution for chlorite end-members, after Vidal et al. (2001), Bourdelle and Cathelineau (2015), and additional studies referenced in the table

	$(T1)_2$	$(T2)_2$	M1	$(M2)_2$	$(M3)_2$	M4
Daphnite/Clinochlore	$(Si)_2$	Si Al	Fe^{2+}, Mg	$(Fe^{2+}, Mg)_2$	$(Fe^{2+}, Mg)_2$	Al
(Fe, Mg)-Amesite	$(Si)_2$	$(Al)_2$	Al	$(Fe^{2+}, Mg)_2$	$(Fe^{2+}, Mg)_2$	Al
(Fe, Mg)-Sudoite	$(Si)_2$	Si Al	□	$(Al)_2$	$(Fe^{2+}, Mg)_2$	Al
Al-free chlorite	$(Si)_2$	$(Si)_2$	Fe^{2+}, Mg	$(Fe^{2+}, Mg)_2$	$(Fe^{2+}, Mg)_2$	Fe^{2+}, Mg
"Pyrophyllite-Gibbsite"	$(Si)_2$	$(Si)_2$	□	$(Al)_2$	$(Al)_2$	□
Ferri-sudoite (Vidal et al. 2016)	$(Si)_2$	Si Al	□	$(Al)_2$	$(Fe^{2+}, Mg)_2$	Fe^{3+}
Diferri-sudoite (Trincal and Lanari 2016)	$(Si)_2$	Si Al	□	$(Fe^{3+})_2$	$(Fe^{2+}, Mg)_2$	Al
Triferri-sudoite (This study)	$(Si)_2$	Si Al	□	$(Fe^{3+})_2$	$(Fe^{2+}, Mg)_2$	Fe^{3+}
Vacant triferri-amesite (This study)	$(Si)_2$	$(Al)_2$	□	$(Fe^{3+})_2$	Fe^{3+} (Fe^{2+}, Mg)	Al

The speciation of iron is a common issue when calculating structural formulas from electron-microprobe analyses of chlorite, and ferric iron has been emphasized as potentially important for thermobarometric estimates (e.g., Vidal et al. 2005; Inoue et al. 2009; Lanari et al. 2014) but also discarded by some other authors (e.g., Bourdelle and Cathelineau 2015). To model the incorporation of Fe^{3+} into the chlorite structure, several substitutions and end-members have been proposed. Homovalent exchange of Al by Fe^{3+} (Al = Fe^{3+}) has been suggested as a possible mechanism both in octahedral (Vidal et al. 2005; Inoue et al. 2009; Lanari et al. 2014) and tetrahedral position to a smaller extent (Lanson et al. 2012; Muñoz et al. 2013). Trincal and Lanari (2016) highlighted a di-trioctahedral substitution $^{VI}\square + 2\ ^{VI}Fe^{3+} = 3\ ^{VI}(Mg,Fe^{2+})$ that they modeled with a "di-ferri-sudoite" end-member in which Fe^{3+} replaces Mg and Fe^{2+} in M2 and M3 sites (see Table 1). Vidal et al. (2016) suggested another "ferri-sudoite" end-member, with one Fe^{3+} ion in the M4 site per formula unit (Table 1), following the cation distribution of their previous model (Vidal et al. 2006).

Unfortunately, methods allowing detailed investigations of the cation distribution (such as single-crystal X-ray diffraction) are difficult to set up for ferric chlorite due to frequent zoning, twinning, and crystal deformation; consequently models ground on a limited set of reliable structure refinements. Most studies concur in allocating Mg and Fe^{2+} to M1, M2, and M3 sites (Smyth et al. 1997; Lougear et al. 2000; Aja et al. 2015), and filling the smaller M4 site with Al (Rule and Bailey 1987; Walker and Bish 1992; Nelson and Guggenheim 1993; Welch and Marshall 2001; Zazzi et al. 2006; Aja et al. 2015). Smyth et al. (1997) and Inoue and Kogure (2016) suggest filling the M4 site with Fe^{3+} when measured, consistent with an Al^{3+} = Fe^{3+} exchange.

The presence of octahedral vacancies in chlorite further complicates the estimation of the Fe^{3+}/Fe_{total} ratio, unlike other structural groups in which full site occupancy allows Fe^{3+} estimation from electron-microprobe data by site-filling methods, as in garnet or chloritoid (e.g., Droop 1987). Estimation of Fe^{3+}/Fe_{total} in chlorite has also been carried out via thermodynamic modeling (e.g., Walshe 1986; Vidal et al. 2006; Lanari et al. 2014; Inoue et al. 2018), however these models are based on a restricted number of analyses with measured iron speciation and little information on cation site distribution. There is a lingering need for measuring and modeling variations in the oxidation state of iron in chlorite, which must be obtained together with major-element composition. Mössbauer spectroscopy (De Grave et al. 1987; Aja and Dyar 2002), electron energy-loss spectroscopy on transmission electron microscope (van Aken and Liebscher 2002; Bourdelle et al. 2013b), photoelectron spectroscopy (Raeburn et al. 1997; Yamashita and Hayes 2008), and EPMA at iron $L\alpha$,β edges (Höfer et al. 1994; Fialin et al. 2001) allow measuring Fe^{3+}/Fe_{total}, but all show disadvantages as compared to X-ray absorption near-edge spectroscopy (XANES) for rapid measurement on samples and over scales consistent with scanning electron microscopy and electron microprobe analysis, with limited alteration effects due to the beam—for example electron beams may induce reduction or oxidation with proton loss in hydrous silicates (e.g., Garvie and Craven 1994; Garvie et al. 2004). XANES has been shown

to be strongly sensitive to both the formal oxidation state and coordination of iron (e.g., Wilke et al. 2001; Newville 2014).

This publication reports on a series of XANES measurements carried out on samples where crystal composition was also measured with scanning electron microscopy and electron microprobe analysis. Iron speciation was measured in oxides and silicates, with emphasis on chlorite, to identify trends in chemical exchanges involving Fe^{3+}. Iron speciation was also mapped in zoned crystals. This effort considerably extends the database for chlorite compositions where iron speciation is known and allows better identification of end-members relevant to ferric chlorite. It is found that the "oxychlorite" component is important even in pristine, apparently unaltered green chlorite. The structure and thermodynamic properties of the ferric end-members remain unknown, however thermodynamic modeling provides first-order constraints on these. Crystal-chemical considerations allow refining the cation site assignment from chlorite electron-microprobe analyses. We propose an alternative algorithm to that of Vidal et al. (2006) for the calculation of end-member activities, which has implications for all compositions and major importance for Fe^{3+}-rich chlorite.

Materials and methods

Twenty-nine samples of chlorite-bearing rocks from various localities have been measured for their texture, composition, and iron speciation. It was aimed to analyze a wide range of compositions to provide a complete view of solid solutions involving ferric iron. Mineral compositions and sample origin are detailed in Supplemental[1] Tables S1, S2, and S3. As thin sections were cut perpendicular to the foliation (if any), most chlorite crystals were oriented with *c*-axis in the section plane.

A compilation of analyses from the literature was used for comparison, taken from Trincal and Lanari (2016) but screened with more stringent criteria:

- Sum of "alkalis" ($Na_2O + K_2O + CaO$) below 0.5 wt% to remove analyses possibly contaminated by illite-like material (see e.g., Bourdelle et al. 2013a),
- Sum of oxides between 80 and 91 wt% (not counting H_2O),
- Discarding incorrectly referenced/used analyses (misidentified chlorite, missing analysis in the original paper, missing reference, duplicates).

Scanning electron microscopy and electron microprobe analysis

Scanning electron microscopy (SEM) was used to complement optical microscopy at ISTeP (Sorbonne Université, Paris) using a Zeiss Supra 55VP apparatus associated to an SSD detector PTG Sahara for imaging and elemental mapping in energy-dispersive spectroscopy mode. Electron probe micro-analyses were then carried out at CAMPARIS (Sorbonne Université, Paris, France) with both Cameca SX-Five and SX-100 instruments. Point measurements were made under classical analytical conditions (15 kV acceleration voltage and 10 nA beam current allowing ~2 µm beam size, in wavelength-dispersive spectroscopy mode) using diopside (Ca, Mg, Si), $MnTiO_3$ (Mn, Ti), orthoclase (K, Al), Fe_2O_3 (Fe), albite (Na), and Cr_2O_3 (Cr) as standards to measure elements indicated in parentheses. Element maps were obtained with similar conditions but counting time lowered to between 50 and 300 ms. For sessions with analysis of oxygen, alumina (Al_2O_3) was used as standard, and absorption coefficients were selected from Bastin and Heijligers (1989). Oxygen measurements were subsequently verified with analyzes of periclase (MgO), quartz (SiO_2), and hematite (Fe_2O_3), yielding an average relative uncertainty of 1.1% (here interpreted as trueness) on the measured value for oxygen. This value is lower than the average standard deviation obtained from the electron microprobe on chlorite analyses, yielding a precision generally around 3% of the measured value (using the manufacturer's software with ZAF correction and the standardization method from this study).

Electron microprobe measurements were combined to iron speciation XANES measurements on the exact same crystals to calculate structural formulas for all minerals. Unless stated otherwise, structural formulas are assumed to be calculated on the basis of $O_{10}(OH)_8$ (i.e., 28 charges) for chlorite, $O_5(OH)_4$ for serpentine, and $O_{10}(OH)_2$ for micas.

X-ray absorption near-edge spectroscopy

X-ray absorption near-edge spectroscopy measurements were carried out for spatially resolved Fe^{3+}/Fe_{total} analysis on both homogeneous and zoned crystals, directly on thin section (i.e., without losing textural information). The oxidation state and coordination number of iron are obtained after spectra processing as detailed below (adapting protocols from White and McKinstry 1966 and Wilke et al. 2001).

Experimental setup. Absorption spectra around the *K* edge of iron were collected on the ID24 beamline at the European Synchrotron Radiation Facility in Grenoble and on the 13-IDE beamline at APS Chicago. Each beamline was dedicated to XANES in fluorescence detection mode. Setups at Grenoble and Chicago were broadly similar, with the difference that the incident beam was linearly polarized at 13-IDE and circularly polarized at ID24. Beam spot size was approximately 5 × 5 µm. Thin sections were mounted on an iron-free plexiglass holder, fixed on a remotely controlled shelf and positioned perpendicular to the X-ray beam direction to minimize self-absorption effects (Tröger et al. 1992; Pfalzer et al. 1999). Detector sensitivity and distance to the sample were manually adjusted as a function of iron content. For maps, a compromise for coexisting iron-rich and iron-poor minerals was searched with the aim of obtaining the best signal-to-noise ratio for chlorite at the expense of other minerals. Dwell times for spot analyzes and maps were adapted as a function of iron concentration and size of mapped areas. Energy calibration was carried out on hematite crystals and Fe foils.

The absorption coefficient µ is defined as $\mu(E) = \log(I_1/I_0)$, where I_0 is the incident beam intensity and I_1 is the intensity of fluorescence. The absorption coefficient µ has been measured from 7109 to 7180 eV at ID24 (Fig. 2) and 7062 to 7756 eV at 13-IDE. Spectra were obtained with 0.1 eV resolution around the pre-edge and lower resolutions at lower and higher energies. Two types of detector were used at ID24, and we retained the best spectra in terms of signal-to-noise ratio. Previous studies have shown that linear polarization of incoming photons impacts XANES spectra of anisotropic crystals, and particularly phyllosilicates (e.g., Dyar et al. 2001; Muñoz et al. 2013; Evans et al. 2014), plaguing earlier mapping attempts. Because of linear polarization of the beam at 13-IDE, each crystal has been measured four times, rotating the sample holder by 30°. Because samples were cut perpendicularly to the foliation (along which the long axis of chlorite crystals is generally oriented), this rotation mainly explored the angle between the *c*-axis of chlorite and the beam with the aim of capturing most of the effect of dichroism on the pre-edge of iron without separating crystals and losing textural information. Spectra were subsequently averaged (see Supplemental[1] Fig. S1 for two examples). Following the analysis of Muñoz et al. (2013), this should average shifting of the pre-edge and limit uncertainties due to linear polarization to about 5% of the calculated Fe^{3+}/Fe_{total} ratio. Mounting of a quarter-wave plate along the incident beam at ID24 allowed transforming the linearly polarized incident X-ray beam into a transmitted (non-deviated) beam with circular polarization (Giles et al. 1994) around the Fe *K*-edge, making corrections for polarization unnecessary and reliable mapping possible. Because of diffraction effects between the X-ray beam and the quarter-wave crystal, all spectra obtained at ID24 showed a systematic shoulder and trough ("glitch") between 7090 and 7105 eV, which has subsequently been considered as part of the background.

The possible effect of beam exposure on iron oxidation state has been tested and dismissed for iron-rich samples via repeated point measurement of the same crystals identified as entirely ferrous or ferric. This is consistent with the study of Fiege et al. (2017) and with results obtained on maps where exposure times were below 30 s per point.

Spectra processing. Figure 2 shows an example of XANES spectrum after normalization and smoothing (using the Savitzky-Golay algorithm). Absorption µ was normalized using intensities measured in the range 7160–7180 eV to correct for variations of iron content. Several functions were tested to remove the baseline below the pre-edge. This is an important step as the form of the baseline function has been shown to have a critical effect on the area of the pre-edge and on the position of its centroid to a lesser extent (Farges et al. 2004). The pre-edge ranges broadly from 7109 to 7116 eV, and these values are affected by iron speciation. It has been found that interpolating the shape of the *K*-edge with piecewise cubic spline interpolation (as used by Wilke et al. 2001; De Andrade et al. 2011) induced bowl shapes under small-intensity pre-edges (i.e., mostly when iron is divalent), overestimating pre-edge areas and at times significantly altering centroid positions. Considering that the first and second energy derivative of the baseline should be positive, and that the *K*-edge of iron should be a pseudo-Voigt function combining a Lorentzian-shaped edge with a Gaussian tail containing the pre-edge stands (see Wilke et al. 2001; Muñoz et al. 2013), we modeled the baseline as purely Gaussian-shaped. A Gaussian function was fitted below each pre-edge using values on each side of the pre-edge as constraints, and defining the pre-edge limits such as (1) the

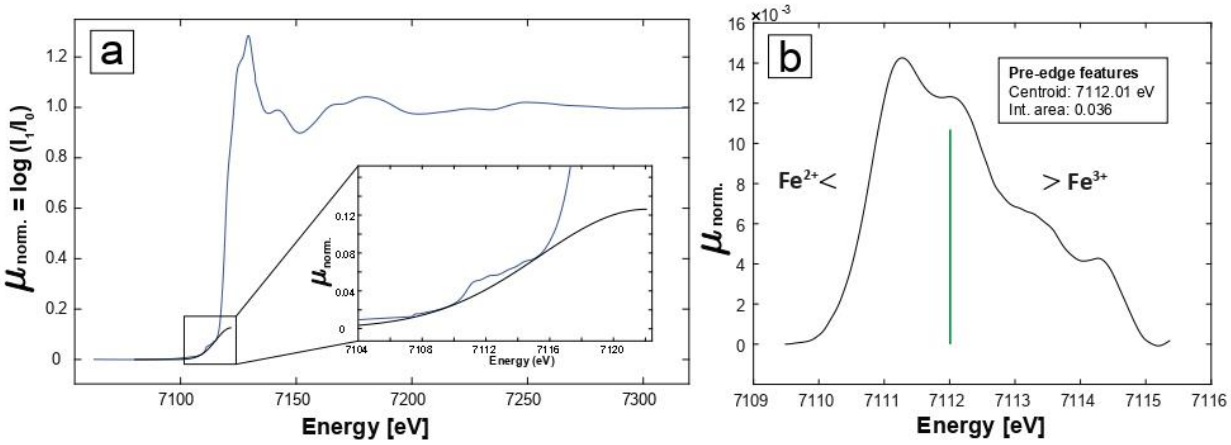

FIGURE 2. Typical XANES spectral features at the Fe *K* edge for chlorite. (**a**) Normalized spectrum. The inset shows the pre-edge and the baseline used for extraction of the pre-edge (details in text). (**b**) Corresponding pre-edge. The vertical line indicates the energy position of the centroid, which increases with increasing Fe^{3+}/Fe_{total} ratio. The area of the pre-edge is sensitive to coordination of Fe, ^{IV}Fe leading to the larger pre-edge area than ^{VI}Fe.

pre-edge is always contained in the range 7109–7116 eV, (2) the pre-edge area is minimum, (3) the baseline has lower intensity than the pre-edge, (4) the baseline has positive first and second derivatives. Due to a large number of analyses carried out here, especially for maps, baseline removal has been automated within an optimization algorithm where points 2 and 3 were equally weighted. Results for all spectra acquired in point mode were manually verified. Some spectra were discarded, in particular spectra containing low signal-to-noise ratio when iron content was too low (detector too far away) and for analyses showing interferences (mostly due to the presence of Mn and Cr).

Propagation of uncertainties

Structural formulas cumulate uncertainties arising from EPMA and XANES analyses. Analytical propagation of these uncertainties is made difficult first by the normalization procedure (either to a fixed number of charges or to the measured oxygen content) that has the effect of correlating all measurements and their uncertainties, second by the distribution of cations on crystal sites using algorithmic techniques (such as $^{IV}Al = 4 - Si$ and $^{VI}\square = 6 - \Sigma octa$ for chlorite and mica) further correlating uncertainties. Uncertainties have therefore been propagated using Monte-Carlo simulations where a large number of structural formulas (typically 300) were calculated for each EPMA+XANES measurement pair, from as many randomly drawn compositions allowed to vary around each measured value within its uncertainty. For EPMA measurements, uncertainties on measured element weight percentage were taken from the standard deviation obtained from the electron microprobe using the manufacturer's software, which are of the order of 2–3% of the measured value for major cations (>5 wt%) and for oxygen where trueness appears better from analysis of standards, to ensure that uncertainties were not under-estimated. For Fe^{3+}/Fe_{total}, we used an absolute 15% uncertainty, as estimated below from the XANES measurements.

In this configuration, after normalization to a fixed number of charges (assuming a fixed anionic basis), uncertainties on structural formulas are in the range 1–3% of the obtained value for major metals—smaller than point size in Figures 5 and 6—excluding Fe. Uncertainties on structural formulas are greater with decreasing concentration (e.g., for Mn), and for Fe^{2+} and Fe^{3+} in Fe-rich minerals where the effect of uncertainties on Fe^{3+}/Fe_{total} is larger. For vacancies, this results in uncertainties typically of the order of 0.02 to 0.1 pfu, depending on vacancy content and on Fe content.

For structural formulas normalized to oxygen, uncertainties are larger due to the propagation of the large error on oxygen: 2–4% of the obtained value for major metals excluding Fe. Again uncertainties on Fe^{2+} and Fe^{3+} are often larger than for other metals and increase with Fe content. Uncertainties on estimated vacancies are much larger than previously, typically in the range 0.2–0.3 pfu. For the estimated number of charges (used to deduce proton content), uncertainties are even larger around 0.5 pfu. Analyses using this method of normalization have only been carried out on homogeneous minerals, uncertainties have been propagated on median values of several measurements and are reported in corresponding figures and tables.

Comparing both methods of normalization, it is emphasized that neither one increases accuracy over *measured* relative proportions of metals (e.g., the Si/Al ratio and its uncertainty are similar with both methods). However, values *estimated after normalization* such as vacancy content are dramatically affected. We conclude below that normalizing to measured oxygen results in much more robust trueness for the estimation of vacancies than using a fixed anionic basis, in addition to allowing for verifying deprotonation via charge balance.

RESULTS

Estimation of iron speciation from XANES spectra

The energy location of the centroid of each pre-edge and its area for each mineral measured in point mode are provided in Supplemental[1] Tables S2 to S4.

As shown in Figure 3, these values plotted in the diagram suggested by Wilke et al. (2001) illustrate variations in terms of iron oxidation state and coordination number between ferrous (low energy) and ferric (high energy) minerals and between tetrahedral (large area) and octahedral (low area) coordination of iron. Noting that our data show a spread substantially larger than the end-members defined by Wilke et al. (2001), and this consistently for measurements from both ID-24 (ESRF) and 13-IDE (APS) beamlines, we re-estimated centroid positions for $^{VI}Fe^{2+}$ and $^{VI}Fe^{3+}$ end-members using hematite for the ferric end-member at an energy of 7114.2 (±0.1) eV and the average value between olivine (from our sample MA15-26B) and chromite (from our sample MA15-31) for the ferrous end-member at an energy of 7111.9 (±0.2) eV (Fig. 3a). This is equivalent to using crystals with well-constrained iron speciation as internal standards, to account for differences observed with the study of Wilke et al. (2001). These discrepancies may originate from (1) differences in baseline removal or in standardization of spectra, (2) effects of fluorescence (our study) vs. transmission (Wilke et al. 2001), and (3) evolution of detectors; regardless of the cause, re-estimating end-member values ensures internal consistency to our study. Iron speciation calculations for all minerals were subsequently made on the assumption that pre-edge centroid positions are proportional to the relative amount of ferrous and ferric end-members in the crystal (as described and discussed by

Bajt et al. 1994 and Wilke et al. 2001). It has been verified from our measurements that an increase in absorption components of the pre-edge that are characteristic of Fe^{3+} leads to a drift of the centroid energy that can be safely assumed as linear, with regard to the precision on the estimation of the centroid.

End-members for octahedral Fe^{2+} and Fe^{3+} differ by ~2.3 eV, compared to ~1.4 eV for previous studies (Wilke et al. 2001; Galoisy et al. 2001), as illustrated in Figure 3. Previous studies suggest 10% uncertainty on Fe^{3+}/Fe_{total} with this technique for minerals (Wilke et al. 2005) and 2.4% for glasses (Fiege et al. 2017), corresponding to uncertainties ranging within 0.1 to 0.3 eV. Analyses carried out on different types of minerals show high reproducibility but considerable scatter, suggesting uncertainties of the order of 0.2 eV on the ferrous end-member. It follows that an absolute uncertainty of 15% on each Fe^{3+}/Fe_{total} estimate seems reasonable for our data set.

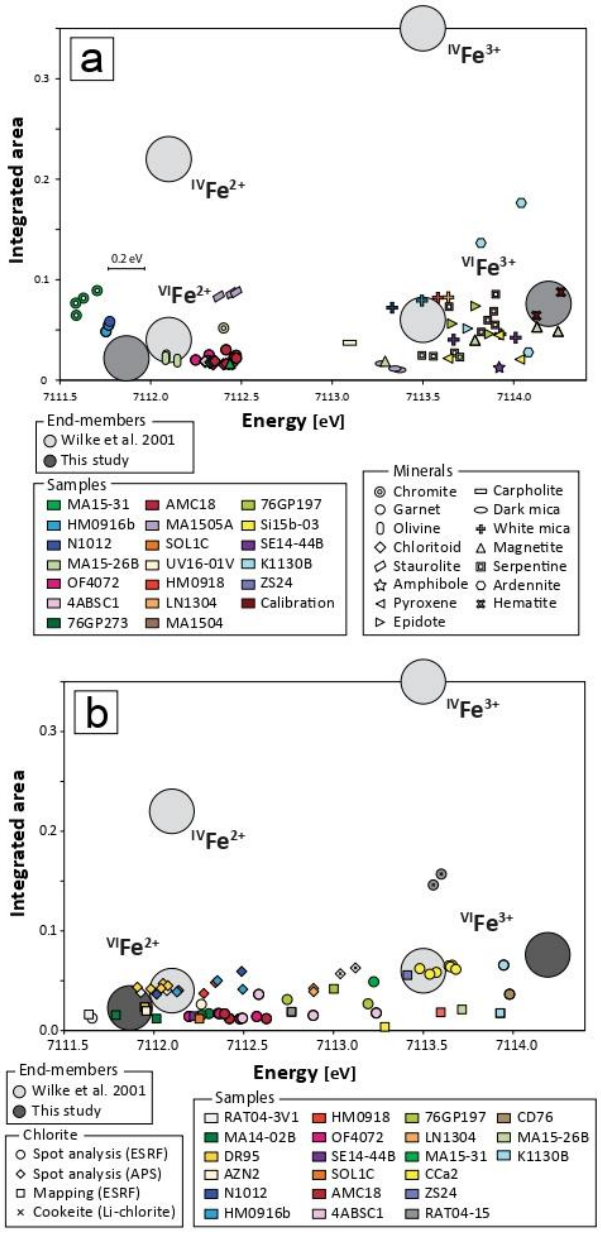

FIGURE 3. XANES results: Integrated area vs. centroid position in energy for (**a**) a selection of oxides and silicates (standards and minerals associated with chlorite in thin sections); (**b**) chlorite. Circles show estimated end-member positions for tetrahedral, octahedral, ferrous, and ferric iron, from the study of Wilke et al. (2001, pale circles) and this study (darker circles for octahedral iron).

Speciation and coordination of iron

Chlorite crystals from this study cover almost the entire range of Fe^{3+}/Fe_{total} ratio, from 0 to 95% (Supplemental[1] Table S1, Fig. 3). The garnet and chloritoid crystals analyzed in point mode are homogeneous and bear almost exclusively ferrous iron. In all serpentine crystals, iron is essentially ferric. No crystal in our collection contains purely tetrahedral iron. Staurolite shows large pre-edge area values, consistent with the presence of both tetrahedral and octahedral iron in its structure (e.g., Smith 1968; Dyar et al. 1991a; Hawthorne et al. 1993). The Mn-Al-arsenatosilicate ardennite also contains a significant proportion of tetrahedral Fe^{3+} (~25% of the ~0.5 wt% $Fe_2O_{3(total)}$ reported by Altherr et al. 2017), which is a new feature. Tetrahedral iron was found making as much as ~25% of total iron in cookeite [Li-rich chlorite with <1 wt% $Fe_2O_{3(total)}$, ideally $LiAl_4Si_3AlO_{10}(OH)_8$], but was below the detection limit for all other chlorite crystals.

Areal variations: Fe^{3+}/Fe_{total} mapping in chlorite-bearing assemblages

One of the goals of this study was to test the feasibility of XANES mapping of sheet-silicates and its suitability to petrological purposes. Out of seven maps acquired, Figure 4 shows results obtained on a rodingite sample bearing andraditic hydrogarnet, pyrite, and two generations of chlorite (10–14 wt% FeO_{total} in the early one, 4–8 wt% FeO_{total} in the late, matrix-forming one). XANES measurements appear clustered (Figs. 4b, 4c, and 4d) and faithfully render the two chlorite generations (cf. EPMA data in Fig. 4a), regardless of the (variable) crystal orientation. The early, Fe-rich generation is less oxidized (Fe^{3+}/Fe_{total} in the range 0.2–0.4) than the late one (Fe^{3+}/Fe_{total} in the range 0.35–0.7; Figs. 4c and 4d). Yet, in spite of the significant increase in the Fe^{3+}/Fe_{total} ratio between the two generations, their Fe^{3+} content remains similar, in the range 0.25–0.35 pfu, as seen in structural formulas given in Table 2 for the areas labeled 1 to 4 on Figure 4. In this case, the Fe^{2+}–Mg exchange explains most of the chemical variability, $X_{Mg} = Mg/(Mg+Fe^{2+})$ passing from 0.81 to 0.97.

Garnet in this sample is Fe^{3+}-rich, and its boundary is hardly identified in the Fe^{3+}/Fe_{total} map (Fig. 4c), suggesting possible contamination of nearby chlorite analyses by fluorescence. However, this effect can be ruled out as both the Fe_{total} map measured by XANES (Fig. 4b) and the Fe_{total} vs. Fe^{3+}/Fe_{total} plot (Fig. 4d) show distinct clusters for garnet and chlorite. The Fe_{total} map measured by XANES compares very favorably with the EPMA Fe map (Figs. 4a vs. 4b), with similarly sharper boundaries for garnet–chlorite grain boundaries than between chlorite generations. Analyses showing contamination appear restricted to the few pixels straddling grain boundaries. This reliability opens good prospects for further petrological applications.

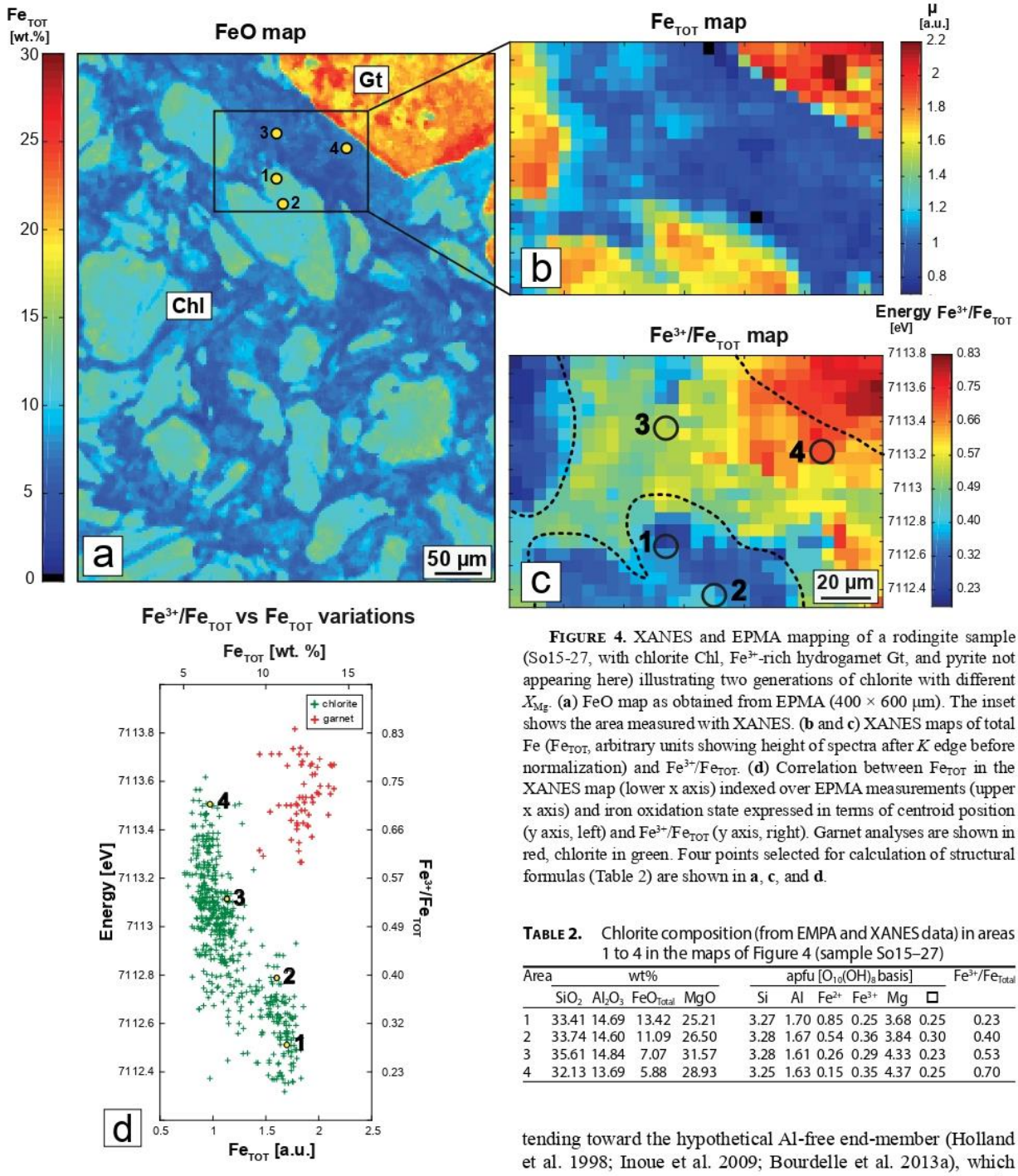

FIGURE 4. XANES and EPMA mapping of a rodingite sample (So15-27, with chlorite Chl, Fe^{3+}-rich hydrogarnet Gt, and pyrite not appearing here) illustrating two generations of chlorite with different X_{Mg}. (**a**) FeO map as obtained from EPMA (400 × 600 µm). The inset shows the area measured with XANES. (**b** and **c**) XANES maps of total Fe (Fe_{TOT}, arbitrary units showing height of spectra after *K* edge before normalization) and Fe^{3+}/Fe_{TOT}. (**d**) Correlation between Fe_{TOT} in the XANES map (lower x axis) indexed over EPMA measurements (upper x axis) and iron oxidation state expressed in terms of centroid position (y axis, left) and Fe^{3+}/Fe_{TOT} (y axis, right). Garnet analyses are shown in red, chlorite in green. Four points selected for calculation of structural formulas (Table 2) are shown in **a**, **c**, and **d**.

TABLE 2. Chlorite composition (from EMPA and XANES data) in areas 1 to 4 in the maps of Figure 4 (sample So15–27)

Area	wt%				apfu [$O_{10}(OH)_8$ basis]						Fe^{3+}/Fe_{total}
	SiO_2	Al_2O_3	FeO_{Total}	MgO	Si	Al	Fe^{2+}	Fe^{3+}	Mg	□	
1	33.41	14.69	13.42	25.21	3.27	1.70	0.85	0.25	3.68	0.25	0.23
2	33.74	14.60	11.09	26.50	3.28	1.67	0.54	0.36	3.84	0.30	0.40
3	35.61	14.84	7.07	31.57	3.28	1.61	0.26	0.29	4.33	0.23	0.53
4	32.13	13.69	5.88	28.93	3.25	1.63	0.15	0.35	4.37	0.25	0.70

Fe^{3+} incorporation in phyllosilicates

The compositional variations of chlorites, serpentines (lizardite, chrysotile) and white micas (phengite, muscovite) are illustrated in an R^{2+}–R^{3+}–R^{4+} plot (Fig. 5a). Most chlorite analyses fall in the classical field between the clinochlore and amesite end-members (see Table 1) with some dioctahedral component toward the sudoite end-member. A few analyses show chlorite compositions more siliceous than clinochlore, i.e., tending toward the hypothetical Al-free end-member (Holland et al. 1998; Inoue et al. 2009; Bourdelle et al. 2013a), which has a serpentine composition but a chlorite structure (14 Å). A more remarkable feature of Figure 5a is that a number of chlorite analyses plot outside but on the opposite side of the classical clinochlore–amesite range, i.e., on the R^{3+}-rich side. These analyses are mostly those of crystals containing more than 0.1 Fe^{3+} pfu (Figs. 5b and 5c). In two samples (4ABSC1 and CD76), chlorite incorporates as much as 1.0 to 2.8 Fe^{3+} pfu (Supplemental[1] Table S1 and Figs. 5b and 5c).

The analyzed micas contain from 0.06 to 0.28 Fe^{3+} pfu

and have Fe^{3+}/Fe_{total} values between 0.62 and 0.92. Serpentine analyses show Fe^{3+} contents ranging from 0.07 to 0.14 pfu and Fe^{3+}/Fe_{total} ratios between 0.75 and 0.87.

In this data set, chlorite, therefore, shows by far the highest Fe^{3+} contents and the largest variations in Fe^{3+}/Fe_{total} ratio, which begs the question of the involved substitutions.

Substitutions and possible ferric end-members for chlorite

Chlorite compositions are shown in Figures 5 and 6 together with literature values.

Low-Fe chlorite: Al-Fe^{3+} exchange. The first group of chlorite analyses was best identified through high Fe^{3+}/Fe_{total}, low iron content (high X_{Mg}, low Fe_{total}) and low vacancy number (Figs. 5b, 5c, 6a, and 6b). Such compositions highlight the need for at least one tri-trioctahedral, magnesian, Al-exchanged ferric end-member (Fig. 6a) such as "ferri-clinochlore" and/or "Mg-ferri-amesite" (the latter being more likely according to Fig. 6b). These end-members remain fictive as none of them is dominant in these samples, but they are needed to encompass the compositional field of ferric chlorites (Fig. 5b).

High-Fe chlorite: Vacancy creation or "oxychlorite"? The second group of compositions stands out by their high Fe^{3+} contents, hence high Fe_{total}. A striking feature of Fe^{3+} incorporation is the increasing octahedral vacancy with increasing Fe^{3+} content (as shown in Fig. 5b). This trend has already been identified by Trincal and Lanari (2016; also Billault et al. 2002, in Fe-rich sudoite) and explained by coupled substitution of three divalent cations by two Fe^{3+} cations, similarly to the di-trioctahedral substitution: $^{VI}\square + 2\ ^{VI}Fe^{3+} = 3\ ^{VI}(Mg,Fe^{2+})$. This exchange reaction must be completed by some $Al = Fe^{3+}$ substitution, first to account for analyses with $Fe^{3+} > 2$ pfu (Figs. 5b and 6b), then to explain deviation from a straight line in Figure 5b, and finally to explain Fe^{3+} incorporation in trioctahedral crystals (i.e., without vacancy, Fig. 6a) forming the first group addressed above. Both substitutions may act concomitantly (Fig. 5c), along the vacancy-creating substitution $^{VI}\square + 2\ ^{VI}R^{3+} = 3\ ^{VI}(Mg,Fe^{2+})$ where R^{3+} may be Al or Fe^{3+}. In other words, incorporation of trivalent cations above 2 apfu appears controlled by the di-trioctahedral substitution (Fig. 5c) with Al and Fe^{3+} exchanging for one another (Fig. 6a).

Vacancy creation during Fe^{3+} incorporation through the

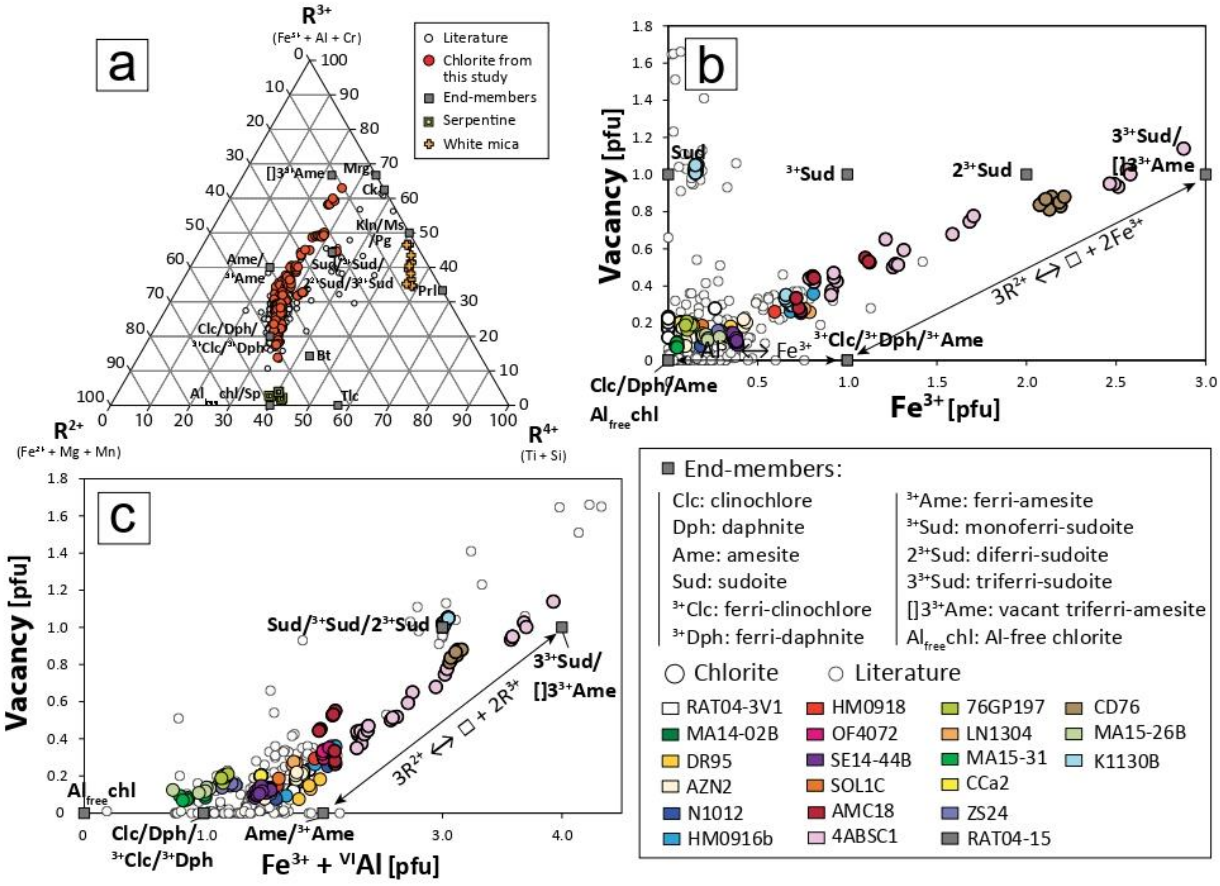

FIGURE 5. Chlorite compositions from this study (color symbols) and from the literature (open symbols) together with possible chlorite end-members as defined in Table 1 (continued in Fig. 6). (**a**) Composition of chlorite, serpentine, and micas in a R^{2+}–R^{3+}–R^{4+} diagram, together with various phyllosilicate end-members. Bt = biotite; Ck = cookeite; Kln = kaolinite; Mrg = margarite; Ms = muscovite; Pg = paragonite; Prl = pyrophyllite; Sp = serpentine; Tlc = talc. (**b** and **c**) Chlorite vacancy content as a function of Fe^{3+} content (**b**), and of the sum of ^{VI}Al and Fe^{3+} (**c**). The trend defined by the di-trioctahedral substitution $^{VI}\square + 2\ ^{VI}R^{3+} = 3\ ^{VI}(Mg, Fe^{2+})$ is shown in **b** and **c**. Bold symbols in **b** show crystals selected for normalization to measured oxygen content (see Fig. 7).

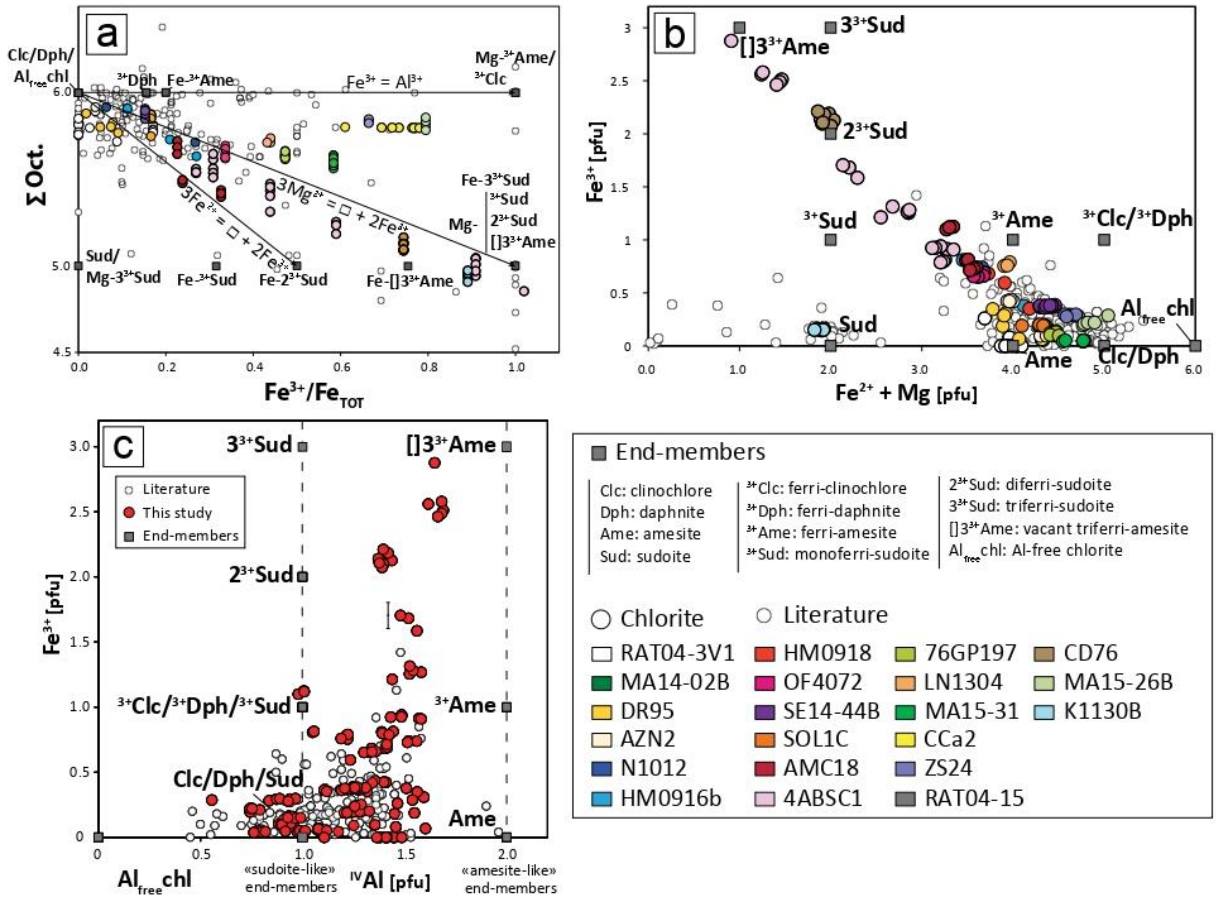

FIGURE 6. The composition of chlorite from this study (color symbols) and from the literature (open symbols) together with possible chlorite end-members (continued from Fig. 5). (**a**) Octahedral sum as a function of the oxidation state of iron, with trends defined by Al–Fe^{3+} exchange and di-trioctahedral exchanges shown for Mg and Fe^{2+}. (**b**) Correlation between Fe^{3+} and the sum of Fe^{2+} and Mg. (**c**) Fe^{3+} content vs. tetrahedral Al.

above equation may be modeled with several di-trioctahedral end-members, either trisilicic (i.e., $Si^{IV}Al = 3$, of the sudoite type) or disilicic (i.e., $Si^{IV}Al = 1$, of the "vacant-amesite" type). Both types allow for several end-members with various Fe^{3+} content, such as "ferrisudoite"-type end-members with formulas $\square(Mg,Fe^{2+})_2Al_{3-x}Fe^{3+}_x(Si_3Al)O_{10}(OH)_8$ where x may vary between 1 and 3 (Table 1). As seen in Figure 6a, analyses tend toward an Mg-rich end-member (of sudoite or amesite type) with some Fe entirely in trivalent state, rather than a Fe_{total}-rich end-member with mixed valence (in which Fe would be found in both ferrous and ferric state). Figure 6c shows that Fe^{3+}-rich analyses fall in the range 1.4–1.6 ^{IV}Al pfu, requiring both disilicic and trisilicic end-members for their formulation.

However, the plausibility of such ferric end-members with dioctahedral character rests heavily on proper estimation of the amount of vacancy, which is fraught with three main sources of error: (1) incorrect definition of the chemical system and neglect of minor elements, (2) cumulating analytical uncertainties, and (3) high sensitivity to the formula normalization basis. The first source of error (overlooked elements) may be ignored when careful EDS measurements lead to estimated vacancy content above 0.5 pfu unless lithium is present. The second source of error (cumulating analytical uncertainties) could not explain either such large vacancy contents if EPMA measurements were carefully carried out. The third source of error is the important one, as shown below, due to possible deprotonation in hydrous silicates, as advocated by Dyar et al. (1993). For chlorite, the standard assumption of a fixed $O_{10}(OH)_8$ anionic basis in the structural formula may lead to a severe bias in vacancy estimation through normalization to 28 negative charges Q_{norm} [18 O^{2-} and 8 H^+ make $Q_{norm} = 18 \times (-2) + 8 = -28$, corresponding to 14 oxygen anhydrous basis]. Indeed, in the case one proton is lost by clinochlore $Mg_5Al_2Si_3O_{10}(OH)_8$ along an exchange vector like $Mg^{2+} + H^+ = Al^{3+}$ (Dyar et al. 1993), the structural formula becomes $Mg_4Al_3Si_3$ with anionic composition $O_{11}(OH)_7$ and 29 negative charges [18 O^{2-} and 7 H^+ make $Q_{norm} = 18 \times (-2) + 7 = -29$]; if proton loss is ignored, the EPMA analysis of this $Mg_4Al_3Si_3O_{11}(OH)_7$ tri-trioctahedral deprotonated chlorite will be expressed as $\square_{0.35}Mg_{3.85}Al_{2.90}Si_{2.90}O_{10}(OH)_8$. In other words, the loss of one proton will lead to the artificial estimation of 0.35 vacancy—and the trend identified between vacancy and Fe^{3+} content (in Fig. 5b and earlier studies) may simply be an artifact resulting from normalization to a fixed number of charges.

Therefore, the key datum to identify the effective substitution(s)

responsible for Fe^{3+} incorporation is the actual number of OH groups pfu—which is at hand if one combines XANES data and EPMA *including oxygen*. Since the total number of oxygen atoms pfu remains unaffected, the actual oxygen content (measured by EPMA) can be used to calculate the formula on the basis of 18 oxygen atoms and, with the Fe^{3+}/Fe_{total} ratio from XANES data as input, *the number of H^+ pfu is then obtained by charge balance*. This calculation admittedly cumulates analytical uncertainties and is sensitive to small deviations in the measured oxygen content (due to, e.g., surface roughness, matrix effects or contamination by minerals with lower OH content). To test the validity of this new approach, oxygen was measured by EPMA (see Materials and methods) on five chlorite-bearing samples covering the compositional range and trends identified in Figures 5 and 6 ($0 \leq Fe^{3+}/Fe_{total} \leq 0.9$; $0 \leq Fe^{3+} \leq 2.2$ pfu; $0 < Fe^{2+} \leq 3.2$ pfu; $0.2 \leq \square \leq 1.1$ pfu) and including sudoite, known to be di-trioctahedral. The results are reported in Figure 7 and, except for the zoned, very heterogeneous sample 4ABSC1, median values given in Table 3.

The spread in H^+ and vacancy values for each homogeneous sample or subsample in Figures 7b and 7c is a direct reflection of the dependency of the estimation on oxygen analysis, which is less precise than for metals (Fig. 7a). Mean vacancy numbers are in the range of 0.2 to 0.4 pfu, except for the sudoite sample (K1130B), gratifyingly close to 1 pfu, thereby lending credence to the oxygen analysis procedure. Mean values of H^+ are in the plausible range 6.0–8.7 pfu for homogeneous samples or subsamples (Table 3), hinting at possible over-estimation of H^+ by about 0.5 proton, especially for the RAT04-3v1 sample, although half a proton pfu is the general uncertainty over estimated H^+ content. For this sample, underestimation of Fe^{3+}/Fe_{total} (by ~25% when neglecting all other sources of uncertainties) would be necessary to explain solely this excessive proton estimate. Yet, the whole procedure is sufficiently precise to establish the following solid results in our data set:

- The iron-rich chlorites are close to trioctahedral ($\square < 0.4$ pfu), regardless of iron oxidation state (cf. CD76 and RAT04-3v1; Fig. 7c, Table 3);
- Deprotonation is an effective process, definitely linked to increasing Fe^{3+} content (Fig. 7b). It reaches and might exceed a loss of 2 H^+ pfu.

These results have important consequences for incorporation mechanisms of Fe^{3+}. The relation found between the number of

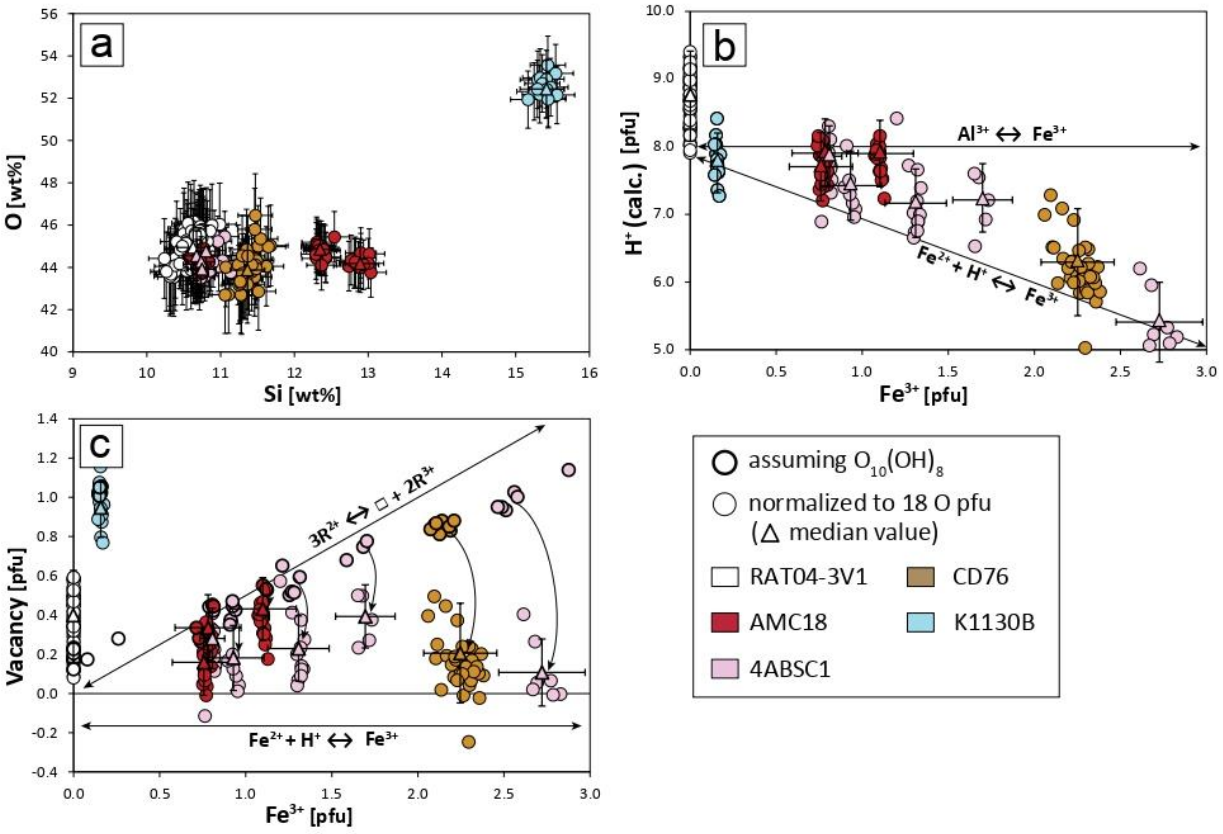

FIGURE 7. The composition of chlorite in five samples measured with EPMA, including oxygen, which is used for normalization to 18 oxygen atoms. Iron oxidation is set with XANES measurements. (**a**) Oxygen content as a function of Si as measured with EPMA. (**b**) The number of protons obtained by charge balance (as explained in the text). The exchange vector $Fe^{2+} + H^+ = Fe^{3+}$ is shown together with the $Fe^{3+} = Al$ exchange. (**c**) Vacancy amount obtained after normalization to oxygen, compared to that obtained by normalization to 28 charges ([i.e., $O_{10}(OH)_8$ anionic basis; bold symbols, as in Fig. 5b]. Arrows highlight the decrease in estimated vacancy content. Note that (1) the sudoite sample (K1130B) is unaffected, and (2) for each sample, scatter increases with normalization to oxygen, due to sensitivity to small variations in oxygen measurement. Uncertainties from EPMA and XANES measurements are propagated on median values for each compositional group as described in the text.

protons and Fe^{3+} content shows that $R^{2+} + H^{+} = Fe^{3+}$ is an effective net exchange in chlorite, as suggested by Dyar et al. (1993) and observed in other hydrous silicates. Most importantly, the trend defined by the $3\ R^{2+} = \square + 2\ Fe^{3+}$ exchange vector (i.e., the vacancy-creating trend) in Figures 5b, 5c, and 6a essentially disappears from our data set after normalization to oxygen (cf. bold and non-bold symbols in Fig. 7c). This casts doubt on conclusions made in the literature from data showing an identical trend of increasing vacancy with Fe^{3+} content, because vacancy may just be the result of normalization to a fixed number of charges, the most common practice with EPMA data.

In any case, our results do not support the existence of di-trioctahedral ferric end-members as recently proposed for common chlorites (Vidal et al. 2016; Trincal and Lanari 2016)—even if at least one is needed to account for Fe^{3+}-rich sudoite (Billault et al. 2002). Rather, the high contents of Fe^{3+} found in our samples are mostly linked to proton loss, with a potential contribution of Al^{3+}-Fe^{3+} exchange. There is no indication of other substitution linked to proton loss such as $R^{2+} + H^{+} = Al^{3+}$.

Discussion

Incorporation of Fe^{3+}

Cation distribution in Fe^{3+}-rich chlorite. Ferric iron exchanging with Al, either as homovalent substitution or through di-trioctahedral [$^{VI}\square + 2\ ^{VI}R^{3+} = 3\ ^{VI}(Mg, Fe^{2+})$] or Tschermak-like ($Si^{4+} + {}^{VI}R^{2+} = {}^{IV}Al^{3+} + {}^{VI}R^{3+}$) substitutions, leads to the possible existence of many ferric end-members. In the absence of structure refinements for these ferric end-members, empirically derived methods of estimation of the enthalpy of formation can be used to test for possible cation distributions after exchange reactions described above, which involve several crystal sites. The polyhedral oxide summation methods of Chermak and Rimstidt (1989) and van Hinsberg et al. (2005) were used and extended to protonated Fe^{3+}-centered octahedra (Fig. 8) to estimate the formation enthalpy of such compounds. A fundamental observation in Figure 8 is that for all components, the formation enthalpy steadily decreases from anhydrous octahedral sites (not found in chlorite) to mica-like OH-bearing octahedra (M1 and M2 sites of chlorite) to octahedra where all oxygen atoms are protonated (M3 and M4 sites of chlorite), which have the most negative enthalpy of formation. This implies that vacancy-rich compounds with chlorite structure are thermodynamically favored when the M3 and M4 sites (hydroxide interlayer) are fully occupied and vacancies are located in the M1 or M2 sites (TOT layer). Depending on the composition, the gain in energy is between 5 and 20 times the uncertainties given by the two methods, which therefore is regarded as robust proof. The same method applied for the enthalpy of formation of sudoite, $\square Mg_2Al_3(Si_3Al)O_{10}(OH)_8$, yields -8647 ± 80 kJ/mol or -8526 ± 73 kJ/mol with van Hinsberg et al. (2005) values, depending on whether the vacancy is located in the TOT octahedral sheet or in the interlayer hydroxide sheet, respectively. These bulk values are not significantly different, but their difference (121 ± 7 kJ/mol) is obtained with a much smaller uncertainty and confirms the preferred occurrence of vacancies in the octahedral sheet of the TOT layer. This analysis is consistent with the abundance of natural examples of di-trioctahedral chlorite (with vacancies in the 2:1 layer such as cookeite and sudoite) and the scarcity of tri-dioctahedral phyllosilicates (among which the zincosilicate franklinfurnaceite is a rare example, Peacor et al. 1988).

In the octahedral sheet of the 2:1 layer, with a multiplicity of 1 pfu and by analogy with the structure of dioctahedral micas (e.g., muscovite), the M1 site is a more likely target for vacancies than M2, as already proposed by Vidal et al. (2001) for their sudoite end-member. The same analysis indicates that for compositions containing proportions of the "pyrophyllite-gibbsite" end-member (proposed by Inoue et al. 2009, and by Trincal and Lanari 2016), with two vacancies, these should be assigned first to M1, then to M4.

A ferric end-member with an octahedral vacancy? Further evidence based on charge distribution may be used to constrain the structure of tentative Fe^{3+}-rich end-members with some di-octahedral character. First, one may simply argue that the exchange due to vacancy creation by substitution of three divalent cations by two trivalent cations is energetically less costly if the trivalent cations compensating the charge deficit are located close to the vacancy (therefore the two trivalent cations should be in the M2 site that has a multiplicity of 2). This is shown in Table 4, which compares a "diferri-sudoite"-type

Table 3. Chemical analyses (averaged) of chlorite based on EPMA (O measured) and XANES data

Sample	Atom wt%								
	Si	Ti	Al	Fe	Mn	Mg	Alk.[a]	O	Total
Rat04	10.60	0.01	13.41	25.86	0.07	3.87	0.13	44.88	98.83
CD76	11.36	0.00	10.51	25.82	0.60	5.32	0.53	43.94	98.10
AMC18	12.35	0.03	9.32	28.93	0.18	4.05	0.94	44.80	100.92
	12.18	0.02	9.44	28.58	0.16	4.50	0.54	44.20	99.87
	12.54	0.01	8.95	29.04	0.17	4.20	0.87	44.55	100.62
K1130B	15.37	0.02	19.31	1.79	0.37	8.33	0.20	52.53	98.83[c]

[a] Alk = Na + Ca + K. [b] X_{Mg} = Mg/(Mg+Fe^{2+}). [c] Includes 0.02 wt% Cr.

(Table extends on next page)

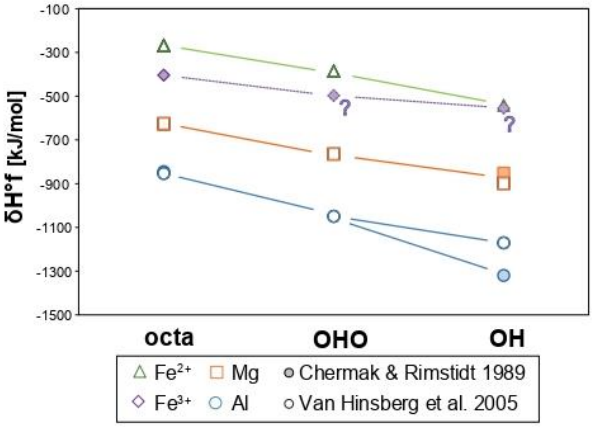

Figure 8. Estimated contribution to the enthalpy of formation for oxide polyhedral components as a function of their protonation. "octa" stands for anhydrous octahedra (e.g., Mg in olivine), "OHO" for partly hydroxylated octahedra as in the TOT layer of chlorite, and "OH" for fully hydroxylated octahedra as in the interlayer hydroxide sheet of chlorite. Values are from Chermak and Rimstidt (1989), van Hinsberg et al. (2005), and estimated for Fe^{3+} in hydroxylated sites (question marks) using the average slope for Al^{3+} from van Hinsberg et al. (2005).

TABLE 3.—*EXTENDED*

Sample	Fe^{3+}/Fe_{Total}	Structural formulas normalized to 18 O														$O_{10}(OH)_8$
		Si	Ti	Al	^{IV}Al	^{VI}Al	Fe^{2+}	Fe^{3+}	Mn	Mg	Alk.[a]	H	Σoct.	X_{Mg}[b]	□	□
Rat04	0.00	2.42	0.00	3.19	1.58	1.61	2.97	0.00	0.01	1.02	0.02	8.7(4)	5.61	0.26	0.36(15)	0.20(4)
CD76	0.74	2.65	0.00	2.55	1.35	1.20	0.79	2.24	0.07	1.44	0.09	6.3(4)	5.74	0.65	0.17 (14)	0.85(2)
AMC18	0.33	2.83	0.00	2.22	1.17	1.05	2.23	1.10	0.02	1.07	0.16	7.8(2)	5.47	0.32	0.37(8)	0.54(1)
	0.24	2.82	0.00	2.28	1.17	1.11	2.56	0.78	0.02	1.21	0.09	7.8(3)	5.67	0.32	0.24(10)	0.450(4)
	0.23	2.89	0.00	2.14	1.11	1.03	2.37	0.99	0.02	1.12	0.15	7.8(2)	5.53	0.32	0.32(6)	0.29(3)
K1130B	0.89	3.00	0.00	3.92	1.00	2.93	0.02	0.16	0.04	1.88	0.03	7.8(3)	5.02	0.99	0.95(8)	1.03(2)

end-member to clinochlore, which has similar $Si/^{IV}Al$ ratio and a well-established structure (e.g., Rule and Bailey 1987; Smyth et al. 1997; Zanazzi et al. 2006). A large charge mismatch (up to 2/3 *e*) is observed between TOT layer and hydroxide interlayer if trivalent cations incorporated during vacancy creation are not located in the TOT layer, whereas there is no charge mismatch if they are in the TOT layer.

Remaining unknowns include Al vs. Fe^{3+} occupancy in the M4 and M2 sites, which is debated (Zheng and Bailey 1989; Smyth et al. 1997; Aja et al. 2015; Inoue and Kogure 2016). The similarly small ionic radii of Al and Fe^{3+} (Shannon 1976) make them both candidates for preferential incorporation into the M4 site, as suggested by Vidal et al. (2006, 2016).

An "oxychlorite" component. The $R^{2+} + H^+ = Fe^{3+}$ exchange observed in the Fe^{3+}-rich chlorite samples requires at least one tri-trioctahedral end-member of "oxychlorite" type, i.e., hydrogen deficient. The term oxychlorite (or oxidized chlorite) is infrequently mentioned in the literature, mostly as a petrographic term for a brownish chlorite with higher birefringence than usual, reminiscent of stilpnomelane or Fe-rich vermiculite (e.g., Chatterjee 1966; Rona 1984; Plunder et al. 2015). "Oxychlorite" remains poorly described, does not currently form a group within phyllosilicates or a subgroup within the chlorite group, and its existence has been questioned (in the review of Foster 1962). Yet, the hydrogen-deficient and 14-Å character of such chlorite were established by Chatterjee (1966), but it remains unclear whether the oxidized character is a secondary, alteration feature or a pristine one. The chlorites with the largest Fe^{3+} contents of our study appear as optically clear, green, unaltered flakes in the hydrothermal vein sample CD76 (Supplemental[1] Fig. S2) and, in metapelite sample 4ABSC1, as olive-green flakes with some brown edges (Supplemental[1] Fig. S3), possibly linked to higher Fe^{3+}/Fe_{total} (but evidence is still lacking as Fe^{3+}/Fe_{total} mapping failed due to beam loss). The "oxy-" concept used here for hydrogen-deficient chlorite is the same as that of micas (e.g., Wones 1963; Dyar et al. 1991b, 1993; Virgo and Popp 2000) and other groups of silicates in which some "oxy-members" have acquired species status ("oxy-tourmalines" in Henry et al. 2011; "oxo-amphiboles" in Hawthorne et al. 2012). It is noteworthy that Walshe (1986) extracted a set of thermodynamic properties for a Fe^{3+}-rich hydrogen-deficient chlorite end-member along the $R^{2+} + H^+ = Fe^{3+}$ exchange vector, with composition $Fe_4^{2+}Fe^{3+}Al_2Si_3O_{11}(OH)_7$. Walshe (1986) estimates the activity of this end-member within a solid solution model as a sole function of the Fe^{3+} amount. However, this analysis relies on a restricted set of measurements, including analyses originating from Emmons and Larsen (1923) showing contamination by mica, which required correction (see Walshe and Solomon 1981).

Whether due to alteration or not, incorporation of Fe^{3+} along the $R^{2+} + H^+ = Fe^{3+}$ exchange vector can be expected to take place in a protonated site, for local charge balance. In the most substituted samples measured in this study (CD76 and 4ASBSC1), about 2 Fe^{3+} are incorporated, and 2 H^+ are lost with respect to standard chlorite. In regard of the chlorite structure (Fig. 1), we suggest that this substitution occurs in the TOT layer (as for hydrogen-deficient mica) rather than in the interlayer hydroxide sheet. In the TOT layer of chlorite, each M1 site shares two hydroxyl groups with M2 sites, whether M1 is filled, *cis*- or *trans*-vacant (see e.g., Sainz-Diaz et al. 2001). Loss of protons from the TOT layer should be energetically more favorable than from the interlayer hydroxide sheet where protons are forming hydrogen bonds with oxygen atoms of the tetrahedral sheets: with proton loss from the hydroxide interlayer, greater loss of symmetry and charge repulsion between the then-unscreened oxygen atoms in tetrahedral sheet and interlayer position are expected, therefore greater crystal strain (which scales positively with the energetic cost of incorporation, Dubacq and Plunder 2018).

TABLE 4. Atom site and charge (Q) distribution of clinochlore (Nelson and Guggenheim 1993; Smyth et al. 1997; Aja et al. 2015) compared to two tentative magnesian di-ferri-sudoite end-members

	$(T1)_2$	$(T2)_2$	M1	$(M2)_2$	$(M3)_2$	M4
	Si_2	Si Al	Mg	Mg_2	Mg_2	Al
Clinochlore	Q = 15		Q = 6		Q = 7	
	Si_2	Si Al	□	Mg_2	$(Fe^{3+})_2$	Al
Diferri-sudoite	Q = 15		Q = 4		Q = 9	
	Si_2	Si Al	□	$(Fe^{3+})_2$	Mg_2	Al
Diferri-sudoite	Q = 15		Q = 6		Q = 7	
	TOT				O	

To these new constraints suggest the following atom site distribution for chlorite, based on that of Vidal et al. (2001, 2006), and including a deprotonation mechanism:

- Al is distributed first in tetrahedral position (with $^{T2}Al = 4 - Si$), which allows for the calculation of octahedral occupancy ($^{VI}Al = Al_{total} - {}^{T2}Al$, $^{M1}□ = 6 - \Sigma oct$);
- Proton loss is balanced by Fe^{3+} (or other trivalent if insufficient Fe^{3+}) in M1 and M2 with random distribution ($H^+_{loss} = 8 - H^+$; $^{M1(H^+)}Fe^{3+} = \frac{1}{3} \times H^+_{loss}$; $^{M2(H^+)}Fe^{3+} = \frac{2}{3} \times H^+_{loss}$);
- Trivalent cations compensating the vacancy-induced charge deficiency are distributed in M2 ($^{M2}R^{3+} = 2\,{}^{M1}□ + {}^{M2(H^+)}Fe^{3+}$);
- The M2 site is completed with divalents ($^{M2}R^{2+} = 2 - {}^{M2}R^{3+}$);
- The M4 site is filled with trivalent cations and completed with divalent cations if necessary ($^{M4}R^{2+} = 1 - {}^{M4}R^{3+}$, as for the Al-free chlorite end-member);
- Remaining trivalent cations are distributed on M1, then M3 if

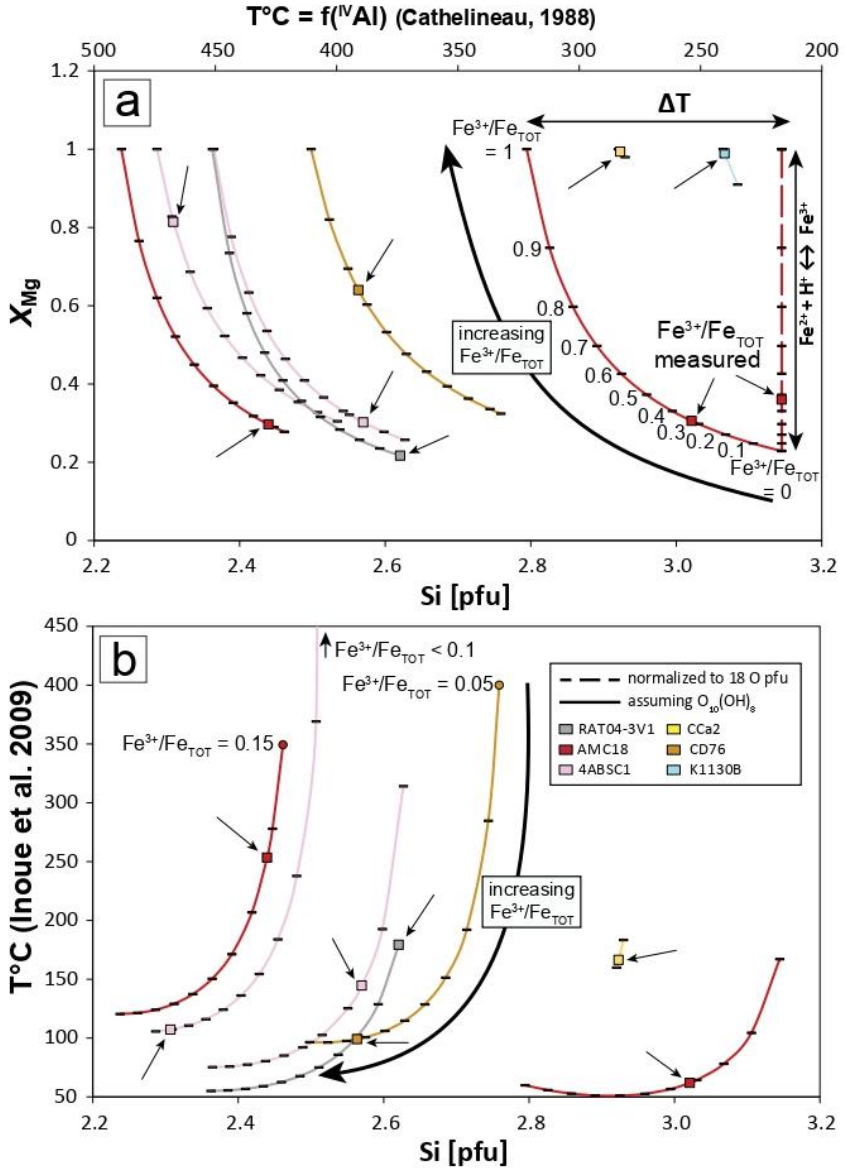

FIGURE 9. Effect of varying Fe^{3+}/Fe_{total} on structural formulas and estimated crystallization temperatures for a selection of Fe-poor (CCa2 and K1130B) and Fe-rich chlorite analyses (Fe_{TOT} = total Fe). Solid lines are calculated for the $O_{10}(OH)_8$ anionic basis from $Fe^{3+}/Fe_{total} = 0$ (low X_{Mg}, higher Si content) to $Fe^{3+}/Fe_{total} = 1$ ($X_{Mg} = 1$, lower Si content). The measured Fe^{3+}/Fe_{total} ratio is shown with a square for each chlorite crystal and highlighted with a black arrow. Note that two analyses are plotted for each of the zoned samples 4ABSC1 and AMC18. (**a**) Evolution of X_{Mg} and Si content with the temperature estimated using the model of Cathelineau (1988). The vertical dashed line shows the effect of proton loss if the anionic basis is allowed to vary, only for sample AMC18 for readability. The Fe^{3+}/Fe_{total} ratio is labeled every 10% for one of the curves; on every other line Fe^{3+}/Fe_{total} increases by 10% between black ticks. (**b**) Evolution of temperature calculated with the model of Inoue et al. (2009) vs. Si content, assuming $O_{10}(OH)_8$ anionic basis. Proton loss alters neither Si content nor temperatures estimated with this model. Chlorite from K1130B (sudoite) is not shown in **b** because its vacancy content is out of the applicability range of the Inoue et al. (2009) model. A similar issue appears with some *T* estimates for 4ABSC1, where low Fe^{3+}/Fe_{total} values cause zero amesite activity and the infinite constant of the reaction.

necessary ($^{M1+M3}R^{3+} = {}^{VI}R^{3+}_{total} - {}^{M4}R^{3+} - {}^{M2}R^{3+}$, $^{M1}R^{2+} = 1 - {}^{M1}R^{3+} - {}^{M1}\square$);

• Fe^{2+} and Mg are distributed following random mixing on all divalent-bearing sites;

• Fe^{3+} is preferentially incorporated in M4 over Al, the remaining Fe^{3+} and Al are randomly mixed in M1 and M3.

The last two steps follow the distribution recommendations of Vidal et al. (2001, 2006, 2016). The new site distribution assumes that the octahedral sum is comprised between 5 and 6 and has been derived in the system Fe^{2+}–Fe^{3+}–Mg–Al–Si–O–H, based on solid solutions with exchange vectors expressed from the "daphnite" end-member. The effect of other cations is not accounted for, although it may be assumed that: (1) tetravalent

cations such as Ti^{4+} behave as in biotite where they occur in tetrahedral and octahedral position depending on concentration (e.g., Namur et al. 2009); (2) trivalent cations in the radius range of Fe^{3+} and Al^{3+} such as Cr^{3+} and Mn^{3+} are globally randomly mixed with the former two; and (3) similarly, divalent cations comparable in size to Fe^{2+} and Mg such as Mn^{2+} are generally randomly mixed.

Improvements compared to the work of Vidal et al. (2001, 2006) consist in (1) differentiated M2 and M3 site distribution for better charge distribution during vacancy creation, (2) allowing for large amounts of Fe^{3+} in the structure (up to 3 pfu), (3) considering proton loss, and (4) explicit extension toward the Al-free chlorite end-member.

IMPLICATIONS

Anionic basis, oxidation state, why bother? Implications for structural formulas and thermobarometry

The effect of varying Fe^{3+}/Fe_{total} in chlorite on the structural formula and on the estimated temperature of crystallization is quantified and illustrated in Figure 9 for representative samples of this study. The empirical thermometer of Cathelineau (1988, based on Si content pfu, Fig. 9a) and the semi-empirical one of Inoue et al. (2009, based on vacancy, Mg, and Si contents, Fig. 9b) are used on structural formulas with varying Fe^{3+}/Fe_{total}, assuming $O_{10}(OH)_8$ basis. Values obtained for measured Fe^{3+}/Fe_{total} ratios are shown as larger squares. The dependency of the temperature estimates and of the structural formulas, taking Si as an example, is particularly strong for chlorites with high Fe contents (4ABSC1 and AMC18): these evolve from low X_{Mg} for $Fe^{3+}/Fe_{total} = 0$ to $X_{Mg} = 1$ for $Fe^{3+}/Fe_{total} = 1$. The Si content decreases by up to 0.3 pfu with increasing Fe^{3+}/Fe_{total}, while estimated temperatures increase by 80 °C with the model of Cathelineau (1988) and decrease by more than 100 °C with the model of Inoue et al. (2009). For the measured values of Fe^{3+}/Fe_{total}, estimated temperatures differ significantly from those obtained assuming that Fe is entirely reduced or oxidized. In short, both thermometers are in general disagreement for crystallization temperature and the effect of Fe^{3+} on it. For Fe-poor chlorites, the effect of Fe speciation is negligible, both on structural formulas and on estimated temperatures (CCa2 and K1130B in Fig. 9).

Assuming now that proton loss is the sole exchange for Fe oxidation, and allowing the anionic basis to vary accordingly along $Fe^{2+} + H^+ = Fe^{3+}$, cations other than Fe^{2+} and Fe^{3+} remain unaffected in the structural formula, as shown by a dashed line in Figure 9a. Consequently, as Fe^{3+}/Fe_{total} goes from 0 to 1, X_{Mg} tends to 1 *without altering estimated crystallization temperatures* (dashed vertical line on Fig. 9a). This result should hold for any thermometer in which Fe^{2+} content is not involved in the thermometric formulation (note that X_{Mg} includes Fe^{2+} content). Conversely, any chlorite thermometer using Fe^{2+}, whether (semi-)empirical or thermodynamic, shall be affected by such Fe oxidation.

Recommendations

A conclusion of this analysis is that, with increasing Fe content, measuring the oxidation state of iron *and* the H content in chlorite becomes increasingly important; chlorite thermometry appears very uncertain (by more than 50 °C) when X_{Mg} is lower than about 0.5 (with all Fe expressed as Fe^{2+}). Measurement of Fe^{3+} content should be systematic when X_{Mg} obtained by EPMA is below ~0.6 (with Fe expressed as Fe^{2+}), and proton loss is estimated if ferric iron is measured and above ca. 0.5 Fe^{3+} pfu. To this end, oxygen measurements with EPMA proved reliable and should be generalized (Table 5). In their absence or in case of doubt, assuming that all iron is divalent and using the anionic basis $O_{10}(OH)_8$ has less impact on the calculated structural formula—in terms of, e.g., ^{IV}Al content and vacancies—than using a (measured) high Fe^{3+}/Fe_{total} ratio but neglecting proton loss, which produces artificial vacancies. However, many thermometers are too sensitive to the octahedral vacancy to justify the neglect of measurement of Fe oxidation state and H content for thermobarometry in Fe-rich chlorite.

For thermodynamic modeling of Fe^{3+} incorporation, at least two ferric end-members are necessary: one with low Fe content (high X_{Mg}) where Fe^{3+} replaces Al, one of the oxychlorite types as suggested by Walshe (1986) but with greater proton loss (with anionic composition $O_{12}(OH)_6$, corresponding to loss of two protons). The need for an additional, di-trioctahedral end-member with high Fe content is debatable, and several end-members are possible. The picture is similar for sudoites: the analysis of Billault et al. (2002) is in favor of a Fe-rich ferric end-member with octahedral sum below 5, but the anionic basis was not verified, and their analyses align along the possibly artificial substitution creating vacancies. In addition, the $Al=Fe^{3+}$ substitution remained important. At the least, an Mg-rich, ferric end-member (with Fe content below 0.5 apfu) appears necessary for sudoites. Basic thermodynamic modeling and charge-balance considerations provide constraints on the crystal chemistry of Fe^{3+}-rich chlorite,

TABLE 5. Chemical analyzes (median values) of chlorite and their uncertainties based on EPMA (O measured) and XANES data

Sample	Atom wt%								Fe^{3+}/Fe_{TOT}	Structural formulas pfu									
	Si	Al	Fe	Mn	Mg	Ca	O	Total		Si	Al	Fe^{2+}	Fe^{3+}	Mn	Mg	Ca	H	Σ cat.	X_{Mg}[a]
Rat04	10.6(2)	13.4(4)	25.9(7)	0.06(8)	3.9(1)	–	44.9(18)	98.8	0.0	2.42(7)	3.19(9)	2.97(9)	0.0	0.01(1)	1.02(3)	–	8.7(7)	9.6(2)	0.255(5)
CD76	11.4(2)	10.5(3)	25.9(7)	0.6(1)	5.3(1)	0.2(1)	43.9(19)	97.7	0.74(15)	2.65(7)	2.56(8)	0.8(2)	2.2(2)	0.07(1)	1.44(4)	0.03(1)	6.3(8)	9.8(3)	0.65(6)
AMC18	12.3(2)	9.3(2)	29.0(7)	0.19(9)	4.0(1)	0.6(2)	44.8(12)	100.7	0.33(15)	2.82(5)	2.22(4)	2.2(2)	1.1(2)	0.02(1)	1.07(3)	0.10(2)	7.9(5)	9.6(2)	0.32(2)
	10.7(2)	12.0(2)	27.0(7)	0.16(9)	4.7(2)	–	44.1(12)	98.8	0.24(15)	2.48(5)	2.89(5)	2.4(2)	0.8(2)	0.02(1)	1.27(3)	–	7.7(5)	9.8(2)	0.35(2)
	12.9(2)	8.3(2)	29.1(7)	0.17(9)	4.4(2)	0.4(2)	44.2(12)	99.4	0.23(15)	2.99(5)	2.00(4)	2.6(2)	0.8(2)	0.02(1)	1.19(3)	0.06(2)	7.9(5)	9.7(2)	0.31(2)
4ABSC1	10.7(2)	12.6(2)	25.5(7)	0.12(8)	4.7(2)	0.2(1)	43.9(12)	97.8	0.91(15)	2.51(5)	3.07(6)	0.3(2)	2.7(3)	0.03(1)	1.28(3)	0.03(1)	5.4(6)	9.9(2)	0.8(1)
	10.8(2)	12.3(2)	25.0(7)	0.17(9)	4.7(2)	0.3(1)	44.7(12)	98.0	0.59(15)	2.47(5)	2.93(6)	1.2(2)	1.7(2)	0.02(1)	1.26(3)	0.05(1)	7.2(5)	9.6(2)	0.52(4)
	10.7(2)	12.5(2)	25.5(7)	0.13(8)	4.6(2)	0.3(2)	44.3(12)	98.0	0.44(15)	2.48(5)	3.01(5)	1.7(2)	1.3(2)	0.02(1)	1.24(3)	0.05(1)	7.2(5)	9.8(2)	0.43(3)
	10.7(2)	12.3(2)	25.5(7)	0.14(8)	4.7(2)	–	43.9(12)	97.6	0.31(15)	2.50(4)	3.00(6)	2.1(2)	0.9(2)	0.02(1)	1.28(3)	–	7.4(5)	9.8(2)	0.38(2)
	10.7(2)	12.4(2)	25.8(7)	0.12(8)	4.7(2)	–	44.5(12)	98.4	0.27(15)	2.46(4)	3.01(5)	2.2(1)	0.8(1)	0.02(1)	1.24(3)	–	7.9(5)	9.7(2)	0.37(1)
K1130B	15.4(2)	19.3(3)	1.8(2)	0.4(1)	8.3(2)	0.2(1)	52.4(14)	97.8	0.89(15)	3.01(5)	3.93(7)	0.02(1)	0.16(2)	0.04(1)	1.88(4)	0.02(1)	7.8(4)	9.1(1)	0.99(1)

Notes: Oxygen and Fe^{3+}/Fe_{TOT} analyses uncertainties are given with two significant digits. Dash = below detection limit (<0.01 wt%).
[a] $X_{Mg} = Mg/(Mg+Fe^{2+})$.

on the basis of which we recommend the improvements made above to the cation site distribution model of Vidal et al. (2001, 2006). Further targets for improvement relate to the competing distribution of Al and Fe^{3+}, and to the tetrahedral population of Fe^{3+}-rich end-members, either disilicic or trisilicic—with the thermodynamic properties of Fe^{3+}-rich chlorite, oxychlorite, and their end-members as the ultimate goal.

In other words, this is nothing else than the early recommendation by Dyar et al. (1993) "that attention be focused on characterizing and understanding the highly variable H^+ and Fe^{3+} contents of rock-forming silicates, with a goal of establishing accurate stoichiometric bases for those minerals." Twenty-five years later, the challenge is still there for chlorite.

Funding

This work was financially supported by the CNRS INSU programs and by French state funds managed by the ANR within the Investissements d'Avenir program under reference ANR-11-IDEX-0004-02, and more specifically within the framework of the Cluster of Excellence MATISSE led by Sorbonne Université, This research used resources of the Advanced Photon Source, a U.S. Department of Energy (DOE) Office of Science User Facility operated for the DOE Office of Science by Argonne National Laboratory under Contract No. DE-AC02-06CH11357.

Acknowledgments

We are grateful to Franck Bourdelle, Loïc Labrousse, Bruno Reynard, and Olivier Vidal for constructive discussion and to Michel Fialin, Nicolas Rividi, Sakura Pascarelli, Olivier Mathon, Antonio Lanzirotti, and Matt Newville for technical advice and support. Thanks are also extended to Rainer Altherr, Guillaume Bonnet, Colette Derré, Anne-Céline Ganzhorn, Michael Jentzer, Loïc Labrousse, Benjamin Lefeuvre, Alexis Plunder, Julien Reynes, Mathieu Soret, and Alberto Vitale-Brovarone for providing some of the chlorite-bearing samples. Constructive reviews by Darby Dyar and Atsuyuki Inoue led to substantial improvements of the manuscript and are gratefully acknowledged.

References cited

Aja, S.U., and Dyar, M.D. (2002) The stability of Fe–Mg chlorites in hydrothermal solutions—I. Results of experimental investigations. Applied Geochemistry, 17, 1219–1239.

Aja, S., Omotoso, O., Bertoldi, C., Dachs, E., and Benisek, A. (2015) The structure and thermochemistry of three Fe-Mg chlorites. Clays and Clay Minerals, 63, 351–367.

Altherr, R., Soder, C., Meyer, H.-P., Ludwig, T., and Böhm, M. (2017) Ardennite in a high-P/T meta-conglomerate near Vitolište in the westernmost Vardar zone, Republic of Macedonia. European Journal of Mineralogy, 29, 473–489.

Bajt, S., Sutton, S., and Delaney, J. (1994) X-ray microprobe analysis of iron oxidation states in silicates and oxides using X-ray absorption near edge structure (XANES). Geochimica et Cosmochimica Acta, 58, 5209–5214.

Bastin, G.F., and Heijligers, H.J.M. (1989) Quantitative electron probe microanalysis of oxygen, 168 p. Eindhoven University of Technology.

Beaufort, D., Rigault, C., Billon, S., Billault, V., Inoue, A., Inoue, S., and Patrier, P. (2015) Chlorite and chloritization processes through mixed-layer mineral series in low-temperature geological systems—a review. Clay Minerals, 50, 497–523.

Billault, V., Beaufort, D., Patrier, P., and Petit, S. (2002) Crystal chemistry of Fe-sudoites from uranium deposits of the Athabasca Basin (Saskatchewan, Canada). Clays and Clay Minerals, 50, 70–81.

Bourdelle, F., and Cathelineau, M. (2015) Low-temperature chlorite geothermometry: a graphical representation based on a T-R^{2+}-Si diagram. European Journal of Mineralogy, 27, 617–626.

Bourdelle, F., Parra, T., Chopin, C., and Beyssac, O. (2013a) A new chlorite geothermometer for diagenetic to low-grade metamorphic conditions. Contributions to Mineralogy and Petrology, 165, 723–735.

Bourdelle, F., Benzerara, K., Beyssac, O., Cosmidis, J., Neuville, D.R., Brown, G.E., and Paineau, E. (2013b) Quantification of the ferric/ferrous iron ratio in silicates by scanning transmission X-ray microscopy at the Fe L_{23} edges. Contributions to Mineralogy and Petrology, 166, 423–434.

Cathelineau, M. (1988) Cation site occupancy in chlorites and illites as a function of temperature. Clay Minerals, 23, 471–485.

Chatterjee, N.D. (1966) On the widespread occurrence of oxidized chlorites in the Pennine zone of the western Italian Alps. Contributions to Mineralogy and Petrology, 12, 325–339.

Chermak, J.A., and Rimstidt, J.D. (1989) Estimating the thermodynamic properties (ΔG_f^0 and ΔH_f^0) of silicate minerals at 298 K from the sum of polyhedral contributions. American Mineralogist, 74, 1023–1031.

De Andrade, V., Susini, J., Salomé, M., Beraldin, O., Rigault, C., Heymes, T., Lewin, E., and Vidal, O. (2011) Submicrometer hyperspectral X-ray imaging of heterogeneous rocks and geomaterials: Applications at the Fe *K*-edge. Analytical Chemistry, 83, 4220–4227.

De Grave, E., Vandenbruwaene, J., and Van Bockstael, M. (1987) ^{57}Fe Mössbauer Spectroscopic Analysis of Chlorite. Physics and Chemistry of Minerals, 15, 173–180.

Droop, G.T.R. (1987) A general equation for estimating Fe^{3+} concentrations in ferromagnesian silicates and oxides from microprobe analyses, using stoichiometric criteria. Mineralogical Magazine, 51, 431–435.

Dubacq, B., and Plunder, A. (2018) Controls on trace element distribution in oxides and silicates. Journal of Petrology, 59, 2, 233–256.

Dyar, M.D., Perry, C.L., Rebbert, C.R., Dutrow, B.L., Holdaway, M.J., and Lang, H.M. (1991a) Mössbauer spectroscopy of synthetic and naturally occurring staurolite. American Mineralogist, 76, 27–41.

Dyar, M.D., Colucci, M.T., and Guidotti, C.V. (1991b) Forgotten major elements: Hydrogen and oxygen variation in biotite from metapelites. Geology, 19, 1029–1032.

Dyar, M.D., Guidotti, C.V., Holdaway, M.J., and Colucci, M. (1993) Nonstoichiometric hydrogen contents in common rock-forming hydroxyl silicates. Geochimica et Cosmochimica Acta, 57, 2913–2918.

Dyar, M.D., Delaney, J.S., and Sutton, S.R. (2001) Fe XANES spectra of iron-rich micas. European Journal of Mineralogy, 13, 1079–1098.

Emmons, W.H., and Larsen, E.S. (1923) Geology and ore deposits of the Creede district, Colorado. USGS Bulletin, 718, 198 p.

Evans, K.A., Dyar, M.D., Reddy, S.M., Lanzirotti, A., Adams, D.T., and Tailby, N. (2014) Variation in XANES in biotite as a function of orientation, crystal composition, and metamorphic history. American Mineralogist, 99, 443–457.

Farges, F., Lefrère, Y., Rossano, S., Berthereau, A., Calas, G., and Brown, G.E. (2004) The effect of redox state on the local structural environment of iron in silicate glasses: A combined XAFS spectroscopy, molecular dynamics, and bond valence study. Journal of Non-Crystalline Solids, 344, 176–188.

Fialin, M., Wagner, C., Métrich, N., Humler, E., Galoisy, L., and Bézos, A. (2001) Fe^{3+}/Σ Fe vs. Fe $L\alpha$ peak energy for minerals and glasses: Recent advances with the electron microprobe. American Mineralogist, 86, 456–465.

Fiege, A., Ruprecht, P., Simon, A.C., Bell, A.C., Göttlicher, J., Newville, M., Lanzirotti, T., and Moore, G. (2017) Calibration of Fe XANES for high-precision determination of Fe oxidation state in glasses: Comparison of new and existing results obtained at different synchrotron radiation sources. American Mineralogist, 102, 369–380.

Foster, M. D. (1962) Interpretation of the composition and a classification of the chlorites. U.S. Geological Survey Professional Paper 414-A, p. A1–A33.

Galoisy, L., Calas, G., and Arrio, M.A. (2001) High-resolution XANES spectra of iron in minerals and glasses: structural information from the pre-edge region. Chemical Geology, 174, 307–319.

Garvie, L.A., and Craven, A.J. (1994) Electron-beam-induced reduction of Mn^{4+} in manganese oxides as revealed by parallel EELS. Ultramicroscopy, 54, 83–92.

Garvie, L.A., Zega, T.J., Rez, P., and Buseck, P.R. (2004) Nanometer-scale measurements of Fe^{3+}/ΣFe by electron energy-loss spectroscopy: A cautionary note. American Mineralogist, 89, 1610–1616.

Giles, C., Malgrange, C., Goulon, J., de Bergevin, F., Vettier, C., Fontaine, A., Dartyge, E., and Pizzini, S. (1994) Energy and polarization-tunable X-ray quarter-wave plates for energy dispersive absorption spectrometer. Nuclear Institute and Methods in Physics Research, 349, 622–625.

Hawthorne, F.C., Ungaretti, L., Oberti, R., Caucia, F., and Callegari, A. (1993) The crystal chemistry of staurolite; I, Crystal structure and site populations. The Canadian Mineralogist, 31, 551–582.

Hawthorne, F.C., Oberta, R., Harlow, G.E., Maresch, W.V., Martin, R.F., Schumacher, J.C., and Welch, M.D. (2012) Nomenclature of the amphibole supergroup. American Mineralogist, 97, 2031–2048.

Henry, D.J., Novák, M., Hawthorne, F.C., Ertl, A., Dutrow, B., Uher, P., and Pezzotta, F. (2011) Nomenclature of the tourmaline supergroup minerals. American Mineralogist, 96, 895–913.

Hillier, S., and Velde, B. (1991) Octahedral occupancy and the chemical composition of diagenetic (low-temperature) chlorites. Clay Minerals, 26, 149–168.

Höfer, H.E., Brey, G.P., Schulz-Dobrick, B., and Oberhänsli, R. (1994) The determination of the oxidation state of iron by the electron microprobe. European Journal of Mineralogy, 6, 407–418.

Holland, T.J.B., and Powell, R. (1998) An internally consistent thermodynamic data set for phases of petrological interest. Journal of Metamorphic Geology, 16, 309–343.

Holland, T., Baker, J., and Powell, R. (1998) Mixing properties and activity–composition relationships of chlorites in the system MgO-FeO-Al_2O_3-SiO_2-H_2O. European Journal of Mineralogy, 10, 395–406.

Inoue, S., and Kogure, T. (2016) High-angle annular dark field scanning transmission electron microscopic (HAADF-STEM) study of Fe-rich 7-Å-14-Å interstratified minerals from a hydrothermal deposit. Clay Minerals, 51, 603–613.

Inoue, A., Meunier, A., Patrier-Mas, P., Rigault, C., Beaufort, D., and Vieillard, P.

(2009) Application of chemical geothermometry to low-temperature trioctahedral chlorites. Clays and Clay Minerals, 57, 371–382.
Inoue, A., Inoué, S., and Utada, M. (2018) Application of chlorite thermometry to estimation of formation temperature and redox conditions. Clay Minerals, 53, 143–158.
Lanari, P., Wagner, T., and Vidal, O. (2014) A thermodynamic model for di-trioctahedral chlorite from experimental and natural data in the system MgO-FeO-Al_2O_3-SiO_2-H_2O: Applications to P-T sections and geothermometry. Contributions to Mineralogy and Petrology, 167, 1–19.
Lanson, B., Lantenois, S., van Aken, P.A., Bauer, A., and Plançon, A. (2012) Experimental investigation of smectite interaction with metal iron at 80 °C: Structural characterization of newly formed Fe-rich phyllosilicates. American Mineralogist, 97, 864–871.
Lougear, A., Grodzicki, M., Bertoldi, C., Trautwein, A.X., Steiner, K., and Amthauer, G. (2000) Mössbauer and molecular orbital study of chlorites. Physics and Chemistry of Minerals, 27, 258–269.
Muñoz, M., Vidal, O., Marcaillou, C., Pascarelli, S., Mathon, O., and Farges, F. (2013) Iron oxidation state in phyllosilicate single crystals using Fe-K pre-edge and XANES spectroscopy: Effects of the linear polarization of the synchrotron X-ray beam. American Mineralogist, 98, 1187–1197.
Namur, O., Hatert, F., Grandjean, F., Long, G.J., Krins, N., Fransolet, A.-M., Vander Auwera, J., and Charlier, B. (2009) Ti substitution mechanisms in phlogopites from the Suwalki massif-type anorthosite, NE Poland. European Journal of Mineralogy, 21, 397–406.
Nelson, D.O., and Guggenheim, S. (1993) Inferred limitations to the oxidation of Fe in chlorite: A high-temperature single-crystal X-ray study. American Mineralogist, 78, 1197–1207.
Newville, M. (2014) Fundamentals of XAFS. Reviews in Mineralogy and Geochemistry, 78, 33–74.
Peacor, D.R., Rouse, R.C., and Bailey, S.W. (1988) Crystal structure of franklinfurnaceite; a tri-dioctahedral zincosilicate intermediate between chlorite and mica. American Mineralogist, 73, 876–887.
Pfalzer, P., Urbach, J.-P., Klemm, M., Horn, S., DenBoer, M.L., Frenkel, A.I., and Kirkland, J.P. (1999) Elimination of self-absorption in fluorescence hard-X-ray absorption spectra. Physical Review B, 60, 9335–9339.
Plunder, A., Agard, P., Chopin, C., Pourteau, A., and Okay, A.I. (2015) Accretion, underplating and exhumation along a subduction interface: From subduction initiation to continental subduction (Tavşanlı zone, W. Turkey). Lithos, 226, 233–254.
Raeburn, S.P., Ilton, E.S., and Veblen, D.R. (1997) Quantitative determination of the oxidation state of iron in biotite using X-ray photoelectron spectroscopy: II. In situ analyses. Geochimica et Cosmochimica Acta, 61, 4519–4530.
Rona, P.A. (1984) Hydrothermal mineralization at seafloor spreading centers. Earth-Science Reviews, 20, 1–104.
Rule, A.C., and Bailey, S.W. (1987) Refinement of the crystal structure of a monoclinic ferroan clinochlore. Clays and Clay Minerals, 35, 129–138.
Sainz-Diaz, I.C., Hernández-Laguna, A., and Dove, T.M. (2001) Theoretical modelling of *cis*-vacant and *trans*-vacant configurations in the octahedral sheet of illites and smectites. Physics and Chemistry of Minerals, 28, 322–331.
Shannon, R.D. (1976) Revised effective ionic radii and systematic studies of interatomic distances in halides and chalcogenides. Acta Crystallographica, 32, 751–767.
Smith, J.V. (1968) The crystal structure of staurolite. American Mineralogist, 53, 1139–1155.
Smyth, J.R., Dyar, M.D., May, H.M., Bricker, O.P., and Acker, J.G. (1997) Crystal structure refinement and Mössbauer spectroscopy of an ordered, triclinic clinochlore. Clays and Clay Minerals, 45, 544–550.
Trincal, V., and Lanari, P. (2016) Al-free di-trioctahedral substitution in chlorite and a ferri-sudoite end-member. Clay Minerals, 51, 675–689.
Tröger, L., Arvanitis, D., Baberschke, K., Michaelis, H., Grimm, U., and Zschech, E. (1992) Full correction of the self-absorption in soft-fluorescence extended X-ray-absorption fine-structure. Physical Review B, 46, 3283–3289.
van Aken, P.A., and Liebscher, B. (2002) Quantification of ferrous/ferric ratios in minerals: New evaluation schemes of Fe $L_{2,3}$ electron energy-loss near-edge spectra. Physics and Chemistry of Minerals, 29, 188–200.
van Hinsberg, V.J., Vriend, S.P., and Schumacher, J.C. (2005) A new method to calculate end-member thermodynamic properties of minerals from their constituent polyhedra I: Enthalpy, entropy and molar volume. Journal of metamorphic Geology, 23, 165–180.
Vidal, O., Parra, T., and Trotet, F. (2001) A thermodynamic model for Fe-Mg aluminous chlorite using data from phase equilibrium experiments and natural pelitic assemblages in the 100°C to 600°C, 1 to 25kb range. American Journal of Science, 301, 557–592.
Vidal, O., Parra, T., and Vieillard, P. (2005) Thermodynamic properties of the Tschermak solid solution in Fe-chlorite: Application to natural examples and possible role of oxidation. American Mineralogist, 90, 347–358.
Vidal, O., De Andrade, V., Lewin, E., Muñoz, M., Parra, T., and Pascarelli, S. (2006) P-T-deformation-Fe^{3+}/Fe^{2+} mapping at the thin section scale and comparison with XANES mapping: Application to a garnet-bearing metapelite from the Sambagawa metamorphic belt (Japan). Journal of Metamorphic Geology, 24, 669–683.
Vidal, O., Lanari, P., Muñoz, M., Bourdelle, F., and De Andrade, V. (2016) Deciphering temperature, pressure, and oxygen activity conditions of chlorite formation. Clay Minerals, 51, 615–633.
Virgo, D., and Popp, R.K. (2000) Hydrogen deficiency in mantle-derived phlogopites. American Mineralogist, 85, 753–759.
Walker, J.R., and Bish, D.L. (1992) Application of Rietveld refinement techniques to a disordered IIb Mg-chamosite. Clays and Clay Minerals, 40, 319–322.
Walshe, J.L. (1986) A six-component chlorite solid solution model and the conditions of chlorite formation in hydrothermal and geothermal systems. Economic Geology, 81, 681–703.
Walshe, J.L., and Solomon, M. (1981) An investigation into the environment of formation of the volcanic-hosted Mt. Lyell copper deposits using geology, mineralogy, stable isotopes, and a six-component chlorite solid solution model. Economic Geology, 76, 246–284.
Welch, M.D., and Marshall, W.G. (2001) High-pressure behavior of clinochlore. American Mineralogist, 86, 1380–1386.
White, E.W., and McKinstry, H.A. (1966) Chemical effect on X-ray absorption-edge fine structure. Advances in X-ray Analysis, 9, 376–392.
Wilke, M., Farges, F., Petit, P.E., Brown, J.G., and Martin, F. (2001) Oxidation state and coordination of Fe in minerals: An Fe *K*-XANES spectroscopic study. American Mineralogist, 86, 714–730.
Wilke, M., Partzsch, G.M., Bernhardt, R., and Lattard, D. (2005) Determination of the iron oxidation state in basaltic glasses using XANES at the K-edge. Chemical Geology, 220, 143–161.
Wones, D.R. (1963) Phase equilibria of "ferriannite," $KFe_3^{+2}Fe^{+3}Si_3O_{10}(OH)_2$. American Journal of Science, 261, 581–596.
Yamashita, T., and Hayes, P. (2008) Analysis of XPS spectra of Fe^{2+} and Fe^{3+} ions in oxide materials. Applied Surface Science, 254, 2441–2449.
Zanazzi, P.F., Montagnoli, M., Nazzareni, S., and Comodi, P. (2006) Structural effects of pressure on triclinic chlorite: A single-crystal study. American Mineralogist, 91, 1871–1878.
Zane, A., Sassi, R., and Guidotti, C.V. (1998) New data on metamorphic chlorite as a petrogenetic indicator mineral, with special regard to greenschist-facies rocks. Canadian Mineralogist, 36, 713–726.
Zazzi, Å., Hirsch, T.K., Leonova, E., Kaikkonen, A., Grins, J., Annersten, H., and Edén, M. (2006) Structural investigations of natural and synthetic chlorite minerals by X-ray diffraction, Mössbauer spectroscopy and solid-state nuclear magnetic resonance. Clays and Clay Minerals, 54, 252–265.
Zheng, H., and Bailey, S.W. (1989) Structures of intergrown triclinic and monoclinic II*b* chlorites from Kenya. Clays and Clay Minerals, 37, 308–316.

MANUSCRIPT RECEIVED JULY 25, 2018
MANUSCRIPT ACCEPTED NOVEMBER 27, 2018
MANUSCRIPT HANDLED BY SASA BAJT

Endnote:

[1]Deposit item AM-19-36766, Supplemental Material and Figure. Deposit items are free to all readers and found on the MSA website, via the specific issue's Table of Contents (go to http://www.minsocam.org/MSA/AmMin/TOC/2019/Mar2019_data/Mar2019_data.html).

Annexe – 2

Disentangling the compositional variations of lawsonite in blueschist-facies metasediments (Schistes Lustrés, W. Alps)

Benjamin Lefeuvre[1,2*], Benoît Dubacq[1], Anne Verlaguet[1], Clément Herviou[1], Stephanie Walker[3], Ethan Baxter[3], Philippe Agard[1]

[1] Sorbonne Université, CNRS-INSU, Institut des Sciences de la Terre de Paris, ISTeP UMR 7193, F 75005 Paris, France

[2] Laboratoire des Fluides Complexes et leurs Réservoirs – IPRA, E2S-UPPA, TotalEnergies, CNRS, Université de Pau et des Pays de l'Adour, UMR5150 Pau, France

[3] Department of Earth and Environmental Sciences, Boston College, 140 Commonwealth Ave, Chestnut Hill, MA02467, USA

*corresponding author: benjamin.lefeuvre@univ-pau.fr

1. Introduction

Sediments undergoing subduction contain large amounts of H_2O (up to 7 wt.% entering the trench globally, Plank and Langmuir, 1998) and release water through metamorphic reactions all along burial (Schmidt and Poli, 1998; Hacker et al., 2003; Van Keken et al., 2011). At depth, fluids play a major role as their migration induces dramatic changes in both mechanical and chemical properties of rocks. Produced amounts of water may be estimated (e.g., via thermodynamic modeling as in Hacker and Abers, 2004, among many others), but pathways and scales of fluid migration remain hard to assess, especially in sedimentary lithologies where alternating horizons show hugely variable permeabilities, and where connection of vein networks may be transient and hardly recorded. In this context, lawsonite is of particular interest as a H_2O host (~12 wt.%), as a primary constituent of calcschists and as a stable mineral over an extended pressure-temperature range (Schmidt and Poli, 1994). In metasediments, lawsonite is also intimately linked to the carbon cycle as its formation reactions involve both devolatilization and dissolution/crystallization of carbonates (Nitsch, 1972; Cook-Kollars et al., 2014; Lefeuvre et al., 2020).

The major element composition of lawsonite has been shown remarkably stable around its ideal composition (CaAl2Si2O7(OH)2.H2O) regardless of pressure-temperature compositions (e.g.,

Okamoto and Maruyama, 1999). Detailed studies of the minor and trace element composition of lawsonite have been performed in mafic blueschists, eclogites, and metasomatic rocks (Ueno, 1999; Tsujimori et al., 2006; Martin et al., 2011; Vitale Brovarone et al., 2014; Vitale Brovarone and Beyssac, 2014; Fornash et al., 2019; Whitney et al., 2020) but fewer studies have focused on metasedimentary lawsonite (Martin et al., 2014; Whitney et al., 2020). Reviews of the trace element contents of lawsonite (Fornash et al., 2019; Whitney et al., 2020) show that lawsonite incorporates preferentially Pb, Sr and rare earths (REE), especially light rare earths (LREE), emphasizing the variability of lawsonite compositions between and within rock types, with implications for element cycling in shallow to deep parts of subduction zones.

During Alpine subduction, fragments of oceanic lithosphere were successively buried along a cold geothermal gradient (~ 8°C/km, Agard et al., 2001a; Agard, 2021; Herviou et al., 2022), sliced from the downgoing plate and exhumed, providing a well-exposed example of a deep accretionary complex (Platt et al., 1986; Marthaler and Stampfli, 1989; Agard et al., 2009; 2018; Agard, 2021). In this zone, known as Liguro-Piemont domain or Schistes Lustrés (SL) complex, metasediments are volumetrically dominant and are cropping out continuously over large distances (e.g. Agard et al., 2009, 2021; Herviou et al. 2021, 2022), allowing studying the production, composition and behavior of fluids in subducted sediments (Agard et al., 2000; Bebout et al., 2013; Herviou et al., 2021). Lawsonite is abundant in these rocks, in a network of high-pressure veins (with carpholite in places) as well as in the surrounding schists (Agard et al., 2000, 2001; Vitale-Brovarone et al., 2014; Lefeuvre et al., 2020; Herviou et al., 2021). Oxygen and carbon isotopic data in the metasediments suggest that most of the fluid present during subduction was locally-derived (Henry et al., 1996; Bebout et al., 2013; Cook-Kollars et al., 2014; Jaeckel et al., 2018; Epstein et al., 2020), consistently with the composition of fluid inclusions in carpholite- and lawsonite-bearing veins (Agard et al., 2000; Herviou et al., 2021; see also Raimbourg et al., 2018; Lefeuvre, 2020). This dataset suggests that metasediments of the Schistes Lustrés complex mostly behaved as a rock-buffered system, with volumetrically large but transient and restricted fluid migration, and limited external fluid infiltration, but the scales of opening and fluid mobility remain poorly known.

In light of the different lawsonite types identified in the Schistes Lustrés (Lefeuvre et al., 2020) and of the very large variability of minor and trace element composition of lawsonite (Fornash et al., 2019; Whitney et al., 2020), this geochemical study provides a petrological model to refine the crystallization history of lawsonite and to shed light over the scale of element mobility in the upper units of the

Schistes Lustrés complex. This is necessary to know whether the composition of lawsonite offers reliable tracers of fluids and their sources or not, and to characterize the scale of fluid circulation in the Schistes Lustrés during prograde and peak metamorphism.

Lawsonite types were measured for major and trace elements in high-pressure veins and the surrounding schists. Bulk-rock compositions (major and trace elements) were measured on 9 samples representative of the calcschist types collected along the transect, to account for the variability of rock composition. Sr isotopic ratios were measured on mineral separates and selected bulk samples**.**

2. Geological setting and lawsonite classification

2.1 The Cottian Alps transect of the Western Alps

The Western Alps result of an east-dipping, slow and cold subduction (~8°C/km at a maximum of 2 cm/year; Agard et al., 2001a; Le Pichon et al., 1988; Lapen et al., 2003) of the Valais and Liguro-Piemont slow-spreading oceans (Lagabrielle and Cannat, 1990) below Adria/Apulia microcontinents. Subduction of these slow-spreading oceanic domains lasted over 35 My before continental subduction (Schmid et al., 2017, Stampfli et al., 1998).

Remnants of Liguro-Piemont oceanic lithosphere are now exposed in the internal domain of the Western Alps and form a nappe-stack known as Liguro-Piemont domain (Agard, 2021; Herviou et al., 2022) or Schistes Lustrés (SL) complex (Caron, 1974; Agard et al., 2001, 2002) owing to their characterising sedimentary features (Fig. 1a; for more details on the overall Alpine structure, see: Coward and Dietrich, 1989; Lagabrielle and Lemoine, 1997; Rosenbaum and Lister, 2005; Handy et al., 2010). Former oceanic sediments (marls, shales and limestones; e.g. Lemoine, 2003) correspond to an initial ~200-400m thick sequence of Upper Jurassic to Late Cretaceous pelagic and hemipelagic seafloor deposits (De Wever and Caby, 1981; Lemoine et al., 1984; Lemoine and Tricart, 1986; Deville, 1986; Deville et al., 1992; Lemoine, 2003). These sediments are volumetrically dominant in this complex and are embedding variable amounts of mafic and ultramafic rocks (e.g. Lagabrielle et al., 2015; Herviou et al., 2022).

During subduction, fragments of the Liguro-Piemont oceanic lithosphere were successively scraped off from the downgoing plate, stacked at depths and exhumed to form a deep accretionary complex built by progressive underplating (Platt et al., 1986; Marthaler and Stampfli, 1989; Agard et al., 2009;

2018; Agard, 2021; Agard and Handy, 2021; Plunder et al., 2012. Herviou et al., 2022). Several units corresponding to independent subduction slices were identified in the Schistes Lustrés complex (Lagabrielle, 1987; Fudral, 1996; Tricart and Schwartz, 2006; Lagabrielle et al., 2015; see Herviou et al., 2022 for a compilation). Recently, based on the compilation of metamorphic, structural, lithostratigraphic and radiochronological data, Herviou et al. (2022) reappraised the overall structure of the complex, highlighting the existence of a trimodal distribution of units with an almost continuous eastward increase in peak burial conditions from the Liguro-Piemont Upper units (LPU; 320-400°C-1.2-1.9 GPa) to the Middle units (LPM; 415-475°C- 1.7-2.2 GPa) and to the Lower units (LPL; 500-580°C- 2.2-2.8 GPa; Fig. 1a-c; For peak metamorphic conditions through the domain see also Agard et al., 2001; Beyssac et al., 2002; Gabalda et al., 2009; Plunder et al., 2012; Angiboust et al., 2012 Schwartz et al., 2013). The LPU and LPM units metamorphosed under blueschist-facies conditions are dominated by sediments (>90%), whereas the LPL units metamorphosed at eclogite-facies are much richer in mafic-ultramafic rocks (>40%; Herviou et al., 2022).

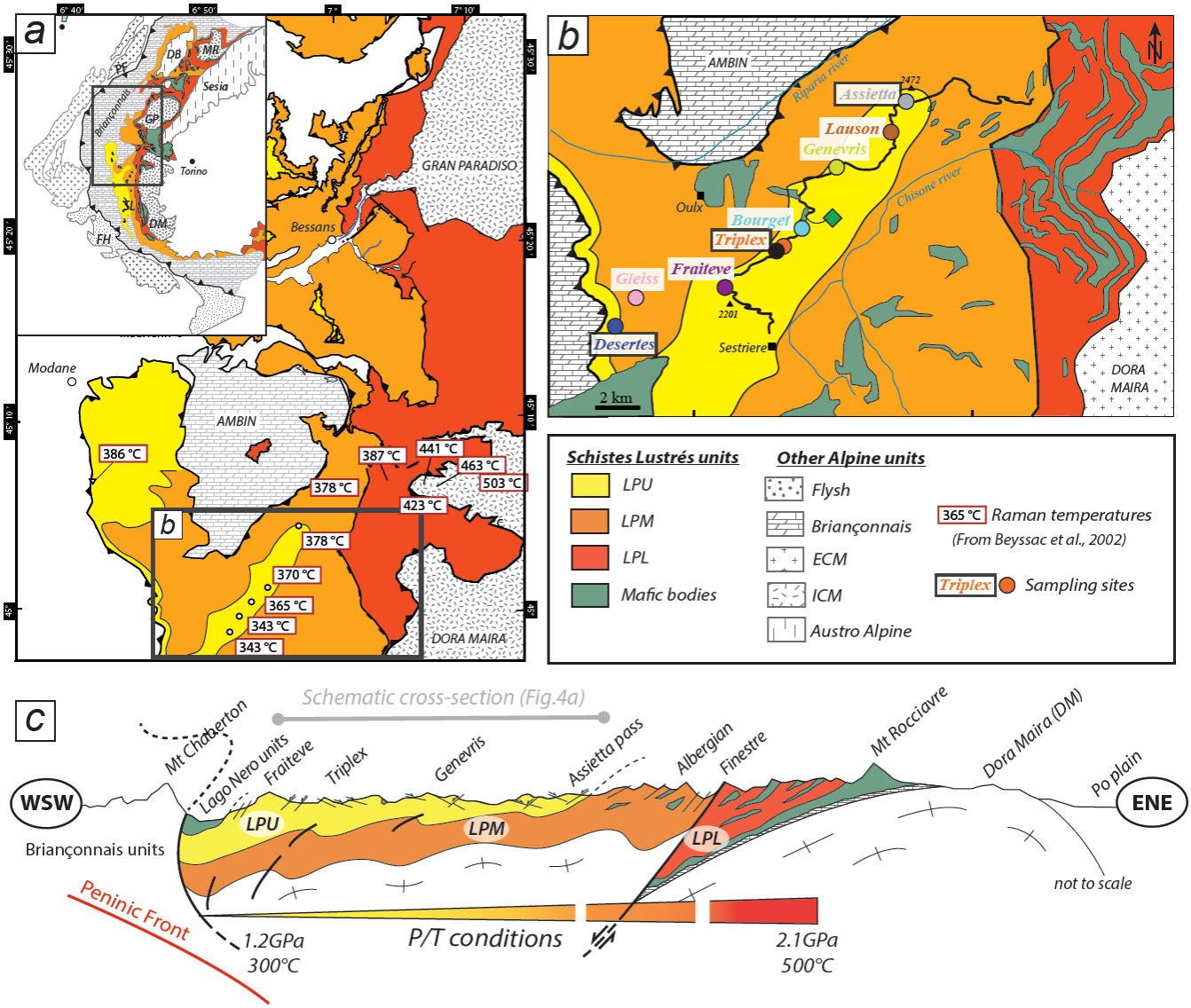

Figure 1 *(previous page): Geolocial setting. (a) Geological map of the Western Alps illustrating the repartition of the different Liguro-Piemont units (yellow: LPU, orange: LPM and red: LPM). RSCM temperatures are indicated (Beyssac et al., 2002, Gabalda et al., 2009; Plunder et al., 2012). (b) Zoom on the cottian Alps andl ocalization of the sites of interest. Mafic and ultramafic bodies are in green. (c) simplified SW-NE cross-section in the studied area. Associated P-T conditions are reported after Agard et al., 2001a. Contours of the units are after Herviou et al. (2022).*

This contribution focusses on the lawsonite types found in high quantities in the LPU unit of Cottian Alps (Lago Nero slice; Polino et al., 2002; Herviou et al., 2022) and more specifically on the Strada dell Assietta transect (Caron, 1974; Lefeuvre et al., 2020; Fig. 1b) between Fraiteve and the Assietta pass, along a ~15 km SW-NE traverse in the French-Italian Cottian Alps (Figs. 1b, c; Caron, 1974; Polino et al., 1984).

2.2. Several types of lawsonite

Lefeuvre et al. (2020) identified four types of lawsonite in these rocks based on varying textures and microstructural occurrences (Fig.2). Thsudo apt updatessis section draws a brief overview, details are available in the original publication. The four lawsonite types were labelled A to D (LwsA, LwsB, LwsC, LwsD) without implying chronological order, and interpreted as generations forming during prograde to peak metamorphic conditions (Fig. 2a). LwsA is the most abundant lawsonite type and occurs as millimetric black prisms closely associated to ankerite crystals, in layers of pelitic schist surrounded by thin carbonate-rich layers (Fig. 2b). The dark colour of LwsA originates from abundant organic matter inclusions. A similar mineral assemblage is found in centimetric tensile veins (as schematized on Fig. 2f), in which cream-coloured LwsC fibres are in textural equilibrium with ankerite and quartz, all growing perpendicular to vein walls. LwsC-bearing veins are scarce in the field and small, largely deformed and sheared, therefore poorly preserved and easy to miss. Yet, LwsC-bearing veins are only found where LwsA is widespread in the schist. LwsA in the schist and LwsC-bearing veins likely formed early on the prograde path (in conditions possibly as low as 0.4 GPa / 180 °C but probably developing over time, Fig. 2a; Lefeuvre et al., 2020). The associated reaction requires small-scale Ca transfer from carbonate horizons towards pelitic layers (sketch on Figs. 2a, b).

In the field, veining is abundant and decimetric to metric veins containing quartz and cream-coloured LwsB fibres dominate (Fig. 2c). LwsB fibres are elongated parallel to the vein walls and suggest incremental crystallization in long-lived veins, now showing superimposed ductile and fragile deformation. Locally, LwsB-bearing veins and the surrounding schist were intimately folded and sheared, resulting in hard-to-interpret outcrops in which schistose fragments are embedded in high-

pressure veins with abundant quartz (Figs. 2e-g). These are referred to as “multiquartz aggregates”. This veining system contains LwsB (labelled LwsB*; Fig. 2f) apparently crystallizing over multiple steps, and therefore likely recording incremental growth during ductile deformation (Fig. 2g). Crystals of LwsA type found in the schistose fragments are noted LwsA*. The multiquartz aggregates also show LwsC tensile veins, generally at the interface between pelitic domains and the quartz-LwsB-bearing vein, as schematized on figure 2f. Rare rectangular white crystals without preferential orientation are found in the vicinity of LwsB-bearing veins and classified as a fourth lawsonite type: LwsD (Fig. 2d).

Figure 2 *(next page): Different types of lawsonite observed in the field. (a) P-T diagram showing the P-T conditions associated with the several lawsonite types encountered in the field (from Lefeuvre et al., 2020). (b) Typical outcrop of the Schistres Lustrés where pelitic layers and carbonate layers are intensely folded. LwsA is found in the pelitic layers and ankerite (Ank) enrichment is found at the edges of carbonate layers and within the pelitic layers. Small quartz-bearing veins are often encountered. (c) LwsB-bearing vein associated with quartz (Qz). (d) LwsD crystals found in the pelitic schist directly next to LwsB vein. Note the presence of ankerite. (e) Multiquartz aggregate observed in the field where pelitic schist fragment are locally incorporated to a LwsB-rich vein. (f) Interpretative sketch of (e). (g) Multiquartz aggregate of larger than (e).*

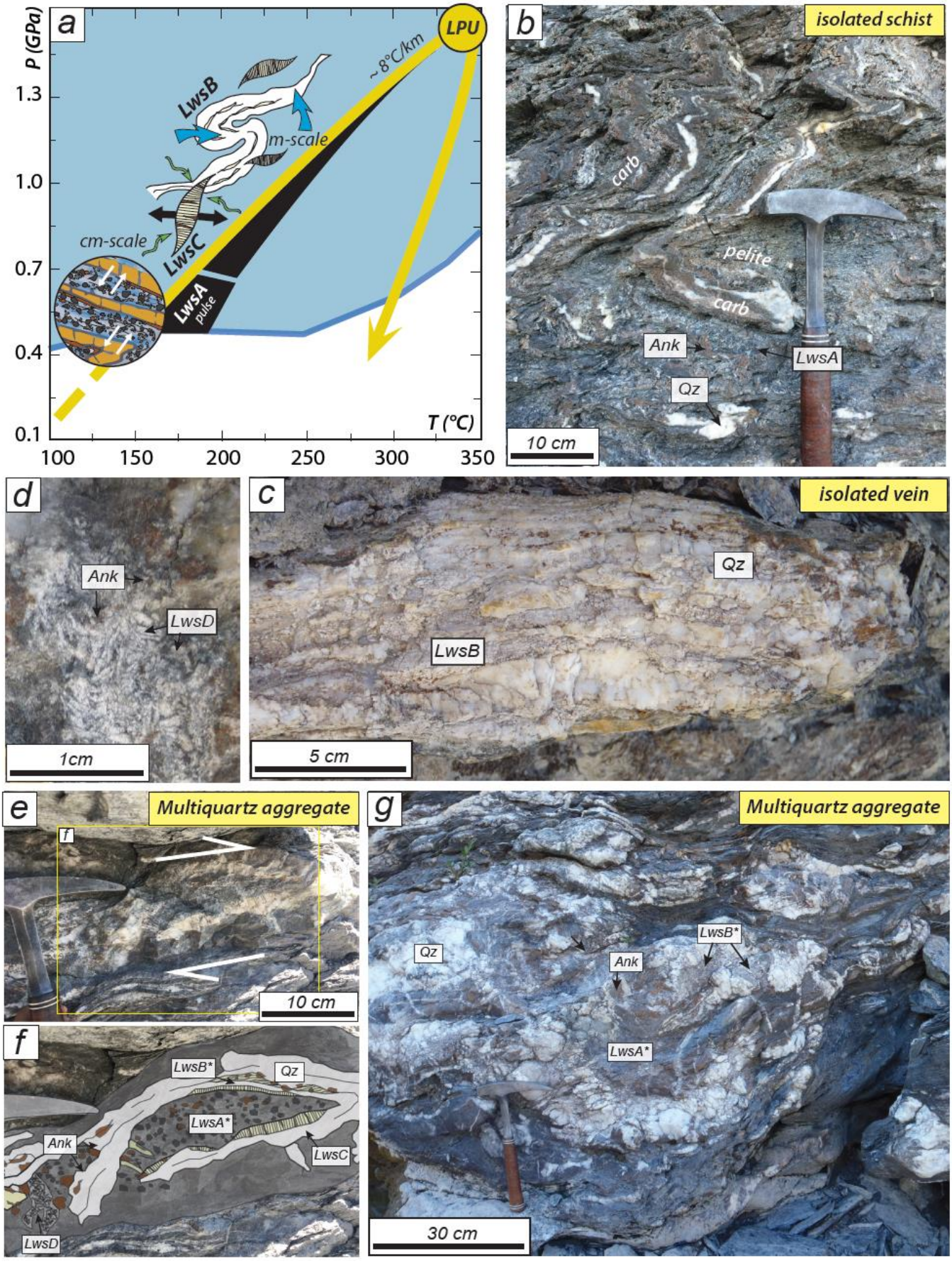
a
P (GPa)
1.3
1.0
0.7
0.4
0.1
100
150
200
250
300
350
T (°C)
LPU
~8°C/km
LwsB
m-scale
cm-scale
LwsC
LwsA
pulse
b
isolated schist
carb
pelite
carb
Ank
LwsA
Qz
10 cm
d
Ank
LwsD
1cm
c
isolated vein
Qz
LwsB
5 cm
e
Multiquartz aggregate
f
10 cm
f
LwsB*
Qz
LwsA*
Ank
LwsC
LwsD
g
Multiquartz aggregate
Qz
LwsB*
Ank
LwsA*
30 cm

2.3. Sampling strategy

Out of 30 samples collected along the Strada dell Assietta transect, 9 have been selected for trace element analysis. In the Triplex area, 6 samples have been selected for their good preservation of lawsonite, with little or no retrograde minerals (generally phengite and chlorite). Two LwsB-bearing samples (one also bearing LwsC) have been analyzed east (Assietta) and west (Desertes) of Triplex for comparison.

Sample SL17-08D3 contains large amounts of centimetric LwsA crystals reaching 40 vol.% of the whole rock (Fig. 3a, b). This sample is hereafter referred to as “isolated schist” as it has been collected from pelitic/carbonate-layers alternation (Fig. 2b) without veins at direct proximity (within 5 meters).

Samples SL17-07A (Triplex), SL17-03B (Triplex) and DS18-02B2 (Desertes) are LwsB-bearing veins mainly composed of quartz and LwsB elongated parallel to vein walls, as shown on Fig. 3c-d. LwsB is often fractured (Fig. 3d) and intimately associated with quartz. Preservation of lawsonite crystals has again been a prevalent criterion for sample selection before laser ablation, as LwsB was often found pseudomorphed into a mixture of phengite and chlorite (Fig. 3d).

Three multiquartz aggregates have been added as potential records of extensive fluid-rock interaction (Figs. 2e-g). Two of them have been collected in the Triplex area (SL16-11E2 and SL17-01(4)), the other one at the Assietta pass (SL18-11(1&2)). Figure 3e illustrates how the types and generations of lawsonite are distributed in multiquartz aggregates. The pelitic schist containing LwsA* is often crosscut by quartz-rich LwsB*-bearing vein. This sample also contains some LwsC fibers present in tensile veins. Near the pelitic fragments, ankerite is abundant and locally grows into the vein. At the contact between pelitic schist fragments and LwsC-bearing veins in sample SL18-11(1&2), LwsC shows epitaxial growth from LwsA* in the schist (Fig. 3g) without clear textural relation with ankerite in this sample.

One LwsD-bearing sample (Fig. 2d) from Triplex area has been selected (SL17-07B). This sample is a pelitic schist in which white LwsD prisms are observed, collected 1 meter away from SL17-07A (LwsB-bearing vein presented above). These lawsonite crystals are locally associated with ankerite (Fig. 2d).

For bulk rock analyses, 10 samples were selected along the transect (Fig. 1d). Nine of them are calcschists, representative of the different calcschist types identified by Lefeuvre et al. (2020), ranging

from pelitic horizons to more carbonated horizons (lithologies 1 to 5; Fig. 4a). Only one pelitic (DS18-02C; type 1) and one carbonate-rich calcschists (GL18-06; type 4) were selected, as lawsonite is scarce in these endmember compositions. Therefore, most of the selected samples (7) are classified as type 2 and type 3 calcschists (Fig. 4a) in which lawsonite is widespread, owing to small-scale chemical exchanges between the dm- to cm-scale pelitic and carbonate-rich horizons (Lefeuvre et al., 2020). For comparison, one mafic sample was also analyzed. SL17-09B is a metamorphosed basaltic pillow breccia body (~10 m long) embedded in calcschists and collected at the Bourget site (20 m away from the Bourget calcschist sample). Metamorphosed volcano-detrital deposits are common in the Schistes Lustrés and are referred to as prasinites (Lagabrielle and Cannat., 1990).

Figure 3 *(next page): Selected lawsonite-bearing samples. Corresponding name is reported for each. sample (a) Isolated schist enriched in LwsA crystals, which are black and associated with ankerite (Ank) and quartz (Qz). Note the peculiar presence of chlorite (greenish mineral observed top left of the sample). (b) Polarized microscopy image of LwsA bearing schist. (c) LwsB-bearing vein where almost no ankerite is observed. (d) Polarized microscopy image of LwsB vein where quartz is associated with LwsB. (e) Multiquartz aggregate hand-size specimen in which several thick-sections have been made, lawsonite contained in the pelitic fragments is referred as LwsA* and lawsonite contained in the quartz-rich vein is referred as LwsB* to avoid confusion between these minerals and LwsA, LwsB observed elsewhere. (f) LwsB* cumulate in a vein from a multiquartz aggregate. (g) LwsA* observed in the pelitic fragment where a LwsC vein crosscut the schist.*

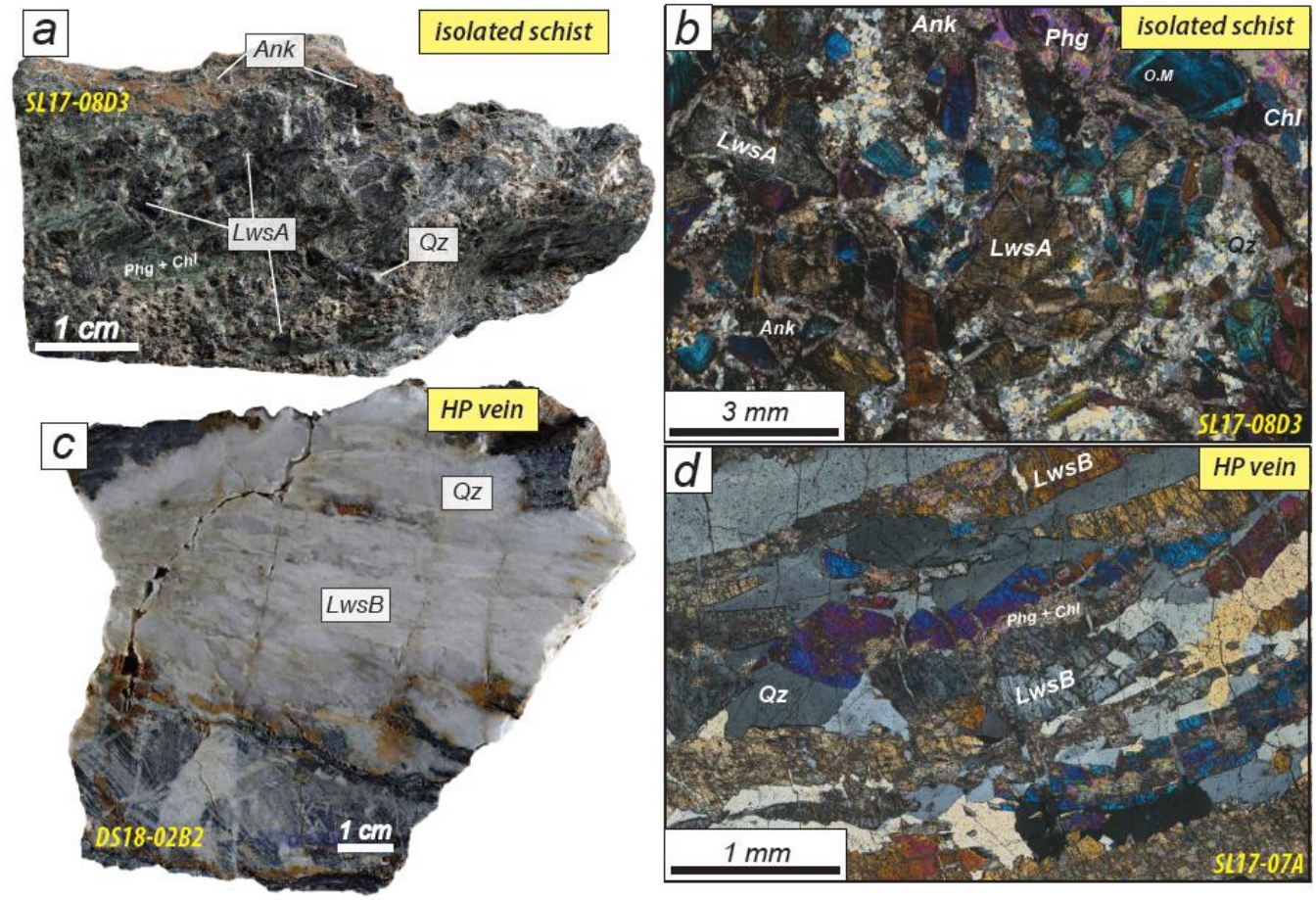
a
isolated schist
Ank
SL17-08D3
LwsA
Qz
Phg + Chl
1 cm
b
Ank
Phg
isolated schist
O.M
Chl
LwsA
LwsA
Qz
Ank
3 mm
SL17-08D3
c
HP vein
Qz
LwsB
DS18-02B2
1 cm
d
LwsB
HP vein
Phg + Chl
Qz
LwsB
1 mm
SL17-07A
e
MultiQz aggregate
Qz
LwsB*
LwsA*
Ank
1 cm
SL17-01(4)
f
SL16-11E2
MultiQz aggregate
Qz
LwsB*
2 mm
g
MultiQz aggregate
Qz
LwsA*
LwsC vein
Ank
LwsC
Qz
2 mm
SL18-11(2)

3. Analytical methods

3.1. Bulk-rock geochemistry

Samples were finely crushed (< 2µm) in an agate mortar. Sample powders were weighed, heated for 1h at 1100°C and weighed again to calculate loss on ignition and to ensure destruction of organic matter. Powders were dissolved at 80°C in closed beakers with HNO_3 and HF overnight. For analysis of major elements, $B(OH)_3$ was introduced quickly after opening the beakers to avoid loss of silica. Further dilution was carried out with 2% HNO_3 before analysis. Both major and trace element compositions were analyzed at ALIPP6 (ISTeP, Sorbonne Université, Paris) using an ICP-OES spectrometer (Agilent 5100 HVDV) for major elements and an ICP-MS/MS (Agilent 8800) for trace elements. Calibration was made using a set of international and in-house standards (RGM-1, BIR-1, AGV-2, LIP, M77-2, GSN, COS, BHVO-2). To characterize the major element budget of these rocks, 10 oxides were measured (SiO_2, TiO_2, Al_2O_3, FeO, MnO, MgO, CaO, Na_2O, K_2O and P_2O_5). A total of 37 minor and trace elements were selected for this study (Li, Be, Sc, V, Cr, Co, Ni, Cu, Zn, Ga, As, Rb, Sr, Y, Zr, Nb, Cs, Ba, Ta, Pb, La, Ce, Pr, Nd, Sm, Eu, Gd, Tb, Dy, Ho, Er, Tm, Yb, Lu, Hf, Th and U).

3.2. Major element analysis and chemical mapping of lawsonite

Major element analysis of lawsonite crystals has been carried out at CAMPARIS (Sorbonne Université, Paris) with a CAMECA SX-FIVE electron microprobe and the data reducing method of Pouchou and Pichoir (1991). Analytical conditions were 15 kV-10 nA in WDS mode for analysis of major elements. Conditions were changed to 25 kV-100 nA when measuring minor elements (Sr, Ti, Cr and Ce). Fe_2O_3 (Fe), $MnTiO_3$ (Mn, Ti), diopside (Mg, Si), Cr_2O_3 (Cr), SrSi (Sr), orthoclase (Al, K), anorthite (Ca) and albite (Na) were used as standards for calibration of elements in parentheses. Qualitative element mapping was carried out with a SUPRA-55VP SEM at ISTeP (Sorbonne Université, Paris) in energy-dispersive spectroscopy (EDS) mode at 15 keV acceleration voltage, 30 nA beam current with a dwell time of 256 µs, analyzing each area up to 10 times for increased signal/noise ratio.

3.3. Trace element analysis of lawsonite

Trace element lawsonite contents were measured at ALIPP6, using a laser ablation ICP-MS/MS (Teledyne Analyte G2 193 nm ArF excimer laser ablation system coupled to an Agilent 8800 ICP-MS/MS) on polished thick sections (100 µm). Lawsonite crystals were ablated for 60 s (frequency of 8 Hz) in a He atmosphere using a 40 µm beam and a laser fluency of 3.54 J/cm^2. Background was measured 18 s before and after sampling ablation. Standardization was carried out using BCR2-G international glass standard, and ^{27}Al as internal standard obtained from electron microprobe analyses. Instrument drift and accuracy were controlled with repeated analyses of the international standards ATHO-G and BHVO2-G. Each and every ablation pattern was verified with an in-house Excel spreadsheet to check for absence of impurities and/or inclusions during ablation (89 out of 400 analyses were discarded).

3.4. Strontium isotopic ratios

Lawsonite strontium isotopic ratios were determined at the Boston College Center for Isotope Geochemistry using an IsotopX Phoenix Thermal Ionization Mass Spectrometer (TIMS). First, lawsonite crystals were separated from the bulk rock after crushing and sieving (see Sup. Mat. 1). Mineral fractions between 500µm and 125µm were separated using sodium polytungstate (density of 2.9 g.cm^{-3}) allowing isolation of the heavy fraction containing lawsonite, ankerite and oxides. Magnetic separation allowed separation of lawsonite from the magnetic phases. Lawsonite grains were subsequently cleaned in ultrasonic baths and handpicked before dissolution for TIMS analysis.

Dissolution was carried out in Boston College following a four-step protocol. Lawsonite separates were partially dissolved in 2mL of glacial acetic acid in an ultrasonic tank allowing the dissolution of mica and remaining carbonates. This first step was repeated twice to purify the lawsonite fraction.

Samples were subsequently dissolved in HF-HNO_3-HCl. Cleaned lawsonite fractions were attacked by 100 µL of HF together with 2 mL of HNO_3 at 120°C overnight. After 12 hours, acids were dried. The same step was repeated with 2 mL of HNO_3 at 120°C. Final dissolution was carried out with 2 mL of HCl at 120°C. Sr was separated using 100 µL micro-columns and pre-cleaned Sr-spec resin. Approximately 100 ng of Sr were loaded onto Re filaments with a TaF activator solution. Samples were analyzed using a multidynamic method, and repeated analysis of Sr standard SRM987 during the duration of the project gave 0.710240 ± 0.000010 (n = 5; 2sd), which is within the long-term average of 0.710242 ± 0.000005 (n=114; 2sd).

This procedure has been applied to bulk rock samples (without preliminary partial dissolution). In total, a set of 7 bulk rocks and 17 lawsonite separates have been analyzed (8 LwsA, 6 LwsB, 1 LwsC and 2 LwsD samples).

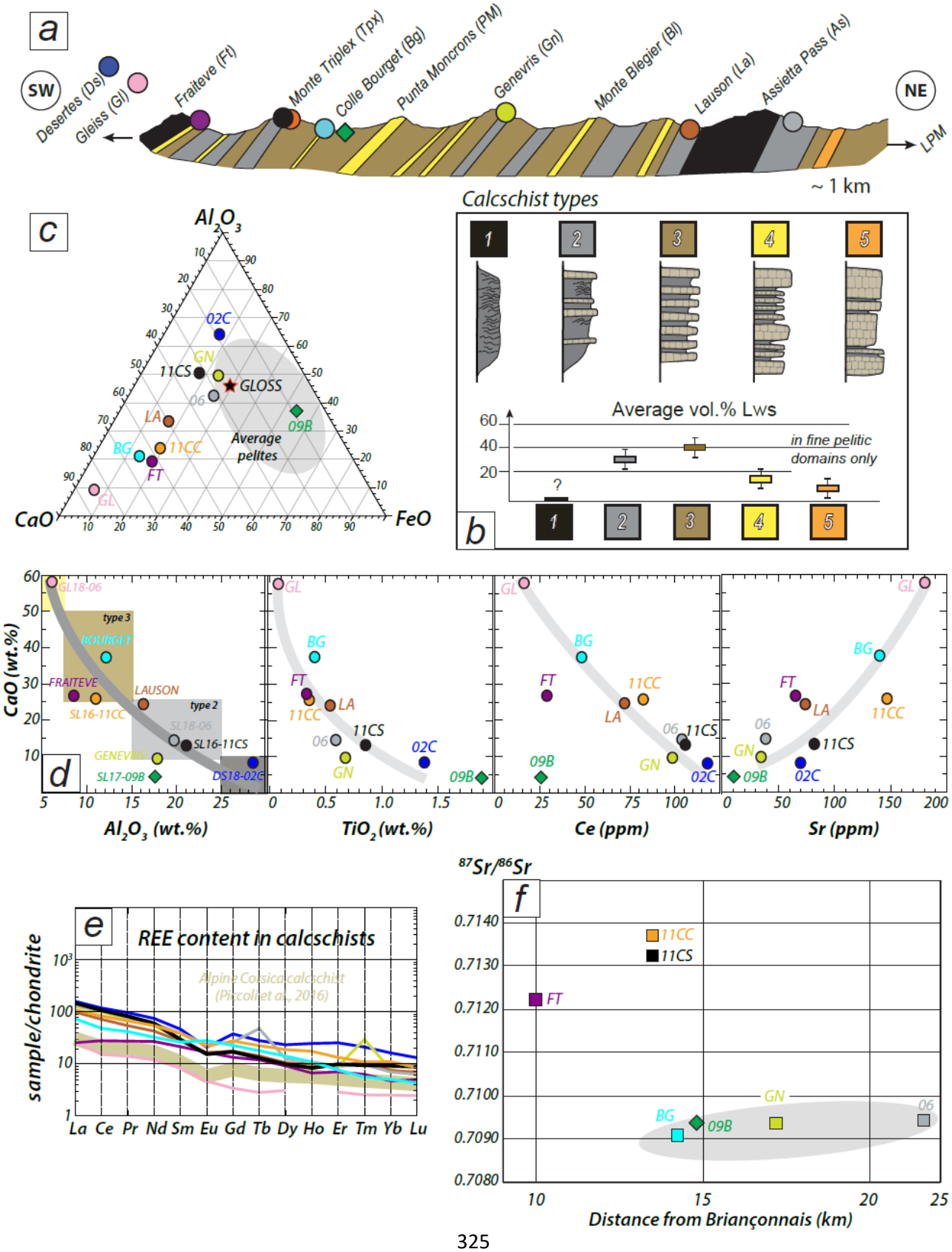

Figure 4 *(previous page): Bulk rock geochemistry. (a) Al_2O_3 (wt.%), TiO_2 (wt.%), Ce (ppm) and Sr (ppm) concentrations versus CaO (wt.%) for the different calcschist types. ACF diagram where the selected bulk rocks mainly plot between CaO and Al_2O_3. (c) Trace element content in lanthanides for each bulk rock. Corsican Schistes Lustrés have been added for comparison (after Piccoli et al., 2016)*

4. Results

4.1. Bulk rock geochemistry

Several calcschist types have been identified along the transect (lithologies 1 to 5; Fig. 3a, b) ranging from pelitic to more carbonated horizons. Bulk geochemistry reflects this classification (Table X, Fig. 4c) where compositions evolve gradually in ACF space between the two endmembers. These rocks exhibit similar FeO contents around 20 % in ACF (Fig. 4c), with the exception of sample 09B as described below. As shown in Fig. 4d, CaO and Al_2O_3 contents show inverse correlation. Pelitic horizons (DS18-02C; type 1) contain > 25 wt. % of Al_2O_3 and < 10 wt. % of CaO, whereas carbonate-rich calcschists (GL18-06; type 4) contain up to 58 wt. % of CaO and ~5 wt.% of Al_2O_3. Type 2 calcschists contain between 15 and 25 wt. % of Al_2O_3 and 10-25 wt. % of CaO, whereas more carbonated type 3 calcschists contain 7 to 15 wt. % of Al_2O_3 and 25 to 50 wt. % of CaO. At first order, TiO_2 and Ce are anti-correlated to CaO content (as for Al_2O_3) but Sr is positively correlated to CaO content (Fig. 4d). TiO_2 is a major component of these rocks (ranging between 0.1 and 1.9 wt. %), and is more concentrated in type 1 pelitic lithologies (> 1 wt. %) than in type 2 (0.5-1 wt. %) or type 3 and 4 (< 0.5 wt. %) more carbonated rocks. Most of the calcschists analyzed here contain less than 100 ppm of Sr (types 1, 2) but Sr reaches 180 ppm in type 4.

The most pelitic type 1 and type 2 calcschists are generally the most concentrated in LREE (Ce > 100 ppm in Figs. 4d, e) while the lowest concentrations are found in type 4 calcschists (Ce < 25 ppm, Fig. 4d). Chondrite-normalized REE patterns (Fig. 4e) show similarly decreasing trends from LREE to HREE for all calcschists, with La/Yb ratios around 20 and negative Eu anomalies (except for the Bourget sample). These patterns compare well with those of Corsican calcschists metamorphosed around 500-550 °C and ~ 2.3 GPa reported by Piccoli et al. (2016). However, Al_2O_3-rich calcschists from our study (types 1 to 3) are one order of magnitude richer in REE (Fig. 4e).

Sample SL17-09B (metamorphosed pillow breccia) shows higher FeO (up to 55 % in the ACF, Fig. 4c) and TiO_2 (~2 wt. %) contents than calcschists, but lower amounts of CaO (5 wt. %), Ce (25 ppm) and Sr (~10 ppm; Fig. 4d).

Strontium isotopic ratios do not correlate with carbonate content inferred by CaO values of bulk rocks. Figure 4f presents measured $^{87}Sr/^{86}Sr$ ratios for bulk rocks with distance to the Briançonnais units. Two groups are identified: one with $^{87}Sr/^{86}Sr$ values around 0.709 (samples BG, 09B, GN and 06) and another one with $^{87}Sr/^{86}Sr$ ratios ranging between 0.7120 and 0.7140 (samples FT, 11CC and 11CS). Interestingly, the pillow breccia (sample 09B) has an $^{87}Sr/^{86}Sr$ ratio similar to surrounding carbonates (Fig. 4f).

4.2. The geochemical signature of lawsonite

4.2.1. Minor and trace elements in lawsonite types

In-situ lawsonite compositions are provided in Table X and presented in figure 5 (normalized to C1 chondrite, McDonough and Sun, 1995) for each lawsonite type and each locality.

Dark LwsA crystals in isolated schist from Triplex area (SL17-08D3, Fig. 5a) display high values for U, Th and REE. Large ion lithophile elements (LILE; K, Cs, Rb, Ba, Pb, Sr) display large variations between samples, sharing high Pb and Sr contents (10 to 100 times chondritic values) but low contents in the other LILE (down to 10^{-3} chondritic values). The dispersion is much lower for Pb and Sr than for other LILE. High field strength elements (HFSE; Zr, Ti, Y, Hf) are also hugely variable: Zr content varies over four orders of magnitude, Hf and Y over three, Ti over two. These lawsonite crystals show peculiar REE patterns, with marked enrichment in LREE content for some, leading to a four order of magnitude dispersion. HREE are also scattered but contained between 10 and 1000 times the chondritic values. Two signatures appear: LREE-enriched LwsA with a negative slope from LREE to HREE (La/Yb ~ 100), and LwsA with flat to curved REE profiles, with an inflection point around Gd. Metallic elements (Fe, Mn, Cr and Ni) are generally low with little dispersion.

LwsB in isolated quartz-bearing veins from Triplex (SL17-07A, Fig. 5b; SL17-03B, Fig. 5c) and Desertes (DS18-02B2, Fig. 5d) shows very similar patterns for most elements. Globally, LwsB shows less dispersion than LwsA, except for LILE in SL17-07A (Fig. 5b) that compare well with those of LwsA (Fig. 5a). U and Th contents are either comparable to those in LwsA (Figs. 5a-d) or lower (between 10 and 200 times chondritic values in SL17-07A). Pb contents are comparable to those of

LwsA, and Sr is slightly higher in LwsB (up to 1000 times the chondritic values). For HFSE, Zr and Hf contents are lower than in LwsA (10^{-1} to 10^{-2} chondritic values) while Ti is similar (1-10, Fig. 5b). However, LwsB from Desertes shows higher content in LILE and HFSE than those from Triplex (Figs. 5b-d). REE patterns of LwsB show a slightly negative slope from LREE to HREE, as commonly observed in lawsonite (see compilation of Whitney et al., 2020). These patterns are consistent with some of the LwsA patterns in isolated schist (Fig. 5a). A small positive anomaly in Eu is observed in sample SL17-07A only (Fig. 5b). Metallic element contents in LwsB from Triplex are comparable to those in LwsA crystals, although Ni is systematically very low (Figs. 5b, c). Desertes locality shows LwsB with the highest content in metallic elements (Fig. 5d).

Lawsonite crystals in multiquartz aggregates (LwsA* and LwsB*) in Triplex (SL16-11E2, Figs. 5e, f; SL17-01(4), Fig. 5g) and Assietta Pass (SL18-11(1&2), Fig. 5h) show compositions overall similar to those of LwsA and LwsB, respectively (Figs. 5a, b). LILE and HFSE contents are globally consistent with similar variability between lawsonite types (LwsA* are comparable to LwsA and LwsB* to LwsB). Yet LwsA* and LwsC from multiquartz aggregate SL17-01(4) (Fig. 5g) show higher content in LILE, U, Th and metallic elements (Cr in particular) than LwsA in isolated schist and LwsA* from other samples. REE patterns are more distinctive: LwsA* and LwsC from multiquartz aggregate SL17-01(4) (Fig. 5g) show pronounced spoon-shaped REE patterns similar to some of LwsA in isolated schist, while LwsA* from sample SL16-11E2 (Fig. 5e) displays flat REE patterns around 10 to 100 times chondritic values, with one crystal showing a spoon-shaped REE pattern. Most LwsB* crystals from Triplex and sample SL18-11(2) from Assietta Pass show REE patterns consistent with those of LwsB (Figs. 5b, 5f, 5h), i.e., with a slightly negative slope and slightly curved. However, in sample SL18-11(1) from the Assietta pass, LwsB* growing with ankerite (Fig. 5h) shows convex REE patterns (i.e., richer in MREE; Figs 5h), which is also observed for a few LwsB* crystals from Triplex (Fig. 5d). In the multiquartz aggregate from the Assietta Pass, LwsC crystals show trace element patterns similar to those of neighboring LwsB* (Fig. 5i), with both spoon-shaped and convex REE patterns.

LwsD crystals (SL17-07B, Fig. 5j) show trace element patterns globally similar to those of LwsA and LwsA*, with somewhat higher Sr and Y values, reaching 2000 times chondritic values. Contents in LILE, U, Th and all metallic elements are as high as for LwsA* and LwsC in multiquartz aggregate SL17-01(4) described above. Part of LwsD crystals show relatively flat patterns from LREE to MREE and an enrichment of HREE starting from Ho, resulting in La/Yb ~10^{-2}. These patterns are similar to

some of LwsA* and LwsC in multiquartz aggregate SL17-01(4). (Fig. 5g, j). The other half of LwsD crystals are comparable with the most REE-enriched LwsA crystals in isolated schist (Fig. 5a, j).

Overall, two major points appear in light of expected lawsonite composition from the literature. First, enrichment in some elements (LREE, U, Th, Pb, Sr) stands out, in particular for LwsA, LwsA* and LwsD crystals. Second, the dispersion of analyses is huge, even within samples. To provide a petrologic explanation for these two points, the distribution of trace elements in lawsonite crystals has been mapped at micrometric scale for selected elements. Results are presented below according to lawsonite type.

It is noteworthy that in some of the maps described below, detection limits may be close to, or above, trace element contents in domains where these elements are depleted, especially for Ce (and for LREE in general): zoning is confidently identified in parts of the crystals, but in depleted domains, information is restricted to “depletion”. Corresponding extended trace element patterns are given for LA-ICP-MS/MS spot analyses next to maps for comparison.

4.2.2. Lawsonite composition in isolated schist (LwsA)

Five areas have been analyzed in a pelitic schist (sample SL17-08D3, LwsA, Fig. 5a), three of them (referred to as C1, C3 and C4 here) are shown in Figs. 6 and 7 (localization on the thick section in Sup. Mat. 2). They contain dark LwsA crystals with hourglass zoning, easily recognized on Ti maps (Figs. 6a, b). Crystals may exhibit both sides of the hourglass (Fig. 6b) or only one (Fig. 6a) due to their orientation. In maps of Figs. 6a and 6b, hourglass zoning is faintly observed for Ce, with enriched domains similar to Ti (blue spots 30 to 35 in C1; spots 13, 14, 16 and 18 in C4) whereas Al is slightly depleted in these domains (C1, Fig. 6a). Ce also shows enrichment in angular sectors in the center of lawsonite crystals, again anti-correlated to Al (Fig 6a) but not linked to specific Ti enrichment (close to spots 37 and 29 in Fig. 6a, and to spot 15 of Fig. 6b), sometimes correlated to Cr enrichment (Fig. 6b).

Figure 5 *(next page): Trace element concentrations for each lawsonite type. The values are normalized to the chondrite CI of McDonough and Sun. (1995). Sample names and number of analysis performed are given in top right, and location is given in top left of each diagram.*

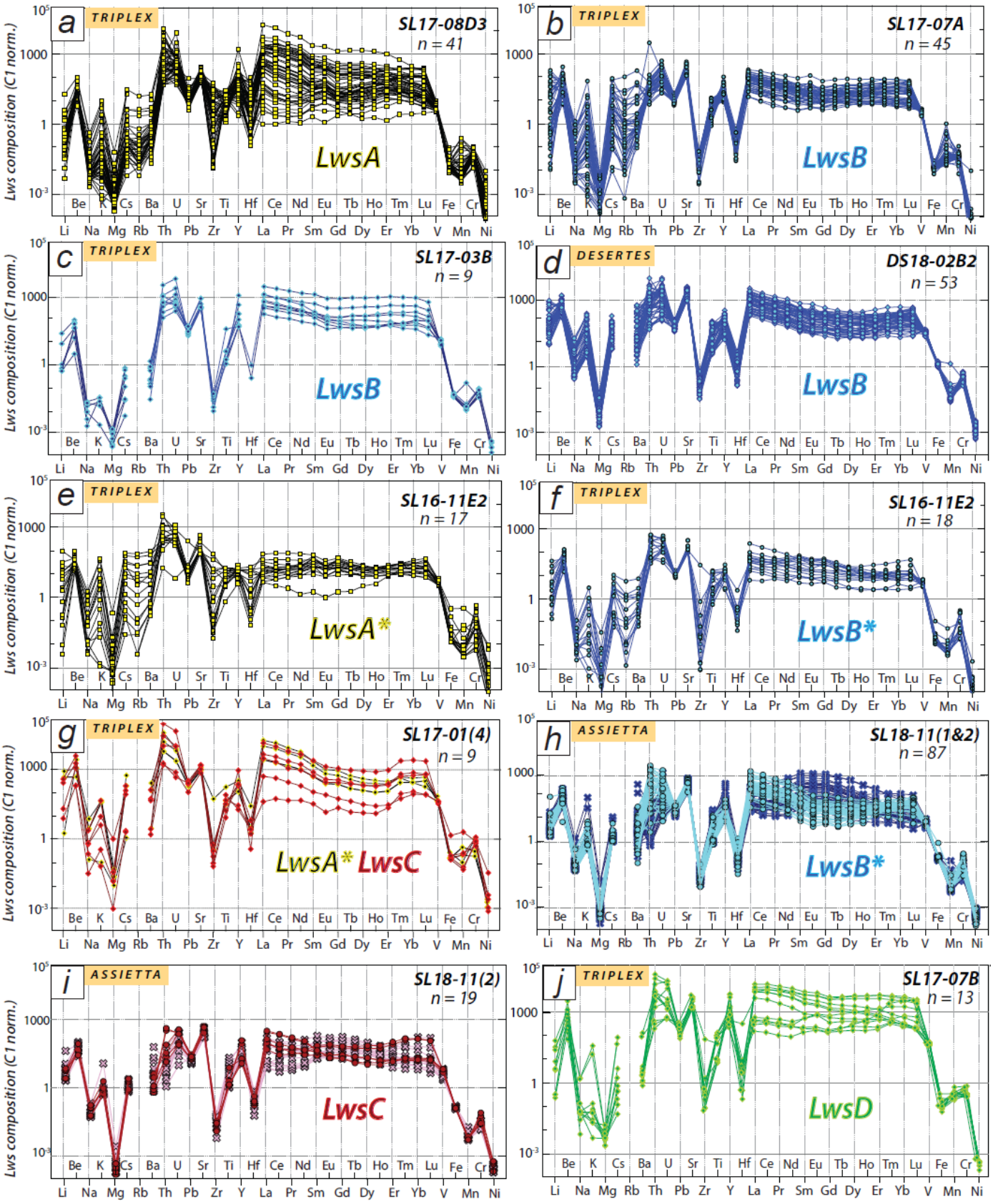
a
TRIPLEX
SL17-08D3
n = 41
LwsA
b
TRIPLEX
SL17-07A
n = 45
LwsB
c
TRIPLEX
SL17-03B
n = 9
LwsB
d
DESERTES
DS18-02B2
n = 53
LwsB
e
TRIPLEX
SL16-11E2
n = 17
LwsA*
f
TRIPLEX
SL16-11E2
n = 18
LwsB*
g
TRIPLEX
SL17-01(4)
n = 9
LwsA* LwsC
h
ASSIETTA
SL18-11(1&2)
n = 87
LwsB*
i
ASSIETTA
SL18-11(2)
n = 19
LwsC
j
TRIPLEX
SL17-07B
n = 13
LwsD
Lws composition (C1 norm.)
Li Na Mg Rb Th Pb Zr Y La Pr Sm Gd Dy Er Yb V Mn Ni
Be K Cs Ba U Sr Ti Hf Ce Nd Eu Tb Ho Tm Lu Fe Cr

Ti-rich hourglass domains on Fig. 6a (blue dots 30 to 35; Fig. 6c) show the highest concentrations in Ti, Zr and Hf and the lowest concentrations in Sr, Y and Mn. REE patterns also show large variations, in terms of slope and absolute values, whether located within or without the Ti-enriched domains. While barely seen on maps (Figs. 6a, b) due to detection limits, core to rim variations appear superimposed to the hourglass domain, in particular in Ti-rich domains (e.g., blue curves 30 to 35 on Fig. 6c, blue and green curves on Fig. 6d): LREE content decreases from core to rim, while HREE values remain almost constant, which tends to flatten the REE pattern slope and generate spoon-shaped patterns. Ti also tends to decrease from core to rim in Fig. 6a, while in Fig. 6b thin Ti-enriched/depleted bands alternate from core to rim. In the crystal core (spot 15 on Fig. 6b), the Ce-enriched Ti-depleted domain shows the highest U, Zr, Y, Hf, REE, Fe, Mn and Cr contents.

The LwsA crystal investigated in the third area (Fig. 7) shows intricate zoning as tentatively illustrated on Fig. 7b. Overall, Ti and Sr maps (Fig. 7a) show a lawsonite core (spots 1 and 8) overgrown by Ti-enriched lawsonite, itself rimmed by a Ti-poor, Sr-rich lawsonite border (green and blue zones on Fig. 7b, respectively). In the lawsonite core, hourglass zoning is observed with two domains: Ti-enriched (dots 01 and 08) and Sr-enriched (depleted triangle-shaped domain immediately below). Additionally, the Ti-rich domain shows variable Ti content (Figs. 7a, b), the lowest contents in Zr, Hf and Ni, and low LREE contents (spots 01 and 08, Fig. 7c). The overgrowing lawsonite (spots 2 to 9) is globally Ti-rich and Sr-poor with much dispersion and patchy domains. LA-ICP-MS analyses in this zone (spots 02, 03, 07, 09) show variable amounts of LREE, with almost similar HREE contents, resulting in flattened and curved patterns similar to those observed in Fig. 6. Finally, the Sr-rich Ti-poor border (spots 10 and 12) rimming LwsA (Fig. 7b) is enriched in Y and HREE, showing spoon-shape REE patterns as observed in Fig. 6c-d.

4.2.3. Lawsonite composition in quartz-rich veins (LwsB)

Cream-colored LwsB crystals have more homogeneous composition than LwsA crystals. None of the investigated LwsB crystals (see Sup. Mat. 3) display hourglass zoning. Nevertheless, zoning has been identified in LwsB crystals as presented on Fig. 8. The Ti map (Fig. 8a) features angular Ti-rich domains in crystal cores (LA-ICP-MS spots 38 to 41) surrounded by Ti-depleted rims (spots 42 and 43). These differences are highlighted on Fig. 8b; it is tempting to interpret these as successive generations of lawsonite. The Ti-poor crystals are enriched in U, Sr, Y and HREE compared to the Ti-rich crystals (Fig. 8b).

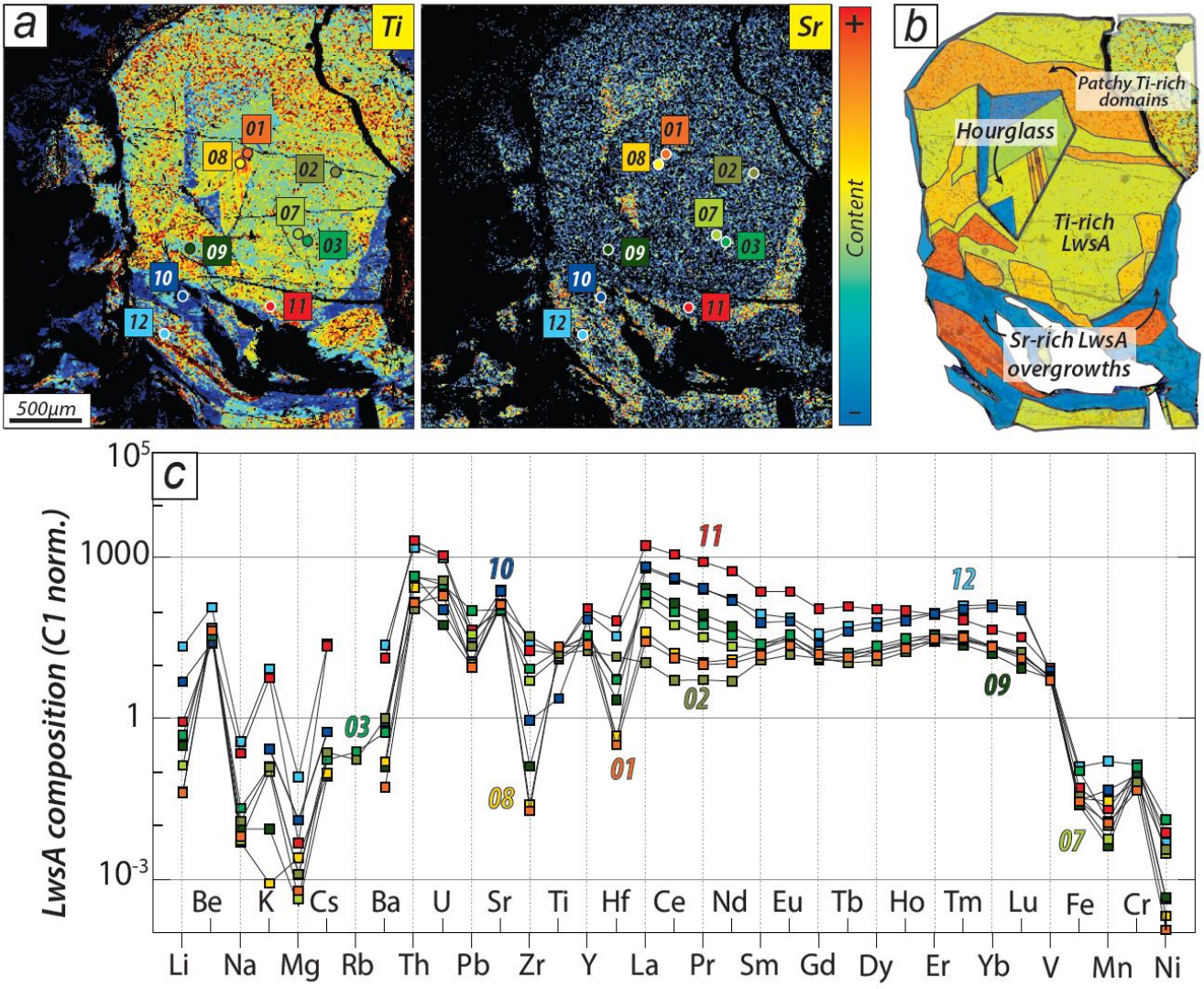

***Figure 7**: LwsA crystal with complex zoning features. (a) Element maps of Ti and Sr. All the analyses spots are reported in colors (ranging from 02 to 12). (b) Interpretative sketch based on the element maps deciphering the complex zonation recorded in this LwsA crystal. (c) Associated trace element contents (normalized to CI chondrite).*

4.2.4. Lawsonite composition in multiquartz aggregates (LwsA & LwsB*)*

Figure 9 shows the composition of LwsA* and LwsB* from multiquartz aggregate SL16-11E2 from Triplex. LwsB* shows the same features as LwsB with Ti-rich cores (Fig. 9a) and Ti-depleted borders that correspond to the highest Sr contents (Fig. 9b). The composition and distribution of the other trace elements (Fig. 9b) compare also well to LwsB.

In the inclusions of pelitic schist, (see Sup. Mat. 4), LwsA* crystals are often overgrown by pale borders (Fig. 9d) enriched in Ti and Cr (Fig. 9c) but not in Ce (spots 2 to 5, Fig. 9c). LwsA* cores (dots 06 to 09) show heterogeneous and patchy Ti-zoning, and are globally enriched in most LILE (and HSFE to a lower extent) but depleted in Pb and Sr (Fig. 9e). A Ce-rich domain in a crystal core is also observed as for LwsA in Fig. 6a-b.

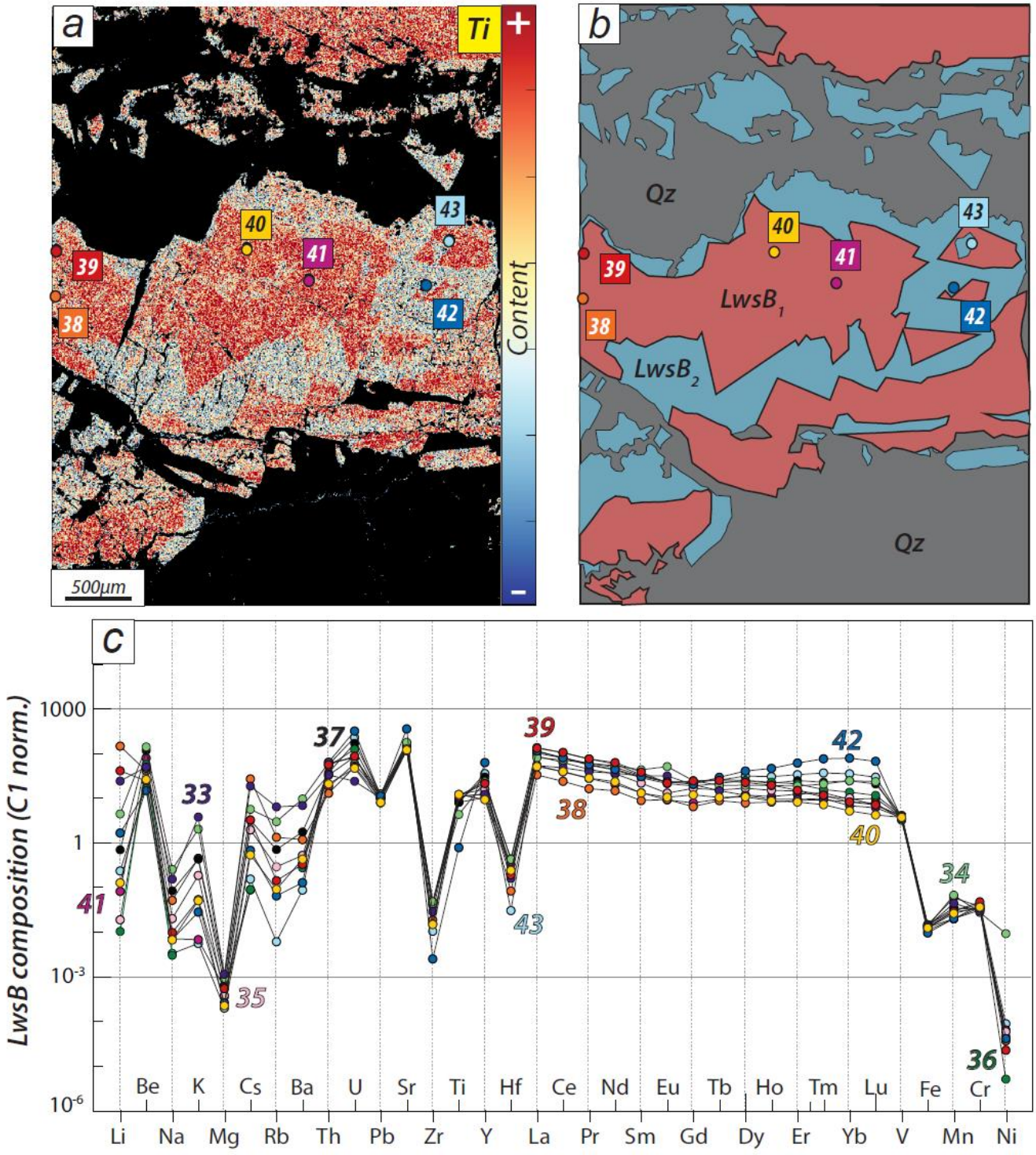

Figure 8. *LwsB zoning patterns. (a) Element map of Ti illustrating two distinct LwsB generations. Colorbar on the right. All the corresponding analyses spots are reported in colors. (b) Interpretative sketch of the Ti map. (c) Corresponding trace elements patterns (normalized to chondrite CI).*

4.3. Lawsonite $^{87}Sr/^{86}Sr$ ratios

The $^{87}Sr/^{86}Sr$ ratios of lawsonite separates are reported on Fig. 10. At first order, lawsonite separates display different signatures along the transect (Fig. 10a) and vary between 0.7113 near the Briançonnais contact (westward) and 0.7145 at Triplex, with ratios around 0.714 at the Assietta pass (eastward). Near the contact with the Briançonnais units, LwsA at Desertes shows higher $^{87}Sr/^{86}Sr$ ratios than LwsB collected directly near the LwsA sample (DS02A). The sample collected at Fraiteve containing LwsD shows a $^{87}Sr/^{86}Sr$ ratio of 0.7126. At Triplex, where the lawsonite content is maximum (see Fig. 4b), all five LwsA samples show very similar $^{87}Sr/^{86}Sr$ ratios (TableX) around 0.7130. LwsB samples collected at Triplex show higher $^{87}Sr/^{86}Sr$ ratios than LwsA and reach 0.7145. LwsD contained in sample SL07B shows values similar to LwsB. At the Assietta pass, LwsA and LwsB show comparable $^{87}Sr/^{86}Sr$ ratios around 0.7140.

Overall, $^{87}Sr/^{86}Sr$ ratios in lawsonite apparently increase eastward (Fig. 10a) with large variability. The $^{87}Sr/^{86}Sr$ ratios in lawsonite are not correlated with the Sr concentration (Fig. 10b). In the bulk rocks, Sr isotopic ratios are inversely correlated to Sr concentration for the least radiogenic group, but not for the more radiogenic samples.

Figure 9 *(next page): Trace elements in lawsonite from a single multiquartz aggregate. (a) Element map of Ti in LwsB*. (b) Trace element content of LwsB* (normalized to chondite CI). (c) Element maps of Ti, Cr and Ce of a LwsA* crystal (d) Analyses spotsof c) (e) Trace element contents of LwsA* (normalized to chondrite CI).*

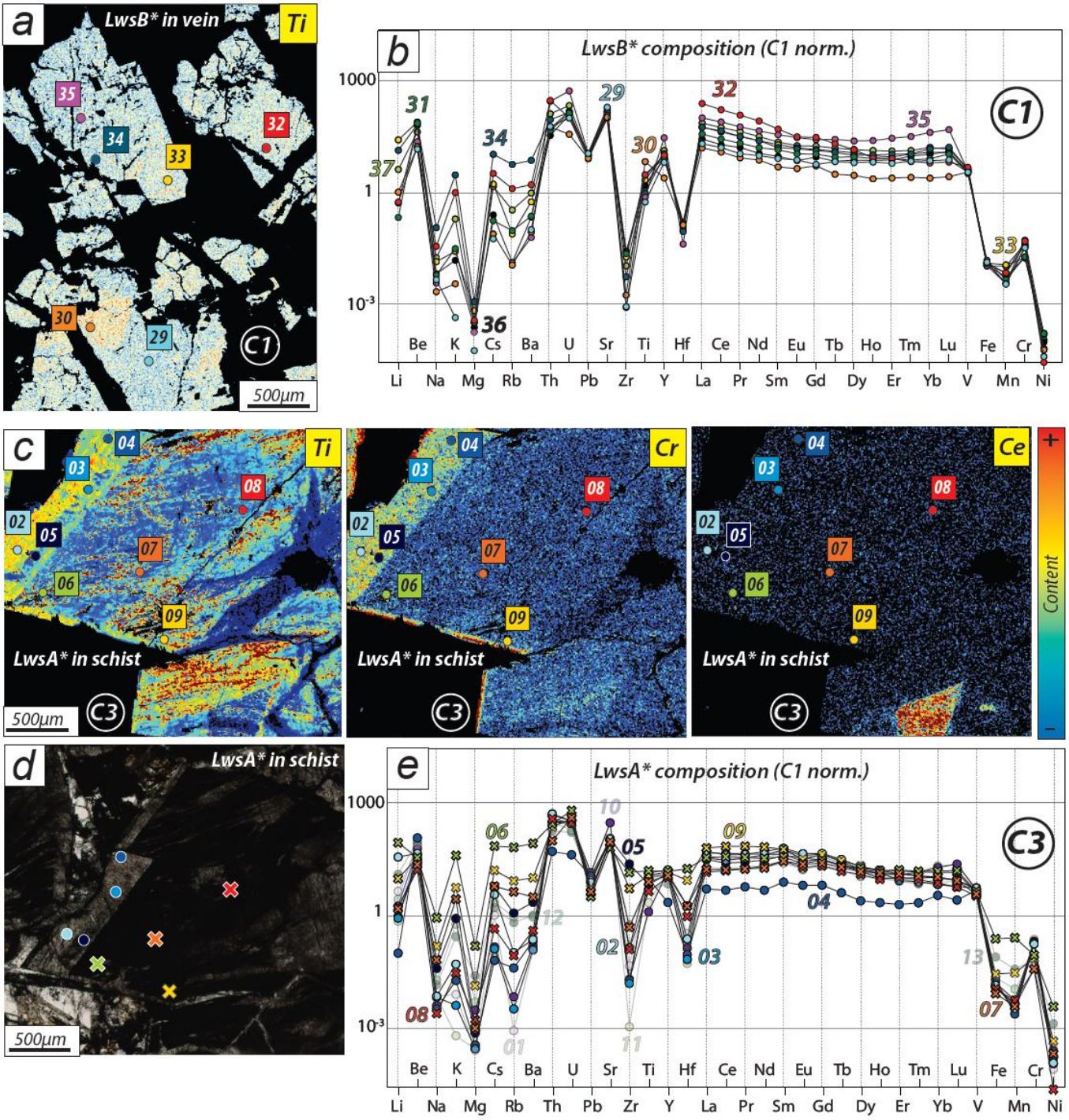

5. Discussion and geological implications

5.1. Distribution of trace elements in lawsonite types

Lawsonite is known to easily incorporate trace elements in its structure owing to multiple potential substitutions on Si, Al and Ca sites, the latter being easily deformed and therefore prone to hosting large cations (Ueno et al., 1999; Dubacq et Plunder, 2018). Itoigawaïte has been recognized as the

Sr equivalent of lawsonite, where Sr occupies the Ca site (Miyajima et al., 1999), suggesting extensive solid solution between the two.

In the following, we study correlations between elements, allowing identification of mechanisms controlling variations in lawsonite composition. Importantly, none of the observed composition variations appear linked to varying pressure-temperature conditions. Rather, these variations seem linked to competing out-of-equilibrium processes and transient system opening, when not due to analytical artefacts. We choose to emphasize the problem of contamination from white mica, which is probably met by many studying lawsonite.

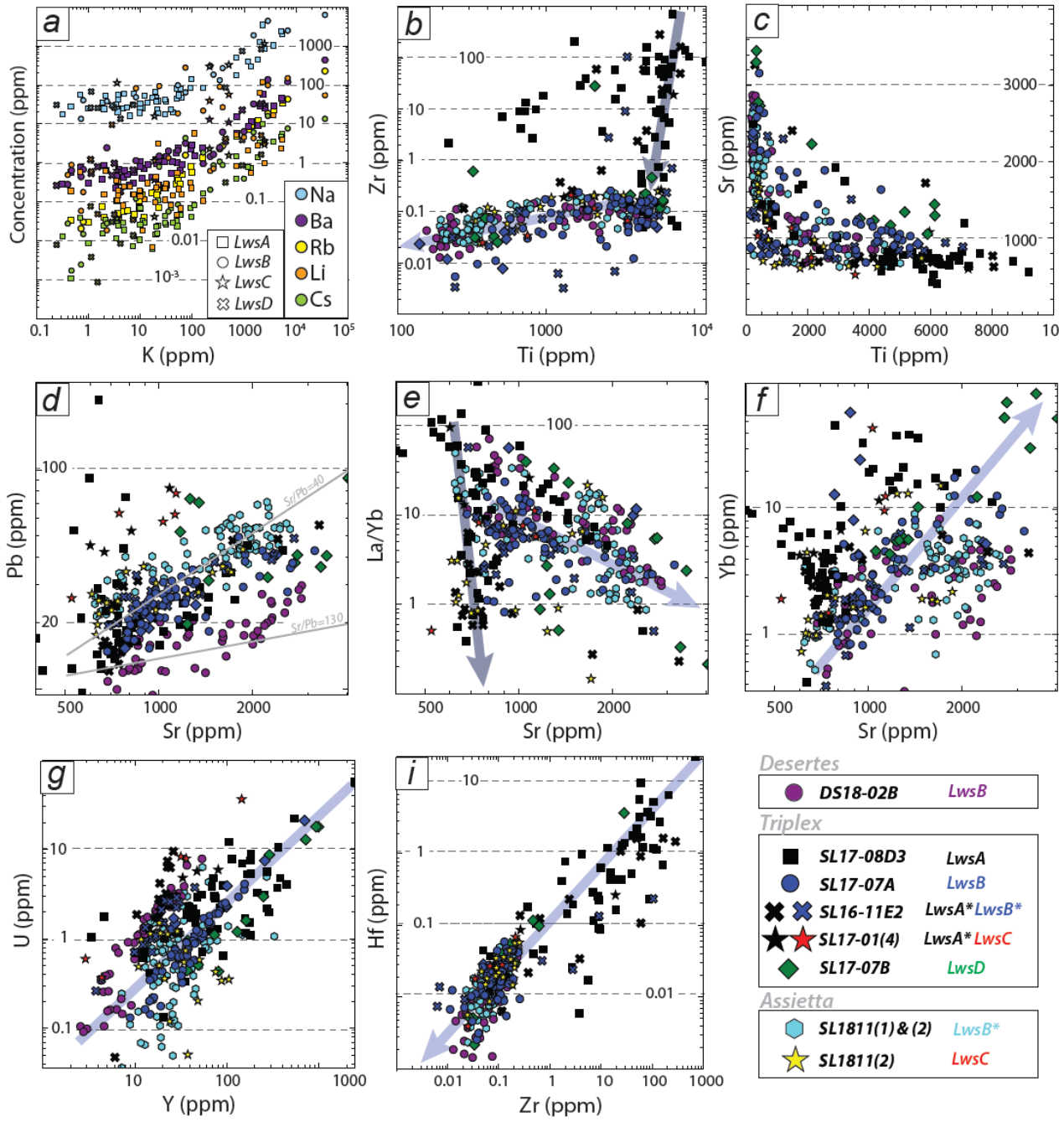

Figure 10 *(previous page): Comparative geochemistry of the several lawsonite types identified in this contribution.*

5.1.1. Univalent cations and white mica contamination

A strongly positive correlation between K content and Na, Ba, Rb and Cs contents is observed (Fig. 11a). These elements are classically enriched in white mica, in substitution of K. As lawsonite is generally devoid of K, these specific enrichments are attributed to white mica contamination (see also Whitney et al., 2020). Even though samples have been selected for good preservation of lawsonite, and each lawsonite ablation pattern has been carefully inspected to detect contamination from inclusions (see analytical methods), contamination remains apparent. Consequently, small mica inclusions have probably been ablated with lawsonite, leading to apparent enrichment of Na, Ba, Rb and Cs. Significant white mica contamination appears limited to these elements as no other correlation with K is observed. Therefore, interpretation of analytical results does not incorporate Na, K, Ba, Rb and Cs in the following. Importantly for mineral separates analyses, neither $^{87}Sr/^{86}Sr$ ratios nor Sr concentrations correlate with K (Fig. 10c, d), indicating negligible mica contamination on the Sr budget of the lawsonite separates and validating the procedure (more on mica contamination of mineral separates? i.e. on Na, Rb). It is also noteworthy that Li appears to show a positive correlation with K, yet much weaker than for other univalent cations (Fig. 11a).

5.1.2. Hourglass sector zoning

Hourglass zoning, observed in LwsA only, dramatically affects Ti (Figs. 6a, b, 7a). Ti-rich domains also correspond to high LREE concentrations, as illustrated on Ce maps (Figs. 6a, b), and to Zr and Hf enrichment (Fig. 6c, 11b, 11c). Preferential incorporation of Ti and LREE is commonly observed in metasedimentary lawsonite (Ueno et al., 1999; Martin et al., 2011; Vitale-Brovarone et al., 2014), while Ti and Fe hourglass zoning are reported for lawsonite in mafic rocks (Fornash et al., 2019). Hourglass zoning is classically observed in magmatic clinopyroxene and metamorphic staurolite (e.g., Hollister, 1970; Hollister and Gancarz, 1971; Dowty, 1976) and appears restricted to specific mineral groups, including lithian tourmaline (Van Hinsberg et al., 2006). Hourglass zoning is attributed to differential uptake of elements on the faces exposed to fluids (Van Hinsberg et al., 2006). Dowty (1976) showed that this preferential incorporation is controlled by the crystal structure: some elements show a higher affinity with some crystal faces due to electrostatic interactions, increasing their

adsorption rate during growth. Hourglass zoning has therefore been identified as an out-of-equilibrium feature, linked to rapid crystallization (Vitale-Brovarone et al., 2014). Practically, crystals showing hourglass zoning are proof that equilibrium was not reached, at least for some elements, with the consequence that thermodynamic modeling and/or partition coefficients based on formula unit properties will fail at reproducing the incorporation of these trace elements in lawsonite.

5.1.3. Concentric growth zoning

In Ti-enriched domains, concentrations of Ti and LREE are not constant. LREE are observed to decrease from core to rim, resulting in flattened REE patterns (Figs. 6c, d). Ti also globally decreases from core to rim in Fig. 6a (patchy domains can be related to interface-coupled dissolution-precipitation, as discussed in the next paragraph). These core-to-rim depletions, also observed in tourmaline by Van Hinsberg et al. (2006), are interpreted as reflecting a reservoir effect consistent with closed-system behavior, as for the classical Mn bell-shaped zoning in prograde garnet sometimes referred to as "garnet fractionation" (Tropper and Recheis, 2003; Kohn, 2005; Skora et al., 2006; Dubacq et al., 2019). Here concentric zoning is observed for notoriously immobile elements (large tri and quadrivalent cations) in lawsonite from pelitic parts (with the lowest permeability) after low-temperature crystallization (180 to 300°C). Assuming at least transient closed-system behavior is therefore reasonable, and backed by previous studies (Henry et al., 1996; Cook-Kollars et al., 2014; Lefeuvre et al., 2020; Herviou et al., 2021). The lack of systematics between cores and rims reflects the transient and local character, with homogenization over small length-scales in isolated parts of the schist. In other words, LwsA preferentially incorporates mobilized Ti and LREE to its hourglass domains, but these elements are probably not distributed homogeneously at the same time in the surrounding schist over more than tens of centimeters, linked to the thickness of pelitic/carbonate alternations in the original sediment.

The combination of hourglass zoning and of the reservoir effect explains the dramatic variations in La/Yb ratios in LwsA crystals (Fig. 11e). Most of available LREE are incorporated to Ti-enriched domains of LwsA while HREE contents remain globally stable (Figs. 6c, d, 7c).

5.1.4. Interface-coupled dissolution-precipitation

A third feature observed on lawsonite chemical maps in the schistose parts (LwsA and LwsA*) relates to patchy zoning, consisting of enriched or depleted domains for some trace elements, cross-cutting

homogeneous or differently-zoned domains for other elements. This is best seen on the Ti map of LwsA* in Fig. 9c, where thin Ti-depleted domains are found together with hair-like Ti-enriched domains with a vague preferential orientation. Patchy Ti zoning is also observed for LwsA, either in the hourglass domain (Fig. 6b) or in overgrowths (Fig. 7a). Ce and Cr also show patchy or angular zoning in LwsA (Figs. 6a, b) and LwsA* (Fig. 9c). This contrast with hourglass zoning and concentric growth zoning in that the domains appear blurry and not linked to crystal axes. The domains cannot be attributed to contamination as depleted and enriched domains alternate (Fig. 6a, 6b, 7a, 9c). Interpretation for these patchy domains involves faster crystal growth than homogenization rate of Ti (or Cr, Ce) in the fluid feeding the crystal at grain boundaries. This has been recognized as interface-coupled dissolution-precipitation, a mechanism leading to spectacular zoning in many mineral groups (including carbonates, apatite, chloritoid, clinopyroxene and garnet) over all metamorphic grades (Martin, 2009; De Andrade et al., 2014; Ruiz-Agudo et al., 2014; Ague and Axler, 2016; Renard et al., 2019; Figowy et al., 2020). This mechanism is not observed in LwsB (grown from fluids in veins), where element mobility is likely much higher than in schistose parts and where crystals grow with much more open space as the veins may represent incrementally opened structures (Lefeuvre et al., 2020). Interface-coupled dissolution-precipitation may lead to zoning reflecting the distribution of immobile elements before crystallization of neoblasts, as suggested by Martin (2009). Combined to sensitivity on element mobility, interface-coupled dissolution-precipitation will therefore lead to decoupling of poorly mobile elements from one another (variably affected) and from more mobile elements (unaffected). Here, this translates as adding noise to correlations with Ti (Fig. 11b, c).

5.1.5. Lawsonite overgrowths and system opening

In the schist, LwsA shows overgrowths with distinct chemical fingerprints, as well as LwsB and LwsB* in HP veins and multiquartz aggregates (Fig. 7b, 8b, 9a). Overgrowths are Ti-depleted (Fig. 7a, 8a, 9a) but enriched in Sr, Y and HREE (Fig. 7a, c, 8c) whether found in veins or in the schist. LREE contents in lawsonite overgrowths are variable but do not show clear systematic differences compared to cores (Figs. 7c, 8c, 9b).

Sr-rich overgrowths show that Sr is released in the fluid during lawsonite crystallization. Contrary to out-of-equilibrium element incorporation described above for LwsA cores, this likely reflects an increased lengthscale for element transfer. Given that Sr is positively correlated to CaO in the bulk rocks and more concentrated in type 4 (carbonate-rich) calcschists (Fig. 4b), and considering that carbonates are the primary reservoir of Sr in these rock units, Sr-rich overgrowths may be interpreted

as evidence of opening of the system to carbonates via fluids. Quantifying this requires modeling the origin and source of Sr in the rocks, for which bulk rock and lawsonite Sr isotopic signatures can yield constraints.

Sr isotopic ratios for all samples (Fig. 10) are more radiogenic than expected from Cretaceous limestones (in the range 0.7073 – 0.7077, McArthur et al., 2001). In bulk samples, the high Sr isotopic ratios are thought to reflect incorporation of terrestrial sediments. This is motivated by the high Sr isotopic ratios of the ~300 to ~500 My crystalline basement from Massif Central, Briançonnais micro continent and Adria, being eroded at the time of deposition of the Schistes Lustrés: commonly in the range 0.703-0.715, ratios as high as 0.731 are reported (e.g. Talbert and Duthou, 1983; Duthou et al., 1984; Downes et al., 1990, 1991; von Raumer et al., 1999). Non-metamorphic Upper Cretaceous sediments of the “nappe des Gets” and Helminthoid flysch, taken as approximate equivalents of the Schistes Lustrés before subduction, contain variable and locally high amounts of terrestrial sediments, mostly in the form of clays but including plagioclase feldspar (Caron and Weidmann, 1967; Caron, 1972; Caron et al., 1981), a favored Sr host. Rock samples with $^{87}Sr/^{86}Sr$ ratios around 0.709 show decreasing isotopic ratios with Sr concentration (Fig. 10b) possibly reflecting the rock pelitic/carbonate proportions. However, for the more radiogenic samples (Fig. 10b) and the lawsonite separates, the absence of correlation between Sr content and isotopic ratio is explained by the wide range of $^{87}Sr/^{86}Sr$ ratios in the pelitic fraction of the sediments: a unique mixing curve is not obtained because of the variability of the pelitic endmember. Incorporation of variable fractions of Hercynian basement-derived,

Figure 11 *(next page): Strontium isotopic ratio of the different lawsonite types.*

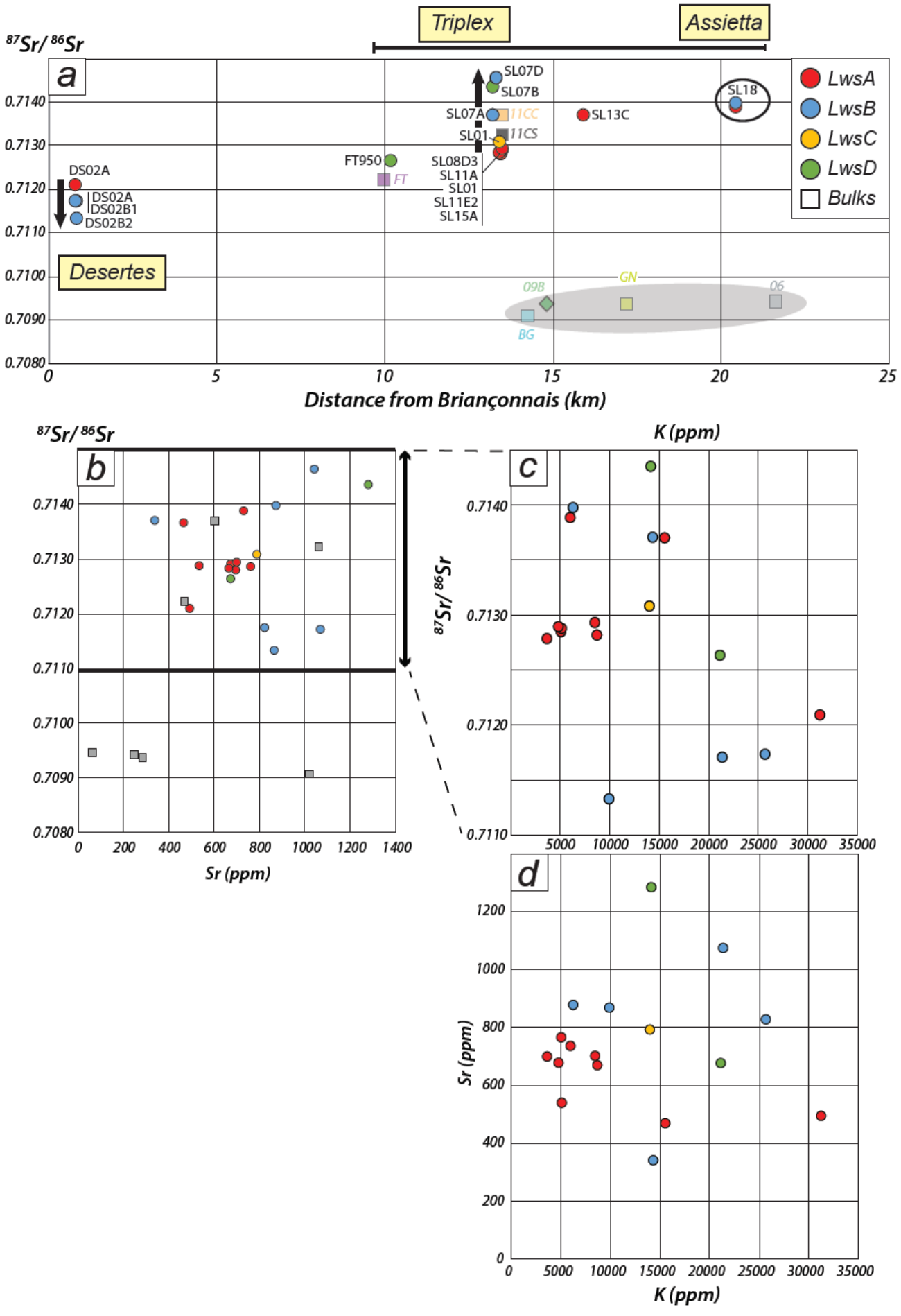
a
$^{87}Sr/^{86}Sr$
Triplex
Assietta
Desertes
LwsA
LwsB
LwsC
LwsD
Bulks
SL07D
SL07B
SL07A
11CC
SL13C
SL01
11CS
SL18
FT950
FT
SL08D3
SL11A
SL01
SL11E2
SL15A
DS02A
DS02A
DS02B1
DS02B2
09B
GN
06
BG
0.7140
0.7130
0.7120
0.7110
0.7100
0.7090
0.7080
0
5
10
15
20
25
Distance from Briançonnais (km)
b
$^{87}Sr/^{86}Sr$
0.7140
0.7130
0.7120
0.7110
0.7100
0.7090
0.7080
0
200
400
600
800
1000
1200
1400
Sr (ppm)
c
K (ppm)
$^{87}Sr/^{86}Sr$
0.7140
0.7130
0.7120
0.7110
5000
10000
15000
20000
25000
30000
35000
d
1200
1000
800
600
400
200
0
Sr (ppm)
0
5000
10000
15000
20000
25000
30000
35000
K (ppm)

variably radiogenic Sr into the rock and/or the lawsonite overgrowths leads to a blurry relationship between content and isotopic signature.

This small-scale variability of $^{87}Sr/^{86}Sr$ ratios and the lack of data on isotopic signatures for lawsonite cores vs rims precludes defining precisely the source of Sr feeding overgrowths. Therefore, Sr-rich overgrowths are proof of increased Sr mobility and consistent with limited system opening, but do not reflect increasing devolatilization of the limestones.

5.2. Evolution of fluid circulation and element mobility length-scale in the Schistes Lustrés metasediments

Trace element distribution and zoning patterns in the different lawsonite types give insight into the evolution of element mobility and fluid circulation length-scales in the calcschists during burial (schematized in Fig. 12a, b).

LwsA (and LwsA*) in isolated schist appears first (Figs. 12a, d; Lefeuvre et al., 2020). Hourglass zoning indicates out-of-equilibrium incorporation for some trace elements, including Ti and LREE. Fine zoning in LREE and Ti shows small-scale migration of poorly mobile elements via interface-coupled dissolution-precipitation. LREE core-to-rim depletion suggests progressive depletion in the surrounding fluid. Altogether, this explains the huge variability of trace element concentrations and the decreasing La/Yb ratios over time, correlating positively with Ti but negatively with Sr (Figs. 5a, c, e, 11c, e). This is consistent with closed-system behavior and element transfer restricted to µm to mm scale. As LwsA starts crystallizing early in the Schistes Lustrés burial (predicted around 0.4 GPa and 180°C by the modeling of Lefeuvre et al., 2020), element mobility was likely restricted by both the small amount of fluid available at grain boundaries and low diffusivity at such low temperature. Sr-rich overgrowths in LwsA (Fig. 10 a-b) probably record limited system opening, with length-scales of element transfer apparently reaching the dm-scale (Fig. 12b). Increasing element mobility is likely due to on-going dehydration reactions (mostly from the pelitic fraction, as modeled by Lefeuvre et al., 2020), as well as increasing temperature and deformation near peak conditions (Figs. 12c, d). The similar Sr isotopic ratios of LwsA separates and bulk samples from Triplex (sample SL11 in particular, Fig. 10) also evidence small-scale element redistribution along LwsA crystallization. The apparent eastward increase of Sr isotopic ratios in LwsA across the Strada dell Assietta transect (Fig. 10a) remains unclear. It is possibly linked to reactions from the pelitic fraction with increasing P-T conditions, including destabilization and dehydration of clay minerals (see Vidal and Dubacq, 2009)

and/or increasing dissolution of detrital plagioclase. Denser sampling and analyses on other phases (calcite and ankerite from the Schistes Lustrés; plagioclases and clays from the Gets units, which represent a non-metamorphic analog) are required to clarify this, as the evolution of the average Sr isotopic ratio of the detrital sediments during deposition is unknown.

Although interpretations for LwsC and LwsD cannot be generalized due to a lack of data for these scarce lawsonite types, it is noteworthy that LwsC veins in multiquartz aggregate present mineral assemblage and trace element patterns similar to the neighboring LwsA* in the schist (Fig. 5g), and LwsD in the schist is very similar to LwsA and LwsA* (Fig. 5j). Therefore, it is hypothesized that LwsC and LwsD formed from the same local fluid, transferring elements at small scale only (possibly below meter).

The elemental homogeneity of LwsB and LwsB* cores (Figs. 8, 9a) suggests that the vein network collecting internally-derived fluids allowed efficient homogenization and element redistribution. As for LwsA, Sr-rich overgrowths (LwsB2, Fig. 8b) likely reflect an increasing distance of element transfer during LwsB crystallization, in agreement with the incremental growth patterns of LwsB fibers (Lefeuvre et al., 2020). LwsB $^{87}Sr/^{86}Sr$ ratios are higher than those of LwsA at Triplex but lower at Desertes and similar at Assietta, which is also consistent with opening of the LwsB vein network to surrounding pelitic/carbonate layers with variable Sr isotopic ratios. LwsB and LwsB* show similar trace element patterns all along the Strada dell Assietta transect, suggesting that similar small-scale processes acted synchronously along the transect, regardless of the varied pressure-temperature conditions. However, the lack of homogenization of their Sr isotopic signature (Fig. 10) suggests that the scale of fluid homogenization in LwsB vein network did not reach the km scale, but was efficient on the order of hundreds of meters (sub-unit scale; Fig. 12c) in a transiently connected LwsB vein network, continually evolving with ductile deformation. This is in line with previous isotopic studies (^{18}O and ^{13}C: Henry et al., 1996; Cook-Kollars et al., 2014; Epstein et al., 2020) that evidenced the closed-system behavior of the Schistes Lustrés sub-units. However, a local and limited influx of fluid containing radiogenic Sr cannot be ruled out at Triplex, where lawsonite separates show both the highest and most variable $^{87}Sr/^{86}Sr$ ratios, and where multiquartz aggregates are numerous. Local fluid infiltration from the underlying Briançonnais margin unit into the LPU has been evidenced by salt-rich fluid inclusions on a southern cross-section (Herviou et al., 2021). Fluid inclusion analysis on the Assietta Pass transect would be necessary to test this hypothesis.

5.3. Upscaling micrometric observations

The geochemical complexity of lawsonite is a tantalizing record of fluid-rock interactions, and upscaling micrometric observations of out-of-equilibrium processes to the scale of the Schistes Lustrés units is challenging.

In line with other studies (Henry et al., 1996; Cook-Kollars et al., 2014; Jaeckel et al., 2018; Epstein et al., 2020, 2021; Herviou et al., 2021), this study shows that element migration and mass transfer in the upper unit of the Schistes Lustrés are limited, even though fluid circulation may be transiently extensive in the vein network. During prograde and peak metamorphism, fluids are internally produced via dehydration reactions in pelitic horizons and devolatilization of carbonates (see also Herviou et al., 2021) but mobilized elements are rapidly trapped in lawsonite and newly-formed carbonates. Growth of LwsA in the schist leads to rapid, effective immobilization of poorly mobile elements like Ti, in addition to consuming water.

Crystallization of lawsonite follows a continuum (see Lefeuvre et al., 2020) starting early in the subduction history and lasting until peak metamorphic conditions (Fig. 12d). Along this continuum, opening of the system appears progressive, with increasing fluid-rock interaction scales (from mm-scale to m-scale, Fig. 12a-c.). This is evidenced i) by incremental growth of LwsA, ii) by appearance of other lawsonite types in veins, iii) by reaction fronts along the carbonate/pelite interfaces, with rock mixing and reaction rates enhanced by deformation (Lefeuvre et al., 2020), and iv) by isotopic disequilibrium of Sr between lawsonite veins and the surrounding schist. Despite evidence for increasing fluid circulation and system opening over time, no evidence for large-scale mass transfer, even close to tectonic contacts, is found. The limited fluid flux in the Schistes Lustrés units compared to studies of lawsonitite at tectonic or lithological contacts explains the important differences in opening state of the system and geochemical behavior of elements during lawsonite crystallization (e.g., Piccoli et al., 2018; Vitale-Brovarone et al., 2020).

Figure 12 *(next page): General sketch illustrating the different steps leading to formation of the distinct lawsonite types describe in this work and during subduction of the Liguro-Piemont ocean.*

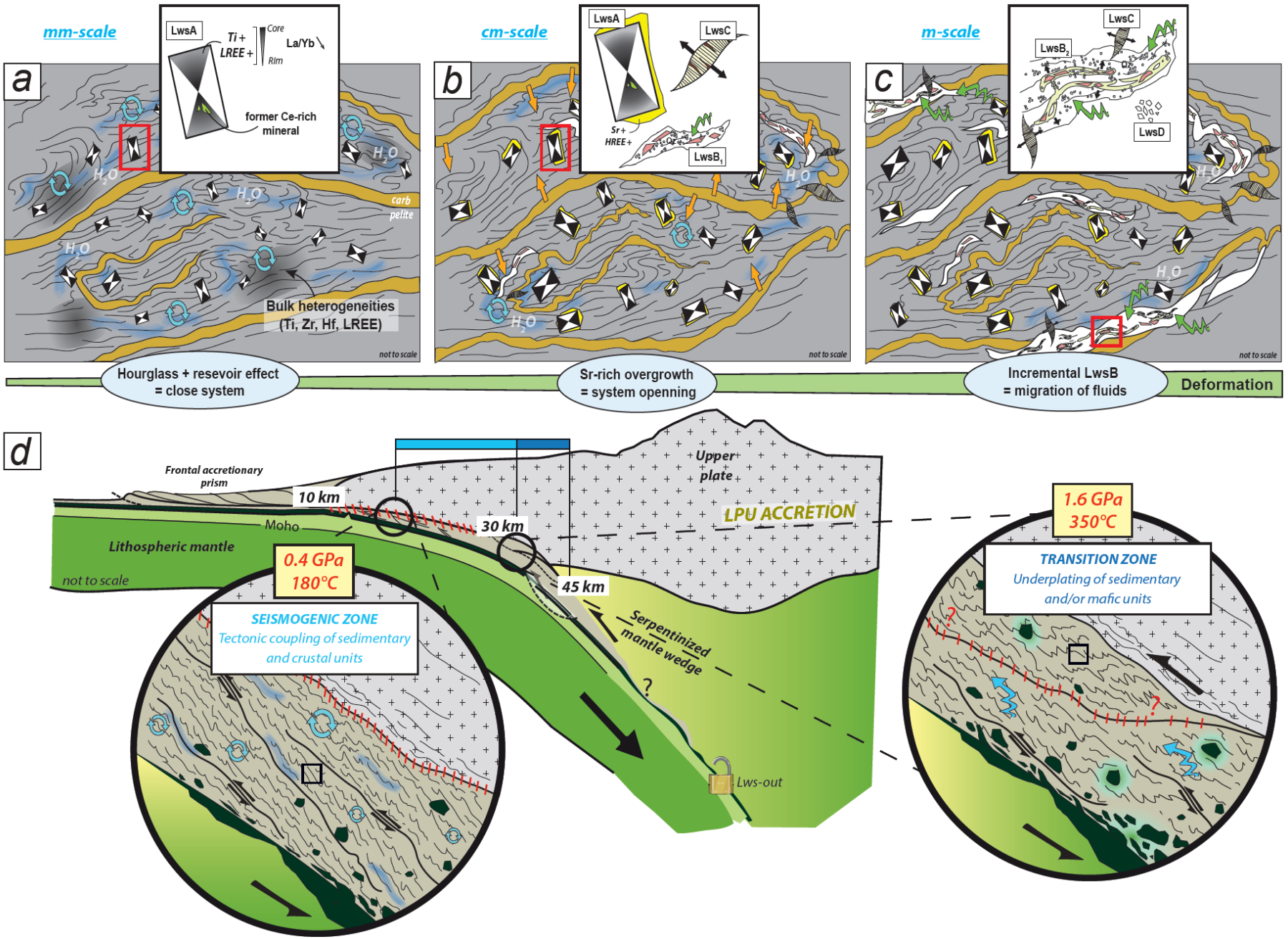
mm-scale
cm-scale
m-scale
a
b
c
LwsA
Ti +
LREE +
Core
La/Yb
Rim
former Ce-rich mineral
H_2O
carb
pelite
Bulk heterogeneities
(Ti, Zr, Hf, LREE)
not to scale
LwsA
LwsC
Sr +
HREE +
Ce/Ce*
$LwsB_1$
LwsC
$LwsB_2$
LwsD
Hourglass + resevoir effect
= close system
Sr-rich overgrowth
= system openning
Incremental LwsB
= migration of fluids
Deformation
d
Frontal accretionary prism
10 km
Moho
Lithospheric mantle
not to scale
0.4 GPa
180°C
SEISMOGENIC ZONE
Tectonic coupling of sedimentary and crustal units
30 km
45 km
Upper plate
LPU ACCRETION
Serpentinized mantle wedge
Lws-out
1.6 GPa
350°C
TRANSITION ZONE
Underplating of sedimentary and/or mafic units

6. Conclusions

The upper unit of the Schistes Lustrés deep accretionary complex shows an intricate record of extensive fluid/rock interactions in sediments metamorphosed in blueschist facies conditions. Lawsonite is ubiquitous there, in veins and in the surrounding schists, and crystallized from early prograde history up to peak conditions. This study based on major, trace elements and Sr isotopic ratios provides a detailed framework for petrological interpretation of the apparently deterring complexity of the geochemical record of lawsonite. White mica contamination is found very hard to avoid and hinders interpretations based on content of univalent cations. For other minor and trace elements, this study shows that several processes affected the composition of lawsonite, decoupling elements from one another, mostly based on their mobility. These processes take place at equilibrium and out-of-equilibrium and result in zoning, apparently unrelated to the changing pressure-temperature conditions. At crystal scale, two main types of zonations are observed: hourglass zoning in the schists and growth zoning both in the schist and in the veins. Hourglass zoning affects preferentially Ti and LREE. Concentric growth zoning is best observed for Ti, REE, Hf and Zr, and probably involves many other elements less dramatically. Combination of these mechanisms results in large variability of trace element contents, especially REE that vary over four orders of magnitude. Over time, the La/Yb ratio decreases strongly (from ~100 to ~1) as La appears much more sensitive than Yb to surface effects leading to hourglass zoning.

Interface-coupled dissolution-precipitation is a third mechanism decoupling elements in the schists, and involves poorly mobile elements. It is again best observed for Ti, but affects REE and Cr too, with the result that correlations between elements are noisy.

Lastly, overgrowths best observed in Sr content show system opening, limited in the schists and clearer in the veins. Sr isotopic ratios rule out limestone devolatilization as the main driver of this event. The overall mineral compositional evolution records progressive and incremental system opening, first limited to tens of centimeters, then to the subunit scale, of the order of hundreds of meters at most. Large-scale mass transfer and fluid influx from external sources are not supported even though the vein network extends over time until peak conditions. This vein network appears fed by internal fluids and enhanced by deformation. In the schists, transfer via fluid advection was limited to mobile elements like Sr during the last growth increments.

Comparison between the composition of lawsonite in veins and in the schist has been found critical for interpretation of varying fluid composition over space and time.

Acknowledgments

This work was financially supported by the SYSTER program of CNRS-INSU, by ISTeP and by the ZIP project (REA grant agreement no. 604713 (ZIP “Zooming In between Plates”) from the People Program (Marie Curie Actions) of the European Union’s Seventh Framework Program FP7/2007-2013). We thank O. Boudouma and D. Deldique for their expertise with SEM characterisation; M. Fialin and N. Rividi for help with EPMA; B. Caron, B. Villemant and J. Noel for ICP-OES and LA-ICP-MS measurements; E. Delairis for making the thin and thick sections. We also thank H. Raimbourg, L. Jolivet, L. Martin, A. Vitale-Brovarone, M. Ballèvre and M. Feineman for insightful discussions during the PhD defense of the first author.

References

Agard, P. (2021). Subduction of oceanic lithosphere in the Alps: Selective and archetypal from (slow-spreading) oceans. Earth-Science Reviews, 103517.

Agard, P., Goffé, B., Touret, J.L.R., Vidal, O., 2000. Retrograde mineral and fluid evolution in high-pressure metapelites (Schistes lustrés unit, Western Alps). Contributions to Mineralogy and Petrology 140, 296–315. https://doi.org/10.1007/s004100000190

Agard, P., Jolivet, L., Goffé, B. (2001). Tectonometamorphic evolution of the Schistes Lustrés complex : implications for the exhumation of HP and UHP rocks in the western Alps. Bulletin de la Société Géologique de France 172, 617–636.

Agard, P., Monié, P., Jolivet, L., Goffé, B. (2002). Exhumation of the Schistes Lustrés complex: in situ laser probe 40Ar/39Ar constraints and implications for the Western Alps. Journal of metamorphic Geology 20, 599–618.

Agard, P., Yamato, P., Jolivet, L., Burov, E., 2009. Exhumation of oceanic blueschists and eclogites in subduction zones: Timing and mechanisms. Earth-Science Reviews 92, 53–79. https://doi.org/10.1016/j.earscirev.2008.11.002

Agard, P., Plunder, A., Angiboust, S., Bonnet, G., Ruh, J., 2018. The subduction plate interface: rock record and mechanical coupling (from long to short timescales). Lithos 320–321, 537–566. https://doi.org/10.1016/j.lithos.2018.09.029

Ague, J.J., Axler, J.A. (2016). Interface coupled dissolution-reprecipitation in garnet from subducted granulites and ultrahigh-pressure rocks revealed by phosphorous, sodium, and titanium zonation. American Mineralogist 101, 1696–1699. https://doi.org/10.2138/am-2016-5707

Angiboust, S., Langdon, R., Agard, P., Waters, D., Chopin, C., 2012. Eclogitization of the Monviso ophiolite (W. Alps) and implications on subduction dynamics. Journal of Metamorphic Geology 30, 37–61. https://doi.org/10.1111/j.1525-1314.2011.00951.x

Ballèvre, M., Camonin, A., Manzotti, P., & Poujol, M. (2020). A step towards unraveling the paleogeographic attribution of pre-Mesozoic basement complexes in the Western Alps based on U–Pb geochronology of Permian magmatism. Swiss Journal of Geosciences, 113(1), 1-28.

Baxter, E. F., & DePaolo, D. J. (2000). Field measurement of slow metamorphic reaction rates at temperatures of 500 to 600 C. Science, 288(5470), 1411-1414.

Baxter, E. F., & DePaolo, D. J. (2002). Field measurement of high temperature bulk reaction rates II: Interpretation of results from a field site near Simplon Pass, Switzerland. American Journal of Science, 302(6), 465-516.

Bebout, G.E., Agard, P., Kobayashi, K., Moriguti, T., Nakamura, E. (2013). Devolatilization history and trace element mobility in deeply subducted sedimentary rocks: Evidence from Western Alps HP/UHP suites. Chemical Geology 342, 1–20. https://doi.org/10.1016/j.chemgeo.2013.01.009

Beyssac, O., Goffé, B., Chopin, C., Rouzaud, J.N. (2002). Raman spectra of carbonaceous material in metasediments: a new geothermometer. Journal of metamorphic Geology 20, 859–871.

Caron, J.M. (1974). Rapports entre diverses “générations” de lawsonite et les déformations dans les Schistes lustrés des Alpes cottiennes septentrionales (France et Italie). Bulletin de la Société Géologique de France 255–263.

Caron, C., & Weidmann, M. (1967). Sur les flysch de la région des Gets (Haute-Savoie). Birkhäuser.

Caron, C. (1972). La Nappe Supérieure des Préalpes: subdivisions et principaux caractères du sommet de l'édifice préalpin.

Caron, C., Hesse, R., Kerckhove, C., Homewood, P., Van Stuijvenberg, J., Tasse, N., & Winkler, W. (1981). Comparaison préliminaire des flyschs à Helminthoïdes sur trois transversales des Alpes. Eclogae Geologicae Helvetiae, 74, 369-378.

Cook-Kollars, J., Bebout, G.E., Collins, N.C., Angiboust, S., Agard, P. (2014). Subduction zone metamorphic pathway for deep carbon cycling: I. Evidence from HP/UHP metasedimentary rocks, Italian Alps. Chemical Geology 386, 31–48. https://doi.org/10.1016/j.chemgeo.2014.07.013

Coward, M., Dietrich, D. (1989). an overview– Alpine tectonics. Geological Society, London, Special Publications 45.

De Andrade, V., Ganne, J., Dubacq, B., Ryan, C.G., Bourdelle, F., Plunder, A., Falkenberg, G., Thieme, J. (2014). Retrieving past geodynamic events by unlocking rock archives with µ-XRF and µ-spectroscopy. J. Phys.: Conf. Ser. 499, 012012. https://doi.org/10.1088/1742-6596/499/1/012012

Deville, E, 1986. La klippe de la Pointe du Grand Vallon (Vanoise-Alpes occidentales) : un lambeau de métasédiments à foraminifères du Maastrichtien supérieur couronnant les nappes de « schistes lustrés ». Comptes rendus de l’Académie des sciences. Série 2, Mécanique, Physique, Chimie, Sciences de l’univers, Sciences de la Terre 303, 1221–1226.

Deville, E., Fudral, S., Lagabrielle, Y., Marthaler, M., Sartori, M. (1992). From oceanic closure to continental collision: A synthesis of the" Schistes lustrés" metamorphic complex of the Western Alps. Geological Society of America Bulletin 104, 127–139.

De Wever, P., & Caby, R. (1981). Datation de la base des schistes lustrés postophiolitiques par des radiolaires (Oxfordien-Kimmeridgien moyen) dans les Alpes Cottiennes (Saint Véran, France). Compte rendu de l'académie des Sciences de Paris, 292, 467-472.

Dorsam, G., Liebscher, A., Wunder, B., Franz, G., & Gottschalk, M. (2007). Crystal chemistry of synthetic Ca2Al3Si3O12OH–Sr2Al3Si3O12OH solid-solution series of zoisite and clinozoisite. American Mineralogist, 92(7), 1133-1147.

Downes, H., Dupuy, C., & Leyreloup, A. F. (1990). Crustal evolution of the Hercynian belt of Western Europe: Evidence from lower-crustal granulitic xenoliths (French Massif Central). Chemical Geology, 83(3-4), 209-231.

Downes, H., Bodinier, J. L., Thirlwall, M. F., Lorand, J. P., & Fabries, J. (1991). REE and Sr-Nd isotopic geochemistry of eastern Pyrenean peridotite massifs: sub-continental lithospheric mantle modified by continental magmatism. Journal of Petrology, (2), 97-115.

Dowty, E. (1976). Crystal structure and crystal growth: II. Sector zoning in minerals. American Mineralogist 61, 460–469.

Dubacq, B., Soret, M., Jewison, E., Agard, P. (2019). Early subduction dynamics recorded by the metamorphic sole of the Mt. Albert ophiolitic complex (Gaspé, Quebec). Lithos 334–335, 161–179. https://doi.org/10.1016/j.lithos.2019.03.019

Duthou, J. L. (1984). Aˆ ge dévonien supérieur (Rb/Sr) des gneiss acordiérite de la carriere du Puy-du-Roi aAubusson (Creuse). Consé quences. 10e Ré un. ann. sci. Terre, Bordeaux.

Enami, M. (1999). CaAl-silicates: an important Sr container in subducted slab. Journal of Geography (Chigaku Zasshi), 108(2), 177-187.

Epstein, G.S., Bebout, G.E., Angiboust, S., Agard, P. (2020). Scales of Fluid-Rock Interaction and Carbon Mobility in the Deeply Underplated and HP-Metamorphosed Schistes Lustrés, Western Alps. Lithos 105229. https://doi.org/10.1016/j.lithos.2019.105229

Feineman, M. D., Ryerson, F. J., DePaolo, D. J., & Plank, T. (2007). Zoisite-aqueous fluid trace element partitioning with implications for subduction zone fluid composition. Chemical Geology, 239(3-4), 250-265.

Figowy, S., Dubacq, B., Noël, Y. (2020). Partitioning of chromium between garnet and clinopyroxene: first-principle modelling versus metamorphic assemblages. Eur. J. Mineral. 17.

Fornash, K.F., Whitney, D.L., Seaton, N.C.A. (2019). Lawsonite composition and zoning as an archive of metamorphic processes in subduction zones. Geosphere. https://doi.org/10.1130/GES01455.1

Fudral, S. (1996). Etude géologique de la suture tethysienne dans les Alpes franco-italiennes Nord-Occidentales de la Doire Ripaire (Italie) à la région de Bourg Saint-Maurice. (France) (Doctoral dissertation, Université de Savoie).

Hacker, B.R., Abers, G.A. (2004). Subduction Factory 3: An Excel worksheet and macro for calculating the densities, seismic wave speeds, and H2O contents of minerals and rocks at pressure and temperature. Geochemistry, Geophysics, Geosystems 5, n/a-n/a. https://doi.org/10.1029/2003GC000614

Hacker, B.R., Peacock, S.M., Abers, G.A., Holloway, S.D. (2003). Subduction factory 2. Are intermediate-depth earthquakes in subducting slabs linked to metamorphic dehydration reactions? Journal of Geophysical Research: Solid Earth 108. https://doi.org/10.1029/2001JB001129

Handy, M.R., M. Schmid, S., Bousquet, R., Kissling, E., Bernoulli, D. (2010). Reconciling plate-tectonic reconstructions of Alpine Tethys with the geological–geophysical record of spreading and subduction in the Alps. Earth-Science Reviews 102, 121–158. https://doi.org/10.1016/j.earscirev.2010.06.002

Hara, T., Tsujimori, T., Chang, Q., & Kimura, J. I. (2018). In-situ Sr-Pb isotope geochemistry of lawsonite: A new method to investigate slab-fluids. Lithos, 320, 93-104.

Hara, T., Tsujimori, T., Flores, K. E., & KIMURA, J. I. (2019). Sr–Pb isotope compositions of lawsonites in a Pacheco Pass metagraywacke, Franciscan Complex, California. Journal of Mineralogical and Petrological Sciences, 114(6), 296-301.

Henry, C., Burkhard, M., Goffé, B. (1996). Evolution of synmetamorphic veins and their wallrocks through a Western Alps transect: no evidence for large-scale fluid flow. Stable isotope, major- and trace-element systematics. Chemical Geology 127, 81–109. https://doi.org/10.1016/0009-2541(95)00106-9

Herviou, C., Verlaguet, A., Agard, P., Locatelli, M., Raimbourg, H., Lefeuvre, B., & Dubacq, B. (2021). Along-dip variations of subduction fluids: The 30–80 km depth traverse of the Schistes Lustrés complex (Queyras-Monviso, W. Alps). Lithos, 394, 106168.

Herviou, C., Agard, P., Plunder, A., Mendes, K., Verlaguet, A., Deldicque, D., Cubas, N. (2022). Subducted fragments of the Liguro-Piemont ocean, Western Alps: spatial correlations and offscraping mechanisms during subduction. Tectonophysics.

Hollister, L.S. (1970). Origin; mechanism, and consequences of compositional sector-zoning in staurolite. The American mineralogist 55, 742–766.

Hollister, L.S., Gancarz, A.J. (1971). Compositional sector-zoning in clinopyroxene from the Narce area, Italy. The American mineralogist 56, 959–979.

Jaeckel, K., Bebout, G.E., Angiboust, S. (2018). Deformation-enhanced fluid and mass transfer along Western and Central Alps paleo-subduction interfaces: Significance for carbon cycling models. Geosphere 14, 2355–2375. https://doi.org/10.1130/GES01587.1

Kohn, M.J. (2005). Geochemical zoning in metamorphic minerals. In: Holland, H.D., Turekian, K.K. (Eds.), Treatise on Geochemistry. Pergamon, Oxford, pp. 229–261.

Lagabrielle, Y., 1987. Les ophiolites : Marqueurs de l'histoire tectonique des domaines océaniques. PhD thesis Brest.

Lagabrielle, Y., Cannat, M. (1990). Alpine Jurassic ophiolites resemble the modern central Atlantic basement. Geology 18, 319–322.

Lagabrielle, Y., Lemoine, M. (1997). Alpine, Corsican and Apennine ophiolites: the slow-spreading ridge model. Comptes Rendus de l'Académie des Sciences-Series IIA-Earth and Planetary Science 325, 909–920.

Lagabrielle, Y., Polino, R. (1985). Origine volcano-détritique de certaines prasinites des Schistes lustrés du Queyras (France) : arguments texturaux et géochimiques. Bulletin de la Société Géologique de France 461–471.

Lagabrielle, Y., Vitale Brovarone, A., Ildefonse, B., 2015. Fossil oceanic core complexes recognized in the blueschist metaophiolites of Western Alps and Corsica. Earth-Science Reviews 141, 1–26. https://doi.org/10.1016/j.earscirev.2014.11.004

Lapen, T.J., Johnson, C.M., Baumgartner, L.P., Mahlen, N.J., Beard, B.L., Amato, J.M. (2003). Burial rates during prograde metamorphism of an ultra-high-pressure terrane: an example from Lago di Cignana, western Alps, Italy. Earth and Planetary Science Letters 215, 57–72. https://doi.org/10.1016/S0012-821X(03)00455-2

Le Pichon, X., Bergerat, F., Roulet, M.-J. (1988). Plate kinematics and tectonics leading to the Alpine belt formation; a new analysis. Geological Society of America Special Papers 218, 111–132.

Lefeuvre B. (2020). La lawsonite dans les métasédiments en base de zone sismogénique : géochimie, échelles de migration des fluides et rôle de la déformation dans les Schistes Lustrés

Lefeuvre, B., Agard, P., Verlaguet, A., Dubacq, B., Plunder, A. (2020). Massive formation of lawsonite in subducted sediments from the Schistes Lustrés (W. Alps): Implications for mass transfer and decarbonation in cold subduction zones. Lithos 105629. https://doi.org/10.1016/j.lithos.2020.105629

Lemoine, M., 2003. Schistes lustrés from Corsica to Hungary : back to the original sediments and tentative dating of partly azoic metasediments. Bulletin de la Société Géologique de France 174, 197–209. https://doi.org/10.2113/174.3.197

Lemoine, M., Marthaler, M., Caron, M., Sartori, M., Amaudric du Chaffaut, S., 1984. Découverte de foraminifères planctoniques du Crétacé supérieur dans les schistes lustrés du Queyras (Alpes occidentales). Conséquences paléogéographiques et tectoniques. Comptes-rendus des séances de l'Académie des sciences. Série 2, Mécanique-physique, chimie, sciences de l'univers, sciences de la terre 299, 727–732.

Lemoine, M., Tricart, P., 1986. Les Schistes lustrés piémontais des Alpes Occidentales : approche stratigraphique, structurales et sédimentologique. Eclogae Geologicae Helvetiae 79, 271–294. https://doi.org/10.5169/SEALS-165835

Manzotti, P., Ballèvre, M., Pitra, P., & Schiavi, F. (2021). Missing lawsonite and aragonite found: P–T and fluid composition in meta-marls from the Combin Zone (Western Alps). Contributions to Mineralogy and Petrology, 176(8), 1-27.

Marthaler, M., Stampfli, G.M., 1989. Les Schistes lustrés à ophiolites de la nappe du Tsaté : un ancien prisme d'accrétion de la marge active apulienne? Schweizerische Mineralogische und Petrographische Mitteilunge 69, 211–216. https://doi.org/10.5169/SEALS-52789

Martin, A.J. (2009). Sub-millimeter Heterogeneity of Yttrium and Chromium during Growth of Semi-pelitic Garnet 15.

Martin, L.A.J., Hermann, J., Gauthiez-Putallaz, L., Whitney, D.L., Vitale Brovarone, A., Fornash, K.F., Evans, N.J. (2014). Lawsonite geochemistry and stability - implication for trace element and water cycles in subduction zones. Journal of Metamorphic Geology 32, 455–478. https://doi.org/10.1111/jmg.12093

Martin, L.A.J., Wood, B.J., Turner, S., Rushmer, T. (2011). Experimental Measurements of Trace Element Partitioning Between Lawsonite, Zoisite and Fluid and their Implication for the Composition of Arc Magmas. Journal of Petrology 52, 1049–1075. https://doi.org/10.1093/petrology/egr018

McArthur, J. M., Howarth, R. J., & Bailey, T. R. (2001). Strontium isotope stratigraphy: LOWESS version 3: best fit to the marine Sr-isotope curve for 0–509 Ma and accompanying look-up table for deriving numerical age. The Journal of Geology, 109(2), 155-170.

McDonough, W.F., Sun, S. (1995). The composition of the Earth. Chemical Geology 223–253.

Miyajima, H., Matsubara, S., Miyawaki, R., Ito, K. (1999). Itoigawaite, a new mineral, the Sr analogue of lawsonite, in jadeitite from the Itoigawa-Ohmi district, central Japan. Mineralogical Magazine 63, 909–916.

Nagasaki, A., & Enami, M. (1998). Sr-bearing zoisite and epidote in ultra-high pressure (UHP) metamorphic rocks from the Su-Lu province, eastern China; an important Sr reservoir under UHP conditions. American Mineralogist, 83(3-4), 240-247.

Nitsch, K.-H. (1972). Das P-T-XCO2 Stabilitätsfeld von Lawsonit. Contributions to Mineralogy and Petrology 34, 116–134.

Okamoto, K., Maruyama, S. (1999). The high-pressure synthesis of lawsonite in the MORB+ H2O system. American Mineralogist 84, 362–373.

Phillips, B. L., McGuinn, M. D., & Redfern, S. A. (1997). Si-Al order and the I1̄-I2/c structural phase transition in synthetic CaAl2Si2O8-SrAl2Si2O8 feldspar: A 29SiMAS-NMR spectroscopic study. American Mineralogist, 82(1-2), 1-7.

Piccoli, F., Vitale Brovarone, A., Beyssac, O., Martinez, I., Ague, J.J., Chaduteau, C. (2016). Carbonation by fluid–rock interactions at high-pressure conditions: Implications for carbon cycling in subduction zones. Earth and Planetary Science Letters 445, 146–159. https://doi.org/10.1016/j.epsl.2016.03.045

Piccoli, F.; Vitale-Brovarone, A. & Ague, J. J. (2018). Field and petrological study of metasomatism and high-pressure carbonation from lawsonite eclogite-facies terrains, Alpine Corsica . Lithos, 2018, 304-307, 16 - 37

Plank, T., Langmuir, C.H. (1998). The chemical composition of subducting sediment and its consequences for the crust and mantle. Chemical Geology 145, 325–394.

Platt, J.P., 1986. Dynamics of orogenic wedges and the uplift of high-pressure metamorphic rocks. Geol Soc America Bull 97, 1037–1053. https://doi.org/10.1130/0016-7606(1986)97<1037:DOOWAT>2.0.CO;2

Plunder, A., Agard, P., Dubacq, B., Chopin, C., Bellanger, M. (2012). How continuous and precise is the record of P-T paths? Insights from combined thermobarometry and thermodynamic modelling into subduction dynamics (Schistes Lustrés, W. Alps). Journal of Metamorphic Geology 30, 323–346. https://doi.org/10.1111/j.1525-1314.2011.00969.x

Polino, R. (1984). Les séries océaniques du Haut val de Suse (Alpes Cottiennes): analyse des couvertures sédimentaires. Ofioliti, 9, 547-554.

Polino, R, Dela Pierre, F, Borghi, A, Carraro, F, Fioraso, G, Giardino, M, 2002. Note illustrative della carta geologica d'Italia alla scala 1:50000: foglio 132-152-153 Bardonecchia. ISPRA, Servizio Geologico d'Italia.

Raimbourg, H., Famin, V., Palazzin, G., Mayoux, M., Jolivet, L., Ramboz, C., Yamaguchi, A., 2018. Fluid properties and dynamics along the seismogenic plate interface. Geosphere 14, 469–491. https://doi.org/10.1130/GES01504.1

Renard, F., Røyne, A., Putnis, C.V. (2019). Timescales of interface-coupled dissolution-precipitation reactions on carbonates. Geoscience Frontiers 10, 17–27. https://doi.org/10.1016/j.gsf.2018.02.013

Rosenbaum, G., Lister, G.S. (2005). The Western Alps from the Jurassic to Oligocene: spatio-temporal constraints and evolutionary reconstructions. Earth-Science Reviews 69, 281–306. https://doi.org/10.1016/j.earscirev.2004.10.001

Ruiz-Agudo, E., Putnis, C.V., Putnis, A. (2014). Coupled dissolution and precipitation at mineral–fluid interfaces. Chemical Geology 383, 132–146. https://doi.org/10.1016/j.chemgeo.2014.06.007

Schmid, S. M., Kissling, E., Diehl, T., van Hinsbergen, D. J., & Molli, G. (2017). Ivrea mantle wedge, arc of the Western Alps, and kinematic evolution of the Alps–Apennines orogenic system. Swiss Journal of Geosciences, 110(2), 581-612.

Schmidt, M.W., Poli, S. (1998). Experimentally based water budgets for dehydrating slabs and consequences for arc magma generation. Earth and Planetary Science Letters 163, 361–379. https://doi.org/10.1016/S0012-821X(98)00142-3

Schmidt, M.W., Poli, S. (1994). The stability of lawsonite and zoisite at high pressures: Experiments in CASH to 92 kbar and implications for the presence of hydrous phases in subducted lithosphere. Earth and Planetary Science Letters 124, 105–118. https://doi.org/10.1016/0012-821X(94)00080-8

Schwartz, S., Guillot, S., Reynard, B., Lafay, R., Debret, B., Nicollet, C., Lanari, P., Auzende, A.L., 2013. Pressure–temperature estimates of the lizardite/antigorite transition in high pressure serpentinites. Lithos 178, 197–210. https://doi.org/10.1016/j.lithos.2012.11.023

Sicard-Lochon, E., & Potdevin, J. L. (1986). Transfert de matière à l'échelle de pseudomorphoses de lawsonite. Réunion annuelle des sciences de la terre, 11.

Skora, S., Baumgartner, L. P., Mahlen, N. J., Johnson, C. M., Pilet, S., & Hellebrand, E. (2006). Diffusion-limited REE uptake by eclogite garnets and its consequences for Lu–Hf and Sm–Nd geochronology. Contributions to Mineralogy and Petrology, 152(6), 703-720.

Stampfli, G. M., Mosar, J., Marquer, D., Marchant, R., Baudin, T., & Borel, G. (1998). Subduction and obduction processes in the Swiss Alps. Tectonophysics, 296(1-2), 159-204.

Talbert, J., & Duthou, J. (1983). Upper carboniferous age (rb-sr) of the meymac granite (french massif central). Ccomptes rendus de l'academie des sciences serie ii, 296(17), 1321-1323.

Tricart, P., Schwartz, S. (2006). A north-south section across the Queyras Schistes lustrés (Piedmont zone, Western Alps): Syn-collision refolding of a subduction wedge. Eclogae Geologicae Helvetiae 99, 429–442. https://doi.org/10.1007/s00015-006-1197-6

Tropper, P., Recheis, A. (2003). Garnet zoning as a window into the metamorphic evolution of a crystalline complex: the northern and central Austroalpine Ötztal-Complex as a polymorphic example. Mitteilungen der Österreichischen Geologischen Gesellschaft 27–53.

Tsujimori, T., Sisson, V., Liou, J., Harlow, G., Sorensen, S. (2006). Very-low-temperature record of the subduction process: A review of worldwide lawsonite eclogites. Lithos 92, 609–624. https://doi.org/10.1016/j.lithos.2006.03.054

Ueno, T. (1999). REE-bearing sector-zoned lawsonite in the Sanbagawa pelitic schists of the eastern Kii Peninsula, central Japan. European Journal of Mineralogy 11, 993–998.

Van Hinsberg, V.J. (2006). Hourglass sector zoning in metamorphic tourmaline and resultant major and trace-element fractionation. American Mineralogist 91, 717–728. https://doi.org/10.2138/am.2006.1920

Van Keken, P.E., Hacker, B.R., Syracuse, E.M., Abers, G.A. (2011). Subduction factory: 4. Depth-dependent flux of H2O from subducting slabs worldwide. Journal of Geophysical Research 116. https://doi.org/10.1029/2010JB007922

Vidal O., Dubacq B. (2009) Thermodynamic modelling of clay dehydration, stability and compositional evolution with temperature, pressure and H2O activity. Geochimica et Cosmochimica Acta 73, 6544 – 6564, doi: 10.1016/j.gca.2009.07.035

Vitale Brovarone, A., Alard, O., Beyssac, O., Martin, L., Picatto, M. (2014). Lawsonite metasomatism and trace element recycling in subduction zones. Journal of Metamorphic Geology 32, 489–514. https://doi.org/10.1111/jmg.12074

Vitale Brovarone, A., Beyssac, O. (2014). Lawsonite metasomatism: A new route for water to the deep Earth. Earth and Planetary Science Letters 393, 275–284. https://doi.org/10.1016/j.epsl.2014.03.001

Vitale Brovarone, A.; Tumiati, S.; Piccoli, F.; Ague, J. J.; Connolly, J. A. & Beyssac, O. (2020). Fluid-mediated selective dissolution of subducting carbonaceous material: Implications for carbon recycling and fluid fluxes at forearc depths. Chemical Geology, 2020, 549, 119682

Von Raumer, J., Abrecht, J., Bussy, F., Lombardo, B., Menot, R. P., & Schaltegger, U. (1999). The Paleozoic metamorphic evolution of the Alpine external massifs. Schweizerische Mineralogische und Petrographische Mitteilungen, 79, 5-22.

Whitney, D.L., Fornash, K.F., Kang, P., Ghent, E.D., Martin, L., Okay, A.I., Vitale Brovarone, A. (2020). Lawsonite composition and zoning as tracers of subduction processes: A global review. Lithos 370–371, 105636. https://doi.org/10.1016/j.lithos.2020.105636

Annexe – 3

Supplementary material II.1: Comparison between microthermometry derived salinity and Raman salinity in the same inclusions and eutectic temperatures in Monviso omphacite vein.

Sample	IF N°	Raman salinity	Tm_{ice}	Microthermometric salinity
1LwsC	IF1	14.7	-10.4	14.4
1LwsC	IF5	13.2	-8.9	12.7
1LwsC	IF8	4.8	-3.2	5.3
1LwsC	IF15	5.4	-3	5.0
1LwsC	IF17	6.6	-4.5	7.2
4LwsB	IF3	11.8	-8.4	12.2
4LwsB	IF8	8.1	-5.6	8.7
4LwsB	IF9	5.8	-3.7	6.0
4LwsB	IF12	6.4	-4.1	6.6
4LwsB	IF16	7.6	-5.2	8.1
4LwsB	IF18	6.2	-4	6.4
4LwsB	IF3	5.8	-3.6	5.9
4LwsB	IF1	8.1	-5.2	8.1
4LwsB	IF4	7.1	-4.5	7.2
9LwsB	IF6	0.0	-0.2	0.4
9LwsB	IF7	0.0	0	0.0
9LwsB	IF8	0.0	-0.3	0.5
9LwsB	IF9	0.0	-0.1	0.2
9LwsB	IF10	1.4	-0.7	1.2
9LwsB	IF12	2.1	-1.3	2.2
9LwsB	IF13	2.7	-1.5	2.6
9LwsB	IF16	0.0	-0.1	0.2
9LwsB	IF18	1.1	-0.9	1.6
9LwsB	IF19	0.9	-0.8	1.4

Sample	IF N°	Eutectic T°C
OmpV1b	IF1	-23.2
OmpV1b	IF2	-23.2
OmpV1b	IF3	-22.9
OmpV1b	IF4	-23.3
OmpV1b	IF5	-24.3
OmpV1b	IF6	-23.6
OmpV1b	IF7	-23.2
OmpV1b	IF8	-22.5
OmpV1b	IF10	-22.8
OmpV1b	IF15	-23.0
OmpV1b	IF16	-22.0

Supplementary material II.2: Comparison between the raman spectrum of the potential hydrocarbons and raman spectra of glue and oil used for sample preparation.

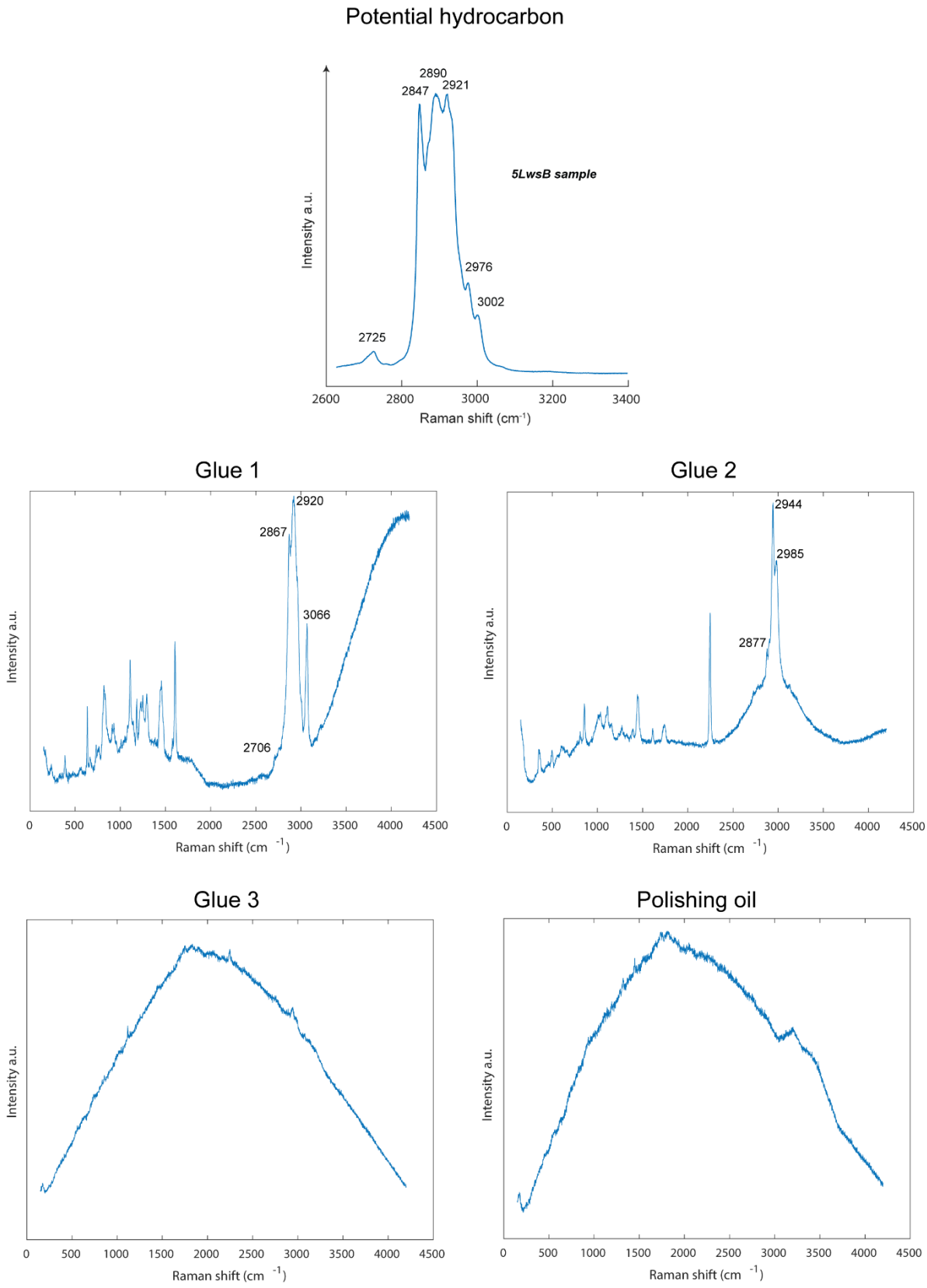

Annexe – 4

Supplementary material III.1: Location, mineral assemblages and RSCM temperatures of our samples and compilation of RSCM temperatures form literature

Sample name	Slice	Unit	Latitude	Longitude	Mineralogy ± Ru-Hem-Ttn	n. spectra	Av. T(°C)	sd	SE
ALB1901	Albergian	LPM	45.00701667	6.991566667	WM-Chl-Qz-Ank	15	450	9	2
ALB1907a	Albergian	LPM	44.95943333	6.986266667	Pseudo Lws-Ep-Tur-WM-Chl-Qz	16	477	18	4
ALB1910	Albergian	LPM	44.96625	6.97875	Tur-WM-Chl-Qz	16	468	17	4
ALB1913D	Albergian	LPM	44.98151667	6.965533333	WM-Chl-Qz	16	454	16	4
ALB1916H	Albergian	LPM	44.99266667	6.975566667	Pseudo Lws-WM-Chl-Qz	16	440	13	3
ALB1918	Orsiera-Rocciavrè	LPL	44.94445	7.053816667	Tur-WM-Chl-Qz-Ab-Cc-Ank	15	499	31	8
ALB1920	Albergian	LPM	44.96246667	7.046266667	Tur-WM-Chl-Qz-Ab-Cc	16	451	14	3
ALB1922	Albergian	LPM	44.9691	7.02015	Ep-Tur-WM-Chl-Qz-Ank	15	491	21	5
ALB2001	Orsiera-Rocciavrè	LPL	45.04072222	7.021388889	WM-Chl-Qz-Cc-Ank	16	483	14	3
ALB2003	Albergian	LPM	44.91922222	7.051361111	Tur-WM-Chl-Qz-Ab-Cc-Ank	16	489	21	5
ALB2004	Albergian	LPM	44.91558333	7.025694444	Pseudo Lws-WM-Chl-Qz-Cc	15	482	18	5
ALB2005	Orsiera-Rocciavrè	LPL	44.90797222	7.059166667	Grt-Cld-WM-Chl-Qz	14	534	50	13
ALB2006	Mirabouc-Bouchet	LPM	44.86086111	7.03475	Pseudo Lws-Tur-WM-Chl-Qz	16	458	13	3
ALB2007	Albergian	LPM	44.88261111	7.038833333	WM-Chl-Qz-Ab	16	428	8	2
ALB2008	Albergian	LPM	44.9812189	6.9241491	Pseudo Lws-WM-Chl-Qz-Cc-Ank	16	442	14	3
ALB2010	Albergian	LPM	44.92177778	6.965166667	Tur-WM-Chl-Qz-Cc	16	461	13	3
ALB2012	Albergian	LPM	44.95066667	6.95	Pseudo Lws-Tur-WM-Chl-Qz-Cc-Ank	16	449	15	4
AM2001	Cerogne-Ciantiplagna	LPM	45.00883333	6.823388889	Pseudo Lws-WM-Chl-Qz	16	373	3	1
AOS2001	By unit	LPM	45.71566667	7.239	WM-Chl-Qz-Cc-Ank	16	512	14	4
AOS2002	By unit	LPM	45.7385811	7.2685045	Tur-WM-Chl-Qz-Ab-Cc-Ank	16	449	18	4
AOS2003	By unit	LPM	45.7507473	7.2784716	Ctd-WM-Chl-Qz-Cc	14	466	18	5
AOS2004	By unit	LPM	45.7274584	7.2596538	Tur-WM-Chl-Qz-Qz-Ab-Cc	16	462	29	7
AOS2005	By unit	LPM	45.7033963	7.2104762	Tur-WM-Chl-Qz-Qz-Cc-Ank	16	497	17	4
AOS2006	By unit	LPM	45.6983553	7.2321025	Pseudo Lws-WM-Chl-Qz-Cc	16	453	22	6

AOS2007	By unit	LPM	45.7025772	7.3053121	Grt-Ep-Tur-WM-Chl-Qz-Ab-Cc-Ank	16	505	21	5
AOS2008	By unit	LPM	45.7475389	7.4727285	WM-Chl-Qz-Cc-Ank	16	488	17	4
AOS2009	By unit	LPM	45.775562	7.4796557	Ctd-Ep-WM-Chl-Qz-Ab-Cc-Ank	15	475	21	5
AOS2010	By unit	LPM	45.7994177	7.4992147	Lws-Ep-WM-Chl-Qz-Cc-Ank	16	523	38	9
AOS2011	By unit	LPM	45.7643564	7.5031853	Ep-Tur-WM-Chl-Qz-Ab-Cc	16	475	22	5
AOS2012	By unit	LPM	45.769527	7.5485911	Ep-WM-Chl-Qz-Cc-Ank	16	492	19	5
AOS2014	Avise-Tasboc-Feluma	LPM ?	45.67647222	7.084833333	Ep-WM-Chl-Qz-Ab-Cc	16	522	20	5
ARG2001	Albergian	LPM	44.88702778	6.957888889	Tur-WM-Chl-Qz-Ab-Cc-Ank	16	461	9	2
ARG2002	Albergian	LPM	44.89491667	6.913361111	Pseudo Lws-WM-Chl-Qz-Cc	16	403	13	3
ARG2003	Albergian	LPM	44.92927778	6.871777778	Tur-WM-Chl-Qz-Ab-Ank	16	386	6	2
ARG2004	Cerogne-Ciantiplagna	LPM	44.93847222	6.873972222	Pseudo Lws-Tur-WM-Chl-Qz-Ab	16	406	7	2
BB1903	Mirabouc-Bouchet	LPM	44.81185	7.015416667	Lws-WM-Chl-Qz-Ank	15	444	14	4
BEA2001	Puys	LPU	45.04027778	6.76425	WM-Chl-Qz-Cc	16	364	6	2
BF2001	Mirabouc-Bouchet	LPM	44.84980556	6.947166667	Lws-WM-Chl-Qz	16	421	8	2
BF2003	Mirabouc-Bouchet	LPM	44.85811111	6.940638889	WM-Chl-Qz-Cc-Ank	16	404	16	4
BF2009	Mirabouc-Bouchet	LPM	44.86328333	6.931369444	Pseudo Lws-Tur-WM-Chl-Qz-Cc-Ank	16	400	10	2
BF2011	Mirabouc-Bouchet	LPM	44.84981944	6.919886111	Pseudo Lws-WM-Chl-Qz-Cc-Ank	16	415	10	3
BL1906	Pelvas-Taillante	LPU	44.66298333	6.925016667	Lws-WM-Chl-Qz-Cc-Ank	16	361	6	2
CH1901	Savoy Middle Unit (Chardonnet)	LPM	45.46646667	6.877516667	WM-Chl-Qz	16	391	8	2
CHE2002	Gondran	Piemont margin ?	44.89219444	6.714472222	Chl-Qz	16	297	6	1
DS1804	Lago-Nero	LPU	44.99433333	6.806166667	Lws-WM-Chl-Qz-Cc-Ank	15	376	15	4
FEN2001	Lago-Nero	LPU	44.98113889	6.79625	Pseudo Lws-WM-Chl-Qz-Ab-Cc	16	366	7	2
FIN2001	Orsiera-Rocciavrè	LPL	45.03455556	7.053972222	Ctd-Ep-Tur-WM-Chl-Qz-Cc-Ank	16	508	27	7
FR2002	Lago-Nero	LPU	45.14480556	6.673333333	Car-WM-Chl-Qz	16	355	7	2

FR2003	Lago-Nero	LPU	45.13488889	6.671277778	Ep-WM-Chl-Qz-Cc	16	423	21	5
FR2004	Lago-Nero	LPU	45.20758333	6.748138889	WM-Chl-Qz-Cc-Ank	16	410	6	2
FR2006	Lago-Nero	LPU	45.21558333	6.778916667	Car-WM-Chl-Qz-Cc	16	390	9	2
FR2007	Lago-Nero	LPU	45.19072222	6.77875	Car-WM-Chl-Qz-Cc	16	379	10	2
FR2008	Lago-Nero	LPU	45.19591667	6.738138889	Car-WM-Chl-Qz-Cc-Ank	16	384	13	3
FR2010	Lago-Nero	LPU	45.18716667	6.700444444	Pseudo Lws-WM-Chl-Qz-Ab-Cc-Ank	15	383	14	4
GA2003	Grivola-Urtier	LPL	45.45763889	7.077694444	Grt-WM-Chl-Qz-Ank	16	479	24	6
GA2005	Grivola-Urtier	LPL	45.456541	7.0728534	Ep-WM-Chl-Qz-Ab-Cc-Ank	15	483	19	5
GL1807a	Aigle	LPU	45.06191944	6.731672222	Chl-Qz-Cc-Ank	16	357	7	2
GRI2001	Grivola-Urtier	LPL	45.60477778	7.203888889	Grt-Cld-Ep-Tur-WM-Chl-Qz	16	534	27	7
GS1802	Savoy Middle Unit (Gde-Sassière)	LPM	45.50573333	6.993633333	WM-Chl-Qz-Cc	16	440	13	3
GU1823	Mirabouc-Bouchet	LPM	44.79561667	7.005016667	Pseudo Lws-WM-Chl-Qz-Cc-Ank	16	376	15	4
GU1901	Calcschist unit	LPU	44.75793333	6.793083333	Lws-WM-Chl-Qz-Cc-Ank	15	358	9	2
GU1912	Calcschist unit	LPU	44.77113333	6.840083333	Lws-WM-Chl-Qz-Cc-Ank	16	360	9	2
GU1817	Calcschist unit	LPU	44.78855	6.886933333	Lws-WM-Chl-Qz-Cc-Ank	16	366	6	2
JA2001	Lago-Nero	LPU	45.08872222	6.716611111	Pseudo Lws-WM-Chl-Qz-Cc	16	371	5	1
JA2002	Lago-Nero	LPU	45.07769444	6.745305556	Pseudo Lws-WM-Chl-Qz-Cc	16	366	5	1
JA2003a	Aigle	LPU	45.06969444	6.766666667	Lws-WM-Chl-Qz-Cc-Ank	17	377	10	2
JA2005a	Vin Vert	LPM	45.08183333	6.805361111	Pseudo Lws-WM-Chl-Qz-Cc-Ank	16	413	12	3
JA2007	Vin Vert	LPM	45.08130556	6.803527778	Pseudo Lws-WM-Chl-Qz-Cc	16	416	17	4
JA2009	Lago-Nero	LPU	45.08519444	6.770861111	WM-Chl-Qz	16	374	4	1
LC2001	Lago-Nero	LPU	44.85155556	6.807027778	Tur-WM-Chl-Qz	15	380	6	2
LC2002	Lago-Nero	LPU	44.83502778	6.813555556	WM-Chl-Qz	15	383	12	3
LC2007	Lago-Nero	LPU	44.85247222	6.797833333	Car-Tur-WM-Chl-Qz	16	376	9	2
MC1803	Savoy Middle Unit	LPM	45.20948333	7.0689	WM-Chl-Qz-Cc-Ank	15	405	9	2

MO2002	Calcschist unit	LPU	44.83697222	6.972694444	Ep-Tur-WM-Chl-Qz-Ab-Cc-Ank	16	437	11	3
MO2003	Mirabouc-Bouchet	LPM	44.82980556	7.008944444	Pseudo Lws-Tur-WM-Chl-Qz-Cc-Ank	16	418	13	3
MO2004	Mirabouc-Bouchet	LPM	44.833	6.992	Lws-WM-Chl-Qz-Cc-Ank	15	423	6	2
MO2005	Calcschist unit	LPU	44.83505556	6.956166667	Pseudo Lws-Tur-WM-Chl-Qz-Cc-Ank	16	422	13	3
MO2006	Calcschist unit	LPU	44.82269444	6.945	Pseudo Lws-WM-Chl-Qz-Ank	16	434	12	3
MO2007	Calcschist unit	LPU	44.80536111	6.929361111	Pseudo Lws-WM-Chl-Qz	15	407	6	2
MTN958b	Lago-Nero	LPU	44.86818889	6.830227778	Car-WM-Chl-Qz-Cc-Ank	13	408	6	2
PL2001	Savoy Upper Unit (Grand Vallon)	LPU	45.32455556	6.849194444	Pseudo Lws-WM-Chl-Qz-Ab-Cc-Ank	16	376	7	2
PS1906	Pelvas-Taillante	LPU	44.69368333	6.99005	Lws-WM-Chl-Qz-Cc-Ank	16	363	6	2
ROC2001	Lago-Nero	LPU	45.11638889	6.750888889	Pseudo Lws-WM-Chl-Qz-Cc-Ank	16	368	10	3
ROC2002	Lago-Nero	LPU	45.07644444	6.713166667	Pseudo Lws-WM-Chl-Qz-Cc-Ank	16	352	4	1
SIC2001	Lago-Nero	LPU	44.96163889	6.818027778	WM-Chl-Qz-Cc	16	356	2	0
SU2001	Savoy Lower Unit	LPL	45.12638889	7.365777778	Ep-Tur-WM-Chl-Qz-Ab	15	530	31	8
SU2002	Savoy Lower Unit	LPL	45.15125	7.381027778	Pseudo Lws-WM-Chl-Qz-Ank	16	471	21	5
SU2003	Savoy Lower Unit	LPL	45.19966667	7.369444444	Ep-Tur-WM-Chl-Qz-Cc	16	507	19	5
SU2004	Savoy Lower Unit	LPL	45.20986111	7.373805556	Cld-Tur-WM-Chl-Qz	14	524	27	7
SU2005	West-Sesia	LPM ?	45.31738889	7.375038889	WM-Chl-Qz-Cc	16	433	36	9
THU2001	Lago-Nero	LPU	44.93433333	6.818944444	WM-Chl-Qz-Cc	16	365	9	2
THU2002	Lago-Nero	LPU	44.92302778	6.823972222	Pseudo Lws-WM-Chl-Qz-Cc	16	358	4	1
UB2005	Pelvas-Taillante	LPU	44.61008333	6.868416667	WM-Chl-Qz-Cc	15	319	10	3
VEN2001	Venaus	LPM	45.14855556	7.010166667	Pseudo Lws-WM-Chl-Qz-Cc-Ank	15	485	27	7
VM2002	Mirabouc-Bouchet	LPM	44.47658333	7.042472222	Pseudo Lws-Cld-Ep-Tur-WM-Chl-Qz-Cc-Ank	16	517	43	11
VM2003	Mirabouc-Bouchet	LPM	44.45166667	7.074083333	Tur-WM-Chl-Qz-Ank	16	389	5	1
VM2004	Mirabouc-Bouchet	LPM	44.51691667	7.056722222	Lws-Tur-WM-Chl-Qz-Ank	16	413	7	2

VM2005	Mirabouc-Bouchet	LPM	44.49658333	7.069611111	Pseudo Lws-WM-Chl-Qz-Cc-Ank	14	411	12	3
VM2006	Mirabouc-Bouchet	LPM	44.48869444	7.068666667	Pseudo Lws-Tur-WM-Chl-Qz-Ank	16	413	9	2
VSL1903	Mirabouc-Bouchet	LPM	44.6796	7.069316667	Ctd-WM-Chl-Qz-Cc	15	464	20	5
VV2001	Mirabouc-Bouchet	LPM	44.6226215	7.0234206	Lws-WM-Chl-Qz-Cc-Ank	16	448	15	4
VV2002	Mirabouc-Bouchet	LPM	44.61052778	7.05625	Pseudo Lws-WM-Chl-Qz-Cc	16	467	7	2
VV2003	Mirabouc-Bouchet	LPM	44.59286111	7.06625	WM-Chl-Qz-Cc-Ank	16	461	13	3
VV2004	Mirabouc-Bouchet	LPM	44.58263889	7.024583333	Pseudo Lws-WM-Chl-Qz-Cc-Ank	16	412	7	2
VV2005	Mirabouc-Bouchet	LPM	44.57977778	7.004333333	Pseudo Lws-WM-Chl-Qz-Cc-Ank	16	379	9	2
VV2007	Mirabouc-Bouchet	LPM	44.54130556	7.095194444	Pseudo Lws-WM-Chl-Qz-Cc-Ank	16	470	9	2
VV2008	Mirabouc-Bouchet	LPM	44.54622222	7.068583333	Tur-WM-Chl-Qz-Cc	16	420	18	5
VV2010	Mirabouc-Bouchet	LPM	44.63494444	7.014527778	Pseudo Lws-WM-Chl-Qz-Cc-Ank	16	419	17	4

Latitude	Longitude	Name	Ref	Unit	Slice
46.0816388888889	7.92227777777778	545	Angiboust et al. (2009)	LPL	Zermatt-Saas
46.0635861111111	7.91750555555556	537	Angiboust et al. (2009)	LPL	Zermatt-Saas
46.0041972222222	7.74588333333333	536	Angiboust et al. (2009)	LPL	Zermatt-Saas
45.9933555555556	7.70975555555556	544	Angiboust et al. (2009)	LPL	Zermatt-Saas
45.8601111111111	7.80233611111111	542	Angiboust et al. (2009)	LPL	Zermatt-Saas
45.8629166666667	7.8455	540	Angiboust et al. (2009)	LPL	Zermatt-Saas
45.8787083333333	7.61330833333333	531	Angiboust et al. (2009)	LPL	Zermatt-Saas
45.863675	7.60291944444444	535	Angiboust et al. (2009)	LPL	Zermatt-Saas
45.8757527777778	7.59168333333333	541	Angiboust et al. (2009)	LPL	Zermatt-Saas
45.7470777777778	7.71281111111111	533	Angiboust et al. (2009)	LPL	Avic
45.7299194444444	7.55856111111111	523	Angiboust et al. (2009)	LPL	Avic
45.7002166666667	7.66083611111111	537	Angiboust et al. (2009)	LPL	Avic
45.6724694444444	7.66844722222222	542	Angiboust et al. (2009)	LPL	Avic
45.6287611111111	7.57637222222222	527	Angiboust et al. (2009)	LPL	Avic
45.9365388888889	7.65945277777778	542	Angiboust et agard (2010)	LPL	Zermatt-Saas

45.9089138888889	7.68009166666667	538	Angiboust et agard (2010)	LPL	Zermatt-Saas
45.9167611111111	7.68368888888889	524	Angiboust et agard (2010)	LPL	Zermatt-Saas
45.881475	7.70844722222222	531	Angiboust et agard (2010)	LPL	Zermatt-Saas
46.0234555555556	7.82035833333333	546	Angiboust et agard (2010)	LPL	Zermatt-Saas
45.7023944444444	7.44558333333333	544	Angiboust et agard (2010)	LPL	Avic
45.6331277777778	7.57134722222222	534	Angiboust et agard (2010)	LPL	Avic
45.6528444444444	7.54602222222222	545	Angiboust et agard (2010)	LPL	Avic
45.6532777777778	7.529975	540	Angiboust et agard (2010)	LPL	Avic
45.641075	7.54352222222222	547	Angiboust et agard (2010)	LPL	Avic
45.6578611111111	7.47160555555556	535	Angiboust et agard (2010)	LPL	Avic
45.6985333333333	7.49325833333333	544	Angiboust et agard (2010)	LPL	Avic
45.9406	7.62575555555556	457	Angiboust et agard (2010)	LPM	By Unit
44.7197222222222	7.09305555555556	549	Angiboust et al. (2012b)	LPL	Lago Superiore
44.7181111111111	7.09155555555555	530	Angiboust et al. (2012b)	LPL	Lago Superiore
44.71625	7.08125	520	Angiboust et al. (2012b)	LPL	Lago Superiore
44.7155833333333	7.08419444444444	544	Angiboust et al. (2012b)	LPL	Lago Superiore
44.7155	7.08497222222222	548	Angiboust et al. (2012b)	LPL	Lago Superiore
44.7128888888889	7.08052777777778	556	Angiboust et al. (2012b)	LPL	Lago Superiore
44.712	7.09444444444444	536	Angiboust et al. (2012b)	LPL	Lago Superiore
44.7096111111111	7.09694444444444	544	Angiboust et al. (2012b)	LPL	Lago Superiore
44.7093611111111	7.07991666666667	541	Angiboust et al. (2012b)	LPL	Lago Superiore
44.7130833333333	7.09113888888889	514	Angiboust et al. (2012b)	LPL	Lago Superiore
44.7007222222222	7.08605555555556	544	Angiboust et al. (2012b)	LPL	Lago Superiore
44.7007222222222	7.08605555555556	531	Angiboust et al. (2012b)	LPL	Lago Superiore
44.6985555555556	7.07602777777778	515	Angiboust et al. (2012b)	LPL	Lago Superiore
44.6931111111111	7.07863888888889	520	Angiboust et al. (2012b)	LPL	Lago Superiore
44.6926111111111	7.08136111111111	532	Angiboust et al. (2012b)	LPL	Lago Superiore
44.6929166666667	7.09527777777778	565	Angiboust et al. (2012b)	LPL	Lago Superiore
44.6890555555556	7.10041666666667	571	Angiboust et al. (2012b)	LPL	Lago Superiore
44.6886388888889	7.08566666666667	538	Angiboust et al. (2012b)	LPL	Lago Superiore
44.6865	7.09327777777778	546	Angiboust et al. (2012b)	LPL	Lago Superiore
44.688675	7.09203055555556	535	Angiboust et al. (2012b)	LPL	Lago Superiore
44.6853333333333	7.07991666666667	524	Angiboust et al. (2012b)	LPL	Lago Superiore
44.6819444444444	7.08333333333333	526	Angiboust et al. (2012b)	LPL	Lago Superiore

44.6857222222222	7.10180555555556	555	Angiboust et al. (2012b)	LPL	Lago Superiore
44.6841944444444	7.11177777777778	555	Angiboust et al. (2012b)	LPL	Lago Superiore
44.6836388888889	7.10447222222222	541	Angiboust et al. (2012b)	LPL	Lago Superiore
44.6810833333333	7.11263888888889	531	Angiboust et al. (2012b)	LPL	Lago Superiore
44.6746944444444	7.12416666666667	532	Angiboust et al. (2012b)	LPL	Lago Superiore
44.6716388888889	7.10380555555555	524	Angiboust et al. (2012b)	LPL	Lago Superiore
44.6675833333333	7.10944444444444	525	Angiboust et al. (2012b)	LPL	Lago Superiore
44.6653333333333	7.11347222222222	524	Angiboust et al. (2012b)	LPL	Lago Superiore
44.6646666666667	7.13063888888889	534	Angiboust et al. (2012b)	LPL	Lago Superiore
44.6636111111111	7.13333333333333	531	Angiboust et al. (2012b)	LPL	Lago Superiore
44.6571111111111	7.12352777777778	548	Angiboust et al. (2012b)	LPL	Lago Superiore
44.6563888888889	7.11277777777778	540	Angiboust et al. (2012b)	LPL	Lago Superiore
44.6459444444444	7.11841666666667	534	Angiboust et al. (2012b)	LPL	Lago Superiore
44.6343888888889	7.12083333333333	523	Angiboust et al. (2012b)	LPL	Lago Superiore
44.6419444444444	7.10861111111111	494	Angiboust et al. (2012b)	LPL	Monviso
44.662	7.10097222222222	489	Angiboust et al. (2012b)	LPL	Monviso
44.7036388888889	7.07461111111111	484	Angiboust et al. (2012b)	LPL	Monviso
44.7156111111111	7.07780555555556	480	Angiboust et al. (2012b)	LPL	Monviso
46.09833333	7.593333333	413	Angiboust et al. (2014)	LPU	Cornet
46.09666667	7.564444444	398	Angiboust et al. (2014)	LPU	Cornet
46.10083333	7.560555556	412	Angiboust et al. (2014)	LPU	Cornet
46.04	7.446666667	364	Angiboust et al. (2014)	LPU	Cornet
45.87027778	7.325	403	Angiboust et al. (2014)	LPU	Cornet
45.87027778	7.325	396	Angiboust et al. (2014)	LPU	Cornet
45.88583333	7.345833333	378	Angiboust et al. (2014)	LPU	Cornet
45.995	7.399722222	422	Angiboust et al. (2014)	LPU	Cornet
45.99388889	7.402222222	367	Angiboust et al. (2014)	LPU	Cornet
46.05166667	7.493333333	402	Angiboust et al. (2014)	LPU	Cornet
46.12138889	7.6475	458	Angiboust et al. (2014)	LPM	By Unit
46.03277778	7.408611111	466	Angiboust et al. (2014)	LPM	By Unit
45.73222222	7.115555556	494	Angiboust et al. (2014)	LPM	By Unit
45.73861111	7.146388889	480	Angiboust et al. (2014)	LPM	By Unit
46.11722222	7.647777778	434	Angiboust et al. (2014)	LPM	By Unit
46.13388889	7.576944444	441	Angiboust et al. (2014)	LPM	By Unit

46.12972222	7.576666667	440	Angiboust et al. (2014)	LPM	By Unit
46.11416667	7.574166667	439	Angiboust et al. (2014)	LPM	By Unit
46.11194444	7.576666667	437	Angiboust et al. (2014)	LPM	By Unit
45.94805556	7.3825	487	Angiboust et al. (2014)	LPM	By Unit
45.96055556	7.388611111	478	Angiboust et al. (2014)	LPM	By Unit
45.97194444	7.368055556	478	Angiboust et al. (2014)	LPM	By Unit
45.98888889	7.355277778	474	Angiboust et al. (2014)	LPM	By Unit
46.0025	7.341388889	457	Angiboust et al. (2014)	LPM	By Unit
45.89027778	7.3375	430	Angiboust et al. (2014)	LPM	By Unit
45.8775	7.3025	466	Angiboust et al. (2014)	LPM	By Unit
44.9755027777778	6.86858611111111	330	Beyssac et al. (2002)	LPU	Lago Nero
44.9908333333333	6.86694444444444	330	Beyssac et al. (2002)	LPU	Lago Nero
44.99833333	6.88444444444444	343	Beyssac et al. (2002)	LPU	Lago Nero
45.0202777777778	6.89722222222222	365	Beyssac et al. (2002)	LPU	Lago Nero
45.0352777777778	6.90888888888889	356	Beyssac et al. (2002)	LPU	Lago Nero
45.0558333333333	6.93527777777778	370	Beyssac et al. (2002)	LPU	Lago Nero
45.0666666666667	6.95361111111111	378	Beyssac et al. (2002)	LPU	Lago Nero
45.0611111111111	6.97222222222222	387	Beyssac et al. (2002)	LPU	Lago Nero
45.0766666666667	6.97944444444444	423	Beyssac et al. (2002)	LPM	Cerrogne-Ciantiplagna
45.0601888888889	7.00334444444444	441	Beyssac et al. (2002)	LPM	Cerrogne-Ciantiplagna
45.0710416666667	7.03362222222222	463	Beyssac et al. (2002)	LPM	Cerrogne-Ciantiplagna
45.0753277777778	7.05908055555556	503	Beyssac et al. (2002)	LPL	Orsiera-Rocciavrè
46.03944444	7.456111111	368	Decrausaz et al. (2021)	LPU	Cornet
46.03888889	7.434722222	376	Decrausaz et al. (2021)	LPU	Cornet
46.03777778	7.4325	373	Decrausaz et al. (2021)	LPU	Cornet
46.07222222	7.458333333	369	Decrausaz et al. (2021)	LPU	Cornet
45.23333333	7	404	Gabalda et al. (2009)	LPU	Savoy Upper Unit (Grand Vallon)
45.33333333	6.866666667	378	Gabalda et al. (2009)	LPU	Savoy Upper Unit (Grand Vallon)
45.15	7.066666667	481	Gabalda et al. (2009)	LPM	Savoy Middle Unit
45.15	7.05	477	Gabalda et al. (2009)	LPM	Savoy Middle Unit
45.3	7.033333333	437	Gabalda et al. (2009)	LPM	Savoy Middle Unit
45.31666667	7.016666667	486	Gabalda et al. (2009)	LPM	Savoy Middle Unit
45.31666667	6.983333333	494	Gabalda et al. (2009)	LPM	Savoy Middle Unit
45.21666667	6.966666667	484	Gabalda et al. (2009)	LPM	Savoy Middle Unit

45.25	6.9	455	Gabalda et al. (2009)	LPM	Savoy Middle Unit
45.28333333	6.883333333	472	Gabalda et al. (2009)	LPM	Savoy Middle Unit
45.31666667	6.916666667	402	Gabalda et al. (2009)	LPM	Savoy Middle Unit
45.33333333	6.85	388	Gabalda et al. (2009)	LPM	Savoy Middle Unit
45.33333333	6.85	384	Gabalda et al. (2009)	LPM	Savoy Middle Unit
45.33333333	6.85	394	Gabalda et al. (2009)	LPM	Savoy Middle Unit
45.36666667	6.933333333	398	Gabalda et al. (2009)	LPM	Savoy Middle Unit
45.33333333	6.966666667	429	Gabalda et al. (2009)	LPM	Savoy Middle Unit
45.3	6.95	442	Gabalda et al. (2009)	LPM	Savoy Middle Unit
45.28333333	6.816666667	395	Gabalda et al. (2009)	LPM	Savoy Middle Unit
45.41666667	7.033333333	440	Gabalda et al. (2009)	LPM	Savoy Middle Unit
45.2	6.966666667	503	Gabalda et al. (2009)	LPM	Savoy Middle Unit
45.1	6.683333333	356	Gabalda et al. (2009)	LPU	Lago Nero
45.2	6.7	373	Gabalda et al. (2009)	LPU	Lago Nero
45.21666667	6.783333333	377	Gabalda et al. (2009)	LPU	Lago Nero
45.21666667	6.766666667	390	Gabalda et al. (2009)	LPU	Lago Nero
45.08333333	6.783333333	386	Gabalda et al. (2009)	LPU	Aigle
45.06666667	7.133333333	527	Gabalda et al. (2009)	LPL	Orsiera-Rocciavrè
45.05	7.133333333	542	Gabalda et al. (2009)	LPL	Orsiera-Rocciavrè
45.05	7.083333333	541	Gabalda et al. (2009)	LPL	Orsiera-Rocciavrè
45.3	7.083333333	513	Gabalda et al. (2009)	LPL	Savoy Lower Unit
45.3	7.05	542	Gabalda et al. (2009)	LPL	Savoy Lower Unit
45.33333333	7.016666667	541	Gabalda et al. (2009)	LPL	Savoy Lower Unit
45.35	7.033333333	507	Gabalda et al. (2009)	LPL	Savoy Lower Unit
45.36666667	7.066666667	535	Gabalda et al. (2009)	LPL	Savoy Lower Unit
45.36666667	7.066666667	546	Gabalda et al. (2009)	LPL	Savoy Lower Unit
45.36666667	7.066666667	542	Gabalda et al. (2009)	LPL	Savoy Lower Unit
45.35	7.066666667	530	Gabalda et al. (2009)	LPL	Savoy Lower Unit
45.38333333	7.033333333	526	Gabalda et al. (2009)	LPL	Savoy Lower Unit
45.87083333	7.326388889	403	Manzotti et al. (2018)	LPU	Cornet
45.87083333	7.326388889	373	Manzotti et al. (2018)	LPU	Cornet
45.87055556	7.325833333	392	Manzotti et al. (2018)	LPU	Cornet
45.87027778	7.325833333	382	Manzotti et al. (2018)	LPU	Cornet
45.87	7.325833333	386	Manzotti et al. (2018)	LPU	Cornet

45.91055556	7.355833333	399	Manzotti et al. (2018)	LPU	Cornet
45.88416667	7.316666667	494	Manzotti et al. (2018)	LPM	By Unit
45.88833333	7.329444444	477	Manzotti et al. (2018)	LPM	By Unit
45.88805556	7.329166667	467	Manzotti et al. (2018)	LPM	By Unit
45.89555556	7.283333333	457	Manzotti et al. (2018)	LPM	By Unit
45.88166667	7.286944444	515	Manzotti et al. (2018)	LPM	By Unit
45.91333333	7.353055556	484	Manzotti et al. (2018)	LPM	By Unit
45.91333333	7.351666667	470	Manzotti et al. (2018)	LPM	By Unit
45.91472222	7.349166667	467	Manzotti et al. (2018)	LPM	By Unit
45.91027778	7.353888889	463	Manzotti et al. (2018)	LPM	By Unit
45.90277778	7.3475	462	Manzotti et al. (2018)	LPM	By Unit
45.88833333	7.307222222	463	Manzotti et al. (2018)	LPM	By Unit
45.87444444	7.31	469	Manzotti et al. (2018)	LPM	By Unit
45.90111111	7.335555556	478	Manzotti et al. (2018)	LPM	By Unit
45.90111111	7.335555556	474	Manzotti et al. (2018)	LPM	By Unit
45.74722222	7.4725	437	Manzotti et al. (2018)	LPM	By Unit
45.75055556	7.478888889	445	Manzotti et al. (2018)	LPM	By Unit
45.76666667	7.466944444	482	Manzotti et al. (2018)	LPM	By Unit
45.76666667	7.466944444	458	Manzotti et al. (2018)	LPM	By Unit
45.79361111	7.49	504	Manzotti et al. (2018)	LPM	By Unit
45.79333333	7.49	506	Manzotti et al. (2018)	LPM	By Unit
45.79638889	7.468888889	439	Manzotti et al. (2018)	LPM	By Unit
45.79277778	7.466944444	467	Manzotti et al. (2018)	LPM	By Unit
45.77972222	7.463611111	464	Manzotti et al. (2018)	LPM	By Unit
45.76611111	7.446111111	495	Manzotti et al. (2018)	LPM	By Unit
45.75777778	7.482777778	446	Manzotti et al. (2018)	LPM	By Unit
45.80083333	7.535555556	445	Manzotti et al. (2018)	LPM	By Unit
45.82722222	7.524444444	445	Manzotti et al. (2018)	LPM	By Unit
45.77666667	7.482777778	453	Manzotti et al. (2018)	LPM	By Unit
46.11785	7.63342	448	Negro et al, (2013)	LPM	By Unit
46.11666	7.57275	454	Negro et al, (2013)	LPM	By Unit
46.13349	7.57667	451	Negro et al, (2013)	LPM	By Unit
45.94402	7.38207	461	Negro et al, (2013)	LPM	By Unit
45.9439	7.38204	478	Negro et al, (2013)	LPM	By Unit

45.93158	7.38002	477	Negro et al, (2013)	LPM	By Unit
45.99113	7.34738	492	Negro et al, (2013)	LPM	By Unit
46.0027	7.34131	494	Negro et al, (2013)	LPM	By Unit
46.08049	7.49553	439	Negro et al, (2013)	LPM	By Unit
45.98938	7.69626	514	Negro et al, (2013)	LPM	By Unit
45.98234	7.67855	475	Negro et al, (2013)	LPM	By Unit
45.98224	7.67618	462	Negro et al, (2013)	LPM	By Unit
45.98206	7.67543	460	Negro et al, (2013)	LPM	By Unit
45.9814	7.67424	453	Negro et al, (2013)	LPM	By Unit
45.98839	7.69529	499	Negro et al, (2013)	LPM	By Unit
45.98795	7.68886	473	Negro et al, (2013)	LPM	By Unit
45.9881	7.69312	530	Negro et al, (2013)	LPM	By Unit
45.98434	7.68257	470	Negro et al, (2013)	LPM	By Unit
45.98373	7.68218	451	Negro et al, (2013)	LPM	By Unit
45.98382	7.6819	457	Negro et al, (2013)	LPM	By Unit
46.01798	7.73325	508	Negro et al, (2013)	LPM	By Unit
46.01652	7.72229	510	Negro et al, (2013)	LPM	By Unit
46.01824	7.70979	501	Negro et al, (2013)	LPM	By Unit
46.02263	7.73853	481	Negro et al, (2013)	LPM	By Unit
46.0249	7.73282	488	Negro et al, (2013)	LPM	By Unit
46.02718	7.72485	494	Negro et al, (2013)	LPM	By Unit
46.03181	7.71761	476	Negro et al, (2013)	LPM	By Unit
46.02674	7.71823	421	Negro et al, (2013)	LPM	By Unit
46.02752	7.72461	503	Negro et al, (2013)	LPM	By Unit
46.02934	7.72317	485	Negro et al, (2013)	LPM	By Unit
46.02821	7.74971	480	Negro et al, (2013)	LPM	By Unit
46.02216	7.79735	523	Negro et al, (2013)	LPM	By Unit
46.02345	7.80481	504	Negro et al, (2013)	LPM	By Unit
46.025	7.80403	498	Negro et al, (2013)	LPM	By Unit
46.02923	7.79269	503	Negro et al, (2013)	LPM	By Unit
46.01649	7.80764	511	Negro et al, (2013)	LPM	By Unit
46.02456	7.81757	516	Negro et al, (2013)	LPM	By Unit
45.87932	7.60459	532	Negro et al, (2013)	LPM	By Unit
45.88023	7.60437	498	Negro et al, (2013)	LPM	By Unit

45.88044	7.60433	504	Negro et al, (2013)	LPM	By Unit
45.87842	7.58695	506	Negro et al, (2013)	LPM	By Unit
45.89257	7.59811	475	Negro et al, (2013)	LPM	By Unit
45.89159	7.5976	466	Negro et al, (2013)	LPM	By Unit
45.88408	7.60062	508	Negro et al, (2013)	LPM	By Unit
45.88728	7.5972	469	Negro et al, (2013)	LPM	By Unit
45.88846	7.59686	455	Negro et al, (2013)	LPM	By Unit
45.89058	7.59702	474	Negro et al, (2013)	LPM	By Unit
45.88792	7.58284	474	Negro et al, (2013)	LPM	By Unit
45.87842	7.58695	513	Negro et al, (2013)	LPM	By Unit
45.98991	7.70485	528	Negro et al, (2013)	LPL	Zermatt-Saas
45.98999	7.70095	495	Negro et al, (2013)	LPL	Zermatt-Saas
46.00073	7.72624	535	Negro et al, (2013)	LPL	Zermatt-Saas
45.972	7.72658	510	Negro et al, (2013)	LPL	Zermatt-Saas
45.97802	7.72309	536	Negro et al, (2013)	LPL	Zermatt-Saas
45.9833	7.78508	521	Negro et al, (2013)	LPL	Zermatt-Saas
45.98484	7.7638	531	Negro et al, (2013)	LPL	Zermatt-Saas
45.98704	7.7606	526	Negro et al, (2013)	LPL	Zermatt-Saas
45.99334	7.75681	543	Negro et al, (2013)	LPL	Zermatt-Saas
46.01568	7.77943	539	Negro et al, (2013)	LPL	Zermatt-Saas
45.87842	7.58695	522	Negro et al, (2013)	LPL	Zermatt-Saas
45.87281	7.60736	541	Negro et al, (2013)	LPL	Zermatt-Saas
46.10362	7.58653	418	Negro et al, (2013)	LPM	Combin/Cornet
45.49985751	6.666979864	376	Plunder et al. (2012)	LPU	Savoy Upper Unit (Jovet)
45.2475	6.906944444	436	Plunder et al. (2012)	LPM	Savoy Middle Unit
45.2225	6.944166667	464	Plunder et al. (2012)	LPM	Savoy Middle Unit
45.23	6.959444444	450	Plunder et al. (2012)	LPM	Savoy Middle Unit
45.32777778	6.9975	482	Plunder et al. (2012)	LPM	Savoy Middle Unit
45.29472222	6.908888889	480	Plunder et al. (2012)	LPM	Savoy Middle Unit
45.26888889	7.02	470	Plunder et al. (2012)	LPM	Savoy Middle Unit
45.42194444	7.040277778	460	Plunder et al. (2012)	LPM	Savoy Middle Unit
45.41916667	7.036388889	476	Plunder et al. (2012)	LPM	Savoy Middle Unit
45.42	7.0275	427	Plunder et al. (2012)	LPM	Savoy Middle Unit
45.49111111	6.964722222	449	Plunder et al. (2012)	LPM	Savoy Middle Unit

45.28833333	7.088055556	570	Plunder et al. (2012)	LPL	Savoy Lower Unit
45.28833333	7.088055556	536	Plunder et al. (2012)	LPL	Savoy Lower Unit
45.27916667	7.088333333	535	Plunder et al. (2012)	LPL	Savoy Lower Unit
45.2725	7.078333333	510	Plunder et al. (2012)	LPL	Savoy Lower Unit
45.28861111	7.105277778	549	Plunder et al. (2012)	LPL	Savoy Lower Unit
45.27472222	7.112222222	547	Plunder et al. (2012)	LPL	Savoy Lower Unit
45.40027778	7.0425	548	Plunder et al. (2012)	LPL	Savoy Lower Unit
45.40055556	7.040833333	518	Plunder et al. (2012)	LPL	Savoy Lower Unit
45.205	7.205	524	Plunder et al. (2012)	LPL	Savoy Lower Unit
45.40138889	7.038055556	508	Plunder et al. (2012)	LPL	Savoy Lower Unit
45.40138889	7.036388889	559	Plunder et al. (2012)	LPL	Savoy Lower Unit
44.74860358	6.778628324	332	Schwartz et al. (2013)	LPU	Calcschist unit
44.74283994	6.795559027	328	Schwartz et al. (2013)	LPU	Calcschist unit
44.7453165	6.829060204	326	Schwartz et al. (2013)	LPU	Calcschist unit
44.72406307	6.823656789	320	Schwartz et al. (2013)	LPU	Calcschist unit
44.67957494	6.856077283	340	Schwartz et al. (2013)	LPU	Calcschist unit
44.77994339	6.85850882	336	Schwartz et al. (2013)	LPU	Calcschist unit
44.64175103	6.876610263	327	Schwartz et al. (2013)	LPU	Calcschist unit
44.69992781	6.92452055	338	Schwartz et al. (2013)	LPU	Calcschist unit
44.68011529	6.959642752	356	Schwartz et al. (2013)	LPU	Calcschist unit
44.65093684	6.956580816	367	Schwartz et al. (2013)	LPU	Calcschist unit
44.70262952	6.971350153	373	Schwartz et al. (2013)	LPU	Pelvas-Taillante
44.71469715	6.987380286	364	Schwartz et al. (2013)	LPU	Pelvas-Taillante
44.77395461	6.95207797	367	Schwartz et al. (2013)	LPU	Pelvas-Taillante
44.73577047	6.951537628	341	Schwartz et al. (2013)	LPU	Pelvas-Taillante
44.80984229	6.997196492	402	Schwartz et al. (2013)	LPM	Mirabouc-Bouchet
44.76098641	6.994404727	389	Schwartz et al. (2013)	LPM	Mirabouc-Bouchet
44.741354	6.990081994	383	Schwartz et al. (2013)	LPM	Mirabouc-Bouchet
44.71739885	7.021241692	445	Schwartz et al. (2013)	LPM	Mirabouc-Bouchet
44.70807796	7.04474655	463	Schwartz et al. (2013)	LPM	Mirabouc-Bouchet
44.68822041	7.056724122	469	Schwartz et al. (2013)	LPM	Mirabouc-Bouchet
44.69578519	7.106075319	519	Schwartz et al. (2013)	LPL	Lago Superiore
44.65219764	7.120484428	493	Schwartz et al. (2013)	LPL	Monviso
44.63116934	7.087433535	476	Schwartz et al. (2013)	LPL	Monviso

44.6508	7.0803	498	Schwartz et al. (2013)	LPL	Monviso
44.8904	6.7233	330	Schwartz et al. (2013)	Piemont margin ?	Gondran
45.00701667	6.991566667	450	This study	LPM	Albergian
44.95943333	6.986266667	477	This study	LPM	Albergian
44.96625	6.97875	468	This study	LPM	Albergian
44.98151667	6.965533333	454	This study	LPM	Albergian
44.99266667	6.975566667	440	This study	LPM	Albergian
44.94445	7.053816667	499	This study	LPL	Orsiera-Rocciavrè
44.96246667	7.046266667	451	This study	LPM	Albergian
44.9691	7.02015	491	This study	LPM	Albergian
45.04072222	7.021388889	483	This study	LPL	Orsiera-Rocciavrè
44.91922222	7.051361111	489	This study	LPM	Albergian
44.91558333	7.025694444	482	This study	LPM	Albergian
44.90797222	7.059166667	534	This study	LPL	Orsiera-Rocciavrè
44.86086111	7.03475	458	This study	LPM	Mirabouc-Bouchet
44.88261111	7.038833333	428	This study	LPM	Albergian
44.9812189	6.9241491	442	This study	LPM	Albergian
44.92177778	6.965166667	461	This study	LPM	Albergian
44.95066667	6.95	449	This study	LPM	Albergian
45.00883333	6.823388889	373	This study	LPM	Cerogne-Ciantiplagna
45.71566667	7.239	512	This study	LPM	By unit
45.7385811	7.2685045	449	This study	LPM	By unit
45.7507473	7.2784716	466	This study	LPM	By unit
45.7274584	7.2596538	462	This study	LPM	By unit
45.7033963	7.2104762	497	This study	LPM	By unit
45.6983553	7.2321025	453	This study	LPM	By unit
45.7025772	7.3053121	505	This study	LPM	By unit
45.7475389	7.4727285	488	This study	LPM	By unit
45.775562	7.4796557	475	This study	LPM	By unit
45.7994177	7.4992147	523	This study	LPM	By unit
45.7643564	7.5031853	475	This study	LPM	By unit
45.769527	7.5485911	492	This study	LPM	By unit
45.67647222	7.084833333	522	This study	LPM ?	Avise-Tasboc-Feluma
44.88702778	6.957888889	461	This study	LPM	Albergian

44.89491667	6.913361111	403	This study	LPM	Albergian
44.92927778	6.871777778	386	This study	LPM	Albergian
44.93847222	6.873972222	406	This study	LPM	Cerogne-Ciantiplagna
44.81185	7.015416667	444	This study	LPM	Mirabouc-Bouchet
45.04027778	6.76425	364	This study	LPU	Puys
44.84980556	6.947166667	421	This study	LPM	Mirabouc-Bouchet
44.85811111	6.940638889	404	This study	LPM	Mirabouc-Bouchet
44.86328333	6.931369444	400	This study	LPM	Mirabouc-Bouchet
44.84981944	6.919886111	415	This study	LPM	Mirabouc-Bouchet
44.66298333	6.925016667	361	This study	LPU	Pelvas-Taillante
45.46646667	6.877516667	391	This study	LPM	Savoy Middle Unit (Chardonnet)
44.89219444	6.714472222	297	This study	Piemont margin ?	Gondran
44.99433333	6.806166667	376	This study	LPU	Lago-Nero
44.98113889	6.79625	366	This study	LPU	Lago-Nero
45.03455556	7.053972222	508	This study	LPL	Orsiera-Rocciavrè
45.14480556	6.673333333	355	This study	LPU	Lago-Nero
45.13488889	6.671277778	423	This study	LPU	Lago-Nero
45.20758333	6.748138889	410	This study	LPU	Lago-Nero
45.21558333	6.778916667	390	This study	LPU	Lago-Nero
45.19072222	6.77875	379	This study	LPU	Lago-Nero
45.19591667	6.738138889	384	This study	LPU	Lago-Nero
45.18716667	6.700444444	383	This study	LPU	Lago-Nero
45.45763889	7.077694444	479	This study	LPL	Grivola-Urtier
45.456541	7.0728534	483	This study	LPL	Grivola-Urtier
45.06191944	6.731672222	357	This study	LPU	Aigle
45.60477778	7.203888889	534	This study	LPL	Grivola-Urtier
45.50573333	6.993633333	440	This study	LPM	Savoy Middle Unit (Gde-Sassière)
44.79561667	7.005016667	376	This study	LPM	Mirabouc-Bouchet
44.75793333	6.793083333	358	This study	LPU	Calcschist unit
44.77113333	6.840083333	360	This study	LPU	Calcschist unit
44.78855	6.886933333	366	This study	LPU	Calcschist unit
45.08872222	6.716611111	371	This study	LPU	Lago-Nero
45.07769444	6.745305556	366	This study	LPU	Lago-Nero
45.06969444	6.766666667	377	This study	LPU	Aigle

45.08183333	6.805361111	413	This study	LPM	Vin Vert
45.08130556	6.803527778	416	This study	LPM	Vin Vert
45.08519444	6.770861111	374	This study	LPU	Lago-Nero
44.85155556	6.807027778	380	This study	LPU	Lago-Nero
44.83502778	6.813555556	383	This study	LPU	Lago-Nero
44.85247222	6.797833333	376	This study	LPU	Lago-Nero
45.20948333	7.0689	405	This study	LPM	Savoy Middle Unit
44.83697222	6.972694444	437	This study	LPU	Calcschist unit
44.82980556	7.008944444	418	This study	LPM	Mirabouc-Bouchet
44.833	6.992	423	This study	LPM	Mirabouc-Bouchet
44.83505556	6.956166667	422	This study	LPU	Calcschist unit
44.82269444	6.945	434	This study	LPU	Calcschist unit
44.80536111	6.929361111	407	This study	LPU	Calcschist unit
44.86818889	6.830227778	408	This study	LPU	Lago-Nero
45.32455556	6.849194444	376	This study	LPU	Savoy Upper Unit (Grand Vallon)
44.69368333	6.99005	363	This study	LPU	Pelvas-Taillante
45.11638889	6.750888889	368	This study	LPU	Lago-Nero
45.07644444	6.713166667	352	This study	LPU	Lago-Nero
44.96163889	6.818027778	356	This study	LPU	Lago-Nero
45.12638889	7.365777778	530	This study	LPL	Savoy Lower Unit
45.15125	7.381027778	471	This study	LPL	Savoy Lower Unit
45.19966667	7.369444444	507	This study	LPL	Savoy Lower Unit
45.20986111	7.373805556	524	This study	LPL	Savoy Lower Unit
45.31738889	7.375038889	433	This study	LPM ?	West-Sesia
44.93433333	6.818944444	365	This study	LPU	Lago-Nero
44.92302778	6.823972222	358	This study	LPU	Lago-Nero
44.61008333	6.868416667	319	This study	LPU	Pelvas-Taillante
45.14855556	7.010166667	485	This study	LPM	Venaus
44.47658333	7.042472222	517	This study	LPM	Mirabouc-Bouchet
44.45166667	7.074083333	389	This study	LPM	Mirabouc-Bouchet
44.51691667	7.056722222	413	This study	LPM	Mirabouc-Bouchet
44.49658333	7.069611111	411	This study	LPM	Mirabouc-Bouchet
44.48869444	7.068666667	413	This study	LPM	Mirabouc-Bouchet
44.6796	7.069316667	464	This study	LPM	Mirabouc-Bouchet

44.6226215	7.0234206	448	This study	LPM	Mirabouc-Bouchet
44.61052778	7.05625	467	This study	LPM	Mirabouc-Bouchet
44.59286111	7.06625	461	This study	LPM	Mirabouc-Bouchet
44.58263889	7.024583333	412	This study	LPM	Mirabouc-Bouchet
44.57977778	7.004333333	379	This study	LPM	Mirabouc-Bouchet
44.54130556	7.095194444	470	This study	LPM	Mirabouc-Bouchet
44.54622222	7.068583333	420	This study	LPM	Mirabouc-Bouchet
44.63494444	7.014527778	419	This study	LPM	Mirabouc-Bouchet

Supplementary material III.2: Representative electron microprobe compositions of phengite.

Sample	UB2005	FR2006	LC2007	PS1903	JA2002	BEA2001	ALB1920	BF2009	VM2002	JA2005a	VSL1903	VV2002	MO2003
SiO_2	49.24	50.79	51.23	51.16	51.58	51.97	51.32	52.02	52.76	53.52	53.53	53.20	53.19
TiO_2	0.11	0.10	0.08	0.10	0.12	0.09	0.17	0.26	0.08	0.11	0.11	0.08	0.13
Al_2O_3	28.77	27.77	27.50	27.38	26.56	26.97	25.26	25.21	25.15	24.95	25.09	23.67	23.04
Cr_2O_3	0.04	0.03	0.05	0.09	0.03	0.03	0.02	0.05	0.00	0.02	0.04	0.03	0.03
FeO	3.41	3.47	2.33	4.32	3.32	3.10	4.08	4.20	3.55	3.36	3.13	4.41	4.20
MnO	0.04	0.01	0.04	0.00	0.00	0.00	0.02	0.02	0.00	0.00	0.05	0.00	0.03
MgO	3.14	2.54	3.26	2.32	3.09	2.85	3.38	2.93	3.33	3.32	3.52	3.22	3.61
CaO	0.18	0.04	0.05	0.04	0.01	0.14	0.01	0.00	0.21	0.00	0.01	0.11	0.00
Na_2O	0.68	0.20	0.34	0.11	0.14	0.31	0.05	0.10	0.03	0.07	0.02	0.05	0.02
K2O	8.97	9.99	9.74	10.15	10.03	9.66	10.32	10.39	10.39	10.30	10.06	10.03	10.27
Total	94.56	94.94	94.62	95.68	94.87	95.12	94.62	95.17	95.50	95.64	95.56	94.80	94.52
Si	3.31	3.40	3.42	3.42	3.45	3.46	3.47	3.50	3.52	3.55	3.55	3.58	3.59
Ti	0.01	0.00	0.00	0.00	0.01	0.00	0.01	0.01	0.00	0.01	0.01	0.00	0.01
Al	2.28	2.19	2.16	2.16	2.10	2.12	2.01	2.00	1.98	1.95	1.96	1.88	1.83
Cr	0.00	0.00	0.00	0.00	0.00	0.00	0.00	0.00	0.00	0.00	0.00	0.00	0.00
Fe	0.19	0.19	0.13	0.24	0.19	0.17	0.23	0.24	0.20	0.19	0.17	0.25	0.24
Mn	0.00	0.00	0.00	0.00	0.00	0.00	0.00	0.00	0.00	0.00	0.00	0.00	0.00
Mg	0.31	0.25	0.33	0.23	0.31	0.28	0.34	0.29	0.33	0.33	0.35	0.32	0.36
Ca	0.01	0.00	0.00	0.00	0.00	0.01	0.00	0.00	0.01	0.00	0.00	0.01	0.00
Na	0.09	0.03	0.04	0.01	0.02	0.04	0.01	0.01	0.00	0.01	0.00	0.01	0.00
K	0.77	0.85	0.83	0.87	0.86	0.82	0.89	0.89	0.88	0.87	0.85	0.86	0.88
XMg	0.62141	0.57	0.71	0.49	0.62	0.62	0.60	0.55	0.63	0.64	0.67	0.57	0.61
Al^{IV}	0.69	0.60	0.58	0.58	0.55	0.54	0.53	0.50	0.48	0.45	0.45	0.42	0.41
Al^{VI}	1.59	1.60	1.59	1.57	1.55	1.58	1.48	1.49	1.50	1.50	1.51	1.46	1.43
sum Alk.	0.87	0.88	0.87	0.88	0.87	0.86	0.90	0.90	0.89	0.88	0.85	0.87	0.89
sum Oct.	2.1	2.05	2.05	2.06	2.05	2.05	2.07	2.04	2.04	2.03	2.04	2.04	2.04

Supplementary material III.3: Selected maximum Si a.p.f.u. values of phengite ($Si^{max}Ph$), RSCM temperature for the same samples and peak pressure estimated by intersection of RSCM temperatures with Si a.p.f.u. isopleths of pseudosection of figure 9a.

Sample	Unit	Slice	Latitude	Longitude	$Si^{Max}Ph$ (apfu)	Reference for $Si^{Max}Ph$	RSCM T° (°C)	Reference for RSCM T°(°C)	Pressure estimated (Gpa)
LC2007	LPU	Lago Nero	44.85247222	6.797833333	3.42	This study	376	This study	1.7
JA2002	LPU	Lago Nero	45.07769444	6.745305556	3.45	This study	366	This study	1.7-1.8
THU2002	LPU	Lago Nero	44.92302778	6.823972222	3.47	This study	358	This study	1.7-1.8
FEN2001	LPU	Lago Nero	44.98113889	6.79625	3.32	This study	366	This study	1.5
ROC2001	LPU	Lago Nero	45.11638889	6.750888889	3.43	This study	368	This study	1.7-1.8
FR2003	LPU	Lago Nero	45.13488889	6.671277778	3.47	This study	423	This study	1.9-2
Agard1	LPU	Lago Nero	44.96972222	6.854444444	3.27	Agard et al. (2001a)	330	Beyssac et al. (2002)	1.3-1.4
Agard2	LPU	Lago Nero	44.96694444	6.857222222	3.28	Agard et al. (2001a)	330	Beyssac et al. (2002)	1.3-1.4
Agard3	LPU	Lago Nero	44.985	6.851666667	3.33	Agard et al. (2001a)	330	Beyssac et al. (2002)	1.4-1.5
Agard5	LPU	Lago Nero	44.98305556	6.844444444	3.31	Agard et al. (2001a)	330	Beyssac et al. (2002)	1.4
Agard6	LPU	Lago Nero	44.97777778	6.860833333	3.28	Agard et al. (2001a)	330	Beyssac et al. (2002)	1.3-1.4
Agard7	LPU	Lago Nero	44.97777778	6.861666667	3.3	Agard et al. (2001a)	330	Beyssac et al. (2002)	1.4
Agard8	LPU	Lago Nero	44.99583333	6.869722222	3.47	Agard et al. (2001a)	343	Beyssac et al. (2002)	1.7-1.8
Agard9	LPU	Lago Nero	44.985	6.880555556	3.43	Agard et al. (2001a)	330	Beyssac et al. (2002)	1.6
Agard10	LPU	Lago Nero	44.98666667	6.875277778	3.44	Agard et al. (2001a)	330	Beyssac et al. (2002)	1.6-1.7
Agard11	LPU	Lago Nero	45.02916667	6.895833333	3.51	Agard et al. (2001a)	365	Beyssac et al. (2002)	1.8-1.9
Agard12(1)	LPU	Lago Nero	45.06138889	6.948055556	3.49	Agard et al. (2001a)	378	Beyssac et al. (2002)	1.8-1.9
60	LPU	Lago Nero	44.98338056	6.780972222	3.32	Liewig et al. (1981)	366	This study	1.5
FR2006	LPU	Lago Nero	45.21558333	6.778916667	3.4	This study	390	This study	1.7-1.8
BEA2001	LPU	Puys	45.04027778	6.76425	3.46	This study	364	This study	1.7-1.8
MO2007a	LPU	Calcschit unit	44.80536111	6.929361111	3.52	This study	407	This study	2
MO2006	LPU	Calcschit unit	44.82269444	6.945	3.4	This study	434	This study	1.8-1.9
GU1817	LPU	Calcschit unit	44.78855	6.886933333	3.47	This study	366	This study	1.8
4b	LPU	Calcschit unit	44.75837222	6.796983333	3.34	Liewig et al. (1981)	332	Schwartz et al. (2013)	1.4
8	LPU	Calcschit unit	44.76846667	6.819127778	3.41	Liewig et al. (1981)	360	This study	1.6-1.7
17	LPU	Calcschit unit	44.80338611	6.831113889	3.4	Liewig et al. (1981)	360	This study	1.6-1.7
21	LPU	Calcschit unit	44.79185556	6.883455556	3.44	Liewig et al. (1981)	366	This study	1.7-1.8
36	LPU	Calcschit unit	44.81291111	6.963461111	3.5	Liewig et al. (1981)	434	This study	2
PS1903	LPU	Pelvas-Taillante	44.69368333	6.99005	3.42	This study	363	This study	1.7
671	LPU	Pelvas-Taillante	44.6783	6.914936111	3.42	Bocquet (1974)	361	Schwartz et al. (2013)	1.7

UB2005	LPU	Pelvas-Taillante	44.61008333	6.868416667	3.31	This study	319	This study	1.4
AM2001	LPU	Cerogne-Ciantiplagna	45.00883333	6.823388889	3.41	This study	373	This study	1.7
Agard13	LPM	Cerogne-Ciantiplagna	45.06944444	7.023611111	3.57	Agard et al. (2001a)	463	Beyssac et al. (2002)	>2.2
ALB1907	LPM	Albergian	44.95943333	6.986266667	3.47	This study	477	This study	2.1
ALB1920	LPM	Albergian	44.96246667	7.046266667	3.47	This study	451	This study	2
ALB2010	LPM	Albergian	44.92177778	6.965166667	3.64	This study	461	This study	>2.2
ARG2002	LPM	Albergian	44.89491667	6.913361111	3.41	This study	403	This study	1.8
ALB2004	LPM	Albergian	44.91558333	7.025694444	3.39	This study	482	This study	1.9-2
ALB2007	LPM	Albergian	44.88261111	7.038833333	3.48	This study	428	This study	2
Agard14	LPM	Albergian	44.98666667	6.955277778	3.49	Agard et al. (2001a)	454	This study	2.1
Agard15	LPM	Albergian	44.95444444	6.940833333	3.61	Agard et al. (2001a)	449	This study	>2.2
Agard16	LPM	Albergian	44.985	6.970555556	3.51	Agard et al. (2001a)	451	This study	2.1
Agard17	LPM	Albergian	44.96972222	7.02	3.61	Agard et al. (2001a)	491	This study	>2.3
JA2005a	LPM	Vin Vert	45.08183333	6.805361111	3.55	This study	413	This study	2.1
VV2004	LPM	Mirabouc-Bouchet	44.58263889	7.024583333	3.5	This study	412	This study	1.9-2
VV2008	LPM	Mirabouc-Bouchet	44.54622222	7.068583333	3.54	This study	420	This study	2.1
BF2001	LPM	Mirabouc-Bouchet	44.84980556	6.947166667	3.48	This study	421	This study	1.9-2
BF2009	LPM	Mirabouc-Bouchet	44.86328333	6.931369444	3.5	This study	400	This study	1.9-2
MO2003	LPM	Mirabouc-Bouchet	44.82980556	7.008944444	3.59	This study	418	This study	>2.1
VV2002	LPM	Mirabouc-Bouchet	44.61052778	7.05625	3.58	This study	467	This study	>2.2
VV2010	LPM	Mirabouc-Bouchet	44.63494444	7.014527778	3.54	This study	419	This study	2.1
VM2004	LPM	Mirabouc-Bouchet	44.51691667	7.056722222	3.46	This study	413	This study	1.9
VM2002	LPM	Mirabouc-Bouchet	44.47658333	7.042472222	3.52	This study	517	This study	>2.4
VSL1903	LPM	Mirabouc-Bouchet	44.6796	7.069316667	3.55	This study	464	This study	2.2-2.3
ALB2005a	LPL	Orsiera-Rocciavrè	44.90797222	7.059166667	3.47	This study	534	This study	>2.5
Agard18	LPL	Orsiera-Rocciavrè	45.0525	7.061388889	3.44	Agard et al. (2001a)	508	This study	2.2
Agard19	LPL	Orsiera-Rocciavrè	45.06583333	7.0525	3.67	Agard et al. (2001a)	503	Beyssac et al. (2002)	>2.5
DM19b-43	LPL	Lago Superiore	44.60888889	7.178611111	3.61	Bonnet et al. (in prep)	493	Schwartz et al. (2013)	>2.4

Annexe – 5

Supplementary material IV.1: Vein thickness.

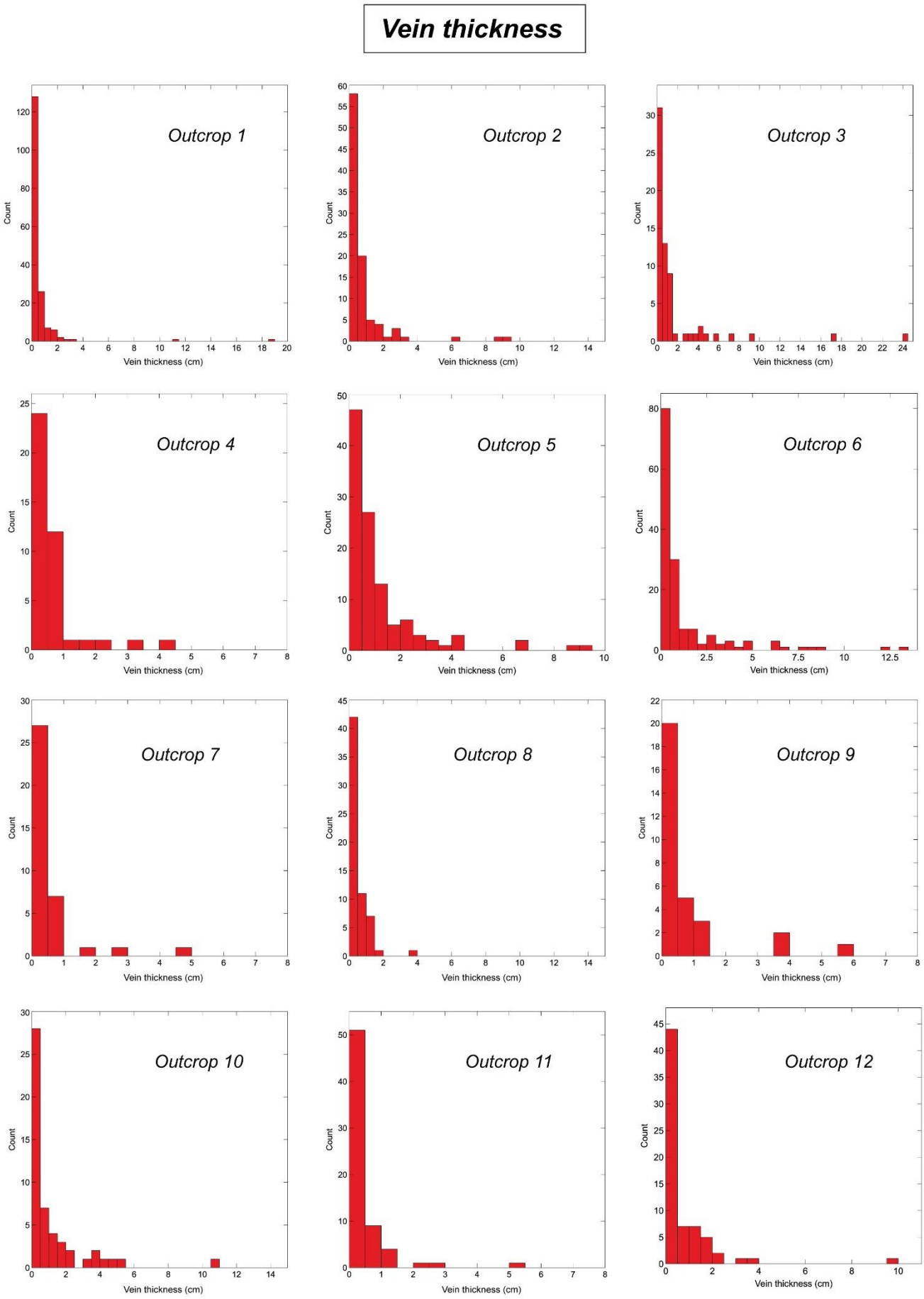

Vein spacing

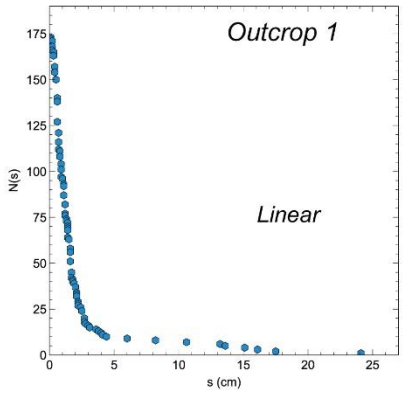

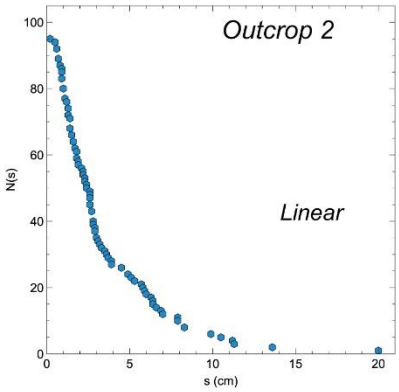

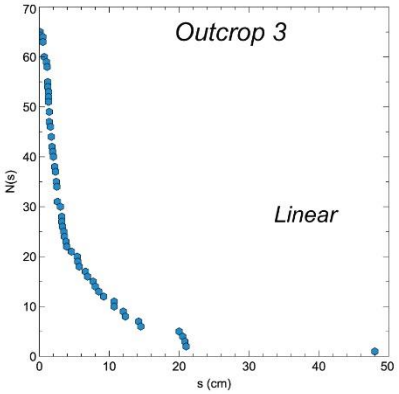

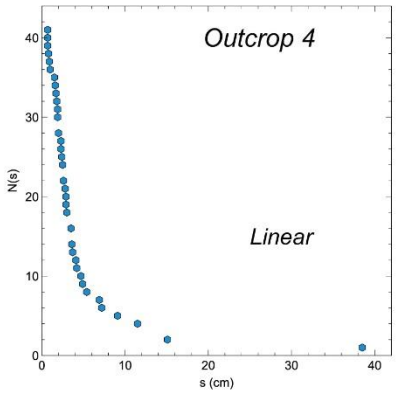

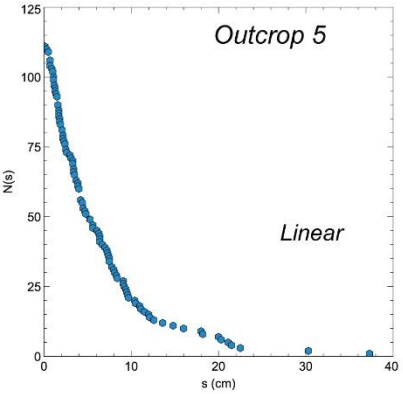

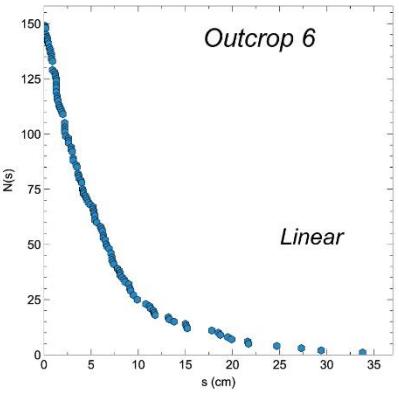

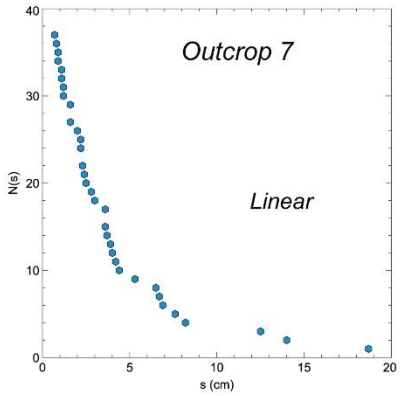

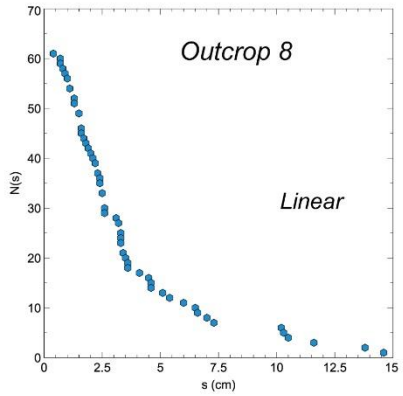

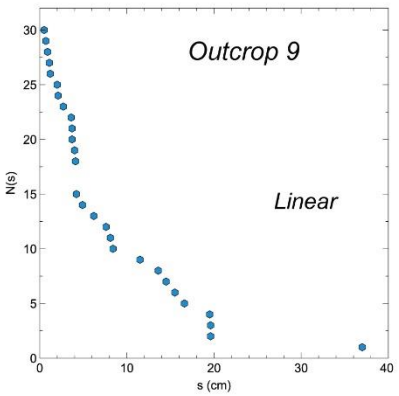

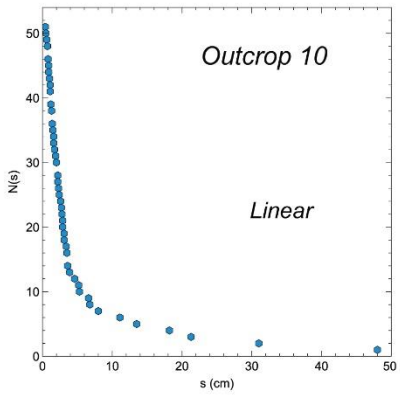

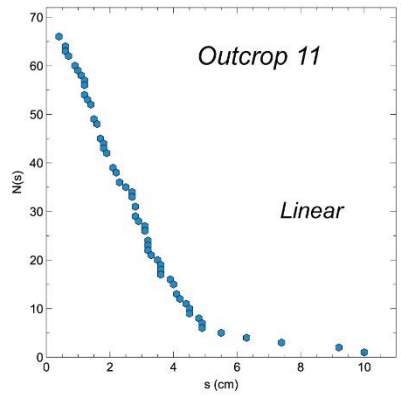

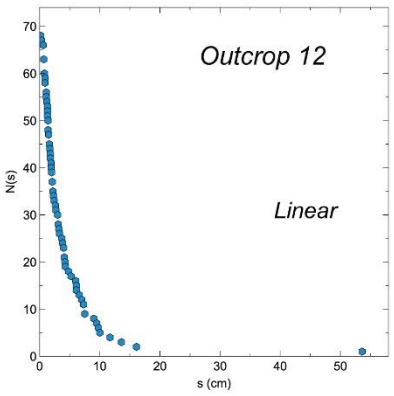

Vein thickness

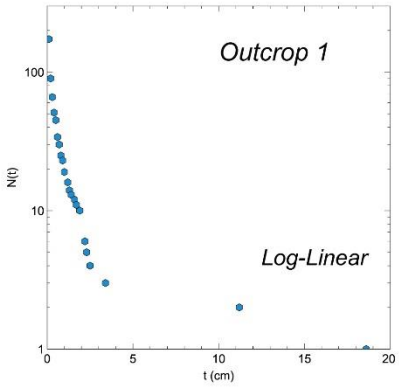

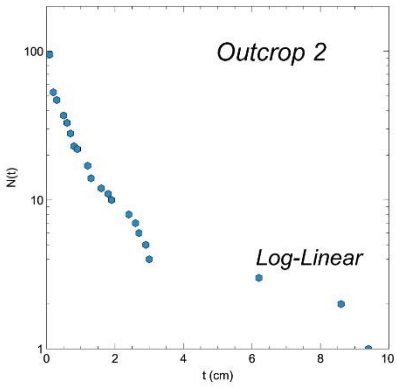

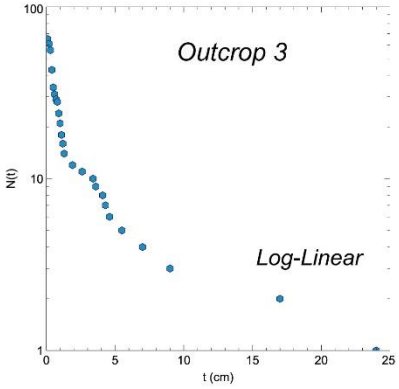

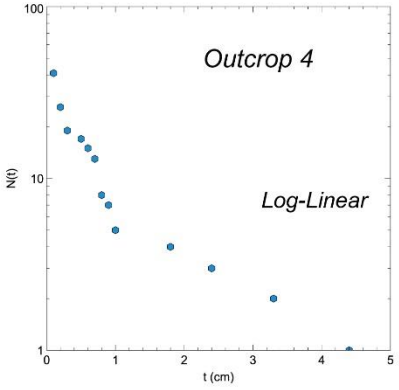

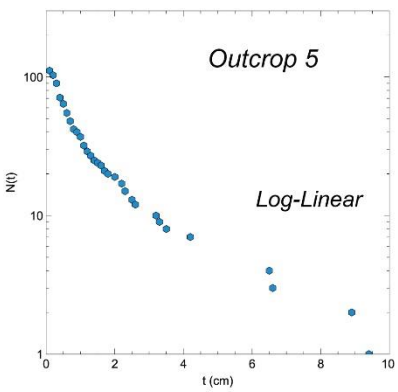

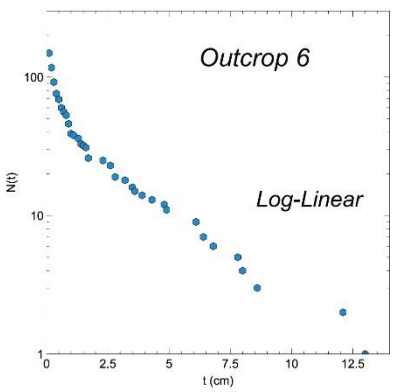

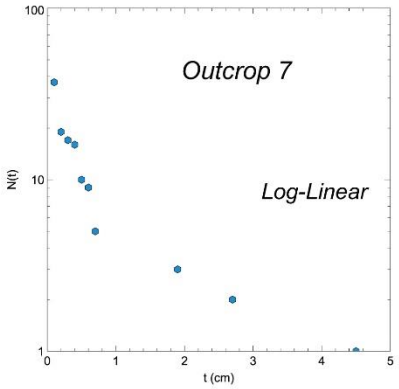

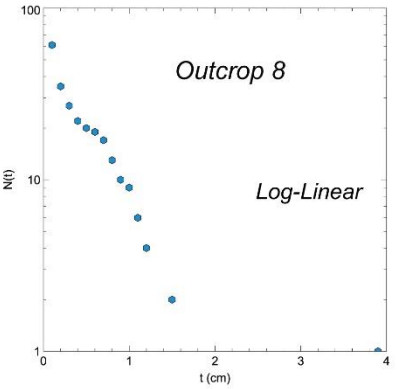

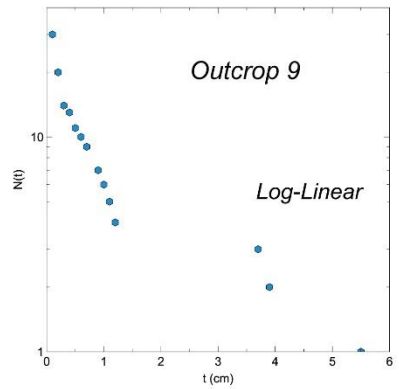

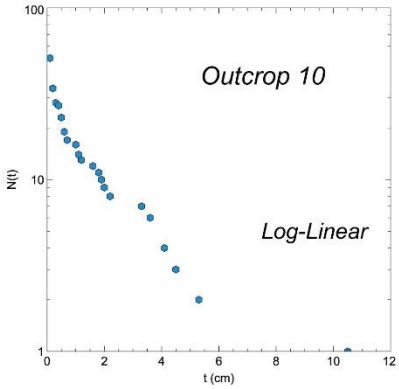

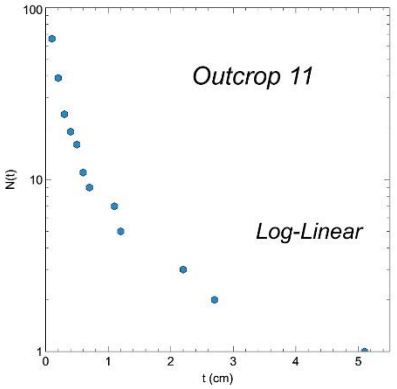

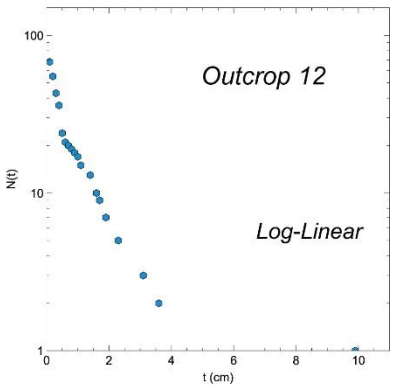

Vein thickness

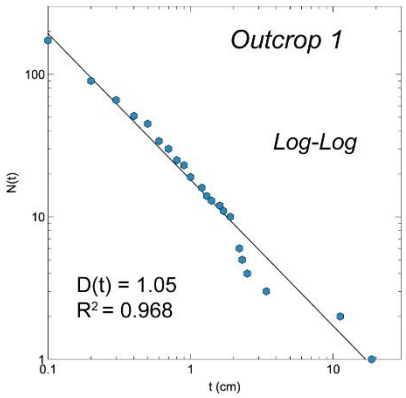

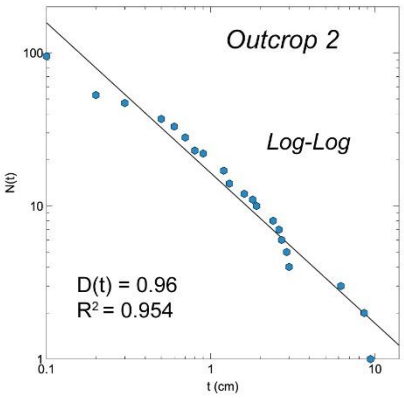

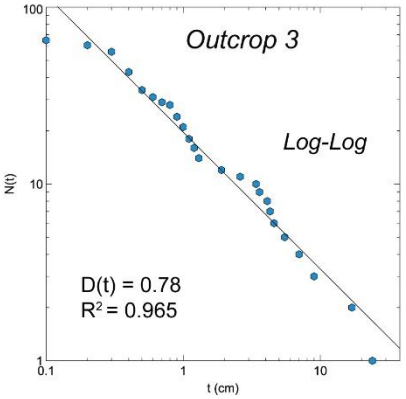

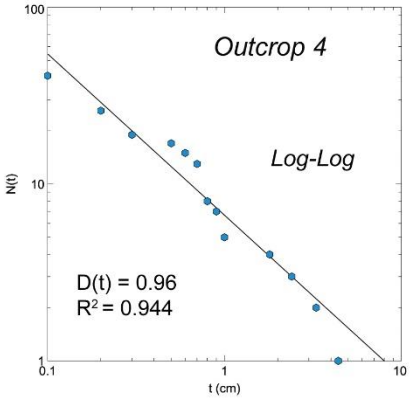

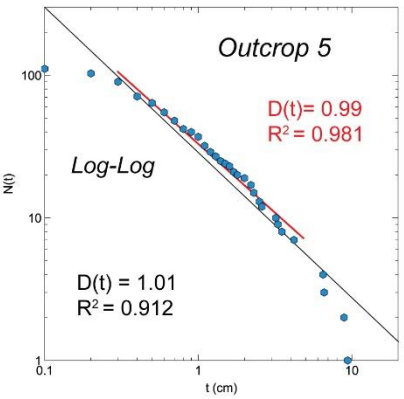

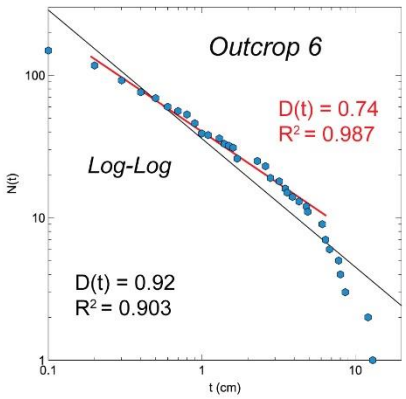

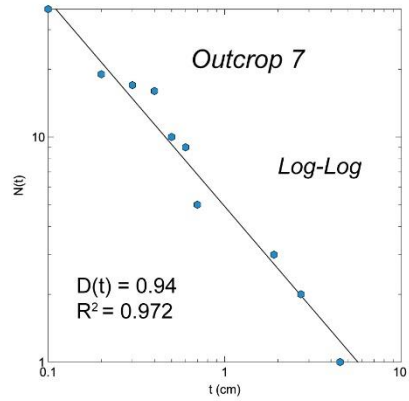

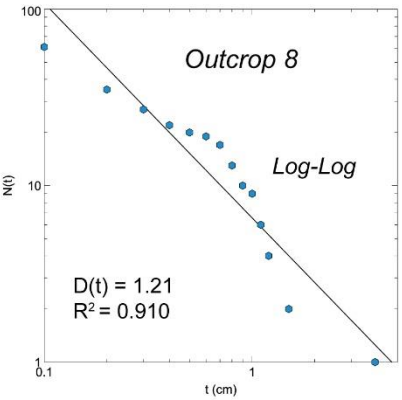

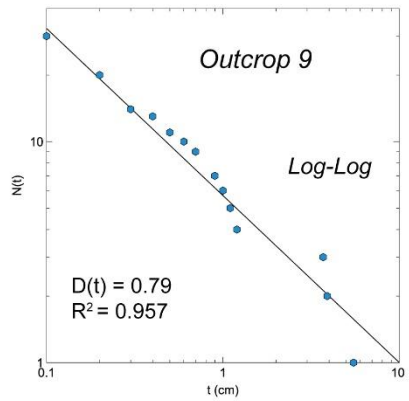

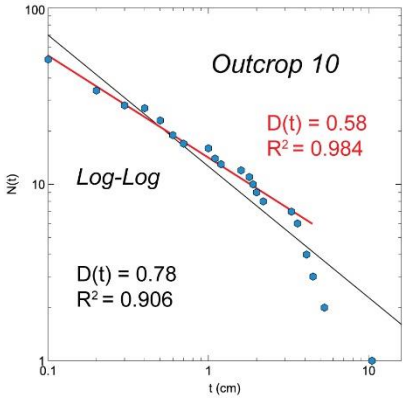

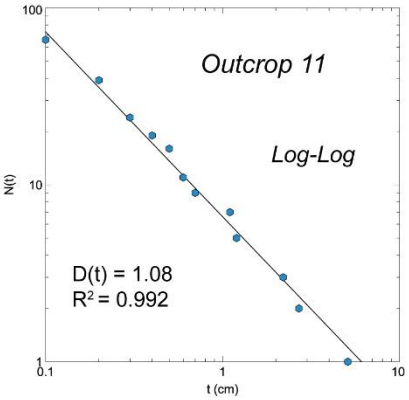

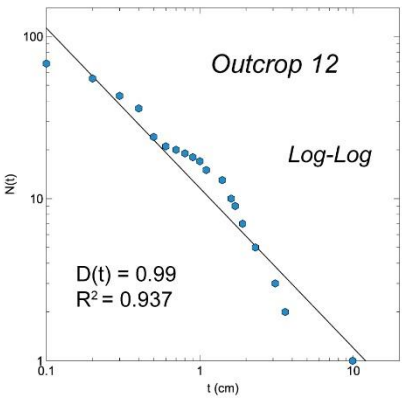

Vein thickness

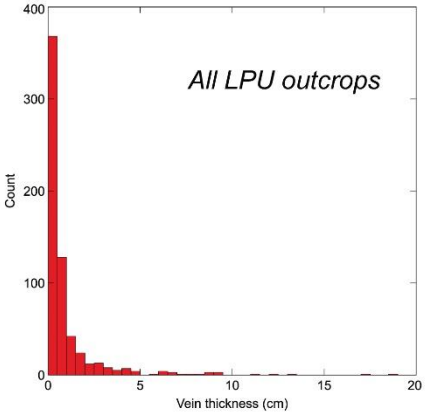

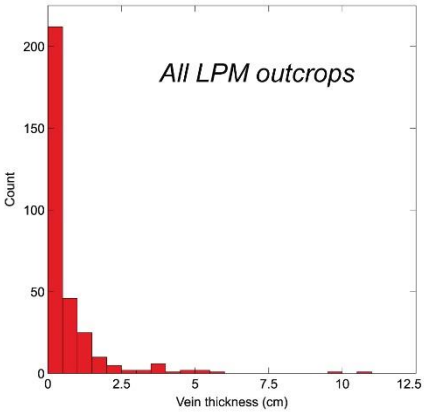

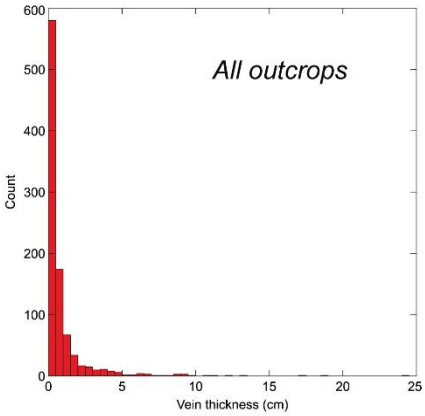

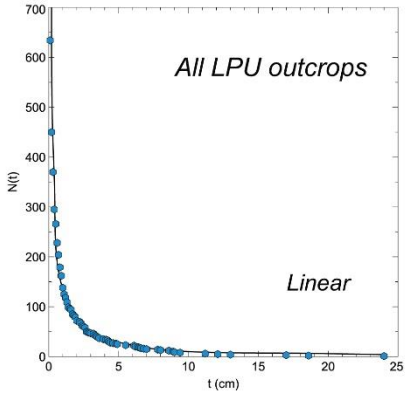

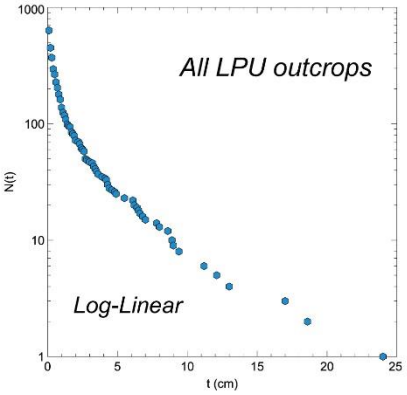

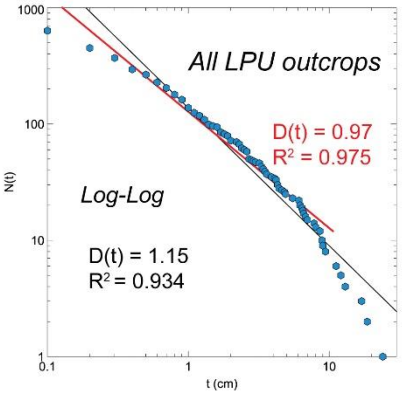

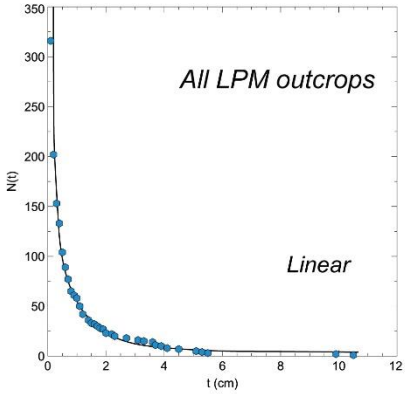

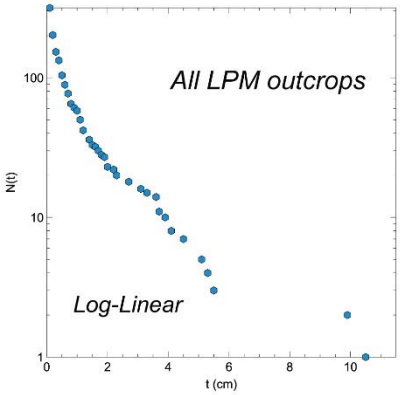

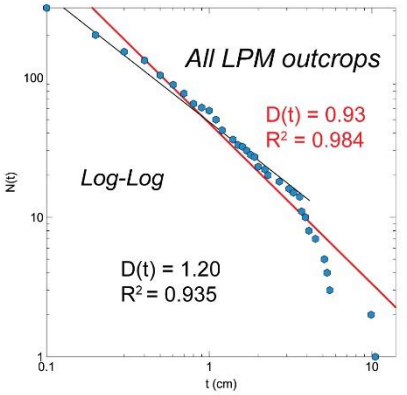

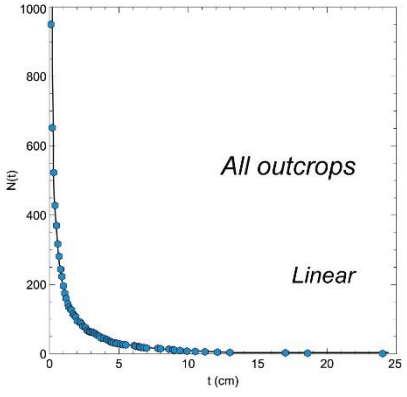

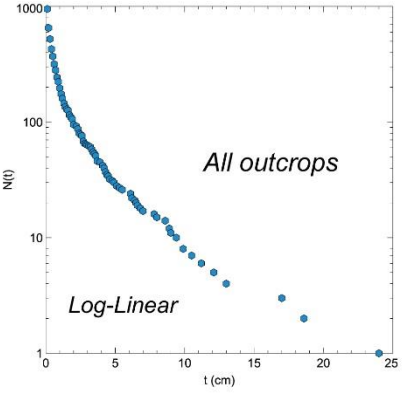

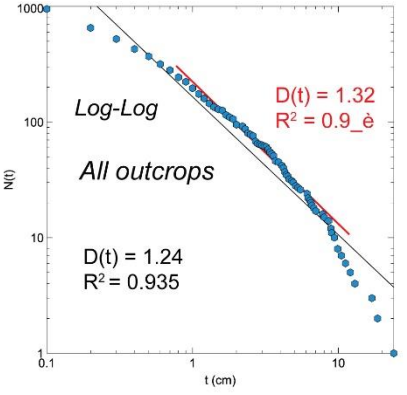

Supplementary material IV.2: Vein spacing.

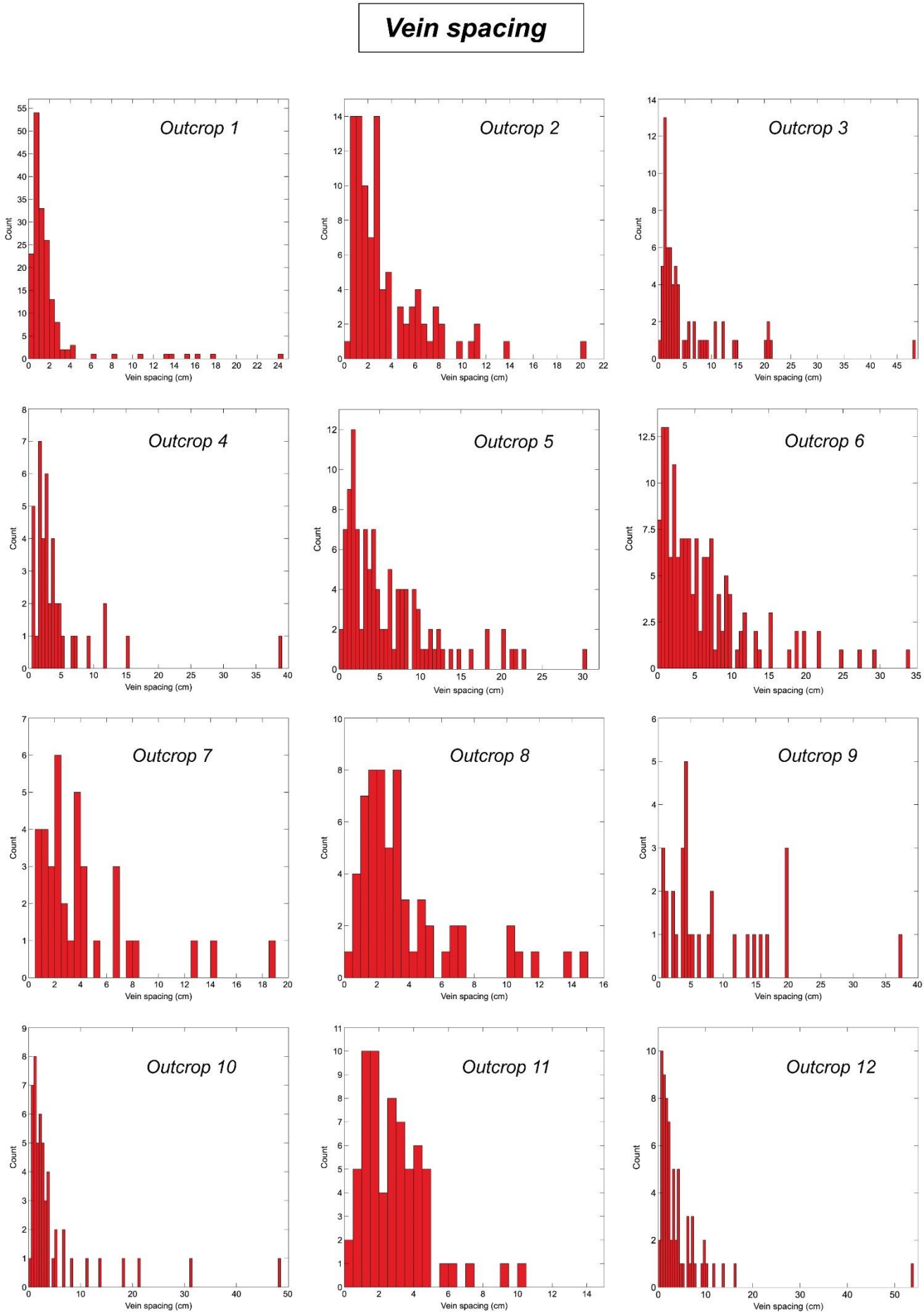

Vein spacing

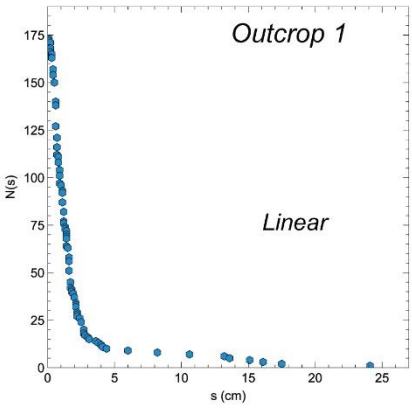

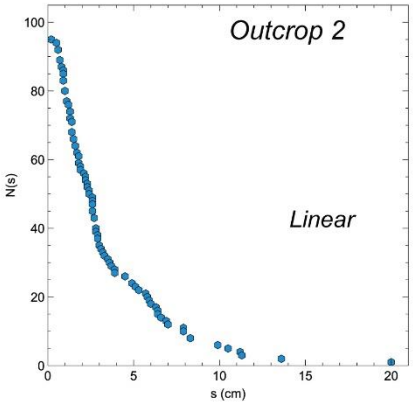

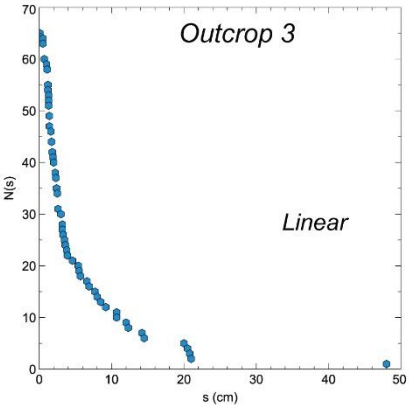

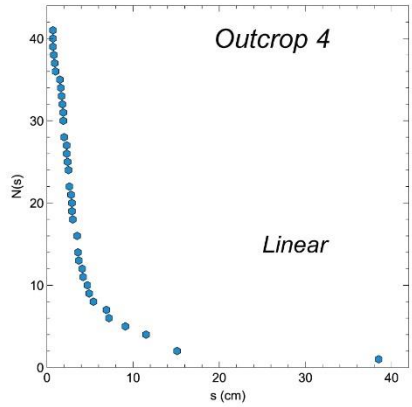

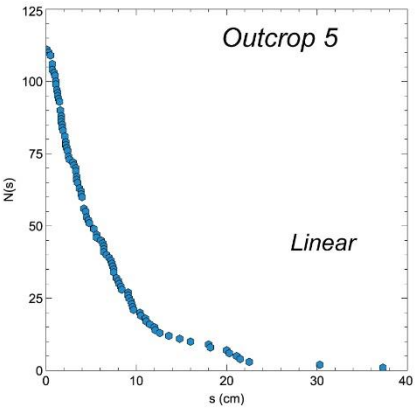

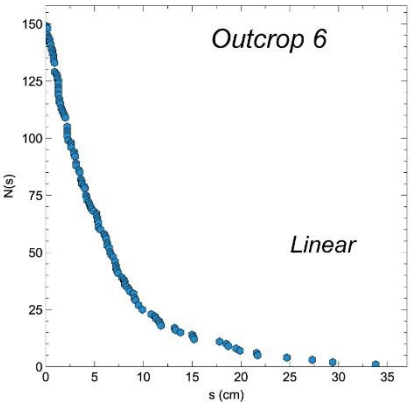

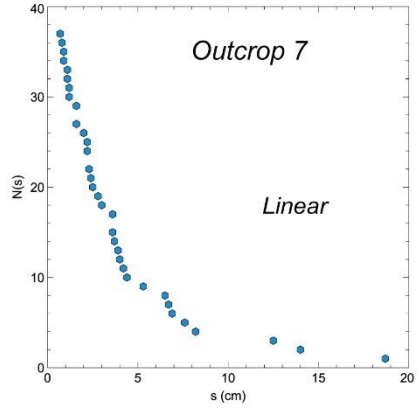

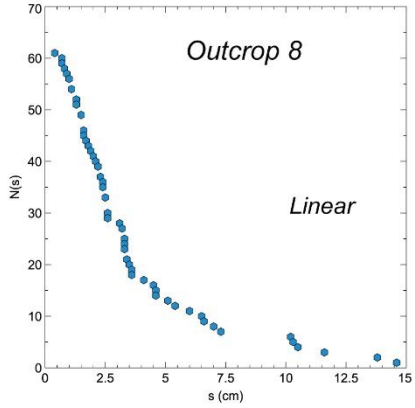

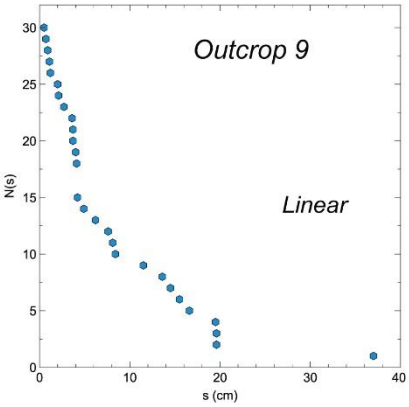

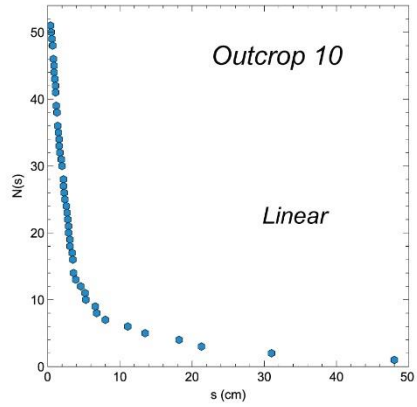

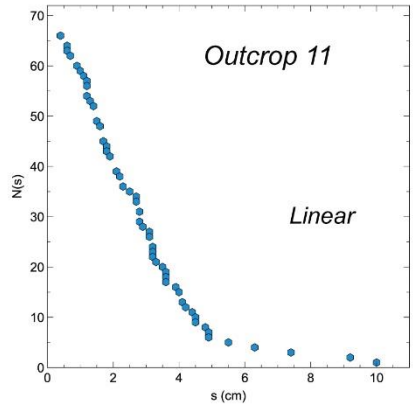

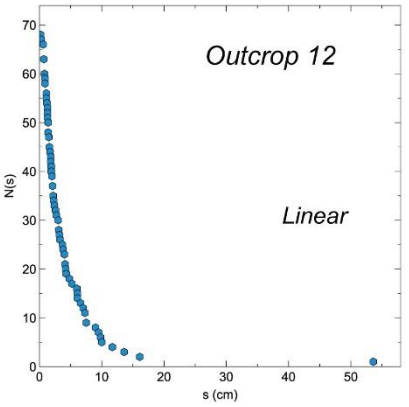

Vein spacing

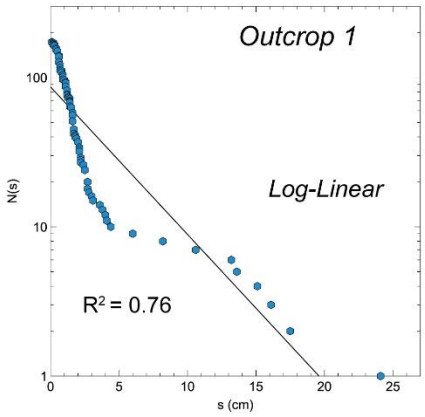

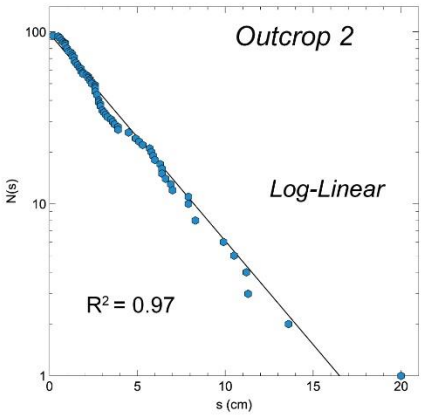

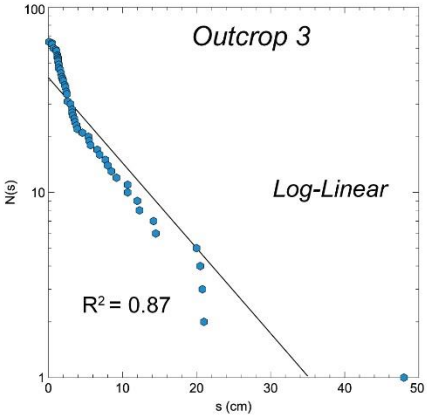

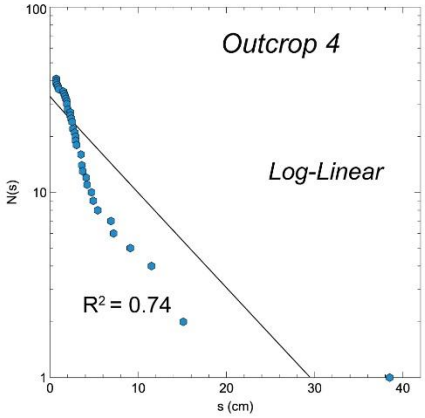

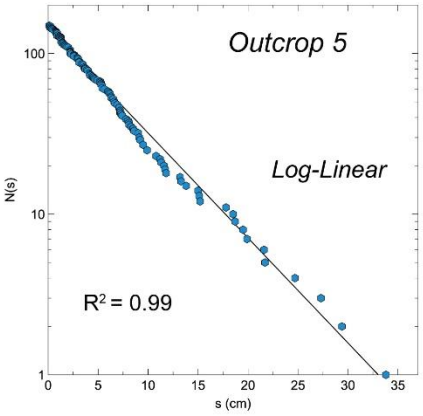

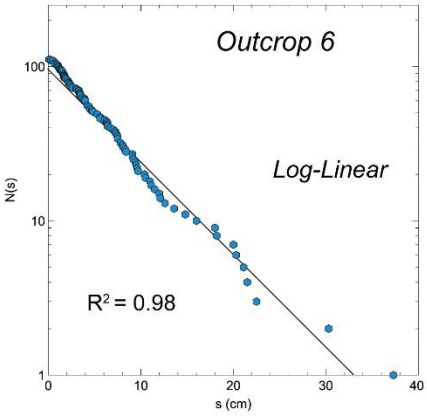

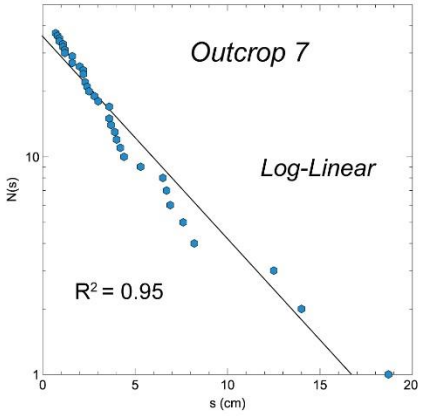

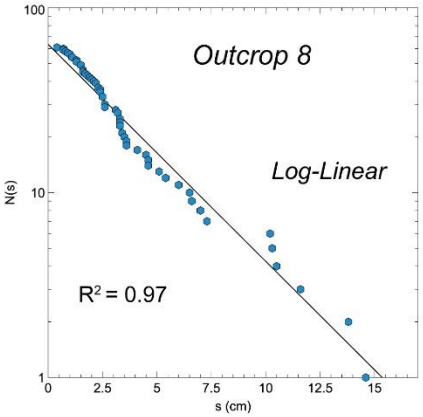

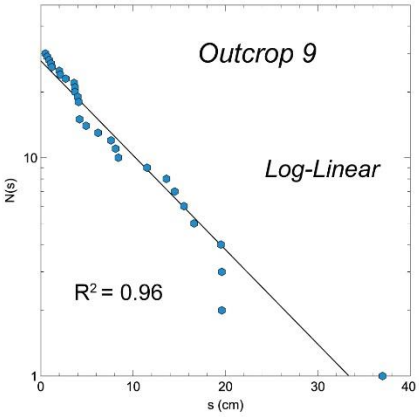

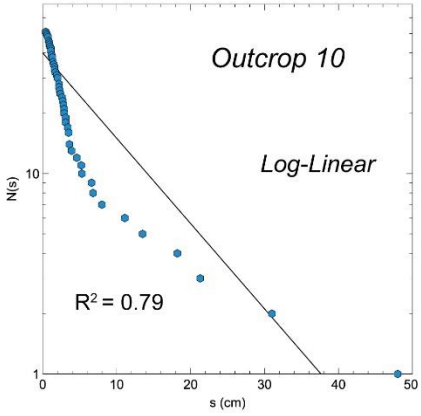

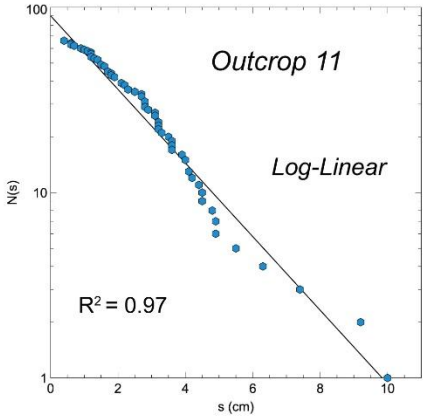

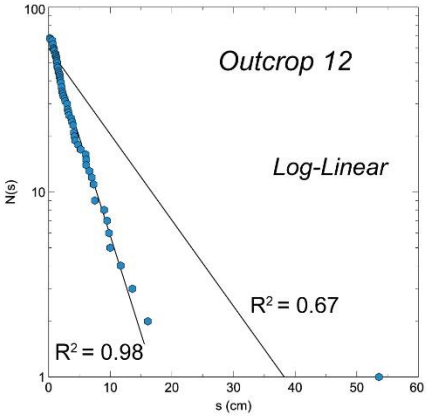

Vein spacing

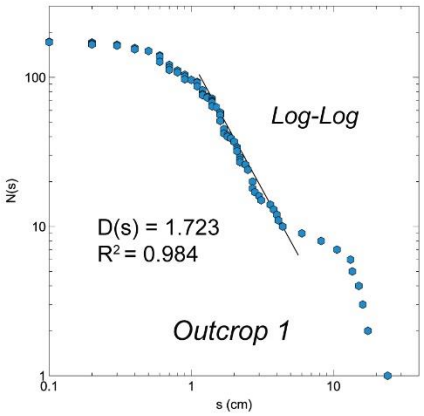

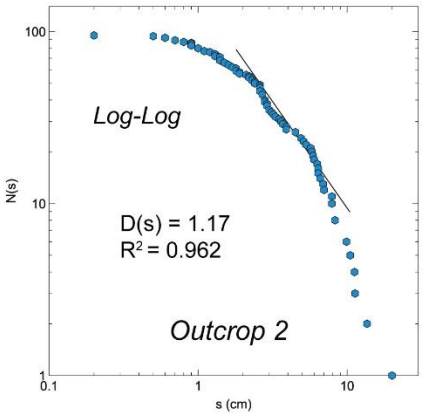

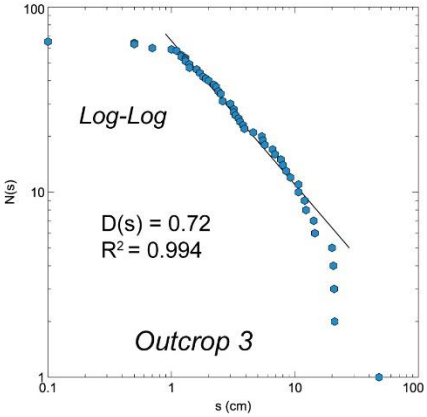

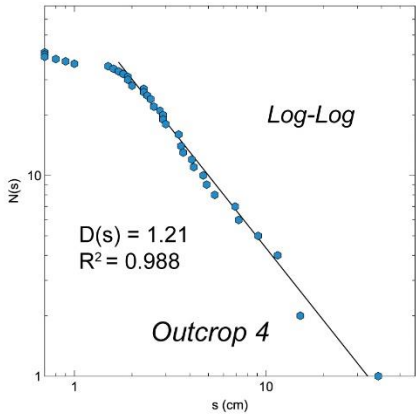

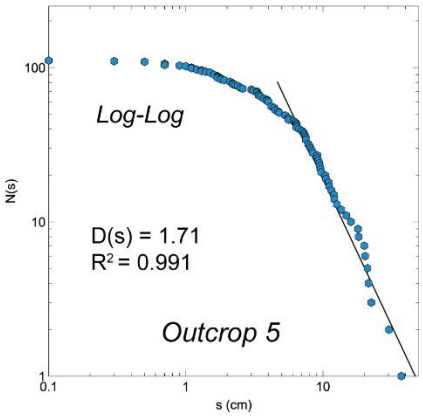

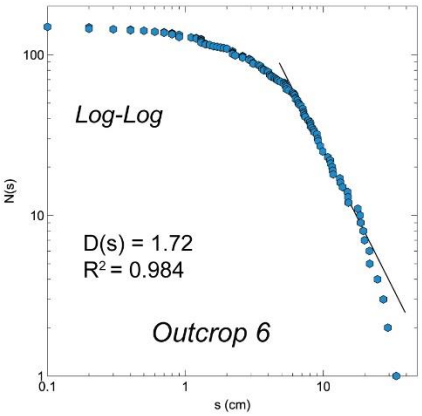

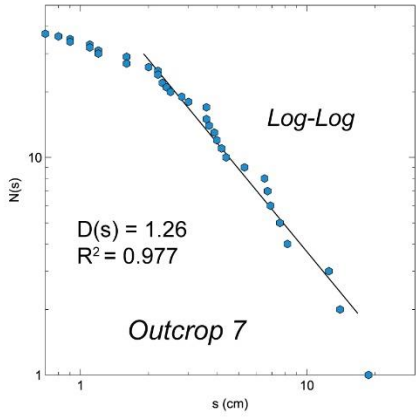

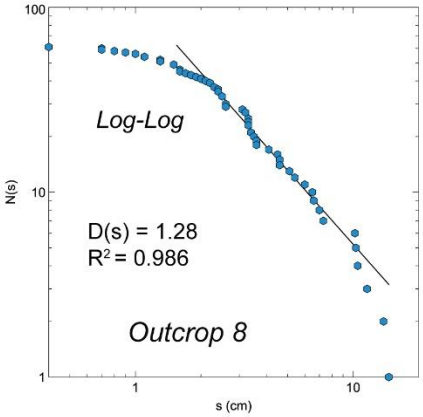

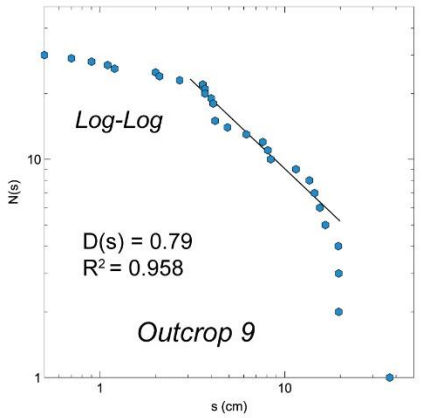

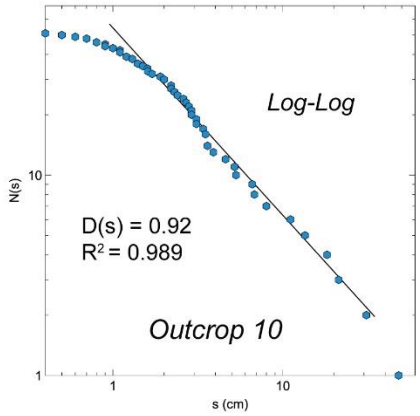

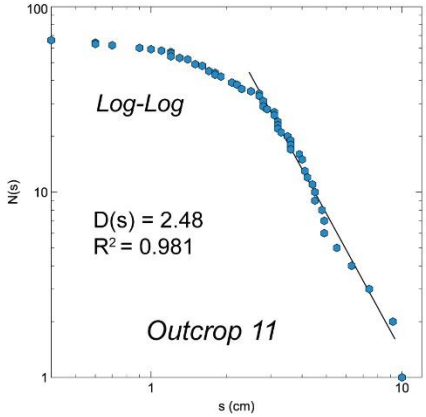

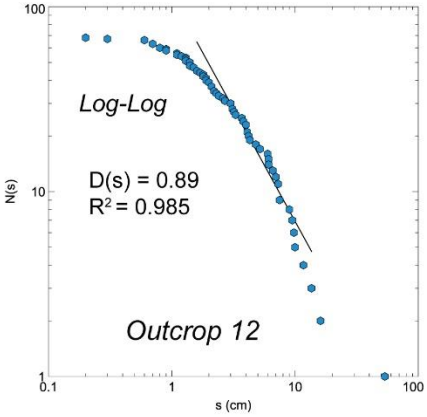

Vein spacing

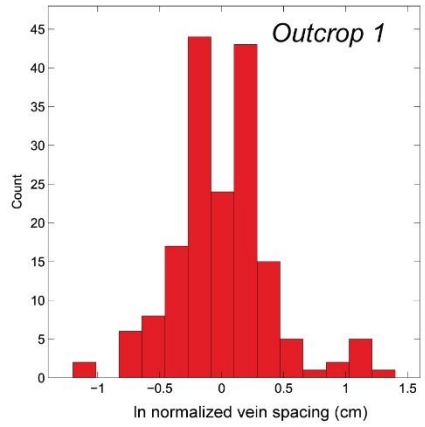

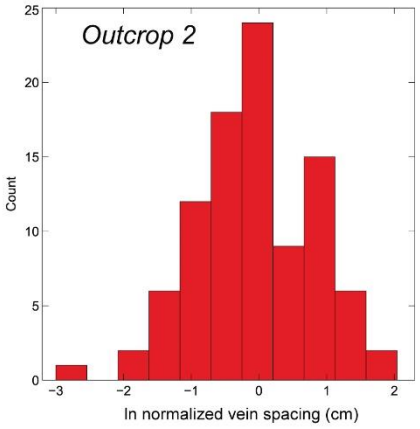

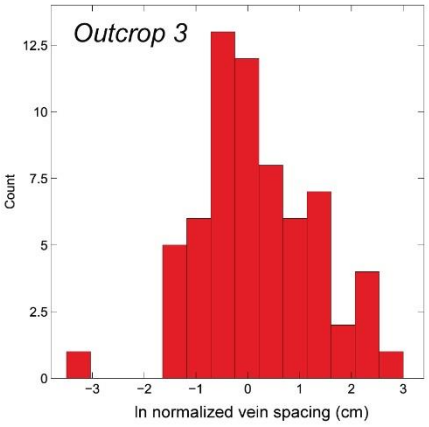

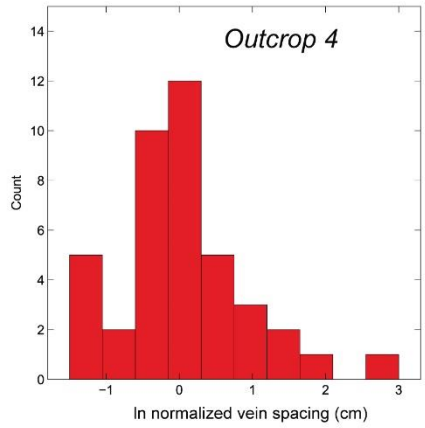

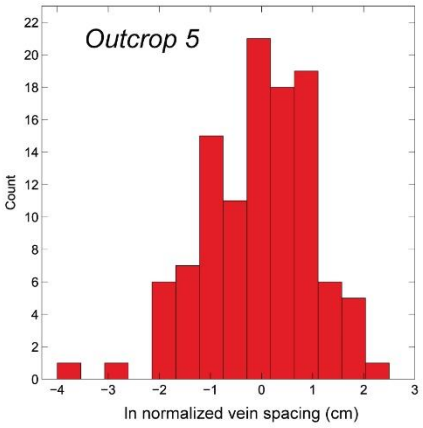

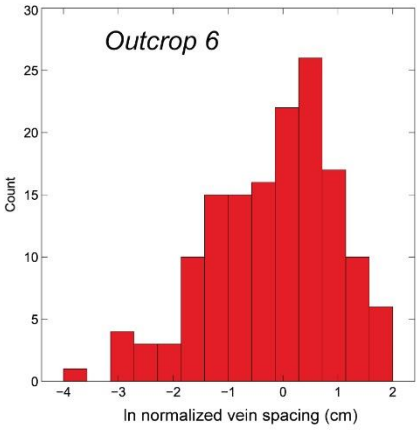

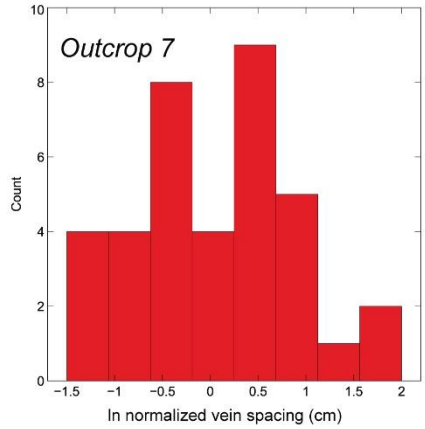

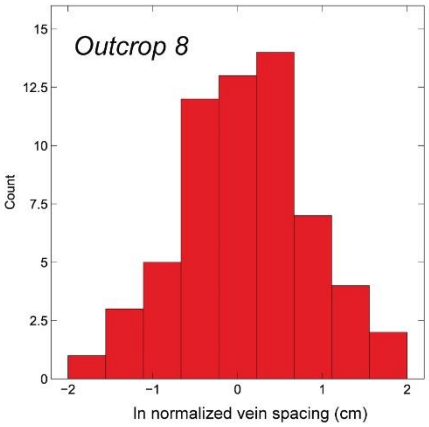

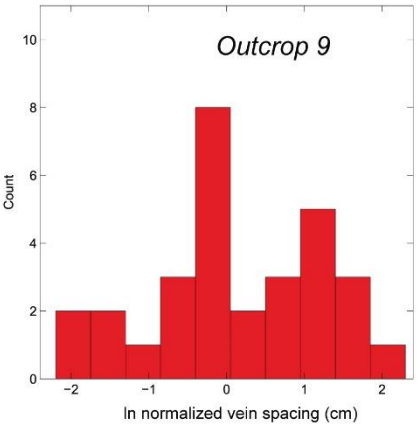

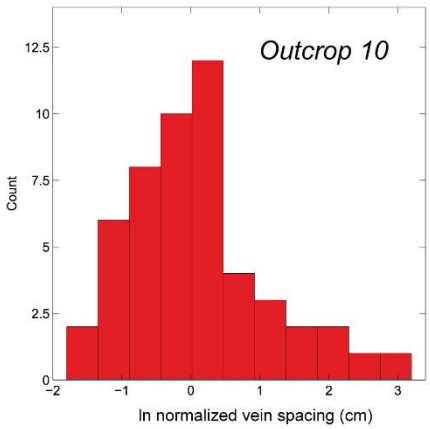

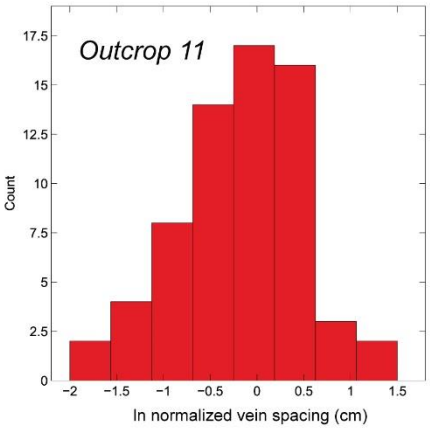

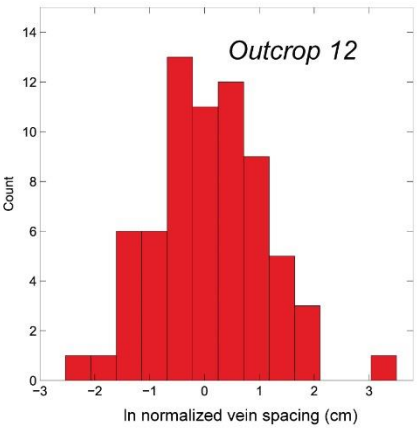

Vein spacing

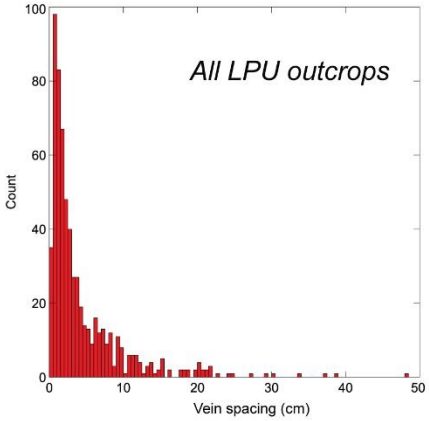

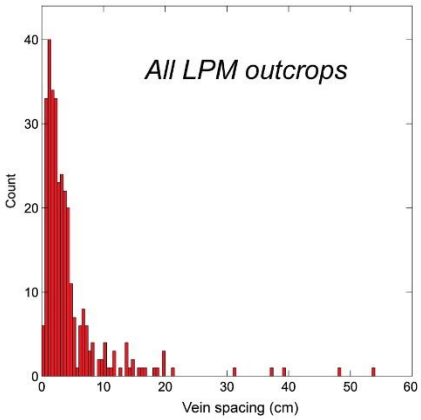

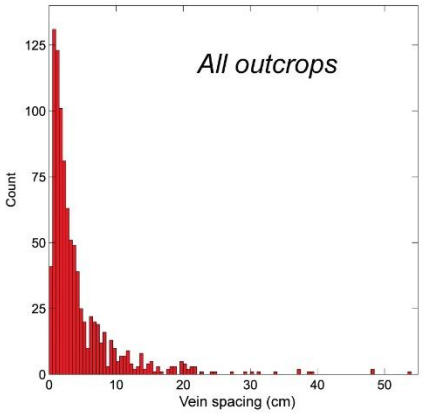

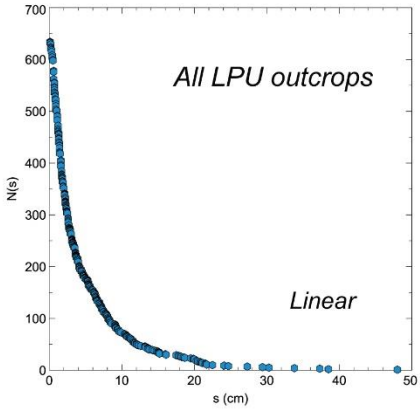

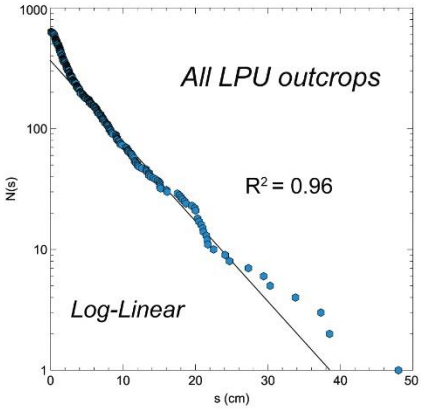

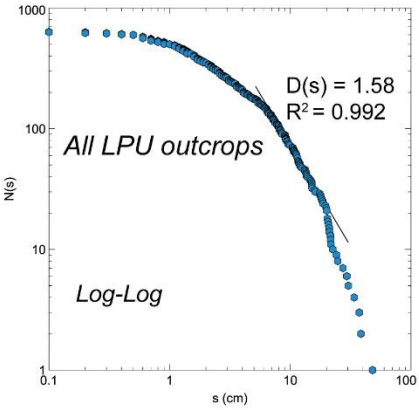

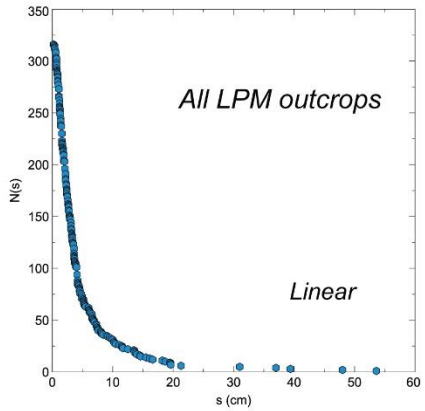

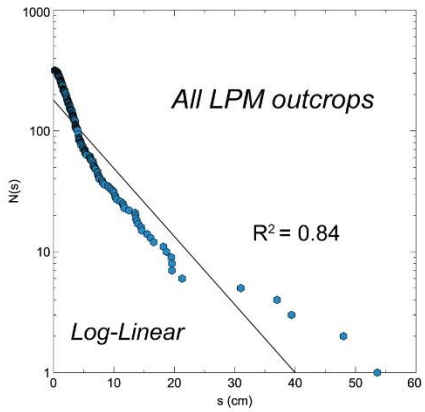

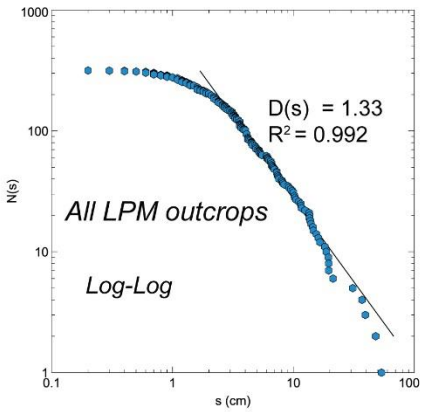

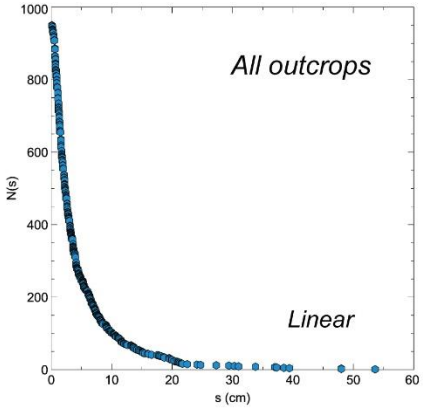

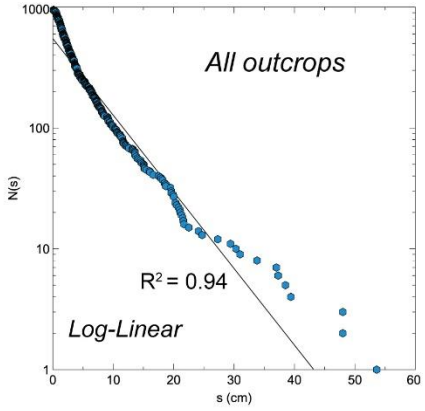

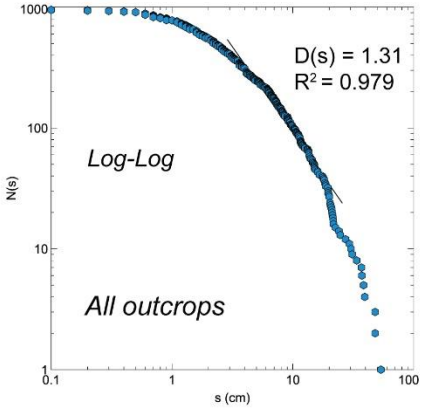

Vein spacing

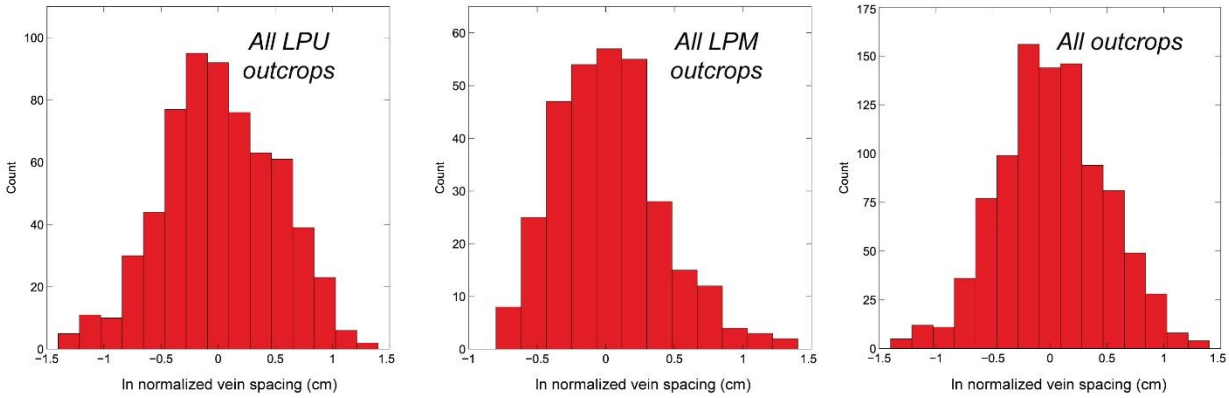

Supplementary material IV.3: Vein clustering.

Vein clustering

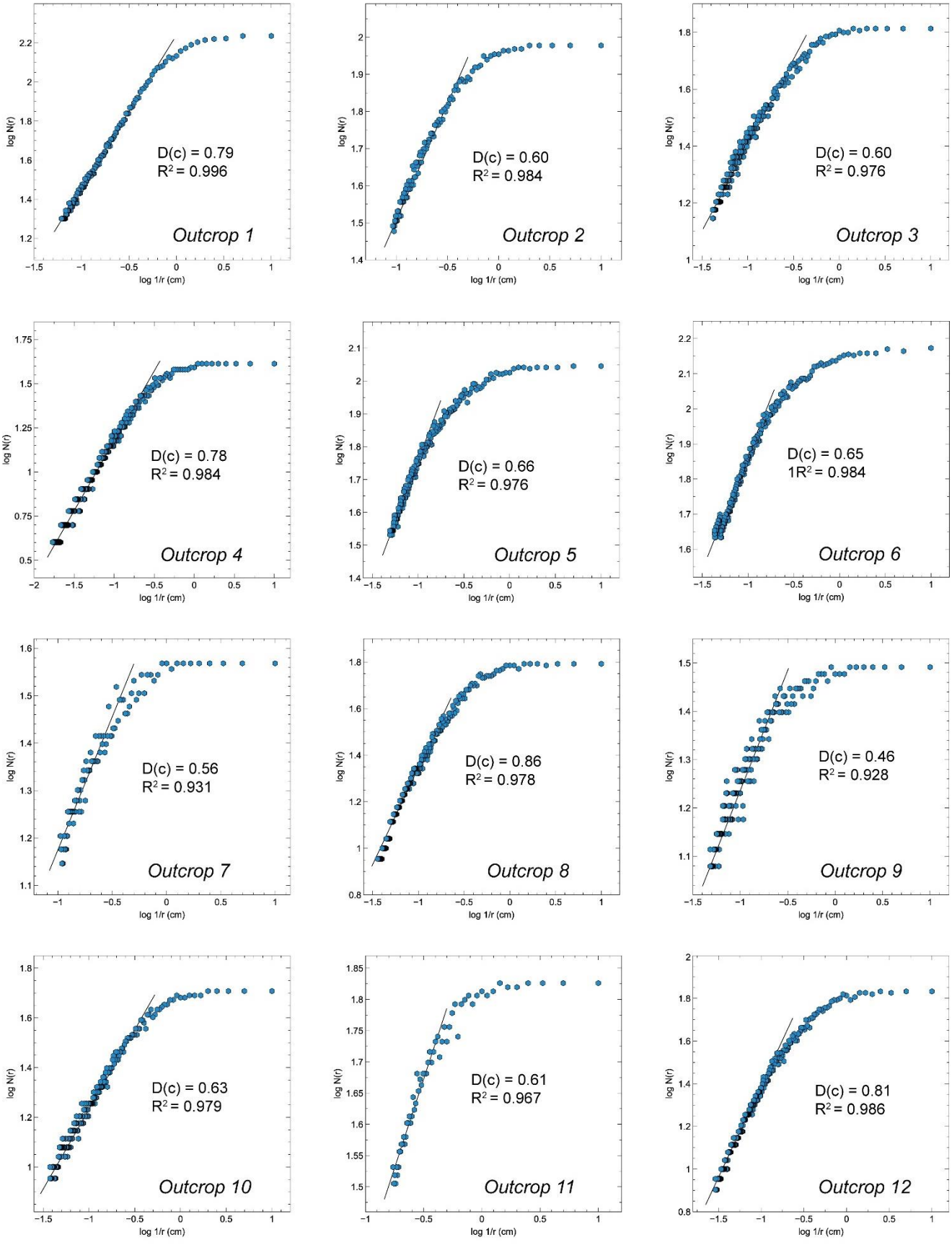

Supplementary material IV.4: Inclusion spacing.

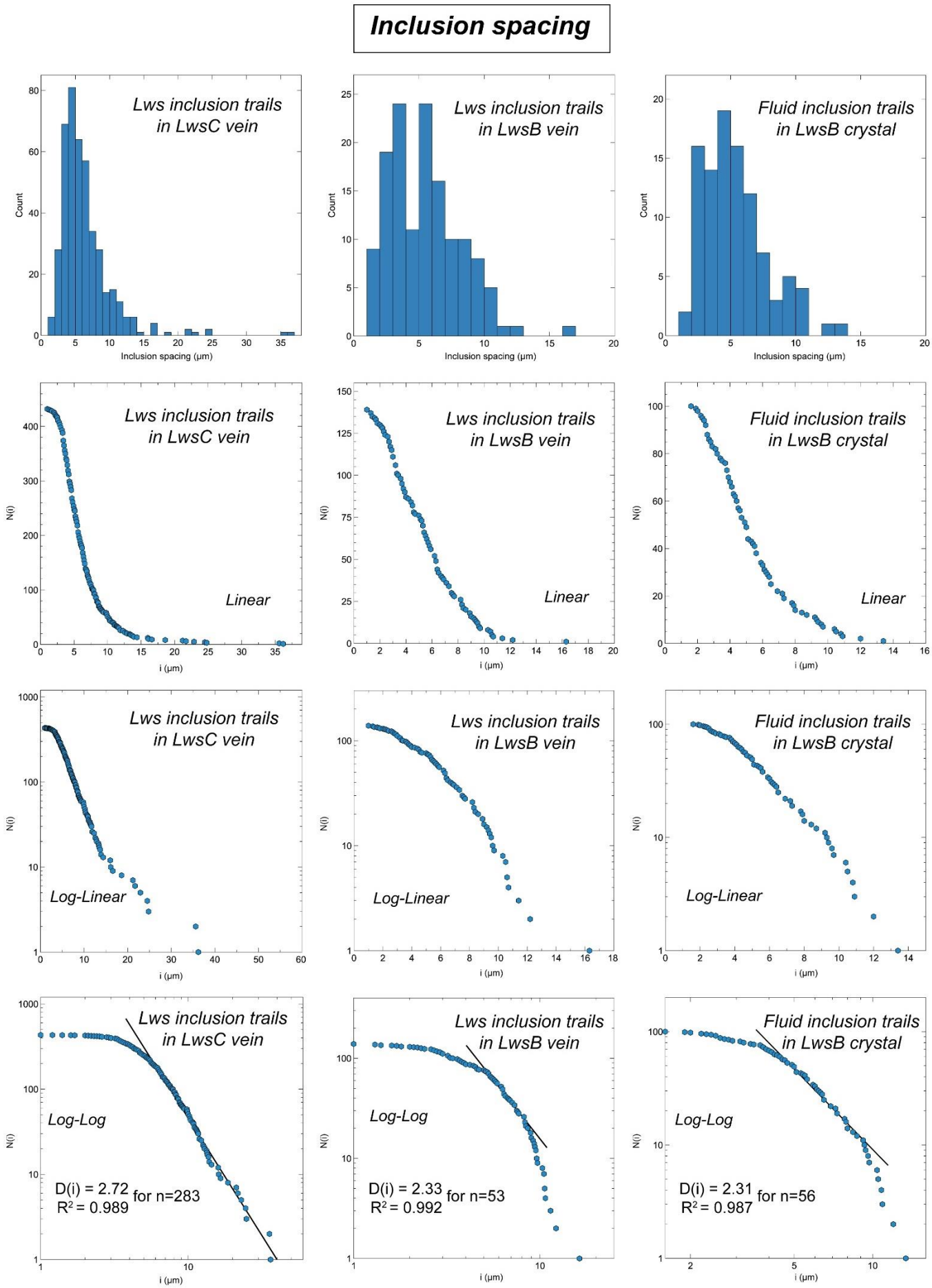

Inclusion spacing

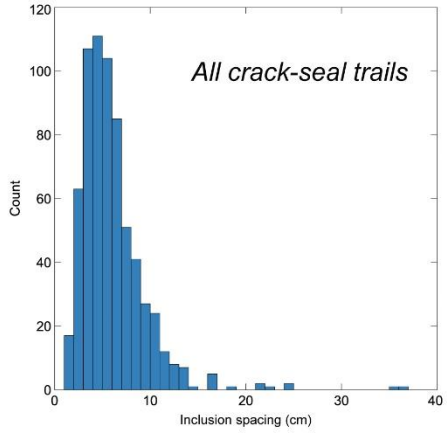

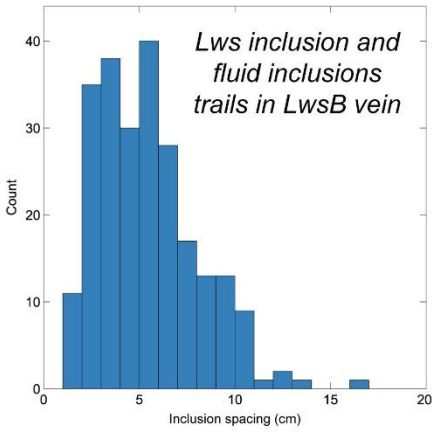

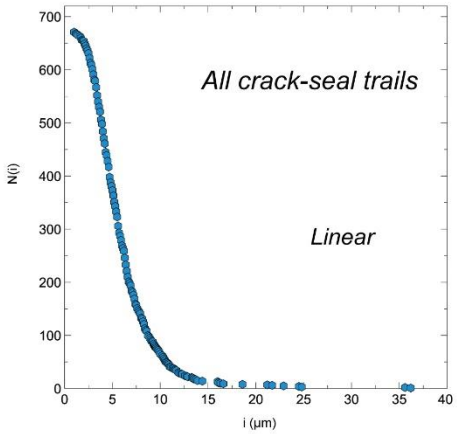

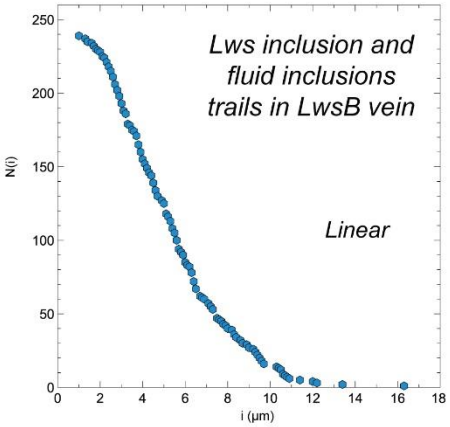

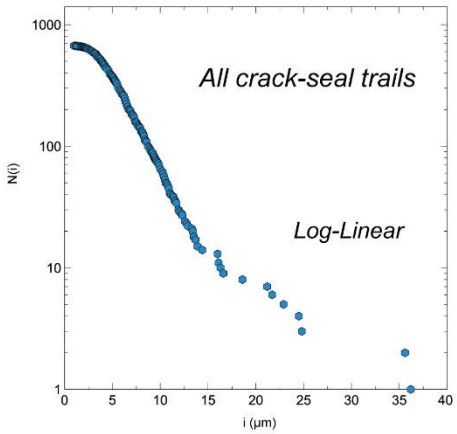

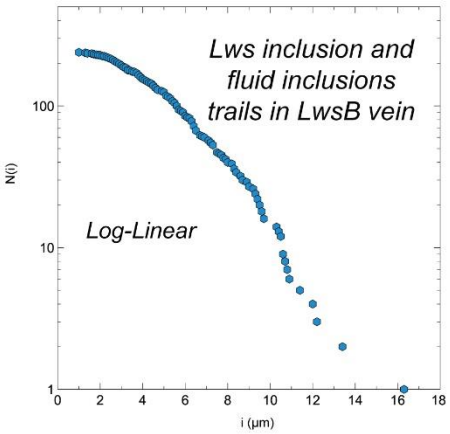

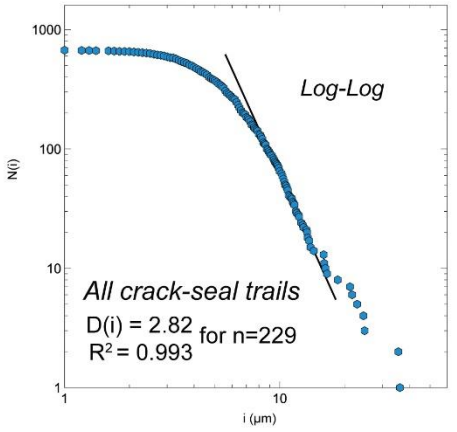

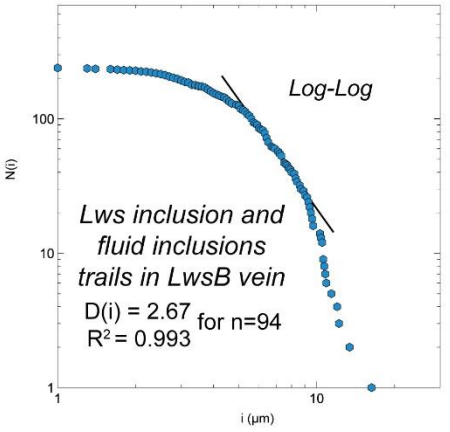

Annexe – 6

Supplementary material V.1: Representative mineral analyses.

	Chlorite	Chlorite	Chlorite	Talc	Talc	Talc	Dolomite	Dolomite	Dolomite
Sample	PS1802	BB1901	SL1907	PS1802	SL1809	BB1901	PS1802	SL1807	SL1809
SiO_2	29.8	28.53	29.22	61.59	61.94	61.32	0.01	0.09	0.01
TiO_2	0.02	0.01	0.03	0.01	0.02	0.03	0.01	0.02	0.05
Al_2O_3	16.2	16.97	15.14	0.02	0.00	0.04	0.00	0.00	0.01
Cr_2O_3	2.35	2.16	5.17	0.10	0.02	0.02	0.01	0.00	0.06
FeO	11.3	11.15	10.14	4.71	4.65	3.82	4.99	4.77	5.10
MnO	0.06	0.09	0.00	0.03	0.04	0.02	0.21	0.30	0.60
MgO	26.1	25.11	25.54	27.76	27.25	27.71	19.93	19.68	19.13
CaO	0.01	0.05	0.02	0.04	0.05	0.01	31.65	31.52	31.29
Na_2O	0.04	0.01	0.01	0.05	0.00	0.03	0.06	0.03	0.01
K2O	0.01	0.01	0.02	0.03	0.00	0.02	0.02	0.01	0.00
Total	86.0	84.10	85.27	94.34	93.99	93.02	56.89	56.42	56.25
Si	2.99	2.93	2.97	4.01	4.04	4.03	0.00	0.01	0.00
Ti	0.00	0.00	0.00	0.00	0.00	0.00	0.00	0.00	0.00
Al	1.92	2.05	1.81	0.00	0.00	0.00	0.00	0.00	0.00
Cr	0.19	0.18	0.41	0.00	0.00	0.00	0.00	0.00	0.00
Fe	0.95	0.96	0.86	0.26	0.25	0.21	0.37	0.35	0.38
Mn	0.01	0.01	0.00	0.00	0.00	0.00	0.02	0.02	0.05
Mg	3.90	3.84	3.86	2.70	2.65	2.71	2.62	2.60	2.55
Ca	0.00	0.01	0.00	0.00	0.00	0.00	2.99	3.00	3.00
Na	0.01	0.00	0.00	0.01	0.00	0.00	0.01	0.00	0.00
K	0.00	0.00	0.00	0.00	0.00	0.00	0.00	0.00	0.00
XMg	0.80	0.80	0.82	0.91	0.91	0.93	0.88	0.88	0.87